

STRUCTURAL BEHAVIOR AND DURABILITY OF MULTIFUNCTIONAL FIBER-REINFORCED POLYMER COMPONENTS

THÈSE N° 3695 (2006)

PRÉSENTÉE LE 21 DÉCEMBRE 2006

À LA FACULTÉ DE L'ENVIRONNEMENT NATUREL, ARCHITECTURAL ET CONSTRUIT

Laboratoire de construction en composites

PROGRAMME DOCTORAL EN STRUCTURES

ÉCOLE POLYTECHNIQUE FÉDÉRALE DE LAUSANNE

POUR L'OBTENTION DU GRADE DE DOCTEUR ÈS SCIENCES

PAR

Florian RIEBEL

Dipl.-Ing., Technische Universität Darmstadt, Allemagne
et de nationalité allemande

acceptée sur proposition du jury:

Prof. E. Brühwiler, président du jury

Prof. T. Keller, directeur de thèse

Prof. P. Hamelin, rapporteur

Prof. J. Lesko, rapporteur

Prof. I. Smith, rapporteur



ÉCOLE POLYTECHNIQUE
FÉDÉRALE DE LAUSANNE

Suisse
2006

Contents

Summary	v
Résumé	vii
Zusammenfassung	ix
Acknowledgments	xi
1. Introduction	1
1.1. Motivation	1
1.2. Multifunctional insulating joint	2
1.3. Objectives	3
1.4. Methodology	4
1.5. Composition of the work	4
2. The state of the art	7
2.1. Introduction	7
2.2. Use of FRP reinforcement in concrete structures	7
2.3. Diffusion into solids	9
2.3.1. General aspects	9
2.3.2. Diffusion into FRPs	10
2.3.3. Mathematical approaches	13
2.4. Degradation of GFRP	16
2.4.1. Degradation of glass fibers	16
2.4.2. Matrix	23
2.4.3. Fiber-matrix interface	28
2.4.4. Composite system degradation	32
2.5. Lifetime predictions	35
2.5.1. Introduction	35
2.5.2. Arrhenius-type prediction	35
2.5.3. Prediction studies	37
2.6. Conclusions	43
3. Multifunctional GFRP elements	45
3.1. Introduction	45
3.2. Description of the CS-element	45
3.3. Mechanical properties of unconditioned CS-elements	47
3.4. Mechanical properties of conditioned CS-elements	50
3.4.1. Experimental procedure	50
3.4.2. Experimental results	52

3.5. Gravimetric studies on the CS-element	55
3.5.1. Experimental procedure	56
3.5.2. Modeling of moisture uptake	57
3.5.3. Results of measurements and modeling	58
3.6. Scanning electron microscope (SEM) investigations on CS-element	63
3.6.1. Experimental procedure	63
3.6.2. Experimental results	65
3.7. Energy dispersive X-ray spectroscopy (EDX)	68
3.7.1. Experimental procedure	68
3.7.2. Experimental results	69
3.8. Discussion of experimental results	70
3.8.1. Alteration of mechanical properties of CS-element	71
3.8.2. Diffusion behavior	71
3.8.3. Microscopic investigations	72
3.8.4. Atomic ion distribution	73
3.8.5. Conclusions	73
3.9. Description of the TS-element	74
4. Experimental investigation of beams with multifunctional insulating and load-bearing joints	77
4.1. Beams with hybrid GFRP/steel insulating joint	77
4.1.1. Introduction	77
4.1.2. Experimental program and set-up	77
4.1.3. Experimental specimens	79
4.1.4. Materials	79
4.1.5. Instrumentation	80
4.1.6. Experimental results	80
4.1.7. Discussion	86
4.1.8. System deformations	92
4.1.9. Conclusions concerning the hybrid steel/GFRP joint	94
4.2. Beams with all-GFRP insulating joint	94
4.2.1. Introduction	94
4.2.2. Experimental program and set-up	95
4.2.3. Experimental specimens	95
4.2.4. Instrumentation	97
4.2.5. Results	97
4.2.6. Discussion	103
4.2.7. Conclusions concerning the all-GFRP joint	109
5. Strength and stiffness prediction for GFRP compression/shear elements	111
5.1. Introduction	111
5.2. Element strength and stiffness requirements after 70 years of service	111
5.3. Strength and stiffness prediction for conditioned CS-elements	112
5.4. Strength estimation in a real concrete environment	121
5.5. Conclusions concerning strength prediction	122

6. Conclusions and future research	125
6.1. Investigations of multifunctional joints	125
6.2. Durability and lifetime prediction	125
6.3. Contribution to the state of the art	126
6.4. Proposals for future work	127
7. List of symbols	129
Bibliography	131
List of Figures	141
List of Tables	151
Curriculum Vitæ	153
<i>Appendices on CD-ROM</i>	
A. Temperature measurement during conditioning	155
B. Compression/shear element – structural behavior	157
B.1. Load-displacement curves of unconditioned elements	157
B.2. Influence of cap-plate thickness and creep	162
B.3. Experimental overview and results	164
B.4. Hairline cracks on element surface	166
B.4.1. Load displacement curves of conditioned elements	167
B.5. Failure Modes	198
B.5.1. Unconditioned elements	198
B.5.2. Conditioned elements	202
C. Gravimetric study	209
C.1. Sealing performance	209
D. Microscopic study	211
D.1. Damage progression by microscopic series	211
D.2. Damage after 800 days exposure at 20°C	216
E. EDX results	217
E.1. Results of EDX material analysis	217
F. Investigations on hybrid joint	219
F.1. Experimental set-up	219
F.2. Calculation of principal stress angle	222
F.3. Load-displacement curves	223
F.3.1. Vertical Displacements	223
F.3.2. Horizontal Displacements	231
F.4. Displacement and deformation patterns	238
F.5. Crack formation on supported beam section	242

E6. Axial strain on steel reinforcement and CS-element	247
E7. Strain on CS-element surfaces	253
E8. Failure modes of hybrid beam	262
E8.1. Concrete Failure at Bottom Side	262
E8.2. Detailed View of Compression Element	270
E9. Second principal stress angle on CS-element	275
G. Investigations on all-FRP joint	285
G.1. Experimental set-up	285
G.2. Instrumentation	288
G.3. Load-displacement curves	290
G.3.1. Vertical Displacements	290
G.3.2. Horizontal Displacements	294
G.4. Crack patterns	298
G.5. Failure modes of all-GFRP beam	301
G.6. Strain on CS-element	305
G.7. Angle of principal stress on the compression element	309
G.8. Measured strain on the tension element's top-side	311
G.9. Measured strain on the tension element's lateral sides	313
G.10. Angle of principal stress at the tension elements middle section	315

Summary

In the context of sustainable development, building insulation represents a major concern as a means of increasing energy efficiency. In order to comply with new norms such as the Passive House standard, locations where load-bearing components must penetrate the building's insulating envelope, such as when cantilevered slabs (e.g. balconies) are anchored to building walls, constitute a particular challenge. With conventional steel reinforcement, thermal bridges are inevitable and insulation is weakened. To overcome this deficiency, a multifunctional joint has been developed in which GFRP (glass-fiber reinforced polymer) elements perform the necessary structural functions without compromising the continuity of the building's insulating envelope. This is due to GFRP materials' low thermal conductivity, which is magnitudes smaller than that of concrete and steel, making them particularly suitable.

The anchorage of balconies requires linkages that can resist shear as well as tensile and compression forces in the upper and lower parts of the slab. In a first step, a hybrid joint was created in which the lower compression steel reinforcement was replaced by a compression-shear (CS-)element made of GFRP. This consisted of a short pultruded profile with cap plates bonded to its cut ends. In addition to compression forces, the element was intended to bear parts of the shear load. The joint was investigated in various full-scale beam specimens each representing a section of the slab. Based on the results, the joint's structural behavior was modeled analytically and structural requirements for the CS-element were determined. It was seen that shear transfer through the element increased with increasing shear-to-moment ratios. In a second step, an all-GFRP joint was created in which, in addition to the element in the compression zone, a tension-shear (TS-)element replaced the remaining steel reinforcement. This element consisted of the same pultruded profile cut to longer sections and penetrating the concrete. To anchor the tensile forces in the concrete, ribs were bonded to its surface. This joint type was also investigated through full-scale beam experiments similar to the hybrid-joint beams. The load transfer through the joint and into the concrete was studied and modeled analytically. The behavior of the all-GFRP joint was as ductile as that of the hybrid joints. The TS-element bore the main portion of the shear load independently of the shear-to-moment ratio however.

The CS-element used in both joint types was of special interest with regard to remaining strength and stiffness after long-term service life. Exposure to alkaline concrete-pore solution represents a particular threat to the polyester matrix and glass fibers inside the GFRP material. Therefore, CS-elements were immersed in alkaline liquids at different temperatures and their compression strength and stiffness were studied during a period of eighteen months. Material degradation was investigated by SEM-microscopic images and EDX-analysis. The observed loss of compressive strength was ascribed to moisture diffusion and chemical degradation of the fibers, matrix, and fiber-matrix interface. It was shown that the strength degradation rate at different temperatures followed the Arrhenius rate law and that remaining strength after long time spans could therefore be projected by extrapolating the

measurements. Remaining strength after 70 years of service life was found to be sufficient for the element never to become the critical failure location and classic concrete theory can be applied to verify the joint. Since stiffness at high temperatures was observed to already remain constant after short exposure times, this value could directly be extrapolated to apply to a 70-year service lifespan.

Keywords: alkalinity; concrete slab; EDX; diffusion; durability; GFRP; glass fibers; moisture; pultrusion; SEM; thermal insulation

Résumé

Dans le cadre du développement durable, l'isolation de bâtiments représente une mesure importante pour augmenter l'efficacité énergétique. Afin de réaliser de nouveaux standards, comme le standard pour les maisons en basse consommation d'énergie, les endroits où l'enveloppe isolatrice d'un bâtiment doit être pénétrée par des éléments structuraux représentent un défi particulier. Un tel cas se présente quand des dalles en porte-à-faux (p. ex. balcons) sont ancrées dans le mur du bâtiment. Lorsqu'on utilise une armature conventionnelle en acier, des ponts thermiques sont inévitables et l'isolation est affaiblie. Pour surmonter cette déficience, un joint multifonctionnel a été développé dans lequel des éléments en GFRP (matériaux composites renforcés par fibres de verre) exercent la fonction structural nécessaire, sans altérer la continuité de l'isolation du bâtiment. La conductivité thermique des matériaux GFRP est inférieure de plusieurs magnitudes par rapport à celle du béton et de l'acier, ce qui les rend particulièrement appropriés.

L'ancrage des balcons requiert des liaisons aptes à résister à l'effort tranchant autant qu'aux forces de traction et de compression dues au moment de flexion. Dans une première étape, un joint hybride a été conçu pour remplacer l'armature de compression par un élément combiné en compression et cisaillement fabriqué en GFRP. Il consiste en un court profilé pultrudé avec des plaques de tête accolées aux surfaces coupées. Au-delà des forces de compression, l'élément est censé de transmettre une partie des efforts tranchants. Le joint a été étudié dans des poutres diverses à l'échelle 1:1, représentant chacune une section de la dalle. Les résultats ont servi à modéliser analytiquement le comportement structural du joint et de déterminer les exigences structurales de l'élément. Il a été observé que les efforts tranchants augmentaient dans un rapport croissant entre cisaillement et moment appliqué. Une deuxième étape a visé à la création d'un joint dans lequel, en plus de l'élément dans la zone de compression, un élément combiné en traction et cisaillement a remplacé l'armature restante en acier. Cet élément consistait en le même profilé pultrudé, mais coupé dans des sections plus longues pénétrant le béton. Pour l'ancrage des forces de traction dans le béton servaient des nervures collées aux surfaces. Similairement au joint hybride, ce joint tout-GFRP a été étudié dans des poutres à l'échelle 1:1. Le transfert de la force à travers le joint et dans le béton a été analysé et modélisé analytiquement. Il a été constaté que le comportement du joint tout-GFRP a été aussi ductile que celui du joint hybride. Indépendamment du rapport entre cisaillement et moment appliqué, l'élément traction/cisaillement transmettait la majorité de l'effort tranchant.

L'élément compression/cisaillement utilisé dans les deux versions du joint était d'un intérêt particulier concernant l'aptitude de résistance et de rigidité au service à long terme. L'exposition aux solutions alcalines des pores du béton représente une menace à la matrice de polyester et aux fibres de verre dans le matériau GFRP, raison pour laquelle les éléments compression/cisaillement ont été immergés dans des liquides alcalins aux différentes températures et leur résistance et rigidité en compression ont été poursuivies pendant une période de dix-huit mois. La dégradation du matériau a été documentée par des images mi-

croscopiques MEB, ainsi que des analyses EDS. La perte de la résistance en compression a été attribuée à la diffusion de liquide et à la dégradation chimique des fibres, de la matrice ainsi que de l'interface entre les fibres et la matrice. Il a été démontré que la dégradation de la résistance suit la Loi d'Arrhenius, grâce à quoi la résistance résiduelle sur de longues périodes peut être déterminée par une extrapolation des mesures. La résistance résiduelle après une durée de vie de 70 ans a été jugée suffisante pour que l'élément ne devienne pas l'endroit critique où la rupture se produit, de sorte que la théorie classique du béton ait pu être appliquée pour vérifier le joint. La rigidité à températures élevées est restée constante déjà peu après le début de l'exposition, il été possible de l'associer directement à une durée de vie de 70 ans.

Mots-clés: alcalinité; dalle en béton; EDS; diffusion; durabilité; polymères renforcés de fibres de verre; fibres de verre; humidité; pultrusion; MEB; isolation thermique

Zusammenfassung

Vor dem Hintergrund nachhaltiger Entwicklung gewinnt die Gebäudedämmung zur Steigerung der Energieeffizienz von Bauwerken zunehmend an Bedeutung. Dies spiegelt sich auch in modernen Normen wider mit erheblich gesteigerten Anforderungen an die Dämmung. Bewehrung, die die äußere Isolationsschicht eines Gebäudes durchdringt, wie es beispielsweise bei Kragplattenverankerungen (z.B. Balkone) der Fall ist, stellen dabei eine besondere Herausforderung bei der Einhaltung dieser neuen Standards dar. Mit herkömmlicher Stahlbewehrung sind Kältebrücken an solchen Durchdringungen unvermeidlich und führen zu einer Schwächung der Dämmung. Um dies zu vermeiden wurden Anschlüsse entwickelt, in denen multifunktionale Bauteile aus GFK (Glasfaserverstärkter Kunststoff) lasttragende Funktionen übernehmen ohne die Gebäudedämmung zu unterbrechen. GFK-Materialien eignen sich besonders für diese Aufgabe, da ihre Wärmeleitfähigkeit die von Stahl oder Beton um mehrere Größenordnungen unterschreitet.

Die Balkonverankerung erfordert Verbindungselemente, die in der Lage sind neben Schub auch Zug- und Druckkräfte im oberen bzw. unteren Plattenbereich abzutragen. In einem ersten Schritt wurde ein gemischter Anschluss entworfen in dem die Druckbewehrung im unteren Plattenbereich durch ein Druck-Schub-Element aus GFK ersetzt wurde. Es bestand aus einem kurzen, stranggezogenen Profil mit an den abgesägten Seiten angeklebten GFK-Kopfplatten. Neben Druckkräften war das Element zur Aufnahme eines Teils der Schubkraft vorgesehen. Dieser Anschluss wurde in verschiedenen maßstäblichen Balken untersucht, die jeweils einen Ausschnitt der Kragplatte darstellten. Basierend auf den Ergebnissen wurde das Tragverhalten des Anschlusses analytisch modelliert und die mechanischen Anforderungen an das Druck-Schub-Element bestimmt. Dabei wurde ein Zusammenhang festgestellt zwischen der Schubübertragung im GFK-Element und dem Verhältnis aus Schub und Moment. In einem zweiten Schritt wurde ein reiner GFK-Anschluss entworfen in dem, zusätzlich zu dem Element im Druckbereich, ein Zug-Schub-Element die verbleibende Stahlbewehrung ersetzte. Dieses Element bestand aus dem gleichen stranggezogenen Profil, welches zu diesem Zweck in längere Abschnitte geschnitten wurde, die beidseitig der Dämmfuge in den Beton eingebettet wurden. Dieser Anschlusstyp wurde ebenfalls in maßstäblichen Balkenversuchen, ähnlich denen des gemischten Anschlusses, untersucht und die Lastübertragung durch Anschluss und in den Beton wurde ermittelt und analytisch modelliert. Die Untersuchungen ergaben ein ähnlich duktilen Verhalten beider Anschlusstypen, jedoch nahm das Zug-Schub-Element unabhängig von der Belastungsart den Hauptteil der Schubkräfte auf.

Ein weiterer Interessenschwerpunkt war das Langzeitverhalten des Druck-Schub-Elements in Hinblick auf Festigkeit und Steifigkeit. Insbesondere der Kontakt mit dem alkalischen Porenwasser des Betons stellt eine Gefährdung für die Polyestermatrix und die Glasfasern im GFK-Werkstoff dar. Aus diesem Grund wurden Druck-Schub-Elemente in alkalische Bäder mit unterschiedlichen Temperaturen gelegt und regelmäßig auf ihre Materialeigenschaften während eines Zeitraums von achtzehn Monaten hin getestet. Die

Materialdegradation wurde unter Zuhilfenahme von Aufnahmen eines Rasterelektronenmikroskops und der Röntgenfluoreszenzanalyse erforscht. Der beobachtete Verlust an Druckfestigkeit wurde auf Diffusion und chemische Degradation der Matrix, der Fasern und der Grenzschicht zwischen Fasern und Matrix zurückgeführt. Es konnte gezeigt werden, dass die Verlustraten für die Festigkeit bei unterschiedlichen Temperaturen dem Arrheniusgesetz folgen und die Restfestigkeiten konnten somit vorhergesagt werden indem die gemessenen Werte zeitlich fortgeschrieben wurden. Die ermittelte Restfestigkeit war ausreichend, damit das Druck-Schub-Element auch nach einer Lebensdauer von 70 Jahren nicht versagensmaßgebend wird und gewöhnliche Bemessungsverfahren für Stahlbeton angewandt werden können um den Anschluss nachzuweisen. Da die Steifigkeit sich schon während der Messungen auf einem konstanten Niveau stabilisierte, war es möglich die gemessenen Werte direkt auf eine Lebensdauer von 70 Jahren anzuwenden.

Schlagwörter: Alkalität, Betonplatte, Dauerhaftigkeit, Diffusion, GFK, Glasfasern, Feuchtigkeit, REM, RFA, Strangziehen, Wärmedämmung

Acknowledgments

This thesis marks the end of almost four years of research, a period during which I often had to rely on a number of people whom I would like to thank here.

Of particular importance for me were the support and confidence of Prof. Thomas Keller. I want to thank him not only for making this project possible, but also for guiding me through the difficult task of combining very diverse research areas to create a cohesive result.

I would also like to thank the thesis defense committee for the time and effort devoted to reading and evaluating this thesis: Prof. Patrice Hamelin, Laboratoire Mécanique Matériaux et Structures, Lyon, Prof. John J. Lesko, Dept. of Engineering Science & Mechanics, Blacksburg, Prof. Ian Smith, IMAC-EPFL, Lausanne and Prof. Eugen Brühwiler, MCS-EPFL, Lausanne. Prof. Lesko in particular was a great help with ideas and discussions on many occasions.

Further I am grateful for the financial support I received from the Swiss Innovation Promotion Agency (contract number 6278.1 KTS) as well as from SFS-Locher AG (Switzerland). At SFS-Locher, I appreciated the constructive discussions and negotiations with Erich Mayer, Ernst Nufer, Rudolf Enzler (ATROF Bauphysik) and Alex Frei during our meetings. My thanks also go to Eduard Frei for his careful checking of the verification programs.

A big thank you is also reserved for Nathan L. Post who is responsible for a large part of the gravimetric studies and SEM microscopy.

This work would not have been possible without the solid support provided by the technicians during the experimental phases. For the full-scale experimental investigations and compression studies I am particularly grateful to Sylvain Demierre, Hansjakob Reist, François Perrin, Gilles Guignet and Roland Gysler. For the high quality microscopic results I want to thank the CIME personnel at the EPFL.

For the realization of the thesis document I want to express my gratitude to Prof. Keller for his careful reading and constructive suggestions as well as Margaret Howett for her scrupulous English corrections.

I am grateful to my colleague Aixi Zhou for directing my thesis for almost two years and the time and effort he spent doing so. Till Vallée for the many many technical questions he had to answer (especially in mechanics), Craig Tracy for being a super cubicle neighbor and thereby training me in image processing – his enthusiasm even made me buy a 1980 photo camera... The whole group was responsible for creating a fantastic atmosphere, making this a very enjoyable experience. Therefore I don't want to leave out Erika Schaumann, Herbert Gürtler, Julia de Castro, Martin Schollmayer, Ye Zhang, Yu Bai, Anastasios Vassilopoulos, Marlène Sommer, Pierre Zurbrügg, Christina Boo, Dan Bolomey, David Guzman and Magdalena Schauenberg as well as the many students present during that time.

Finally I am very grateful to my family, especially to my mother Annegret, and my friends who encouraged me to decide to do a PhD and further supported me during the many crises that occur during such an endeavor.

1. Introduction

1.1. Motivation

In today's context of sustainable development in construction, the energy consumption of buildings and structures represents an important issue. The development of construction methods with high thermal insulation is on-going and new standards such as the Passive House standard reduce linear thermal bridge allowances to less than $0.3 \text{ W}/(\text{m}\cdot\text{K})$, cp. SIA 380 [6]. Therefore it is possible to build highly insulated and self-sustaining houses without, for example, the need for heating systems. Another reason to increase thermal insulation is that insufficient insulation may lead to physical problems on inner building surfaces. Thus a reduction of the inner surface temperature below the dew point of the air in rooms can cause surface condensation and fungal growth. Finally, for thermal comfort in interior rooms, the average surface temperature should not fall more than 3°C below the room air temperature, cp. SIA 180 [5].

Table 1.1: Thermal conductivity λ of construction materials at 20°C (Özişik [79])

Material	$\lambda \left[\frac{\text{W}}{\text{m}\cdot\text{K}} \right]$
Steel B500B	60
Stainless steel	15
Concrete	2.1
GFRP (pultruded)	0.3
Timber	0.18
Styrofoam	0.04
Stationary air	0.03

In view of these considerations, the insulating facade becomes a central concern and weak locations such as thermal bridges, allowing unwanted heat transfer between inside and outside, have to be avoided. Such locations are present whenever structural members penetrate the facade, such as concrete slabs for balconies. As shown in Table 1.1, traditional construction materials such as concrete or steel exhibit relatively high thermal conductivity. Steel reinforcement therefore causes thermal bridges with substantial heat losses. Consequently, starting from the 1st-generation all-steel joint, shown in Figure 1.1, multifunctional joint elements have been developed to ensure structural continuity of the concrete slab through the facade and to provide a certain level of thermal insulation. These new joint elements incorporate glass-fiber reinforced polymer (GFRP) materials, which are placed in the facade's insulating layer. From the table it can be seen that in addition to their structural advantages

GFRP materials display very low thermal conductivity, lower than that of normal steel by a factor of 200. Furthermore, GFRP outperforms concrete by a factor of seven.

1.2. Multifunctional insulating joint

Anchorage of cantilevered slab-concrete members to an insulated building represents the joint's general mechanical purpose. The moment and shear, which result from vertical loads on the slab, create tension forces in the upper part of the slab, compression forces in its lower part and shear that must all be transmitted through the insulating layer. To date, these tasks have been performed by an all-steel joint generation with three special kinds of steel reinforcement: one horizontal in the top, and another in the bottom of the slab, and diagonal bars crossing the insulating layer as shown in Figure 1.1. To reduce thermal bridges caused by the high thermal conductivity of the steel, in this work a new hybrid GFRP/steel joint has been conceived in which the lower steel reinforcement was replaced by an existing GFRP compression-shear (CS-)element, cp. Figure 1.2. The number and distribution of CS-elements can, as with steel reinforcement, be varied to accommodate various application requirements, e.g. loading conditions and geometries. A possible combination is shown in Figure 1.3. Investigations concerning the technical feasibility and marketability of this joint, including the structural behavior of the whole joint and especially that of the CS-element, had to be carried out however. Here, questions regarding possible geometric optimization and durability had to be answered. A second development step aimed to completely replace all steel reinforcement by GFRP elements. For this purpose, a tension-shear (TS-)element will have to be developed to replace the upper and shear bars. By replacing the steel reinforcement, thermal conductivity can effectively be reduced from 0.4-0.6 W/(m·K) for the all-steel joint to 0.1-0.2 W/(m·K) for the hybrid joint. The thermal conductivity for the all-GFRP joint was anticipated to be 0.05-0.1 W/(m·K), corresponding to an overall reduction of 90% compared to the all-steel joint.

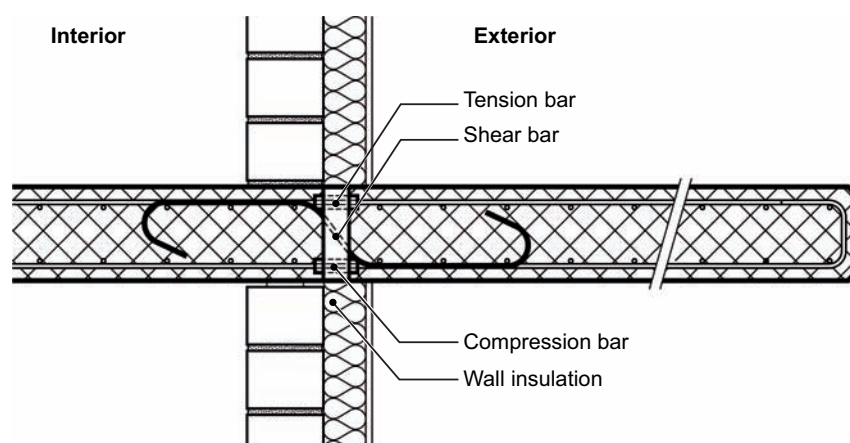


Figure 1.1: 1st-generation all-steel insulating joint

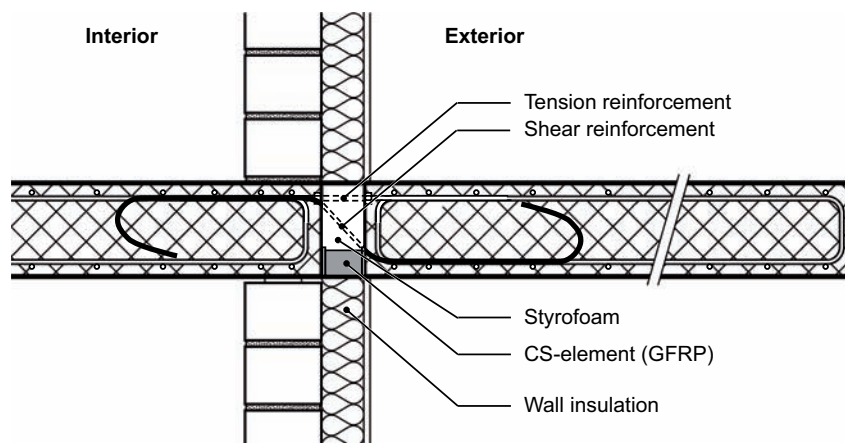


Figure 1.2: 2nd-generation hybrid GFRP/steel insulating joint

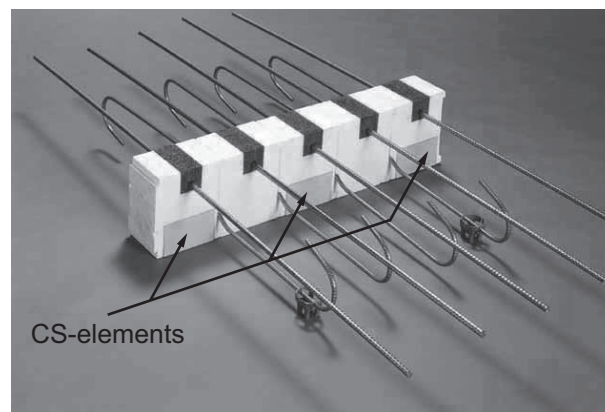


Figure 1.3: Prefabricated insulating joint with three GFRP elements embedded in styrofoam insulation and stainless steel bars (*isolan[®] plus* joint) [105].

1.3. Objectives

The objective of this research was to develop thermal-insulating and load-bearing GFRP components for cantilevered concrete members anchored in insulating facades and to describe their static short- and long-term behavior. Specifically, the following problems had to be solved:

Hybrid joint investigation The investigations on the hybrid joint were aimed at gaining an understanding of the structural behavior. Experimental data should provide a basis for analytical models, which lead to a design method that can be used in practice.

All-GFRP joint investigation The final joint (3rd generation) should be composed of only two GFRP elements replacing the steel reinforcement, both of which bear a part of the shear load. Therefore, a TS-element bearing tensile and shear forces had to be designed and integrated into the hybrid joint. Besides the shear distribution between

the CS- and TS-elements, the load-transfer mechanisms in the TS-element and the load-transmission behavior into the concrete had to be determined and modeled.

Durability and lifetime prediction The GFRP elements as central components in both hybrid and all-GFRP joints are exposed to alkaline concrete-pore solution. Moist and alkaline environments, however, are harmful to GFRP materials. Chemical and physical processes acting on the material in this aggressive environment had to be identified and their impact on the GFRP elements' material properties evaluated. Since the insulating joints are intended for service lifetimes of 70 years, the remaining material properties of the GFRP-elements after this time span had to be determined.

1.4. Methodology

To achieve these objectives, experimental and analytical procedures were used and the following approaches were chosen:

- The CS-element's structural behavior in compression was investigated experimentally, accompanied by a durability analysis to assess its long-term performance. This part included a thorough review of literature concerning the chemical and physical impacts of alkaline environments on GFRP.
- The degradation mechanisms of the GFRP material were detected by SEM microscopy and EDX material analysis. The ingress of alkaline liquids was measured by a weight-gain analysis.
- The hybrid steel/GFRP and all-GFRP joints were investigated by means of full-scale experimental series whereby several parameters influencing structural behavior were examined.
- The structural behavior of both joints (hybrid and all-GFRP) was subsequently modeled analytically. The results obtained for the hybrid joint should be directly applicable in practice.

1.5. Composition of the work

This work is structured as follows:

- Chapter 2 summarizes the state of the art:
 1. The use of GFRP reinforcement in concrete structures is reviewed to situate the present research in this field.
 2. Diffusion into isotropic and orthotropic materials is reviewed and specific problems related to resin degradation are dealt with.
 3. The degradation mechanisms acting on the fibers, matrix and fiber-matrix interphase and their impact on material strength are examined.

4. The theoretical approach to the Arrhenius rate law is described and applied research is reviewed.
- Chapter 3 describes the CS- and TS-elements. The CS-element, whose development should lead to direct application in practice, is addressed in depth with regard to its behavior in the joint. In addition to initial strength and stiffness, the impact of alkaline concrete-pore solution on material properties is shown and diffusion as well as the microscopic investigations are described.
 - In Chapter 4 the insulating joints are investigated. Both the hybrid and all-GFRP joints are explained in detail, the experimental procedures are shown and results are discussed. Structural models describing the load-carrying behavior of both joint types are developed and compared to the obtained results.
 - In Chapter 5 the strength degradation is extrapolated by means of the Arrhenius rate law. Acceleration factors and activation energies are given for CS-elements and placed in context with results from previous research. Finally, the obtained strength in the alkaline solution is transferred to the real application and the safety of the insulating joint is discussed.
 - Chapter 6 summarizes the obtained results and puts forward proposals for future work.

2. The state of the art

2.1. Introduction

GFRP materials are increasingly used in construction due to their special characteristics such as light weight, high specific strength and corrosion resistance. However, used in combination with concrete structures, two major disadvantages, which have detrimental effects on FRP material properties, are moisture in the form of concrete-pore solution and the resulting strong alkaline environment. The degradation is physical, due to ingressing moisture resulting in swelling and cracking of the matrix and fiber-matrix interface, and chemical, due to decomposing matrix and glass fibers. To understand the complex degradation process, the interacting physical and chemical mechanisms have to be analyzed. Degradation will depend on diffusion velocity, which differs in orthotropic composite materials in the longitudinal and transverse directions. Once alkaline moisture has penetrated the material, chemical reactions occur between the hydroxide ions in the moisture and resin as well as the glass fibers. The pathways created by the swelling along the fiber-matrix interface will constitute preferred locations for the chemical onset. An understanding of the combined degradation processes is a precondition for applying life-time predictions based on the Arrhenius rate law.

2.2. Use of FRP reinforcement in concrete structures

The idea of using FRP materials not only as self-supporting elements but also as reinforcement for concrete structures emerged in the 1960s in North America and in the 1970s in Europe and Japan. The justifications and motivation for these new developments were manifold. In Japan, the prime interest was in the development of construction materials and methods that could enhance prefabrication, automation, labor savings and generally a cleaner and more efficient construction process, Nakagawa [76]. In North America, replacement of the corroding infrastructure represented a strong need for non-corroding materials. The use of salt on roads and bridges for all-weather driving conditions led to serious deterioration of the steel reinforcement in concrete structures and bridge decks, Dolan [35], Prince [92]. Finally, in Europe, the large number of historical buildings in need of repair led to increased interest in strengthening/rehabilitation products, Nanni [77]. Here too however applications in the infrastructure in the form of pre-stressed tendons were investigated from the beginning stages. Furthermore, the low heat conductivity was used to produce elements to thermally insulate the warm interior of a building from the exterior parts of the construction, Taerwe and Matthys [115]. Finally, FRP reinforcement may be the choice if there is need for electromagnetic transparency in certain industrial constructions, Bakis et al. [13].

FRP used for internal concrete reinforcement assumes the role of traditional steel reinforcement and therefore adopts its forms and shapes. The rebars and tendons made from FRP are typically made by the pultrusion process. Close variants exist such as pull-winding

or pull-forming, which allow for integrating cross-layers and final shaping after the profile left the forming die. The bars can be assembled into 2- or 3-dimensional shapes in the same way as steel bars. Unlike steel bars, however, the production of curved FRP bars is difficult, resulting in a number of restrictions. Furthermore multi-axial reinforcements may also be fabricated using complex braiding techniques, cp. Figure 2.1, the joints in such woven structures being stronger than those in structures connected on the construction site.


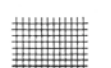
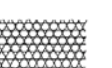
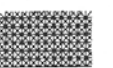

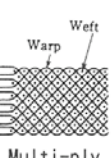
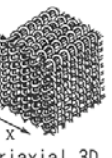



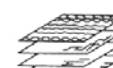


Axis		1	2	3	4~		
Dimension		Mono-axial	Biaxial	Triaxial	Multi-axial		
1D		Pultrusion rod	—	—	—		
2D		 Pre-impregnation sheet	 Plane weave	 Triaxial weave	 Multi-axial weave		
3D	Linear element	 3D braid	 Multi-ply weave	 Triaxial 3D weave	 4-axial	 5-axial	 6-axial
	Plane element	 Laminate type	 H or I beam	 Honey-comb type	—		

Figure 2.1: Fiber configurations for composite materials (taken from Nanni [76])

To improve the bond between the rebar and the concrete, surface deformations are applied. Cosenza et al. [30] distinguish two major deformation categories: either deformations are applied to the outer surface (ribbed, indented, braided) or the bar surface is covered with grains (sanded). By testing bars with different surfaces, it was possible to classify different surface treatments according to their effective bond behavior. In any case, smooth FRP rebars are inadequate for use as concrete reinforcement. In contrast, deformed bars offer a variety of bond mechanisms that depend on the shape of the outer surface, the compressive strength of the concrete, and the mechanical properties of the bar itself. In all cases the rebar surface has to provide enough lateral confinement to activate a bearing-type mechanism and to create a dependency between bond strength and the concrete compressive strength. Sanded surfaces also offer good bond resistance, but the interface between sand grains and bars detached abruptly, leading to brittle bond failure. Glued spirals and twisted strands proved less effective than deformed or sanded bars. Glued spirals on the rebar surface did not result in a significantly improved bond compared to smooth bars. The glued parts detached from the bars without causing any damage to the concrete. Twisted strands provided slightly higher bond strength than smooth rebars.

Additional challenges regarding the application of FRP rebars arise from their lower elastic modulus with resulting higher tensile elongations compared to steel, as was found by Pecce et al. [82]. An important factor is also the higher Poisson's ratio, which leads to a reduc-

tion in the transverse diameter. The resulting lower shear strength and stiffness of the ribs can influence mechanical interlocking and failure mechanisms in both splitting and pull-out failure. Another important difference between FRP and steel bars is the brittle behavior of the former. While steel offers a large ductile behavior, the brittle characteristic of the glass fibers leads to sudden failure. In order to avoid such failure modes, efforts have been made to develop pseudo-ductile hybrid FRP rebars using fibers with different material properties to generate a high initial modulus, a definite yield point and a high level of ultimate strain. Somboonsong et al. [111] investigated hybrid bars of 3- and 5-mm diameter, produced with a braiding technology. The core yarn was made from high-modulus carbon fibers, while for the braiding and rib yarn softer aramid fibers were used that are known to fail in a ductile manner. Experimental tensile investigations showed large ductile plateaux, which were reproducible by analytical models.

2.3. Diffusion into solids

Compared to materials like steel, FRPs are characterized by a rather open molecular structure allowing the penetration of moisture. Furthermore, they possess several characteristics that complicate the diffusion process. Embedded fibers lead to orthotropic diffusion properties, with faster diffusion in fiber direction due to wicking action. This effect is increased by several physical and chemical processes, which occur at the fiber-matrix interface. Further, the matrix' chemical structure is altered by the ingressing moisture influencing the possible maximum moisture content. In this respect, cracks resulting from swelling stresses after moisture has entered the material have an even greater influence. Research was carried out in order to take these effects into account. The objectives were to model them analytically and to ascertain the limits of their applications.

2.3.1. General aspects

Diffusion in general is always driven by a concentration gradient. A distinction must moreover be made between physical and chemical diffusion, physisorption and chemisorption, where physisorption concerns the penetration of liquids into pores inside the material and chemisorption describes the chemical inclusion of the contaminant into the substrate, where the adsorbed molecules are linked to the surface by chemical bonds. Chemisorption can be a consequence of physisorption once reacting molecules are transported to surface-active sites inside a material. Chemisorption is considered to be irreversible if the chemical nature of the adsorbent is altered by surface dissociation or reaction, Everett and Koopal [43]. If the rate of diffusion is not diffusion-controlled, i.e. the material is not altered in such a way that the diffusion coefficient changes, the rate of both types of diffusion (chemical and physical) can be described by Fick's First Law, shown in Equation 2.1.

$$F = -D \frac{\partial C}{\partial x} \quad (2.1)$$

where F [mol/(m² s)] is the rate of transfer (flux) per unit area perpendicular to the diffusion, C [mol/m³] is the concentration of the diffusing substance, x [m] is the space coordinate in diffusion direction (normal to the surface) and D [m²/s] is the corresponding diffusion coefficient, constant with respect to concentration C , dimension x and time. This equation is equivalent to the theory of heat transfer through materials described in 1822 by Fourier [46] and was first used for the description of diffusion kinetics in 1855 by Fick [44]. However, this equation assumes that the concentration within the diffusion volume does not change with respect to time ($F_{in} = F_{out}$). When the concentration within the diffusion volume changes with respect to time, Fick's Second Law (Equation 2.2) establishes the relation between the concentration of the substance and time, t [31].

$$\frac{\partial C}{\partial t} = D \frac{\partial^2 C}{\partial x^2} \quad (2.2)$$

Fickian diffusion is defined as a process that is accurately described by Fick's equation and consequently, any diffusion process that differs from the assumption of constant diffusion is termed non-Fickian. In reality any diffusion into polymers is non-Fickian since the contaminant will always provoke some chemical reactions inside the material, which change the diffusion rate. This is particularly true after extended exposure to the diffusion substance. However, often the initial diffusion stages can be approximated as Fickian since this process occurs more rapidly than the chemical reactions. An alternative approach that attempts to better describe chemical processes in diffusion using rate constants is the Langmuir model. However, the components and chemical molecular states of the reacting substances must be known in depth, which is rarely the case, Merdas [75]. Therefore, this approach will not be further explored in the following.

In addition to uniform diffusion with identical diffusion parameters in different directions, the heterogeneous character of the material, in which wicking processes through the fiber-matrix interface play an important role, marks the moisture uptake into FRPs. The process along and in between fibers and rovings is similar to that observed in concrete and was investigated by Keller [61]. The diffusion was described as a function of maximum aggregate size where the moisture searches for the shortest ways between two aggregates. Around the aggregate a weak area of cement matrix is built up and leads to increased flux activity. The wicking moisture in the cement-aggregate interface creates pathways and accelerates the diffusion. These pathways are preferred areas for the onset of cracks. The same mechanism was verified in E-glass fiber-reinforced polyester by Prian and Barkatt [91], who found areas of transformed fiber-matrix interfaces due to reactions of the surrounding liquid with the glass. These weakened areas also served as pathways for liquid in the composite. These pathways were shown by Karbhari [60] in E-glass reinforced vinylester composites, cp. Figure 2.2.

2.3.2. Diffusion into FRPs

Some of the earliest applied research on moisture ingress in fiber-reinforced polymer composites was undertaken by Springer et al. in the 1970s and 1980s [109]. Springer's studies included the application of Fickian diffusion principals to orthotropic polymer composites.

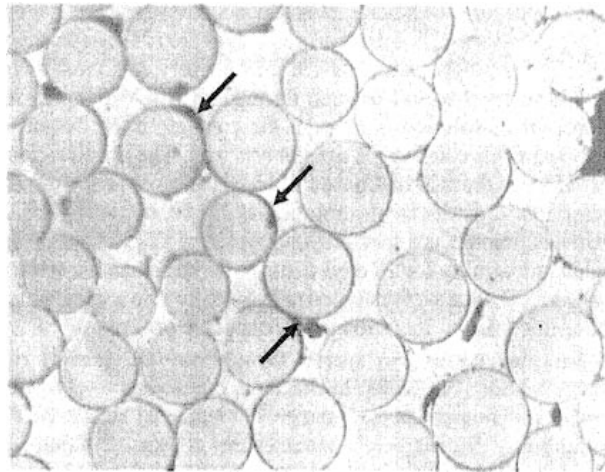


Figure 2.2: Fiber debonding in E-glass fiber-reinforced vinyl ester (taken from Karbhari and Chu [60])

A diffusion coefficient D_x was used to describe the diffusion normal to a specimen's surface independent of the fiber direction. To incorporate the orthotropic character, D_x was approximated by using the fiber angle normal to the specimen surface together with either the known diffusion coefficients parallel and normal to the fiber direction or the specimen's fiber-volume fraction. Once D_x was obtained, correction factors taking into account the specimen's dimensions were calculated for experiments where diffusion through the edges could not be neglected. The theoretical approach was verified by means of moisture uptake experiments on unidirectional graphite composites under various conditions. Comparison between the calculation and experimental data showed good agreement.

Although most of Springer's work was focused on epoxy matrix composites, Loos and Springer [71] also reported on the moisture diffusion of several polyester/E-glass composites. Experiments were performed on a series of chopped strand mat composites with various polyester-based matrix materials under conditions of humid air, distilled water, salt water, and several industrial chemicals. The composite was assumed to have isotropic diffusion characteristics. Weight gain measurements indicated a decreasing weight of the composites in distilled water at elevated temperature (50°C) after about 20 days and demonstrated widely varying non-Fickian behavior depending on the type of solution used. However, no attempt was made to explain why this was the case. Fickian diffusion coefficients were calculated based on a maximum moisture content value chosen at the point where the weight gain first leveled off.

However, this maximum moisture content was only an approximation and its determination always poses problems because of the weight losses, which already happen during initial stages, especially at high temperatures. Abeysinghe et al. [1] provided some insight into the weight losses in polyester resins immersed in water at elevated temperatures. They performed experiments on five isophthalic polyester resins, an orthophthalic resin and a vinyl ester resin, cured in neat samples and then immersed in distilled water and salt solution baths at temperatures between 30 and 65°C. In addition to noting the change in weight during immersion, the weight after removing and thoroughly drying the samples was recorded

and a chemical analysis of the remaining solution in the baths was performed by gas liquid chromatography. Based on these results, the true water uptake weight was determined by adding the weight of leached material to the measured mass of the sample. By doing so it could be shown that the water content inside the material remained relatively constant for most resin samples after the initial saturation. The same study also included a chemical analysis to explain the weight loss. This part of the study is reviewed in Section 2.4.2.

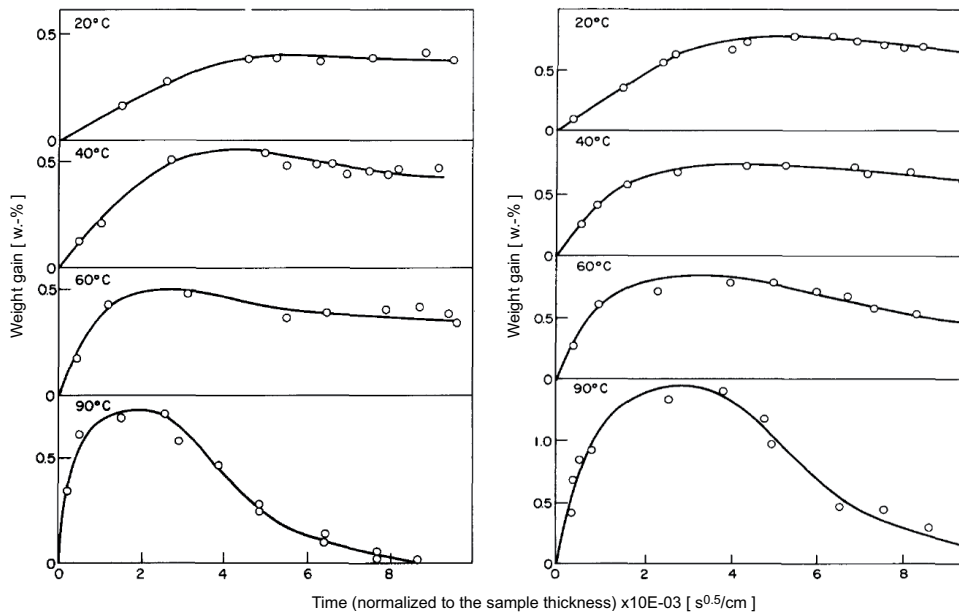


Figure 2.3: Weight gain of pure resin (left) and GRP composites (right) immersed in water at different temperatures (taken from Apicella et al. [8])

Especially for unsaturated polyester resins, weight losses at high temperatures make the determination of diffusion coefficients problematic, since the maximum moisture content, necessary for the fitting of the Fickian Law, cannot be precisely determined. A study concerning the subject of weight loss was undertaken by Apicella et al. [8], who investigated the weight losses of pure polyester resins and glass fiber composites (GRP) immersed in water. The temperatures were chosen between 20 and 90°C and the weight gain for pure resin samples and the GRP composite material was measured. The results are shown in Figure 2.3. It can be seen that after an initial gain, the weight decreased gradually. This phenomenon became progressively more pronounced as the temperature was increased. After an equivalent aging time of $8000 \sqrt{s}/\text{cm}$, the samples were desiccated and weighed. In the dry material, weight losses ranged from 0.38 to 1.12 % for the pure resin and from 0.53 to 2.41 % in the case of the GRP. Further, the actual moisture uptakes of both types of samples were calculated by using the effective final dry weight. From this it was evident that the maximum moisture content of the pure resin samples did not change for temperatures between 20 and 60°C and remained constant at $\sim 0.78\%$. It was therefore concluded that in this temperature range the sorption process was athermal. However, pure resin samples immersed at 90°C showed noticeably higher maximum moisture contents, which was attributed to microcavitation damage. In addition to these results, the equilibrium water uptake and weight losses of the

GRP samples were influenced by the fibers. The water uptake was higher, especially at high temperatures, which was attributed to debonding of the fibers and localized water entrapment in the cavities. The debonding was confirmed by SEM micrographs.

2.3.3. Mathematical approaches

Apart from the Langmuiran approach, which takes chemical reactions into account, the Fickian diffusion represents the only possibility for modeling moisture ingress. Since the Langmuiran approach depends on many specific parameters, nearly every study of moisture diffusion in materials relies on the application of Fick's Law as shown in Equation 2.1. It is usually employed only in one dimension where the concentration, C , as a function of time, t , and the spatial dimension, x , is found by solving Equation 2.2.

1D-Fickian diffusion into infinite plates

1D-Fickian diffusion can be applied if no interactions between different edges of a specimen exist. This would be the case for diffusion in the through-thickness direction of an infinite plate with thickness h . The boundary conditions for this purpose are:

$$\begin{aligned} C &= C_0 & 0 < x < h & \quad t = 0 \\ C &= C_\infty & x = 0; x = h & \quad t \geq 0 \end{aligned} \quad (2.3)$$

The solution in terms of the moisture content M as a function of time t is provided as

$$\frac{M_t - M_0}{M_\infty - M_0} = 2 \left(\frac{\sqrt{Dt}}{h} \right) \left[\frac{1}{\sqrt{\pi}} + 2 \sum_{j=0}^{\infty} (-1)^j \operatorname{ierfc} \frac{jh}{\sqrt{Dt}} \right] \quad (2.4)$$

where $\operatorname{ierfc}(x)$ is the integral complementary error function, defined by

$$\operatorname{ierfc}(x) = \frac{1}{\sqrt{\pi}} \exp(-x^2) - x \int_x^{\infty} \exp(-v^2) dv. \quad (2.5)$$

Here, h is the plate thickness, M_0 the initial moisture content, M_t the moisture content at time t and M_∞ the maximum moisture content. For short times the diffusion weight gain will be a linear function of \sqrt{t} and the unknown diffusion coefficient D in through-thickness direction used in Equation 2.4 can be found experimentally by plotting M_t vs. \sqrt{t} as shown in Figure 2.4 and determining the slope during the initial portion of the curve shown by Shen and Springer [108] as

$$D = \pi \left(\frac{h}{4M_\infty} \right)^2 \left(\frac{M_1 - M_2}{\sqrt{t_1} - \sqrt{t_2}} \right)^2. \quad (2.6)$$

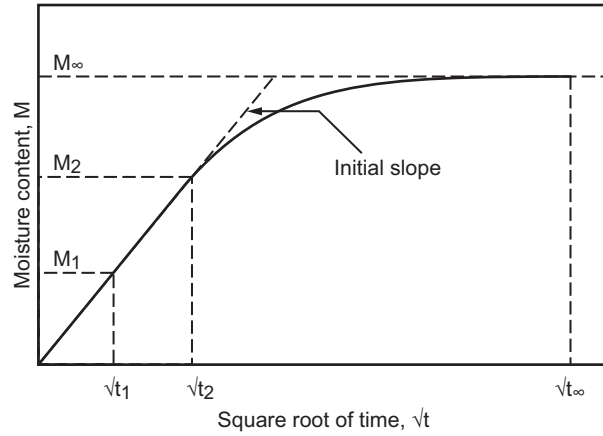


Figure 2.4: Gravimetric curve for 1D-Fickian absorption

Introduction of edge effects

The one-dimensional approach is good for relatively thin samples and situations where diffusion can be assumed to be in one direction normal to large surfaces. Once the sample has finite dimensions with edge lengths l and k , the diffusion in different directions interacts, which has to be taken into account. If the material shows orthotropic diffusion behavior, two more diffusion coefficients in directions 1 and 2 are introduced. A widely used method to calculate the weight gain with orthotropic diffusion behavior and edge effects was developed by Shen and Springer [108] using Equation 2.7.

$$M_t = \frac{4M_\infty}{h\sqrt{\pi}} \left(\frac{h}{l} \sqrt{D_1} + \frac{h}{k} \sqrt{D_2} + \sqrt{D_3} \right) \sqrt{t} \quad (2.7)$$

where D_1 and D_2 correspond to diffusion in the length (l) and width (k) directions respectively. By testing specimens of different surface-to-thickness ratios, it is possible to obtain diffusion coefficients D_1 , D_2 , D_3 and calculate an equivalent moisture diffusion coefficient, D , using Equation 2.8.

$$D = D_3 \left(\frac{h}{l} \sqrt{\frac{D_1}{D_3}} + \frac{h}{k} \sqrt{\frac{D_2}{D_3}} + 1 \right)^2 \quad (2.8)$$

This method, however, has substantial limitations. One problem is the need for samples of significantly different aspect ratios, especially if the diffusion properties are highly orthotropic. Another is the requirement that the maximum moisture content has to be known. This is easily determined for samples that follow true Fickian behavior and reach saturation in a reasonable amount of experimental time. However, it is often desirable to model the diffusion properties of materials that either require too much time to reach equilibrium or become non-Fickian due to degradation or other chemical changes after some time and

never reach a true moisture equilibrium level. For these cases, Pierron et al. [86] developed a novel approach using a solution to the full 3-dimensional diffusion equation.

3D-Fickian diffusion modeling

For an orthotropic thick rectangular plate of finite dimensions, the three-dimensional Fick's equation is

$$\frac{\partial C}{\partial t} = D_1 \frac{\partial^2 C}{\partial x_1^2} + D_2 \frac{\partial^2 C}{\partial x_2^2} + D_3 \frac{\partial^2 C}{\partial x_3^2} \quad (2.9)$$

with the boundary conditions

$$C = C_0 \text{ for } \begin{cases} -l/2 \leq x_1 \leq l/2 \\ -k/2 \leq x_2 \leq k/2 \\ -h/2 \leq x_3 \leq h/2 \end{cases} \text{ at } t = 0 \quad (2.10)$$

$$C = C_\infty \text{ for } \begin{cases} x_1 = \left| \frac{l}{2} \right| \\ x_2 = \left| \frac{k}{2} \right| \\ x_3 = \left| \frac{h}{2} \right| \end{cases} \text{ at } t \geq 0 \quad (2.11)$$

The closed-form solution to Equations 2.9, 2.10 and 2.11 is given as

$$\frac{C_t - C_0}{C_\infty - C_0} = 1 - \frac{64}{\pi^3} \sum_{m=0}^{\infty} \sum_{n=0}^{\infty} \sum_{p=0}^{\infty} \frac{(-1)^m (-1)^n (-1)^p \exp(-At)}{(2m+1)(2n+1)(2p+1)} \cos \frac{(2m+1)\pi x_1}{l} \cos \frac{(2n+1)\pi x_2}{k} \cos \frac{(2p+1)\pi x_3}{h} \quad (2.12)$$

with

$$A = \pi^2 \left[D_1 \left(\frac{2m+1}{l} \right)^2 + D_2 \left(\frac{2n+1}{k} \right)^2 + D_3 \left(\frac{2p+1}{h} \right)^2 \right] \quad (2.13)$$

Pierron integrates this result on the space variables, l , k and h (where l is the 1-direction and k , h are the 2- and 3-direction respectively) to find the total mass in the specimen as a function of time.

$$\frac{M_t}{M_\infty} = 1 - \left(\frac{8}{\pi^2} \right)^3 \sum_{m=0}^{\infty} \sum_{n=0}^{\infty} \sum_{p=0}^{\infty} \frac{1}{(2m+1)^2 (2n+1)^2 (2p+1)^2} \exp(-At) \quad (2.14)$$

In Equation 2.14 there are four unknowns, D_1 , D_2 , D_3 and M_∞ . Since it is not possible to solve for these explicitly from gravimetric data, an optimization routine has to be employed to minimize the least squared error between the calculated prediction and the experimental

data for i time steps, as shown in Equation 2.15.

$$q = \sum_i \left[M(t_i)^{(\text{calc})} - M(t_i)^{(\text{exp})} \right]^2 \quad (2.15)$$

Using several samples with different aspect ratios or boundary conditions enables the diffusion coefficients and maximum moisture content to be determined from the early diffusion data only. Thus, the maximum moisture content can actually be predicted for cases where non-Fickian behavior makes measurement impossible. By running a number of simulations using this approach, it was possible to show that the optimization solution is very robust when predicting the samples that are not fully soaked and which are, since M_∞ is missing, impossible to calculate with the method using correction terms for edge effects.

Several researchers have also applied various types of finite-element simulations to predict the moisture diffusion behavior of undamaged and damaged composite FRP materials with good results [99][100][57][127]. However, significant requirements for these types of models are well-defined composite component properties and micro-scale geometry and, as long as there are no complex interior configurations in the material structure, analytical solutions provide results of similar accuracy.

2.4. Degradation of GFRP

FRP composites used in concrete structures are prone to degrade due to the humid and especially the alkaline environment of the concrete. Moisture will diffuse into the material and provoke swelling with accompanying cracks and a general softening of the matrix material. Above all, the excess of hydroxide ions present in the alkaline concrete-pore solution will decompose glass fibers and the matrix. The principal impact of this material degradation concerns its strength, but its creep, relaxation and fatigue behavior will also be influenced, cp. Balázs and Borosnyói [14]. This section treats the different degradation mechanisms acting on the three components: glass fibers, the matrix and the fiber-matrix interface. In addition the impact on whole composite parts is reviewed in the last section of this chapter. In view of the application in question, the review is limited to E-glass and polyester composites. However, where principal mechanisms are concerned, different materials are included and, especially between vinylester and polyester resins, comparisons are made and discussed.

2.4.1. Degradation of glass fibers

Glass composition

Glass fibers are made from commercial silicate glasses. The most common glasses used in GFRPs are E-glasses (E for electrical grade) mainly because of their chemical durability and higher strength as well as their low price. E-glasses belong to the group of aluminosilicates, which are characterized by their relatively high proportion of aluminum oxide content (Al_2O_3 , cp. Table 2.1). Furthermore this type of glass has a low sodium (Na) fraction, which increases resistance to water attack as will be explained below. Since glass fibers are also used to directly reinforce cement and concrete, a special composition with a higher resistance to the alkaline environment was created by adding zirconium oxide (ZrO_2). This is referred to

as AR-glass (AR for alkali-resistant), cp. Majumdar and Ryder [72]. Table 2.1 shows common compositions for both types of glasses.

Table 2.1: Exemplary composition [w.-%] of E- and AR-glass [37][126]

	SiO ₂	ZrO ₂	Na ₂ O	CaO	K ₂ O	Al ₂ O ₃	B ₂ O ₃	others
E-glass	55	-	1	21	1	15	7	-
AR-glass	62.5	16.5	14.6	5.5	0.2	0.5	-	0.2

From the table it can be seen that in both cases the main constituent is silicon oxide (SiO₂) with more than 50 % in weight. For AR-glass, the increased proportion of zirconium oxide (ZrO₂) is apparent and the amount of aluminum oxide (Al₂O₃) is drastically reduced compared to E-glass. Zirconium oxide leads to the creation of a protecting layer as will be explained below, while aluminum oxide has been found to lead to low corrosion resistance against hydrochloric acid as shown by Ehrenstein and Staude [40]. The incorporation of zirconium oxide into the AR-glass is a complex process and explains the relatively high proportion of sodium oxide (Na₂O), which is generally added to lower the melting temperature during production.

Glass fibers used in composites are treated to promote fiber-matrix adhesion. The treatment consists of removing a weak surface layer of the fiber and adding additional chemicals, which allow the fiber and the matrix to react with one another. Two major treatments are applied to the glass fibers, the so called *sizing* and *finish*, cp. Jayaraman et al. [58]. The first thing applied to the fiber is the sizing, which contains ingredients to provide surface lubricity and binding action but, unlike a finish, contains no coupling agent. It is said to protect the fiber surface and ease processing and handling during fabrication. It also seem to play a significant role as a barrier to water migration to the fiber surface, as was found by Zhang et al. [128]. The sizing is usually removed before the finish is applied. The finish is a mixture of processing aids, usually containing the coupling agent, which enhance the fiber's wettability allowing the resin to flow freely around it and bond to it. In addition, it protects the fiber from abrasive damage during handling and protects fiber surface reactivity. For detailed information concerning the coupling agent, see page 28.

Glass is one of the most chemically inert of all commercial materials and does not react with hardly any gases or liquids below 300°C. The processes explained in the following, therefore, occur very slowly and may even stop at some point. Figure 2.5 shows the two principle types of glass alteration and degradation. It can be seen that possible attack can be either in the form of ion exchange (interdiffusion) between hydrogen ions in the attacking liquid and alkaline ions in the glass, known as *leaching*, cp. Figure 2.5a, or in the form of destruction of the silica-oxygen network by hydroxide ions, known as *etching* and depicted in Figure 2.5b.

These two processes are not independent, however. Leaching may create more dense layers at the glass surface that slow down the leaching and possible etching, while at the same time, free sodium resulting from leaching at the fiber surface provokes glass etching. The etching process prevents the creation of these dense layers, which directly influences the leaching rate. If both processes occur, temperature has an influence on whether leaching

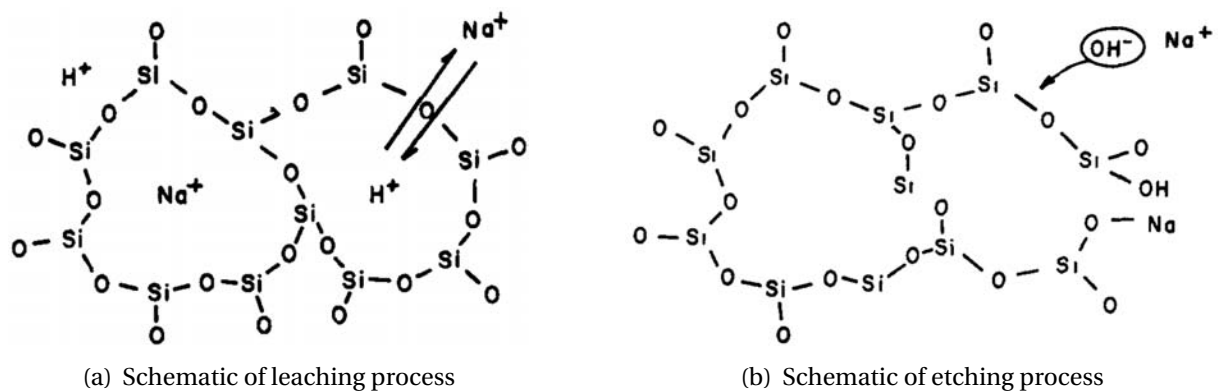
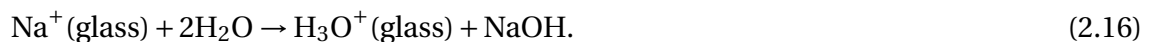


Figure 2.5: Two principle types of glass degradation (taken from Adams [2])

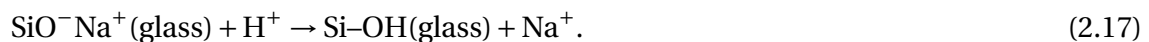
or etching is rate controlling. Leaching occurs predominantly at temperatures below 30°C, while for temperatures above 85°C, the etching process predominates, Alaily [41].

Ion exchange and layer formation (leaching)

The ion exchange mechanism takes place in the form of an interdiffusion between hydrogen ions (H) from the solution and alkaline ions (e.g. sodium) from the glass. It is the predominant process in neutral and acidic solutions, which contain an excess of hydrogen, cp. Devreux [34] and Schreiner [103]. Water is a neutral solution containing hydrogen ions and the ion exchange will occur as shown by Doremus [37] [38] as



The resultant substances from this reaction are hydronium (H_3O) in the glass and sodium hydroxide (NaOH) in the liquid, whose hydroxide ions (OH^-), in turn, attack the silica-oxygen network as will be discussed later in this section. The special role of the hydrogen ions in the interdiffusion process is shown by Scholze [101] as



The sodium (Na) in the glass is exchanged with the hydrogen ion. Sodium is assumed to be the only mobile charge carrier and hence small sodium concentrations in the glass decelerate the ion exchange process, cp. Lanford et al. [67]. Therefore, glasses containing less sodium (e.g. E-glass, cp. Table 2.1) show higher resistance to leaching. Reaction 2.17 is shown schematically in Figure 2.5a. An excess of positively charged hydrogen ions is a criterion for acidic solutions ($\text{pH} < 7$) and, since it is the hydrogen ions that characterize the water attack, the reaction between the water and glass can be classified as acidic.

From Figure 2.5a it can be seen that the ion exchange process leaves the silica-oxygen network intact. Instead, it forms a hydrated layer that grows from the surface into the glass, cp. Lanford et al. [67], Scholze [101] and Tomozawa and Capella [117]. The concentration profiles of the sodium and hydrogen ions are shown in Figure 2.6. It can be seen that the

hydrated layer is characterized by an excess of hydrogen ions together with a concurrent reduction in sodium. The glass network in the hydrated layer may become more dense and stable than the original glass since the structure of the silica-oxygen network rearranges, with the distance between two Si atoms becoming smaller, cp. Scholze [102]. Therefore, the produced layer will, with increasing thickness, protect the subjacent glass. If the silica-oxygen network is not otherwise altered, the layer grows diffusion-controlled at a constant rate with the square root of time and stops after several tenths of μm as shown by Lanford et al. [67].

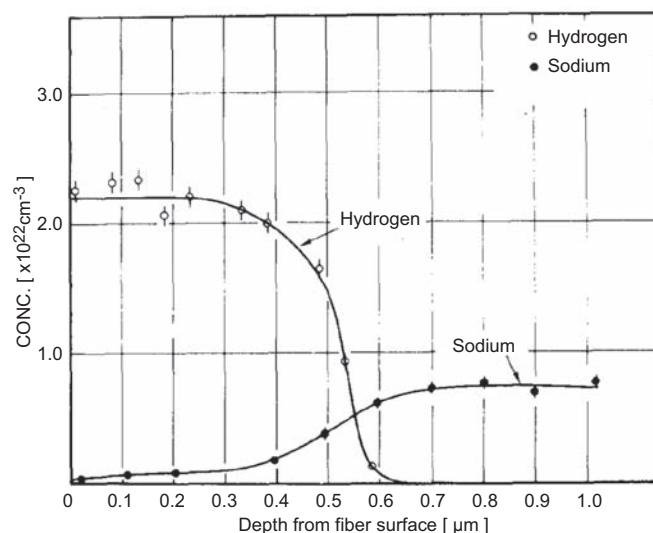


Figure 2.6: Na and H concentration of a hydrated glass surface (taken from Lanford et al. [67])

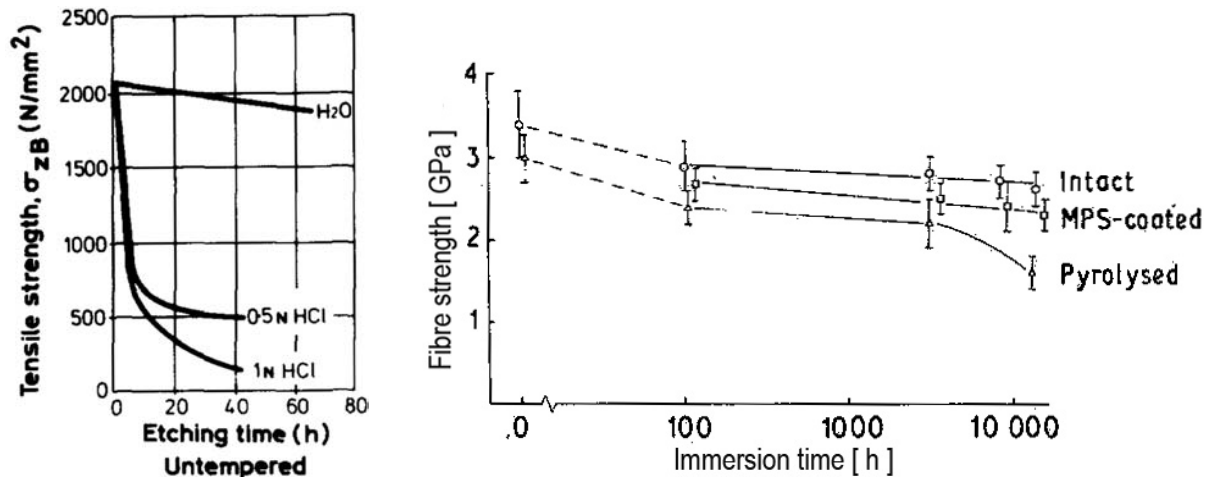
Leaching appears to have a non-negligible impact on fiber strength. The difference between acidic and neutral liquids was shown by Ehrenstein and Spaude [40], who immersed different kinds of glass fibers in neutral and acidic liquids at various temperatures. The remaining strength of E-glass fibers at 80°C is shown in Figure 2.7a¹. While in water, strength decreases were only small, in acid liquids, fiber strength drops to $\sim 10\%$ of its initial strength after only forty hours. The authors conclude from these results that absorbed water influences fiber strength. The presence of aluminum oxide (Al_2O_3) in the glass was found to be a major cause of weakening of the glass. Indeed, glass fibers without aluminum oxide performed much better.

In accordance with Ehrenstein and Spaude, Chua et al. [26] found similar tensile strength degradation rates for E-glass fibers in 60 and 75°C water. The differing parameter in their study was the fiber coating. The fibers were investigated with the original coating intact, coated with a special MPS² coating, and without coating (pyrolysed). Figure 2.7b shows the remaining fiber tensile strength. In the first 100 hours, strength losses were greatest with 10% (MPS-coated), 12% (coating intact) and 20% (pyrolysed coating). The coated fibers, therefore, exhibited a decrease rate of 3% per decade, while bare fibers showed a much higher

¹Note that the term 'etching' used in this figure does not correspond to the definition used in this work. Although some etching will certainly occur, the principal process will be 'leaching'.

² γ -methacryloxypropyltrimethyl siloxane

decrease rate after 300 h. A temperature of 22°C had very little effect on fiber strength, while an increase to 75°C produced similar results to the 60°C treatment.



(a) Tensile strength decrease of E-glass fibers at 80°C (taken from Ehrenstein and Spaude [40])

(b) Effect on fiber strength of immersion in water at 60°C (MPS-coated fibers with same initial strengths as pyrolysed fibers)(taken from Chua et al. [26])

Figure 2.7: Remaining glass fiber tensile strength at different temperatures in neutral and acid liquids

Apart from the fiber strength, failure mode also changes with progressive alterations in the glass structure. This is indicated by a changing fracture surface. Liao et al. [69] exposed E-glass fiber-reinforced composites to water and salt solutions (pH<7) at 25 and 75°C and tested their tensile strength. To investigate changes in the glass, they measured the size of the mirror of broken fibers, one of three phenomena observed on broken fiber surfaces, cp. Figure 2.8a. They were assuming the relationship between the mirror size on the fiber's fractured surface and fiber strength as

$$\sigma \cdot \sqrt{r} = \text{const.} \quad (2.18)$$

with σ = breaking stress and r = mirror radius. This relationship was investigated by Shand [106], who showed that measurements of the mirror size of fracture surfaces can be used to determine approximate values of breaking stresses in glass. The change in the fracture surface implies a change in the material provoked by the hydrolysis of the glass. Liao et al. measured the mirror sizes from selected fibers of each specimen, ranked them in descending order and assigned a probability of failure to each of the broken fibers. Figure 2.8b shows these probabilities of failure for the glass fibers as a function of mirror radius in the different solutions. It can be seen that fibers in 'as-received' specimens have smaller probabilities for smaller mirror sizes - and hence higher strength - than aged specimens. It can also be seen that strengths of fibers aged in hot water are not significantly different from those of fibers in specimens aged in water at room temperature.

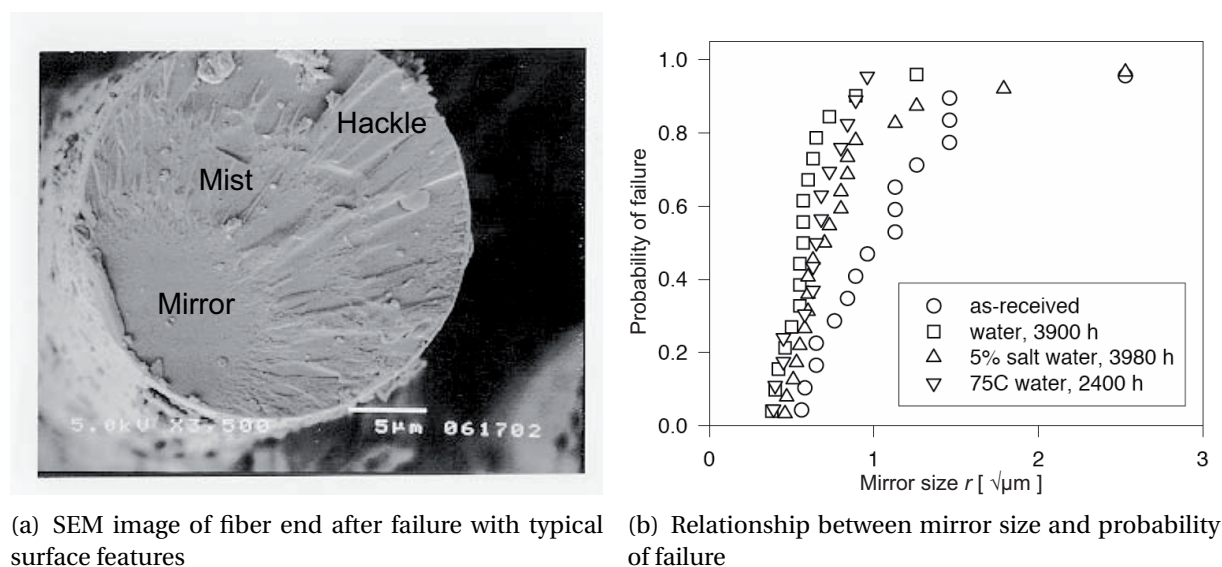


Figure 2.8: Features on broken-fiber surfaces and their relationship to failure probability (taken from Liao et al. [69])

SiO₂ network destruction and glass dissolution (etching)

Etching is a bond-breaking process that attacks the silica-oxygen network and leads to glass dissolution. The etching process occurs predominantly in alkaline solutions (pH>7) with an excess of hydroxide ions (OH⁻) and proceeds faster with increasing pH. In water (pH 7), glass will dissolve through a hydrolyzing process as shown in Equation 2.19.



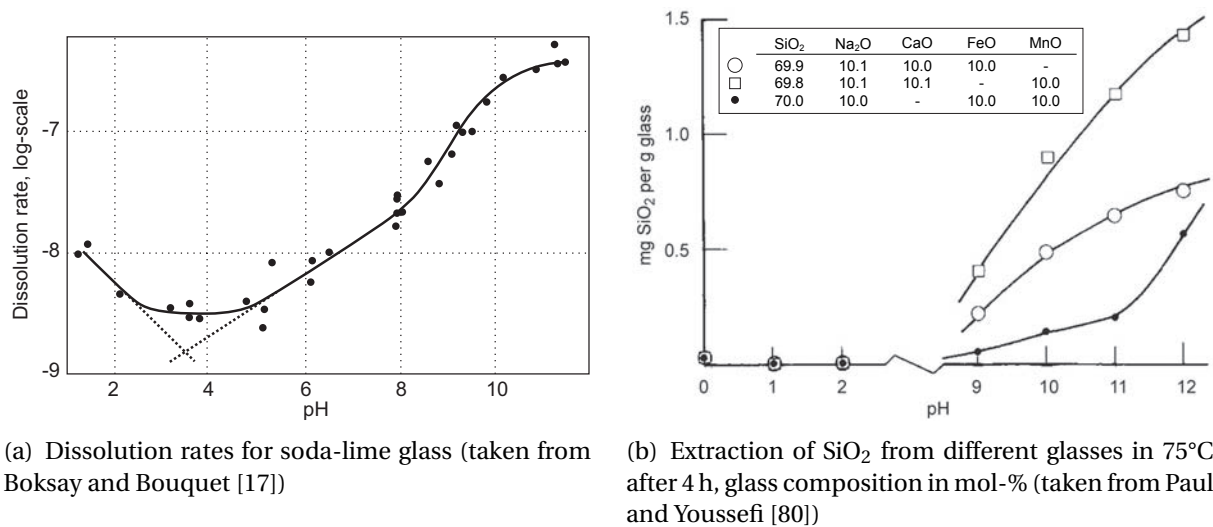
This process occurs by water molecules penetrating into the glass and successively breaking up the silica-oxygen network by hydrolysis, forming immobile hydroxide, as shown by Doremus [36], Perera and Doremus [83] as



As a result, permanently new surfaces are exposed to the water and the process will, in contrast to leaching, continue at a constant rate. This means that etching will control glass degradation in basic solutions after long periods, since hydrolyzed layers produced by leaching slow down and may stop the interdiffusion process.

The growing abundance of negatively charged hydroxide ions (OH⁻) increases a solution's alkalinity. In addition to the glass-water reactions shown above, the presence of hydroxide ions will severely increase the rate of the bond-breaking process between the silica and the oxygen leaving a terminal Si-OH surface group as shown in Equation 2.21, cp. Charles [20], Yilmaz [124] [125].

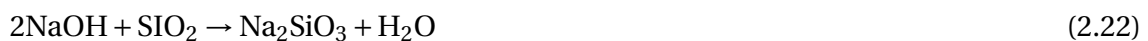




(a) Dissolution rates for soda-lime glass (taken from Boksay and Bouquet [17]) (b) Extraction of SiO₂ from different glasses in 75°C after 4 h, glass composition in mol-% (taken from Paul and Youssefi [80])

Figure 2.9: Rate of the etching mechanism at different pH

Negatively charged hydroxide ions are an intrinsic part of all hydroxides, large amounts of the water-soluble sodium hydroxide (NaOH) and potassium hydroxide (KOH) being found in concrete-pore solutions. Figure 2.5b shows schematically the reaction of glass with sodium hydroxide. For this reaction, Adams [2] proposes Equation 2.22, where sodium hydroxide breaks the bond between the hydrogen and the oxygen by separating a water molecule.



Etching proceeds at different rates depending on the pH of the solution. Doremus [37] reports constant rates between pH 2-8 for amorphous silica. Below pH 2, the dissolution rate decreases, while for pH > 8, in the presence of hydroxide ions (OH⁻), an ionization of the silicic acid (H₄SiO₄) accelerates the process. Boksay and Bouquet [17], however, found a further decrease of the dissolution rate for soda-lime glass beneath pH 8 with a regain for pH 2 and lower, while for pH 11 and higher it became almost constant, cp. Figure 2.9a. Paul and Youssefi [80] investigated the dissolution of the SiO₂ from the glass into the surrounding liquid. Figure 2.9b shows the extraction of SiO₂ from different glasses found in the solution. It is obvious that the bond-breaking process only begins once the liquid is of an alkaline nature (pH > 7). The presence of manganese oxide (MnO) slows down the etching rate, especially for high pH.

The etching mechanism will proceed at a constant rate, in an ideal case following the Arrhenius rate law, Adams [2]. To slow down the reaction rate, Larner et al. [68] found a protective surface layer was created by adding zirconia³ to the glass. Indications showed that the Zr-O bonds, compared to those of Si-O, were only slightly attacked by the OH⁻. The same effect is assigned to zirconium hydroxide (Zr(OH₄)) and other oxides, Scholze [101]. The layer developed only after some surface corrosion had taken place.

³This effect was used to create AR-glass, cp. Table 2.1 (ZrO₂).

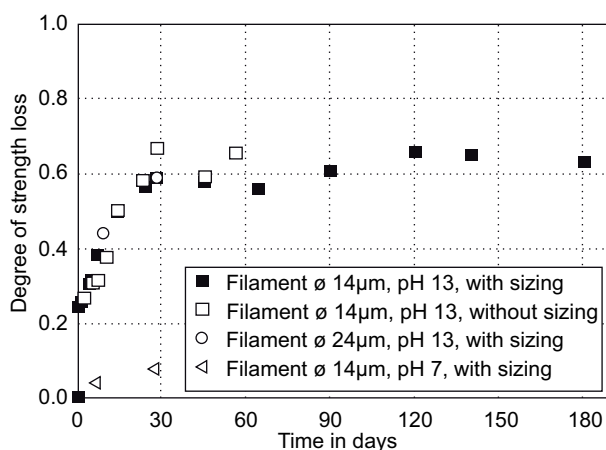


Figure 2.10: AR-glass filament strength reduction in neutral and alkaline liquids at 50°C (taken from Orłowski et al. [78])

This initial surface corrosion seems however to already have a decisive influence on fiber tensile strength, as Orłowski et al. [78] found. They investigated the impact of alkaline solutions on the tensile strength of AR-glass fibers. When AR-glass filaments of different diameters were immersed in 50°C alkaline solution (pH 13.5), strength reductions of up to 60% occurred within the first 30 days, independent of applied sizing, cp. Figure 2.10. Reference filaments in distilled water showed strength reductions of only ~10%, the remaining reduction being assumed to result from the etching process explained above. The authors supposed that areas in the glass containing low proportions of zirconia will lead to etching and widening of initial flaws, which, in turn, will be responsible for the observed strength reduction. This seemed to be confirmed by measurements of fiber diameter, which did not change sufficiently during conditioning to explain strength decrease by a simple reduction of fiber cross-section. After 40% of initial strength was attained, practically no further reductions were observed. This observation, in accordance with Larner et al., was explained by the fact that the etching process reaches the deeper layer of the glass with increased zirconium concentration. This significantly retards further diffusion and recondensation of silanol groups at the weak surface layer with a destroyed glass network, slowing down access of the OH^- to the non-corroded glass structure.

2.4.2. Matrix

Once exposed to environmental impacts such as temperature, water or chemicals dissolved in water, matrix resins undergo changes in their material properties, weight and ability to interact with fibers. The immediate change in the resin is swelling through the inclusion of water molecules in the molecular resin network, shown schematically in Figure 2.11. This process occurs by diffusion and will stop once the material is fully soaked. The process is reversible if accompanying swelling stresses induce no secondary damage. Once liquid reaches the interior of the polymer material, reactions between free radicals in the resin and the attacking liquid (hydrolysis) will cause the resin to shrink.

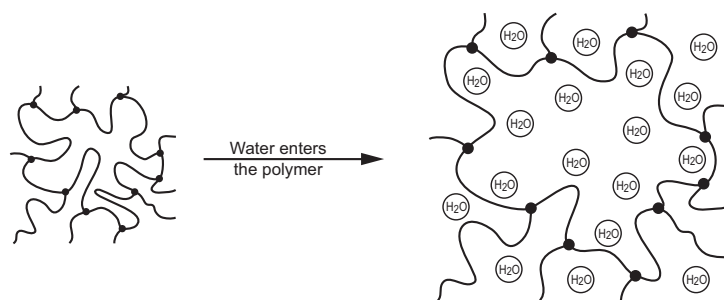


Figure 2.11: Polymer swelling through water inclusion

Resistance to water diffusion and chemical attacks varies with resin type. Johnson [59] (see also Schutte [104]) found the relative hydrolysis rate of polyester resins to be fastest in orthophthalic ester, followed by isophthalic ester > vinyl ester > bisphenol-A ester. While the hydrolysis in itself is to some extent a reversible reaction, it leads to the leaching of low molecular weight material, causing irreversible damage to the resin.

The controversial resin reactions of swelling and shrinking were investigated by Ashbee et al. [10], who studied the impact of water on polyester resins at different temperatures. They immersed specimens composed of three different polyester resins in 60°C distilled water for 16 weeks and in 100°C distilled water for three days and studied the effects by means of optical and electron microscopy. The findings were classified into two categories: internal cracking in the form of isolated disk-shaped cracks and surface cracking resembling the crazing of a ceramic glaze. The internal cracking was in several cases parallel to the surface, from which it was concluded that it was due to either external tension or internal pressure. The hypothesis was that scission of the polymer chain, provoked by hydrolysis, allows free radicals to interact and extra cross-link, resulting in shrinkage of the material near the scission as water diffusion proceeds. Therefore, swelling provokes shrinkage with stresses and accompanying cracks.

The extra cross-linkage will continue as long as there are free radicals present in the resin. The influence of different environments on the magnitude of the shrinkage was investigated by Ashbee et al. [11], who conducted a second study in which they measured the dimensions of polyester resins in 60 and 100°C immersion as well as in 100°C air for up to 2 000 hours. The results are shown in Figure 2.12. It can be seen that in 100°C air, no swelling was detected and shrinkage amounted to ~1 %, where it remained constant. In 60°C immersion, the shrinkage superseded the swelling process after only 30 min but also subsequently remained constant at ~1 %. After the same time in boiling water, however, shrinkage of ~8 % occurred. Accompanying measurements revealed that the considerable shrinkage did not involve any change in density. From this it was concluded that extra cross-linkage cannot be the only reason for shrinkage and it was suggested that leaching of low molecular weight material from the bulk resin, followed by a closing-in of the copolymer network to fill the 'holes' left by the extracted molecules, may be responsible. A correlation was found between volume shrinkage and weight loss, demonstrating their interdependence. It was already assumed that hydrolysis of ester linkages in the main chain, as shown in Figure 2.13a, is responsible for deterioration of the resin. The diffusion and material leaching processes therefore can-

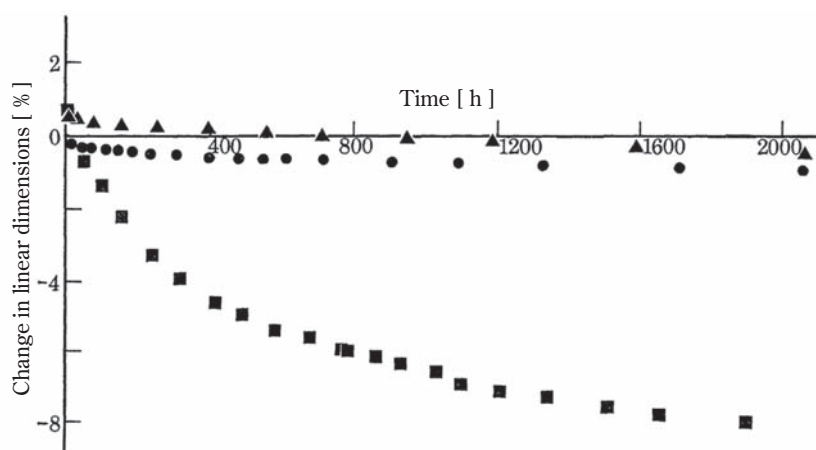
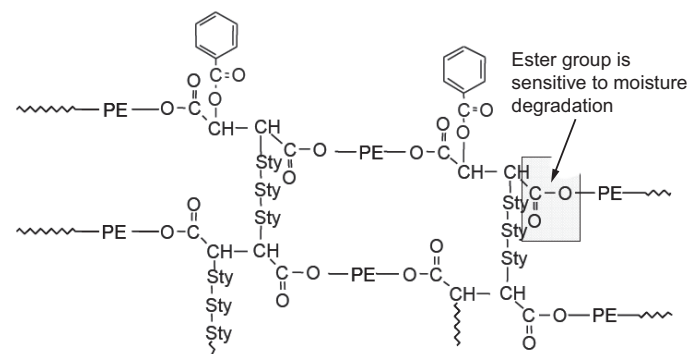


Figure 2.12: Linear dimensional changes of resin. ●, Post-cure in air at 100°C; ▲, water immersion at 60°C; ■, 3-day post-cure in air followed by immersion in boiling water (taken from Ashbee et al. [11])

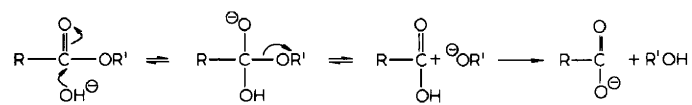
not be separated and total weight change is always the sum of water uptake, on one hand, and weight loss provoked by leached matter on the other. These combined processes also explain weight losses observed in diffusion studies as soon as the liquid becomes aggressive, cp. Figure 2.3.

The irreversible damage to the polyester resin induced by swelling cracks was investigated by Tsai [119], who described the crack creation along an advancing front of the swollen outer layer. At the front line between the glassy inner material and the swollen outer layers, high tension stresses occur and, once exceeded, lead to cracks in the matrix. Ascertaining the role of the so-called osmotic cracking as mechanical accelerator for further degradation constituted an important step towards understanding matrix degradation. In view of the impact these stresses have on a fiber-reinforced polymer, it can be inferred from the foregoing that these swelling stresses are even higher in the proximity of fibers and have a more destructive effect on the fiber-matrix interface. Cohn and Marom [28] studied this phenomenon on the basis of an epoxy resin. They found a highly anisotropic hygroelastic behavior at the swelling front, which was controlled by the size and relative dimensions of the specimens. The embedded non-swelling and stiff fibers especially will provoke stress concentrations. In accordance with the theory of Tsai, Cohn and Marom, Mensitieri et al. [74] report swelling stresses at the front of moisture uptake of the order of 10 MPa.

The impact on material properties of the combined mechanisms of swelling and shrinkage were also investigated by Apicella et al. [8]. Polyester resins were exposed to water at temperatures between 20 and 90°C for a time period of 15 days. A general embrittlement was observed, together with increased stiffness (+33 to +108 %) and reduced elongation at break at temperatures above 40°C. The embrittlement was attributed to the leaching of low molecular weight groups, which dominated the softening by water plasticization. Combined with the embrittlement and leaching of matter in water, the high swelling stresses led to matrix cracking. In a second study Apicella et al. [9] showed that water plasticization decreases resin stiffness, making it more compliant, while weight losses increase it. They subjected different composites and their pure resins to water at temperatures between 20 and 90°C. Their tensile



(a) Chemical composition of an unsaturated polyester resin (taken from Riffle and Lesko [96])



(b) Hydrolysis of an ester by a hydroxide ion (taken from Abeysinghe et al. [1])

Figure 2.13: Chemical structure of polyester resins and ester hydrolysis

stiffness was tested after 15 and 50 days. For 20°C and short time exposure, a plasticization and stiffness decrease were observed, since the water uptake dominated weight losses. However, at 90°C stiffness increased, which was ascribed to a domination by the weight loss of the moisture uptake. Generally it was found that specimens desiccated before testing showed higher strength and stiffness than wet specimens. This was, however, not explained. Furthermore, it was shown that the chemical stability of the resins used depended directly on the number of ester groups in their molecular lattice – a strong indication of their responsibility in the hydrolysis process. The embrittlement of the resin in hot water was confirmed by Mensitieri et al. [74], who conducted tensile experiments on polyester resins conditioned for 15 days in 90°C water. In accordance with Apicella et al. they observed increased stiffness (+18 %) with a reduction of the elongation at break (-70 %) and ascribed this to the same mechanisms.

The influence of the pH of the solution on resin degradation was investigated by Abeysinghe et al. [1]. Several polyester resins were immersed in distilled water, sulphuric acid (H₂SO₄), sodium chloride (NaCl) and sodium hydroxide (NaOH) solutions at temperatures of 30, 50 and 65°C. It was shown that hydrolysis is more rapid in alkaline environments because of the formation of a resonance-stabilized carboxylate anion exhibiting little tendency to react with alcohol. The hydrolysis reaction with hydroxide ions acting on the ester was described in four steps, cp. Figure 2.13b. Here it can be seen that an organic group, R', is separated from the ester group and, therefore, this reaction leads to non-bound, free matter inside the resin. This matter consists of isophthalic acid and large quantities of free propylene glycol. The total amount of leached matter gave a clear indication concerning the aggressive effect of alkalines on the polyester: while for NaCl, H₂SO₄ and H₂O solutions, the percentage of leached matter ranged between 0.5 and 2.7 %, the amount was 32 % for the NaOH (alkaline)

solution at 65°C after 8 000 h. They also noted an acceleration of the resin destruction by osmotic cracking. Osmotic cracking and therefore a diffusion-controlled degradation was also suggested by Bellenger et al. [16]. They assumed that the scission of the ester groups results in the lowering of the plastic flow ability of the polymer, leading to embrittlement. In accordance with Abeysinghe et al., great amounts of isophthalic acid were found in the immersion baths. Further, a special role in the scission process was assigned to the ester groups, which were sensitized to the hydrolysis reaction by terminal isophthalic acid groups. The higher resistance of vinyl ester resins, compared to polyesters, is due to the fact that their ester functional groups are terminal and shielded by methyl groups, whereas in polyesters they are distributed along the main chain and therefore more susceptible to reactions.

Gu et al. [54] observed mass losses of up to 6 % of polyester films after 50 days in alkaline solutions at room temperature. This was almost as much as observed by Ashbee et al. in boiling water (100°C) and demonstrates once again the aggressiveness of the hydroxide ion to the ester linkages. They also assumed Abeysinghe's hydrolysis reaction in Figure 2.13b to be responsible for the mass reduction and that mass and water-soluble fragments of the polyester are leached into the solution.

The absorption rate inside the resin is controlled by the matrix structure or morphology and increases with a more open polymer network, as was found by Cohn and Marom [29], who studied the effect of polymer morphology on hygroelastic behavior by changing the polymer network structure. The matrix morphology, however, is not homogeneous and is influenced by the reaction of free radicals during the curing process. The result is areas with higher and lower crosslink density. Jacobs and Jones [56] found that areas with a lower crosslink density are more efficiently plasticized by water than highly crosslinked areas with a more distinct reduction in stiffness and glass transition temperature (T_g). Raghavan and Egwim [95] came to the same conclusion by investigating the degradation of polyester films exposed to an alkaline environment at 24°C. The heterogeneous structure with hard and soft regions in the resin was detected by atomic force microscopy (AFM) imaging before testing and was assumed to be a result of the entrapment of oligomers⁴/unreacted molecules in a sea of cured polymer film. After 21 days of exposure they found pits in which the microstructure was different from the surrounding material. They assumed the soft regions to be responsible for the faster degradation, leaving behind by-products as mentioned by Abeysinghe et al. [1], Bellenger et al. [16] and others. These pits were assumed to connect and provide channels for corrosive ions, which produce further degradation and confirm the assumption of diffusion-controlled degradation.

To ascertain the impact of combined swelling and shrinkage on tensile strength, Chin et al. [23] exposed dogbone specimens made of polyester resins to different solutions (water, salt-enriched and alkaline-enriched) at temperatures between RT and 90°C. While an increase in temperature had a detrimental effect on tensile strength, independent of the chosen solution, the alkaline-enriched solution accounted for the highest strength loss. For 90°C, for example, zero strength was reached after five weeks. The embrittlement was therefore shown to be solution-dependent with the alkaline composition having the strongest effect. Since the chemical processes were known, it could be shown that tensile strength depends directly on these reactions.

⁴Oligomers consist of a finite number of monomer units.

2.4.3. Fiber-matrix interface

To clarify the subject matter, the terms *interface* and *interphase* have to be differentiated. In general the term 'interface' is employed when there is no specific description that follows. The assumption in this case is a two-dimensional border separating fiber and matrix. However, to investigate this abstract border further, it can no longer be treated in two dimensions but a distinct and mechanically separable entity must be introduced. This 'interphase' has its own mechanical properties and its chemical composition can be altered by environmental influences. In the following, the fiber-matrix interface will therefore be considered as an interphase.

A composite, defined as a material system in which two or more distinct components interact synergistically to produce a superior material, is dependent not only on its distinct components but to a large extent on their synergistic interaction. The ability to interact is provided by their interphase, whose effectiveness is often limited to two extreme cases: perfect bonding or perfect debonding. The actual behavior will however be somewhere between these two extremes. Swain et al. [114] investigated hitherto microstructural models describing composite stiffness and strength properties. They found that these models do not take into account the mechanical properties of the interphase properly. In fact, they all assume perfect bonding, an unreal extreme case that reduces the interphase to a two-dimensional interface. To demonstrate the importance of real interphase properties, Drzal and Madhukar [39] conducted a comprehensive study of carbon fiber-epoxy composites in which they changed the interfacial shear strength (ISS) by different fiber surface treatments and studied the effect on composite strength and stiffness properties. They found that not only off-axis properties, i.e. transverse to the fiber direction, but also on-axis properties, i.e. in fiber direction, of the composite system are, sometimes considerably, affected by changing the ISS. This was true not only in terms of absolute values but also in changing failure modes. In fact, an excessive ISS may have detrimental effects, e.g. for longitudinal tensile strength, since the failure mode shifts from interfacial to matrix and the composite behaves like a brittle material, i.e. becomes 'notch-sensitive'. These reflections lead to the conclusion that a modern approach to understanding mechanisms in the composite system must take interphasial properties and changes into account.

The fiber-matrix interphase is essentially built up through the application of coupling agents. Coupling agents contain chemical functional groups that can react with silanol groups (SiOH^-) on glass, cp. Figure 2.14. The attachment to the glass is obtained by covalent bonds. In addition, coupling agents contain at least one other, different functional group which could co-react with the laminating resin during cure, Plueddemann [87]. The quality of the interphase is influenced by fiber surface treatment.

In addition to development of the interfacial bond, the coupling agent has the function of displacing absorbed water and creating a surface which can be fully wetted. For thermosetting resins, these three functions are best achieved by using silane coupling agents. In its aqueous size, its silanol groups hydrolyze leaving behind different deposits on the glass surface. Based on this, Jones [120] proposes a multi-monolayer model for the interphase. Figure 2.14 illustrates this with a γ -MPS⁵ silane coupling agent. A first strongly chemisorbed monolayer is found at the immediate glass surface (INT), followed by several

⁵ γ -methacryloxypropyltrimethoxy

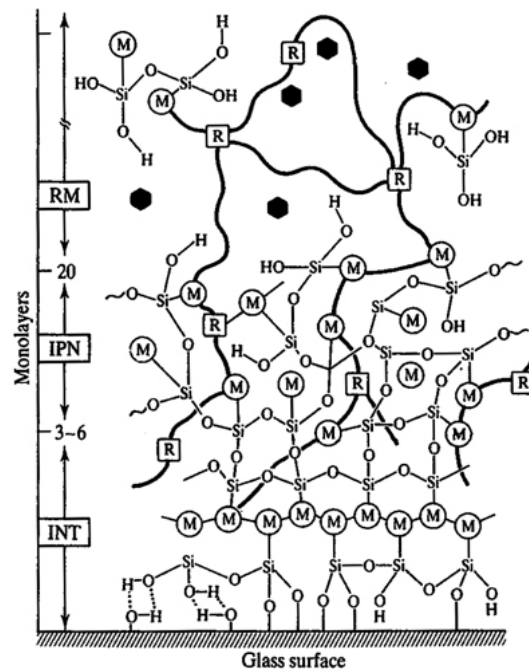


Figure 2.14: Multi-monolayer model after Jones [120]: INT: interface, IPN: interpenetrating network, RM: interpenetrating copolymer with resin matrix, (M): part of coupling agent, (●): dissolved binder and/or size

loosely chemisorbed and physisorbed overlayers (IPN, RM). Note that the term ‘interface’ used in the figure does not have the meaning of a two-dimensional layer as explained above, but describes a part of the interphase.

However, the reality is not as perfect as this theoretical construct. By-products of the coupling agent and poor fabrication lead to considerable differences in interphase properties and therefore affect the composite as a whole. Thomason [116] investigated the interphase of fifteen glass-epoxy composites using various techniques and found that the total amount of coating material on continuous glass fibers varied between 0.2 and 1.0 w.-%. Only 10-20 % was actually bonding to the glass and could not be removed with hot acetone. These alterations had a direct influence on interlaminar shear strength (ILSS), which varied between 55 and 90 MPa. Since direct experimental investigation of the interphase is complex, the ILSS is often taken as an indicator of interphasial shear strength, ISS, and therefore the quality of the interfacial bond.

The interphase will resist stresses perpendicular to the fiber surface, which will influence the composite’s off-axis properties, as well as those parallel to the fiber in the form of the ISS. The latter will influence the compression, tension and shear strength of the composite covering therefore the overwhelming part of possible composite solicitations and will be discussed in the following. To determine the ISS, one or very few single fibers embedded in a matrix are generally investigated. This system is very delicate and susceptible to all kinds of falsifying influences due to the experimental procedure. Friction between the fiber and matrix but also between the fiber and experimental set-up for instance are possible causes

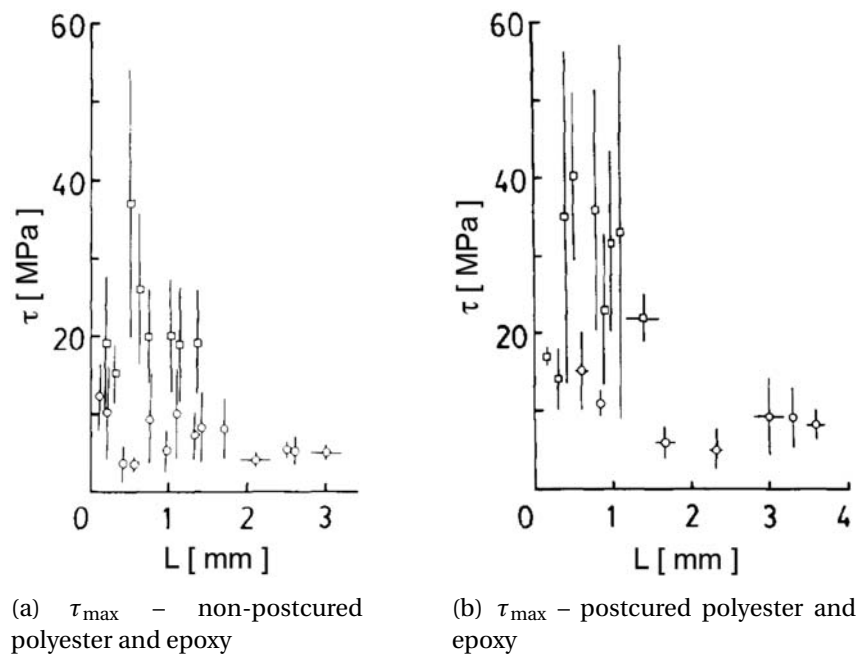


Figure 2.15: ISS of E-glass fiber-polyester (○) / epoxy (□) systems (taken from Chua and Piggott [27])

of unreliability. Chua and Piggott [27] investigated E-glass fibers embedded in polyester and epoxy resins. Their experimental procedure consisted of pulling three fibers synchronically out of the matrix. By means of a special experimental set-up, it was possible to vary the embedded fiber length between 0.1 and 3.5 mm. Their results are shown in Figure 2.15a and b. It can be seen that the ISS was generally higher in the epoxy than the polyester matrix. Also, the values decrease independently of the chosen resin type up to an embedding length of 1.9 mm, after which they remained constant. In the case of a postcured polyester matrix the average maximum ISS increased from 7 to 10 MPa, while in case of an epoxy matrix the increase was from 21 to 34 MPa.

Cheng et al. [110] investigated different sized E-glass fibers in vinylester and epoxy resins by means of the single fiber fragmentation test. The ISS for vinylesters varied between 16 MPa (warm water sized fibers) and 38 MPa (hot water sized fibers). They found an ISS of > 40 MPa independent of sizing; fibers without a silane coupling agent performed better than untreated fibers however. This illogical result was explained by the fact that even non-coupled fibers showed a tenacious layer on the fiber surfaces. It was concluded that a thin layer of coupling agent performs better than a thick one, which is in agreement with the model shown in Figure 2.14 with a layer thickness of only several nanometers. Also the findings of Thomason [116], who was unable to remove all the coupling agent, indicates a thin chemical-bonded layer. This thin layer seems to be the ideal case for a maximum ISS. Pavlidou and Papaspyrides [81] investigated its influence on the ISS in comparison with bare fibers. They conducted short-beam shear tests on woven E-glass fabric/polyester composite systems. Fabrics coated with different coupling agents as well as de-sized fabrics were considered. The de-sizing procedure included pyrolyzing the size by heating the fabrics at

600°C for 2 h. Since from microscopic observations it was obvious that failure took place in the fiber-matrix interphase, the ILSS was taken as the ISS. The ISS for silane-coupled fabrics was determined as being between 25 and 30 MPa and did not change as a result of water exposure cycles. On fabrics without coupling agents, the ISS fell to ~17 MPa and was slightly affected by water exposure cycles. From these results it was concluded that indeed the coupling agent increased the ISS because the bond was chemical rather than mechanical. This means that the de-sizing procedure must have removed the coupling agent and organic impurities completely this time, as compared with the study of Cheng et al.

As the composite is exposed to moisture, the matrix deforms due to swelling and shrinking (see above). Resulting stresses and chemical reactions in the interphase can lead to its failure, with subsequent debonding between the fiber and matrix. A first attempt to quantify ISS degradation was made by Ashbee et al. [11], who measured the optical retardation produced by stresses in the fiber and surrounding matrix in glass/polyester composites. By comparing retardation between the matrix and the fiber, they were able to detect the amount of interfacial shear transferred between the components, which will be zero in the case of debonding. In composites with uncoated E-glass fibers in 20°C water, measurements revealed the initiation of debonding after approximately 20 min and complete debonding after approximately 1.75 h. At 100°C exposure, debonding occurs within a few minutes. The authors claimed that at no stage was any damage visible under a scanning electron microscope and that therefore the debonding process would not have been detectable visually. The situation changed when the fibers were coated with a coupling agent. Now, during a period of 10 months, no fiber debonding was observed for composites immersed in 20°C water. Even in boiling water, the interphase withstood 60-80 h before there was no longer any shear transfer measured. By means of transmission-optical micrographs, the debonding process was identified as an accumulation of single 'bubbles' that develop after approximately four hours and subsequently interconnect to form a continuous debonding.

The fiber-matrix interface is a preferred pathway for ingressing moisture. Once the ingressed moisture begins to react chemically with the glass, accelerated degradation of a composite's ISS is also caused by the leaching of alkaline components from the glass, in turn increasing the concentration of OH⁻ ions in the interphase. By comparing a glass fiber/vinylester composite immersed in phenol red solution for 40 minutes and three weeks, Prian and Barkatt [91] observed an increase in the pH of the solution. According to Chateaubenois [21], such a process will accelerate debonding and open channels for the penetration of the attacking medium.

A quantitative measurement was performed by Gaur and Miller [48], who investigated the ISS of E-glass and Kevlar-reinforced epoxy resins using a microbond technique, whereby a fiber is pulled out of a droplet of resin deposited around the fiber. For the E-glass fibers, the initial ISS was between 40 and 45 MPa, which is in good agreement with the values of post-cured epoxy from Chua and Piggott [27]. After only 15 minutes in 88°C water, however, the ISS dropped to approximately 50 % of the initial value to 20-30 MPa and remained constant thereafter. The same initial drop was seen on Kevlar fibers in epoxy resin (cp. Figure 2.16a). Similar results were obtained by Chua et al. [26], who immersed E-glass fiber-reinforced polyester in hot water at temperatures of 22, 60 and 75°C and measured the ISS for up to 13 000 hours. They found almost complete debonding in the case of the 75°C immersion after 300 hours, whereas even after the 13 000 hours, specimens conditioned at 22°C

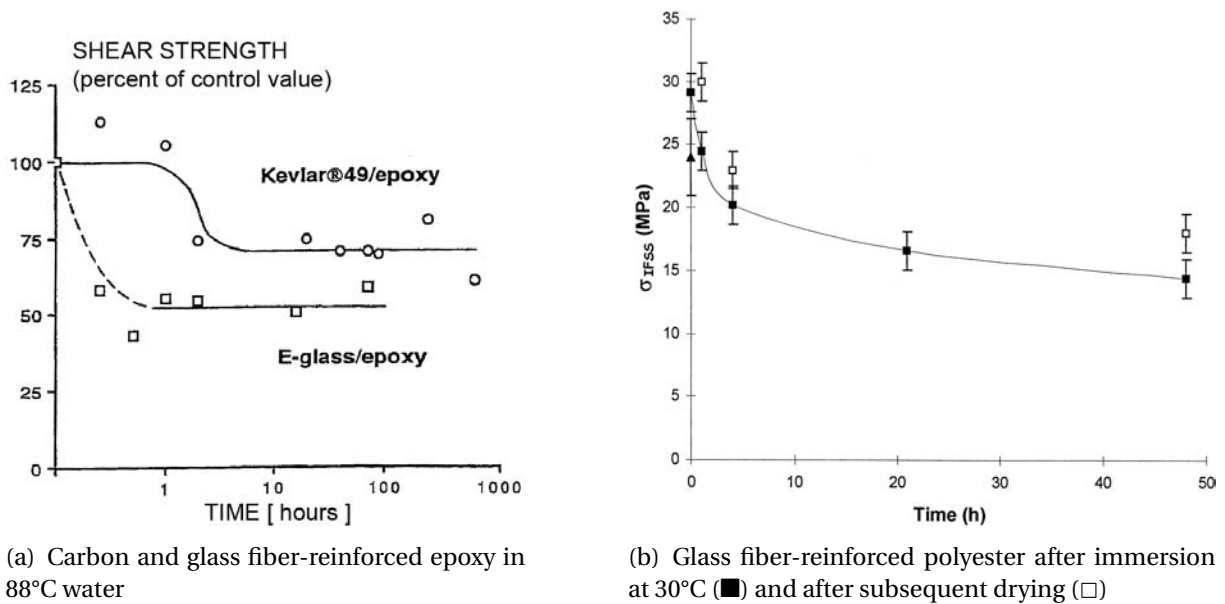


Figure 2.16: ISS degradation (taken from Gaur and Miller [48] and Gautier et al. [49])

showed only a small degradation of ~13 % compared to initial values. Gautier et al. [49] were able to measure the ISS degradation of glass fiber-reinforced polyester composites by using the same microdroplet test as Gaur and Miller [48]. The immersion medium was water and the temperature 30°C. The curve is shown in Figure 2.16b. After a time span of 50 hours the ISS dropped by 50 % and still showed a tendency to fall. After several immersion periods the specimens were dried and tested for their strength. From the figure it can be seen that the strength recovery remained constant at ~5 MPa over the whole observation period, initially resulting in a complete recovery of the initial values. From this observation it was concluded that damage induced in the first four hours was reversible, whilst subsequent damage was irreversible. By comparing Figure 2.16a and b, the initial drop can be seen in the E-glass/epoxy as well as in the E-glass/polyester system. At the lower temperature of 30°C, however, the initial drop is decelerated and strength falls to only ~70 % of its initial value, with a subsequent decrease.

2.4.4. Composite system degradation

In an effort to evaluate the suitability of composites made of isophthalic polyester (IPE) resins compared to vinylesters (VE) in civil engineering applications, Dagher et al. [32] reviewed twenty durability studies on both composite types that took place between 1995 and 2002. In addition to the general observation that composite resistance to chemical impact depends to a large extent on manufacturing process and exposure type, making comparison rather difficult, the authors concluded that there is little difference in tensile strength loss between IPE and VE in concrete-pore solutions (alkaline environments) if cast resin types, which do not represent the real end products, are being used. In a composite system, however, the VE showed superior properties. The situation seems to change when acid environ-

ments are used - here the IPE shows a slightly better performance than the VE. Concerning diffusivity and resistance to chemical attack in non-alkaline environments, the VE showed the better performance, which is in agreement with Johnson [59], cp. page 24. At high temperatures, both resin types showed adverse effects, which were more pronounced in the case of IPE.

In general, the presence of moisture has the strongest impact on composite degradation. Weitsman [122] pointed out that moisture absorption, desorption and resorption curves in composites do not replicate each other, a fact that is amplified by external loads. This is considered to be a result of accompanying internal damage and contradicts the theory of reversible damage from diffusion and swelling.

Fried [47] reports on the compressive strength behavior of 'early types'⁶ of polyester laminates exposed to sea water at sea temperature. All curves showed a period of relatively rapid degradation at the beginning of the exposure, followed by a period of diminution of degradation rate, and finally a flattening-out, with no further degradation after further time exposure. Stiffness, however, was affected to a much lesser degree (if at all) by water immersion, which was demonstrated with epoxy laminate exposed to sea water at 917 bar over a time span of twelve months. It had already been estimated that a 'two-hour boil' is equivalent to approximately one month's exposure to water at room temperature.

The combined impact of moisture and temperature on polymers was investigated by Gopalan and Somashekar [53]. Measurements of the stiffness and ultimate strength of several types of E-glass/epoxy composites showed a decrease in both material properties after immersion in 70°C water for 20 days. The lowest degradation was found for unidirectional fiber alignments, followed by bidirectional and, finally, randomly distributed fiber alignments in the composite. By means of combined acoustic emissions and strength measurements, however, the hygrothermal conditioning was found to alter the failure mechanism from gradual to brittle and catastrophic. This would make sense in light of the findings concerning the degradation mechanisms of the resin matrix, cp. Section 2.4.2.

Ghosh and Bose [52] compared the tension and flexural strength of N- and E-glass reinforced isophthalic polyester rods with N-glass fibers having higher proportions of SiO₂, Na₂O and K₂O compared to the E-glass fibers. The rods were immersed in different solutions (10 % HCL, 0.5 % NaOH and 10 % NaCl) at 100°C up to a time span of 350 h. The E-glass fiber-reinforced composite showed a sharp loss (~60 %) of flexural strength within the first 20-30 h in the HCL and NaOH solutions, and even in the NaCl solution a loss of ~50 % was seen within the first 100 h. Afterwards the strength reduction rate diminished abruptly. N-glass reinforced composites, in contrast, only showed gradual flexural strength decreases. Accordingly, SEM images made of both composites after 24 h boiling in the HCL and NaOH solutions should show a more severe degradation of the E-glass reinforced composite. The difference in strength decrease was confirmed by SEM-microscopic images, which showed comparable conditions for untreated composites. However, once exposed to the chemical solutions the E-glass reinforced composite suffered to a much higher degree than the N-glass variant and showed severe debonding of the glass strands. This was assumed to be the reason for the difference in strength decrease.

⁶181-Garan, 1000-Volan, 1½OZ. Mat-Garan and Woven Roving-Garan

Sonawala and Spontak [112] investigated the flexural and tensile behavior of polyester- (IPE) and vinylester- (VE) based composites in two solutions containing 5 % of NaCl and 10 % of NaOH, respectively, at 25°C over a time period of up to 270 days. After exposure to the NaCl solution, they observed a tensile strength reduction of 31 % for the IPE, which they attributed to fiber-matrix debonding and water-induced polyester plasticization. Contrary to that which occurred at high temperatures however, no sudden strength reduction was observed. The VE showed a better performance and lost only 16 %. Regarding flexural behavior, however, the polyester composite performed better, which was ascribed to a crack blunting of the liquid once the moisture concentration inside the resin reaches a level of ~0.32 %, making the composite more flexible. In the NaOH solution, maximum moisture content for the IPE was over 10 %, while the VE absorbed only approximately 1 %. Contrary to the NaCl solution, the tensile strength of the IPE fell dramatically (by about 85 %) in the first 30 days and afterwards remained constant at ~10 % of the original value. The explanation for this dramatic change in behavior was seen in the simultaneous destruction of the resin and glass fibers. The deterioration of the fibers will contribute once more to the destruction process through the accumulation of degrading chemical residues in the fiber-matrix interface (cp. also Prian and Barkatt on page 31). It was emphasized that the IPE's ester linkages are especially prone to hydrolysis in the presence of an alkali. The flexural strength decrease for both composites in the NaOH solution was more pronounced than in NaCl, with the retention for the IPE being only 20 % of its original value. The VE performed much better however with a strength retention of 70 %.

Chin et al. [25] exposed vinylester- and polyester-based composites to de-ionized water, salt and alkaline solutions at room temperature for a time span of 54 days and tested their tensile strength. The results differ significantly from those observed by Sonawala et al. While Chin et al. observed almost no changes in values and even some strength gain, Sonawala and Spontak measured strength decreases throughout and particularly in the NaOH solution. In view of the large standard deviations in the measurements of Chin et al., the values for the NaCl solution may be explained, but in the case of the alkaline environment, no explanation for the high values can be given.

Shao and Kouadio [107] immersed glass reinforced polyester specimens made from sheet piles in tap water at 23 and 70°C for up to 260 days. Measurements concerned the moisture uptake and mass loss as well as tension strength and elastic modulus in the pultrusion direction. The maximum moisture content was ensured by specimens immersed in 100°C tap water, which were also corrected for mass loss. The mechanical properties were measured at the same time as moisture content. It was thus possible to link mechanical properties directly to moisture content. As could be predicted, tensile strength decreased with an increasing percentage of moisture and was higher at 70°C than 23°C. The maximum strength reduction was estimated as 60 % of the original value. Interestingly, however, the elastic modulus of the aged composites remained almost constant, irrespective of test temperature and age in water.

Kootsookos and Mouritz [65] investigated glass fiber-reinforced polyester and vinylester composites. Weight gain measurements in sea water at 30°C showed a chemically less stable polyester system, which was ascribed to the susceptibility of the polyester resin to hydrolysis and the leaching of ester species with hydroxide end groups and other low molecular weight material. Flexural measurements revealed no obvious correlation between flexural

modulus and immersion time. Interestingly, the flexural strength of the vinyl ester composite decreased to a greater extent than that of the polyester composite, which was not explained.

2.5. Lifetime predictions

2.5.1. Introduction

In civil engineering, the lifetimes of buildings and constructions are of several decades, drastically increasing durability claims in comparison with aircraft or vehicle construction. They therefore have to be designed using materials that guarantee reliable service for decades thanks to their durability. Since these properties also have to be specified for new materials that have not yet withstood environmental impact over such long periods, artificial laboratory treatment, accelerating the aging process, is essential. Degradation may be accelerated by exposure to elevated temperatures, exposure to increased moisture concentrations, increased chemical concentration or fatigue treatment at high frequencies.

Rostasy [98] reports on several methods of investigating long-term behavior. Investigations concerning stress-rupture behavior in dry air (20°C and 65 % RH) showed a characteristic long-term (10^6 h) strength of 70 % of initial strength. Exposed to permanent contact with dissolved alkali (1.0N NaOH and cementitious extract at 23°C), glass fiber rovings exhibited a significant loss of short-term tensile strength within 1 000 h. If degradation is accelerated by an increase in temperature, it is possible to determine its rate and quantify a specific state of degradation. This quantification is based on the Arrhenius rate law. Prediction, however, relies on certain preconditions concerning the degradation mechanism that have to be verified.

2.5.2. Arrhenius-type prediction

The relationship between chemical reaction rate, k , and temperature, T , was developed at the end of the 19th century. It was found that an experimental plot of ' $\ln k$ vs. $1/T$ ' appeared to be approximately linear with a negative slope and several equations were suggested. It was not until the 1920s, however, that the approach proposed by van't Hoff (1884), Arrhenius (1889) and Kooij (1893) was recognized as being the most accurate, cp. Laidler [66]. It became known as the *Arrhenius rate law* and is shown in Equation 2.23. According to this, the reaction rate, k , is the product of a pre-exponential or frequency⁷ factor, A , and an exponential term as

$$k = A \cdot \exp \frac{-E_A}{RT} \quad (2.23)$$

where E_A [J/mol] is the activation energy, $R = 8.314$ [J/(K mol)] is the universal gas constant and T [K] is the absolute thermodynamic temperature. If the difference between two temperatures is small, A and E_A can be treated as constant. In case of wide temperature ranges and more precise rate-temperature data, A is usually allowed to be proportional to T raised to the power m as shown in Equation 2.24, where A' is temperature-independent, cp. Lai-

⁷This factor takes into account the frequency of collisions between atoms and varies slightly with temperature.

der [66]. For engineering purposes, however, this variant is rather of theoretical interest and will not be treated further.

$$k = A'T^m \exp \frac{-E_A}{RT} \quad (2.24)$$

The activation energy, E_A , is the energy that must be overcome in order for a chemical reaction to occur. Activation energy may otherwise be denoted as the minimum energy necessary for a specific chemical reaction to occur. A graphical representation is shown in Figure 2.17, where an endothermic reaction only proceeds after the necessary activation energy is added to the products before they lose a thermodynamic quantity, E_{RXN} . Since each chemical process has its own activation energy, values obtained from material strength degradation will represent a mean value of several chemical processes involved.

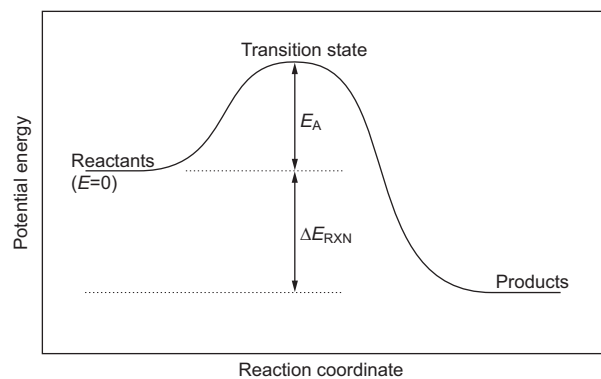


Figure 2.17: Input and output energies in chemical reactions, E_A and E_{RXN} (thermodynamic quantity)

Equation 2.23 shows that, if A and E_A remain constant, the reaction rate, i.e. the speed of a chemical reaction, will increase with increasing temperatures. The chemical process at a high temperature will pass through the same stages as at a lower temperature but in less time. This means that in the same time span, therefore, it is possible to predict the future progress of a chemical reaction by increasing the temperatures. The amount by which the reaction can be accelerated is expressed by a time-shift factor, α_T , which is equal to the ratio of two reaction rates at different temperatures⁸. Equation 2.25 shows the calculation where $T_2 > T_1$.

$$\alpha_T = \frac{k_2}{k_1} = \frac{A \cdot \exp \frac{-E_A}{T_2 \cdot R}}{A \cdot \exp \frac{-E_A}{T_1 \cdot R}} = \exp \left[\frac{E_A}{R} \cdot \left(\frac{1}{T_2} - \frac{1}{T_1} \right) \right] \quad (2.25)$$

It can be seen that, once the activation energy is known, the acceleration between two temperatures can be calculated independent of the temperatures applied in the experi-

⁸E.g. $\alpha_T = 2$ means that the higher temperature T_2 , reduces the time to reach a given remaining strength by 50%. The length of the time interval can therefore be multiplied by two.

ments. In a plot ' α_T vs. T ', the activation energy can be obtained by fitting Equation 2.23. If the measured process is composed of several chemical reactions, which all follow the Arrhenius rate law, the calculated activation energy represents a weighted average of all the reactions involved. In accelerated aging experiments, aggressive chemical reactions will lead to degradation of the material entailing a reduction of its mechanical properties. If the relationship between chemical reactions and resulting strength reduction is proportional, the measured strength can be predicted.

2.5.3. Prediction studies

In the 1970s, the need to predict the long-term performance of the newly introduced FRPs (cp. Section 2.2) motivated researchers from the beginning to carry out accelerated aging studies. Thus, in 1971 Moehlenpah et al. [3] reinforced epoxy resin with different types of fillers: continuous glass fibers, glass beads and air (foam). The specimens were tested for their elastic properties in tension, compression and flexure in a dry environment at temperatures between -1 and 107°C and at strain rates between $(10^{-4} \div 10 \text{ in.})/(\text{in. min})$. It was found that the initial tangent moduli, stress relaxation and yield⁹ stress data of epoxy composites can be correlated by 'time-temperature shift factors'. For the initial tangent moduli and stress relaxation, shift factors were identical. In all cases, they were independent of loading mode and filler type, despite the fact that the actual values of yield stress and strain as well as transition temperatures for failure modes were affected by these variables. From these findings it was concluded that shift factors were a property of the matrix only and independent of the state of stress.

In 1974, Hojo et al. [55] investigated epoxy resins with added silica particulate filler of different diameters at temperatures between 25 and 110°C for tensile, flexural, creep rupture and impact material properties. Short-term strength was generally found to decrease with the increase of both temperature and filler size. Additionally, an Arrhenius plot of failure times ($\log(t_{\text{failure}})$ vs. $1/K$) for various filler sizes and contents converged at the glass transition temperature of the material. By means of this relationship, it was possible to modify the Larson-Miller master rupture curve¹⁰ to take filler size into account and predict the long-term strength of particulate-filled epoxy composites.

A pioneering study in which accelerated degradation was used to predict quantified long-term behavior was made in 1981 by Litherland et al. [70]. They investigated the flexural strength of Cem-FIL AR glass fiber mats in rapid-hardening Portland cement flat sheets immersed in water at temperatures varying between 4 and 80°C. They found two distinct phases of strength development over time, which were more pronounced for high temperatures and inexistent at 4°C: one initial steady fall followed by a constant/near-constant strength region, the remaining strength. In the first phase, strength decreased more rapidly with increasing temperatures as shown in Figure 2.18. The remaining strength appeared to be independent of temperature. By plotting the curves against a logarithmic time axis, the initial strength degradations at different temperatures were parallel. The similar strength characteristics at different temperatures indicated that the chemical reactions leading to strength degradation

⁹Here 'yielding' refers to polymers in a rubbery state.

¹⁰The Larson-Miller relationship is an extrapolation often used to describe the time to rupture based on temperature and stress.

follow the Arrhenius rate law. Real weathering studies at different mean ambient temperatures showed a similar strength decrease to laboratory testing, confirming the assumption of the Arrhenius-type behavior. A normalized Arrhenius plot made it possible to extrapolate the measured data up to a factor of 100 and more. However, it was not clear at that time whether the observed, and therefore predicted, remaining stress level would also occur in reality. For this reason Aindow et al. [4] tested the strength of additional glass fiber-reinforced concrete (GRC) composites weathered over 5-6 years in a number of hot climates and transposed the results to the colder temperatures for which the data of Litherland et al. also apply. By doing so it was proven that the lower strength limit exists and that, therefore, the shift from the 80 to the 4°C curve produced reliable results.

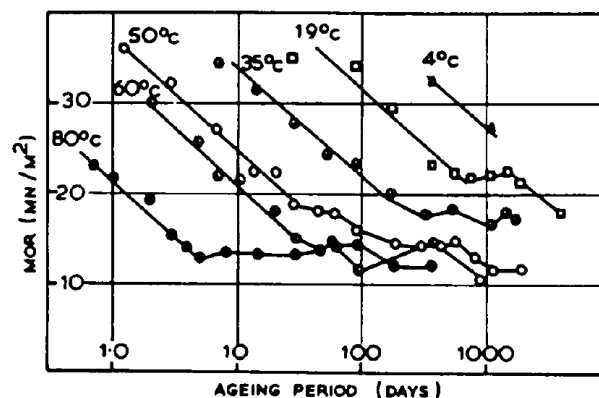


Figure 2.18: Strength retention of glass fiber-reinforced concrete (GRC) specimens at different temperatures (taken from Litherland et al. [70])

The time-shift factors obtained from the Litherland study with the close correlation between predicted and measured values were used afterwards in other studies to justify long-term behavior. Thus, Porter and Barnes [88] used the obtained time-shift factor of 279, which represents the difference between the 60°C alkaline bath and 'real-world age' to predict the tensile and pull-out strength development of E-glass fiber-reinforced vinylester composites in alkaline solutions at 60°C. A second study relying on the Litherland data was performed by Vijay and GangaRao [121]. They investigated the tension strength of E-glass fiber-reinforced rebars conditioned in alkaline and salt solutions over a period of 15 months. They found their strength development qualitatively similar to Litherland's, but three times faster. They calibrated the original data to their local mean temperatures and obtained an acceleration factor of 17, which they multiplied conservatively by two instead of three with their final time-shift factor hence being 34.

In an effort to predict the tensile strength of glass fiber-reinforced polyester laminates, Pritchard and Speake [93] measured the water absorption kinetics of cast resin and laminates at temperatures between 30 and 100°C. In addition to water absorption, the laminates were tested for their strength and stiffness, which proved to be functions of the absorbed moisture content. By extrapolating the diffusion curves to an assumed temperature of 15°C, they were able to predict the tensile strength for a time period of 25 years. The 30°C curves for tensile strength and stiffness predicted from the 90°C measurements were compared to

actual results at this temperature measured over a period of three years. The agreement was satisfactory and therefore the authors concluded that it is possible to extrapolate accelerated processes beyond the experimental period. The relationship between moisture uptake and stiffness was explained by Martin and Campion [73], who reasoned that if diffusion and chemical reactions both follow the Arrhenius rate law and there is a linear relation between network density and stiffness, increased temperatures can be used to accelerate the aging process.

The Arrhenius rate law was increasingly accepted as a reliable tool to predict long-term strength for FRP. Gerritse [51] discussed the possibilities of accelerated aging methods. From results showing no strength degradation for Arapree[®] FRP tendons in pre-stressed concrete after three years and 60°C and the Arrhenius extrapolation, he concluded that it is “obvious that the tested aramid-based tendons do retain more than 80 % of their original capacity after 100 years at room temperature.” Further he concluded from the uniformity and parallelism of the strength degradation lines over time that “investigating one single point (e.g. 180 days in alkaline solution at 80°C) can already indicate an extrapolated residual strength of over 80 % after 100 years in real time”.

With the advent of FRP rebars reinforcing concrete structures, the Arrhenius rate law was applied to confirm the long-term behavior of these products in the aggressive alkaline environment in the concrete. Porter and Barnes [89] used their own results for GFRP rebars in alkaline solutions (pH 12.5-13.0) at 60°C, that they tested for their tensile strength over a period of 2-3 months. They compared their data to results obtained from natural weather exposure by Proctor et al. [94] and elaborated accelerating factors for different mean annual temperatures (reference temperatures). For a reference temperature of 10°C they obtained the relationship¹¹

$$\text{Age}(\text{days}/\text{day}) = 0.2 \cdot \exp(0.0935 \cdot T). \quad (2.26)$$

They expressed some reserve concerning the use of this formula for applications in a real environment. It was considered rather as a tool providing indications and it was recommended that results be analyzed with some caution. Some further retention in applying the Arrhenius rate law for life-time prediction came from Prian and Barkatt [91]. They measured fiber dissolution as a function of time, hydrolytic depolymerization of the matrix surrounding the fibers and crack formation in the matrix. The materials were E-glass fiber-reinforced vinylester and polyester composites, which were immersed in deionized water at temperatures between RT and 80°C. They found an increased pH in the fiber-matrix interface, which could only have resulted from the leaching of the fibers. The increased pH was responsible for accelerated degradation of the fibers and resin. Since the destroyed interface served as a pathway for the attacking liquid, destruction processes are accelerated in aqueous media. Consequently, even when the mechanical properties follow the Arrhenius rate law initially, delayed rises in degradation rates can occur in the course of exposure. The authors conclude that this additional degradation must be quantified in order to apply the Arrhenius rate law to predict long-term behavior.

An extensive study concerning the durability of GFRP re-bars in alkaline solution was

¹¹The exponential term is recalculated here to apply to °C.

undertaken by Dejke [33], who tested up to 1400 specimens immersed at temperatures between 20 and 80°C. The time-shift factors (α_T) as obtained by applying the Arrhenius rate law are shown in Table 2.2. Four different types of rebars, differing in their resin (vinylester/polyester) and fiber (E-/AR-glass) composition, were investigated (nomenclature in Table 2.2). In contrast to lower temperatures, the polyester rebars exposed to the 60°C solution lost all matrix material after approximately two months and weight gain was of 80%. The specimens became very soft and practically fell apart when taken out of the baths. From this it was deduced that the degradation process was different at 60°C and the Arrhenius prediction was only applied to the vinylester bars. There, α_T at 60°C amounts to ~ 30 in cases of the gray and yellow bars and ~ 80 in the case of the Fiberbar. This remarkable difference in prediction ability was not discussed. However, the bar diameter was smaller in the case of the Fiberbar and this may have influenced the degradation speed at 60°C. It was furthermore suggested that α_T obtained at a temperature of 80°C would be “somewhat questionable”.

Table 2.2: Obtained α_T for a reference temperature of 10°C (designations taken from [33])

Bar	Fiber	Resin	Temperature [°C]			
			20	40	60	80
Gray bar	E-glass	Vinylester	2.1	8.4	28.2	82.3
Yellow bar	AR-glass	Vinylester	–	–	28.2	–
Green bar	AR-glass	Polyester	No prediction			
Fiberbar	E-glass	Vinylester	–	–	81.4	–

Another application was presented by the Naval Facilities Engineering Service Center [19]. They tested the bending stiffness for glass and carbon fiber-reinforced polyester, vinylester and epoxy composites exposed to salt vapor at 35, 49 and 71°C over a period of three months. Using the Arrhenius rate law they obtained time-shift factors of 4.5 and were able to predict 13.5 months for a reference temperature of 26.7°C.

A precondition for the application of the Arrhenius rate law is that chemical reactions at all used temperatures remain unchanged, which can be shown by means of an Arrhenius plot ($\log(t_{\text{failure}})$ vs. $1/K$). If the chemical reactions are following the Arrhenius rate law, the relationship between temperature and failure criterion should be linear in the plot as was the case with Litherland et al., who showed a very close linear dependency between data in laboratory testing and in the outdoor environment. Chin et al. [24] immersed vinylester and polyester composites in water, salt water and artificial concrete-pore solution. By testing the interlaminar shear strength at RT, 40, 60 and 80°C, they obtained the Arrhenius plot for the time to 30% strength reduction. They observed good correlation (0.94–0.99) for all vinylesters and polyesters in water and salt water. For the polyester in the pore solution, however, correlation was only 0.84. From this observation they concluded that “accelerated aging methods utilizing temperature as the acceleration factor are not valid for exposures in which severe resin degradation was observed.” However, this conclusion is arguable, since the Arrhenius plot for this experimental combination was almost constant and the correla-

tion, therefore, is highly susceptible to small changes¹². The same subject was part of another study conducted by Chin et al. [23]. They presented Arrhenius plots of the natural log of time to reach 70 % of the original tensile strength vs. $1/T$ of vinylester and polyester pure resins immersed in water, salt water and artificial pore solution and tested them for their tensile strength. The combinations of both resins with water and salt water could be fitted with correlations above 95 %. However, pore solution data for vinylester and polyester did not fall on a line, from which the authors inferred that accelerated aging methods utilizing temperature as accelerating factor may not be valid in hot environments owing to exaggerated matrix degradation.

In 2002, Bank et al. [15] and Gentry et al. [50] presented an accelerated-test-based specification for FRP in structural systems, which includes vinylester, epoxy and isophthalic polyester resins reinforced with glass and carbon fibers. The medium chosen was de-ionized water at a maximum temperature of $T_{\text{ref}} = 0.8 \cdot T_g$. Altogether four temperatures have to be applied, of which the three lower ones are $T_{\text{ref}} - (1, 2, 3) \cdot \Delta T$ with $\Delta T = \frac{T_{\text{ref}} - 40^\circ\text{C}}{3}$. Specimens have to be immersed for periods of 28, 56, 112 and 224 days and tested in tension and short-beam shear. Specimens exhibiting gripping problems can also be tested in three-point bending. To demonstrate the methodology, flexural bending and short-beam shear tests were performed on pultruded E-glass/vinylester rods. Temperatures were 40, 60 and 80°C, with durations of between seven and 224 days. The Arrhenius plot showed linear relationships between the different temperatures, thereby confirming the validity of the method. Using this data it was possible to predict a strength degradation of 50 % after 49 years. The limits of the method are reached once the strength-time curves of different temperatures cross, which would imply a given time at which the material degrades to the same extent at two different temperatures. This would, therefore, contradict the inherent assumption of increased degradation at increased temperatures.

In an effort to establish criteria for a finite difference diffusion/finite element stress code, Phifer and Lesko [85] investigated the diffusion characteristics and strength reduction of hygrothermally-aged vinylester/E-glass pultruded composites. Tensile strength data was collected during 600 days in water at temperatures between RT and 80°C. It was found that the diffusion and maximum moisture content were following the Arrhenius rate law. The strength reduction could be modeled by a double exponential equation in the form shown in Equation 2.27. Here the two exponential terms refer to different damage mechanisms (fiber degradation and resin or interface degradation).

$$\sigma(t) = \sigma_1 \cdot \exp\left(-\frac{t}{\tau_1}\right) + \sigma_2 \cdot \exp\left(-\frac{t}{\tau_2}\right) \quad (2.27)$$

The terms in brackets represent the mechanism's reaction rate, which was found to follow the Arrhenius rate law, and therefore

$$\frac{1}{\tau_i} = k = \frac{1}{\tau_{0,i}} \exp\left(\frac{-E_A}{RT}\right) \quad (2.28)$$

¹²Good correlation between two sets of data signifies that they are linearly related. A correlation coefficient of 1/-1 signifies perfect linear dependency while 0 signifies no correlation at all. Data in which one set remains constant signifies, therefore, no dependency between sets.

with $\tau_{0,i}$ and σ_i as constants ($i = 1, 2$). Furthermore, a linear relationship between moisture content and tensile strength was apparent and therefore maximum moisture content served as an indicator for strength behavior. An Arrhenius analysis of moisture content revealed that after 600 days only 10 % of its maximum value had been achieved and that the point in time at which equilibrium moisture content is reached would not occur before 21 years at 25°C, 8.7 years at 35°C and 3.7 years for 45°C immersion.

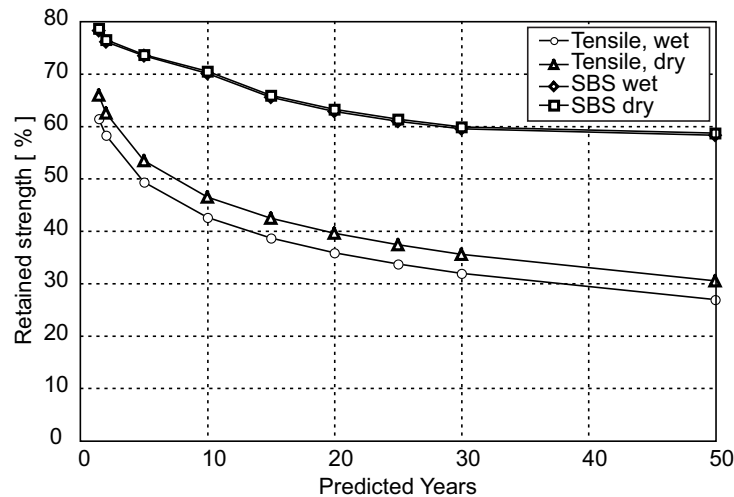


Figure 2.19: Predicted values of strength retention - tensile and short-beam shear (taken from Karbhari and Chu [60])

Karbhari and Chu [60] immersed E-glass/vinylester composites in alkaline environments (pH 11.5) at temperatures between 23 and 80°C. It was argued that, if diffusion coefficients have a linear relationship with applied temperature, which was the case ($E_A = 15.15$ kJ/mol), Equation 2.23 could be applied to predict long-term behavior. Based on these assumptions, behavior in tension and interlaminar shear was extrapolated to a time span of 50 years ($\alpha_T = 34.7$) for a reference temperature of 20°C. Figure 2.19 shows the curves for wet specimens tested immediately after removal from the bath and specimens that were dried before testing. It can be seen that there is significant strength regain for specimens tested in tension, but no regain for specimens tested in short-beam shear. From this it was concluded that the damage to the composite consisted primarily of fiber-matrix debonding, which influences interlaminar shear strength to a much higher degree than tensile strength.

Chen et al [22] immersed E-glass fiber-reinforced vinylester rebars in two different alkaline solutions with pH of 13.6 and 12.7 at temperatures of 20, 40 and 60°C. The different solutions represented normal and high performance concrete, respectively. The bars were taken off the baths and tested for their tensile strength after time spans between 60 and 240 days. The degradation curves for the different temperatures were parallel in an Arrhenius plot and yielded acceleration factors α_{20-60} of 1.8 (pH 13.6) and 7.5 (pH 12.7). The authors conclude consequently that master curves obtained from different solutions are not interchangeable.

2.6. Conclusions

The state of the art regarding the use of FRP materials for reinforcing concrete structures showed that development has focused entirely on one-dimensional elements (rebars) loaded in tension. Three-dimensional structures were obtained by linking these elements together rather than using the pultrusion technique to create them directly. Therefore, the structural behavior of such elements as concrete reinforcement has never been investigated and nothing is known about their performance.

Since the 1970s when research on diffusion into FRP began, mature methods have been developed to model the orthotropic diffusion behavior of liquids in the profile. The degradation mechanisms of the matrix and the principal mechanisms in the glass and the fiber-matrix interface are also well understood. Little interest has been expressed in their impact on strength degradation in compression however. Research on fiber-matrix interfacial strength degradation over time is still particularly inadequate and observations are required for each specific case.

Lifetime predictions based on the Arrhenius rate law have been applied to FRP materials since the beginning of the 1980s. Subsequently, a number of studies carried out entirely in tension showed that material and strength degradation are proportional and thus that the Arrhenius rate law is applicable in tension. In compression, however, no such analysis has ever been carried out. Apart from one example of a multi-exponential approach for modeling strength degradation over time, all existing studies suggest a logarithmic fitting function, which in most cases offers a satisfactory solution.

3. Multifunctional GFRP elements

3.1. Introduction

In order to create the hybrid GFRP/steel joint shown in Figure 1.2, a GFRP compression-shear element (CS-element) was designed. To further develop the hybrid joint into an all-GFRP joint comprising only two bearing elements as shown in Figure 3.1, in addition to the CS-element a tension-shear element (TS-element) was developed. Since the hybrid joint was of direct practical interest, while the all-GFRP joint remained an earlier development stage, the CS-element already employed in the hybrid joint was investigated in detail, while the TS-element is presented at the end of this chapter.

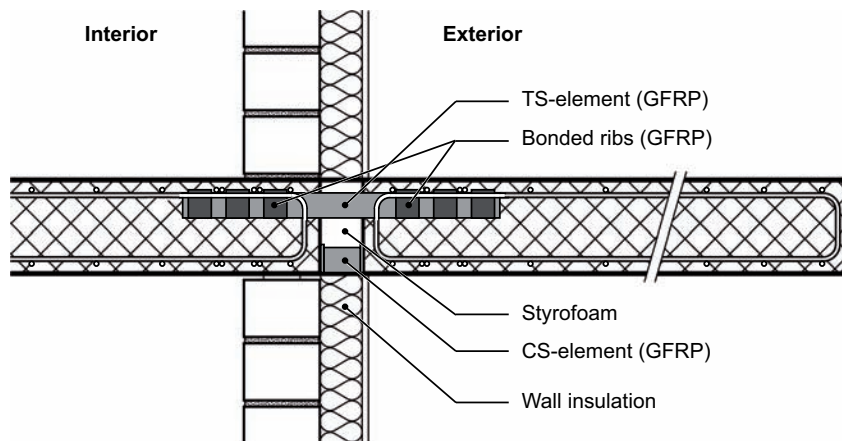


Figure 3.1: New thermally- insulating all-GFRP joint in balcony slab at insulating-layer location of facade

The use of GFRP elements in a concrete environment exposes the material to moist and alkaline impact, which will degrade the material, cp. Section 2.4. The CS-element's remaining compression strength after material degradation must be known in order to apply it in practice. Therefore, several studies including compression experiments on elements exposed to alkaline artificial concrete-pore solution, diffusion behavior and microscopic investigations were conducted to investigate the element's long-term behavior.

3.2. Description of the CS-element

The CS-element consists of a pultruded profile with two bonded cap plates. Its design was determined by four criteria:

- Economic considerations
- Resistance against buckling under compressive loading

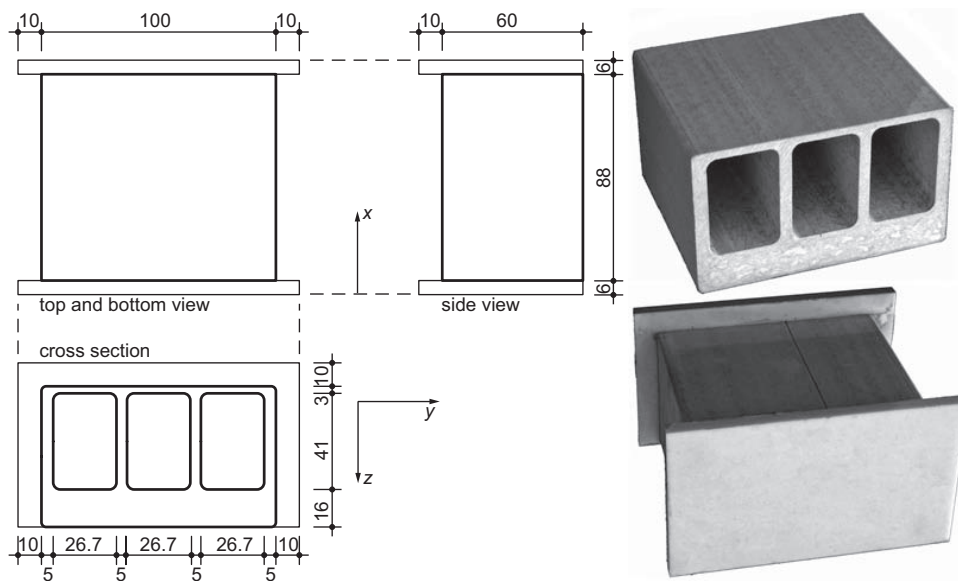


Figure 3.2: GFRP CS-element uncapped and capped - appearance and dimensions

- Ability to transfer shear through the webs
- Resistance against alkaline impact

The optimized profile is pultruded in one step and has a width×depth cross section of 100×60 mm, cp. Figure 3.2. Its upper flange is 3 mm thick and the lower flange has a thickness of 16 mm. The flanges are connected by four webs each with a thickness of 5 mm. The GFRP material was chosen because it combines low thermal conductivity with high strength. The pultrusion process was the preferred method since it enables the rapid, highly automated production of individual constant cross sections of good quality. Owing to the required resistance to buckling and shear-transfer capabilities, the profile's cross section comprised three cells. To prevent buckling of the lower flange, which bears most of the compression load, it was deeper than the webs and the upper flange. The webs were dimensioned to bear parts of the shear load and stabilize the flanges.

The CS-element is positioned with the profile's pultrusion direction in line with the compressive load. GFRP-plates of 120×70×6 mm dimensions are bonded to the sawed ends of the profile using a two-component epoxy adhesive (SikaDur[®]-330). They are cantilevered by 10 mm at the top and sides of the profile. The cap plates provide better distribution of the concentrated compression loads transferred from the lower GFRP flange into the concrete and protect the sawed surfaces of the pultruded part against alkaline moisture ingress from the concrete. During construction, the elements are integrated into the formwork of the adjacent concrete slabs since without this protection, cut surfaces would be exposed to the wet concrete during pouring and setting. As shown below, moisture uptake through the cut surfaces occurs rapidly and the protection they provide is therefore highly important particularly in this initial stage after concreting. The final dimensions of the profile, as shown in Figure 3.2, were the result of several optimization steps in which pultruded channel and plate sections were bonded together [42].

Table 3.1: Proportions of resin and fibers in GFRP profile

Part	Weight	Weight	Resin	Fibers		Fibers	
	before burn-off	after burn-off		(mats)	(unidirectional)		
	[g]	[g]	[w.-%]	[w.-%]	[vol.-%]	[w.-%]	[vol.-%]
1	5.5	3.1	43.6	16.4	11.7	40.0	28.7
2	5.2	3.3	36.5	15.4	10.4	48.1	32.6
3	5.0	3.2	36.0	16.0	10.4	48.0	31.3
4	11.4	7.1	37.7	13.2	9.8	49.1	36.5
5	11.2	6.6	41.1	20.5	12.5	38.4	23.3
6	54.7	39.4	28.0	5.9	4.3	66.2	49.1

The material used for the profile and cap plates is an isophthalic polyester resin as matrix material in which E-glass fibers are embedded. The fiber-volume fraction of the profile parts was determined by burn-off tests according to ASTM D2734-94(2003) [12]. Table 3.1 shows the fiber and mat weight fractions as well as the fiber-volume fraction¹. The part numbering refers to Figure 3.3a, where the sections, which were investigated separately, are shown. It can be seen that the lower flange (part 6) contained the most unidirectional fibers by volume (49.1 %). The webs (parts 1-4) follow with a fiber content of between 28.7 and 36.5 vol.-%, while the thin flange (part 5) contained the smallest amount of fibers by volume (only 23.3 vol.-%). The cap plates had a fiber-volume fraction of 25 % in the form of short E-glass fiber mats. The glass transition temperature of an E-glass fiber reinforced polyester was determined by Tracy [118] using DMA analysis. T_g was found to be 117°C with an onset at 85°C.

To show the mat architecture, a second burn-off test was performed on a 5-mm thick full profile. After burning the resin, the unidirectional fibers were removed so that only the mats remained, which are shown in Figure 3.3b. It can be seen that two mats embrace the outer profile dimensions, while each inner cell is also lined by one mat. A surface veil is applied above each mat.

3.3. Mechanical properties of unconditioned CS-elements

The mechanical behavior of the CS-element was investigated by concentric compression experiments conducted on 14 profiles with cap plates (capped elements) and 10 profiles without cap plates (uncapped elements) to determine the element's strength and stiffness in compression. The compression tests were performed using a servo-hydraulic machine with a maximum load capacity of 1 000 kN and a 250-mm travel, see Figure 3.4. Two displacement transducers with a travel of ± 20 mm and a precision of 0.01 mm were fixed on each side of the piston. The load was applied displacement-controlled at a rate of 0.4 mm/min. Since all elements failed after a displacement of ~ 2 mm, the time to failure was always approximately five minutes.

¹Assumed fiber density: $\rho_{\text{glass}} = 2.56 \text{ g/cm}^3$

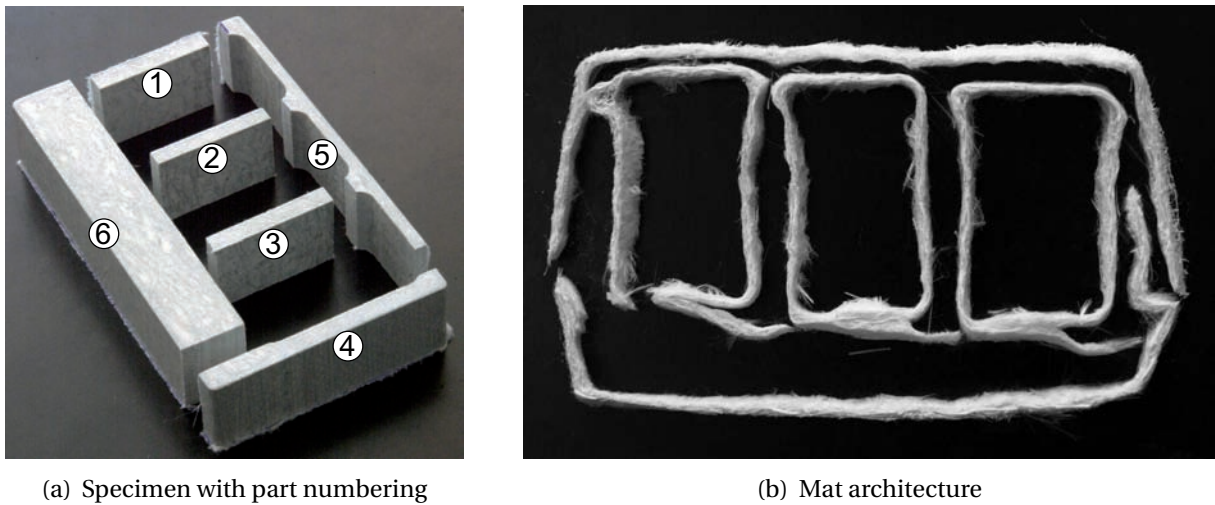


Figure 3.3: Specimen for the burn-off test with part numbering before and after the test.

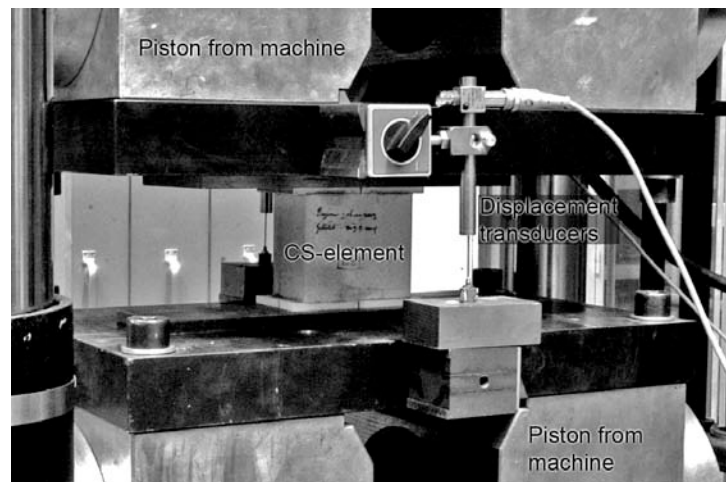


Figure 3.4: Capped CS-element inside the testing machine with applied displacement transducers

Each compression experiment produced a curve similar to that shown in Figure 3.5. After a soft behavior at small displacements in which the machine's piston attained full contact with the CS-element, the load-deformation response of both element types was almost linear-elastic up to brittle failure at F_u . The element system stiffness was calculated in this linear section of the curve as shown. The failure for unconditioned elements was brittle and catastrophic and accompanied by an abrupt drop in strength. Since the load was applied displacement-controlled, it suddenly decreased and built up only when the piston reached the remaining bearing parts of the element. Afterwards, the retained strength, F_{ret} , was maintained by the failed element, i.e. by the remaining crushed material. The measured curves are summarized in Appendix B.1.

Failure of the uncapped elements was announced by several cracking noises followed by an abrupt outward crushing of the sawed ends of the lower flange on one side of the element,

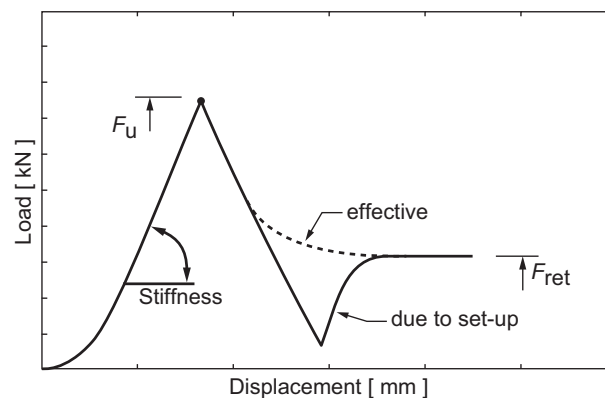


Figure 3.5: Schematic load displacement curve of a CS-element

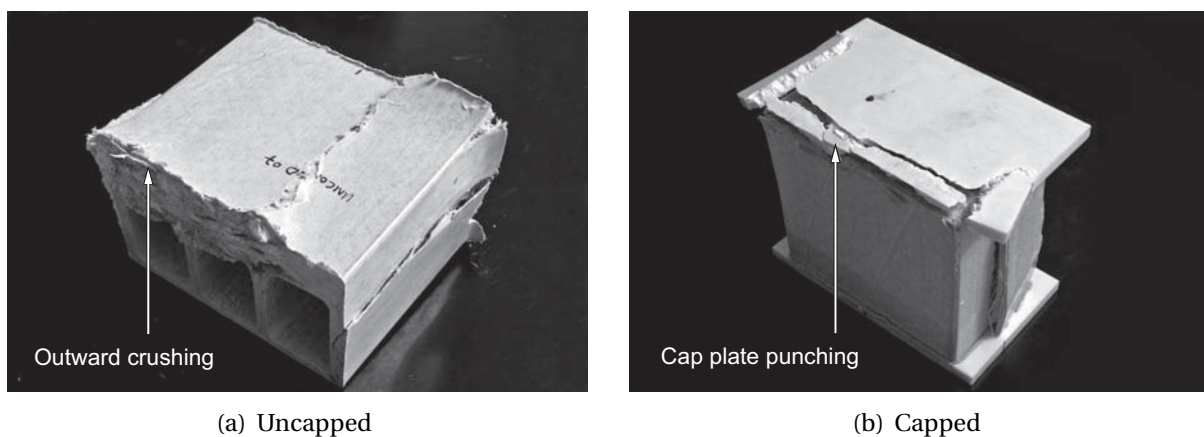


Figure 3.6: Typical failure of unconditioned elements

cp. Figure 3.6a. Subsequently, longitudinal cracks parallel to the pultrusion direction formed in the element flanges and webs. Failure of the capped elements occurred by the punching of the thick element flange through one of the cap plates, thereby crushing the sawed ends of the profile, cp. Figure 3.6b, less severely however than in the uncapped elements. Subsequently, the high compression forces of the thick flange, no longer supported by the crushed cap plate, were deviated towards the still supported thin webs. This deviation caused transverse tensile forces in the webs and corresponding cracks developed from the crushed end parallel to the pultrusion direction at the junctions of the thick flange and webs and led to a brittle ultimate failure. In addition, local wrinkling occurred at the sides of some elements.

The mean values of the obtained results are shown in Table 3.2. It can be seen that the ultimate compression strength for capped elements (727 kN on average) was only 80 % of the uncapped element's strength (917 kN on average). The reason for this difference was found to be the 'premature' punching of the cap plates at the junction between the profile's thick flange and the webs. The stiffness is also lower (with capped elements showing only 66 % on average of the stiffness of the uncapped elements), which is ascribed to the lower

Table 3.2: Mechanical material properties of the CS-element

		Uncapped	Capped
F_u	[kN]	910±60	730±60
F_{ret}	[kN]	160±40	120±30
E-Modulus	[MPa]	24 300±502	16 050±530

transverse stiffness of the cap plates. From the measured system and the profile stiffness, the E-modulus of the cap plates can be estimated by Equation 3.1 as 4 600 MPa. They are, therefore, much softer than the profile.

$$\begin{aligned} \frac{\text{Total length}}{\text{System stiffness}} &= \frac{\text{Cap plate thickness}}{\text{Cap plate stiffness}} + \frac{\text{Profile thickness}}{\text{Profile stiffness}} \\ \frac{100 \text{ mm}}{16050 \text{ MPa}} &= \frac{12 \text{ mm}}{E_{\text{cap plate}}} + \frac{88 \text{ mm}}{24300 \text{ MPa}} \\ E_{\text{cap plate}} &= 4600 \text{ MPa} \end{aligned} \quad (3.1)$$

With a view to further optimizing of the CS-element, the influence of cap-plate thickness on compression strength and stiffness was investigated with 8- and 10-mm thick cap plates. The results are summarized in Appendix B.2, Figure B.25. Both thicker cap plates resisted higher loads than the 6-mm thick cap plates. However, beyond 8 mm no further strength increase was measured, suggesting a threshold at ~8 mm after which further increase of cap-plate thickness no longer leads to higher strength.

3.4. Mechanical properties of conditioned CS-elements

The alkaline and moist environment present in concrete degrade GFRPs. To investigate the CS-element's remaining strength and stiffness in such environments, capped and uncapped CS-elements were immersed in alkaline liquid baths at different temperatures during a period of ~18 months and tested regularly in compression. The chosen set-up exaggerates the attack on the composite material and, besides easy handling and control, this choice was made because it represents a worst case scenario.

3.4.1. Experimental procedure

The conducted study included the immersion of capped and uncapped elements in baths filled with an alkaline solution for a total time span of 548 days in the case of uncapped and 430 days in the case of capped elements. Three baths were employed of three different temperatures, 20, 40 and 60°C. The different temperatures were chosen to accelerate the degradation process and predict the element's long-term behavior in compression using the Arrhenius rate law. To fit the exponential Arrhenius equation (cp. Chapter 5), at least three

different temperatures are necessary, the lowest one of which should be close to the temperature for which the prediction is made, whilst the highest one should remain well below the material's glass transition temperature.

The 40 and 60°C baths were identical single-chamber, general purpose heated baths whose inner sheets were made of seamless 304 stainless steel. Such a bath, opened and filled with CS-elements, is shown in Figure 3.7. Their dimensions were: working depth \times length (mean) \times width (mean) = 16.5 \times 68.0 \times 37.5 cm with a capacity of \sim 43 liters each. To keep the temperature gradient over the liquid depth as small as possible, styrofoam covers, with thicknesses of 4 and 6 cm for the 40 and 60°C temperatures respectively, were added. The bath containing the 20°C liquid was placed inside a temperature-controlled climate tent and was made from high-density polyethylene (HDPE) with the depth \times length \times width dimensions being 30.5 \times 60.7 \times 30.5 cm and comprising \sim 57 liters. In the heated 40 and 60°C baths, two thermocouples fixed underneath each bath and just beneath the liquid surface allowed the temperature to be tracked. The temperature of the 20°C bath was measured and controlled outside the bath in the climate tent. The recorded curves are shown in Appendix A. The temperature loss inside the heated baths was very small over time with a maximum recorded difference in the 60°C bath of \sim 3°C. Fluctuations remained, with some exceptions, within \pm 5°C.



Figure 3.7: Heated bath with inserted CS-elements before covering

The solution consisted of de-ionized water as a basis and was enriched with 2.52 g/ℓ NaOH and 31.08 g/ℓ KOH. This composition yields a theoretical pH of 13.8. To maintain the alkaline level and an even temperature distribution, the plastic cover was attached to the bath by adhesive tape, making it airtight. The solution's alkaline level was monitored and adjusted during the experiment if necessary. The effective pH was found to be between 12.8 and 13.4. In general the above-mentioned theoretical pH of 13.8 will not prevail in the concrete throughout its life because the pH-causing chemicals are not renewed, Karbhari and Chu [60].

During immersion, elements were periodically taken out of the baths, dried and examined in compression within 10-30 minutes using tests identical to those performed for the

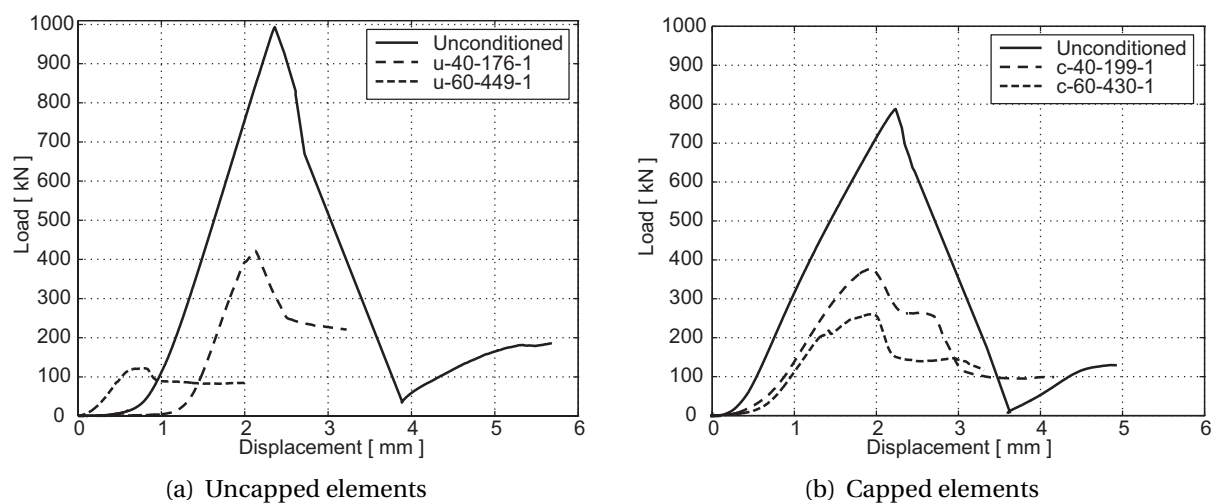


Figure 3.8: Load-displacement curves for conditioned uncapped and capped elements after approximately the same time intervals

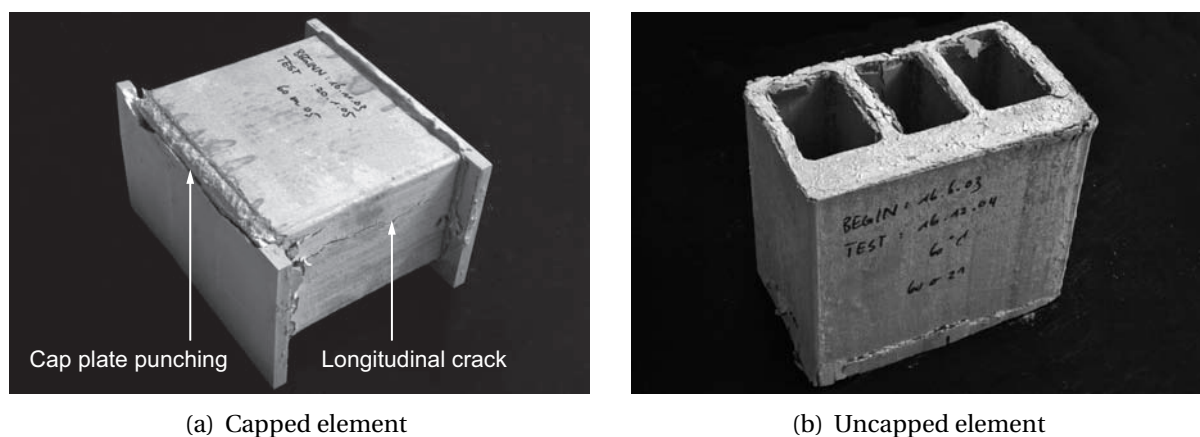


Figure 3.9: Typical failure of elements after long-term exposure at 60°C

cp. Figure B.29. Failure was no longer accompanied by noise and the elements exhibited less visible destruction after failure. This concerned the cracks parallel to the pultrusion direction as well as the punching of the cap plates, cp. Figure 3.9a. The failure mode of uncapped elements changed slightly in that cracks parallel to the pultrusion direction became less frequent and developed at arbitrary locations. Also, no outward crushing occurred and the element crumbled in the proximity of a sawed end, cp. Figure 3.9b. A representative selection of elements after failure is shown in Appendix B.5.

The development of remaining compressive strength for uncapped and capped elements for all applied temperatures is shown in Figure 3.10a and b. Uncapped elements showed a sharp strength decrease within the first ~20 days from 917 kN (average) to values between 600 kN (65 %) at 20°C and 400 kN (45 %) at 60°C. Subsequently the strength reduction rate was less rapid and remained almost constant over time at 20 and 40°C. The remaining strength

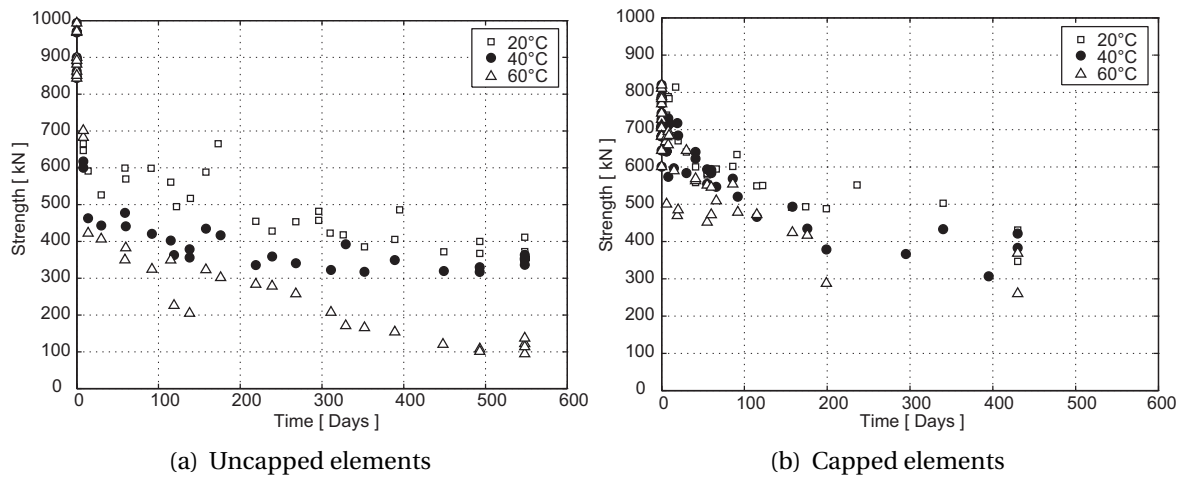


Figure 3.10: Development of ultimate failure load F_u over time as a function of temperature

of the 40°C elements was consistently between the 20 and 60°C values. Capped elements did not exhibit the distinct two-phase behavior observed for the uncapped elements. The initial strength decrease from the unconditioned average value of 727 kN was much smaller than for uncapped elements and lasted much longer – approximately 200 days. Subsequently, values tended to stabilize between 450 kN at 20°C and 300 kN at 60°C. However, since many of the cap plates debonded after 200 days, there were few remaining data points.

The remaining stiffness for both element types at all applied temperatures is shown in Figure 3.11 a and b. The values for uncapped elements show wide scatter. However, a loss of stiffness within the first 100 days from the unconditioned average value of 24.3 GPa to approximately 17 GPa was observed, corresponding to a loss of 30%. Subsequently, the stiffness for the 20 and 40°C elements remained almost constant, while the stiffness of the 60°C elements continued to decrease at a constant rate to approximately 9 GPa after 548 days. Compared to uncapped elements, stiffness values for capped elements showed much smaller scatter and no clear distinction could be made between different temperatures. The values decreased from unconditioned 16 GPa to approximately 12 GPa, corresponding to a loss of 25%.

Figure 3.12a and b shows the retained strength, F_{ret} , for uncapped and capped elements. Uncapped elements showed a tendency to decrease, especially for 40 and 60°C that flattened out only after ~400 days and remained constant at approximately 75 kN for 60°C elements and 160 kN for 20 and 40°C elements. Capped elements showed, once again, a different behavior to that of uncapped elements. The initial retained strength of 122 kN was approximately 26% lower than for uncapped elements. After immersion, no increase in values was observed; they remained constant throughout the whole observation period exhibiting no differences at different temperatures. Scatter was generally smaller than for uncapped elements. This was difficult to assess however owing to the small amount of data available after 200 days.

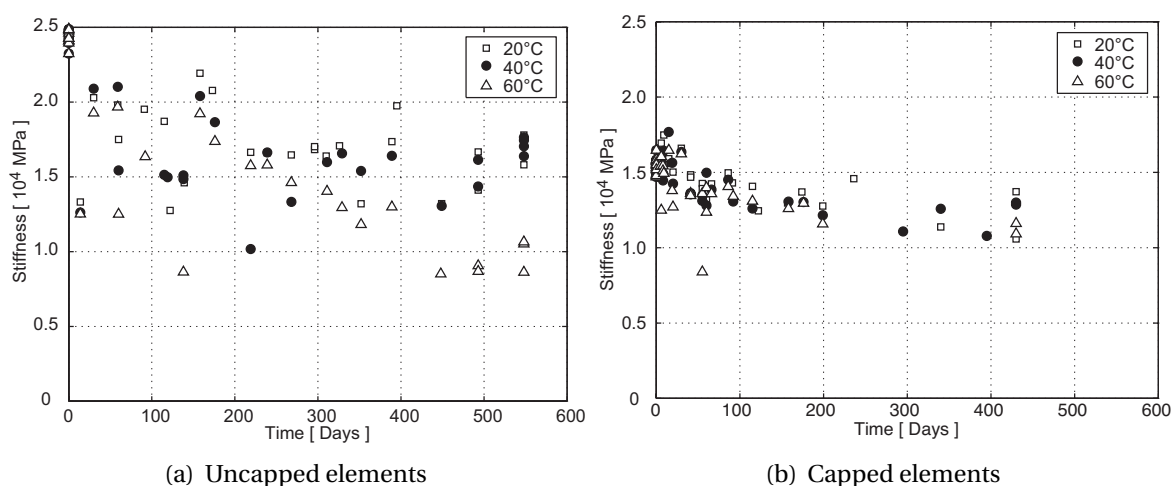


Figure 3.11: Development of stiffness over time as a function of temperature

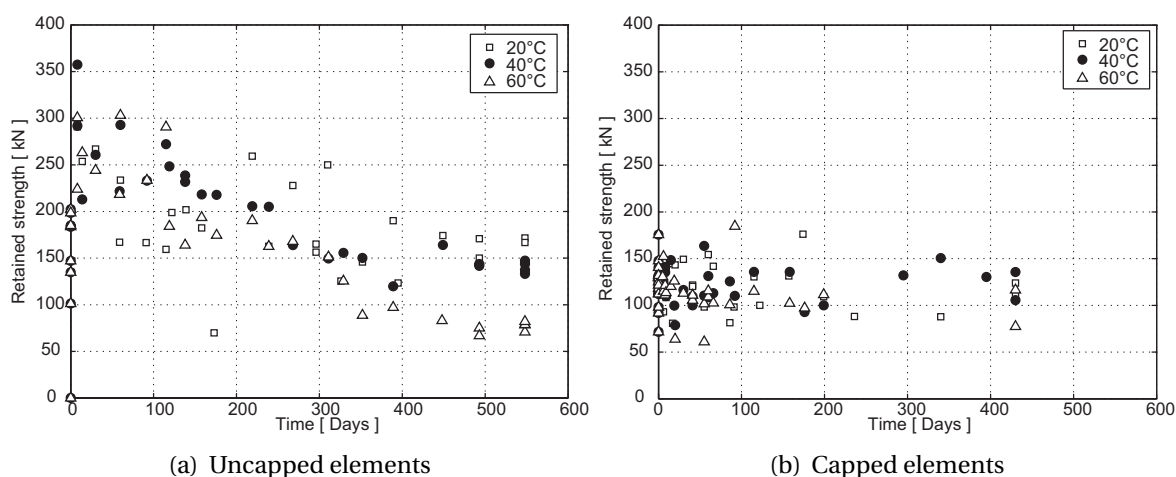


Figure 3.12: Development of retained strength over time as a function of temperature

3.5. Gravimetric studies on the CS-element

The development of strength and stiffness is closely linked to the presence of moisture in the composite material, cp. Section 2.4.2. For this reason, knowledge concerning the amount and distribution of moisture over time contributes towards understanding the element's structural behavior. The aims of the gravimetric study were a) to investigate the moisture diffusion of individual profile sections, b) compare the results to the diffusion of whole elements, c) model it numerically at different temperatures and finally d) investigate the need for the cap plate. As described by Apicella et al. [8] or Prian and Barkatt [91], wicking through the fiber-matrix interface in the fiber direction is the predominant moisture ingress mechanism apart from diffusion into the matrix. This causes different diffusion behavior in longitudinal (pultrusion) and transverse directions. The resulting different diffusion coefficients

and the equilibrium moisture content of different profile sections at different temperatures was the principal interest of the investigation. To obtain these results, specimens were immersed in alkaline liquids and tested for weight gain during a period of several weeks until the material was completely soaked. This study was principally conducted by Nathan L. Post and is described in detail in Post et al. [90].

3.5.1. Experimental procedure

The specimens for this study included profile sections and full profiles. Parts of the specimens' surfaces were sealed using a commercial sealing material (SikaGard-63N[®]). Since the burn-off tests had shown different fiber contents for the flanges and webs, cp. Table 3.1, the profile was analogously segmented and numbered as shown in Figure 3.3a except that section 4 was cut in the same way as sections 1 to 3. Besides the top flange (section 5) with a length of 44 mm (in the pultrusion direction), all sections had a length of 88 mm. The shorter length for section 5 was necessary because it was too thin for the full dimension to be cut without damage. The full profiles had a length of 88 mm (in the pultrusion direction). To test the sealing material's efficiency, eight sealing specimens with areas of 18×73 mm and depths between 3 and 11 mm were fabricated.

With the aim of modeling full-profile diffusion behavior, profile section surfaces resulting from the cuttings in longitudinal direction and normally not exposed to liquid were always sealed to prevent moisture ingress. Further sealing was applied on half of all specimens (profile sections and full profiles) on the transverse cut surfaces, exposing the unprotected unidirectional fiber ends. Specimens with this sealing are designated *sealed*, while the others are designated *unsealed*. The composition of all specimens used for the study is shown in Table 3.3.

Table 3.3: Number of specimens tested with different sealings at different temperatures

Section	① + ④	② + ③	⑤	⑥	Full profile		
Temperature	20°C				20°C	40°C	60°C
Number of specimens							
Sealed	2	2	2	2	3	3	3
Unsealed	2	2	2	2	3	3	3
Dimensions ^a [mm]							
<i>x</i>	88.0	88.0	44.4	88.0	88.0	88.0	88.0
<i>y</i>	5.4	4.7	99.9	99.9	-	-	-
<i>z</i>	34.8	34.8	3.1	15.9	-	-	-
Transversal cross sections related to full profile ^b							
[mm ²]	225.2	196.5	309.7	1588.4	2739	2739	2739
[%-total]	8.2	7.2	11.3	57.9	100	100	100

^aCompare coordinates in Figure 3.2

^bSince the cross sections are related to the full profile, the *z*-value for sections 1-4 is 41 mm and not 34.8 mm as indicated. The lower value in the table is due to the sawing (~3 mm losses on each end). Further, 3.2 mm² are added to each web due to the corner arcs, cp. Figure 3.2.

All specimens were dried in an oven at 50°C for eight hours prior to the weight gain study. As shown in Table 3.3, each two replicates of the profile sections were subsequently immersed in the 20°C alkaline bath, described above. The full profiles were immersed in 20, 40 and 60°C liquids. The sealing material was only tested at 20°C. This procedure was consistent with the environment used to test the structural behavior of the CS-elements (cp. Section 3.4).

During immersion, all specimens were tested for weight gain, the sections over a period of 48.2 days and sealed full profiles over a period of 43.2 days. The period for unsealed profiles was extended to 800 days. Sealed profiles were not immersed for such a long period since the performance of the sealing material could not be guaranteed. The sealing material itself was investigated over a period of 41 days. To perform a weight test, a specimen was taken out of the bath, quickly towed dry to remove water from the surface and then weighed using a precision balance before it was returned to the bath. Testing took place at time intervals of 30 minutes at the beginning, which increased gradually as the rate of weight change decreased.

The percentage moisture content, M_t , inside the material was determined from the weight gain of a specimen and calculated by

$$\begin{aligned} M_t \text{ [\% per weight]} &= \frac{(M_{t, \text{specimen}} - M_{\text{sealing}}) - (M_{0, \text{specimen}} - M_{\text{sealing}})}{M_{0, \text{specimen}} - M_{\text{sealing}}} \cdot 100 \\ &= \frac{M_{t, \text{specimen}} - M_{0, \text{specimen}}}{M_{0, \text{specimen}} - M_{\text{sealing}}} \cdot 100 \end{aligned} \quad (3.2)$$

The subtraction of the sealing weight took into account the assumption that the sealing material does not absorb any moisture, while representing a significant proportion of the whole specimen mass. This assumption was confirmed by the measured diffusion coefficients, which were orders of magnitude smaller than those of the composite material, cp. Appendix C, Figure C.1. The resulting diffusion coefficients are shown in Table 3.4. Since, with these low diffusion rates, no equilibrium moisture content, M_∞ , was attained during the observation period, the value indicated in Table 3.4 was obtained by fitting and extrapolating.

3.5.2. Modeling of moisture uptake

From the weight gain measurements of individual profile sections, their longitudinal (D_1) and transversal ($D_{2/3}$) diffusion coefficients as well as the equilibrium moisture content (M_∞) were calculated. Here, by assumption, D_1 was zero when the transversal cut ends were sealed. To calculate the diffusion coefficients, two different mathematical approaches were adopted. The difference in weight gain between sealed and unsealed specimens from section 6 allowed the application of the three-dimensional approach presented by Pierron et al. [86] and described in Section 2.3.3. Since for the remaining sections an insignificant difference in weight gain between sealed and unsealed specimens was found, cp. Figure 3.13, a one-dimensional approach as also explained in Section 2.3.3 (Equation 2.6) was used.

To model the diffusion behavior of the full profile, the moisture uptake of all sections was totaled. Because of the webs, a total length of 20 mm inside of sections 5 and 6 was not exposed to the liquid. Therefore, the width of both sections was reduced to 90 mm (10 mm

on each side). To check the accuracy of the calculations, the modeling results for sealed and unsealed full profiles were compared to the actual measured moisture uptake at 20°C.

Since it was desirable to model diffusion behavior at any temperature and the individual sections were only immersed at 20°C, the Arrhenius rate law, Equation 3.3, was employed to extrapolate diffusion coefficients from 20°C to 40 and 60°C. Here, the pre-exponential coefficient D_0 and the activation energy E_A are temperature-independent. In a first step, E_A was chosen arbitrarily and D_0 in both directions was calculated with the diffusion coefficients at 20°C. In the following, it was assumed that both diffusion directions had the same activation energy and thus D_0^{long} and D_0^{trans} were obtained with the optimization algorithm explained in Section 2.3.3, Equation 2.15, already used to fit the diffusion coefficients at 20°C. This time, the algorithm was employed to minimize the error between measured and calculated moisture uptake at 40 and 60°C. With the resulting diffusion coefficients, D_0 and E_A were obtained iteratively. The detailed calculation is shown in Post et al. [90]. With the calculated diffusion coefficients, the specific weight gain was simulated and the resulting curves were compared to the full profile weight gain measurements at 40 and 60°C.

$$D = D_0 \cdot \exp \frac{E_A}{R \cdot T} \quad (3.3)$$

As discussed in Section 2.4.2, the matrix material is susceptible to alkaline attack and mass losses quickly occur after exposure. Since mass losses are greater at higher temperatures, the measured equilibrium moisture content (M_∞) for 40 and especially 60°C was falsified and could not be used. This applied to both individual sections and full profiles. Therefore, M_∞ was assumed to be temperature-independent and the values obtained at 20°C, where no mass losses occurred, were also used for 40 and 60°C.

When comparing the curve from measured moisture uptake on sealed profiles and capped elements, the fact that diffusion into sealed profiles occurs from the exterior as well as from the inside of the cells must be taken into account. Therefore, sealed profiles simulated the situation when the adhesive bond-line between the profile and the cap plate fails and liquid enters the interior parts. Since total debonding of the cap plates occurred only after several hundred days in severe environmental conditions, the diffusion measured in sealed profiles will always be higher than that measured on intact capped elements.

3.5.3. Results of measurements and modeling

Diffusion coefficients of profile sections

The calculated moisture uptake for all profile sections during the first 49 days is shown in Figure 3.13, with each curve representing the mean of two tested specimens. The diffusion rates for sections 1-5 were similar and showed little difference between sealed and unsealed specimens. For section 6 however, the diffusion rate was significantly lower and was influenced by the sealing. Also, all sections except section 6 with sealed ends attained an apparent equilibrium. The equilibrium moisture content of the different sections varied significantly with section 6 absorbing approximately 2.9 % and the other sections absorbing 3.7-3.9 % on

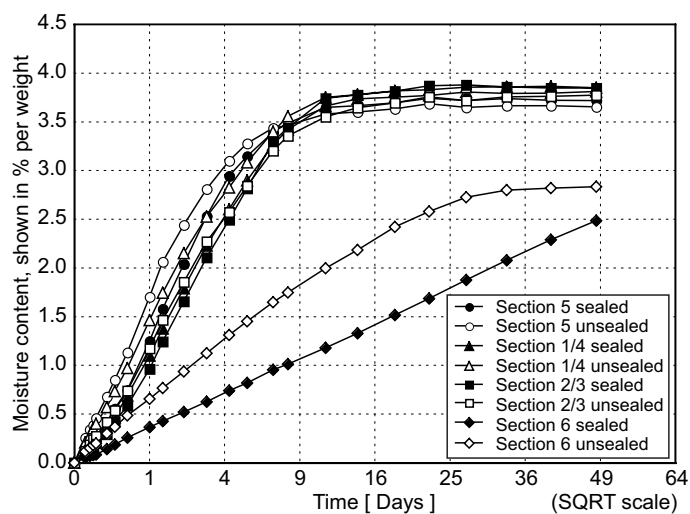


Figure 3.13: Moisture ingress in profile sections

average. This difference was almost proportional to the fiber-volume fraction of the different profile sections, cp. Table 3.1, since the glass fibers absorb no moisture.

Table 3.4: Measured and calculated diffusion coefficients

Temperature [°C]	Sections	D_1 [E-04 $\frac{\text{mm}^2}{\text{sec}}$]	$D_{2/3}$ [E-04 $\frac{\text{mm}^2}{\text{sec}}$]
20	1-5	3.34	0.05
	6	3.34	0.07
40	1-5	8.83	0.13
	6	8.83	0.18
60	1-5	20.79	0.31
	6	20.79	0.42

The calculated diffusion coefficients are shown in Table 3.4. For section 6, the smallest error in the optimization routine was found by setting M_∞ to 2.9%, with $D_1 = 3.34 \cdot 10^{-4}$ and $D_{2/3} = 0.0681 \cdot 10^{-4} \text{ mm}^2/\text{sec}$. As shown in Figure 3.14b, the moisture content modeled with these values was not perfect as it tended to deviate earlier than the measured data. However, it was reasonably close for most of the diffusion process and the error was no longer visible when the full profile was modeled, cp. Figure 3.15.

Since for sections 1-5 no distinctive difference in data was found between sealed and unsealed specimens, it was not possible to calculate the longitudinal diffusion coefficient, D_1 . Instead, the value obtained from section 6 ($D_1 = 3.34 \cdot 10^{-4} \text{ mm}^2/\text{sec}$) was assumed for these sections and used later to model the full profile diffusion. The diffusion coefficients $D_{2/3}$, calculated using the one-dimensional approach, varied between $0.026 \cdot 10^{-4}$ and $0.075 \cdot 10^{-4} \text{ mm}^2/\text{sec}$ with an average of $0.05 \cdot 10^{-4} \text{ mm}^2/\text{sec}$, which was very close to the

transverse diffusion coefficient of section 6. With these coefficients the modeled diffusion behavior of sections 1-5 followed the measured data well, as shown in Figure 3.14a.

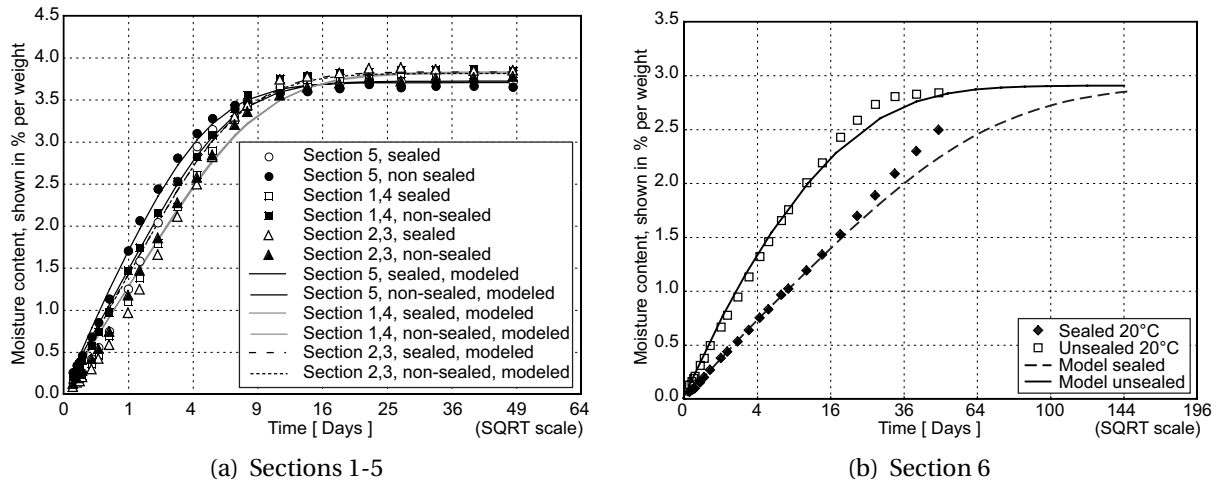


Figure 3.14: Measured and calculated moisture ingress in profile sections

The measured transverse diffusion coefficients are at the high end of the range of values reported in the literature, while the longitudinal coefficient was even two orders of magnitude higher as for non-pultruded composites. In addition, despite relatively high fiber-volume fraction, the equilibrium moisture contents are higher than for most literature experiments with non-pultruded composites, which are between 0.5 and 2.5 %, cp. Post et al. [90].

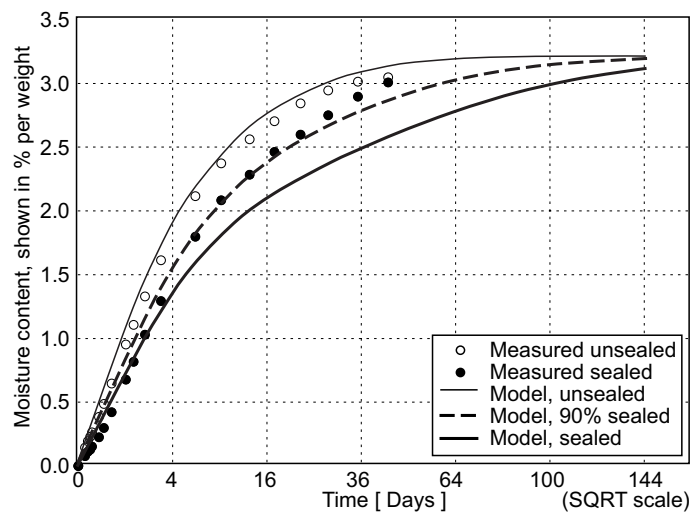


Figure 3.15: Measured and calculated moisture ingress of full profile at 20°C

Full-profile diffusion

Once the diffusion coefficients of single sections were obtained, the full profile diffusion behavior was calculated by totaling the moisture uptake from individual sections. The validity of this calculation could be assessed by comparing the resulting curve to the measured moisture uptake of the full profiles, as in Figure 3.15. It can be seen that for unsealed full profiles, the modeled curve fits well and is only slightly above the measured values. The comparison of modeled and measured uptake for sealed profiles, however, shows the model-curve deviating too early, suggesting a slower uptake than that which occurred in reality. This signifies that the sealing efficiency was overestimated with $D_1 = 0$ and moisture must have entered through the sealed profile ends. To quantify the amount of moisture ingress, the diffusion coefficient was adjusted so that the model curve fitted the data. The result was a diffusion that was reduced by 90 % ($D_1 = 3.34 \cdot 10^{-6} \text{ mm}^2/\text{sec}$). This curve is also shown in the figure and fits the measured sealed moisture uptake well.

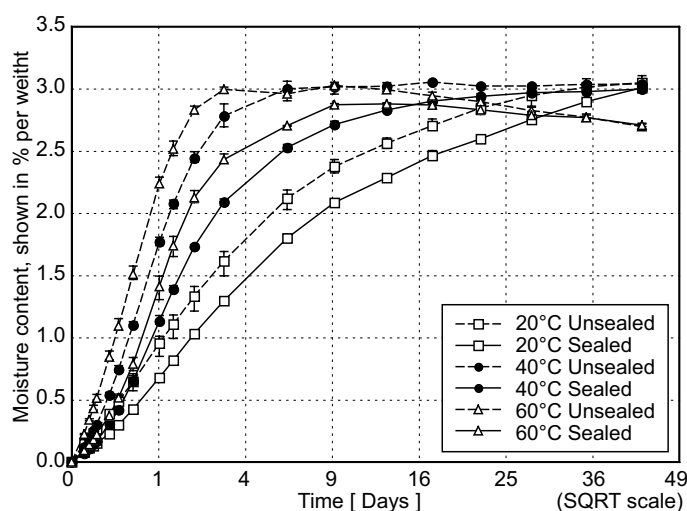


Figure 3.16: Measured diffusion in full profiles – average value curves for each three specimens with error-bars

As described above, the Arrhenius rate law, as shown in Equation 3.3, was used to extrapolate the diffusion coefficients to 40 and 60°C. The obtained temperature-independent values are the pre-exponential factors $D_0^{\text{long}} = 1360$, $D_0^{\text{trans}} = 20.7$ and the activation energy $E_A = 37.1 \text{ kJ/mol}$. The resulting mean diffusion coefficients for 40 and 60°C are shown in Table 3.4. The measured curves for moisture uptake into full profiles at 20, 40 and 60°C are shown in Figure 3.16. Figure 3.17 compares the modeled diffusion curves to measured data for unsealed full profiles at 20, 40 and 60°C. Both extrapolated curves show slower moisture uptake than the measured data, especially at 40°C. A possible explanation for the error made by the model is that the equilibrium moisture content of the profiles at elevated temperatures actually increases due to the mass loss, which is especially pronounced for polyester resins in pultruded composites. However, this was difficult to confirm with the data available.

The average moisture uptakes resulting from the long-term diffusion study on unsealed profiles are shown in Figure 3.18. In elements immersed at 20°C the rapid moisture uptake

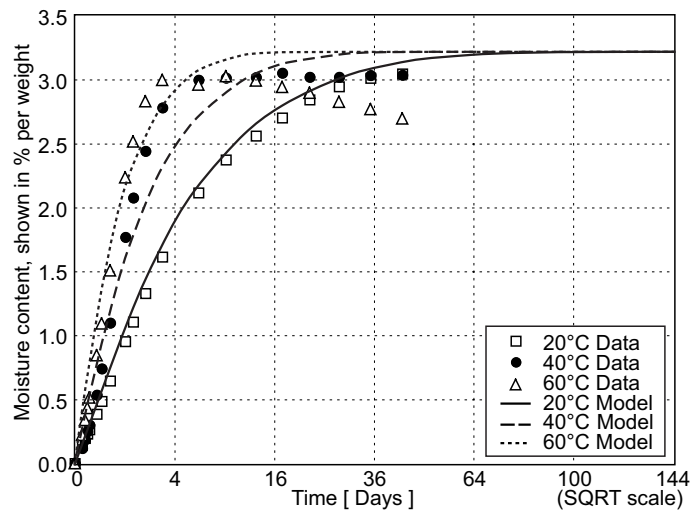


Figure 3.17: Comparison between measured and calculated diffusion in unsealed full profiles at 20, 40 and 60°C

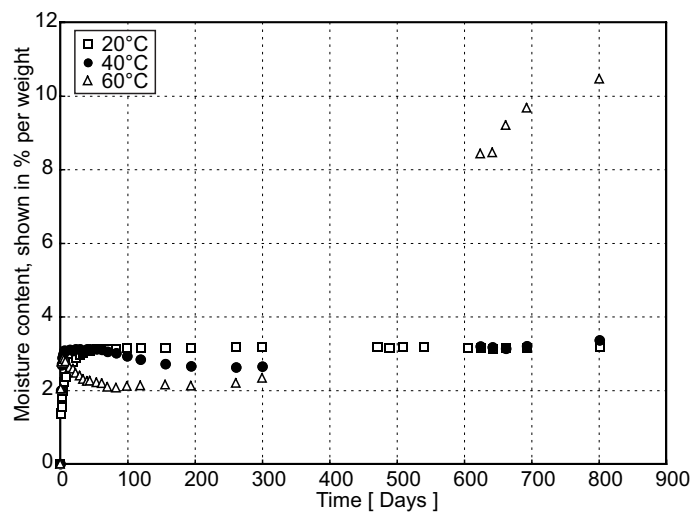


Figure 3.18: Long-term measured weight-gain of unsealed full profiles at 20, 40 and 60°C

stopped at ~3% and did not increase until the end of the observation period. The mass losses already observed during short-term immersion at 40 and 60°C amplified during the first 200 to 300 days. Subsequently, at 40°C a slight increase in weight was visible after 300 days, which finally reached the values at the first peak. At 60°C, however, the profiles gained a lot of weight after a first mass loss and finally showed a weight increase of 10% towards the end of the observation period. This abnormal behavior is explained by substantial resin degradation causing large voids inside the material into which the moisture entered.

3.6. Scanning electron microscope (SEM) investigations on CS-element

The rapid compression strength reduction and moisture uptake of the profiles observed at the beginning of the immersion (cp. Figure 3.10) suggest that resin swelling and subsequent damage in the material take place immediately a profile is immersed in liquid. Therefore, to detect qualitative changes in the material occurring during the initial three-week immersion phase, detailed scanning electron microscopic (SEM) investigations were conducted. Specimens cut from the profile were immersed in the 20 and 60°C alkaline liquid described above and analyzed during a time span of three weeks (short-term). In addition, specimens from profiles conditioned for 650 days at 20°C and for 800 days at 20 and 60°C were investigated for long-term damage.

3.6.1. Experimental procedure

The investigated specimens for the short-term study originated from the roving region of section 6, cp. Figure 3.3a. They had a cubic form with an edge length of 3 mm and were cut and polished in the transverse, longitudinal and inclined directions relative to the pultrusion direction. This produced specimens on which it was possible to examine surfaces with circled fiber cross sections, elliptic fiber cross sections and the fiber's longitudinal cross section, cp. Figure 3.19. However, the elliptic shape had the advantage of increasing the length of the fiber-matrix interface, which was of special interest, while at the same time making it possible to analyze the fiber's diameter since the whole fiber cross-section was visible. Therefore, images of circled and longitudinal fiber cross sections were not repeated for 60°C.

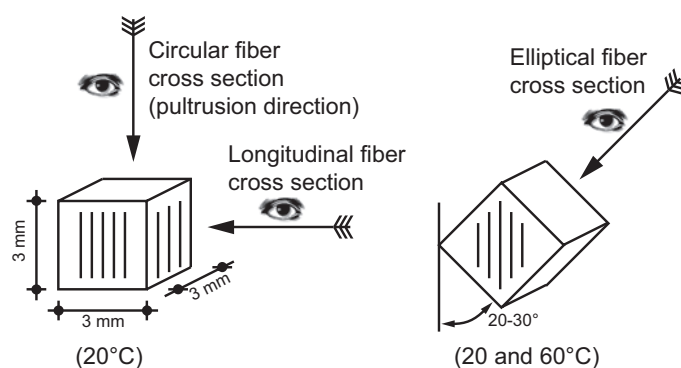


Figure 3.19: Observation angles on microscopic specimens

The amount of damage caused by the specimen fabrication and preparation process (cutting and polishing) was recorded before immersion into the baths. The specimens were carbonated² and maps of each surface were generated in which certain locations were chosen for comparison, see also Post et al. [90]. After immersion the same locations were investigated during 19 days at 20 and 60°C to document changes. The result was a series of images

²FRPs are non-conducting materials and in order to prevent charging effects from the electron beam, carbon layers are applied to specimens used for SEM.

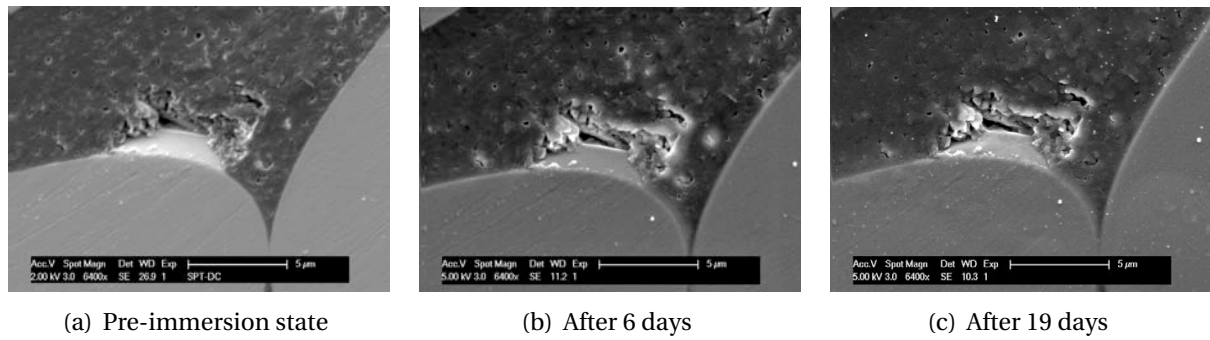


Figure 3.20: SEM-image comparison of specimen with elliptic fiber cross sections immersed at 20°C

Table 3.5: Microscopic investigation program

Surface	Temperature [°C]	Time [Days]	Location of number
Circled	20	0, 6, (19)	4 (series)
Longitudinal	20	0, 6, 19	4 (series)
Elliptic	20	0, 6, 19	4 (series)
Elliptic	60	0, 13	5 (series)
Elliptic	60	13	9 (individual)
Elliptic (near cut edge)	20	650	6 (individual)
Elliptic (near center)	20	650	10 (individual)
Elliptic (near cut edge)	20	800	10 (individual)
Elliptic (near cut edge)	60	800	17 (individual)
Elliptic (near center)	60	800	14 (individual)

of the same location at different time intervals as shown in Figure 3.20. To avoid additional damage, specimens were not repolished once the pre-immersion state had been recorded. Therefore, because of the chemical deposit from the bath and the additional carbonization before each session, image quality worsened somewhat with increasing immersion time.

Table 3.5 summarizes the experimental program. Time intervals of 6 and 19 days after immersion were chosen for 20°C specimens and 13 days for 60°C specimens to limit damage to that of the swelling process, while excluding chemical changes as far as possible. For the images taken after 650 days at 20°C, a profile immersed for this time span was removed from the bath and allowed to dry. Two cubes were then cut inclined to the pultrusion direction from section 6 and polished: one cube approximately 10 mm from the cut end of the profile and another near to its center. In addition, using the same procedure, two cubes were extracted from a full profile immersed for 800 days in 20 and 60°C, respectively. In addition to the microscopic evidence, a burn-off test as described above was conducted on a rectangular specimen (10×10×16 mm) extracted from section 6 near the cut end of a profile immersed for 800 days at 60°C.

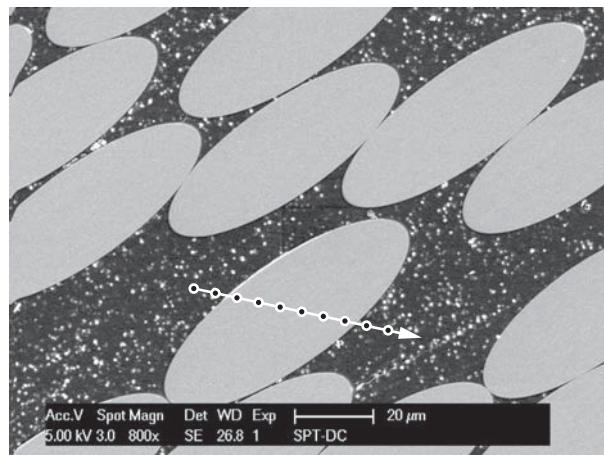


Figure 3.21: SEM image from unconditioned specimen (with marked EDX path)

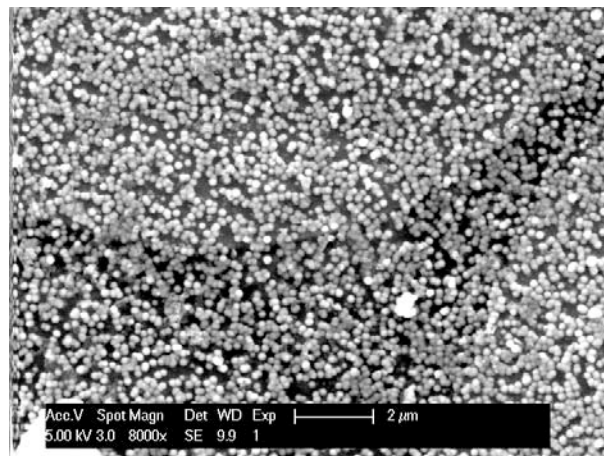


Figure 3.22: SEM image from specimen at 20°C after 19 days – material deposition

3.6.2. Experimental results

As can be seen in Figure 3.21, unconditioned specimens from the element's roving region showed perfectly embedded fibers in the matrix, which exhibited only small voids, no cracks or debonding from the fibers. The series of images, in general, showed no notable difference to this state, cp. Figure 3.20. A global inspection of the specimen's surface confirmed that the series was representative for 20°C. The specimen in 20°C with circular fiber cross-sections showed large amounts of deposited material over the whole surface after 19 days of immersion, cp. Figure 3.22. The reason for this was not clear and the specimen was not used further, reducing this series to two images for each location (cp. Table 3.5). Some representative series are shown in Appendix D.1, Figures D.1-D.4.

In the case of the 60°C specimen, distinctive features were observed outside the selected locations that did not occur in pre-immersed specimens. Therefore, additional images were taken after 13 days outside the series program. A representative selection is shown in Fig-

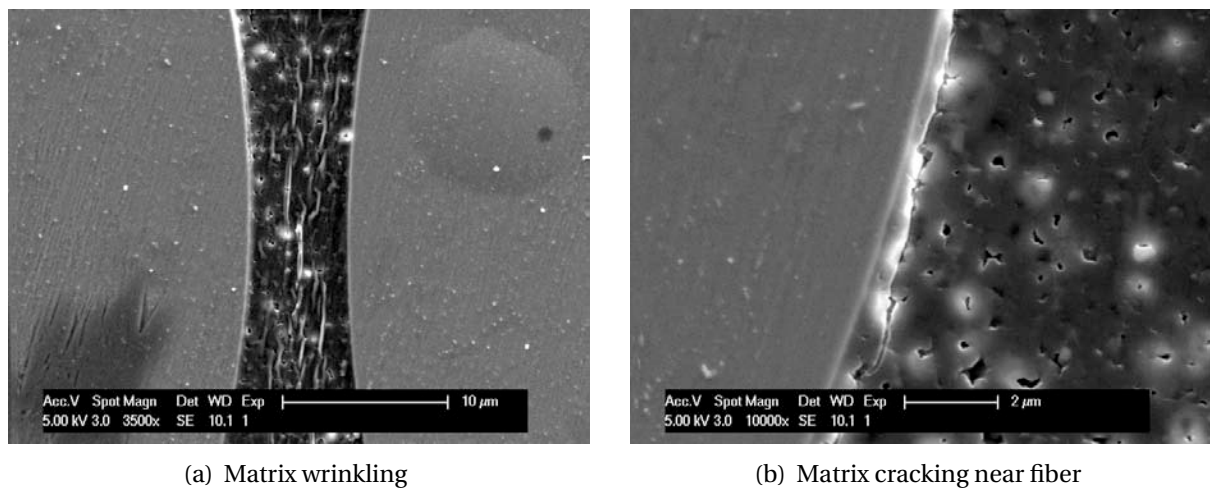


Figure 3.23: SEM images from specimen exposed at 60°C for 13 days

ure 3.23. Some wrinkling or fracturing on the matrix surface between fibers was visible, cp. Figure 3.23a. This kind of damage occurred only when distances between fibers were between 5-6 microns. In addition, matrix cracking was observed on many occasions very close to the fibers, cp. Figure 3.23b. Contrary to older specimens, where the interphase failed leading to fiber-matrix debonding (see below), this matrix cracking took place approximately half a micron away from the interphase.

The profile immersed for 650 days at 20°C was investigated near the cut end and the center. No differences were observed between the locations however. Figure 3.24a shows a specimen extracted near the profile's cut end, while Figure 3.24b shows an image made near its center. Several types of damage, which are not characteristic of the pre-immersed specimens, were visible. In contrast to the matrix cracking close to the fiber surface, shown in Figure 3.23b, these specimens exhibited fiber-matrix interfacial degradation in the form of debonding fibers. The resulting gaps are primarily in the polishing direction, cp. Figure 3.24a. Although fiber diameters did not change, fiber edges along these gaps appeared rough and irregular compared to those along gaps in pre-immersed specimens, cp. Figure 3.24b. More images are shown in Appendix D.1, Figure D.6.

The profile immersed in 20°C liquid for 800 days was only investigated near the cut end. Damage was similar to that exhibited by specimens investigated after 650 days at 20°C. Again, interfacial debonding was observed, accompanied by matrix shrinking and degradation. Also, fiber diameters showed no changes compared to specimens prior to immersion.

The profile immersed for 800 days at 60°C was investigated near the center and the cut end. Near the center, substantial fiber-matrix debonding was observed, indicated in Figure 3.25a by white areas around the fibers. On fiber surfaces, cracks occurred in arbitrary directions, cp. Figures 3.25b. These fiber cracks were not observed in any other specimens. In addition general matrix shrinkage was observed as can be seen in the center of Figure 3.25a, where the resin bulk recedes evenly from all surrounding fibers. As in the specimen in 20°C liquid, no decrease in fiber diameter was observed.

Figure 3.26 shows images from a specimen extracted near a cut edge of the profile, which

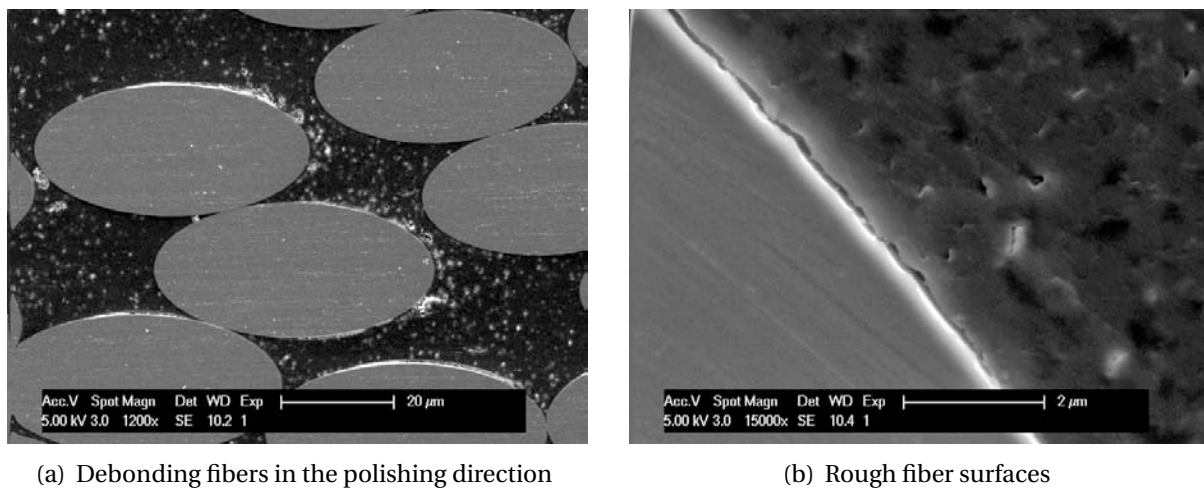


Figure 3.24: SEM images from profile section exposed at 20°C for 650 days

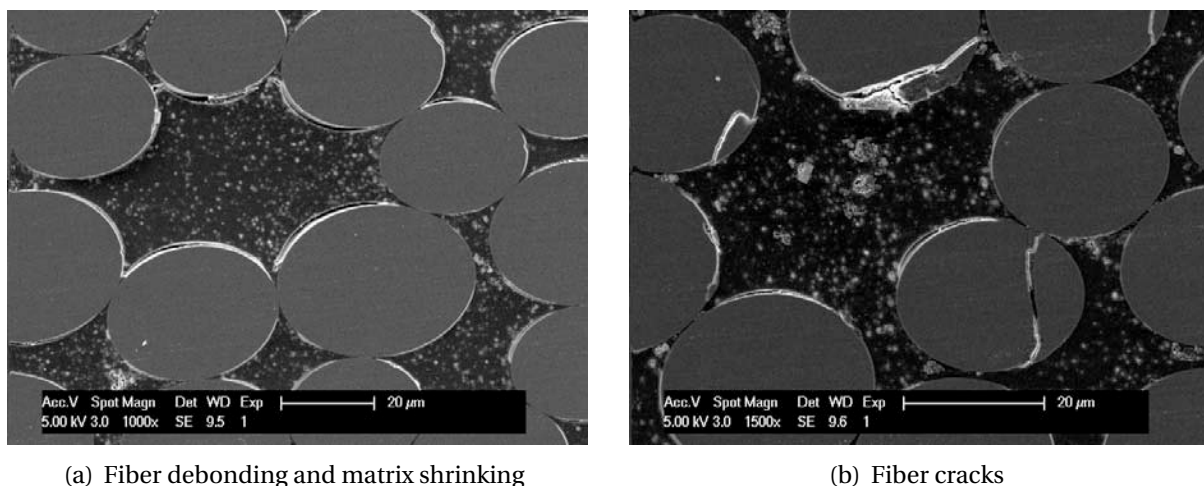


Figure 3.25: SEM images from profile section (near center) exposed to 60°C liquid for 800 days

was immersed for 800 days at 60°C. During the polishing procedure large portions of the specimen detached, revealing a significant reduction in matrix cohesion. In those areas that were still coherent, ubiquitous interfacial degradation and the formation of large voids were visible, cp. Figure 3.26. Corresponding material deposits were observed in the alkaline liquid baths. In addition, as for all previous specimens immersed at 650 and 800 days, roughened fiber surfaces were observed, which are also visible in Figure 3.26b, while the diameter did not change.

Because of the unchanged fiber diameter and rough fiber surfaces after long-term immersion, especially at 60°C, an additional burn-off test was conducted. This revealed a complete change in the flexibility of the fibers. In contrast to the very flexible fibers of the unconditioned elements, the fibers after conditioning were very brittle and crumbled immediately when bent and rubbed between the fingers.

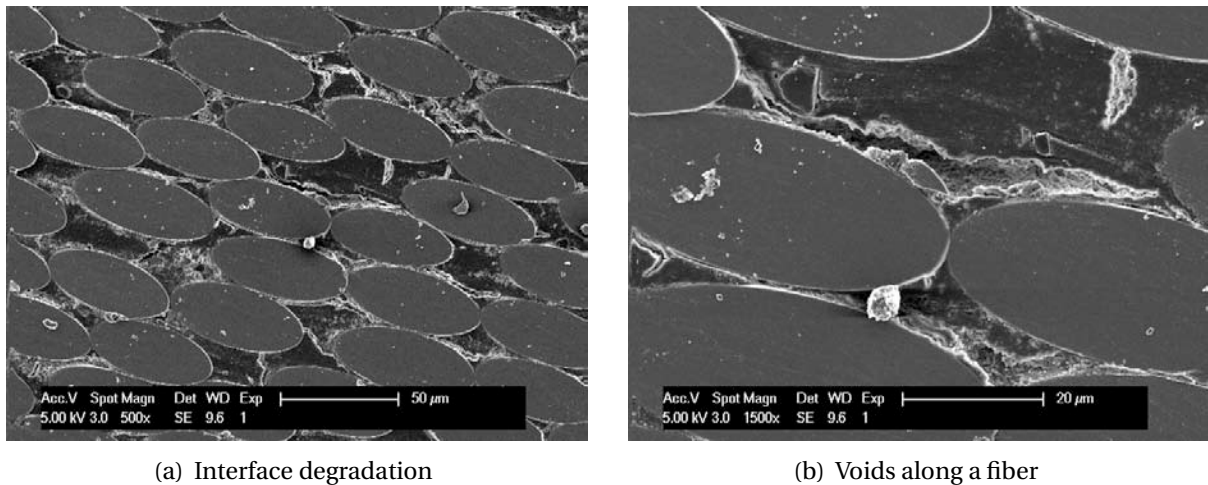


Figure 3.26: SEM images from profile section (near cut end) immersed at 60°C for 800 days

3.7. Energy dispersive X-ray spectroscopy (EDX)

Once alkaline moisture enters the composite, several chemical processes occur as described in Section 2.4. To investigate the chemical alteration of the elements, a study was conducted to determine the atomic distribution of elements from the liquid and composite materials. To determine the differences before and after immersion, cubic specimens, as described in Section 3.6.1, were extracted from unconditioned and conditioned elements and investigated by energy dispersive X-ray (EDX) analysis.

3.7.1. Experimental procedure

The EDX method is an analytical tool used to non-destructively determine the atomic composition of small volumes of solid materials inside an SEM microscope. The investigated material is excited by the SEM electron beam and electrons near an atomic core are removed. This enables electrons from higher energy levels to fill the gap and attain a lower energy level. The energy emitted in the form of X-rays is measured by a detector and since every element has a different structure, the measured X-rays provide information concerning the material's atomic composition. This method can detect elements with an atomic number higher than 9 (fluorine), which means that hydrogen ions (atomic number 1) are non-detectable.

The study was performed on unconditioned and conditioned (800 days at 60°C) cubic specimens with inclined fiber direction, extracted from section 6 near the cut ends. Altogether three locations were investigated for each unconditioned and conditioned specimen. The procedure consisted of scanning the material along a predefined path and extracting information at equidistant test points on this path. Paths were always chosen across a fiber and care was taken to ensure that at least one test point lay outside the fiber in the matrix in order to observe differences. Figure 3.21 (page 65) shows the surface of a specimen extracted from an unconditioned element seen through an SEM microscope. A typical EDX path is marked in white with the test points in black. The recorded elements were oxygen

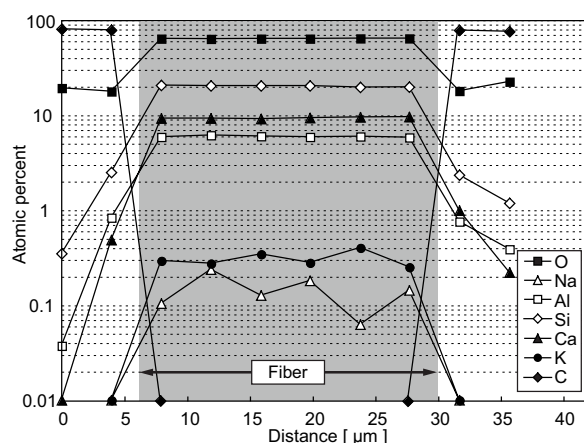


Figure 3.27: Measuring path and results of EDX analysis on unconditioned element

(O), sodium (Na), aluminum (Al), silicon (Si), calcium (Ca) and potassium (K), magnesium (Mg) and carbon (C). Specimen surfaces were covered with a carbon layer to prevent charging, which amounted to 10-15 %. This influenced the real carbon proportion inside the material. However, since the fiber glass contains no carbon, the proportions in the matrix was estimated by subtracting the average value measured in the fiber from the values measured in the matrix.

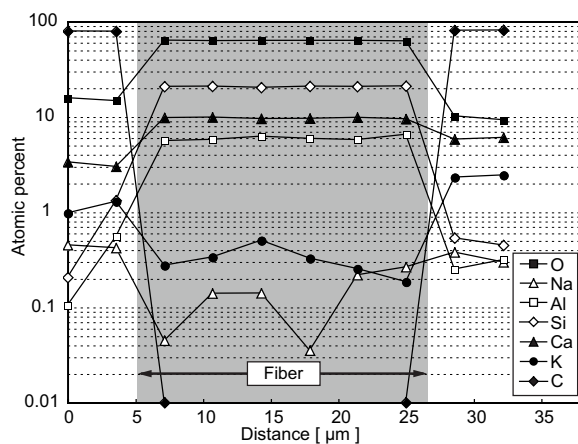
3.7.2. Experimental results

Figures 3.27 and 3.28 show typical results of the EDX material analysis. The magnesium ion distribution is not shown for clarity, however mean values are added in Table 3.6. In Figure 3.27, the atomic composition of an unconditioned specimen is shown in logarithmic scale on a path from the matrix through one fiber back to the matrix again, cp. Figure 3.21. The proportion of carbon in the matrix was 80 % for all specimens and decreased rapidly inside the fiber. In the fiber, oxygen ions represented the biggest proportion, which decreased strongly in the matrix region. Silicon, calcium and aluminum ions attained values of between 6 and 20 % inside the fiber, but decrease to insignificant amounts in the matrix however. The same applies to sodium and potassium ions that decrease from fractions of 0.2 and 0.4 % respectively in the fiber to non-detectable values in the matrix.

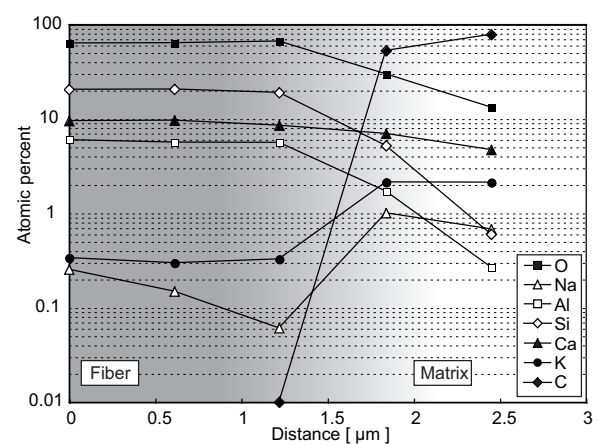
Figure 3.28a shows the atomic composition along a similar path on a specimen conditioned for 800 days at 60°C. Mean values from each three analyzed specimens are given in Table 3.6. Figure 3.28b focuses on the fiber-matrix interface with a higher density of test points. The figure shows a significant increase in potassium, sodium and calcium ions in the matrix and interface of the conditioned specimens. Furthermore, the amount of sodium ions inside the fiber and especially towards the fiber-matrix interface was slightly reduced to beneath 0.1 % on average compared to unconditioned specimens where the content was ~0.2 %. The oxygen ion content did not change inside the fiber (65 %) and decreased slightly in the matrix. Silicon ion content remained constant in the fiber at 20 % and increased slightly from an average of 0.4 to an average of 1.6 % in the matrix. The aluminum ion concentration also

Table 3.6: Mean atomic ion distribution in fibers and matrix (values in [%])

Element	Unconditioned		Conditioned	
	Fiber	Matrix	Fiber	Matrix
C	0.00	74.65	0.00	72.94
O	63.64	20.97	62.84	17.49
Na	0.17	0.07	0.13	0.48
Mg	0.30	0.07	0.30	0.26
Al	6.07	0.78	6.00	0.36
Si	20.20	2.39	20.93	0.96
K	0.27	0.05	0.33	2.01
Ca	9.36	1.02	9.47	5.58



(a) Results of measurements over a whole fiber



(b) Results of measurements on fiber-matrix interface

Figure 3.28: EDX material analysis of conditioned element after 800-day exposure at 60°C

did not change inside the fiber (6%) and increased slightly by an average of 0.17 to 0.6% in the matrix. The close-up of the interface confirms the sharp transition between fiber and matrix. Results from all six investigated locations are shown in Appendix E.1.

3.8. Discussion of experimental results

Summarizing the results of the strength measurements, gravimetric and microscopic data, the CS-element's behavior in alkaline environments was governed by initial rapid moisture uptake followed by chemical degradation of matrix, fibers and fiber-matrix interphase. All processes are accelerated by higher temperatures.

3.8.1. Alteration of mechanical properties of CS-element

Initial compression strength was higher for uncapped elements than for capped elements. This was explained by the lower strength of the cap plates leading to their premature failure, which deviated the entire compression load onto weaker parts of the profile. During conditioning, a sharp strength drop in a short first phase is followed by a subsequent, gradual strength decrease in a longer, second phase. This development, although with different intensity, was observed likewise for uncapped and capped elements and was more pronounced with increasing temperatures. Strength decrease of 60°C elements was retarded for some days due to partial compensation of strength decrease by post-curing processes. Based on the close relationship between moisture uptake and strength decrease, the first drop in strength must have been primarily correlated to moisture uptake: the loss of matrix stiffness, caused by its plasticization during moisture diffusion, decreased the lateral resistance of the compressed fibers to buckling, leading to the rapid loss of compressive strength observed. In the case of uncapped elements, the effect of this phenomenon on strength was much greater compared to studies with tensioned fibers, where the observed strength loss was much smaller during this first phase, cp. Dejke [33]. For capped elements, the rapid strength drop in the first phase was not as significant as for uncapped elements since profile's strength decrease did not change the failure mechanism for capped elements, explained above. After the profile's compression strength underwent the capped element's strength, both curves were similar. During the second phase, strength decrease was ascribed to chemical degradation of the composite material caused by the chemical attack explained below.

The initial stiffness of uncapped elements was significantly higher than capped elements. This was explained by the softness of the cap plates in comparison with the profile, allowing greater deformation. Once exposed to alkaline moisture, the measured data for uncapped elements showed large scatter. However, a rapid reduction in stiffness to ~70 % of its initial value could be seen, which remained stable for 20 and 40°C, but decreased further at low rates for 60°C elements. Capped elements did not show the initial drop, scatter was much smaller and no differences at different temperatures were observed. The small scatter was explained by the fact that the stiffness measured for capped elements could be assumed to be primarily that of the cap plates, since they were softer than the profile. In contrast to the profile, however, cap-plate stiffness was independent on influences created by imperfections during manufacture. Therefore, capped-element values showed very small scatter and a relatively small loss of stiffness during immersion. The stiffness of uncapped elements, in contrast, was that of the profile, influenced by imperfections due to fabrication. This resulted in scatter, which was amplified by size effect. For uncapped elements at 60°C, the stiffness decrease in the second phase was ascribed mainly to chemical processes, which led to a further degradation of fibers, matrix and fiber-matrix interfaces.

3.8.2. Diffusion behavior

The investigation concerning moisture uptake revealed different coefficients in longitudinal and transversal pultrusion directions. In the longitudinal direction diffusion was much faster due to the wicking effect along the fiber-matrix interface. Apart from section 6, however, transversal diffusion filled up the thin profile parts so rapidly that no differences were

observed between sealed and unsealed sections. The full profile diffusion behavior could be approximated by the Fickian diffusion law, which showed high accuracy especially at 20°C. The profile with unsealed ends was saturated after 30 days in 20°C liquid and the sealing of the ends had little effect on these values. A comparison between the diffusion rate and the first important strength decrease of uncapped elements suggested a close relationship between these phenomena. Elements immersed in 60°C liquid were seen to lose weight after only nine days, cp. Figure 3.15. Long-term observation showed the same effect in 40°C elements, cp. Figure 3.18, while no reduction was seen in 20°C elements. Weight losses indicate material degradation and confirm the assumption that the composite components degrade faster at increased temperatures.

3.8.3. Microscopic investigations

The SEM image series revealed no visible short-term (19 days) changes in specimens at 20°C. This result is in contrast to the sharp drop in compression strength observed during this period. Hence, the strength decrease must have been triggered by a significant loss in stiffness of the matrix during moisture uptake, which led to decreased lateral resistance to buckling of the compressed fibers. Possible fiber-matrix debonding, which is optically not visible, would be in accordance with Ashbee et al. [11], cp. Section 2.4.3, who detected non-visible debonding only by measuring changing interfacial stresses. In specimens immersed for 13 days at 60°C, cracks were seen to occur in the proximity of the fiber-matrix interface as accompanied by matrix wrinkling between fibers. Both types of damage indicated thermal incompatibility between resin and fiber, causing stresses and internal damage once the temperature changed. The wrinkling was ascribed to the swelling of the resin, whose expansion was hindered by the rigid fibers on both sides.

Elements immersed for 650 and 800 days at 20°C showed no difference in degradation, independent of location (near center/cut ends). This was in agreement with the constant weight at 20°C observed in the long-term diffusion study, cp. Figure 3.18. Once the temperature is increased to 60°C, the degree of degradation in the form of matrix degradation (voids and shrinkage) and fiber-matrix debonding was generally greater and changed according to profile location. Unlike the profile center, matrix degradation near the cut ends was so severe that it was no longer possible to polish the specimen without significant material losses. The amount and size of voids also increased appreciably, cp. Figures 3.25 and 3.26. It was, therefore, assumed that degradation levels off with decreasing temperature and towards the more protected and inaccessible profile center. Matrix degradation initiated in the fiber-matrix interface and spread towards resin-rich areas. The chemical attack continued and penetrated the whole element until the entire matrix is decomposed. Fiber diameter did not change. However, combined with brittle fiber behavior and brittle fracture surfaces, rough fiber surfaces were evidence of advanced fiber degradation. Combined with the findings from the EDX, the degradation mechanism was identified as being mainly a bond-breaking process acting on the glass atomic structure. It was assumed that, in contrast to fiber-reinforced cement, where, due to the open porous structure of the cement matrix degraded glass was washed away, cp. Yilmaz et al. [126], degraded fiber glass in the composite was held in place by the relatively tight surrounding polyester matrix.

3.8.4. Atomic ion distribution

The increasing amounts of sodium and potassium ions near the fibers proved that the matrix was permeable to alkaline chemicals, which were consequently in direct contact with the glass fibers. Calcium was not added to the liquid and the increase in the matrix can not be explained. The initial sodium proportion of 0.17 % in the fiber glass is rather small compared to approximately 1 % for E-glass reported in the literature, cp. Table 2.1. These small amounts and the high precision scale of 0.1 % made it difficult to draw conclusions, however, on average the amount of sodium ions reduced in conditioned specimens. This corresponded to the described interdiffusion process occurring between hydrogen ions and sodium. The small amounts of sodium towards the fiber surface observed in several specimens (cp. close-up in Figure 3.28b) corresponded especially to the advancing hydrated layer described in Figure 2.6. The constant proportion of silicon ions in the glass confirmed the observations of non-changing fiber diameters under the SEM. If the liquid penetrated into the composite, the tight polyester matrix did not allow any flow to wash out the detached atoms in the glass. This situation was expected to change once the matrix decomposed to a stage where pores became large enough to allow some flow. However, this was not observed. Also, in light of only three specimens in conditioned and unconditioned elements, the statistical certitude, especially for small observed changes, has to be taken into account.

3.8.5. Conclusions

The first sharp drop in strength could be ascribed to moisture diffusion. This was confirmed by the observed moisture uptake, which occurred in the same time span. The ingressed moisture entered the matrix causing swelling and decreasing stiffness, which, in turn, decreased the lateral resistance to buckling of the compressed fibers. The experimental evidence concerning degradation of the fiber-matrix interface was inconsistent: the higher diffusion coefficient in the pultrusion direction signified that wicking along the fiber-matrix interface must have occurred. However, if this caused fiber-matrix debonding, it was not detectable with SEM. Also, elevated temperatures (60°C) provoked cracks near the fiber-matrix interface, implying an intact interface after this period, cp. Figure 3.23b. Matrix wrinkling and cracks near the fiber-matrix interface at 60°C indicated further matrix swelling, causing stresses beyond the matrix strength. The result was significantly higher losses of compression strength in the initial phase at elevated temperatures.

The gradual strength decrease after the initial drop was mainly due to chemical degradation of the fibers, matrix and fiber-matrix interface. Weight losses after the initial moisture uptake evidenced decomposing matrix material, which was washed out into the baths. This corresponds to the large voids in the matrix observed with the SEM. The observed matrix shrinkage after long observation times was assigned to additional monomer reactions in the matrix, which were confirmed by EDX showing alkaline chemicals present in the matrix after material saturation. Increasing void content and shrinkage led to matrix embrittlement. In addition to matrix degradation, substantial fiber-matrix debonding allowed alkaline chemicals to enter into direct contact with fibers. The consequent fiber degradation was assigned mainly a bond-breaking process. Indications for this conclusion were dissolved fiber surfaces found with SEM and fiber embrittlement evidenced by physical observation after burn-

off tests. EDX analysis also indicated that interdiffusion had taken place, although to a lesser degree.

3.9. Description of the TS-element

The TS-element was planned to be employed in the all-GFRP joint, cp. Figure 3.1. It was designed to carry tensile loads and shear through the joint and anchor them in the concrete. Its purpose to bear axial and shear forces similar to the CS-element made the application of the same pultruded profile a preferred choice. To maximize the lever arm between the compression and the tension force from the moment, the profile was turned upside down with the thicker 16-mm flange on top, as shown in Figure 3.29. In addition to the compressive material properties, cp. Table 3.2, the tensile material properties were investigated separately for each flange and the webs. The results are shown in Table 3.7.

Table 3.7: Profile material properties in tension

Part		Flange 16 mm	Webs	Flange 3 mm
σ_u	[MPa]	538± 13	407±34	366±57
E-Modulus	[MPa]	40 520± 560	29 170± 3 750	30 500± 2 290
μ	[-]	0.35	0.22	0.31

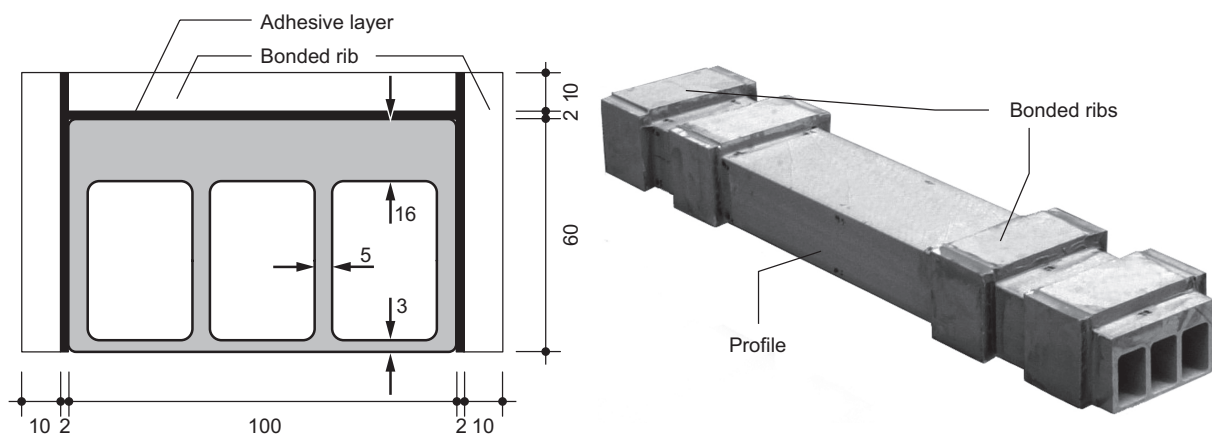


Figure 3.29: TS-element cross section with anchorage ribs

In contrast to the CS-element, which transfers incoming forces by simple contact pressure and static friction, the TS-element had to penetrate the concrete section and anchor the tensile forces. This was achieved by ribs bonded on the profile's upper and lateral sides, cp. Figure 3.29. Each rib had a depth of 10 mm and was cut from flat pultruded sections. The TS-element was made with two different rib distributions: one with two ribs bonded on each side of the insulating section, the total length of the profile being 680 mm, and another with three ribs on each side with a total profile length of 1020 mm. The different rib distribution

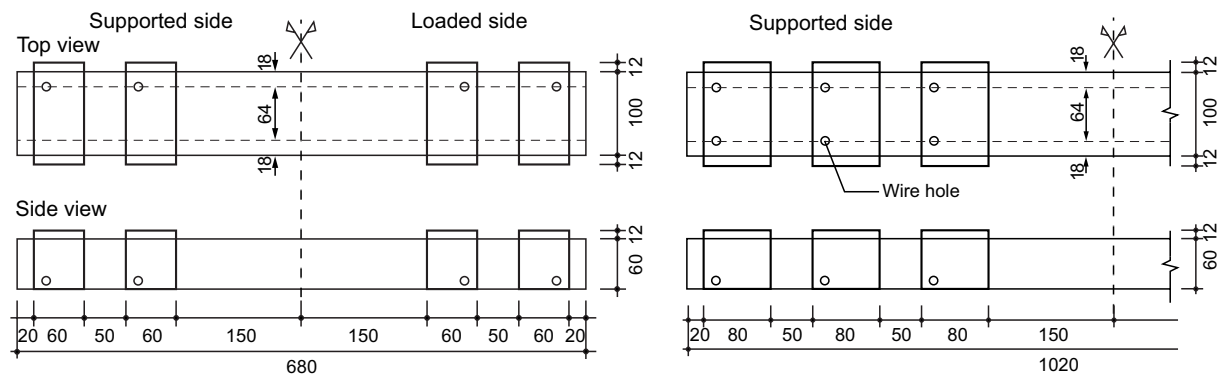


Figure 3.30: Side and top view of two- and three-rib TS-element with strain gage arrangement

was chosen to investigate anchorage behavior. Thus, applied in a joint with end support, the shorter anchorage length with only two ribs was expected to lead to failure at the ribs (anchorage failure), while the longer length was expected to cause shear failure in the profile and concrete failure in the joint's compression zone. Both versions are shown in Figure 3.30.

In the three-rib combination, each rib had a length of 80 mm, while in the two-rib combination, rib length was 60 mm. The rib length was based on an adhesive-joint design according to Keller and Vallée [63]. The inter-rib distance of 50 mm was the same for both cases to provide sufficient space for shear stirrups, cp. Figure 4.18 and 4.19a. The distance between the rib nearest to the insulating section on each side and the concrete edge was 100 mm in order to introduce the anchorage force of the first rib into the concrete. Before bonding the ribs to the profile, the surfaces were sanded and degreased. The adhesive used was SikaDur[®]-330, a two-component epoxy adhesive. Adhesive thickness was 2 mm to accommodate strain-gage wiring. Precise thickness was ensured by inserting $\varnothing 2$ -mm steel balls. The ends of each tension element were closed by means of bonded completion plates flush with profile dimensions.

4. Experimental investigation of beams with multifunctional insulating and load-bearing joints

4.1. Beams with hybrid GFRP/steel insulating joint

4.1.1. Introduction

An intermediate step in the development of the final all-GFRP insulating joint was a hybrid joint, in which only the steel compression reinforcement was replaced by the GFRP CS-element described in Chapter 3. The “hybrid” designation refers to the two materials involved, GFRP and steel. The hybrid joint is shown in Figure 1.2 on page 3 and will reduce the thermal conductivity by 70 % compared to the all-steel joint (from 0.4-0.6 to 0.1-0.2 W/(m·K)). The replacement of the compression steel reinforcement was chosen as a first step because the transfer of compression forces by contact pressure was easier to realize than tensile force transfer. Focusing particularly on the possible tilting of the CS-element, the transmission of forces through the insulating section and the consequences on displacements were investigated experimentally and modeled analytically.

4.1.2. Experimental program and set-up

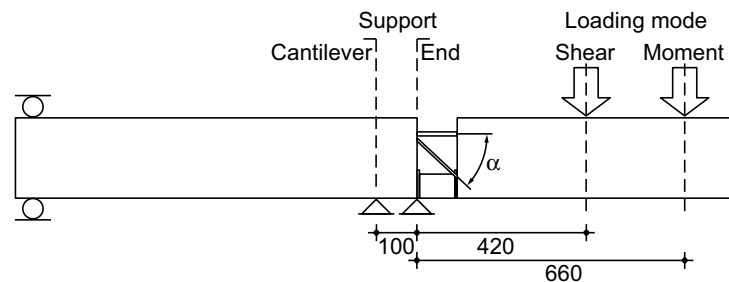
Considering the configuration of the element being tested, it was assumed that the behavior of beams with one incorporated CS-element could be used to directly deduce the behavior of slabs. Figure 4.1 shows the designed beam system. The beams were divided into three sections: one section represented the building’s interior with both ends simply supported. A second concrete section, representing the balcony slab, was fixed on one side through the joint and subjected to a vertical downward load. The two concrete sections were connected by the insulating section containing the CS-element, which was the focus of this research. The concept of the experimental set-up was derived from preexisting joint types with pure steel reinforcement. There are two kinds of joints on the market: one designed to predominantly transfer bending moments and another to transfer predominantly shear. Accordingly, the set-up was designed to consider a *moment mode* with predominant moment transfer and a *shear mode* with predominant shear transfer. This was achieved by applying the load using different lever arms of 420 and 660 mm as shown in Figure 4.1. In moment mode, concrete failure was expected to occur during yielding of the upper steel bars without yielding of the shear bars. In shear mode, concrete failure should occur during yielding of both steel reinforcements (upper tension and shear).

In practice, two principal positions of the wall, on which the slab is anchored, are possible. One possibility, shown in Figure 1.2, is a wall directly adjoining the insulating joint. The compression forces in the CS-element can in this case be directly introduced into the supporting wall. A second possibility is to shift the wall away from the insulating section so that no immediate vertical distribution of the compression forces is possible. The first case

Table 4.1: Composition of hybrid GFRP/steel experiments

Support	End support				Cantilever support			
Loading mode	Moment		Shear		Moment		Shear	
Depth [mm]	200	240	200	240	200	240	200	240
Type of beam	M200E1	M240E1	S200E1	S240E1	M200C1	M240C1	S200C1	S240C1
	M200E2	M240E2	S200E2	S240E2	M200C2	M240C2	S200C2	S240C2
Enhanced bond of cap plates:			S200E3	S240E3				

is designated an *end support* condition, while the second is designated a *cantilever support* condition. Thus in the set-up, the support adjacent to the insulating section was adjustable to obtain both support conditions. An end support produces a three-dimensional stress state in the concrete due to confinement, leading to higher strength, which is also accountable in SIA 262 [7]. If the support is shifted, this effect is lost and the concrete strength decreases to normal values.

**Figure 4.1:** Structural system with varying support conditions and loading (dimensions in mm)

To cover the most commonly used floor depths, two different depths of the beam's cross section were used (200 and 240 mm). Each beam depth was examined with both loading positions, which in turn were duplicated with both support conditions (end and cantilever). Each combination was investigated twice, amounting to the 16 experiments summarized in Table 4.1. The beams were designated *M* in the case of moment mode and *S* in the case of shear mode. This letter was followed by the beam depth (mm), the support condition (*E* for end support and *C* for cantilever support) and a replicate index. Experiments S200E1/2 and S240E1/2 revealed weak adhesion between the cap plates and GFRP profile provoking premature failure in the bond line in shear mode with end support. Therefore, these configurations were repeated for both beam depths. The additional experiments differed from their predecessors in that the cap plates were sanded and degreased before they were bonded to the profile to improve adhesion. The experimental set-up is shown in Appendix F.1 in Figure F.1, page 219.

The load was applied displacement-controlled at a speed of 10 mm/min. A theoretical ultimate failure load, $F_{u,est}$, was estimated in advance with the concrete compression strength

according to SIA 262. The loading path was divided into four cycles. The first loading cycle reached $\sim 30\%$ of $F_{u,est}$ and was expected to show a fully elastic behavior. To investigate plastic load-deformation behavior, two further loading cycles reaching $\sim 60\%$ and $\sim 90\%$ of $F_{u,est}$ were conducted before the load was increased up to failure (F_u).

4.1.3. Experimental specimens

In Figure 4.2, the dimensions and reinforcement of one of the 18 tested beams are shown. The beam's concrete cross section had a width of 270 mm and a depth, d , of 200 or 240 mm. The beam's total length was 1 800 mm with the simply supported concrete section having a length of 1 000 mm, the cantilevered concrete section a length of 700 mm and the insulating section a length of 100 mm.

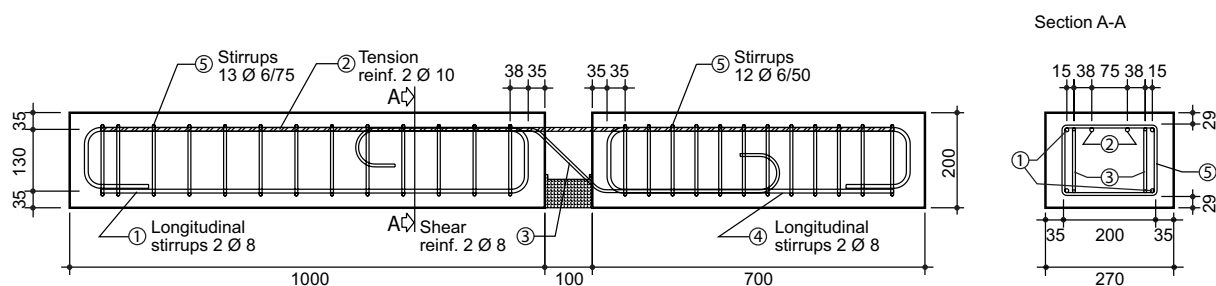


Figure 4.2: Reinforcement and dimensions of the hybrid GFRP/steel experimental beams

The hybrid joint in the insulating section consisted of one CS-element in the lower part, steel reinforcement with two bars ($\text{Ø} 10$ mm) in the upper tension zone and two diagonal bars to take shear. In moment mode, the diameter of the shear bars was 8 mm to prevent yielding and failure in the shear bars while in shear mode, the bar diameter was reduced to 6 mm to provoke yielding in the shear bars. The shear bar's angle α , cp. Figure 4.1, changed with beam depth: 43° for $d = 200$ mm and 51° for $d = 240$ mm. During the production of the beams, the three parts were held together by a styrofoam body also used in real applications.

4.1.4. Materials

The steel reinforcement crossing the insulating section was made from a stainless ribbed rebar (type 1.4462.lwp) with a yielding strength $f_{sk} = 800$ MPa and an ultimate tensile strength $f_{tk} = 900$ MPa, $E_s = 195$ GPa and an elongation at failure $\varepsilon_{tk} = 15\%$ (designation according to SIA 262 [7]). The yielding strain of this steel was assumed as being $\varepsilon_{sk} = f_{sk}/E_s = 800/195000 = 0.41\%$. For the remaining steel reinforcement (pos. 1, 4 and 5 in Figure 4.2), a standard B500 steel was used. The concrete strength $f_{c,cube}$ after 28 days was obtained by three cubic specimens (edge length of 150 mm) and the average strength was transformed into prism strength $f_{c,cyl}$ (80% of $f_{c,cube}$). The results are shown in Table F.2, page 220 and Table 4.2, page 83. For a detailed description of the CS-element, see Section 3.1.

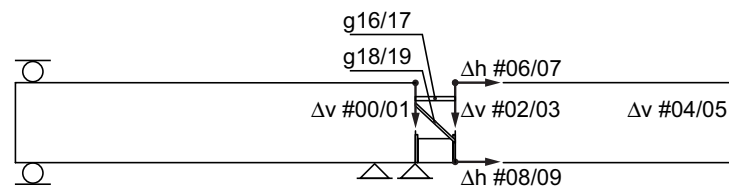


Figure 4.3: Beam with cantilevered support condition. Positioning of displacement transducers and strain gages

4.1.5. Instrumentation

The system's behavior was recorded by displacement transducers in horizontal and vertical directions along the beam and strain gages on the reinforcement and CS-element. The load was measured by a load cell under the load application point.

Displacement transducers

A total of ten displacement transducers were applied on each beam. Their positioning is shown in Figure 4.3 and was independent of the beam's depth or loading position. In the case of the end-support condition, displacement transducers no. 00 and 01 were not used. In Figure 4.3, Δh describes a measurement in the horizontal direction whereas Δv is for the vertical direction. The measurements in Figure 4.3 were made on the left and right sides of the beam. All displacement transducers had an accuracy of 0.01 mm and their travel was 50 mm, except transducers no. 04 and 05 with a travel of 100 mm.

Strain gages

A total of twenty strain gages were used for each beam. The moment and the shear reinforcement bars were prepared each with one strain gage glued to the middle section of its free length inside the insulating section. The numbering of the four strain gages on the steel reinforcement is also shown in Figure 4.3. Figure 4.4 shows the development of a CS-element together with applied strain gages. Dashed lines show the positions of the four webs in the case of top and bottom views or the thickness of the flanges in the case of lateral views. The CS-element was inserted into the insulating section in such a way that gages g00, g01, g06 and g07 faced towards the loaded side. With this arrangement it was possible to measure the strain distribution on the element surfaces at expected stress concentrations and thus determine the principle flow of force. Gages g08-g10 and g12-g14 were gathered into two rosettes respectively with a distribution of 0-45-90°. With this arrangement it was possible to calculate the principal stress angle inside the CS-element. The calculation is explained in Appendix F.2, page 219.

4.1.6. Experimental results

Load-displacement responses

Vertical displacements were measured on both sides of the insulating section (nos 00 and 01, nos 02 and 03 in Figure 4.3), and at the end of the cantilevered beam section (nos 04

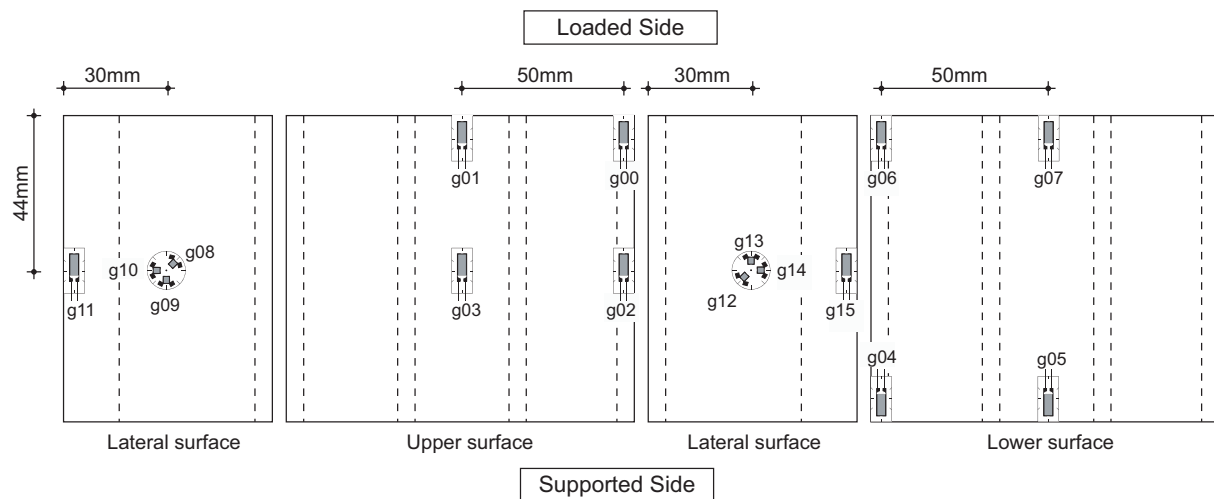


Figure 4.4: Positioning of strain gages on CS-element

and 05). They showed linear-elastic behavior during the first loading cycle. For the three following cycles, the response was elastic-plastic. In Figures 4.5 and 4.6, four typical load-displacement diagrams of the final loading cycle are shown. The curves begin slightly shifted from the point of origin proving that plastic deformations had already occurred during previous loading cycles. Measurements between two corresponding displacement transducers agreed very well for all beams. In Appendix F3.1, all load-displacement diagrams in vertical and horizontal directions are shown for each loading cycle.

In Table 4.2, the elastic limit loads, F_{el} , defined as the load after which deformations became plastic, are shown together with ultimate failure loads, F_u . Generally, beams with a depth of 240 mm showed higher ultimate failure loads than 200-mm deep beams (+30 % on average for all beams). In general, beams in shear mode accepted significantly higher ultimate failure loads compared to moment mode (+33 % on average for all beams). The different support conditions showed no significant influence on ultimate failure loads in moment mode. In shear mode, however, beams with end-support condition showed higher ultimate failure loads than those with cantilever-support condition. The increase was +12 % on average for all beams.

The displacements of the cantilevered beam section consist of a rotation around the support point and a vertical offset of the joint. The contribution of each motion can be found by comparing the vertical displacements at the beginning (transducers nos 02 and 03) and at the end of the section (transducers nos 04 and 05). In moment mode, the rotation dominated, while in shear mode the offset was predominant, resulting in a tilting CS-element. Figure 4.7 shows the displacements after failure for beam S200C1 with a predominant offset deformation. In Appendix F4, page 238 the displacements of all beams after failure are shown.

Load-strain responses

Figures 4.8 and 4.9 show typical measured axial strains on the steel reinforcement and on the lower side of the CS-element in moment mode and shear mode. It can be seen that in

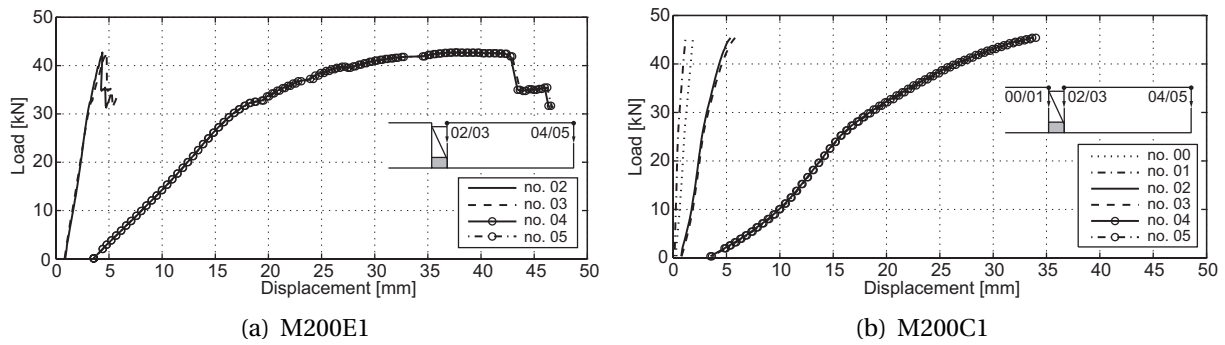


Figure 4.5: Vertical displacements in failure cycle - moment mode

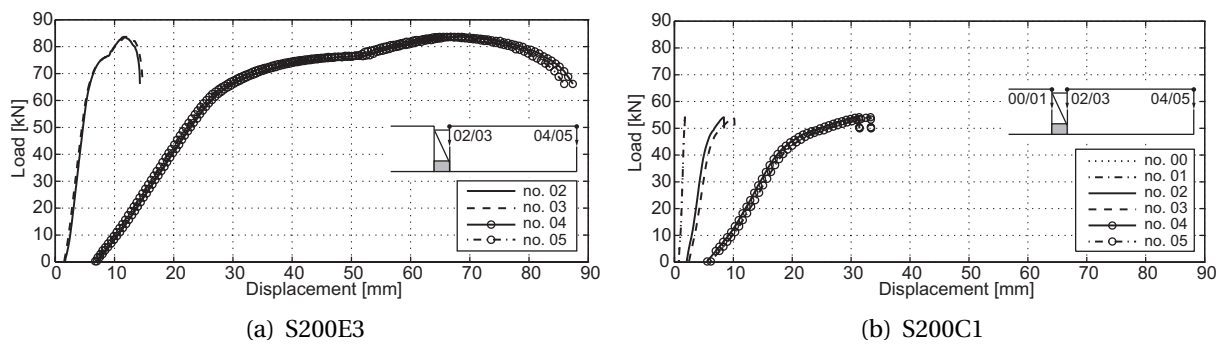


Figure 4.6: Vertical displacements in failure cycle – shear mode

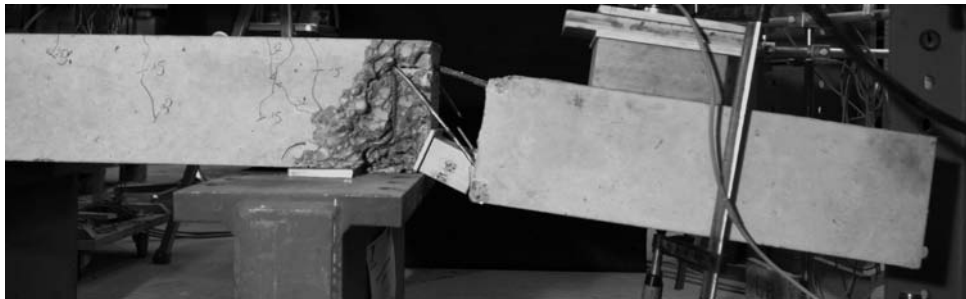


Figure 4.7: Failure mode of beam S200C1 – tilting of CS-element and predominant offset deformation

moment mode the upper bars always yielded, while strain in the shear bars remained in the elastic range. In shear mode yielding occurred in all steel reinforcement, but was more pronounced however in the shear bars, cp. Figure 4.9b. Furthermore, strains measured on the lower side of the CS-element were always greater in moment mode than in shear mode at the same load. In Appendix F.6, page 247, the axial strains are shown in the first and failure cycles.

Figure 4.10 shows typical strain measurements on the GFRP CS-elements on the upper surface, both lateral surfaces and the lower surface during the third loading cycle. The third loading cycle was chosen because in the failure cycle, measurements often became unstable

Table 4.2: Measured cylinder compression strength of concrete, elastic and ultimate limit loads

Specimen	$f_{c,cyl}$ [MPa]	F_{el} [kN]	F_u [kN]
M200E1	31.4	29	42.6
M200E2	38.1	29	47.9
M240E1	31.4	39	54.4
M240E2	38.1	41	64.6
S200E1	35.7	44	60.0
S200E2	38.7	50	64.3
S200E3	34.4	61	83.8
S240E1	35.7	49	69.6
S240E2	38.7	47	70.3
S240E3	34.4	59	81.6
M200C1	37.6	28	45.1
M200C2	44.6	26	44.5
M240C1	37.6	36	59.6
M240C2	44.6	30	54.8
S200C1	40.5	33	53.8
S200C2	43.6	43	53.8
S240C1	40.5	49	77.2
S240C2	43.6	47	72.9

and reliable values could no longer be obtained. In moment mode almost no strain was measured on the upper flange in contrast to large strains on the lower flange that increased towards the supported side. In contrast to the moment mode, in shear mode the upper flange exhibited small strains at the supported side that increased towards the loaded side. The lower flange showed large strains on the supported side that decreased towards the loaded side. In Appendix F.7, page 253, all CS-element strain measurements are shown.

The angles of second principal stress, φ , were measured by the rosettes on the CS-element's lateral surfaces. Figure 4.11 shows an example of φ in the third loading cycle of beam S200E3. The resulting angle, related to the horizontal axis, was approximately 40° and remained almost constant with increasing load. The measured graphs of all angles are shown in Appendix F.9, page 275, in the third and failure cycles. The third loading cycle is added because of measurement instabilities that often occurred in the last cycle. In addition, Table 4.3, page 90, gives the measured angles of second principal stress in the CS-elements in all other beams. The average values from both webs in the third loading cycle are listed.

Crack formation in concrete

Cracks along both concrete sections were mapped after each of the first three loading cycles and after failure and marked with the corresponding load. In general, cracks appeared only after the second loading cycle, mainly on the supported concrete section, cp. Figure 4.7, as

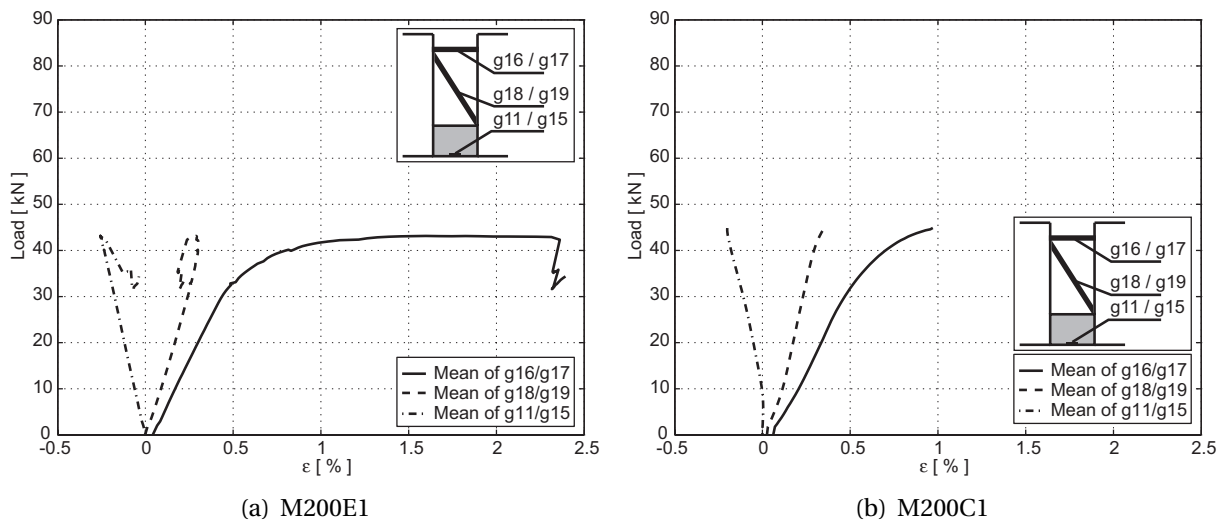


Figure 4.8: Axial strain in failure cycle – moment mode

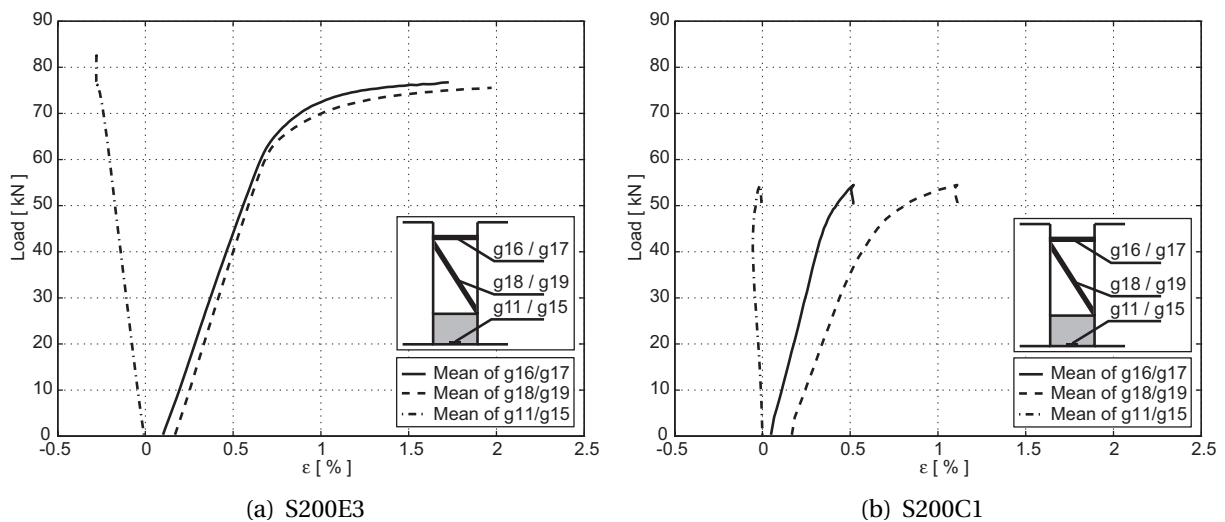
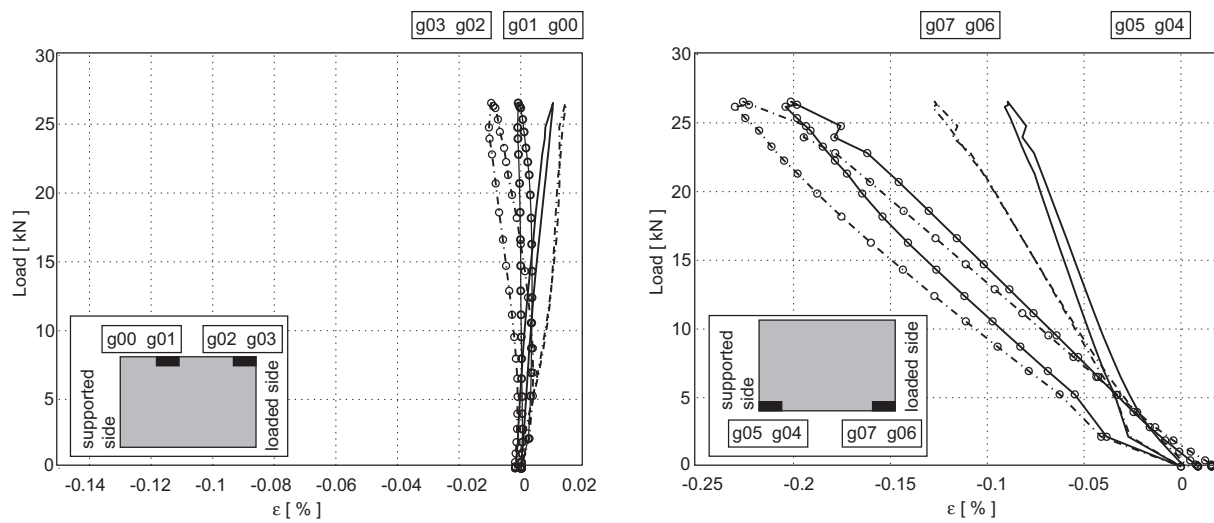


Figure 4.9: Axial strain in failure cycle – shear mode

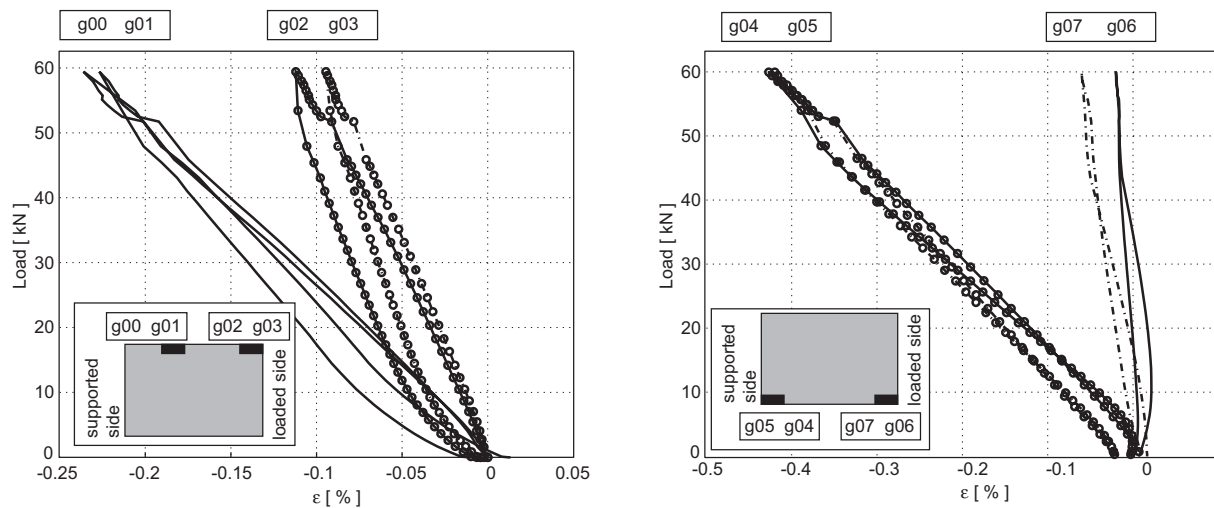
shown in Appendix E.5, page 242. Due to an upward curving of the supported concrete section, cracks developed from the top to the bottom of the beam. The tension force in the curved shear reinforcement caused the concrete to split on top of the supported concrete section near the insulating section. The splitting of the concrete was announced by longitudinal cracks above the reinforcement. The cutting of the shear reinforcement amounted to several centimeters, cp. Figure 4.7 and Appendix E8.2, page 270.

Failure modes

Generally, yielding of the steel reinforcement was followed by global failure through crushing of the concrete. Exceptions were beams in shear mode with end support, where either the cap plates debonded because of the weak adhesion between profile and cap plates, or the



(a) Moment mode (M200E2)



(b) Shear mode (S200E3)

Figure 4.10: Measured axial strain on CS-element surface

steel reinforcement failed in the case of improved adhesion. The failure characteristics are shown in Figures 4.12 and 4.13 by photographs and schematic drawings. It can be seen that failure locations changed depending on loading modes and support conditions.

In moment mode, the concrete failed throughout on the CS-element's lower surface in the cap plate concrete interface. On the element's upper surface, an opening gap between the cap plate and the supported concrete section was observed. With end support, failure took place on the loaded side (Figure 4.12a), while with cantilevered support it occurred at the supported side, (Figure 4.12b). After concrete failure, secondary failure occurred in the CS-element in the form of longitudinal cracks at the junction between the outer webs and lower flanges as can also be seen in the figure.

In shear mode with end-support condition, debonding of the cap plate was the initial fail-

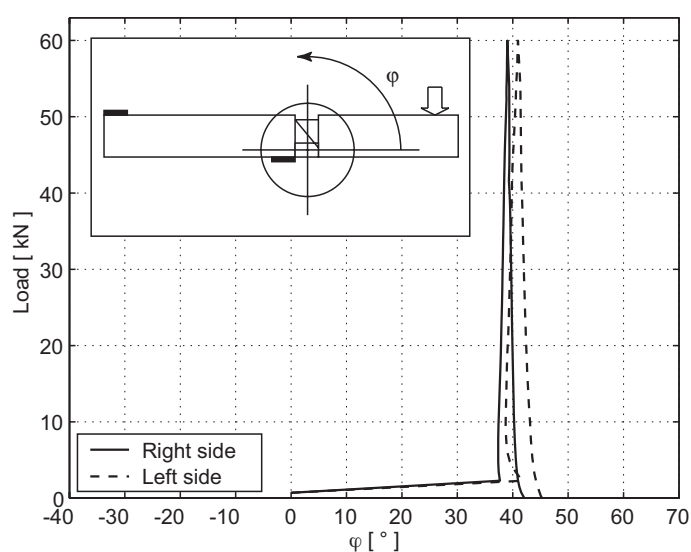


Figure 4.11: Angle of second principal stresses, φ , from rosette gages on CS-element's webs in third loading cycle (S200E3)

ure in the first two beams of each depth. In the third beam of each depth, with improved cap-plate adhesion, failure occurred in the steel bars. In beam S200E3, the upper bars failed, while in S240E3 the upper and the shear bars failed at the same time. In all cases an opening gap was observed at the interface between the cap plate and the concrete on the supported side at the element's upper part and on the loaded side at the element's lower part, indicating a tilting of the element, compare schemata in Figure 4.13. Also in the third series a debonding cap plate was observed, but this time as secondary failure (Figure 4.13a). The concrete on both sides remained undamaged. Beams with cantilever-support condition failed similarly to the corresponding beams in moment mode: the concrete failed on the supported side during yielding of the upper steel bars and remained undamaged on the loaded side (Figure 4.13b). As for beams with end-support condition, a tilting behavior of the CS-element could be observed. Secondary failure occurred in the junctions between the outer webs and upper flanges and in the adhesive layer between the profile and cap plate on the loaded side, cp. Figure 4.13b. All failure modes are shown in Appendix F.8.1, page 262.

4.1.7. Discussion

Load transfer through the CS-element

The strain measurements on the GFRP element's surfaces showed that in moment mode the strain was insignificant on the upper flange, but far greater in the lower flange, cp. Figure 4.10a. This led to the conclusion that most of the compression force was transferred through the lower flange. Small measured angles of principal compression stress (8-28° related to the horizontal axis, cp. Table 4.3) showed that almost no shear was transferred by the webs. The shear transfer was indicated by the increased axial strains in the lower flange towards the support, shown in Figure 4.10a (right), resulting from the co-action of the

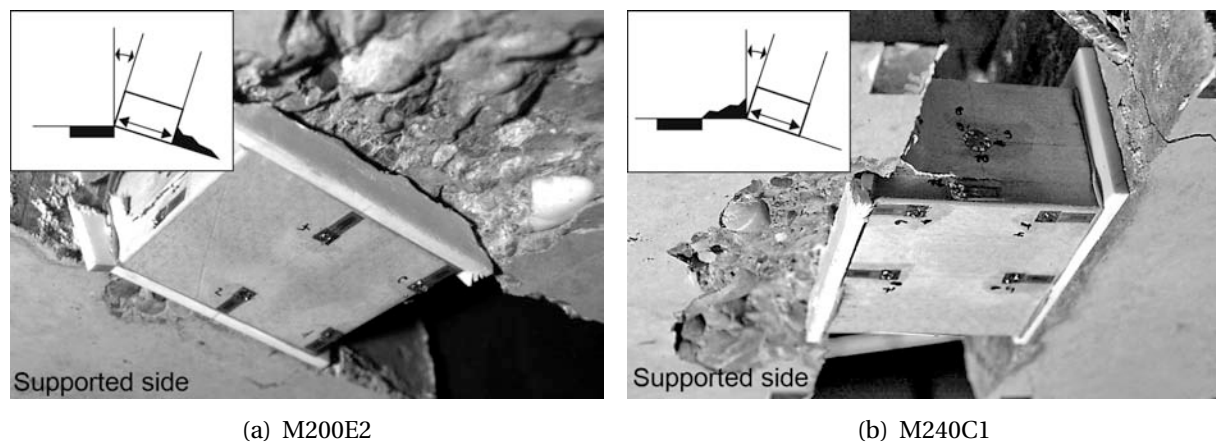


Figure 4.12: Failure modes in moment mode, view from below. (a) Concrete failure at loaded side, no damage at supported side; (b) Concrete failure at supported side, no damage at loaded side

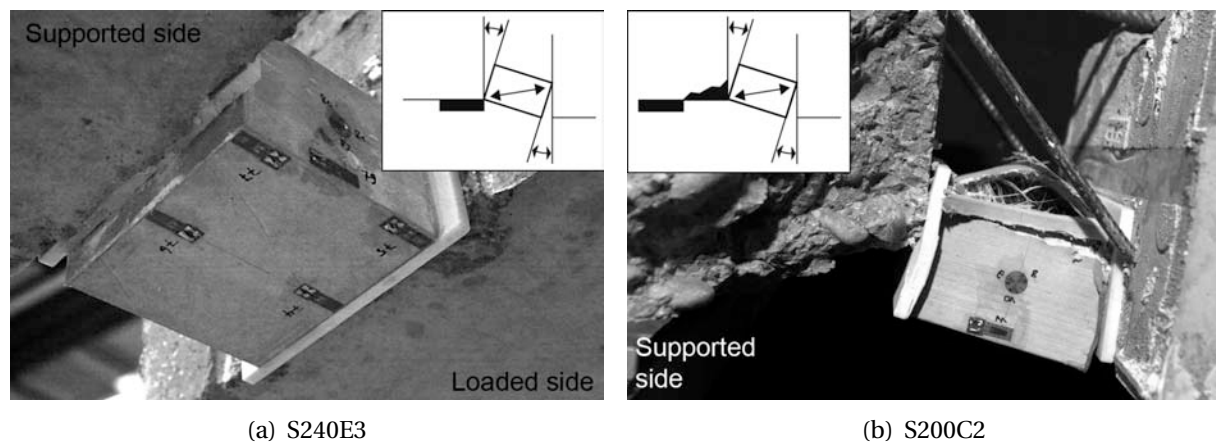


Figure 4.13: Failure modes in shear mode, view from below. (a) Concrete undamaged, steel bar failure, debonding failure (secondary); (b) Concrete failure at supported side, no damage at loaded side

compression force from the moment and the horizontal component of the diagonal force in the webs. In view of the amplitude of this additional strain ($\sim -0.1\%$), the element's relatively small elastic compression modulus of 16 000 MPa in the longitudinal direction, cp. Section 3.2, and the small angles of principal stress in the webs, the vertical shear portion must have been small, as explained in the following.

In shear mode, both axial strain measurements and angles of second principal stress showed a load transfer from the upper flange on the loaded side to the lower flange on the supported side (high strain on both locations, cp. Figure 4.10b). This observation corresponded with the measured angles of principal stress, 24-41°, which were greater than in moment mode and scattered around the geometric diagonal of the element (34°). Further, the strain measurements corresponded to the observed element's tilting explained above. Since the lower flange on the loaded side was almost unstressed, no load was transferred at this point.

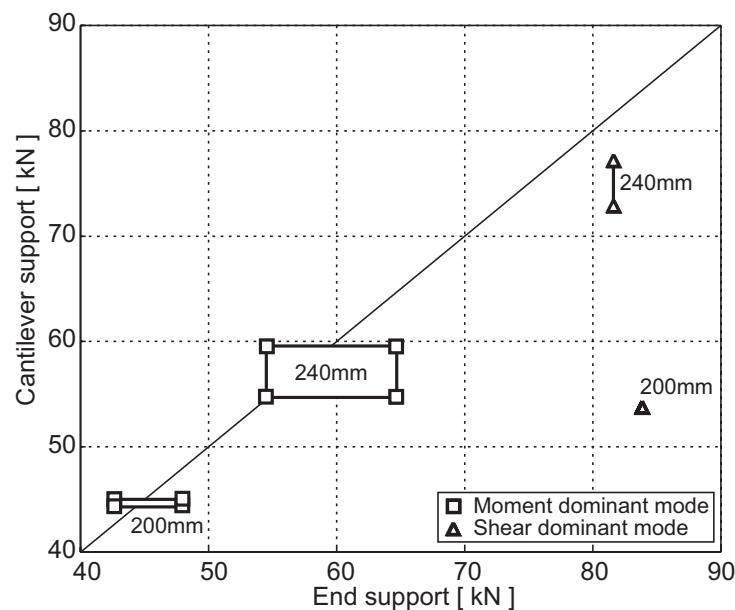


Figure 4.14: Influence of loading mode, support condition and beam depth on ultimate failure loads

The CS-elements with good bond quality were never the first parts in the joint to fail. In fact, their failure was always preceded by that of either the concrete or the steel bars. The pultruder indicates general shear strength of 25 MPa for standard profiles. The actual shear strength of the GFRP profile was not investigated: however, since the highest calculated shear stress at failure was ~ 44 MPa for beam S200E3¹, the actual shear strength was assumed to lie above 25 MPa. The highest axial compression stresses at failure also occurred in beam S200E3 and amounted to 189 MPa^2 , which is below its measured compression strength of 265 MPa, cp. Table 3.2.

Influence of loading mode, support condition and beam depth

Figure 4.14 shows the influences of loading mode, support condition and beam depth on ultimate failure load, F_u . In shear mode, only the beams with good bonding were considered. From this it can be seen that beams with a depth of 240 mm accepted generally higher ultimate failure loads than those with a depth of only 200 mm. This was independent of loading mode and support condition.

In moment mode, F_u was not influenced by the support condition. With end-support condition, the concrete failed at the loaded side since the concrete strength on the supported side was increased by the confinement provided by the support. With the cantilevered support, the confinement on the supported side was removed and the concrete failed here because of the slight increase in force towards the support as described above. The difference, however, was as already mentioned too small to cause any significant variations between the two support conditions but sufficient to change the failure location.

¹ $V_{\text{FRP}} = 52.9 \text{ kN}$, cp. Table 4.3, divided by the area of the profile's webs ($4 \cdot 5 \cdot 60 = 1200 \text{ mm}^2$).

² $C_{\text{FRP}} = 302.5 \text{ kN}$, cp. Table 4.4, divided by the area of the lower flange (1600 mm^2).

In shear mode and end-support condition, the highest failure loads were observed. This was due to the fact that the load, as explained above, was transferred from the upper flange at the loaded side to the lower flange at the supported side. Therefore, on both occasions the confinement increased the concrete compression strength. The concrete remained intact and the steel bars failed instead. The confinement effect on the loaded side is explained by the fact that the point of load introduction was moved to approximately 60 mm above the lower beam edge. This mechanism worked for each support condition. In shear mode with cantilever support, the confinement on the supported side was removed and since the compression strength of the concrete thus returned to normal, failure occurred at this location. The ultimate failure loads were therefore smaller compared to shear mode with end-support condition but considerably higher compared to the corresponding beams tested in moment mode due to the smaller moment-to-shear-force ratio.

Shear transfer capacity of the CS-element

With a view to the development of the all-GFRP joint, it was important to ascertain the amount of shear transfer through the CS-element. The proportion of shear transferred through the CS-element, V_{FRP} , was indirectly determined from the measured axial strains in the shear bars, $\varepsilon_{s,meas}$, and was calculated as follows:

$$V_s = \varepsilon_{s,meas} \cdot E_s A_s \cdot \sin \alpha \leq V_{sk} = \varepsilon_{sk} \cdot E_s A_s \cdot \sin \alpha \quad (4.1)$$

with E_s and A_s being the elastic modulus and cross section of the shear bars and α designating their angles as shown in Figure 4.1, $\varepsilon_{sk} = 0.41\%$ is the steel bar's yielding strain, while V_{sk} is the resulting shear load of the beams when the shear bars yield. The shear transfer in the upper steel bars due to dowel action and inclination was only approximately 1-2% and was disregarded. Therefore, the total amount of shear taken by the shear reinforcement (V_s) and the CS-element (V_{FRP}) must be equal to the applied load, hence:

$$V_s + V_{FRP} = F_u \quad (4.2)$$

where F_u = ultimate failure load. In Table 4.3, V_s and V_{FRP} are listed. The results show that in moment mode, almost no shear was transferred by the CS-element. In shear mode, however, the CS-element transferred between 43-63% of the shear force through the webs at ultimate limit state, independent of the support condition. The results corresponded to the measured angles of principal stress discussed earlier (smaller angles in moment mode and greater angles in shear mode). In shear mode, the shear reinforcement yielded throughout when the ultimate load was approached and the remaining shear force was taken by the CS-element.

Influence of confinement on concrete strength

The present system had two points where local confinement is present: on the supported side with end-support condition at the lower edge of the CS-element and on the loaded side at its upper edge, since in both cases the forces can be distributed in the surrounding ma-

Table 4.3: Shear forces transferred by CS-element (* steel bar yielding, ** at onset of yielding)

Specimen	Failure load measured F_u [kN]	Shear portion shear bars V_s [kN]	Shear portion FRP element V_{FRP} [kN]	Shear proportion FRP element V_{FRP} [%]	Angle of principal stress φ [°]
M200E1	42.6	41.4	1.2	3	21
M200E2	47.9	50.8	0	0	21
M240E1	54.4	56.4	0	0	10
M240E2	64.6	57.9	6.7	10	8
S200E1	60.0	30.9 *	29.1	49	32
S200E2	64.3	30.9 *	33.4	52	38
S200E3	83.8	30.9 *	52.9	63	40
S240E1	69.6	35.2 *	34.4	49	34
S240E2	70.3	35.2 *	35.1	50	24
S240E3	81.6	35.2 *	46.4	57	38
M200C1	45.1	44.1	1.0	2	8
M200C2	44.5	54.8 **	0	0	17
M240C1	59.6	62.5 **	0	0	10
M240C2	54.8	62.5 **	0	0	16
S200C1	53.8	30.9 *	22.9	43	26
S200C2	53.8	30.9 *	22.9	43	30
S240C1	77.2	35.2 *	42	54	33
S240C2	72.9	35.2 *	37.7	52	35

terial. The resulting compressive strength at the loaded side on the bottom edge of the CS-element, σ_{cu} , was calculated using Equation 4.3.

$$\sigma_{cu} = \frac{C_{FRP}}{A_{c0}} = \frac{1}{A_{c0}} \cdot \left(\frac{M_u}{h} + \frac{V_{FRP}}{\tan \varphi} \right) \quad (4.3)$$

with C_{FRP} as the contact force in the lower CS-element's flange at failure and A_{c0} as the equivalent contact area, shown in Figure 4.15. A_{c0} resulted from the expansion of the area of the lower GFRP flange (100 mm · 16 mm) through the cap-plate thickness, and was increased due to a partial contribution of the webs. The resulting area was $26 \cdot 112 = 2912 \text{ mm}^2$. $M_u = F_u \cdot e$ is the bending moment at failure with e = lever arm from the support to the load, $h = d - d_s - \frac{d_c}{2}$ is the lever arm between tension and compression forces in the beam, with $d_s = 40 \text{ mm}$ consisting of the concrete cover (35 mm) plus half of the bar diameter and $d_c = 26 \text{ mm}$ is the depth of A_{c0} .

The calculated values for C_{FRP} and the resulting compression strength σ_{cu} are listed in Table 4.4. The latter is compared to $f_{c,cyl}$, the uni-axial prism strength of the concrete, cp. Table 4.2. The Swiss Code SIA 262 [7] takes the confinement effect into account by a factor

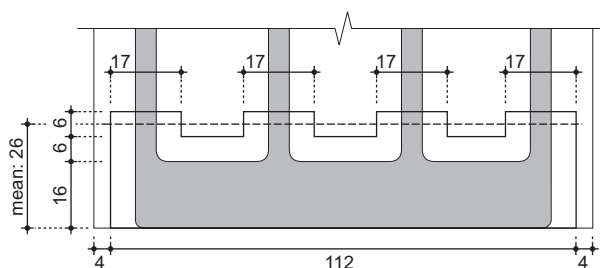


Figure 4.15: Contact area A_{c0} between cap plate and concrete (units in [mm])

$k_{c,SIA}$:

$$k_{c,SIA} = \sqrt{\frac{A_{c1}}{A_{c0}}} \geq 3.0. \quad (4.4)$$

Here, A_{c1} is the area of possible expansion in a certain depth inside the concrete body, cp. Figure 4.16. On concrete failure locations, (supported side with cantilever support and loaded side in moment mode and end support), only horizontal expansion from the cap plate ($b_1 = 112$ mm) to the beam width ($b_2 = 270$ mm) could be taken into account since the equilibrium of forces did not permit vertical expansion. The resulting factor $k_{c,SIA}$ in this case was 1.55. On the supported side with end-support condition and on the loading side in shear mode, where the vertical part of the expansion could be taken into account, $k_{c,SIA}$ reached the limit of 3.0 imposed by SIA 262, the calculated value being 3.10.

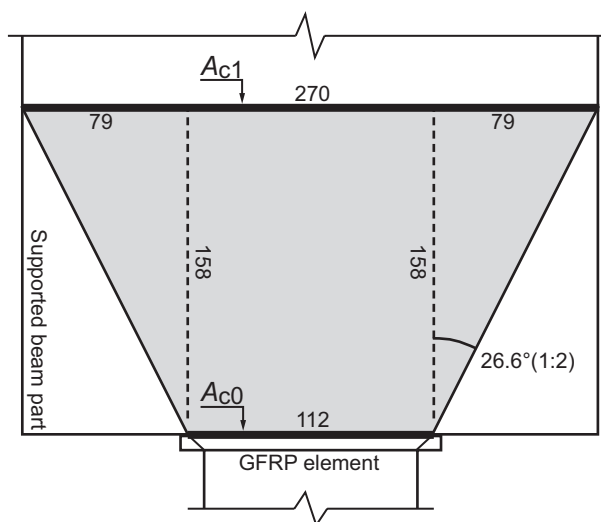


Figure 4.16: Identification of A_{c0} and A_{c1} for cantilever-support condition (top view of horizontal expansion)

The confinement factors resulting from the experiments, k_c , were calculated according to

Equation 4.5:

$$k_c = \frac{\sigma_{cu}}{f_{c,cyl}} \quad (4.5)$$

In Table 4.4, the values resulting from the experiments (k_c) and from the SIA code ($k_{c,SIA}$) are compared. It can be seen that beams with failure on the supported side (cantilever support) showed good agreement between k_{cm} (1.72) and $k_{c,SIA}$ (1.55) with a deviation of 10%. On those specimens without concrete failure, k_{cm} (2.27) was clearly below $k_{c,SIA}$ (3.10). For concrete failure on the loaded side, finally, k_{cm} (2.03) exceeded $k_{c,SIA}$ (1.55) by 31%. On the loaded side, no gap was observed in these cases (cp. also Figure 4.10a, schematic drawing) and, although no stress transfer in the upper edge was measured, cp. Figure 4.10a, it was assumed that the load-transmitting contact area was deeper than the above-mentioned 26 mm.

Table 4.4: Comparison of confinement factors for concrete strength from experiments and Swiss Code SIA 262

Specimen	M_u [kNm]	h [m]	M_u/h [kN]	$V_{FRP}/\tan\varphi$ [kN]	C_{FRP} [kN]	σ_{cu} [MPa]	k_c [-]	k_{cm} [-]	$k_{c,SIA}$ [-]
M200E1	28.1	0.147	191.2	-	191.2	65.6	2.03	2.03 loaded side	1.55
M200E2	31.6	0.147	215.0	-	215.0	73.8	1.94		
M240E1	35.9	0.187	192.0	-	192.0	65.9	2.10		
M240E2	42.6	0.187	227.8	-	227.8	78.2	2.05		
S200E1	25.2	0.147	171.4	46.6	218.0	74.9	2.10	2.27 supported side	3.10
S200E2	27.0	0.147	183.7	42.8	226.5	77.8	2.01		
S200E3	35.2	0.147	239.5	63.0	302.5	103.9	3.02		
S240E1	29.2	0.187	156.1	51.0	207.1	71.1	1.99		
S240E2	29.5	0.187	157.8	78.8	236.6	81.3	2.10		
S240E3	34.3	0.187	183.4	59.4	242.8	83.4	2.42		
M200C1	29.8	0.147	202.7	0.1	202.8	69.7	1.85	1.72 supported side	1.55
M200C2	29.4	0.147	200.0	0.0	200.0	68.7	1.54		
M240C1	39.3	0.187	210.2	0.0	210.2	72.2	1.92		
M240C2	36.2	0.187	193.6	0.0	193.6	66.5	1.49		
S200C1	22.6	0.147	153.7	47.0	200.7	68.9	1.70		
S200C2	22.6	0.147	153.7	39.7	193.4	66.4	1.52		
S240C1	32.4	0.187	173.3	64.7	238.0	81.7	2.02		
S240C2	30.6	0.187	163.6	53.8	217.4	74.7	1.71		

4.1.8. System deformations

The insulating joint is less stiff than the rest of the beam. The deformations in the joint are composed of a vertical displacement and a rotation. The vertical displacement at serviceability limit state was always in the range of 0.5-2 mm (cp. Appendix F.3.1, page 223, first

cycle), which in most practical cases is negligible. The rotation, however, can lead to large deformations with increasing cantilevered spans. It can be calculated from the strain on the upper steel reinforcement and the lower CS-element, whereas only the lower flange of the CS-element is taken into account.

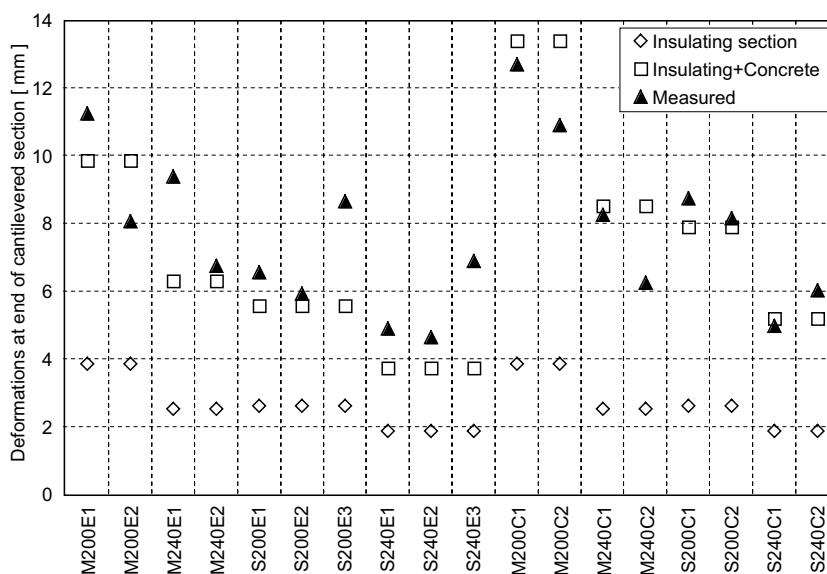


Figure 4.17: Comparison of calculated and measured deformations of the hybrid GFRP/steel system

In Figure 4.17, the calculated and measured vertical displacements at the end of the cantilevered section are compared. The calculated vertical displacements due to joint deformations are shown separately, whereas the vertical offset in the joint was very small and has been disregarded. Deformations in the concrete were obtained using an approximative calculation, König and Tue [64]. The method uses a representative flexural beam stiffness and the lever arm between upper steel reinforcement and the center point of the lower compression zone. Since an applied load of 26 kN was chosen for all experiments, only elastic deformations were exhibited by all beams. Generally, the calculated and measured displacements were of the same order of magnitude. Therefore, and also in view of the simplicity of the calculation, the small amount of experimental evidence and the sometimes large scatter of measured results, the agreement between measured and calculated values proves that it is possible to estimate deformations by traditional beam and concrete theory.

In addition, possible creep deformations had to be considered. In general creep in FRP is known to occur predominantly near the beginning of the load application. Therefore, a creep study over a time span of 50 hours during which a CS-element was subjected to a constant compression load of 16 kN was conducted. During this time span no signs of creep were observed and hence it was concluded that creep was not relevant. The graph is shown in Appendix B.2, page 163.

4.1.9. Conclusions concerning the hybrid steel/GFRP joint

In this section, the first step towards an all-GFRP insulating joint was presented, in which the CS-element replaced the compression steel reinforcement. An experimental series involving beams representing slab systems was conducted to investigate the CS-element, the hybrid GFRP/steel joint and the overall system behavior. The following conclusions were drawn:

- The study proved that the CS-element was never of critical concern at ultimate limit state. The beams failed either in the concrete adjacent to the CS-element or in the steel bars in shear mode in the case of good bond between the element's cap plates and the profile. Therefore, normal concrete theory can be used to dimension this joint, which is an important advantage in practice where FRP dimensioning concepts are still not very common.
- The CS-element transferred the compression force from the moment in all loading modes. In addition, shear was transferred through the tilting element in shear mode with portions between 43-63 % at ultimate failure load. These observations show a promising potential with regard to the intended development of an all-GFRP TS-element, which could exclude the use of steel shear bars. In the case of high shear forces (shear-dominated loading mode), the CS-element will contribute to shear transfer and mitigate the intensity of forces in the TS-element.
- Due to its rotation, the joint causes additional deformations of the concrete structure. This rotation can be considered as a supplement to global deformations and can be determined based on traditional beam theory.

4.2. Beams with all-GFRP insulating joint

4.2.1. Introduction

In addition to the CS-element replacing the compression steel reinforcement in the hybrid joint, in the all-GFRP joint the upper and shear steel reinforcements were replaced by a single GFRP tension-shear (TS-)element as introduced in Section 3.9. The joint, shown in Figure 3.1, is intended to provide a similar load transfer to the hybrid joint, while reducing the thermal conductivity by another 50 % in comparison with the hybrid joint (0.05-0.1 W/(m·K)).

Since only brittle materials are used in the joint, system ductility, which has to be guaranteed as being acceptable in practice, has to be provided by the steel reinforcement and interaction between the different components and the concrete. The system behavior was investigated through a series of full-scale experiments. To establish the limits beyond which the GFRP-material controls failure, different layouts of the TS-element were investigated. Also of interest were the shear-load distribution between the CS- and TS-elements and the transmission of anchorage forces from the ribs into the concrete. Finally, the joint system was modeled analytically.

4.2.2. Experimental program and set-up

As for the hybrid joint, beam cut-outs were intended to adequately represent slab systems. Since with the set-up of the hybrid joint it was possible to record all desired results as well as maintain consistency, the set-up for the all-GFRP joint was identical, although the loading frame was different. Contrary to the hybrid joint, only beams with a depth of 240 mm were investigated and the experimental series consisted of only eight beams. Different support conditions and loading modes, as explained in Section 4.1.2, were combined with two TS-elements that differed in their rib arrangement, cp. Section 3.9. The complete program is shown in Table 4.5, the beams being labeled *M/S* for 'moment' or 'shear' mode, followed by the number of ribs on each side of the TS-element, and *E/C* for 'end' of 'cantilever' support, followed by a replicate index.

Table 4.5: Composition of all-GFRP joint experimental series

Number of ribs per side	2 ribs		3 ribs	
Loading mode Support condition	Moment / End	Shear / Cantilever	Moment / End	Shear / End
Type of Specimen	M2E1 M2E2	S2C1 S2C2	M3E1 M3E2	S3E1 S3E2

The combinations were chosen as follows: in moment mode, no cantilever support condition was applied since results from the hybrid joint experiments showed only a small difference between changing support conditions. Instead, since the tensile forces are highest in moment mode, the influence of different rib numbers was investigated. For beams M2E1/2 anchorage failure and for beams M3E1/2 concrete failure at the lower edge of the loaded side were expected. The beams corresponded to M240E with a hybrid joint. In shear mode, S3E1/2 (corresponding to S240E) and S2C1/2 (corresponding to S240C) were chosen, in which S3E1/2 was expected to provoke the highest shear load with accompanying shear failure in the TS-element, while for the S2C1/2 combination concrete failure on the supported side was expected. Calculations proved that tensile failure in the TS-element would never occur because of its high tensile strength.

The loading frame is explained in Appendix G.1, page 285. The loading cylinder had a maximum loading capacity of 300 kN and a travel of 150 mm. The load was applied displacement-controlled at a rate of 5.0 mm/min. The loading procedure was divided into four cycles: 0-20 kN, 0-40 kN, 0-60 kN and 0-failure. During each loading cycle the crack pattern was recorded together with the corresponding load.

4.2.3. Experimental specimens

Figure 4.18 shows the dimensions and the reinforcement of a two-rib beam and the placement of the TS- and CS-elements in the concrete section. The outer concrete dimensions were the same for all beams and identical to those of the hybrid-joint specimens with two

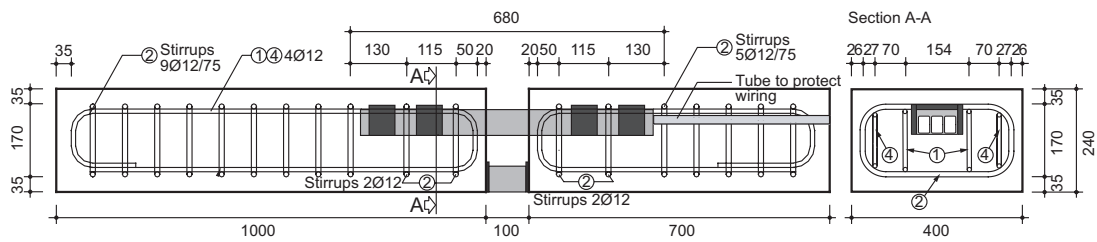
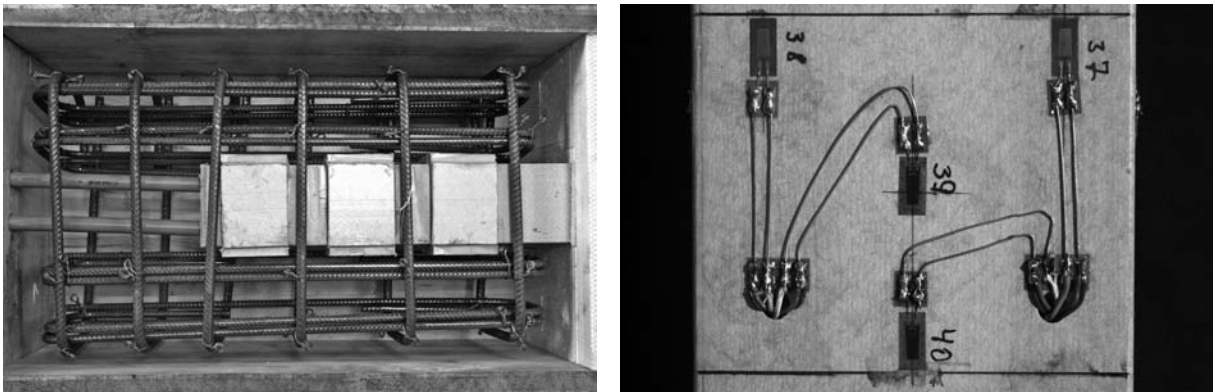


Figure 4.18: Reinforcement and dimensions of the all-GFRP beam specimen



(a) Anchorage part of a three-rib element installed in the formwork of the loaded beam side (top view) (b) Strain gage and wire arrangement in an upper 80-mm rib

Figure 4.19: Anchorage of TS-element and strain gages with wiring

exceptions: firstly, the width had to be increased from 270 to 400 mm due to the required stirrup diameter of 12 mm. This diameter resulted from an estimation of the transverse tensile forces due to horizontal spreading of the concentrated loads introduced by the upper ribs into the concrete. Secondly, only beams with a depth of 240 mm were investigated. A more detailed description of the arrangement of the remaining steel reinforcement in the concrete parts and its dimensions, also for the three-rib beams, is shown in Appendix G.1, Figures G.2 and G.3, page 287.

The reinforcement in the concrete parts consisted of a B500 steel according to SIA 262. The concrete strength, $f_{c,cube}$, after 28 days was obtained by three cubic specimens (edge length of 150 mm) and the average strength was transformed into prism strength, $f_{c,cyl}$ (80 % of $f_{c,cube}$). These values are shown in Table 4.7 on page 102 (detailed data in Appendix G.1, Table G.1, page 286). Both GFRP elements are described in Chapter 3. The arrangement and position of the CS-element in the all-GFRP joint remained unchanged compared to the hybrid joint. The TS-element was positioned upside down with the stirrups from the steel shear reinforcement applied between the ribs, cp. Figure 4.19a. The concrete cover over the steel stirrups was 35 mm thick and which also applied to the ribs, since their depth was the same as the stirrup diameter.

4.2.4. Instrumentation

The system behavior was recorded by displacement transducers in horizontal and vertical directions along the beam. They were aligned in the same manner as for the hybrid beam. The different numbering is shown in Figure G.4, page 288.

In addition to displacement transducers, the CS- and TS-elements were equipped with a total of 61 strain gages for two-rib beams and 81 strain gages for three-rib beams. The configuration of the strain gages on the CS-element was identical to that of the hybrid joint series. Their different numbering is shown in Figure G.5, page 288. On the TS-element, strain was measured under each rib on the upper surface and both lateral surfaces. In addition, eight strain gages were applied at the symmetry axis inside the insulation section. Figure 4.20 shows top and lateral views of both elements. Complete plans with all strain gages and numbering are shown in Figure G.6, page 289.

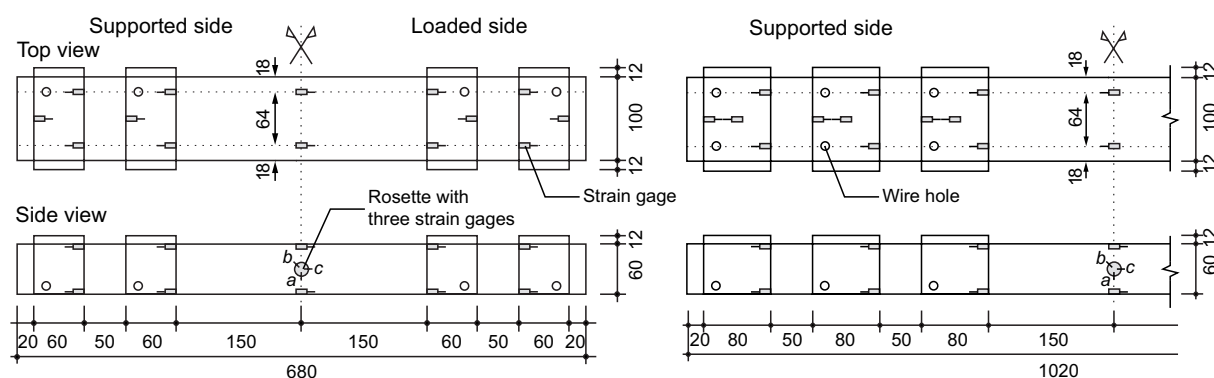


Figure 4.20: Side and top view of two- and three-rib TS-element with strain gage arrangement

To determine the angle of principal stress, two rosettes with a 0-45-90° strain gage arrangement were applied on each of the TS- and CS-element's lateral surfaces. The calculation of the angles from the obtained measurements is explained in Appendix F.1 and the assignment is shown in Appendix G.2 on page 288.

To wire the strain gages, holes were drilled through the thick flange under each rib as shown in Figures 4.20 and 4.19b. The wires were passed through the profile in the loaded beam section and through an outlet in the completion plate. To bridge the distance between tension elements and formwork and protect the cables, the wiring was passed through two tubes (outer \varnothing 20 mm) as shown in Figure 4.19a.

4.2.5. Results

Load-displacement responses

Figures 4.21 and 4.22 show four examples of load-displacement diagrams during the failure cycle. It can be seen that three-rib beams bore higher loads than two-rib beams. Further, in shear mode ultimate failure loads were higher than in moment mode, this difference being more significant for three-rib beams, cp. Table 4.7. As to deflections at ultimate failure load, no significant differences were observed at the end of the cantilevered beam sec-

tion (displacement transducers nos 18/19). Deflections at the beginning of the cantilevered beam section (displacement transducers nos 16/17) were slightly higher in shear mode; however, no significant differences were seen between three- and two-rib beams. Comparison at equal loads before ultimate failure load showed that three-rib beams in shear mode had the smallest deformations, while two-rib beams in moment mode deformed the most. This was due to greater elongations of the tension element in moment mode as well as plastic deformations of the retaining upper steel bars in the concrete.

From a comparison of measurements from nos 16/17 and nos 18/19 it could be seen that the deformations were caused by two major motions: a vertical offset of the cantilevered beam section and its rotation around its supporting point. The main deformation in the joint was an almost parallel offset of the two adjacent beam parts due to predominant shear deformation causing rhomboidal deformations in the TS- and CS-elements. This is illustrated in Figure 4.28b. The rotation of the joint was comparatively small, particularly in shear mode. In Appendix G.3, page 290, the remaining load-displacement diagrams during the failure cycle are shown.

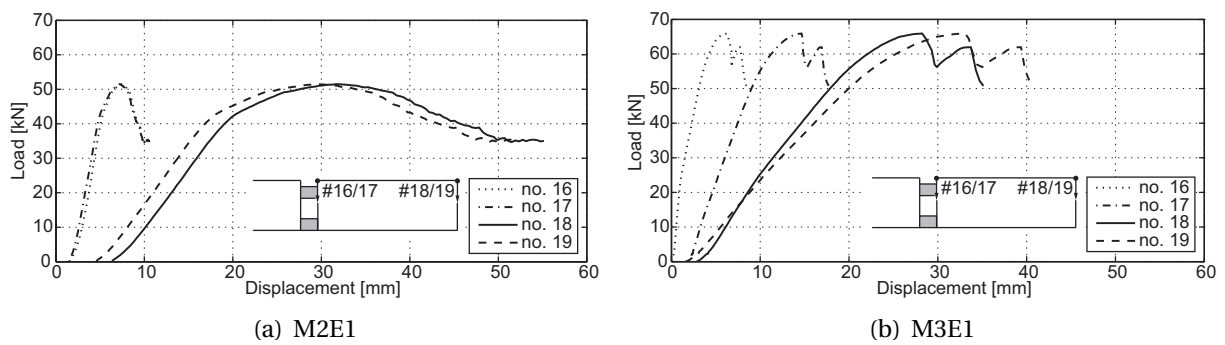


Figure 4.21: Vertical displacements in failure cycle – moment mode

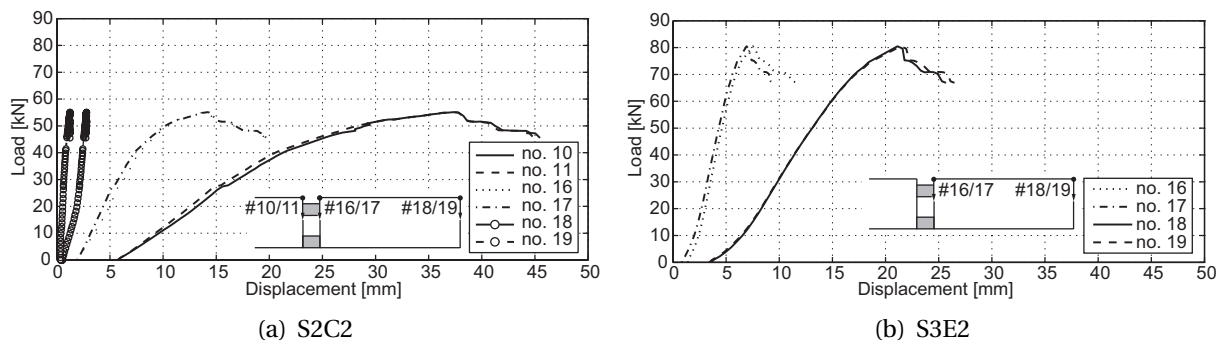


Figure 4.22: Vertical displacements in failure cycle – shear mode

Load strain response on CS-elements

Figure 4.23 shows a typical example of measured strain on the CS-element (beam M2E2). The upper flange shows high strains on the loaded side that decrease towards the supported

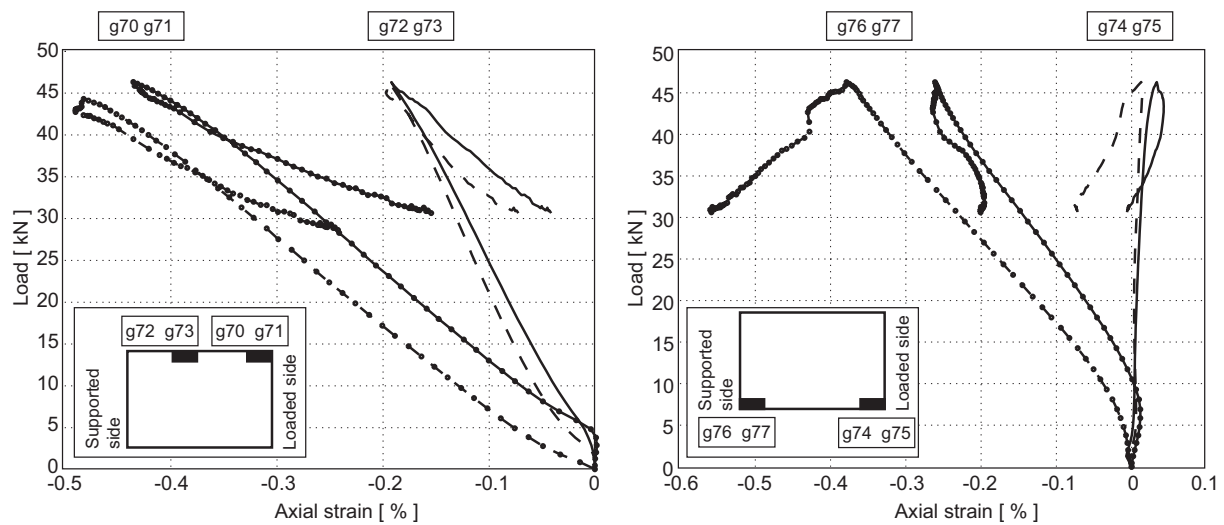


Figure 4.23: Measured axial strains on the upper and lower flanges of CS-element (M2E2)

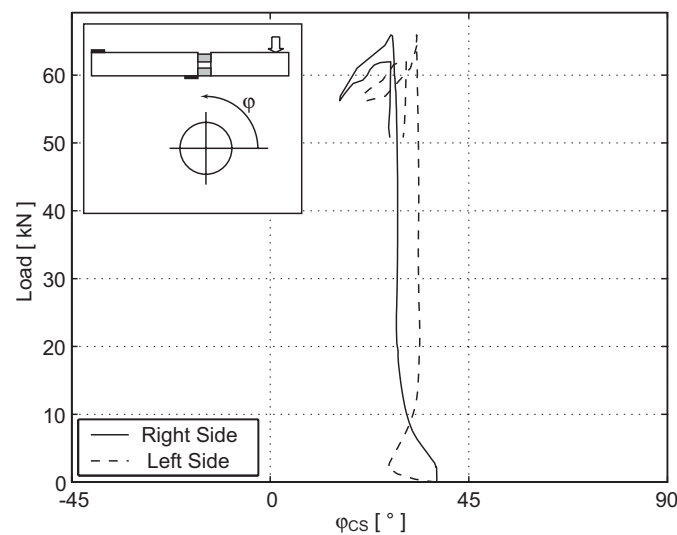


Figure 4.24: Angle of second principal stresses, φ_{CS} , on CS-element webs in failure cycle (M3E1)

side, while on the element’s lower surface the strain increases towards the supported side. Appendix G.6 on page 305 shows measured axial strains on the CS-element for all beams.

The angles of second principal stresses on the CS-element, φ_{CS} , obtained from the lateral rosettes, are given in Table 4.6; Figure 4.24 shows an example from beam M3E1 in the failure cycle that explains the measuring direction. The angles remained almost constant with increasing load up to failure and varied between 20° and 46° on average. This corresponds to the geometric diagonal of the element (34°). In Appendix G.7 on page 309 all principal stress angles are shown.

Table 4.6: Angles of second principal stresses and calculated shear forces transferred in the upper TS- and lower CS-elements

Specimen	Failure load measured F_u [kN]	TS angle of 2 nd principal stress φ_{TS} [°]	CS angle of 2 nd principal stress φ_{CS} [°]	Shear TS / CS element [%]	Shear TS element V_{TS} [kN] (τ_{av} [MPa])	Shear CS element V_{CS} [kN] (τ_{av} [MPa])
M2E1	51.5	45	35	59 / 41	30.3 (25)	21.2 (18)
M2E2	46.5	45	46	49 / 51	22.8 (19)	23.7 (20)
M3E1	65.9	50	30	67 / 33	44.4 (37)	21.5 (18)
M3E2	62.1	42	35	56 / 44	34.9 (29)	27.2 (23)
S3E1	71.7	44	20	73 / 27	52.1 (43)	19.6 (16)
S3E2	80.5	46	42	53 / 47	43.1 (36)	37.4 (31)
S2C1	49.1	45	26	67 / 33	33.0 (28)	16.1 (13)
S2C2	55.1	46	23	71 / 29	39.1 (33)	16.0 (13)
Av \pm sdv	60.3 \pm 11.9	45 \pm 2	32 \pm 9	62 / 38	37.5 (31)	22.8 (19)

Load-strain response of TS-elements

Figure 4.25 shows the axial strain distribution along the upper tensile flange of the TS-elements in beams M3E1 and S3E1 at ultimate failure. Strain measurements beneath the ribs and in the middle of the joint showed that, generally, measured strains were higher on the supported side and decreased from the joint to the element ends, i.e. that axial stresses were transferred from the TS-element through the ribs to the upper steel reinforcement. All strains along the element's upper surface are shown in Appendix G.8, page 311. Figure 4.26 shows the corresponding distributions measured on the elements' lateral surfaces of beam M3E1 (average of both sides) through the depth of the profile's cross section at different locations. The resulting distributions are discussed together with the modeling in Section 4.2.6. The distributions are representative for all other beams, which showed similar results with similar accuracy. Appendix G.9 on page 313 shows all measured lateral strains.

At the TS-element's middle section, two rosettes measured the angle of principal stress in the same manner as on the CS-element, cp. Figure 4.24. The measured angles remained constant over the whole loading cycle up to failure load. They are shown in Table 4.6 (φ_{TS}). This time, independent of beam type, the angles lay between 42° and 50°, and were thus bigger than the geometric diagonal (34°).

Crack formation

Generally cracks formed predominantly at the supported side. They initiated at the upper side of the concrete section and spread downwards. For two-rib beams, cracks initiated during the first loading cycle at 12 kN on average, while for three-rib beams crack initiation took place during the second loading cycle at a load of 24 kN on average. Beams in moment mode developed five cracks and beams in shear mode developed only three cracks. Figure 4.27

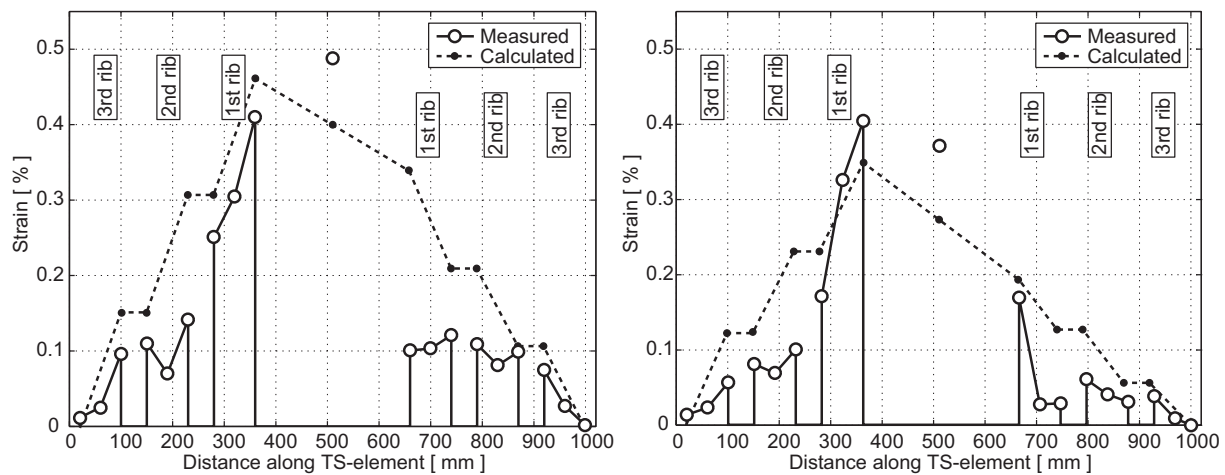


Figure 4.25: Measured and calculated axial strain distribution on the upper tensile flange of TS-element in beams M3E1 (left) and S3E1 (right) at ultimate failure

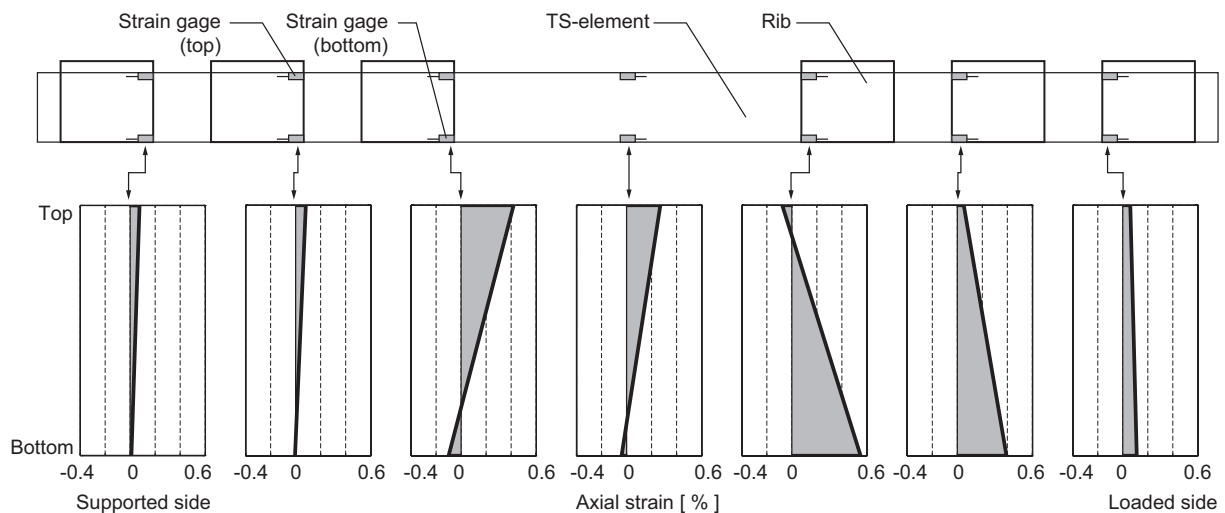


Figure 4.26: Measured axial strain distribution on TS-element's lateral surfaces (average of both sides) through the depth of its cross section at ultimate failure load (S3E1)

shows the crack formation of beam M2E1 after failure. There it can be seen that cracks spread far behind the element end, which proves good load transfer from the element to the longitudinal steel reinforcement. In Appendix G.4 on page 298 all final crack formations are shown.

Failure modes

Figure 4.28 shows the failure mode of beam M2E1. Table 4.7 summarizes all failure modes and loads. Half of the beams, mainly in moment mode, showed anchorage failure on either the loaded or supported side. The TS-elements were pulled out of the concrete, while the retaining steel stirrups showed plastic deformations, cp. Figure 4.28a. Beam M3E1 failed due to upward buckling of the upper flange of the CS-element. Beams in shear mode, except

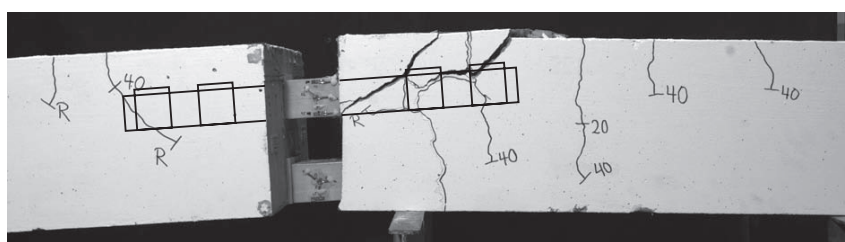
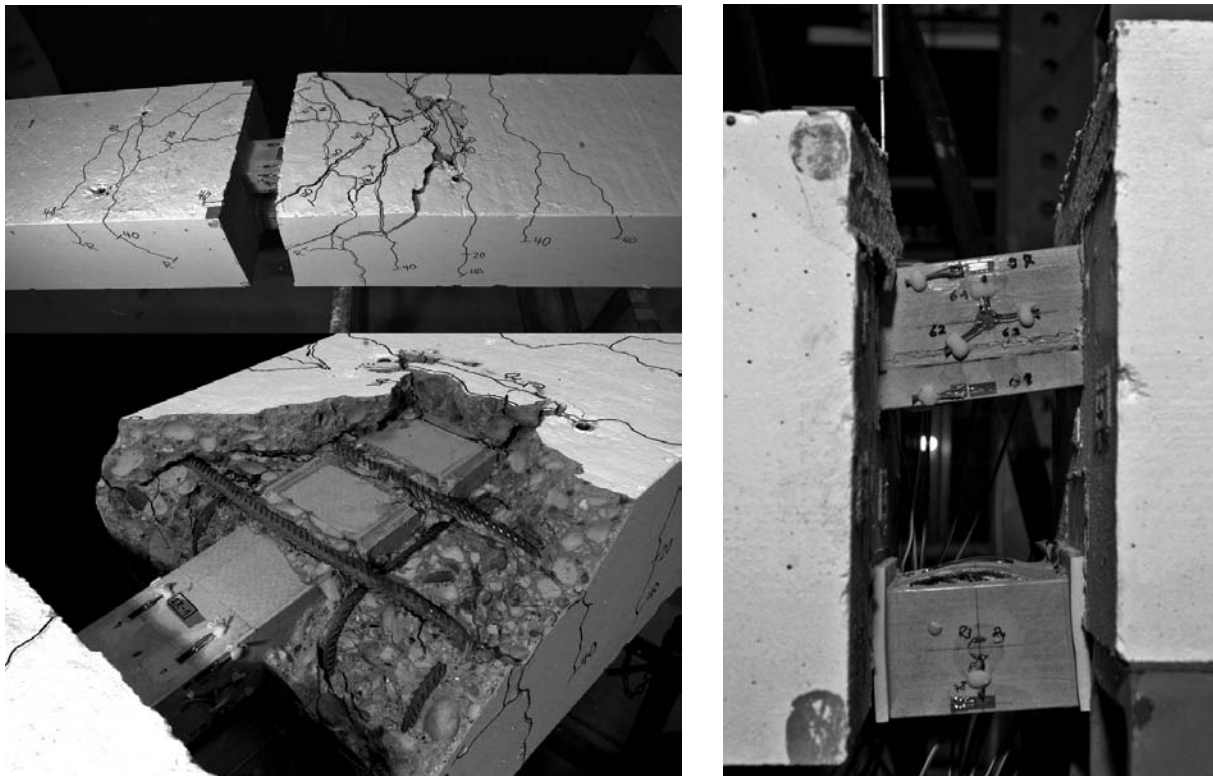


Figure 4.27: Crack pattern on beam M2E1 (20, 40 kN and R for rupture)

S2C1, failed due to shear failure of the TS-element. In the TS-element's profile, horizontal cracks developed along the outer webs, cp. Figure 4.28b. The upward buckling of the upper flange in the CS-element, also visible in the figure, was a secondary failure. The bond layer between the TS-element and the ribs never failed. Appendix G.5, page 301, shows the failure modes of all beams from three perspectives: the lateral view of the insulating section, an overview of the crack pattern and a more detailed view of the concrete failure near the insulating section. As to failure load, the beams could be classified into two-rib beams, which showed the lowest failure load (51 kN on average), three-rib beams in moment mode with a medium failure load of 64 kN on average, and three-rib beams in shear mode for which the highest failure load was measured (76 kN on average).

Table 4.7: Concrete strength, failure loads and modes

Specimen	Concrete strength $f_{c,cyl}$ [MPa]	Failure load F_u [kN]	Failure mode 1st failure
M2E1	34.4	51.5	Anchorage failure on supported side
M2E2	34.4	46.5	Anchorage failure on loaded side
M3E1	32.7	65.9	Flange buckling in CS-element
M3E2	32.7	62.1	Anchorage failure on loaded side
S3E1	32.7	71.7	Shear failure in TS-element
S3E2	32.7	80.5	Shear failure in TS-element
S2C1	34.4	49.1	Anchorage failure on loaded side
S2C2	34.4	55.1	Shear failure in TS-element



(a) Anchorage failure of beam M2E1 on supported side, deformed retaining steel bars

(b) Shear failure in TS-element and secondary failure of upper flange in CS-element (S3E1)

Figure 4.28: Failure modes of all-GFRP insulating sections

4.2.6. Discussion

Transfer of shear forces through the insulating joint

The shear force, V , on the loaded side ($V = F_u$ at ultimate failure) can be divided into two parts: V_{CS} , which is transferred by the webs of the CS-element, and V_{TS} , transferred by the webs of the TS-element to the supported side in accordance with Equation 4.6.

$$V = V_{TS} + V_{CS} = F_u \quad (4.6)$$

As observed and described in Section 4.2.5, page 97, the main motion was an almost vertical offset between both concrete sections and thus, the shear-load distribution between TS- and CS-elements can be directly derived from the measured angles of second principal stress, φ_{TS} and φ_{CS} . In case of parallel offset, the horizontal components of the principal

stresses must be identical in the compression and tension sections. Since the angles of principal stresses are known, the horizontal components can be equated as follows

$$\frac{V_{TS}}{\tan \varphi_{TS}} = \frac{V_{CS}}{\tan \varphi_{CS}} \quad (4.7)$$

Combining Equations 4.6 and 4.7 yields

$$V_{CS} = F_u \cdot \frac{\tan \varphi_{CS}}{\tan \varphi_{CS} + \tan \varphi_{TS}} \quad (4.8)$$

and so

$$V_{TS} = F_u - V_{CS}. \quad (4.9)$$

The forces have to be transferred through the webs of both elements. Table 4.6 summarizes the thus calculated shear forces in both elements. The TS-element was thus able to bear 62 % on average, while the CS-element bore only 38 %. This was apparently due to the fact that the TS-element with its fixed support conditions attracted higher loads than the CS-element, which was not anchored in the concrete and was therefore less stiff. Table 4.6 lists also the resulting average shear stresses, τ_{av} , in the elements' webs. τ_{av} was calculated by dividing the shear force by the area of the four webs ($4 \cdot 5 \cdot 60 \text{ mm} = 1200 \text{ mm}^2$). The highest value for the CS-element was seen in beam S3E2 (31 MPa), which did not provoke failure. In the TS-elements' webs, the highest shear stresses were observed in beams S3E1/2 and M3E1. In those TS-elements that failed in shear (S3E1/2 and S2C2), the pultruder's shear strength of 25 MPa was exceeded by up to 72 % (43, 36, 33 MPa).

Transfer of bending moment in the joint

The bending moment at ultimate failure at the supported joint edge was equal to $F_u \cdot e$ (e = lever arm from the support to the load) and produced a tension force in the TS-element and a compression force of the same magnitude in the CS-element. Assuming that these forces were transferred by the 16-mm flanges of both elements, they could be calculated by dividing the incoming moment by the internal lever arm, h , between the centers of gravity of the upper and lower 16-mm flanges:

$$T = C = \frac{F_u \cdot e}{h} \quad (4.10)$$

$$h = 172 \text{ mm} = d - d_T - d_C \quad (4.11)$$

with $d = 240$ mm being the total depth of the beams, $d_T = 35 + 12 + 8 = 55$ mm the distance between the upper edge of the beam and the center of gravity of the upper 16-mm flange and finally $d_C = 26/2 = 13$ mm the distance between the lower edge of the beam's cross section and the center of gravity of the equivalent area, A_{c0} , cp. Figure 4.15, page 91. The resulting tension forces, T , are listed in Table 4.8. A comparison between shear and moment modes revealed a surplus of 38 % for beams in moment mode while three-rib beams generally bore ~ 37 % higher tension forces than two-rib beams.

In the TS-element, the shear load transfer (V_{TS}) produced a negative moment, $-T' \cdot h'$, at its supported side and a positive moment, $+T' \cdot h'$, at its loaded side due to the fixed supports at both sides of the insulating section. In between these two maximums, moment distribution was linear. The local moments in the TS-element produced a tension (supported side) and compression (loaded side) force in the upper flange in addition to the tension force T from the global moment. Since the local moment was mainly transferred by the TS-elements' upper and lower flanges, the additional forces could be calculated by

$$T' = \frac{V_{TS} \cdot a}{2h'} \quad (4.12)$$

with $a = 100$ mm being the joint length and $h' = 60 - 8 - 1.5 = 50.5$ mm being the distance between the centers of gravity of the upper (16-mm) and lower (3-mm) flanges of the GFRP profile. Superposing the additional forces to the global tension force, T , the resulting force in the tension element's upper flange at the supported (T_s) and loaded (T_l) sides in the insulating joint could be calculated by

$$\begin{aligned} T_s &= T + T' \\ T_l &= T - T' \end{aligned} \quad (4.13)$$

Based on the assumption that the tension force was mainly transferred through the upper flange ($A_T = 16 \cdot 100$ mm) with a tensile modulus $E_T = 40.5$ GPa, cp. Table 3.2, page 50, the resulting axial strain in the upper flange of the TS-element could be calculated by

$$\begin{aligned} \varepsilon(T_s) &= \frac{T_s}{A_T \cdot E_T} \\ \varepsilon(T) &= \frac{T}{A_T \cdot E_T} \\ \varepsilon(T_l) &= \frac{T_l}{A_T \cdot E_T}. \end{aligned} \quad (4.14)$$

T_s and T_l and the resulting axial strains at ultimate failure are shown in Table 4.8. In Figure 4.25, they are shown as dashed lines and compared to the measured values for a beam in moment and shear mode. Considering the simplicity of the applied analytical model and the inherent scatter of single strain measurements, the calculated axial tensile strains compared

well over the joint length and enabled the combined tensile-shear load transfer mechanisms in the TS-element to be understood.

Table 4.8: Tension forces and corresponding strain in TS-elements

Specimen	T [kN]	T' [kN]	T_s [kN]	T_l [kN]	$\varepsilon(T)$ [%]	$\varepsilon(T_s)$ [%]	$\varepsilon(T_l)$ [%]
M2E1	198	30	228	168	0.31	0.36	0.26
M2E2	178	23	201	156	0.28	0.31	0.24
M3E1	253	44	297	209	0.40	0.46	0.33
M3E2	238	35	273	204	0.37	0.43	0.32
S3E1	175	52	227	124	0.27	0.35	0.19
S3E2	197	43	239	154	0.31	0.37	0.24
S2C1	120	33	153	87	0.19	0.24	0.14
S2C2	135	39	173	96	0.21	0.27	0.15

With the compression force C in the lower CS-element's flange being the same as the tension force in the upper TS-element's flange (Equation 4.10), the resulting stress in the concrete and the confinement factors at the supported side could be calculated in the same manner as for the hybrid steel/GFRP joint, cp. Section 4.1.7, Equations 4.3 and 4.5, page 90. The compression force, C , the resulting stress in the contact zone, σ_{cu} , and the confinement factor, k_c , are listed in Table 4.9 and compared to the confinement factors $k_{c,SIA}$ according to the Swiss Code SIA 262 [7], cp. Equation 4.4, page 91 and Figure 4.16, with the beam width being 400 mm this time. It can be seen that in no case were the maximum possible confinement factors reached, which explains the fact that, contrary to the hybrid GFRP/steel joint, concrete failure never occurred as observed in the experiments.

Table 4.9: Concrete compression forces and stresses; comparison of concrete confinement factors from experiments and according to Swiss Code SIA 262

Specimen	C [kN]	σ_{cu} [MPa]	k_c [-]	$k_{c,SIA}$ [-]
M2E1	-198	-68	1.97	3.28
M2E2	-178	-61	1.78	3.28
M3E1	-253	-87	2.66	3.28
M3E2	-238	-82	2.50	3.28
S3E1	-175	-60	1.84	3.28
S3E2	-197	-68	2.06	3.28
S2C1	-120	-41	1.20	1.89
S2C2	-135	-46	1.34	1.89

Anchorage of the TS-element

As expected, the two-rib TS-elements were pulled out of the concrete, the only exception being beam S2C2 where the shear failure in the TS-element triggered the global failure, cp. Table 4.7. This behavior was in contrast to the three-rib beams, where only the TS-element of beam M3E2 was pulled out of the concrete. Inspections of this beam after the experiment, however, showed misalignment of the first steel stirrups and therefore reduced retention of the element. It could be assumed that, without the weakening of the steel reinforcement, the element would have performed in the same manner as beam M3E1 without pull-out failure.

The strain measurements under the ribs showed that the TS-element was always more highly loaded on the supported side with T_s according to Equation 4.14. At the loaded side, the smaller load T_l had to be anchored. A linear load distribution between the ribs was assumed, with each rib bearing 33 % of the anchored loads T_s and T_l in the case of a three-rib beam and 50 % in the case of a two-rib beam. The load transfer inside a rib from the edge facing the middle section towards the opposite side was assumed to be linear, although stress concentration at the beginning of the rib is well known. The comparison of the calculated to the measured strains in Figure 4.25 showed good agreement when the possible scatter in single strain measurements was taken into account. The good agreement between measurements and calculations showed that the assumption of a stepwise load transfer from the element's ribs to the axial steel reinforcement was justified and that it was possible to apply a simple calculation method to model the complex load-carrying behavior of the beam.

Figure 4.26 shows the axial strain distribution through the thickness of the cross sections. The three graphs in the middle (supported joint edge (left), middle of the joint and loaded joint edge (right)) show the influence of local bending due to shear transfer. The strain distribution in the middle cross section was not influenced by the local bending moment, while strains resulting from the negative and positive moments were added at the adjacent cross sections.

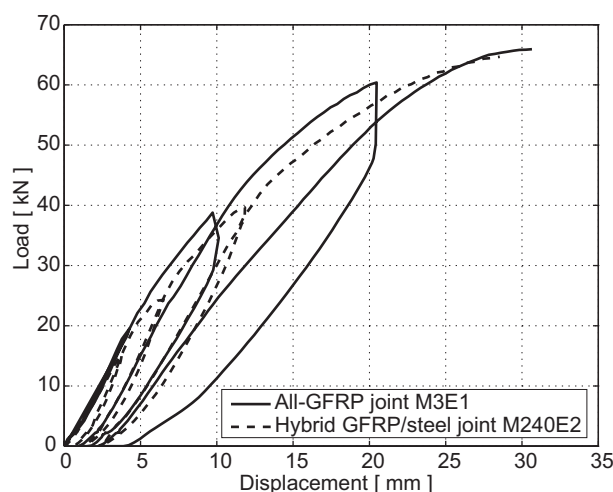
Comparison of all-GFRP and hybrid GFRP joint performance

Table 4.10 compares the failure loads, the percentage shear transmission through the CS-element and the measured angles of second principal stress in the CS-elements of the hybrid and all-GFRP joints. The ultimate failure loads in each loading mode compare well, as does the shear transfer through the CS-element in shear mode: both systems show similar portions and angles of second principal stress. In moment mode, however, in the case of the hybrid joint, the CS-element bore almost no shear load and the angles of principal stress were very small. This was in contrast to the all-GFRP joint where no differences between moment and shear mode were observed, since the parallel shift between the concrete sections dominated the rotation in all experiments.

Figure 4.29 compares the load displacement curves for corresponding beams of both joints in moment mode (M3E1 and M240E2) through all loading cycles. It can be seen that both curves compared well with the hybrid system, showing classic concrete failure during yielding of the steel bars, while the all-GFRP joint also developed ductile behavior due to three different mechanisms:

Table 4.10: Comparison of results from hybrid GFRP/steel and all-GFRP joints

Specimen	Joint type	Failure load measured F_u [kN]	Shear portion CS-element [%]	Angle of 2 nd principal stress φ_{CS} [°]
M3E1	all-GFRP	65.9	33	30
M3E2	all-GFRP	62.1	44	35
M240E1	hybrid-GFRP	54.4	0	10
M240E2	hybrid-GFRP	64.6	10	8
S3E1	all-GFRP	71.7	27	20
S3E2	all-GFRP	80.5	47	42
S240E3	hybrid-GFRP	81.6	57	38

**Figure 4.29:** Comparison of load-displacement response of all-GFRP joint (M3E1) and hybrid-GFRP/steel joint (M240E2)

- yielding of the upper steel bars in the concrete on the supported side of the joint (beams M2E1/2, M3E1/2, S3E1/2);
- plastic deformations of restraining steel stirrups during anchorage failure (beams M2E1/2, M3E2 and S2C1);
- pseudo-ductile GFRP failure in the CS-element of beam M3E1 and TS-element of beams S3E1/2 and S2C2 (pseudo-ductile defined according to Keller and de Castro [62]).

Furthermore, as can be seen from the curve of the all-GFRP joint after the third cycle, a certain visco-elastic behavior of the GFRP components, i.e. a partial recovery of residual deformations after the third cycle, took place.

4.2.7. Conclusions concerning the all-GFRP joint

The hybrid joint, described in Section 4.1, was further developed to an all-GFRP joint by replacing the remaining steel reinforcement with a pultruded TS-element anchored in both sides of the joint in the concrete. The CS-element remained unchanged. The system's quasi static behavior was investigated by full-scale experiments in which the loading mode, support condition and arrangement of ribs on the TS-element's surface were changed. The following conclusions were drawn from the experiments:

- The load-displacement curves showed a similar ductile behavior for both the all-GFRP element and the hybrid version in the case of TS-elements equipped with three ribs per side. Contrary to the hybrid beams, however, the failure took place in the GFRP-elements and not in the concrete during yielding of the steel bars.
- The transfer of the bending moment occurred in the upper flange of the TS-element and the lower flange of the CS-element. This behavior was similar to the hybrid joint, where the tension force was transferred through the upper steel bars.
- It could be shown that the anchorage of the TS-element in the concrete with two or three ribs adhesively bonded to the element on each joint side provided a linear, step-wise transfer of tensile forces from the element to the parallel steel reinforcement bars in the concrete.
- The shear force was shared by both GFRP elements. The portion borne by the TS-elements was 50 % higher compared to the CS-element, due to its fixed support conditions. Shear in the TS-element was transferred through the joint by local bending that increased the tension force in the upper flange at the supported joint edge by 20 %. Contrary to the hybrid joint, the CS-element also transferred considerable amounts (~ 43 % on average) of shear in moment mode.
- It was shown that the load system behavior could be approached by a simple analytical model that fitted well the measurements.

5. Strength and stiffness prediction for GFRP compression/shear elements

5.1. Introduction

FRP materials used in structures such as bridges and buildings are intended to remain in service for between 70 and 100 years. Since serviceability after such long periods has to be assured, long-term durability becomes a major concern. In the joint described in Chapter 4, the CS-element, as a central component, has to bear high compression loads, while being exposed to the concrete-pore solution during pouring and setting. Since moisture uptake occurs rapidly, cp. Section 3.5, the presence of alkaline moisture inside the material has to be taken into account when predicting long-term performance.

5.2. Element strength and stiffness requirements after 70 years of service

Experiments on hybrid and all-GFRP joints, cp. Chapter 4, showed that the greatest compression stresses in the joint occur at the lower part of the compression element's cap plate at the interface to the concrete on the supported side. To verify the joint in accordance with standard concrete theory, the CS-element should not initiate failure. Therefore, its compression strength should never be lower than that of the concrete. Combining Equations 4.3 and 4.5 on page 92, the average compression force at concrete failure, C_{cm} , that can be introduced through the equivalent contact area, A_{c0} , into the concrete is

$$C_{cm} = k_{c,SIA} \cdot f_{cm} \cdot A_{c0} = 1.16 \cdot 33 \cdot 2912 \cdot 10^{-3} = 111 \text{ kN.} \quad (5.1)$$

The average compression strength for unconditioned CS-elements of the lower flange, $C_{FRP,0m}$, however, amounts to 424 kN, which is almost four times higher than the concrete strength, cp. Equation 5.2.

$$C_{FRP,0m} = f_{FRP,0m} \cdot A_{flange} = 265 \cdot 1600 \cdot 10^{-3} = 424 \text{ kN} \quad (5.2)$$

where $f_{FRP,0m}$ is the unconditioned CS-element's compressive system strength as shown in Table 3.2 on page 50 and A_{flange} is the area of the lower element flange ($16 \cdot 100 = 1600 \text{ mm}^2$). The required remaining average compression strength of an element after 70 year of service, $C_{FRP,70m}$, can be estimated as shown in Equation 5.3, assuming that flange compression

strength can decrease from $C_{FRP,0m}$ to $C_{FRP,70m} = C_{cm}$ without creating a reduction in joint strength.

$$C_{FRP,70m} = \frac{F_{0m}}{C_{FRP,0m}/C_{cm}} = \frac{727}{424/111} = 190 \text{ kN} \quad (5.3)$$

where F_{0m} is the average strength of unconditioned CS-elements. With regard to long-term service requirements, the hybrid GFRP/steel joint contributes to the overall concrete slab deflection through an additional local rotation, cp. Section 4.1.8. For cantilevering spans of up to 2.5 m (balconies), a possible reduction in the elastic system stiffness of the CS-element of 20 % during the 70 years of service life seems permissible in order to remain within acceptable deflection limits. The required remaining average system stiffness of the CS-element, $E_{FRP,70m}$, is therefore 12.9 GPa, cp. Equation 5.4.

$$E_{FRP,70m} = 0.8 \cdot E_{FRP,0m} = 0.8 \cdot 16.1 = 12.9 \text{ GPa} \quad (5.4)$$

where $E_{FRP,0m}$ is the average CS-element compressive system stiffness for unconditioned CS-elements, cp. Table 3.2, page 50.

5.3. Strength and stiffness prediction for conditioned CS-elements

To verify the CS-element after continuous alkaline attack from concrete-pore solution, its structural behavior under these circumstances had to be predicted after 70 years of service. A convenient method of extrapolating laboratory data is the Arrhenius rate law, cp. Equation 2.23, page 35. Here it was applied to the remaining compression strength obtained from the durability study presented in Section 3.4. Since in reality only the cap plates are exposed to the concrete-pore solution, full immersion of the elements was much too severe and did not correspond to the real situation. In view of the high allowable strength decrease of the elements from 727 kN to 190 kN, however, the argument was that if the extrapolated strength under these extreme conditions did not fall below 190 kN, the long-term durability of the elements could be assumed.

A precondition for applying the Arrhenius rate law to extrapolate measured data is that all chemical processes causing strength degradation have to be accelerated approximately to the same extent with increasing temperature, following the Arrhenius rate law. As shown in Figure 5.1, chemical reactions and moisture diffusion inside the material modify the composite's mechanical integrity, which in turn has an impact on its strength. To use the resulting measured strength as an indication of the Arrhenius-type acceleration of the degradation processes involved, it has to be shown that matrix-softening from diffusion and later chemical degradation of the composite material are linearly related to the composite strength decrease. The strength decrease, as shown in Figure 3.10, p. 54 in linear timescale, therefore, has to be explained mechanically.

Failure of unidirectional FRPs in compression is caused by fiber microbuckling leading either to fiber fracture or to shear failure of the fiber-matrix interface, explained by Budian-

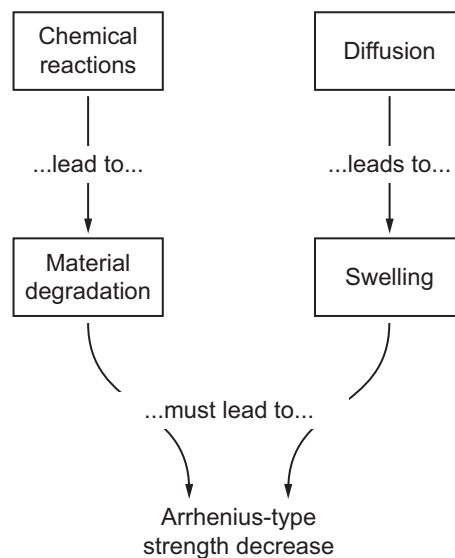


Figure 5.1: Processes leading to Arrhenius-type strength decrease

sky [18] and Steif [113]. The fiber buckling length is influenced by fiber and matrix stiffness, cp. Li et al. [123], and failure depends on interfacial shear and fiber strength. Models exist for calculating a theoretical composite compression strength. However, these values exceed the measured strength by a factor of ~ 4 , cp. Fleck and Budiansky [45], which is due to fiber misalignments and flaws inside the resin. Therefore, calculation-based compressive strength of FRP can only be approximate with high variations. Calculated results become even more unreliable if changes in material properties also have to be correctly modeled. The precise calculation of compressive strength decrease is thus practically impossible and instead, the impact of material degradation on strength decrease is explained qualitatively below.

If perfect fiber-matrix bonding is assumed, the principal interaction between fibers and matrix can be approximated by the theory of a beam on an elastic foundation, cp. Roik [97], where the beam represents the fiber and the elastic foundation represents the matrix. In this case the buckling load, N_{Ki} , is expressed as

$$N_{Ki} = EI \left(\frac{m\pi}{l} \right)^2 + c \left(\frac{l}{m\pi} \right)^2, \quad (5.5)$$

where m is the number of buckling waves, l is the buckling length, EI is the flexural stiffness of the fiber and c is the stiffness of the foundation. The wavelength at buckling depends on the relationship between the flexural stiffness of the fiber and the stiffness of the foundation. A soft foundation combined with a stiff fiber yields long wavelengths, while with a stiff foundation combined with a soft fiber, the wavelength shortens in order to find the

minimum energy necessary for buckling. If the wavelength is a whole-number factor of the whole beam length, the minimum buckling load is calculated by

$$N_{K_i, \min} = EI \sqrt{\frac{c}{EI}} + c \sqrt{\frac{EI}{c}} = 2\sqrt{cEI}. \quad (5.6)$$

During moisture uptake the matrix stiffness will decrease proportionally to the quantity of moisture absorbed, while the fiber flexural stiffness remains constant. The buckling load is thus a function of the form

$$N_{K_i} = 2\sqrt{k c}, \quad (5.7)$$

where k is a constant representing the fiber flexural stiffness. As shown in Section 3.5, the moisture uptake, $M(t)$, plotted on a square-root timescale, proceeds linearly ($M(t) = \text{const.} \cdot \sqrt{t}$). Thus the relationship between moisture uptake and strength decrease can be expressed as:

$$N_{K_i}(t) = N_{K_i,0} - k_1 \sqrt{k_2 \sqrt{t}} = N_{K_i,0} - k_3 \sqrt[4]{t}, \quad (5.8)$$

where k_i are constants. This time-strength dependence, almost linear on a logarithmic time-scale, will apply until saturation occurs after several weeks. Since N_{K_i} , via the matrix stiffness, is a function of diffusion, which in turn follows the Arrhenius rate law, the decrease of N_{K_i} at different temperatures will also follow the Arrhenius rate law.

In addition to strength loss due to matrix-softening, chemical degradation significantly contributes to further strength decrease after saturation. The beginning of this phase is dominated by increasing fiber-matrix slippage due to interfacial degradation. Models are proposed to take this effect into account, cp. Li Xu et al. [123]. However, with continuing degradation, linear elastic theory will no longer be applicable since embrittlement of fibers and matrix, as well as voids emerging in the matrix, prevent elastic interactions. Strength decrease after saturation is thus a direct consequence of both progressive embrittlement of fibers and matrix, and emerging voids in the matrix resulting from chemical attack. This development can also be seen from the changing failure modes, which became less catastrophic with increasing immersion time, cp. Figure 3.6 (p. 49) before conditioning and Figure 3.9 (p. 53) after conditioning. Since the rates of the responsible chemical reactions at different temperatures follow the Arrhenius rate law, strength decrease also accelerates in the same way.

In Figure 3.10, page 54, it can be seen that the compression strength of capped and uncapped CS-elements decreases with increasing temperature at all times during the investigated period. On a linear timescale the curves for all temperatures show an initial sharp strength drop followed by a subsequent gradual decline. Plotted on a logarithmic timescale, the strength decrease becomes linear. This is shown in Figure 5.2, where the remaining-strength data from Figure 3.10 is plotted on a logarithmic timescale. Note that strength for

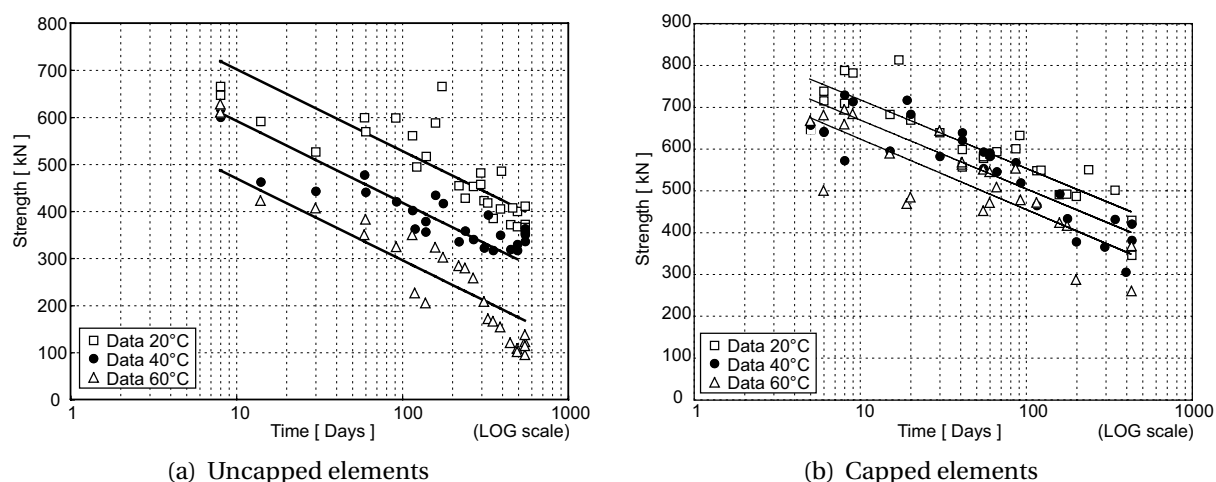


Figure 5.2: Logarithmic regression on remaining-strength data

Table 5.1: Correlation coefficients R for logarithmic fitting functions of uncapped and capped elements

Temperature	Uncapped	Capped
20°C	0.66	0.77
40°C	0.83	0.77
60°C	0.90	0.69

unconditioned elements at time ‘zero’ cannot be displayed in logarithmic scale. In addition to the data points, the remaining strength for each temperature was approximated with a logarithmic function. The fitted lines were averaged to be parallel. The resulting correlation coefficients, shown in Table 5.1, showed large correlation for both element types.

From the regression lines obtained, the time needed to attain different percentages of F_{0m} can be read off and plotted against the reciprocal absolute applied temperature (Arrhenius plot). This is shown in Figure 5.3, where the time required for uncapped and capped elements to attain 60, 50 and 30 % of F_{0m} is shown. It can be seen that there is a linear relationship between time and temperature for a constant percentage of remaining strength. In the figure, this was emphasized by fitted linear regression lines. A linear correlation in Arrhenius plots indicates that the Arrhenius rate law is valid.

After having shown that degradation characteristics are similar at different temperatures and can be described by the Arrhenius rate law, a reference temperature, T_{ref} , was chosen for which strength will be predicted. In a first step, this temperature will be the lowest one used in the study (20°C) to determine the activation energy, which is constant for different temperatures, cp. Section 2.5, page 35. Once the activation energy is known, any temperature can be used as a reference. The data for the reference temperature (20°C) describes behavior during the experimental period in real time, while data for higher temperatures will retrace the same course and show the degradation for much longer time spans. Therefore the curves

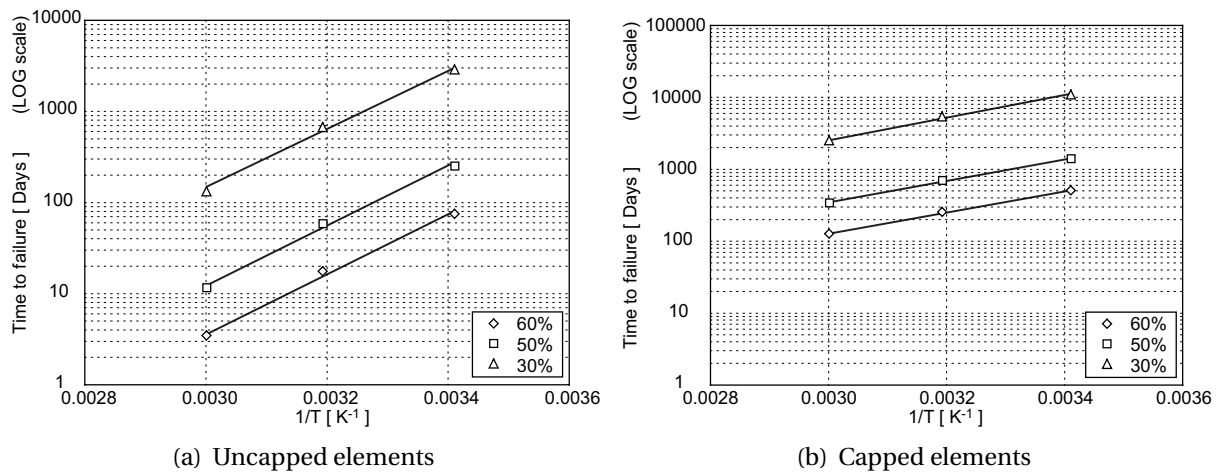


Figure 5.3: Arrhenius plots of compression-strength decrease

for higher temperatures can be shifted on the logarithmic time axis until they superpose the curve for the reference temperature. The amount of shift is described by the time-shift factor, α_T , cp. Section 2.5.

As can be seen in Figure 5.2, the distances between straight lines for capped elements are much smaller than for uncapped elements, reflecting a smaller impact of temperature on failure load. The reasons for this are different failure mechanisms as explained in Section 3.8. The shifted data and the regression lines are shown in Figure 5.4. After twenty years the recorded data for uncapped elements shows greater degradation than predicted. This corresponds to observations from Deijke [33], who observed intensified degradation of polyesters in 60°C alkaline solution and Prian and Barkatt [91], who reported non-Arrhenius behavior for long-term exposure. The scatter for capped elements was larger than for uncapped elements, cp. also correlation coefficients in Table 5.1, but remained constant and of the same magnitude for all applied temperatures.

The shift for uncapped elements was much greater than for capped elements, and consequently, the prediction period that can be verified with data points amounts to ~ 35 years for the former, while data from the latter covered only ~ 5 years. The corresponding α_T are shown in Table 5.2. Since the prediction was made for 20°C, the time-shift factor for this temperature is 1.0. The highest determined time-shift factors for this reference temperature were those between 20 and 60°C, which was 21.9 in the case of uncapped elements and 4.5 in the case of capped elements.

Having determined α_T for three temperatures, Equation 2.25, page 36, can be used to solve for the activation energy, E_A , by setting T_1 to 20°C and varying T_2 and the corresponding α_T . The activation energy determines how much energy is necessary to activate a chemical process – in the present case the combined degradation processes in the composite material. From Table 5.2 it can be seen that E_A remained constant over the investigated temperature range. The mean value was 62.7 kJ/mol for uncapped elements and 30.3 kJ/mol for capped elements. Since from Equation 2.25 it is obvious that α_T and E_A are linearly related, the amount of activation energy is an indication of how effectively a chemical process can be

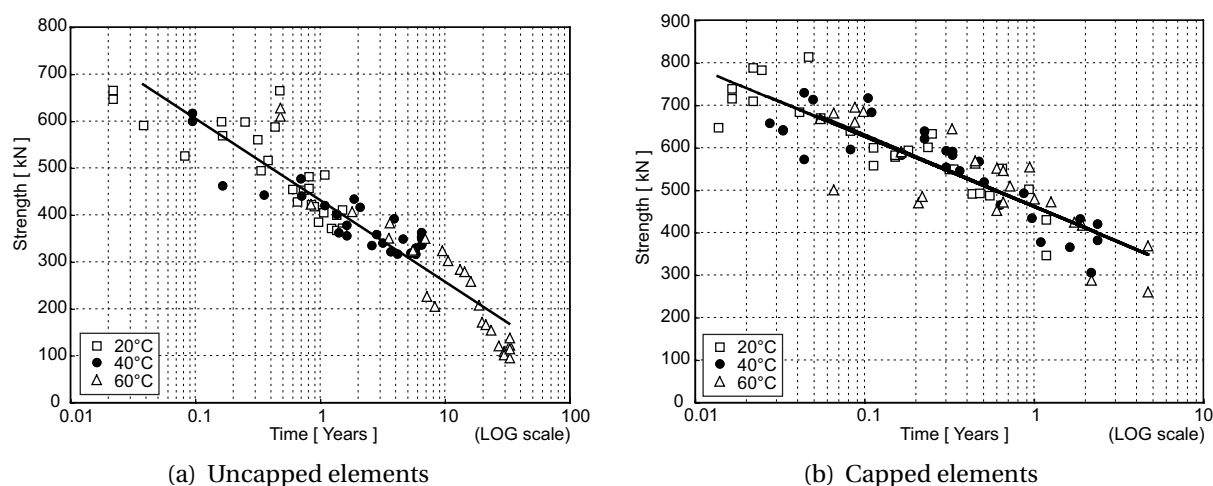


Figure 5.4: Overlapping regression lines of shifted data for a reference temperature of 20°C

Table 5.2: Time-shift factors and activation energies for uncapped and capped elements at $T_{\text{ref}} = 20^\circ\text{C}$

	Uncapped elements		Capped elements	
	α_T [-]	E_A [kJ/mol]	α_T [-]	E_A [kJ/mol]
20-20°C	1.0	-	1.0	-
20-40°C	5.2	62.8	2.2	30.1
20-60°C	21.9	62.6	4.5	30.5
Average	-	62.7	-	30.3

accelerated by an increase in temperature. With the activation energies, time-shift factors for any other reference temperature can be calculated. In Figure 5.5, the obtained curves are shown for both element types for reference temperatures between 5 and 20°C, where the circles mark the measured α_T and the thick line represents the already fitted curve by which E_A was determined. It can be seen that strength development of uncapped elements can be strongly accelerated at 60°C with time-shift factors of $\alpha_{10-60} = 54.3$ for a reference temperature of 10°C, while for capped elements the acceleration remains moderate with values below 10 even at a reference temperature of 5°C.

In Figure 5.6, the predicted curves for reference temperatures of 10 and 20°C are shown for both element types. The shifted experimental data, not inserted for reasons of clarity, covered the functions of time spans between 4.5 years for capped elements at $T_{\text{ref}} = 20^\circ\text{C}$ and 81.5 years for uncapped elements at $T_{\text{ref}} = 10^\circ\text{C}$. It can be seen that at 20°C the strength generally decreased faster than at 10°C. Also, at 20°C the capped elements showed higher remaining strength than the uncapped elements. At 10°C, however, this difference disappeared almost entirely due to the higher time-shift factors for uncapped elements. With regard to application of the CS-element in an outdoor climate, an average service temperature of 10°C

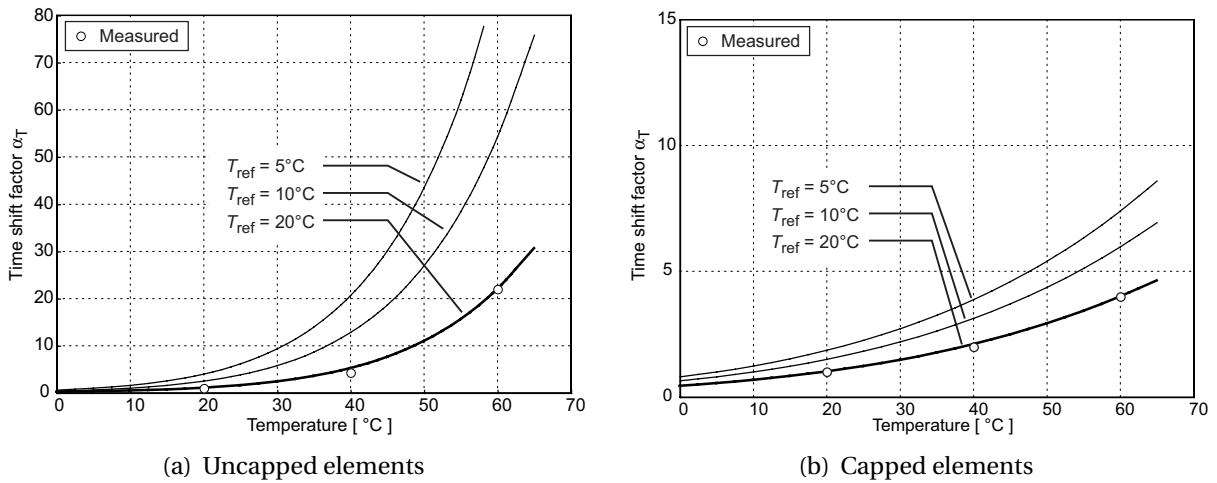


Figure 5.5: Time-shift factors for reference temperatures of 5, 10 and 20°C

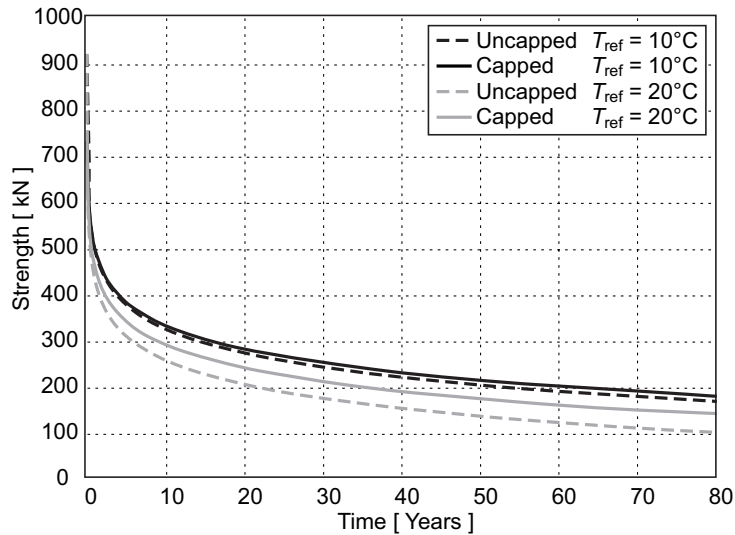


Figure 5.6: Compressive strength prediction for 70 years' service life at 10 and 20°C average reference temperature

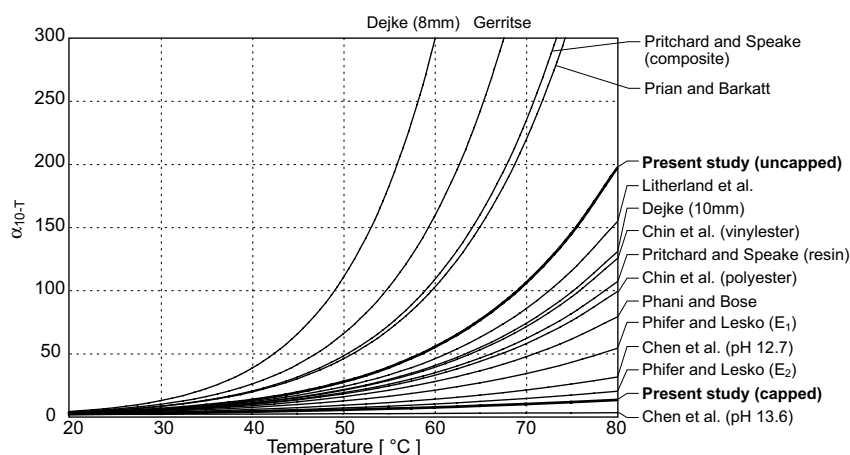
can be assumed in Switzerland. Therefore, the 10°C curves were chosen to predict strength and stiffness after a service life of 70 years.

Table 5.3 shows the predicted strength and stiffness after 70 years of service life. It can be seen that even the predicted remaining strength of 180 kN is almost sufficient and is only 5 % less than the required value of 190 kN. With regard to stiffness, Figure 3.11 shows that the remaining compression stiffness already approached an almost temperature-independent constant value of 12.0 GPa after only 430 days. Assuming that this value does not decrease further, it is only 7 % below the required value of 12.9 GPa after 70 years.

From the overlapping of the curves, it was concluded that the cap plates do not significantly influence the strength development of the totally immersed elements. The cap plates

Table 5.3: Required and estimated capped-element strength and stiffness after 70 years at 10°C reference temperature

Capped element	Required	Estimated	Difference
Compression strength			
$C_{FRP,70m}$ [kN]	190	180	-5 %
Compression stiffness			
$E_{FRP,70m}$ [GPa]	12.9	12.0	-7 %

**Figure 5.7:** α_T for $T_{ref} = 10^\circ\text{C}$ as function of applied temperature for different studies shown in Table 5.4

only reduced the rate of the strength decrease during the first days, which is not apparent in Figure 5.6. However, in real applications, only the cap plates are exposed to the alkaline solution and the pultruded profile remains in a dry environment. Therefore, the cap plates certainly decrease water absorption through the sawed surfaces, particularly in the important first days during concrete pouring and setting when a high moisture level exists. In this respect, as already mentioned, the experimental conditions were much too severe and in reality strength degradation will be much slower.

To situate the activation energies obtained from this study in relation to previous studies, Table 5.4 gives an overview of activation energies resulting from some of the studies already discussed in Section 2.5 and the corresponding reactions. By applying Equation 2.25, it is possible to show α_T graphically for a chosen reference temperature as a function of applied temperature in laboratory treatment. In Figure 5.7 this is done for the studies shown in Table 5.4 for a reference temperature of 10°C. It is therefore possible with this figure to estimate the resulting time-shift factors for a given mechanism and temperature.

From the table and the figure it can be seen that shift factor α_T tends to remain below 50 for $T_{ref} = 10^\circ\text{C}$ and an applied temperature of 60°C. The present study provides shift factors encompassing most of the results, with the highest factor for uncapped and the lowest factor for capped elements. Outside this range, Dejke [33] obtained a high shift factor on

Table 5.4: Activation energies for different mechanisms, materials and conditioning

Reference	Material	Exposition	Reaction	E_a [kJ/mol]
Litherland et al. [70]	CEM-Fill AR glass fiber strands	Concrete-pore solution 4 – 80°C	Tensile strength decrease	59.8
Phani and Bose [84]	E-glass/polyester	Distilled water 42 – 90°C	Interlaminar shear strength decrease	51.8
Pritchard and Speake [93]	E-glass/polyester	Water 30 – 100°C	Diffusion in resin	55.4 (resin) 73.4 (composite)
Gerritse [51]	Aramid/epoxy (tendon)	CaOH ₂ solution 20 – 100°C	Tensile strength decrease	~79.4
Prian and Barkatt [91]	E-glass/vinylester	De-ionized water 23 – 80°C	Silica leaching from composite	70-75
Chin et al. [23]	Vinylester (VE) and polyester (PO) resins	Alkaline solution (pH ~13.5) 22 – 90°C	Time to attain 70 % of tensile strength	57.3(VE)/ 54.5(PO)
Dejke [33]	E-glass/vinylester Ø8 mm, Ø10 mm	Alkaline solution (pH ~13.4) 20 – 80°C	Tensile strength decrease	57.8 (10 mm)/ 89.3 (8 mm)
Phifer and Lesko [85]	E-glass/vinylester	Water 23 – 80°C	Tensile strength decrease (double exponential approach)	47.3 (E_1)/ 35.4 (E_2)
Chen et al [22]	E-glass/vinylester	Alkaline solution (pH 12.7/13.6) 20 – 60°C	Tensile strength decrease	40.73/11.76
Present study	E-glass/polyester	Alkaline solution (pH ~13.4) 20 – 60°C	Compression strength decrease uncapped (unc) / capped (c)	62.7 (unc) / 30.3 (c)

E-glass/vinylester rebars with an 8-mm diameter. However, when rebar diameter was increased to 10 mm, the activation energy, and thus the shift factors, decreased significantly. Gerritse [51] also obtained very high shift factors for the residual strength of aramid/epoxy rebars. In view of the high values obtained in comparison with most other studies, the conclusion drawn by Gerritse that one single point obtained after 180 days at 80°C, for example, might be sufficient to extrapolate residual strength to 100 years should be treated with caution. Pritchard and Speake [93] obtained high shift factors for diffusion into composites and argued that this behavior could be transferred to residual mechanical properties. The same study showed that for pure resin the shift factors decreased significantly. Another high shift factor was obtained by Prian and Barkatt [91] for the leaching mechanism of silica out of glass fibers. Since most studies investigating composite strength yield much lower shift factors, the leaching mechanism may be identified as being very susceptible to temperature changes and contributing to an overall acceleration of strength decrease.

5.4. Strength estimation in a real concrete environment

Since the chemical attack simulated by the experimental set-up was far more severe than that to which the element in the joint is exposed in real conditions, simple model calculations are used to estimate the real case and resulting degradation of the capped CS-elements. Because only the cap plates are exposed to the concrete-pore solution, diffusion into the cap plates also controls diffusion into the profile, which has a much higher coefficient of $D_1 = 3.34 \cdot 10^{-4}$. The diffusion coefficient for the cap plates was assumed to be equal to the transversal diffusion coefficient found in the profile, $D_{2/3} = 0.06 \cdot 10^{-4}$. A further assumption was that the ingressing moisture together with the chemicals would, once they entered the CS-element, distribute uniformly inside the element. Swelling would not be complete and the accompanying cracking would be less, while chemical degradation would proceed at a lower rate. The strength degradation was assumed to be linearly dependent on the amount of liquid inside the material, and therefore the remaining strength could be estimated directly once the amount of liquid was known.

Three scenarios were selected to represent different forms of moisture ingress. In general, moisture diffusion was assumed to stop after two days since the concrete is then set. In a first scenario, it was assumed that the concrete-pore solution would diffuse through the cap plates during two days. A second scenario simulated the complete debonding of the cap plates after one day of exposure with moisture ingressing through the adhesive joint during the remaining day. Since the penetration depth of liquid into the cap plates after one-day was less than 6 mm (5.88 mm), this could be treated as a simple one-day exposure of the profile without cap plates. A third scenario assumed a partial debonding of the cap plates after one day, exposing a three-millimeter-wide band on the profile cross section at the cut ends through which the moisture would diffuse for one day.

A two-day permanent exposure of the cap plates will allow moisture to penetrate 11.8 mm on both sides of the profile (= 23.6 mm in total). The moisture-penetration depth into the profile amounts to 11.6 mm after subtraction of the 2 · 6-mm cap-plate thickness. This corresponds to 13.1 % of M_∞ and will produce a strength decrease of only 71.7 kN compared to the 547 kN observed in the baths ($0.131 \cdot 547$ kN). The remaining strength is 655 kN. If the cap

plates debond after one day, the penetration depth amounts to 28.5 mm on each side. This corresponds to 64.8 % of M_{∞} and leads to a strength decrease of 354.4 kN. The remaining strength for this scenario is 373 kN. In the third scenario, the area through which moisture diffuses is limited to $2 \cdot 100 \cdot 3 + 2 \cdot 60 \cdot 3 = 960 \text{ mm}^2$. The penetration depth for this part of the cross section is 28.5 mm on each side. The remainder of the profile is penetrated to a depth of 8.8 mm on each side. The total moisture content corresponds to 31.2 % of M_{∞} and leads to a strength reduction of 170.7 kN. The remaining strength for this scenario amounts to 556 kN.

Table 5.5: Summary of the chosen scenarios to model real environmental conditions

Scenario	Moisture content [% of M_{∞}]	Strength decrease [kN]	Remaining strength [kN]
Two-day moisture on cap plates	13.1	71.7	655
Complete debonding after one day	64.8	354.4	373
Partial debonding after one day	31.2	170.7	556

Table 5.5 summarizes the results of the three scenarios. Even allowing for the simple assumptions it is nevertheless obvious that the real remaining strength is far above the observed strength of 180 kN. Even after a complete debonding of the cap plates, the element still bears over 350 kN after 70 years in service. Also the stiffness reduction will be less due to less moisture being present inside the material. However, since stiffness is almost independent of moisture content, the difference between measured and real values will be negligible.

5.5. Conclusions concerning strength prediction

Strength degradation for the CS-element in alkaline solution was predicted for a service time of 70 years. It was considered that compression strength results from several interacting mechanisms and strength degradation results from diffusion and chemical reactions acting on the fibers, matrix and fiber-matrix interface. It has been shown that the Arrhenius rate law accounts for GFRP compression strength. Since the permitted strength reduction of the CS-element after 70 years was very high (from 727 to 190 kN), an easy-to-handle experimental investigation in a harsh environment was chosen to simulate the worst case and guarantee the necessary remaining strength.

It was shown that the activation energies of chemical reactions in compression lay within a reasonable range already observed in previous studies. The acceleration of the degradation processes, expressed by time-shift factors, α_T , was different for capped and uncapped elements. While capped elements exhibited only time-shift factors below ten even for low reference temperatures, uncapped elements had time-shift factors $\alpha_{T-60} = 21.9$ for a reference temperature $T_{\text{ref}} = 20^\circ\text{C}$ and $\alpha_{T-60} = 54.3$ for $T_{\text{ref}} = 10^\circ\text{C}$. Due to these differences the

predicted curves differed for $T_{\text{ref}} = 20^{\circ}\text{C}$ and overlapped almost entirely at $T_{\text{ref}} = 10^{\circ}\text{C}$, for which the prediction was required. From this it was concluded that the cap plates do not significantly influence strength reduction for the chosen experimental set-up.

The final predicted remaining strength was shown to be only 5 % below the required strength in the harsh environment. This was acceptable since estimated transfers from harsh environment to real outdoor conditions showed huge reserves. Thus, even for the worst chosen scenario of complete debonding after one day, the remaining strength was still 196 % of the required strength of 190 kN. Concerning stiffness, measured data approached an almost temperature-independent constant value of 12.0 GPa after only 430 days. Assuming that this value does not decrease further throughout the whole service life, it is only 7 % below the required stiffness after 70 years of 12.9 GPa.

6. Conclusions and future research

The replacement of steel reinforcement penetrating insulating layers on building facades by multifunctional GFRP elements is an important step towards insulating buildings effectively. In this thesis the structural behavior of two different joint types was investigated and structural models were developed. To evaluate the performance of the CS-element in alkaline environments, a durability analysis was carried out and long-term strength reductions were determined by means of accelerated aging techniques.

6.1. Investigations of multifunctional joints

Experiments on hybrid joints demonstrated that the CS-element was never a critical concern; failure always initiated either in the concrete or in the steel reinforcement. Therefore ultimate limit loads and deformations could be modeled on the basis of normal concrete theory. This is important for the engineer in practice since GFRP design concepts are still fairly uncommon. Transfer of shear force through the CS-element increased with decreasing moment-to-shear ratio. The high levels of transferred shear observed in the shear-dominated loading mode showed potential with regard to the development of the all-GFRP joint since they reduce shear forces in the TS-element.

Experiments on all-GFRP joints showed full load transfer and deformations similar to those of the hybrid joint when three ribs were attached to the TS-element. Failure, however, initiated also in the GFRP elements and no longer only in the concrete. Shear was borne by both GFRP elements, with the TS-element bearing loads approximately 50 % higher than the CS-element. This distribution was not influenced by the moment-to-shear ratio. The flow of forces in the all-GFRP joint, and especially through the TS-element, could be modeled analytically. By means of principal stress angles, it was possible to determine the shear distribution between the TS- and the CS-elements. Subsequently, the amount of stress in the upper flange of the TS-element was modeled. It was shown that resulting stresses are caused by a combination of the linear stepwise transfer of tensile forces from the element into the concrete at the rib locations and additional stresses from the local bending moment by which shear was transferred through the joint.

6.2. Durability and lifetime prediction

Once immersed in alkaline liquids, the reduction of the CS-element's compression strength occurred in two phases, characterized by a sharp drop in strength at the beginning of the conditioning with a subsequent gradual decrease. The initial sharp drop was attributed to moisture diffusion, while the subsequent gradual decrease was ascribed to chemical degradation of the fibers, matrix and fiber-matrix interface. The diffusion occurred mainly in the fiber direction through wicking effects. It was shown to be of Fickian type and followed the

Arrhenius rate law. The maximum moisture content inside the composite material was influenced by the fiber-volume fraction. Chemical degradation was analyzed by SEM and EDX. The SEM images showed extensive fiber matrix debonding and emerging pores in the matrix. Material losses were also indicated by decreasing weight after saturation at 40 and 60°C. Although fiber diameters did not change during the immersion period, EDX analysis revealed the interdiffusion of hydrogen and sodium ions. In addition, brittle fiber behavior and rough fiber surfaces towards the end of the conditioning indicated etching of the SiO network.

Based on the durability study the CS-element's long-term compression strength was predicted. It could be shown that acceleration of the compression strength reduction of GFRP in alkaline solutions at different temperatures follows the Arrhenius rate law as had been shown previously for tension strength. It was possible to extrapolate the measured data for up to 70 years' service life. Cap plates were found to only delay strength reduction, while exhibiting a similar remaining strength after the full immersion of the elements. In practice, however, the cap plates will protect the sensitive sawed surfaces from moisture ingress during pouring and setting of the concrete. Accordingly, simulations of the real environment, in which moisture only penetrates through the cap plates, showed a remaining strength of almost double the requirements.

A comparison of time-shift factors in tension from previous studies with those obtained in the present study showed that possible acceleration is similar in tension and in compression. It can therefore be assumed that acceleration factors for the TS-element are of the same magnitude. While the degradation of uncapped elements could be considerably accelerated and marked an upper limit in relation to most of the studies considered, the possible acceleration was greatly reduced by the cap plates and thus represented a lower limit. This, however, had little impact on the final remaining compression strength since strength degradation curves developed similarly.

6.3. Contribution to the state of the art

This work concerns the structural behavior of GFRP elements integrated in concrete slabs as well as theoretical approaches for determining the long-term strength of GFRP loaded in compression.

- The principal goal of this work was to develop multifunctional load-bearing and insulating components. It was shown that GFRP profiles used in construction effectively combine physical and static performance. Compared to the all-steel joint, the hybrid joint reduced thermal conductivity by ~70 % (from 0.4-0.6 to 0.1-0.2 W/(m·K)). The all-GFRP joint actually reduced it to 0.05-0.1 W/(m·K), which corresponds to a 90 % reduction.
- Up until now, the introduction of new applications incorporating GFRP materials has often been hampered by the lack of experience of engineers in this domain. In this work, the load-bearing behavior of both joint types was described analytically and it was shown that even the complex behavior of the all-GFRP joint can be described by simple analytical models. This will enhance confidence in the application of such new

materials and acceptance to profit from the multifunctional behavior of FRPs in insulating joints. Beyond the proposed joints, the participating GFRP elements can also be used in a wide range of applications. Thus, besides the combination of TS- and CS-elements in cases of bending, pure tension forces might only require TS-elements. If pure compression forces are to be borne, it is also possible to only apply CS-elements.

- Concerning the lifetime prediction, previous studies only investigated accelerated aging of GFRP loaded in tension. In the present work, it has been shown that the Arrhenius rate law also applies to GFRP loaded in compression, despite the fact that structural behavior was much more complex due to fiber-matrix interaction and buckling. For the present application it was possible to fit the resulting data with a logarithmic function as was done in tension. A comparison to previous studies in tension showed that the obtained acceleration factors in compression are in the same range as in tension.

6.4. Proposals for future work

This thesis has provided valuable results concerning the structural behavior of GFRP used in insulating joints and questions concerning their durability. To further develop this material as a multifunctional reinforcement in concrete sections, it is suggested that the following work should be carried out.

- The successful application of multifunctional GFRP elements in insulating joints has now been demonstrated. However, the TS-element in its current form is too heavy and uneconomical. A further step, therefore, would be to adapt the TS-element's form to the flow of forces found in this work. A possible example is shown in Figure 6.1. Such forms can no longer be pultruded and it is suggested that molding techniques are used instead. The present results provide a solid basis for further development. In addition to changes in the form of the profile, the layout of the ribs should be a subject of further investigations. Depth and distribution should be studied further to optimize material use.

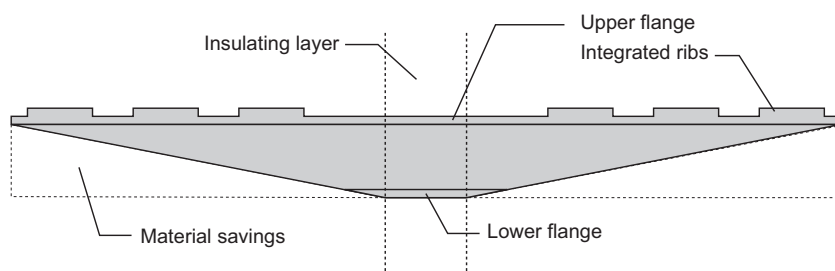


Figure 6.1: Possible improvements to the TS-element with load-adapted form

- The experimental investigation showed that the TS-element works at full capacity. In its current form, therefore, a strength reduction due to alkaline attack as was observed

in the case of the CS-element could not be permitted. For it to be feasible, the next version of the TS-element must be modified to decrease strength reductions. It is therefore proposed that materials less susceptible to alkaline attack, such as vinylester, should be investigated or that a coating should be applied.

To further increase the reliability of GFRPs' long-term prediction, the following proposals are made.

- As has been shown in this work, compression strength drops very sharply at the beginning of immersion and decreases further for high temperatures. Here, the data was fitted with logarithmic curves, which however were not able to fit the last strength decrease for 60°C correctly. Therefore, other possibilities such as multi-exponential fitting-functions, as proposed by Phifer and Lesko [85] might be a promising alternative to describe different degradation mechanisms separately. Also, with this approach individual time-shift factors for fiber, matrix and interfacial degradation could be calculated. It would be possible to verify whether all mechanisms undergo Arrhenius-type acceleration or if there are exceptions.

To do so, the failure mechanisms have to be investigated in more detail. In the present case it was assumed that an initial elastic interaction between fibers and matrix tends to turn into a general crushing after saturation. Although this was evidenced globally by changing failure modes, i.e. less pronounced crushing with increasing immersion time, no actual failure initiation and propagation during degradation was traced and recorded. Therefore, compression tests on unconditioned and conditioned coupon specimens should be carried out and imaged to identify the triggering mechanism.

- The Arrhenius-type acceleration of strength reduction was applied in compression. Efforts have been made to classify the obtained acceleration factors in earlier research. For general application of this method in compression, however, the procedure must be standardized as was proposed in tension, cp. Bank et al. [15]. It is thus suggested that a database should be systematically created including different materials and geometries to obtain empirical acceleration factors as guidelines.
- The fact that the CS-elements were not loaded during conditioning may lead to an underestimation of the strength decrease. In the present application, the stresses at serviceability limit state are very low and therefore this effect was considered negligible. However, once higher loads at serviceability have to be borne, this effect has to be taken into account.

7. List of symbols

General subscripts

∞	Property after $t = \infty$
0	Initial property at $t = 0$
0m	Initial mean property
70m	Required mean property after 70 years of service
av	Average
c	Concrete
cm	Mean concrete property
cu	Action on concrete at ultimate load
C	Compression
CS	Compression shear element
cyl	Cylinder
est	Estimated
FRP	Property of GFRP material
m	Mean/average
meas	Measured
s	Steel
TS	Tension shear element
T	Tension
u	Property at ultimate load

Capital letters

A	Area
A_{c0}	Contact area between CS-element and concrete
A_{c1}	Area of stress distribution inside the concrete
C	Compression force, concentration
D	Diffusion coefficient

E	E-modulus
E_A	Activation energy
EDX	Energy dispersive X-ray spectroscopy
F	Force/load, flux
F_{ret}	Retained compression strength
GFRP	Glass fiber reinforced polymer
GRC	Glass fiber reinforced concrete
HDPE	High-density polyethylene
IFSS	Interfacial shear strength
IPE	Isophthalic polyester
M	Moment, moisture content
R	Universal gas constant
RT	Room temperature
S	Strength
SEM	Scanning electron microscope
T	Global tension force/temperature
T'	Tension forces from local moment in TS-element
T_g	Glass transition temperature
T_l	Resulting tension forces in TS-element on loaded side
T_{ref}	Reference temperature
T_s	Resulting tension forces in TS-element on supported side
V	Shear force
VE	Vinylester

Lower case letters

a	Joint width
d	Beam depth

d_s	Concrete cover
e	Lever arm
f	Strength
f_{sk}	Characteristic yielding strength
f_{tk}	Characteristic tensile strength
f_{u0m}	Unconditioned CS-element's compressive system strength
g	Strain gage
h	Inner beam lever arm, depth
h'	Inner profile lever arm
k	Reaction rate
k_c	Concrete confinement factor
$k_{c,SIA}$	Concrete confinement factor from code SIA 262
r	Radius
t	Time

Greek letters

α	Angle of shear reinforcement
α_T	Time shift factor
Δ	Difference
Δh	Horizontal displacement
Δv	Vertical displacement
ε	Strain
μ	Poissons ratio
φ	Angle of principal compression stresses
ρ	Density
σ	Normal stress
τ	Shear stress, arbitrary variable

Bibliography

- [1] H.P. Abeysinghe, W. Edwards, G. Pritchard, and G. J. Swampillai. Degradation of crosslinked resins in water and electrolyte solutions. *Polymer*, 23(12):1785–1790, November 1982.
- [2] P.B. Adams. Glass corrosion, a record of the past? A predictor of the future? *Journal of Non-Crystalline Solids*, 67:193–205, 1984.
- [3] O. Ishai A.E. Moehlenpah and A.T. Dibenedetto. The effect of time and temperature on the mechanical behavior of epoxy composites. *Polymer Engineering & Science*, 11(2):129–138, 1971.
- [4] A.J. Aindow, D.R. Oakley, and B.A. Proctor. Comparison of the weathering behaviour of GRC with predictions made from accelerated ageing tests. *Cement and Concrete Research*, 14(2):271–274, March 1984.
- [5] Anon. *Swiss Code SIA 180: Wärme- und Feuchteschutz im Hochbau*. Schweizerischer Ingenieur- und Architektenverein, 1999.
- [6] Anon. *Swiss Code SIA 380/1: Thermische Energie im Hochbau*. Schweizerischer Ingenieur und Architektenverein (SIA), Zürich, Switzerland, 2001.
- [7] Anon. *Swiss Code SIA 262: Betonbau*. Schweizerischer Ingenieur- und Architektenverein, 2003.
- [8] A. Apicella, C. Migliaresia, L. Nicodemoa, L. Nicolaisa, L. Iaccarinob, and S. Roccotelli. Water sorption and mechanical properties of a glass-reinforced polyester resin. *Composites*, 13(4):406–410, October 1982.
- [9] A. Apicella, C. Migliaresia, L. Nicolaisa, L. Iaccarinob, and S. Roccotelli. The water ageing of unsaturated polyester-based composites: influence of resin chemical structure. *Composites*, 14(4):387–392, October 1983.
- [10] K.H.G Ashbee, F.C. Frank, and R.C. Wyatt. Water Damage in Polyester Resins. *Royal Society of London Proceedings Series A*, 300(1463):415–419, September 1967.
- [11] K.H.G Ashbee and R.C. Wyatt. Water Damage in Glass Fibre/Resin Composites. *Royal Society of London Proceedings Series A*, 312(1511):553–564, September 1969.
- [12] ASTM International. *D2734-94(2003) Standard Test Methods for Void Content of Reinforced Plastics*.

- [13] C.E. Bakis, L.C. Bank, V.L. Brown, E. Cosenza, J.F. Davalos, J.J. Lesko, A. Machida, S.H. Rizkalla, and T.C. Triantafillou. Fiber-Reinforced Polymer Composites for Construction - State-of-the-Art Review. *Journal of Composites for Construction*, 6(2):73–87, May 2002.
- [14] G.L. Balázs and A. Borosnyói. Long-term behavior of FRP. In *Composites in Construction - A Reality, Proceedings of the International Workshop*, pages 84–91, Capri, Italy, 20-21 July 2001. ASCE.
- [15] L.C. Bank, T.R. Gentry, B.P. Thompson, and J.S. Russel. A model specification for FRP composites for civil engineering structures. *Construction and Building Materials*, 17(6-7):405–437, September-October 2003.
- [16] V. Bellenger, M. Ganem, B. Mortaigne, and J. Verdu. Lifetime prediction in the hydrolytic ageing of polyesters. *Polymer Degradation and Stability*, 49(1):91–97, 1995.
- [17] Z. Boksay and G. Bouquet. PH dependence and an electrochemical interpretation of the dissolution rate of a silicate glass network. *Physics and Chemistry of Glasses*, 21(3):110–113, June 1980.
- [18] B. Budiansky. Micromechanics. *Computers & Structures*, 16(1-4):3–12, 1983.
- [19] A. Caceres, R.M. Jamond, T.A. Hoffard, and L.J. Malvar. Accelerated Testing of Fiber Reinforced Polymer Matrix Composites -Test Plan-. Special publication, Naval Facilities Engineering Service Center, 2000.
- [20] R.J. Charles. Static Fatigue of Glass 1. *Journal of Applied Physics*, 29(11):1549–1553, November 1958.
- [21] A. Chateauminois, B. Chabert, J.P. Souilier, and L. Vincent. Hygrothermal ageing effects on the static fatigue of glass/epoxy composites. *Composites*, 24(7):547–555, October 1993.
- [22] Y. Chen, J.F. Davalos, and I. Ray. Durability Prediction for GFRP Reinforcing Bars Using Short-Term Data of Accelerated Aging Tests. *Journal of Composites for Construction*, 10(4):279–286, July/August 2006.
- [23] J.W. Chin, K. Aouadi, M.R. Haight, W.L. Hughes, and T. Nguyen. Effects of water, salt solution and simulated concrete pore solution on the properties of composite matrix resins used in civil engineering applications. *Polymer Composites*, 22(2):282–297, Apr 2001.
- [24] J.W. Chin, W.L. Hughes, and A. Signor. Elevated Temperature Aging of Glass Fiber Reinforced Vinyl Ester and Isophthalic Polyester Composites in Water, Salt Water, and Concrete Pore Solution. In *Proceedings of the 16th Technical Conference*, pages 1–12. American Society for Composites, 2001.

- [25] J.W. Chin, T. Nguyen, and K. Aouadi. Effects of Environmental Exposure on Fiber-Reinforced Plastic (FRP) Materials Used in Construction. *Journal of Composites Technology & Research*, 19(4):205–213, 1997.
- [26] P.S. Chua, S.R. Dai, and M.R. Piggott. Mechanical properties of the glass-fiber polyester interphase. 2. Effect of water on debonding. *Journal of Materials Science*, 27(4):919–924, February 1992.
- [27] P.S. Chua and M.R. Piggott. The glass fibre-polymer interface: II—Work of fracture and shear stresses. *Composite Science and Technology*, 22(2):107–119, 1985.
- [28] D. Cohn and G. Marom. Deformation and Failure of Polymeric Matrices under Swelling Conditions. *Journal of Applied Polymer Science*, 28(6):1981–1992, June 1983.
- [29] D. Cohn and D. Maron. The effect of the morphology on the hygroelastic behaviour of polyester and epoxy resins. *Polymer*, 24(2):223–228, February 1983.
- [30] E. Cosenza, G. Manfredi, and R. Realfonzo. Behavior and Modeling of Bond of FRP Rebars to Concrete. *Journal of Composites for Construction*, 1(2):40–51, May 1997.
- [31] J. Crank. *The Mathematics of Diffusion*. Clarendon Press, second edition, 1986.
- [32] H.J. Dagher, A. Iqbal, and B. Bogner. Durability of isophthalic polyester composites used in civil engineering applications. *Polymers & Polymer Composites*, 12(3):169–182, 2004.
- [33] V. Dejke. *Durability of FRP Reinforcement in Concrete - Literature Review and Experiments*. PhD thesis, Chalmers University of Technology, Göteborg, Sweden, 2001.
- [34] F. Devreux, Ph. Barboux, M. Filoche, and B. Sapoval. A simplified model for glass dissolution in water. *Journal of Material Science*, 36(6):1331–1341, March 2001.
- [35] C.W. Dolan. FRP Prestressing in the USA. *Concrete International*, 21(10):21–24, October 1999.
- [36] R.H. Doremus. Time dependence of the reaction of water with glass. *Nuclear and Chemical Waste Management*, 2(2):119–123, 1981.
- [37] R.H. Doremus. *Glass Science*. John Wiley, 2 edition, 1994.
- [38] R.H. Doremus, Y. Mehrotra, W.A. Lanford, and C. Burman. Reaction of water with glass: influence of a transformed surface layer. *Journal of Material Science*, 18:612–622, 1983.
- [39] L.T. Drzal and M. Madhukar. Fibre-matrix adhesion and its relationship to composite mechanical properties. *Journal of Materials Science*, 28(3):569–610, February 1993.
- [40] G.W. Ehrenstein and R. Spaude. A study of the corrosion resistance of glass fibre reinforced polymers. *Composite Structures*, 2(3):191–200, 1984.

- [41] N.A. El-Alaily, E.M. Ezz-Eldin, and H.A. El-Batal. Durability of some Gamma-irradiated Alkali Borate Glasses. *Radiation Physics and Chemistry*, 44(1-2):45–51, July-August 1994.
- [42] EMPA. Statische Belastungsversuche bis zum Bruch Kragplatten-Isolierelement, System "isolan@plus" Typ MV. Technical report no. 421'928, EMPA, Dübendorf, Switzerland, 2002.
- [43] D.H. Everett and L.K. Koopal. Chemisorption and physisorption. "http://www.iupac.org/reports/2001/colloid_2001/manual_of_s_and_t/node16.html", 2001.
- [44] A. Fick. Über Diffusion. *Annalen der Physik und Chemie*, 94:59–86, 1855.
- [45] N.A. Fleck and B. Budiansky. Compressive Failure of Fibre Composites Due to Microbuckling. In G.J. Dvorak, editor, *Inelastic Deformation of Composite Materials, IUTAM Symposium Troy/New York 1990*, pages 235–273. Springer, 1991.
- [46] Joseph Fourier. *Théorie de la Chaleur*. Libraires pour les Mathématiques, L'Architecture hydraulique et la Marine. Firmin Didot, 1822.
- [47] N. Fried. Degradation of Composite Materials: The Effect of Water on Glass-reinforced Plastics. In F.W. Wendt, H. Liebowitz, and N. Perrone, editors, *Mechanics of Composite Materials, Proceedings of the Fifth Symposium on Naval Structural Mechanics*, pages 813–837. Pergamon Press, 1967.
- [48] U. Gaur and B. Miller. Effects of Environmental Exposure on Fiber/Epoxy Interfacial Shear Strength. *Polymer Composites*, 11(4):217–222, August 1990.
- [49] L. Gautier, B. Mortaigne, and V. Bellenger. Interface damage study of hydrothermally aged glass-fibre-reinforced polyester composites. *Composite Science and Technology*, 59(16):2329–2337, December 1999.
- [50] T.R. Gentry, L.C. Bank, B.P. Thompson, and J.S. Russel. An Accelerated-Test-Based Specification for Fiber Reinforced Plastics for Structural Systems. In B. Benmokrane and E. El-Salakawy, editors, *Second International Conference on Durability of Fibre Reinforced Polymer (FRP) Composites for Construction*, pages 13–20, Montréal (Québec) Canada, May 29-31 2002.
- [51] A. Gerritse. Durability criteria for non-alkaline tendons in an alkaline environment. In *Proceedings of the 1st International Conference on Advanced Composite Materials in Bridges and Structures*, pages 129–137, Sherbrooke, Quebec, Canada, October 1992. Canadian Society of Civil Engineers.
- [52] P. Ghosh and N.R. Bose. Comparative-evaluation of N-glass and E-glass fibers with special reference to their use in FRP composites. *Journal of Material Science*, 26(17):4759–4764, September 1991.

- [53] R. Gopalan, B.R. Somashekar, and B. Dattaguru. Environmental Effects on Fibre-Polymer Composites. *Polymer Degradation and Stability*, 24(4):361–371, 1989.
- [54] X. Gu, D. Raghavan, T. Nguyen, M.R. VanLandingham, and D. Yebassa. Characterization of polyester degradation using tapping mode atomic force microscopy: exposure to alkaline solution at room temperature. *Polymer Degradation and Stability*, 74(1):139–149, 2001.
- [55] H. Hojo, W. Toyoshim, M. Tamura, and N. Kawamura. Short-term and long-term strength characteristics of particulate-filled cast epoxy resin. *Polymer Engineering & Science*, 14(9):604–609, September 1974.
- [56] P.M. Jacobs and F.R. Jones. Influence of heterogeneous crosslink density on the thermomechanical and hygrothermal properties of an unsaturated polyester resin: 2. Hygrothermal studies. *Polymer*, 34(10):2122–2127, 1993.
- [57] P.A. Jayantha and I.W. Turner. Generalised finite volume strategies for simulating transport in strongly orthotropic porous media. *ANZIAM J.*, 44:C443–C463, 2003.
- [58] K. Jayaraman, K.L. Reifsnider, and R.E. Swain. Elastic and Thermal Effects in the Interphase: Part I. Comments on Characterization Methods. *Journal of Composites Technology & Research*, 15(1):3–13, March 1993.
- [59] A.F. Johnson. *Engineering Design Properties of GRP*, chapter 14, pages 157–163. Crown, 1979.
- [60] V.M. Karbhari and W. Chu. Degradation kinetics of pultruded E-glass/vinylester in alkaline media. *ACI Materials Journal*, 102(1):34–41, January-February 2005.
- [61] T. Keller. *Dauerhaftigkeit von Stahlbetontragwerken, Transportmechanismen - Auswirkung von Rissen*. PhD thesis, Eidgenössische Technische Hochschule Zürich, 1991.
- [62] T. Keller and J. de Castro. System ductility and redundancy of FRP beam structures with ductile adhesive joints. *Composites Part B: Engineering*, 36(8):586–596, December 2005.
- [63] T. Keller and T. Vallée. Adhesively bonded lap joints from pultruded GFRP profiles. Part II: joint strength prediction. *Composites Part B: Engineering*, 36(4):341–350, June 2005.
- [64] G. König and N. Tue. *Grundlagen des Stahlbetonbaus: Einführung in die Bemessung*. Teubner Verlag, 1998.
- [65] A. Kootsookos and A.P. Mouritz. Seawater durability of glass- and carbon-polymer composites. *Composites Science and Technology*, 64(10-11):1503–1511, August 2004.
- [66] K.J. Laidler. The development of the Arrhenius equation. *Journal of Chemical Education*, 61(6):494–498, 1984.

- [67] W.A. Lanford, K. Davis, P. Lamarche, T. Laursen, and R. Groleau. Hydration of soda-lime glass. *Journal of Non-Crystalline Solids*, 33(2):249–266, June 1979.
- [68] L.J. Larner, K. Speakman, and A.J. Majumdar. Chemical interactions between glass fibres and cement. *Journal of Non-Crystalline Solids*, 20(1):73–74, January 1976.
- [69] K. Liao, C.R. Schultheisz, and D.L. Hunston. Effects of environmental aging on the properties of pultruded GFRP. *Composites Part B: Engineering*, 30(5):485–493, July 1999.
- [70] K.L. Litherland, D.R. Oakley, and B.A. Proctor. The use of accelerated aging procedures to predict the long term strength of GRC composites. *Cement and Concrete Research*, 11(3):455–466, 1981.
- [71] A.C. Loos, G.S. Springer, B.A. Sanders, and R.W. Tung. Moisture Absorption of Polyester-E Glass Composites. *Journal of Composite Materials*, 14:142–154, April 1980.
- [72] A.J. Majumdar and J.F. Ryder. Glass fiber reinforcement of cement products. *Glass Technology*, 9(3):78–84, 1968.
- [73] R. Martin and R. Champion. The effects of ageing on fibre reinforced plastics. *Materials World*, 4(4):200–202, April 1996.
- [74] G. Mensitieri, M.A. Delnobile, A. Apicella, and L. Nicolais. Moisture-matrix interactions in polymer-based composite-materials. *Revue de l'Institut Français du pétrole*, 50(4):551–571, July-August 1995.
- [75] I. Merdas, F. ThomINETTE, A. Tcharkhtchi, and J. Verdu. Factors governing water absorption by composite matrices. *Composite Science and Technology*, 62(4):487–492, 2002.
- [76] H. Nakagawa, M. Kobayashi, T. Suenaga, T. Ouchi, S. Watanabe, and K. Satoyama. Three-dimensional fabric reinforcement. In A. Nanni, editor, *Fiber-Reinforced-Plastic (FRP) Reinforcement for Concrete Structures: Properties and Applications*, volume 42 of *Developments in Civil Engineering*. Elsevier, 1993.
- [77] A. Nanni. FRP reinforcement for prestressed and non-prestressed concrete structures. In A. Nanni, editor, *Fiber-Reinforced-Plastic (FRP) Reinforcement for Concrete Structures: Properties and Applications*, volume 42 of *Developments in Civil Engineering*. Elsevier, 1993.
- [78] J. Orłowsky, M. Raupach, H. Cuyper, and J. Wastiels. Durability modelling of glass fibre reinforcement in cementitious environment. *Materials and Structures*, 38(276):155–162, March 2005.
- [79] M.N. Özişik. *Basic Heat Transfer*. Krieger Publishing, 1987.
- [80] A. Paul and A. Youssefi. Alkaline durability of some silicate glasses containing CaO, FeO and MnO. *Journal of Materials Science*, 13(1):97–107, 1978.

- [81] S. Pavlidou and C.D. Papaspyrides. The effect of hygrothermal history on water sorption and interlaminar shear strength of glass/polyester composites with different interfacial strength. *Composites Part A: Applied Science and Manufacturing*, 34(11):1117–1124, November 2003.
- [82] M. Pecce, G. Manfredi, R. Realfonzo, and E. Cosenza. Experimental and Analytical Evaluation of Bond Properties of GFRP Bars. *Journal of Materials in Civil Engineering*, 13(4):282–290, July-August 2001.
- [83] G. Perera and R.H. Doremus. Dissolution Rates of Silica Glasses in Water at pH 7. *J. Am. Ceram. Soc.*, 74(6):1269–1274, 1991.
- [84] K.K. Phani and N.R. Bose. Temperature Dependence of Hydrothermal Ageing of CSM-Laminate During Water Immersion. *Composite Science and Technology*, 29(2):79–87, 1987.
- [85] S.P. Phifer and J.J. Lesko. Moisture absorption and strength characterization of hygrothermally aged neat and clay filled vinyl ester and pultruded vinyl ester E-glass laminates. In B. Benmokrane and E. El-Salakawy, editors, *Second International Conference on Durability of Fibre Reinforced Polymer (FRP) Composites for Construction (CDCC'02)*, pages 485–497, 2002.
- [86] F. Pierron, Y. Poirrette, and A. Vautrin. A Novel Procedure for Identification of 3D Moisture Diffusion Parameters on Thick Composites: Theory, Validation and Experimental Results. *Journal of Composite Materials*, 36(19):2219–2243, 2002.
- [87] E.D. Plueddemann. *Silane Coupling Agents*. Plenum Press, 1982.
- [88] M.L. Porter and B.A. Barnes. Accelerated Aging Degradation of Glass Fiber Composites. In H. Saadatmanesh and M.R. Ehsani, editors, *Proceedings of the 2nd International Conference on Composites in Infrastructure, ICCI '98*, pages 446–459, Tucson, Arizona, 5-7 January 1998. Department of Civil Engineering and Engineering Mechanics, University of Arizona.
- [89] M.L. Porter and B.A. Barnes. Accelerated Durability of FRP Reinforcement for Concrete Structures. In B. Benmokrane and H. Rahman, editors, *Durability of Fibre Reinforced Polymer (FRP) Composites for Construction, Proceedings of the first International Conference (CDCC'98)*, 1998.
- [90] N.L. Post, F. Riebel, A. Zhou, and T. Keller. Investigation of the moisture ingress behavior of pultruded FRP E-glass/polyester composite and subsequent damage under alkaline solution by gravimetric and SEM methods. Internal report, August 2005.
- [91] L. Prian and A. Barkatt. Degradation mechanism of fiber-reinforced plastics and its implications to prediction of long-term behavior. *Journal of Material Science*, 34(16):3977–3989, 1999.
- [92] K. Prince. Fighting corrosion with composites. *Reinforced Plastics*, 46(10):36–37, October 2002.

- [93] G. Pritchard and S.D. Speake. The use of water absorption kinetic data to predict laminate property changes. *Composites*, 18(3):227–232, July 1987.
- [94] B.A. Proctor, D.R. Oakley, and K.L. Litherland. Development in the assessment and performance of GRC over 10 years. *Composites*, 13(2):173–179, April 1982.
- [95] D. Raghavan and K. Egwim. Degradation of polyester film in alkali solution. *Journal of Applied Polymer Science*, 78(14):2454–2463, December 2000.
- [96] J. Riffle and J.J. Lesko. Composites and adhesives for infrastructure renewal - Introduction to polymers. Lecture notes.
- [97] Karl-Heinz Roik. *Vorlesungen über Stahlbau: Grundlagen*. Ernst & Sohn, 1983.
- [98] F.S. Rostásy. On durability of FRP in aggressive environments. In *Proceedings of the Third International Symposium on Non-Metallic (FRP) Reinforcement for Concrete Structures*, volume 2, pages 107–114. Japan Concrete Institute, Japan Concrete Institute, October 1997.
- [99] S. Roy and W. Xu. *Recent Developments in Durability Analysis of Composite Systems.*, volume 103, chapter Modeling of hygrothermal effects in composite and polymer adhesive systems, pages 211–219. Balkema, 2000.
- [100] S. Roy, W. Xu, S. Patel, and S. Case. Modeling of moisture diffusion in the presence of bi-axial damage in polymer matrix composite laminates. *International Journal of Solids and Structures*, 38:7627–7641, 2001.
- [101] H. Scholze. Chemical durability of glasses. *Journal of Non-Crystalline Solids*, 52(1-3):91–103, December 1982.
- [102] H. Scholze. Glass-water interactions. *Journal of Non-Crystalline Solids*, 102:1–10, 1988.
- [103] M Schreiner, G. Woisetschläger, I. Schmitz, and M. Wadsak. Characterisation of surface layers formed under natural environmental conditions on medieval stained glass and ancient copper alloys using SEM, SIMS and atomic force microscopy. *Journal of Analytical Atomic Spectrometry*, 14(3):395–403, 1999.
- [104] C.L. Schutte. Environmental Durability of Glass-Fiber Composites. *Material Science & Engineering R-Reports*, 13(7):265–323, November 1994.
- [105] SFS-Locher. Online product information – isolan and isolan plus. "<http://www.sfslocher.biz/>", 2006.
- [106] E.B. Shand. Breaking stress of glass determined from dimensions of fracture mirrors. *Journal of the American Ceramic Society*, 42(10):474–477, 1959.
- [107] Y. Shao and S. Kouadio. Durability of Fiberglass Composite Sheet Piles in Water. *Journal of Composites for Construction*, 6(4):280–287, November 2002.

- [108] C.H. Shen and G.S. Springer. Moisture Absorption and Desorption in Composite-Materials. *Journal of Composite Materials*, 10(1):2–20, January 1976.
- [109] C.H. Shen and G.S. Springer. *Moisture absorption and desorption of composite materials*, volume 1 of *Environmental Effects on Composite Materials*, chapter 3, pages 15–33. Technomic Publishing Company, Ann Arbor, Michigan, George S. Springer edition, 1981.
- [110] T.-H. Sheng, F.R. Jones, and D. Wang. Effect of fibre conditioning on the interfacial shear strength of glass-fibre composites. *Composite Science and Technology*, 48(1-4):89–96, 1993.
- [111] W. Somboonsong, F.K. Ko, and H.G. Harris. Ductile hybrid fiber reinforced plastic reinforcing bar for concrete structures: Design methodology. *ACI Materials Journal*, 95(6):655–666, November-December 1998.
- [112] S.P. Sonawala and R.J. Spontak. Degradation kinetics of glass-reinforced polyesters in chemical environments (Part 1). *Journal of Materials Science*, 31(18):4745–4756, September 1996.
- [113] P.S. Steif. A simple model for the compressive failure of weakly bonded, fiber-reinforced composites. *Journal of Composite Materials*, 22(9):818–828, 1988.
- [114] R.E. Swain, K.L. Reifsnider, K. Jayaraman, and M. El-Zein. Interface/interphase concepts in composite material systems. *Journal of Thermoplastic Composite Materials*, 3:13–23, January 1990.
- [115] L. Taerwe and S. Matthys. FRP for Concrete Construction: Activities in Europe. *Concrete International*, 21(10):33–36, October 1999.
- [116] J.L. Thomason. The interface region in glass fibre-reinforced epoxy resin composites: 3. Characterization of fibre surface coatings and the interphase. *Composites*, 26(7):487–498, July 1995.
- [117] M. Tomozawa and S. Capella. Microstructure in Hydrated Silicate Glasses. *Journal of the American Ceramic Society*, 66(2):C–24, 1983.
- [118] C. Tracy. *Fire Endurance of Multicellular Panels in an FRP Building System*. PhD thesis, EPFL-CCLab, 2005.
- [119] S.W. Tsai. Environmental Factors in the Design of Composite Materials. In F.W. Wendt, H. Liebowitz, and N. Perrone, editors, *Mechanics of Composite Materials, Proceedings of the Fifth Symposium on Naval Structural Mechanics*, pages 749–767. Pergamon Press, 1967.
- [120] I. Verpoest and M. Desaeger. *Handbook of Polymer-Fibre Composites*, chapter 4.6/4.7 Interfacial bond strength determination, pages 230–238. Polymer Science and Technology Series. Longman Scientific and Technical, Essex, England, F.R. Jones edition, 1994.

- [121] P.V. Vijay and H.V.S. GangaRao. Accelerated and Natural Weathering of Glass Fiber Reinforced Plastic Bars. In C.W. Dolan, S.H. Rizkalla, and A. Nanni, editors, *Fiber Reinforced Polymer Reinforcement for Reinforced Concrete Structures, Proceedings of the Fourth International Symposium*, pages 605–614. ACI International, 1999.
- [122] Y.J. Weitsman. Effects of fluids on polymeric composites. In Y. Miyano, A.H. Cardon, K.L. Reifsnider, H. Fukuda, and S. Ogihara, editors, *Durability Analysis of Composite Systems 2001*, pages 123–128. Swets & Zeitlinger, 2002.
- [123] Y.L. Xu and K.L. Reifsnider. Micromechanical Modeling of Composite Compressive Strength. *Journal of Composite Materials*, 27(6):572–588, 1993.
- [124] V.T. Yilmaz. Chemical attack on alkali resistant glass-fibres in a hydrating cement matrix - Characterization of corrosion products. *Journal of Non-Crystalline Solids*, 151(3):236–244, December 1992.
- [125] V.T. Yilmaz and F.P. Glasser. Reaction of alkali-resistant glass-fibers with cement. 1. Review, assessment, and microscopy. *Glass Technology*, 32(3):91–98, June 1991.
- [126] V.T. Yilmaz, E.E. Lachowski, and F.P. Glasser. Chemical and Microstructural Changes at Alkali-Resistant Glass Fiber-Cement Interfaces. *Journal of the American Ceramic Society*, 74(12):3054–3060, 1991.
- [127] Y.T. Yu and K. Pochiraju. Three-Dimensional Simulation of Moisture Diffusion in Polymer Composite Materials. *Polymer-Plastics Technology and Engineering*, 42(5):737–756, 2003.
- [128] J.S. Zhang, V.M. Karbhari, F. Isley, and J. Neuner. Fiber-Sizing-Based Enhancement of Materials Durability for Seismic Retrofit. *Journal of Composites for Construction*, 7(3):194–199, August 2003.

List of Figures

1.1.	1st-generation all-steel insulating joint	2
1.2.	2nd-generation hybrid GFRP/steel insulating joint	3
1.3.	Insulating joint with three GFRP elements	3
2.1.	Fiber configurations for composite materials	8
2.2.	Fiber debonding in E-glass fiber-reinforced vinylester.	11
2.3.	Weight gain of pure resin and composites in water at different temperatures . . .	12
2.4.	Gravimetric curve for 1D-Fickian absorbtion	14
2.5.	Principle glass degradation	18
2.6.	Hydrated layer and effect on E-glass fiber tensile strength	19
2.7.	Remaining glass fiber strength at different temperatures in neutral and acid liquids	20
2.8.	Features on broken-fiber surfaces related to their failure probability	21
2.9.	Rate of the etching mechanism at different pH	22
2.10.	AR-glass filament strength reduction in neutral and alkaline liquids	23
2.11.	Polymer swelling through water inclusion	24
2.12.	Linear dimensional changes in resin	25
2.13.	Chemical structure of polyester resins and ester hydrolysis	26
2.14.	Multi-monolayer model after Jones	29
2.15.	ISS of E-glass-polyester/epoxy systems	30
2.16.	ISS degradation in composite systems	32
2.17.	Input and output energies in chemical reactions	36
2.18.	Strength retention of glass fiber-reinforced concrete at different temperatures . .	38
2.19.	Predicted strength retention values (tensile and short-beam shear)	42
3.1.	Thermally insulating all-GFRP joint in balcony slab	45
3.2.	GFRP CS-element - appearance and dimensions	46
3.3.	Specimen for the burn-off test.	48
3.4.	CS-element in testing machine	48
3.5.	Schematic load displacement curve of a compression experiment	49
3.6.	Typical failure of unconditioned elements	49
3.7.	Heated bath with inserted CS-elements before covering	51
3.8.	Load-displacement curves for conditioned uncapped and capped elements . . .	53
3.9.	Typical failure of elements after long-term exposure	53
3.10.	Remaining ultimate failure load at different temperatures	54
3.11.	Remaining stiffness at different temperatures	55
3.12.	Remaining retained strength at different temperatures	55
3.13.	Moisture ingress in profile sections	59
3.14.	Measured and calculated moisture ingress in profile sections	60
3.15.	Measured and calculated moisture ingress of full profile at 20°C	60

3.16.	Measured average diffusion in full profiles	61
3.17.	Comparison between measured and calculated diffusion in unsealed full profiles	62
3.18.	Long-term measured weight-gain on unsealed full profiles	62
3.19.	Observation angles on microscopic specimens	63
3.20.	SEM-image comparison of specimen at 20°C	64
3.21.	SEM image from unconditioned specimen (with marked EDX path)	65
3.22.	SEM image from specimen in 20°C after 19 days – material deposition	65
3.23.	SEM images from specimen at 60°C after 13 days	66
3.24.	SEM images from profile section at 20°C after 650 days	67
3.25.	SEM images from profile section (near center) after 800 days at 60°C	67
3.26.	SEM images from profile section (near cut end) at 60°C after 800 days	68
3.27.	EDX analysis, unconditioned element	69
3.28.	EDX material analysis of conditioned element after 800-day exposure at 60°C . .	70
3.29.	TS-element, cross section and 3D-view	74
3.30.	Side and top view of two- and three-rib TS-element	75
4.1.	Structural system	78
4.2.	Reinforcement and dimensions of the hybrid beams	79
4.3.	Positioning of displacement transducers and strain gages on beam specimen . .	80
4.4.	Positioning of strain gages on CS-element	81
4.5.	Vertical displacements - moment mode	82
4.6.	Vertical displacements – shear mode	82
4.7.	Failure mode of beam S200C1	82
4.8.	Axial strain – moment mode	84
4.9.	Axial strain – shear mode	84
4.10.	Measured strain on CS-element surface (examples)	85
4.11.	Angle of second principle stresses on CS-element (S200E3)	86
4.12.	Failure modes – moment mode (examples)	87
4.13.	Failure modes – shear mode (examples)	87
4.14.	Ultimate failure loads – influence of loading mode, support condition and beam depth	88
4.15.	Contact area between cap plate and concrete	91
4.16.	Identification of A_{c0} and A_{c1} for cantilever-support condition	91
4.17.	Comparison of calculated and measured deformations	93
4.18.	Reinforcement and dimensions of the all-GFRP beam specimen	96
4.19.	Anchorage of TS-element and strain gages with wiring	96
4.20.	Strain gage arrangement on TS-elements	97
4.21.	Vertical displacements – moment mode	98
4.22.	Vertical displacements – shear mode	98
4.23.	Axial strains on CS-element	99
4.24.	Angle of second principal stresses on CS-element, M3E1	99
4.25.	Measured and calculated axial strain of TS-element's top side	101
4.26.	Measured axial strain on TS-element's lateral surfaces	101
4.27.	Crack pattern	102
4.28.	Failure modes of all-GFRP insulating sections	103

4.29.	Load-displacement response of hybrid and all-GFRP joints	108
5.1.	Processes leading to Arrhenius-type strength decrease	113
5.2.	Logarithmic regression on remaining-strength data	115
5.3.	Arrhenius plots of compression-strength decrease	116
5.4.	Shifted regression lines	117
5.5.	Time-shift factors for reference temperatures of 5, 10 and 20°C	118
5.6.	Compressive strength prediction for $T_{ref} = 10$ and 20°C	118
5.7.	Different α_T for several accelerated aging studies	119
6.1.	Possible improvements to the TS-element	127
A.1.	Measured temperatures in baths and climate tent	155
B.1.	Uncapped element - 01	157
B.2.	Uncapped element - 02	157
B.3.	Uncapped element - 03	157
B.4.	Uncapped element - 04	157
B.5.	Uncapped element - 05	158
B.6.	Uncapped element - 06	158
B.7.	Uncapped element - 07	158
B.8.	Uncapped element - 08	158
B.9.	Uncapped element - 09	158
B.10.	Uncapped element - 10	158
B.11.	Capped element - 01	159
B.12.	Capped element - 02	159
B.13.	Capped element - 03	159
B.14.	Capped element - 04	159
B.15.	Capped element - 05	159
B.16.	Capped element - 06	159
B.17.	Capped element - 07	160
B.18.	Capped element - 08	160
B.19.	Capped element - 09	160
B.20.	Capped element - 10	160
B.21.	Capped element - 11	160
B.22.	Capped element - 12	160
B.23.	Capped element - 13	161
B.24.	Capped element - 14	161
B.25.	Comparison of mean failure loads for varying cap-plate thicknesses	162
B.26.	Load-displacement diagrams	163
B.27.	Results from creep study	163
B.28.	Allowable compression area for overlapping cap plates	163
B.29.	Hairline cracks on conditioned element	166
B.30.	Load-deformation – 8 days	167
B.31.	Load-deformation – 8 days	167
B.32.	Load-deformation – 14 days	168

B.33.	Load-deformation – 30 days	168
B.34.	Load-deformation – 59 days	169
B.35.	Load-deformation – 59 days	169
B.36.	Load-deformation – 91 days	170
B.37.	Load-deformation – 115 days	170
B.38.	Load-deformation – 120 days	171
B.39.	Load-deformation – 138 days	171
B.40.	Load-deformation – 138 days	172
B.41.	Load-deformation – 158 days	172
B.42.	Load-deformation – 176 days	173
B.43.	Load-deformation – 219 days	173
B.44.	Load-deformation – 239 days	174
B.45.	Load-deformation – 268 days	174
B.46.	Load-deformation – 296 days	175
B.47.	Load-deformation – 296 days	175
B.48.	Load-deformation – 310 days	176
B.49.	Load-deformation – 328 days	176
B.50.	Load-deformation – 352 days	177
B.51.	Load-deformation – 389 days	177
B.52.	Load-deformation – 395 days	178
B.53.	Load-deformation – 449 days	178
B.54.	Load-deformation – 493 days	179
B.55.	Load-deformation – 493 days	179
B.56.	Load-deformation – 548 days	180
B.57.	Load-deformation – 548 days	180
B.58.	Load-deformation – 548 days	181
B.59.	Load-deformation – 548 days	182
B.60.	Load-deformation – 5 days	183
B.61.	Load-deformation – 6 days	183
B.62.	Load-deformation – 6 days	184
B.63.	Load-deformation – 8 days	184
B.64.	Load-deformation – 8 days	185
B.65.	Load-deformation – 9 days	185
B.66.	Load-deformation – 15 days	186
B.67.	Load-deformation – 18 days	186
B.68.	Load-deformation – 20 days	187
B.69.	Load-deformation – 30 days	187
B.70.	Load-deformation – 41 days	188
B.71.	Load-deformation – 41 days	188
B.72.	Load-deformation – 55 days	189
B.73.	Load-deformation – 55 days	189
B.74.	Load-deformation – 60 days	190
B.75.	Load-deformation – 60 days	190
B.76.	Load-deformation – 66 days	191
B.77.	Load-deformation – 86 days	191

B.78. Load-deformation – 92 days	192
B.79. Load-deformation – 115 days	192
B.80. Load-deformation – 122 days	193
B.81. Load-deformation – 158 days	193
B.82. Load-deformation – 175 days	194
B.83. Load-deformation – 199 days	194
B.84. Load-deformation – 236 days	195
B.85. Load-deformation – 295 days	195
B.86. Load-deformation – 340 days	196
B.87. Load-deformation – 395 days	196
B.88. Load-deformation – 430 days	197
B.89. Load-deformation – 430 days	197
B.90. Failure of unconditioned uncapped element 01	198
B.91. Failure of unconditioned uncapped element 02	198
B.92. Failure of unconditioned uncapped element 05	199
B.93. Failure of unconditioned uncapped element 06	199
B.94. Failure of unconditioned uncapped element 07	199
B.95. Failure of unconditioned capped element 03	200
B.96. Failure of unconditioned capped element 05	200
B.97. Failure of unconditioned capped element 10	201
B.98. Failure of unconditioned capped element 11	201
B.99. Failure of uncapped element – 20°C, 59 days	202
B.100. Failure of uncapped element – 40°C, 59 days	202
B.101. Failure of uncapped element – 60°C, 59 days	202
B.102. Failure of uncapped element – 20°C, 219 days	203
B.103. Failure of uncapped element – 40°C, 219 days	203
B.104. Failure of uncapped element – 60°C, 219 days	203
B.105. Failure of uncapped element – 20°C, 448 days	204
B.106. Failure of uncapped element – 40°C, 448 days	204
B.107. Failure of uncapped element – 60°C, 448 days	204
B.108. Failure of uncapped element – 20°C, 548 days	205
B.109. Failure of uncapped element – 40°C, 548 days	205
B.110. Failure of uncapped element – 60°C, 548 days	205
B.111. Failure of capped element – 20°C, 91 days	206
B.112. Failure of capped element – 40°C, 091 days	206
B.113. Failure of capped element – 60°C, 91 days	206
B.114. Failure of capped element – 20°C, 340 days	207
B.115. Failure of capped element – 40°C, 340 days	207
B.116. Failure of capped element – 60°C, 199 days	207
B.117. Failure of capped element – 20°C, 430 days	208
B.118. Failure of capped element – 40°C, 430 days	208
B.119. Failure of capped element – 60°C, 430 days	208
C.1. Weight gain of sealing material	209

D.1.	Comparison of SEM images taken on a specimen with circled fiber surfaces . . .	211
D.2.	Comparison of SEM images taken on a sample polished parallel to the pultrusion direction	212
D.3.	Comparison of SEM images taken on a sample polished at an angle to the pultrusion direction	213
D.4.	Comparison of SEM images taken on a sample polished at an angle to the pultrusion direction	214
D.5.	SEM images taken on a sample polished at an angle to the pultrusion direction and then exposed at 60°C for 13 days	215
D.6.	SEM on profile after 800 days at 20°C (near cut end)	216
E.1.	Results of the EDX material analysis - unconditioned specimens	217
E.2.	Results of the EDX material analysis for conditioned specimens	218
F.1.	Experimental set-up of hybrid beams	219
F.2.	Reinforcement and dimensions	221
F.3.	Strain measurements with rosettes - directions	222
F.4.	Scheme to develop the angle φ	222
F.5.	Vertical displacements for M200E1	223
F.6.	Vertical displacements for M200E2	223
F.7.	Vertical displacements for M240E1	224
F.8.	Vertical displacements for M240E2	224
F.9.	Vertical displacements for S240E1	225
F.10.	Vertical displacements for S240E2	225
F.11.	Vertical displacements for S200E3	226
F.12.	Vertical displacements for S240E3	226
F.13.	Vertical displacements for M200C1	227
F.14.	Vertical displacements for M200C2	227
F.15.	Vertical displacements for M240C1	228
F.16.	Vertical displacements for M240C2	228
F.17.	Vertical displacements for S200C1	229
F.18.	Vertical displacements for S200C2	229
F.19.	Vertical displacements for S240C1	230
F.20.	Vertical displacements for S240C2	230
F.21.	Horizontal displacements for M200E1	231
F.22.	Horizontal displacements for M200E2	231
F.23.	Horizontal displacements for M240E1	232
F.24.	Horizontal displacements for M240E2	232
F.25.	Horizontal displacements for S200Ea	233
F.26.	Horizontal displacements for S240Ea	233
F.27.	Horizontal displacements for M200C1	234
F.28.	Horizontal displacements for M200C2	234
F.29.	Horizontal displacements for M240C1	235
F.30.	Horizontal displacements for M240C2	235
F.31.	Horizontal displacements for S200C1	236

F32.	Horizontal displacements for S200C2	236
F33.	Horizontal displacements for S240C1	237
F34.	Horizontal displacements for S240C2	237
F35.	Global failure M200E2	238
F36.	Global failure M240E2	238
F37.	Global failure M200C2	238
F38.	Global failure M240C1	238
F39.	Global failure M240C2	239
F40.	Global failure S200E2	239
F41.	Global failure S240E1	239
F42.	Global failure S240E2	239
F43.	Global failure S200E3	240
F44.	Global failure S240E3	240
F45.	Global failure S200C1	240
F46.	Global failure S200C2	241
F47.	Global failure S240C1	241
F48.	Global failure S240C2	241
F49.	Crack pattern M200E1	242
F50.	Crack pattern M200E2	242
F51.	Crack pattern M240E1	242
F52.	Crack pattern M240E2	242
F53.	Crack pattern M200C1	243
F54.	Crack pattern M200C2	243
F55.	Crack pattern M240C1	243
F56.	Crack pattern M240C2	243
F57.	Crack pattern S200E1	244
F58.	Crack pattern S200E2	244
F59.	Crack pattern S200E3	244
F60.	Crack pattern S240E1	244
F61.	Crack pattern S240E2	244
F62.	Crack pattern S240Ea	245
F63.	Crack pattern S200C1	245
F64.	Crack pattern S200C2	245
F65.	Crack pattern S240C1	246
F66.	Crack pattern S240C2	246
F67.	Strain on tension & shear reinforcement - M200E1	247
F68.	Strain on tension & shear reinforcement - M200E2	247
F69.	Strain on tension & shear reinforcement - M240E1	247
F70.	Strain on tension & shear reinforcement - M240E2	248
F71.	Strain on tension & shear reinforcement - S200E1	248
F72.	Strain on tension & shear reinforcement - S200E2	248
F73.	Strain on tension & shear reinforcement - S200E3	249
F74.	Strain on tension & shear reinforcement - S240E1	249
F75.	Strain on tension & shear reinforcement - S240E2	249
F76.	Strain on tension & shear reinforcement - S240E3	250

F.77.	Strain on tension & shear reinforcement - M200C1	250
F.78.	Strain on tension & shear reinforcement - M200C2	250
F.79.	Strain on tension & shear reinforcement - M240C1	251
F.80.	Strain on tension & shear reinforcement - M240C2	251
F.81.	Strain on tension & shear reinforcement - S200C1	251
F.82.	Strain on tension & shear reinforcement - S200C2	252
F.83.	Strain on tension & shear reinforcement - S240C1	252
F.84.	Strain on tension & shear reinforcement - S240C2	252
F.85.	Element-strain - M200E	253
F.86.	Element-strain - M240E	254
F.87.	Element-strain - S200E	255
F.88.	Element-strain - S240E	256
F.89.	Element-strain - S200E3 & S240E3	257
F.90.	Element-strain - M200C	258
F.91.	Element-strain - M240C	259
F.92.	Element-strain - S200C	260
F.93.	Element-strain - S240C	261
F.94.	Concrete failure - bottom side M200E1	262
F.95.	Concrete failure - bottom side M200E2	262
F.96.	Concrete failure - bottom side M240E1	263
F.97.	Concrete failure - bottom side M240E2	263
F.98.	Concrete failure - bottom side M200C1	264
F.99.	Concrete failure - bottom side M200C2	264
F.100.	Concrete failure - bottom side M240C1	265
F.101.	Concrete failure - bottom side M240C2	265
F.102.	Concrete failure - bottom side S200E1	266
F.103.	Concrete failure - bottom side S200E3	266
F.104.	Concrete failure - bottom side S240Ea	267
F.105.	Concrete failure - bottom side S200C1	267
F.106.	Concrete failure - bottom side S200C2	268
F.107.	Concrete failure - bottom side S240C1	268
F.108.	Concrete failure - bottom side S240C2	269
F.109.	Failure in insulating section - MDM	270
F.110.	Failure in insulating section - MDM	270
F.111.	Failure in insulating section - SDM	271
F.112.	Failure in insulating section - SDM	271
F.113.	Failure in insulating section - SDM	272
F.114.	Failure in insulating section - MDM	272
F.115.	Failure in insulating section - MDM	273
F.116.	Failure in insulating section - SDM	273
F.117.	Failure in insulating section - SDM	274
F.118.	Main stress axis - M200E1	275
F.119.	Main stress axis - M200E2	275
F.120.	Main stress axis - M240E1	276
F.121.	Main stress axis - M240E2	276

F.122.	Main stress axis - S200E1	277
F.123.	Main stress axis - S200E2	277
F.124.	Main stress axis - S200E3	278
F.125.	Main stress axis - S240E1	278
F.126.	Main stress axis - S240E2	279
F.127.	Main stress axis - S240E3	279
F.128.	Main stress axis - M200C1	280
F.129.	Main stress axis - M200C2	280
F.130.	Main stress axis - M240C1	281
F.131.	Main stress axis - M240C2	281
F.132.	Main stress axis - S200C1	282
F.133.	Main stress axis - S200C2	282
F.134.	Main stress axis - S240C1	283
F.135.	Main stress axis - S240C2	283
G.1.	Experimental set-up of all-FRP beams	285
G.2.	Reinforcement and dimensions of two-rib beam	287
G.3.	Reinforcement and dimensions of a three rib beam	287
G.4.	Positioning of displacement transducers	288
G.5.	Distribution of strain gages on CS-element	288
G.6.	Distripution of strain gages on TS-elements	289
G.7.	Vertical displacements for M2E1	290
G.8.	Vertical displacements for M2E2	290
G.9.	Vertical displacements for M3E1	291
G.10.	Vertical displacements for M3E2	291
G.11.	Vertical displacements for S2C1	292
G.12.	Vertical displacements for S2C2	292
G.13.	Vertical displacements for S3E1	293
G.14.	Vertical displacements for S3E2	293
G.15.	Horizontal displacements for M2E1	294
G.16.	Horizontal displacements for M2E2	294
G.17.	Horizontal displacements for M3E1	295
G.18.	Horizontal displacements for M3E2	295
G.19.	Horizontal displacements for S2C1	296
G.20.	Horizontal displacements for S2C2	296
G.21.	Horizontal displacements for S3E1	297
G.22.	Horizontal displacements for S3E2	297
G.23.	Crack pattern for M2E1	298
G.24.	Crack pattern for M2E2	298
G.25.	Crack pattern for M3E1	298
G.26.	Crack pattern for M3E2	299
G.27.	Crack pattern for S2C1	299
G.28.	Crack pattern for S2C2	299
G.29.	Crack pattern for S3E1	300
G.30.	Crack pattern for S3E2	300

G.31. Failure mode for M2E1	301
G.32. Failure mode for M2E2	301
G.33. Failure mode for M3E1	302
G.34. Failure mode for M3E2	302
G.35. Failure mode for S2C1	303
G.36. Failure mode for S2C2	303
G.37. Failure mode for S3E1	304
G.38. Failure mode for S3E2	304
G.39. M2E1 (left) & M2E2 (right)	305
G.40. M3E1 (left) & M3E2 (right)	306
G.41. S2C1 (left) & S2C2 (right)	307
G.42. S3E1 (left) & S3E2 (right)	308
G.43. Angle of principal stresses on CS-element - M2E	309
G.44. Angle of principal stresses on CS-element - M3E	309
G.45. Angle of principal stresses on CS-element - S2C	310
G.46. Angle of principal stresses on CS-element - S3E	310
G.47. Strain on tension element's top side – M2E	311
G.48. Strain on tension element's top side – M3E	311
G.49. Strain on tension element's top side – S2C	312
G.50. Strain on tension element's top side – S3E	312
G.51. Strain on tension element's lateral side – M2E1	313
G.52. Strain on tension element's lateral side – M2E2	313
G.53. Strain on tension element's lateral side – M3E1	313
G.54. Strain on tension element's lateral side – M3E2	313
G.55. Strain on tension element's lateral side – S2C1	314
G.56. Strain on tension element's lateral side – S2C2	314
G.57. Strain on tension element's lateral side – S3E1	314
G.58. Strain on tension element's lateral side – S3E2	314
G.59. Principal stress angle - M2E	315
G.60. Principal stress angle - M3E	315
G.61. Principal stress angle - S2C	316
G.62. Principal stress angle - S3E	316

List of Tables

1.1. Thermal conductivity of construction materials	1
2.1. Exemplary glass composition	17
2.2. Obtained α_T from durability study (Dejke [33])	40
3.1. Proportions of resin and fibers in GFRP profile	47
3.2. Mechanical properties of CS-element	50
3.3. Gravimetric study – specimen composition	56
3.4. Measured and calculated diffusion coefficients	59
3.5. Microscopic investigation program	64
3.6. Mean atomic ion distribution in fibers and matrix	70
3.7. Profile material properties in tension	74
4.1. Composition of hybrid GFRP/steel experiments	78
4.2. measured concrete strength, elastic and ultimate loading	83
4.3. Shear forces transferred by CS-element	90
4.4. Comparison of confinement factors for concrete strength	92
4.5. Composition of all-GFRP joint experimental series	95
4.6. Angles of second principal stresses and shear force transfer in TS- and CS-elements	100
4.7. Concrete strength, failure loads and modes	102
4.8. Tension forces and corresponding strain in TS-elements	106
4.9. Concrete compression forces, stresses and resulting confinement factors	106
4.10. Comparison of results from hybrid GFRP/steel and all-GFRP joints	108
5.1. Correlation coefficients R	115
5.2. Time-shift factors and activation energies for $T_{ref} = 20^\circ\text{C}$	117
5.3. Required and estimated capped-element strength and stiffness	119
5.4. Activation energies for different mechanisms, materials and conditioning	120
5.5. Summary of chosen scenarios to model real environmental conditions	122
B.1. Cap-plate variation, overview	162
B.2. Structural behavior for conditioned, uncapped elements	164
B.3. Structural behavior for conditioned, capped elements	165
F.1. Pouring and testing plan	220
F.2. Compressive strength of concrete specimens	220
G.1. Compressive strength of concrete after 28 days.	286

Curriculum Vitæ

Florian Riebel

Date of birth: December 29th, 1976 in Heidelberg / Germany
Nationality: German
E-mail: florian.riebe1@epfl.ch

Education

2003–2006 *Swiss Federal Institute of Technology Lausanne (EPFL) – ENAC*
PhD-candidate,
Thesis entitled preliminary:
“Fiber-reinforced polymer thermal-insulating and load-transmitting components for concrete structures”

1997–2003 *Technical University of Darmstadt*
Diplom Ingenieur in Civil Engineering,
Diploma at the EPFL entitled:
“Numerical analysis of adhesively bonded GFRP double-lap joints”

1996 *Gymnasium Heidelberg College*
Diploma from German secondary school qualifying for university admission or matriculation

Work experience

2003–2006 *Composite Construction Laboratory*
Scientific experience in testing and experimental examination

2000–2002 *Institute of Steel Construction*
Student tutor

Additional information

Languages German: mother tongue, French and English: very good

Informatics Office suites, Data processing (MatLab, Octave),
Design and Image editing, object-oriented programming,
FEM (Ansys), Text processing (L^AT_EX)

Appendix A.

Temperature measurement during conditioning

Figure A.1 shows the measured temperatures during conditioning. In 40 and 60°C baths the temperatures were measured directly in the baths, while for the 20°C bath they were measured in the climate tent. The electronic recording for 40 and 60°C was installed only after 157 days, so data were only available from this point. Analysis of the data output for measurements in the 20°C climate tent revealed malfunction of the recording after 428 days. The subsequent temperature was displayed and checked but not recorded.

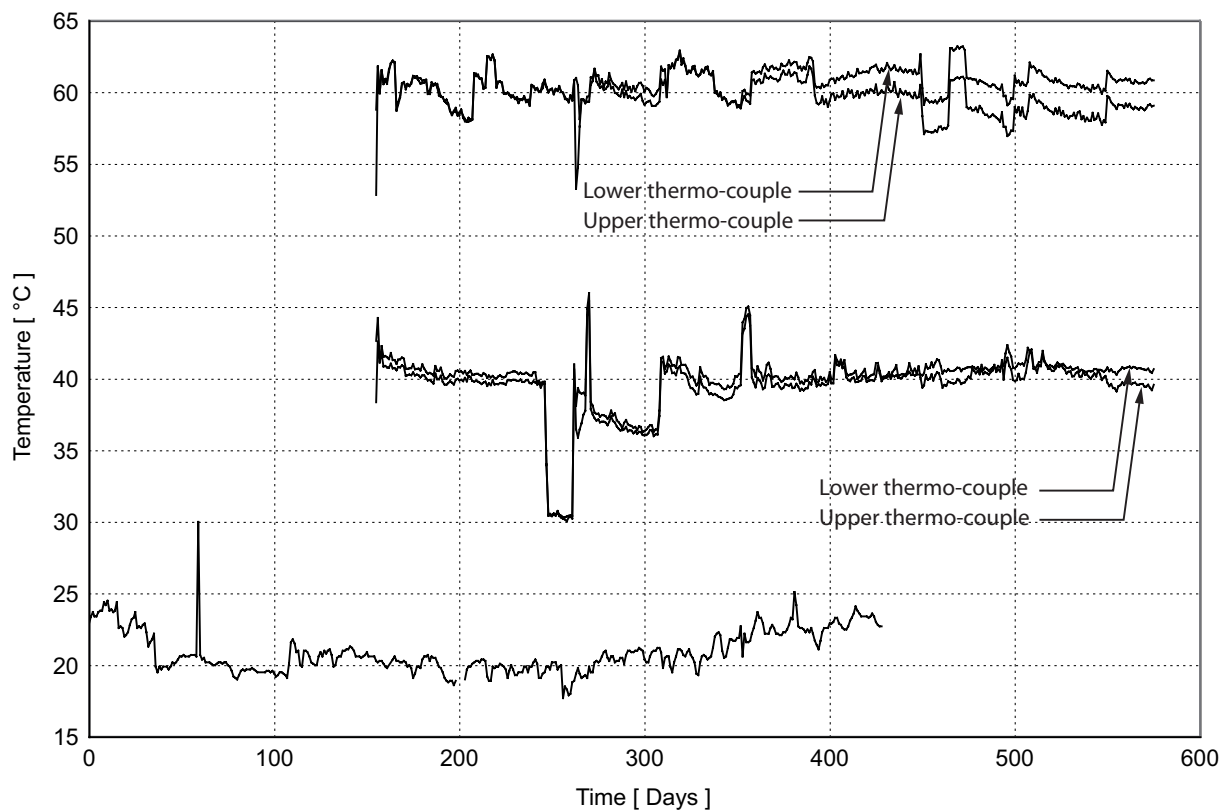


Figure A.1: Measured temperatures in baths and climate tent

Appendix B.

Compression/shear element – structural behavior

B.1. Load-displacement curves of unconditioned elements

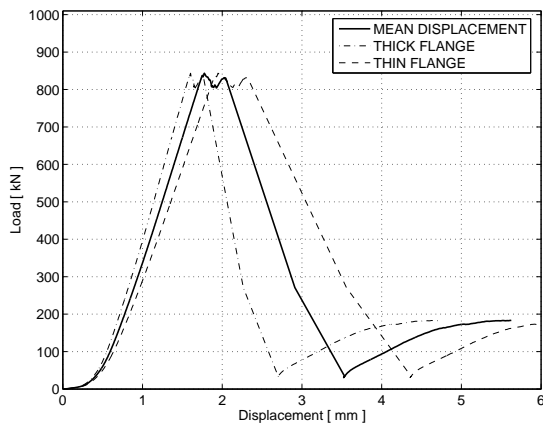


Figure B.1: Uncapped element - 01

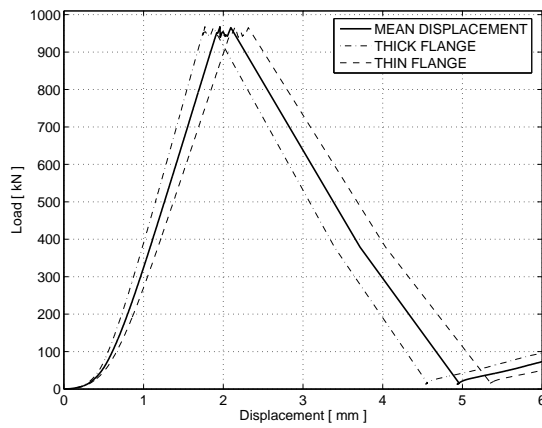


Figure B.2: Uncapped element - 02

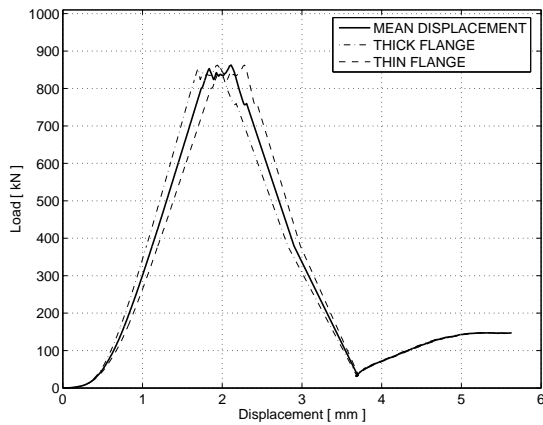


Figure B.3: Uncapped element - 03

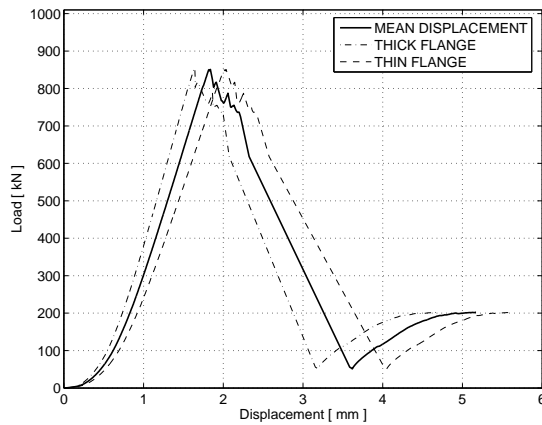


Figure B.4: Uncapped element - 04

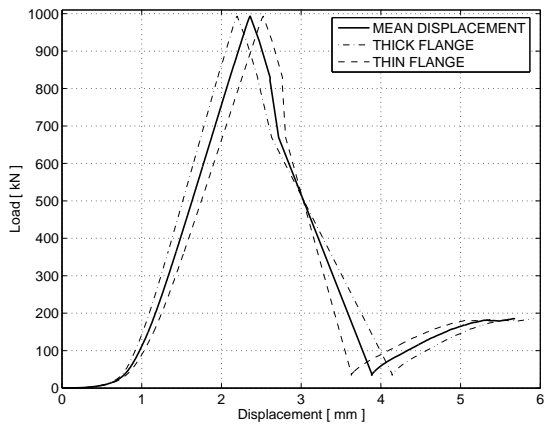


Figure B.5: Uncapped element - 05

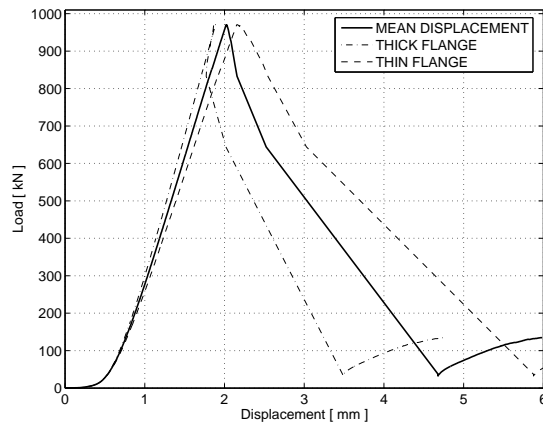


Figure B.6: Uncapped element - 06

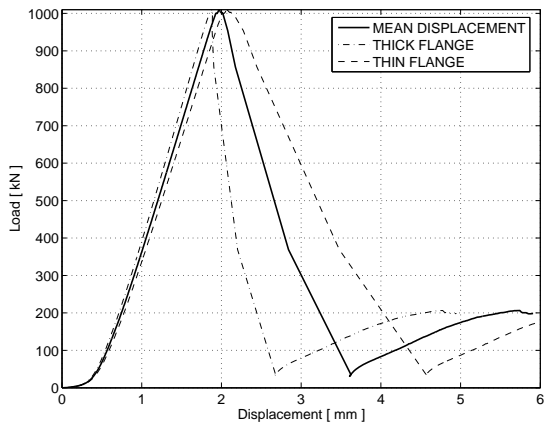


Figure B.7: Uncapped element - 07

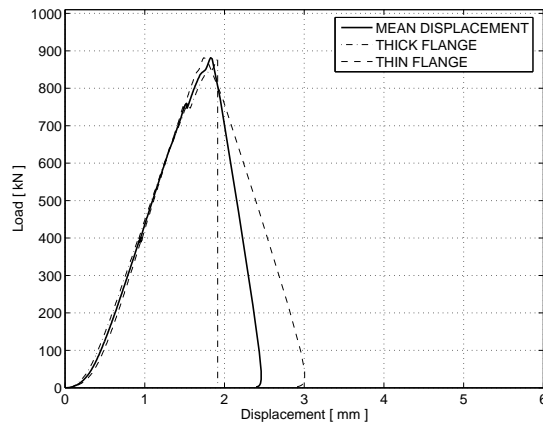


Figure B.8: Uncapped element - 08

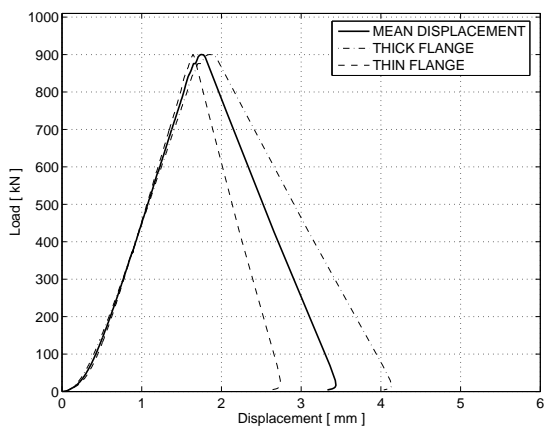


Figure B.9: Uncapped element - 09

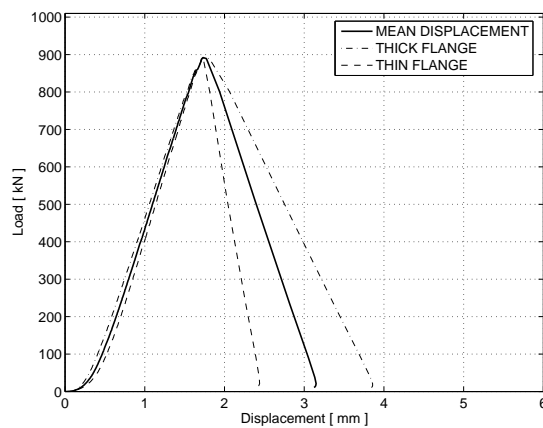


Figure B.10: Uncapped element - 10

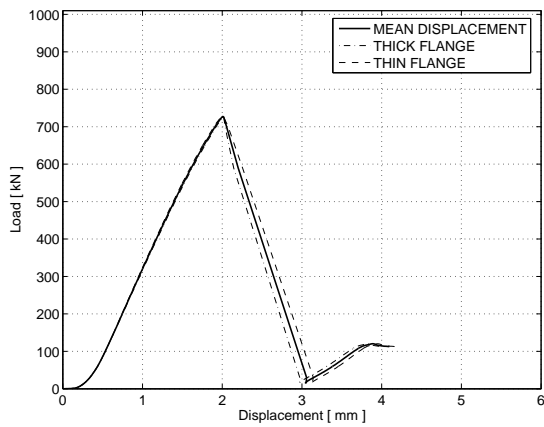


Figure B.11: Capped element - 01

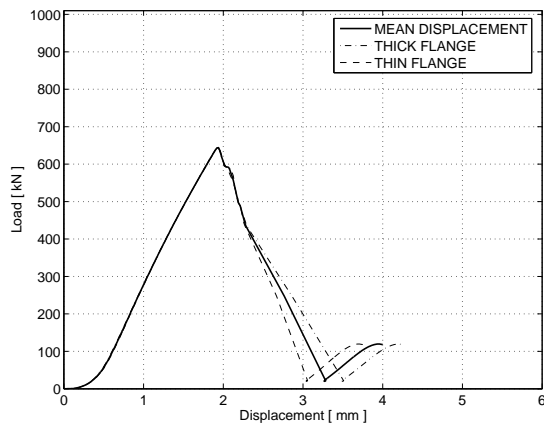


Figure B.12: Capped element - 02

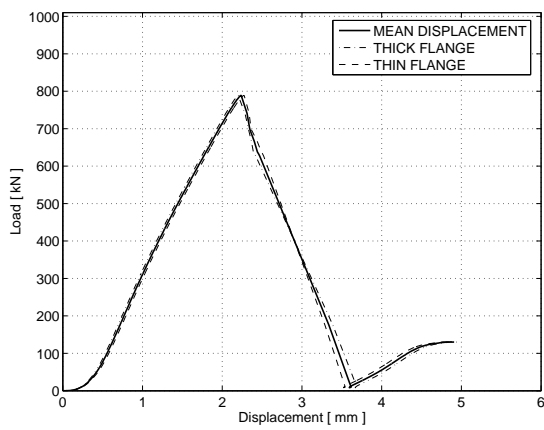


Figure B.13: Capped element - 03

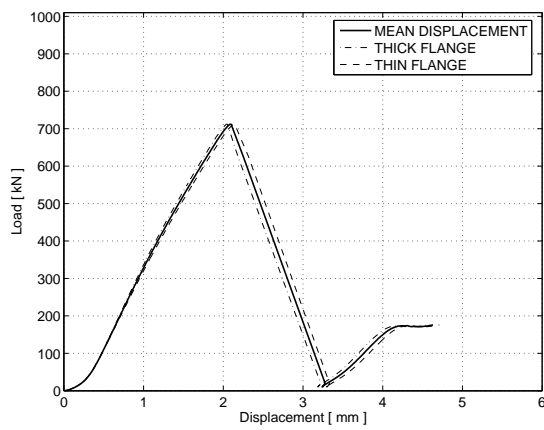


Figure B.14: Capped element - 04

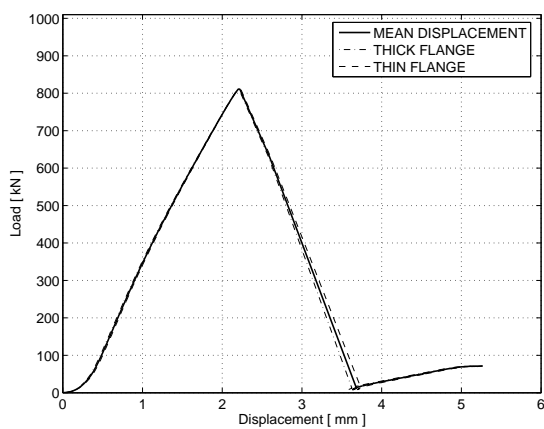


Figure B.15: Capped element - 05

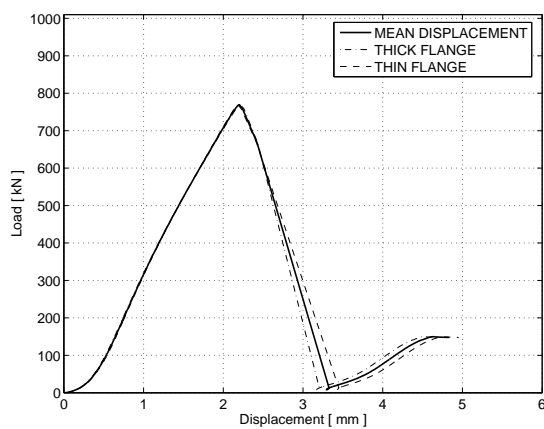


Figure B.16: Capped element - 06

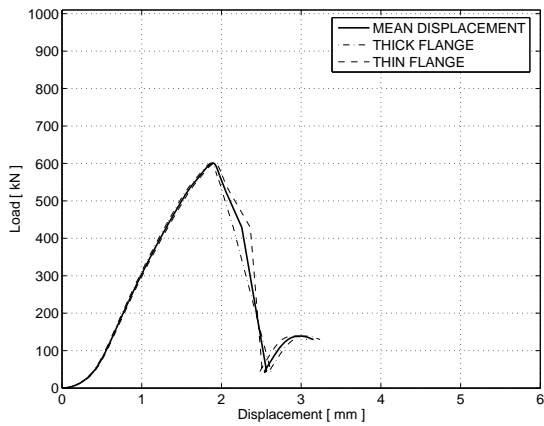


Figure B.17: Capped element - 07

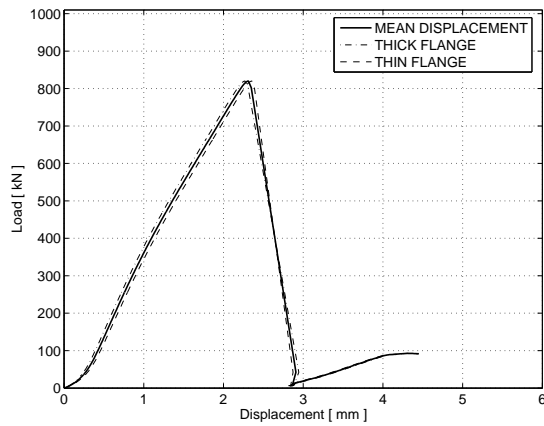


Figure B.18: Capped element - 08

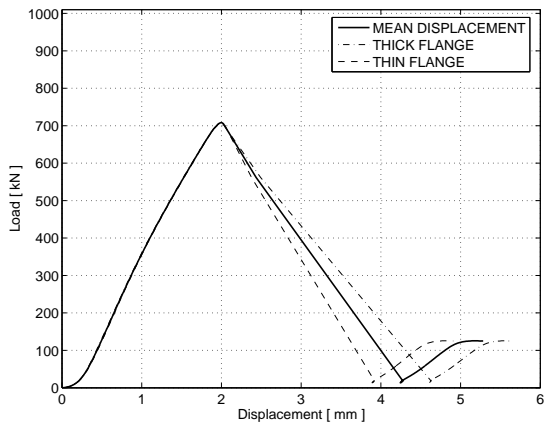


Figure B.19: Capped element - 09

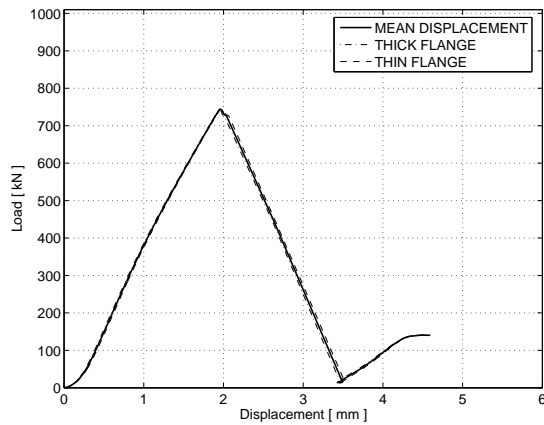


Figure B.20: Capped element - 10

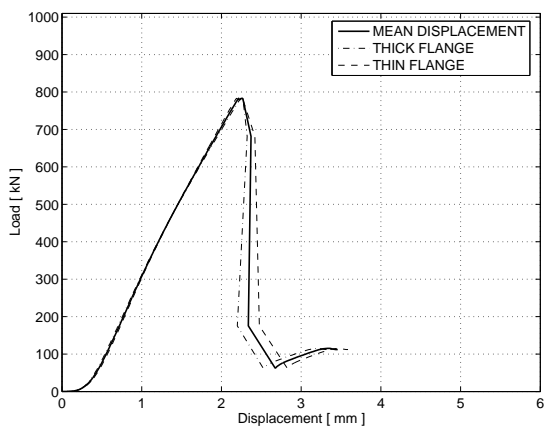


Figure B.21: Capped element - 11

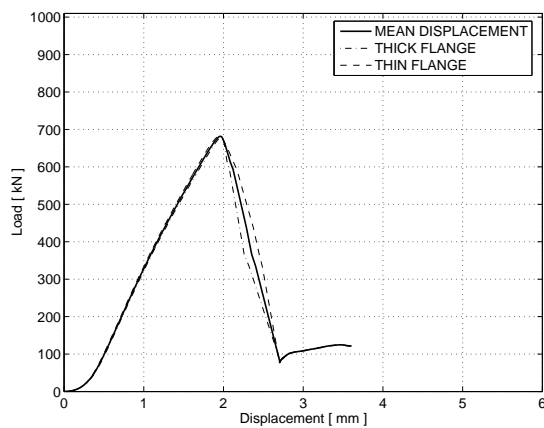


Figure B.22: Capped element - 12

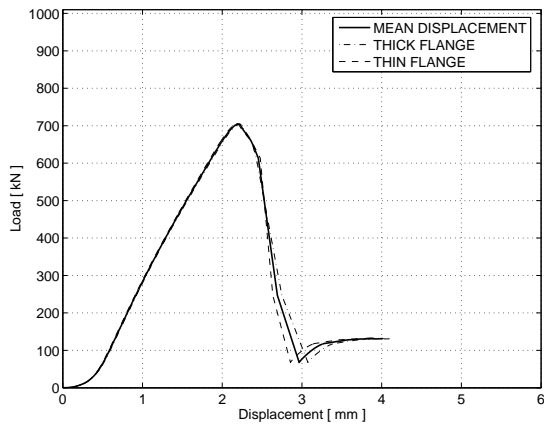


Figure B.23: Capped element - 13

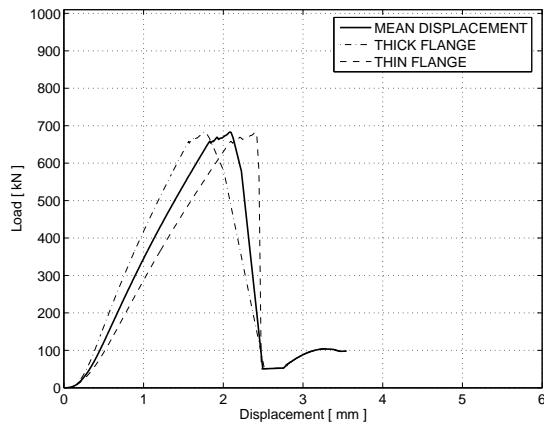


Figure B.24: Capped element - 14

B.2. Influence of cap-plate thickness and creep

In Table B.1 the number of elements tested for each configuration and the results are summarized. Figure B.25 illustrates the maximum failure loads, F_u , for uncapped and capped compression elements. In addition to elements with aligned cap plates, elements with 8-mm overlapping cap plates at the lower edge were tested for compression strength. The obtained strength and stiffness are also shown in Table B.1. Figure B.26 shows the load-displacement diagrams of all elements with aligned cap plates.

Table B.1: Cap-plate variation, overview

Specimen	No. of elements	Average strength [kN]	Average stiffness [MPa]
Uncapped	14	912	24 300
Capped 6 mm	10	729	16 050
Capped 8 mm, aligned	5	818	15 522
Capped 8 mm, overlapping	5	864	12 487
Capped 10 mm, aligned	4	834	15 581

The compression strength of capped elements is always lower than that of uncapped elements. For capped elements, a maximum strength is apparent for the 8-mm cap-plate thickness and does not vary between aligned and overlapping cap plates. The stiffness of capped elements decreased significantly. For capped elements, however, small changes were observed. Stiffness for elements with overlapping cap plates decreased by $\sim 3\,000$ MPa.

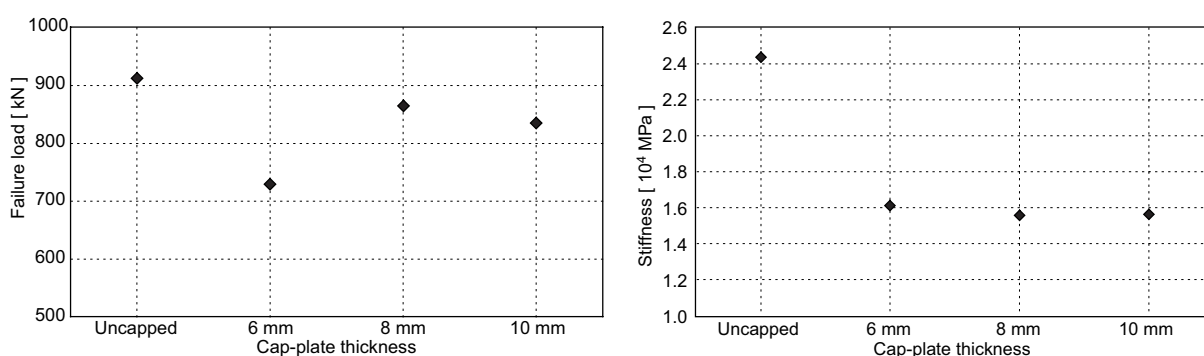


Figure B.25: Comparison of failure load for varying cap-plate thicknesses

Unlike aligned cap plates, cp. Figure 4.15, page 91, the allowable contact area, A_{c0} , for overlapping cap plates will propagate in all directions as shown in Figure B.28.

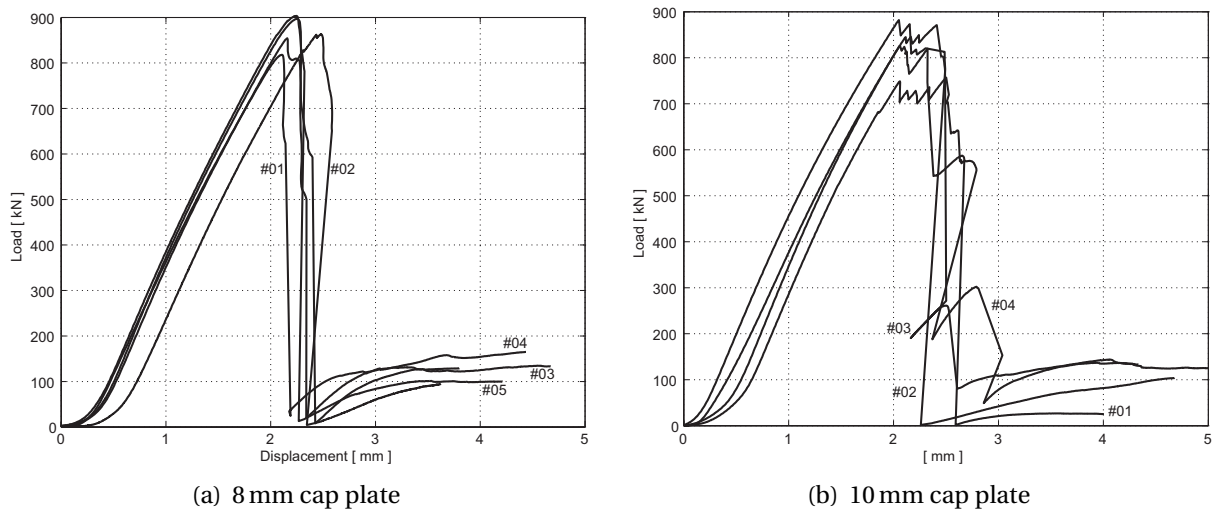


Figure B.26: Load-displacement diagrams of CS-elements with different cap-plate thicknesses

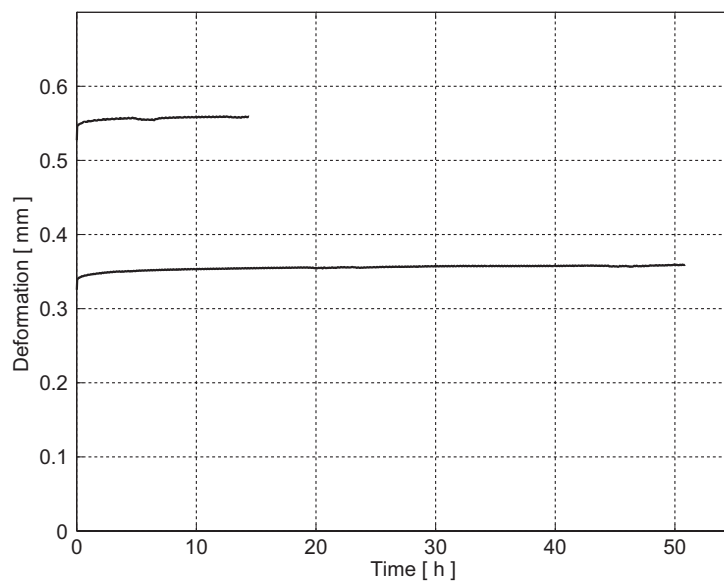


Figure B.27: Results from creep study

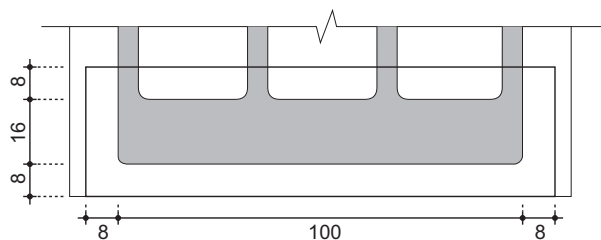


Figure B.28: Allowable compression area, A_{c0} , for CS-elements with overlapping cap plates

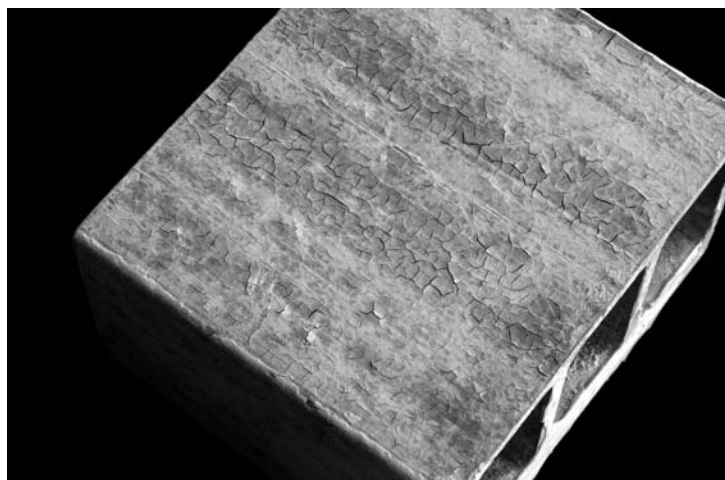
B.3. Experimental overview and results

Table B.2: Structural behavior for conditioned, uncapped elements

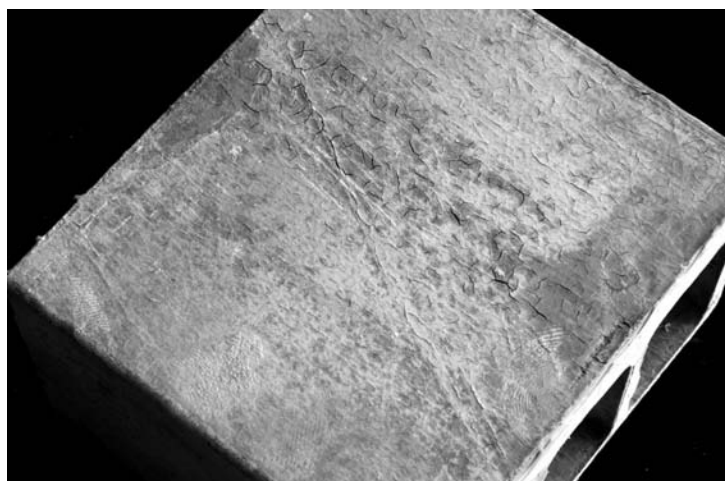
Conditioned at 20°C				Conditioned at 40°C				Conditioned at 60°C			
Name	F_u [kN]	F_{ret} [kN]	E-Modulus [MPa]	Name	F_u [kN]	F_{ret} [kN]	E-Modulus [MPa]	Name	F_u [kN]	F_{ret} [kN]	E-Modulus [MPa]
Unc.	917.3	164.7	24302	Unc.	917.3	164.7	24302	Unc.	917.3	164.7	24302
u-20-8-1	647.1	294.0	–	u-40-8-1	617.5	357.4	–	u-60-8-1	682.7	223.9	–
u-20-8-2	665.5	290.9	–	u-40-8-2	600.2	291.7	–	u-60-8-2	701.4	300.6	–
u-20-14-1	591.3	253.6	13321	u-40-14-1	462.9	213.0	12618	u-60-14-1	422.4	263.1	12516
u-20-30-1	526.5	267.0	20295	u-40-30-1	443.1	260.7	20898	u-60-30-1	406.5	244.1	19272
u-20-59-1	599.3	167.1	19812	u-40-59-1	477.7	221.8	21031	u-60-59-1	349.7	218.3	19674
u-20-60-1	569.6	233.7	17500	u-40-60-1	440.9	292.8	15429	u-60-60-1	382.6	303.2	12508
u-20-91-1	598.8	166.6	19522	u-40-92-1	420.6	233.1	4276	u-60-92-1	324.2	233.4	16349
u-20-115-1	561.1	159.4	18717	u-40-115-1	402.3	272.1	15136	u-60-115-1	349.4	290.6	4294
u-20-122-1	494.6	198.9	12752	u-40-119-1	362.9	248.4	14978	u-60-119-1	226.0	184.1	994
u-20-139-1	516.8	201.9	14611	u-40-138-1	378.8	238.7	14849	u-60-138-1	204.6	164.0	8634
u-20-158-1	588.3	182.4	21930	u-40-138-2	356.2	231.7	15103	u-60-158-1	323.1	193.5	19226
u-20-173-1	665.5	69.9	20783	u-40-158-1	434.5	218.2	20404	u-60-176-1	301.8	174.5	17374
u-20-219-1	454.8	259.4	16646	u-40-176-1	416.8	217.8	18658	u-60-219-1	283.6	190.2	15753
u-20-239-1	428.0	162.7	16614	u-40-219-1	335.8	205.7	10171	u-60-239-1	278.6	162.6	15799
u-20-268-1	453.4	227.9	16468	u-40-239-1	358.8	205.1	16635	u-60-268-1	257.6	167.9	14623
u-20-296-1	457.2	156.4	16827	u-40-268-1	340.6	163.9	13328	u-60-311-1	207.4	151.2	14038
u-20-296-2	481.8	165.0	17023	u-40-311-1	322.4	149.6	15981	u-60-329-1	171.2	125.4	12950
u-20-310-1	422.6	250.0	16396	u-40-329-1	392.4	155.6	16567	u-60-352-1	165.6	88.7	11818
u-20-326-1	418.0	125.5	17080	u-40-352-1	317.3	150.2	15397	u-60-389-1	153.8	97.2	12993
u-20-352-1	385.3	145.9	13202	u-40-389-1	349.6	119.8	16414	u-60-448-1	120.2	83.0	8511
u-20-389-1	405.6	190.1	17359	u-40-449-1	319.5	164.1	13061	u-60-493-1	108.0	75.1	9058
u-20-395-1	485.7	123.3	19753	u-40-493-1	317.0	143.8	14353	u-60-493-2	101.1	66.8	8678
u-20-449-1	372.0	174.2	13207	u-40-493-2	330.1	141.8	16141	u-60-548-1	94.7	70.8	552
u-20-493-1	367.4	150.1	14118	u-40-548-1	363.3	137.5	17450	u-60-548-2	122.2	78.6	10513
u-20-493-2	399.9	170.9	16665	u-40-548-2	350.4	133.2	17039	u-60-548-3	113.9	78.7	8625
u-20-548-1	372.3	139.5	17799	u-40-548-3	354.1	143.8	16380	u-60-548-4	137.2	82.1	10655
u-20-548-2	366.0	171.6	15812	u-40-548-4	336.5	147.4	17642				
u-20-548-3	411.4	166.8	17318								

Table B.3: Structural behavior for conditioned, capped elements

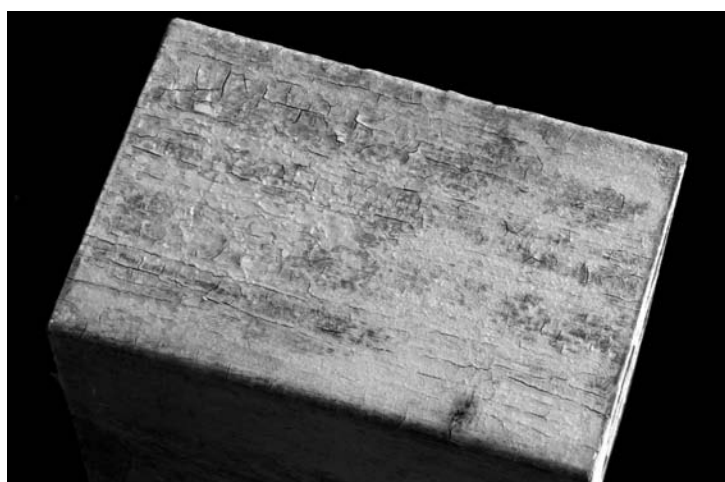
Name	Conditioned at 20°C			Conditioned at 40°C			Conditioned at 60°C				
	F_u [kN]	F_{ret} [kN]	E-Modulus [MPa]	Name	F_u [kN]	F_{ret} [kN]	E-Modulus [MPa]	Name	F_u [kN]	F_{ret} [kN]	E-Modulus [MPa]
Unconditioned	727.1	122.0	15386	Unconditioned	727.1	122.0	15386	Unconditioned	727.1	122.0	15386
c-20-5-1	648.0	129.7	16627	c-40-5-1	658.3	119.5	16090	c-60-5-1	667.9	130.6	15403
c-20-6-1	739.2	132.5	16942	c-40-6-1	642.9	124.2	15566	c-60-6-1	681.2	115.2	16044
c-20-6-2	716.1	93.1	15772	c-40-6-2	641.3	112.8	14700	c-60-6-2	500.5	152.4	12493
c-20-8-1	788.8	113.6	16298	c-40-8-1	573.4	135.6	14463	c-60-8-1	659.4	111.2	15435
c-20-8-2	710.2	136.6	15578	c-40-8-2	730.5	141.0	14911	c-60-8-2	695.4	121.4	15105
c-20-9-1	783.3	108.4	17485	c-40-9-1	714.4	109.9	16431	c-60-9-1	684.7	113.7	14937
c-20-15-1	684.0	144.7	15906	c-40-15-1	596.7	148.5	17683	c-60-15-1	589.9	120.3	16469
c-20-17-1	814.3	80.8	15595	c-40-19-1	717.8	99.8	15639	c-60-19-1	469.6	126.0	13795
c-20-20-1	670.3	143.3	15022	c-40-20-1	684.3	78.8	14256	c-60-20-1	485.0	63.9	12705
c-20-30-1	640.1	149.3	16600	c-40-30-1	583.7	116.5	16356	c-60-30-1	644.3	113.0	16232
c-20-41-1	558.3	121.8	14839	c-40-41-1	640.1	100.0	13618	c-60-41-1	563.3	105.4	13607
c-20-41-2	600.2	120.3	14682	c-40-41-2	622.1	109.7	13544	c-60-41-2	568.6	110.9	13463
c-20-55-1	578.9	98.3	14259	c-40-55-1	554.8	110.5	13469	c-60-55-1	452.1	101.7	8391.7
c-20-55-2	583.0	110.3	13924	c-40-55-2	593.9	163.7	13113	c-60-55-2	551.5	60.9	13597
c-20-60-1	588.6	154.4	13186	c-40-60-1	591.9	108.8	14975	c-60-60-1	471.8	109.0	13989
c-20-66-1	594.6	141.8	14237	c-40-60-2	583.7	131.4	12799	c-60-60-2	545.9	115.6	12357
c-20-86-1	601.6	81.4	14972	c-40-66-1	546.8	113.0	13862	c-60-66-1	509.2	102.6	13587
c-20-91-1	633.4	98.2	14305	c-40-86-1	568.8	125.6	14507	c-60-86-1	554.2	100.7	14062
c-20-115-1	549.2	130.5	14075	c-40-92-1	520.2	110.2	13066	c-60-92-1	478.6	184.7	13413
c-20-122-1	550.4	100.0	12449	c-40-115-1	466.2	135.9	12600	c-60-115-1	472.3	115.1	13091
c-20-157-1	492.0	131.6	12974	c-40-158-1	493.6	135.9	13061	c-60-158-1	424.0	102.2	12600
c-20-174-1	493.4	176.2	13698	c-40-176-1	434.8	92.9	13026	c-60-176-1	416.9	97.2	12953
c-20-199-1	488.0	109.4	12766	c-40-199-1	378.9	100.0	12160	c-60-199-1	287.6	111.6	11577
c-20-236-1	551.8	88.2	14582	c-40-295-1	366.6	132.1	11084	c-60-430-1	260.2	116.5	10921
c-20-340-1	502.6	87.8	11379	c-40-340-1	433.0	150.6	12582	c-60-430-2	368.7	77.4	11611
c-20-430-1	346.8	123.9	10587	c-40-395-1	306.7	130.4	10780				
c-20-430-2	430.7	110.4	13720	c-40-430-1	383.0	105.6	12863				
				c-40-430-2	421.5	135.7	13000				

B.4. Hairline cracks on element surface

(a) Top side



(b) Bottom side

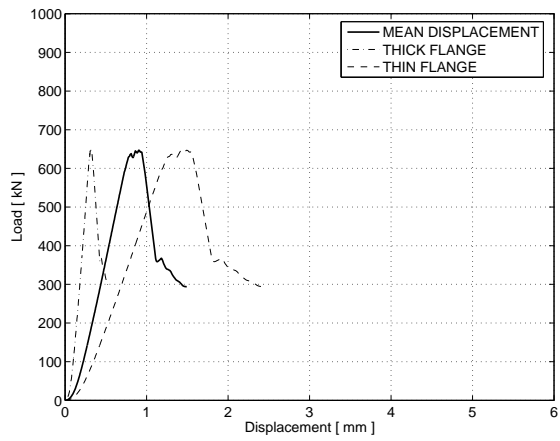


(c) Lateral side

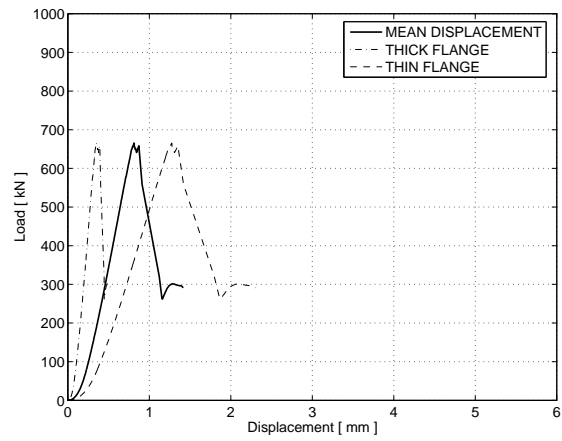
Figure B.29: Hairline cracks on conditioned element (60°C, 800 days)

B.4.1. Load displacement curves of conditioned elements

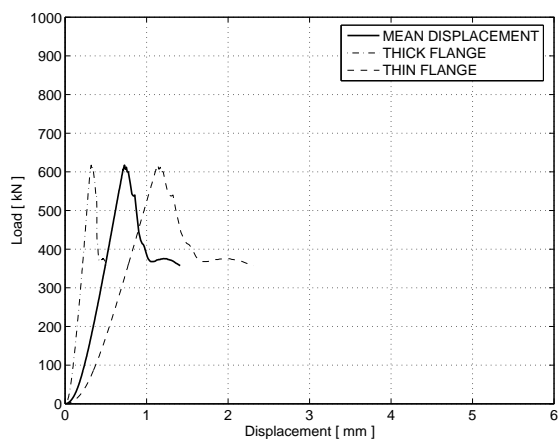
Uncapped elements



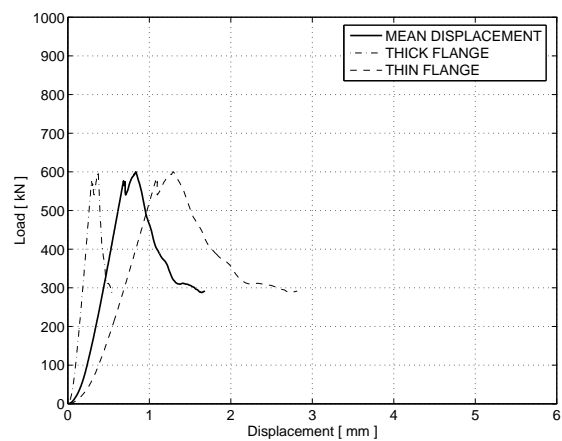
(a) 20°C



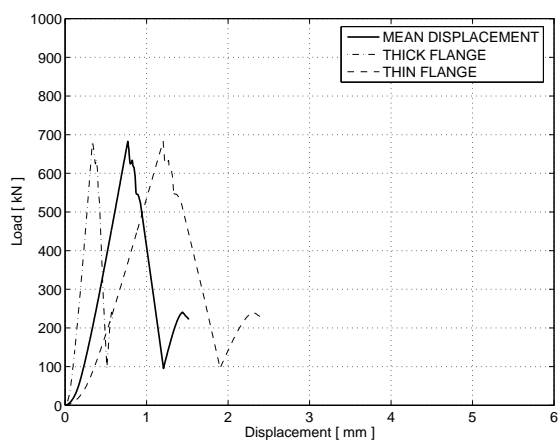
(a) 20°C



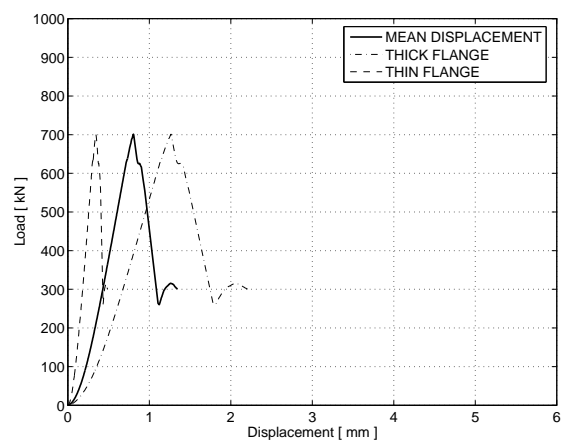
(b) 40°C



(b) 40°C



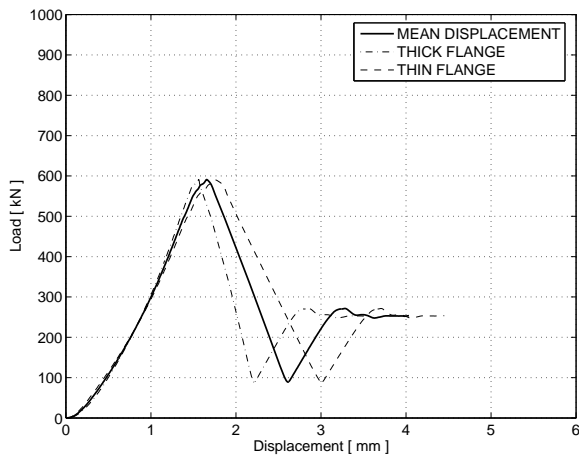
(c) 60°C



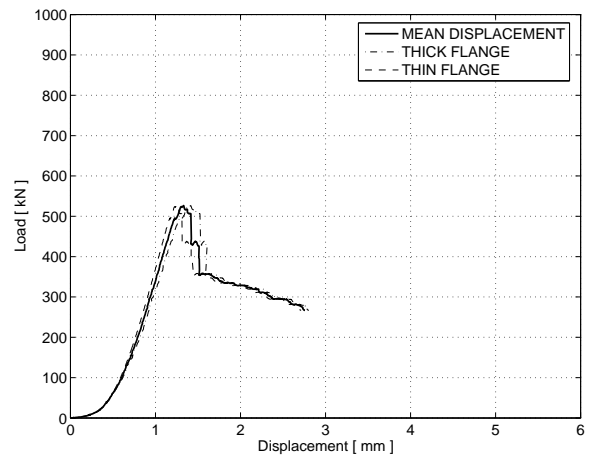
(c) 60°C

Figure B.30: Aging time: 8 days

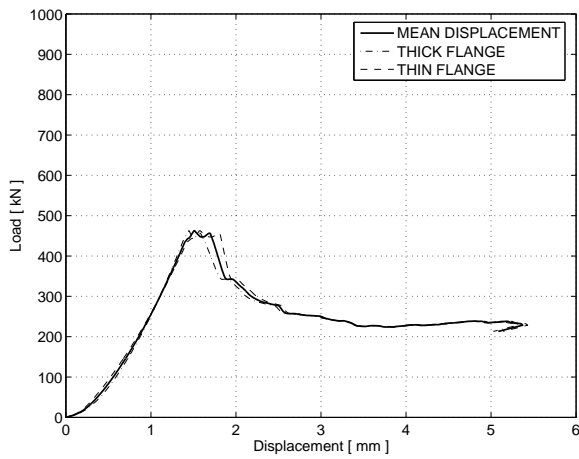
Figure B.31: Aging time: 8 days



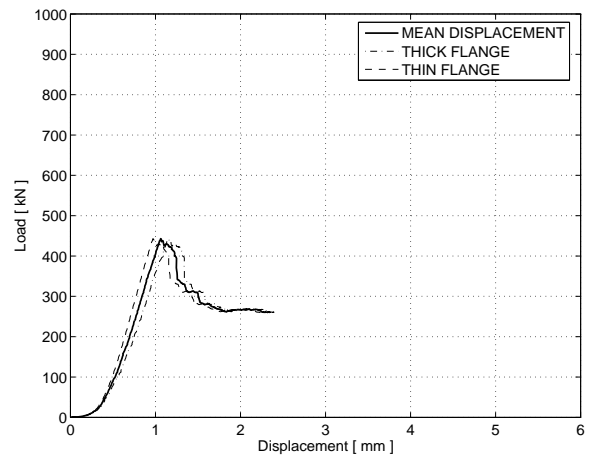
(a) 20°C



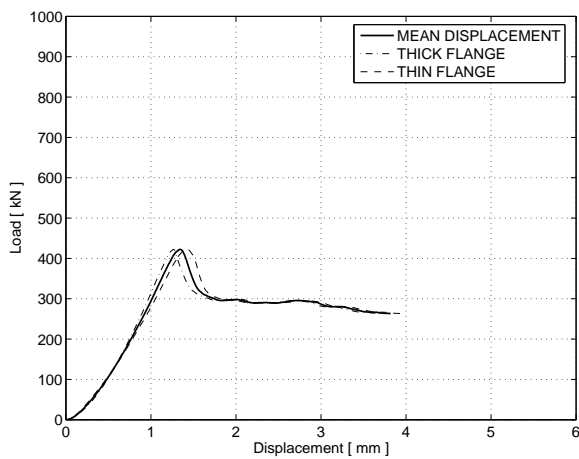
(a) 20°C



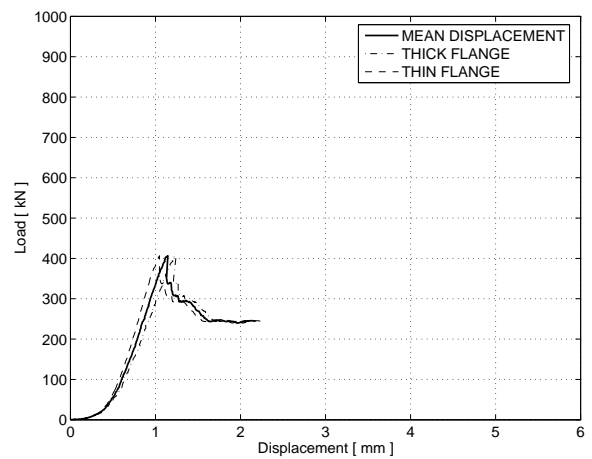
(b) 40°C



(b) 40°C



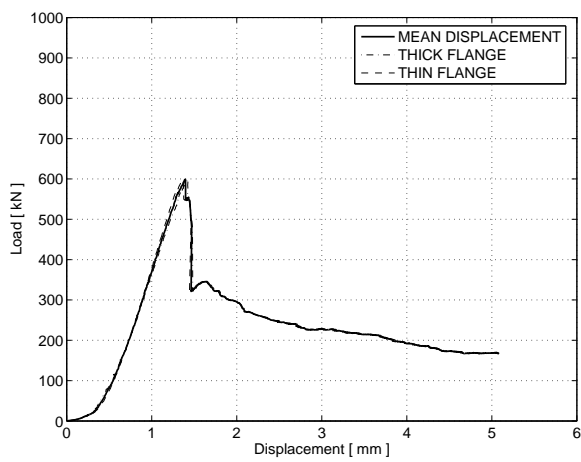
(c) 60°C



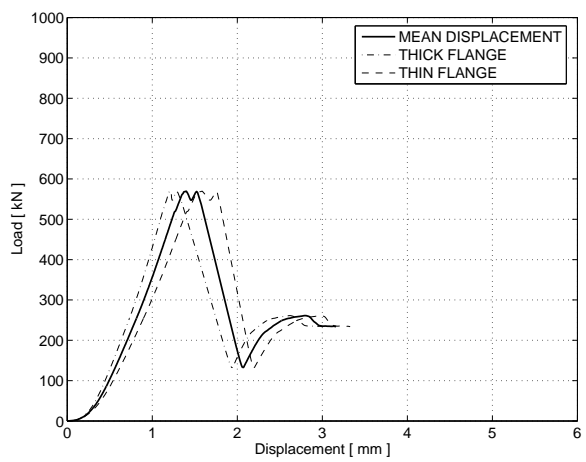
(c) 60°C

Figure B.32: Aging time: 14 days

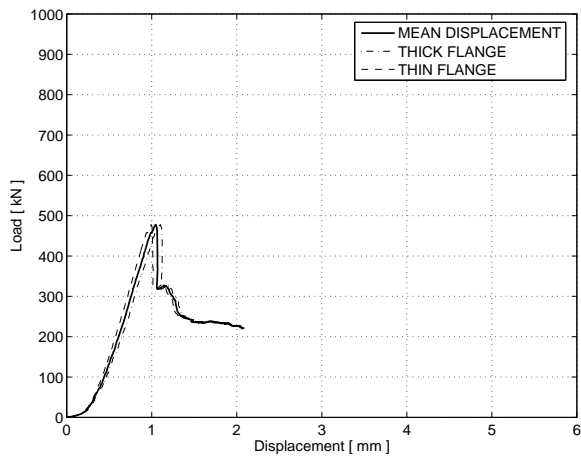
Figure B.33: Aging time: 30 days



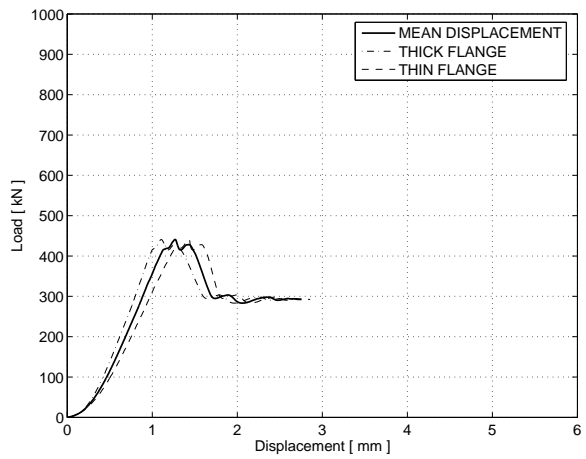
(a) 20°C



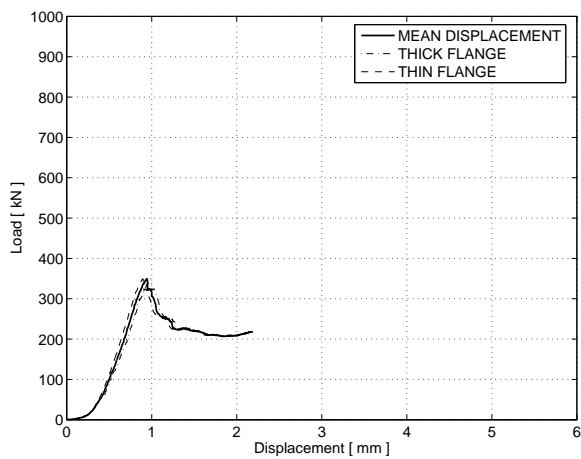
(a) 20°C



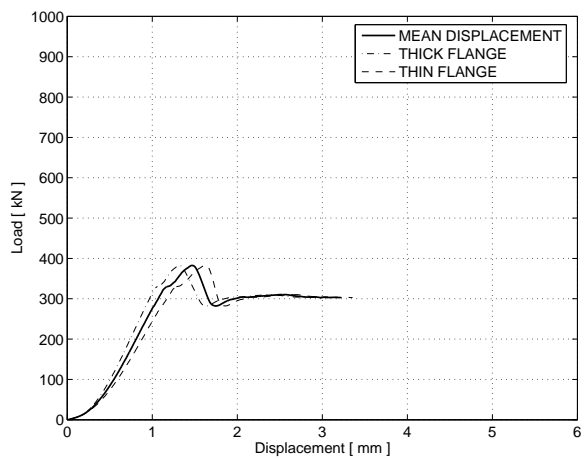
(b) 40°C



(b) 40°C



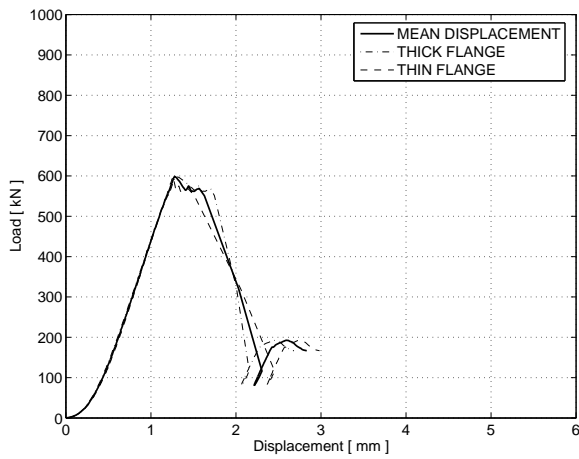
(c) 60°C



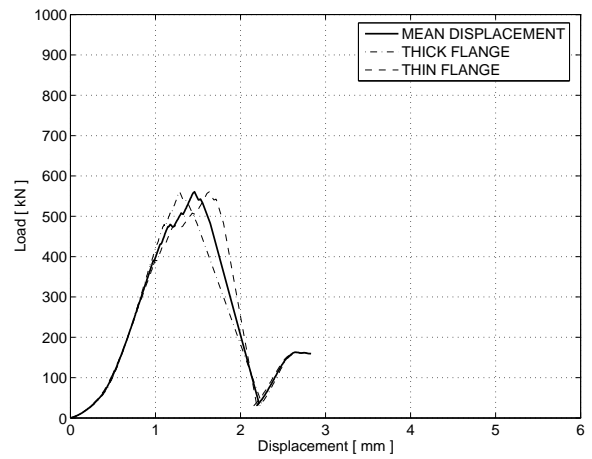
(c) 60°C

Figure B.34: Aging time: 59 days

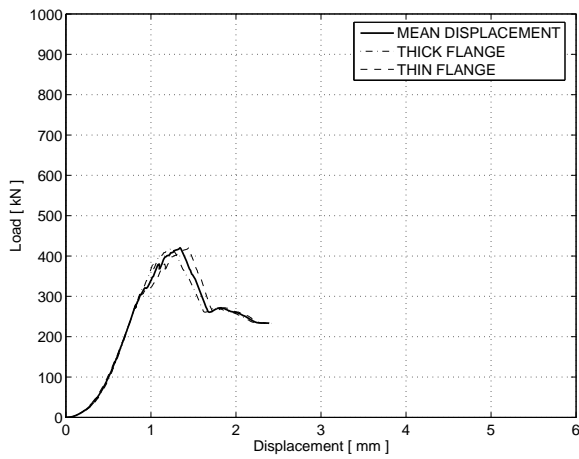
Figure B.35: Aging time: 59 days



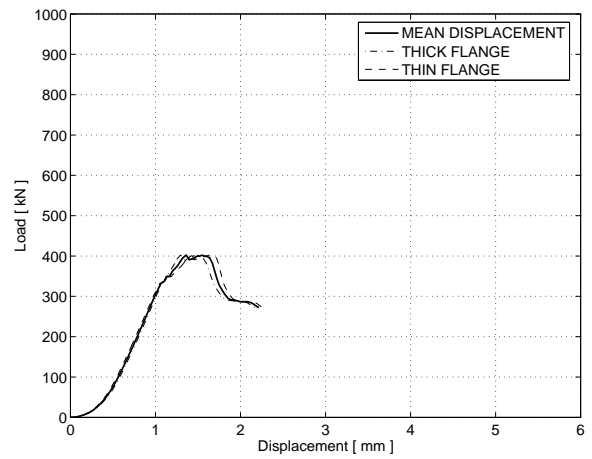
(a) 20°C



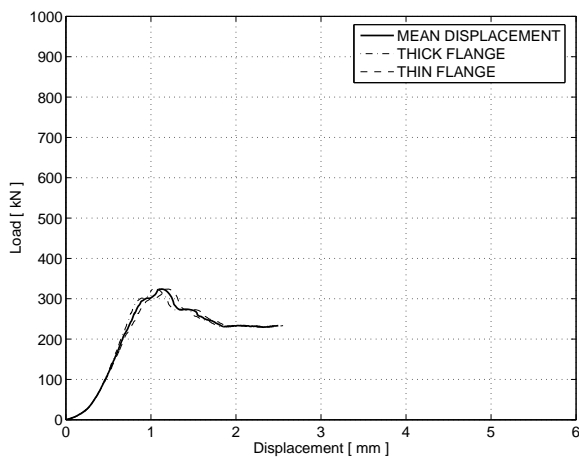
(a) 20°C



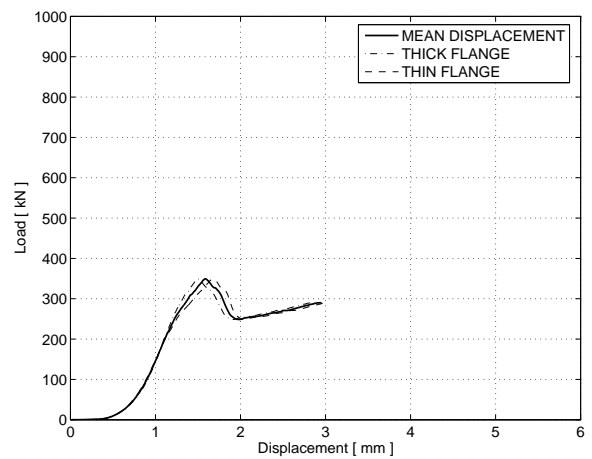
(b) 40°C



(b) 40°C



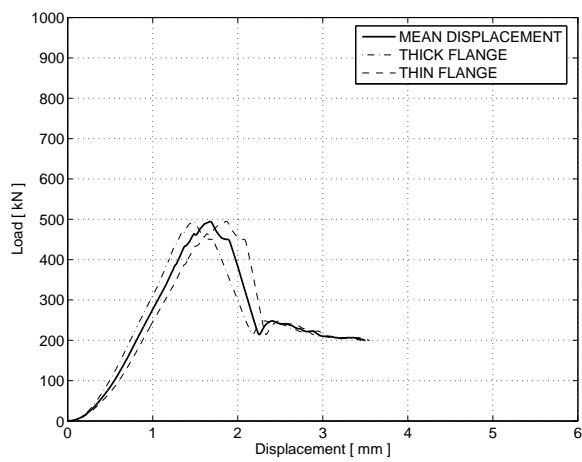
(c) 60°C



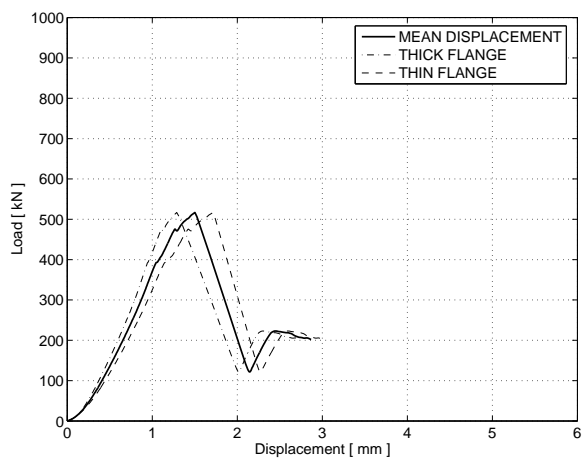
(c) 60°C

Figure B.36: Aging time: 91 days

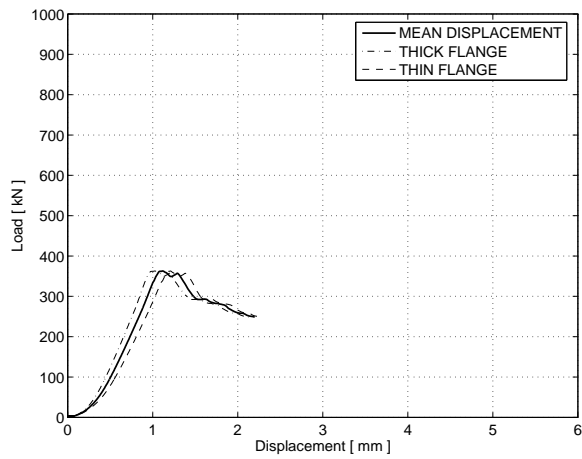
Figure B.37: Aging time: 115 days



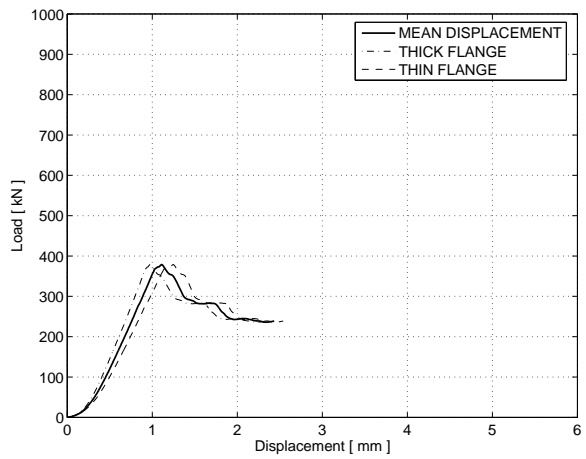
(a) 20°C



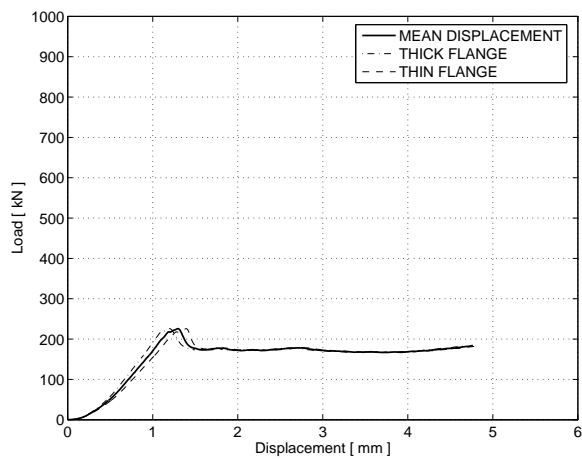
(a) 20°C



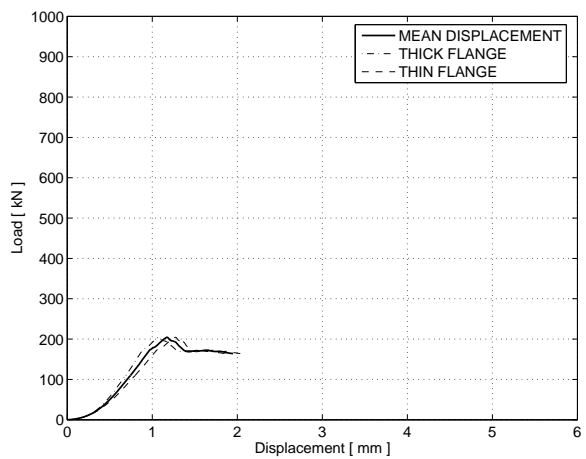
(b) 40°C



(b) 40°C



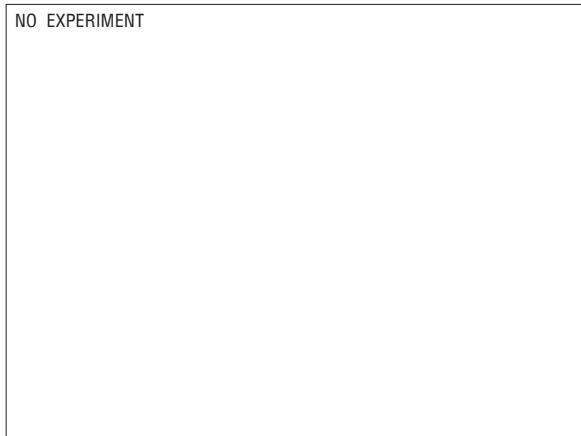
(c) 60°C



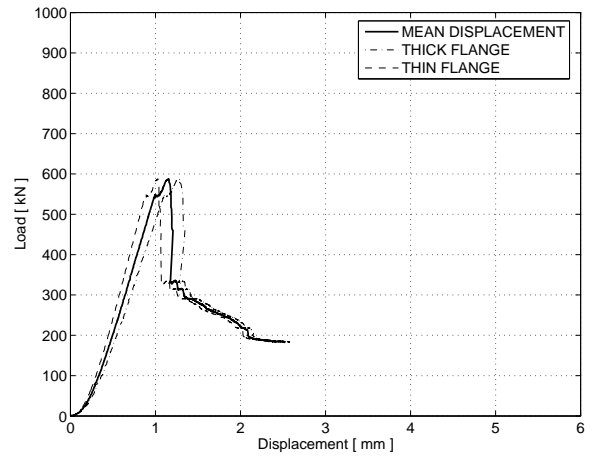
(c) 60°C

Figure B.38: Aging time: 120 days

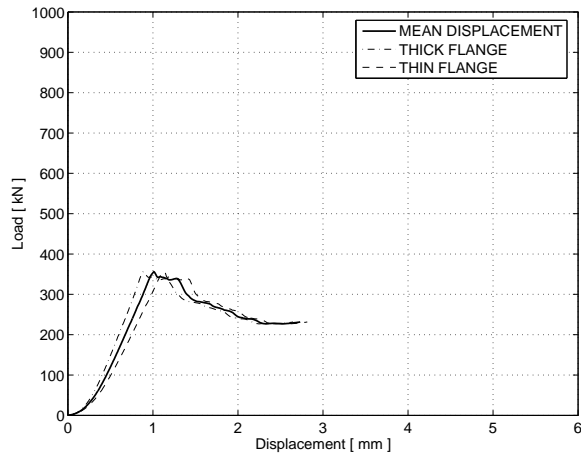
Figure B.39: Aging time: 138 days



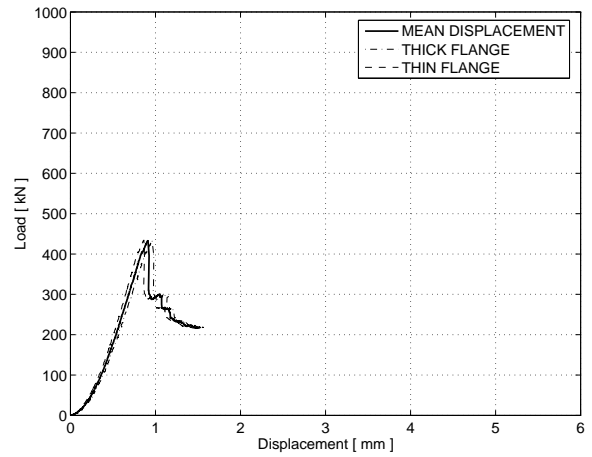
(a) 20°C



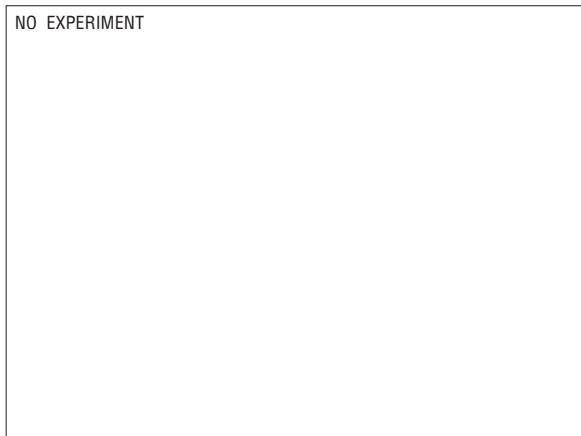
(a) 20°C



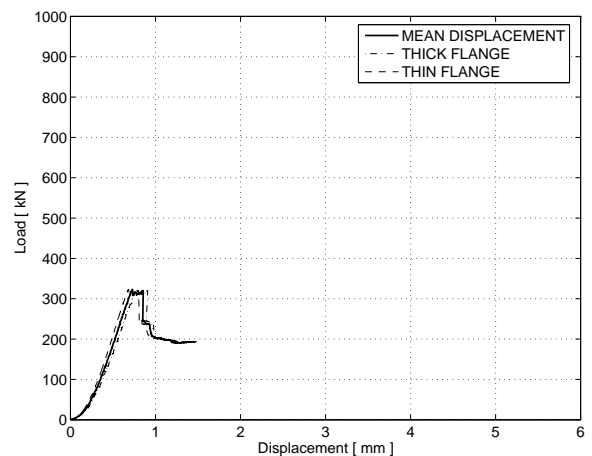
(b) 40°C



(b) 40°C



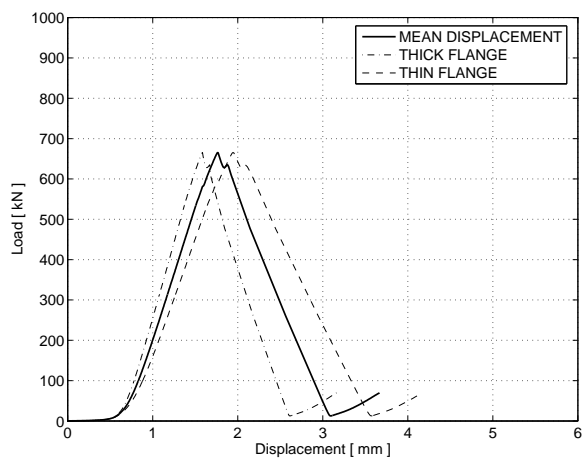
(c) 60°C



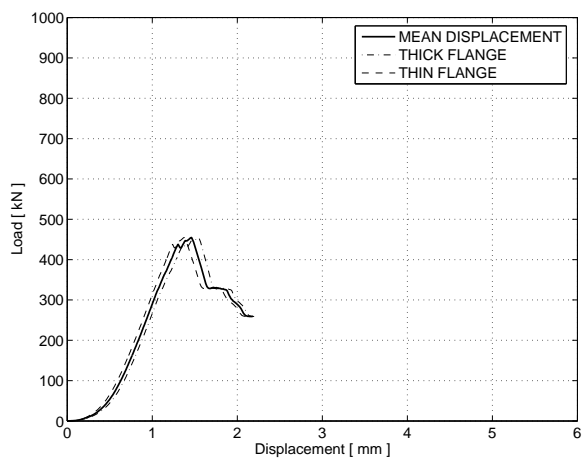
(c) 60°C

Figure B.40: Aging time: 138 days

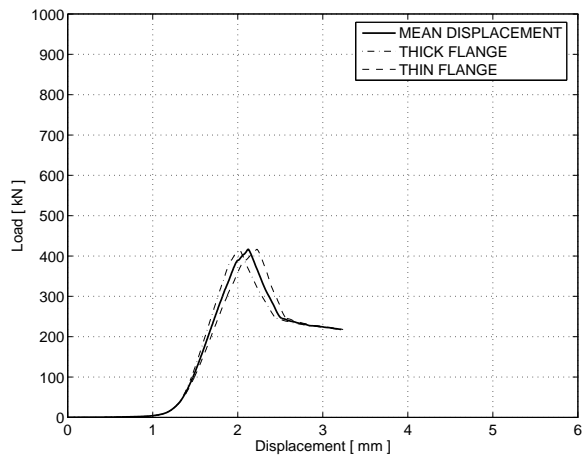
Figure B.41: Aging time: 158 days



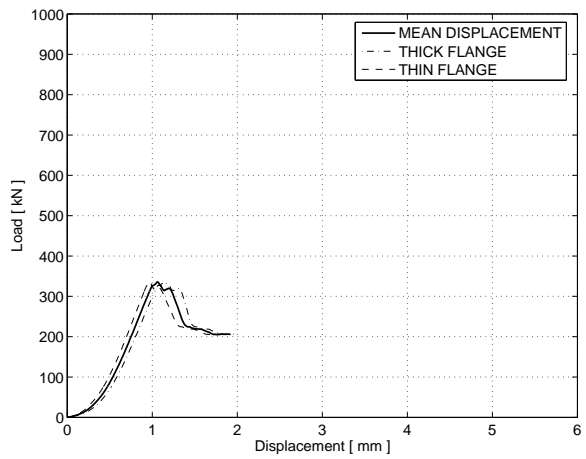
(a) 20°C



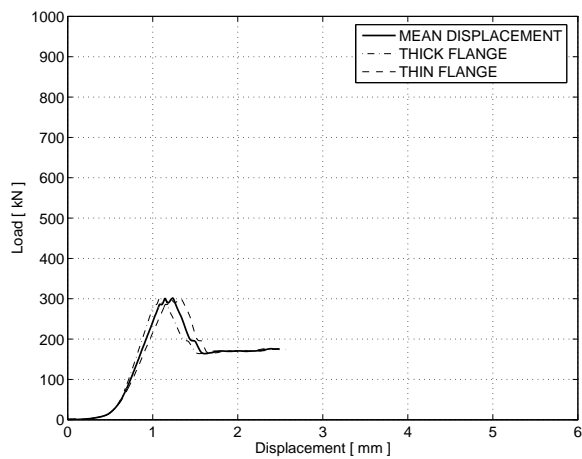
(a) 20°C



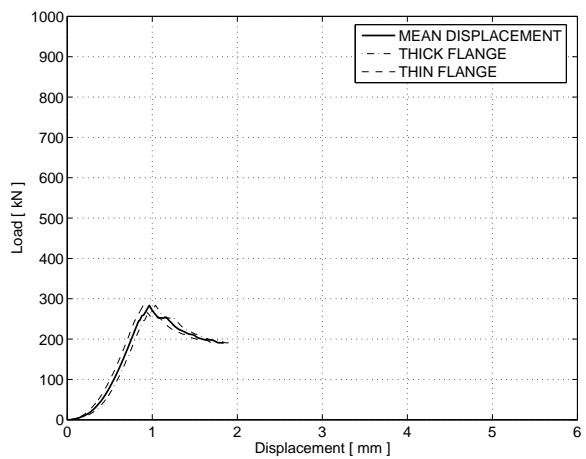
(b) 40°C



(b) 40°C



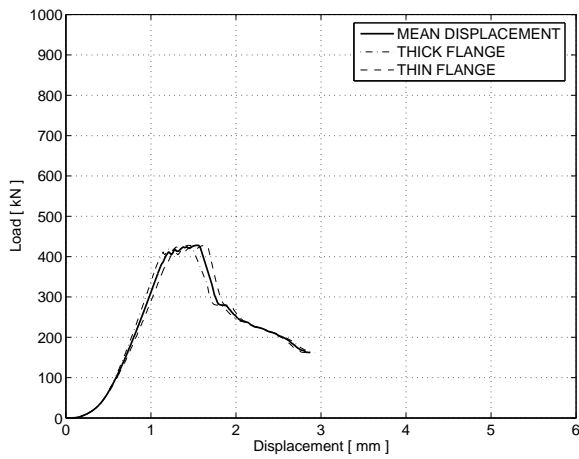
(c) 60°C



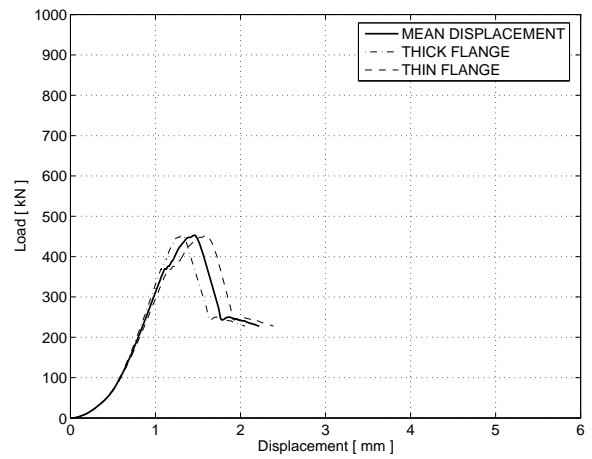
(c) 60°C

Figure B.42: Aging time: 176 days

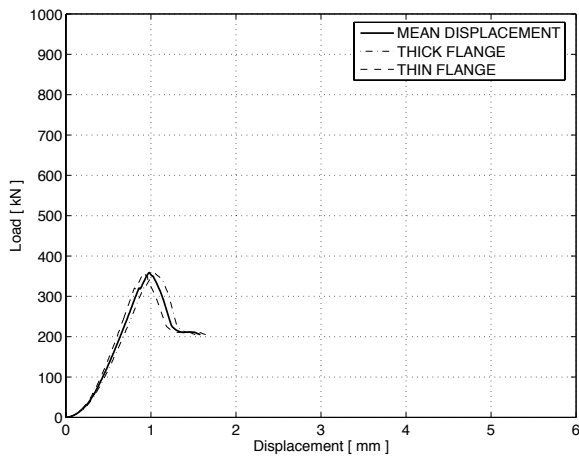
Figure B.43: Aging time: 219 days



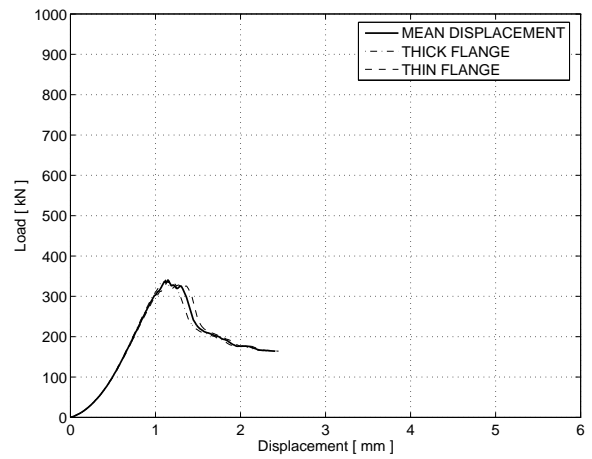
(a) 20°C



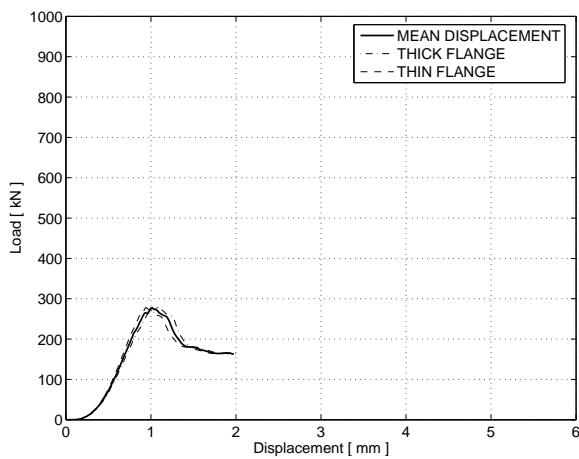
(a) 20°C



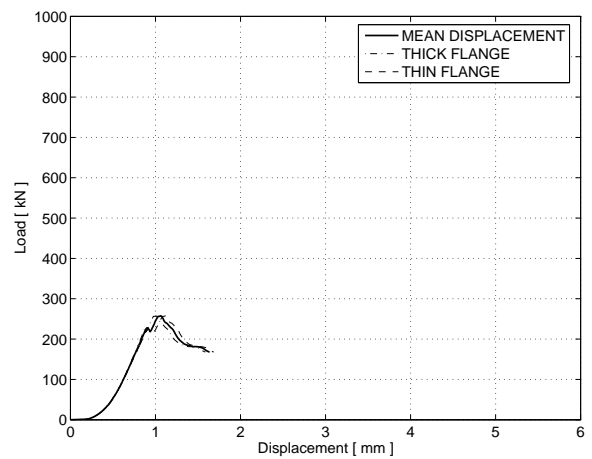
(b) 40°C



(b) 40°C



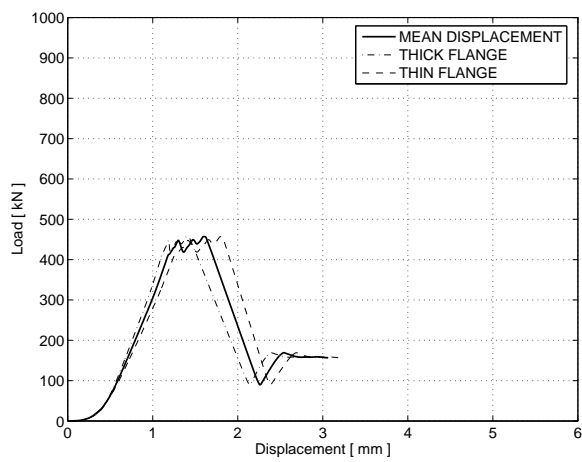
(c) 60°C



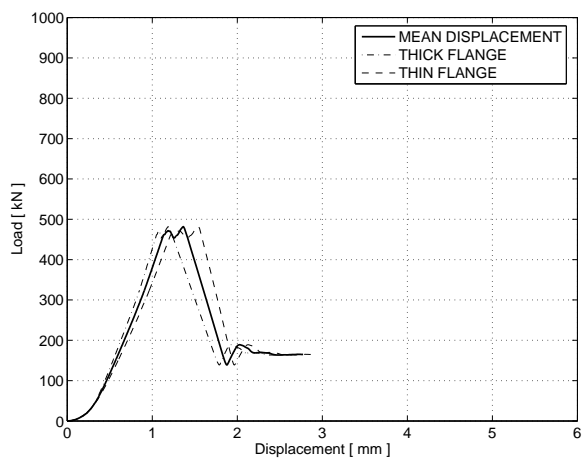
(c) 60°C

Figure B.44: Aging time: 239 days

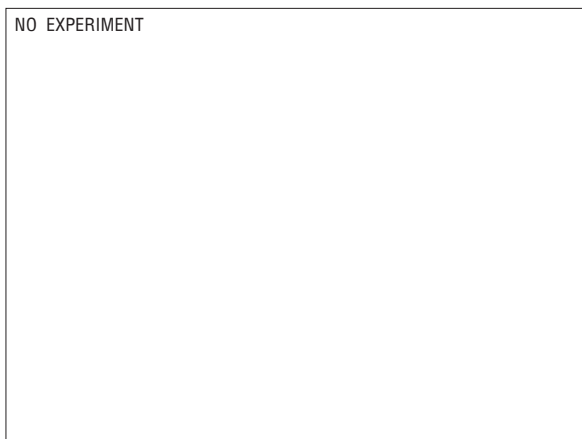
Figure B.45: Aging time: 268 days



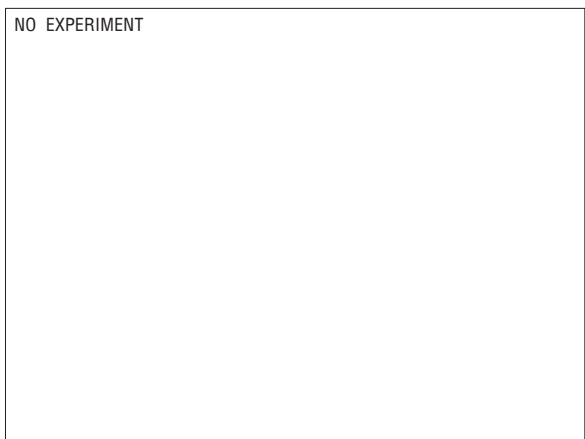
(a) 20°C



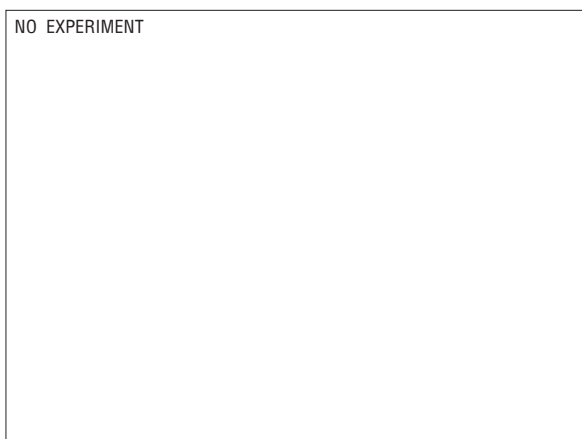
(a) 20°C



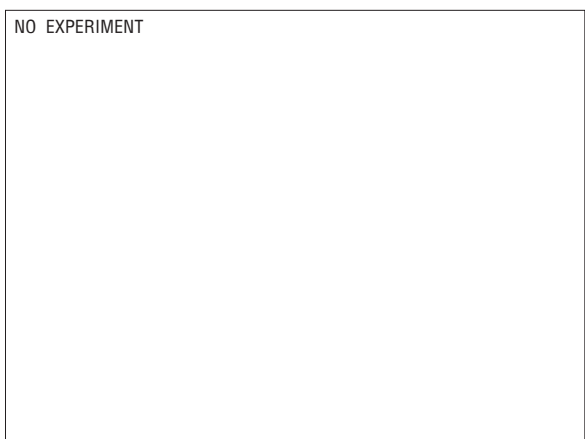
(b) 40°C



(b) 40°C



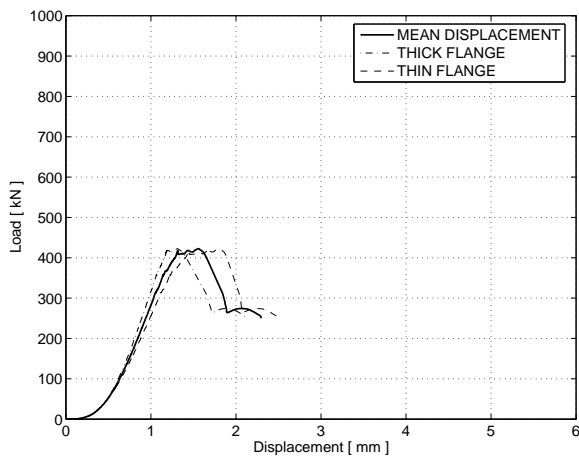
(c) 60°C



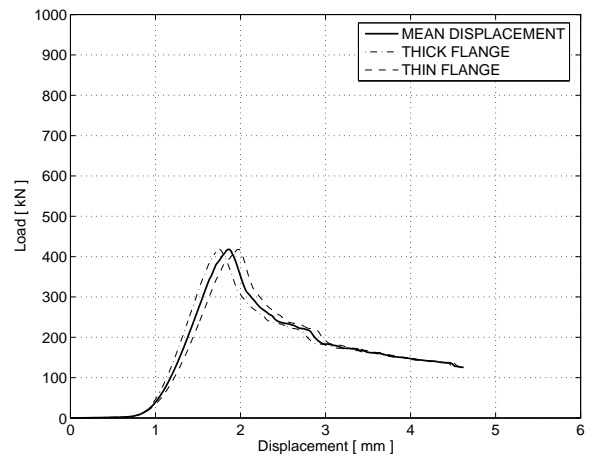
(c) 60°C

Figure B.46: Aging time: 296 days

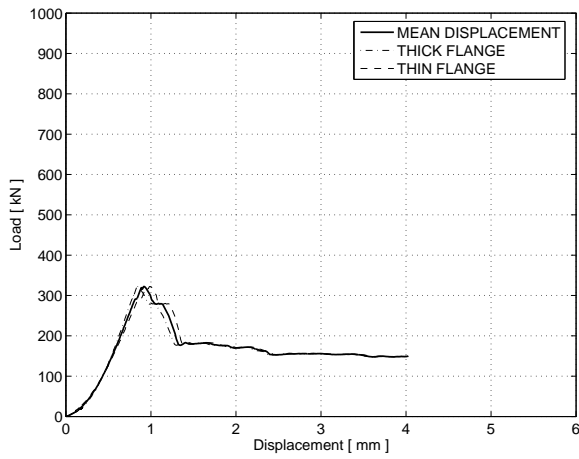
Figure B.47: Aging time: 296 days



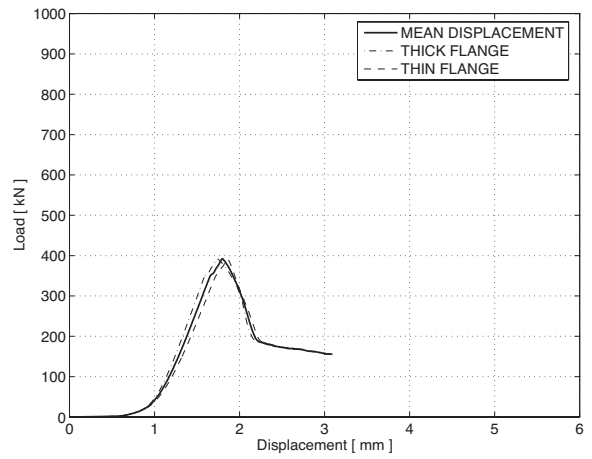
(a) 20°C



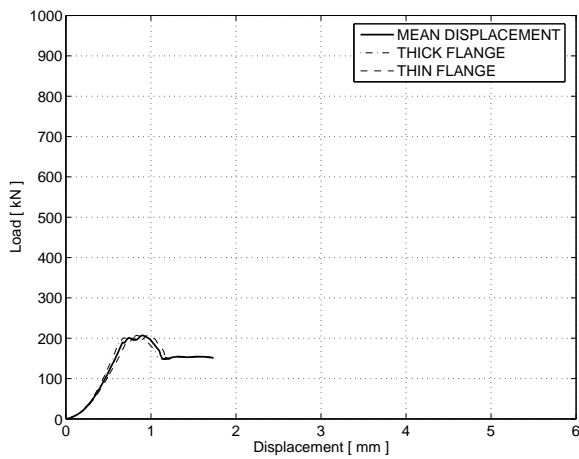
(a) 20°C



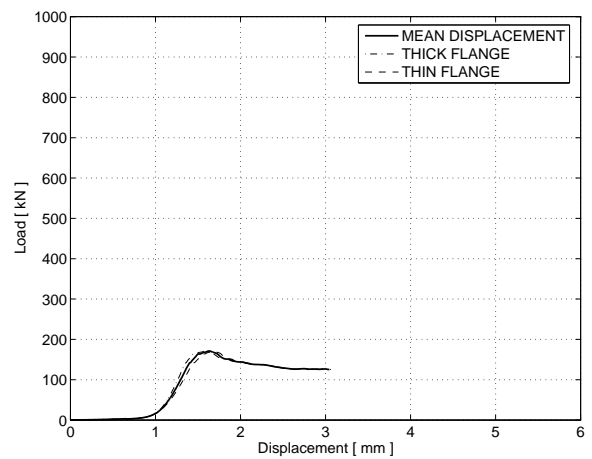
(b) 40°C



(b) 40°C



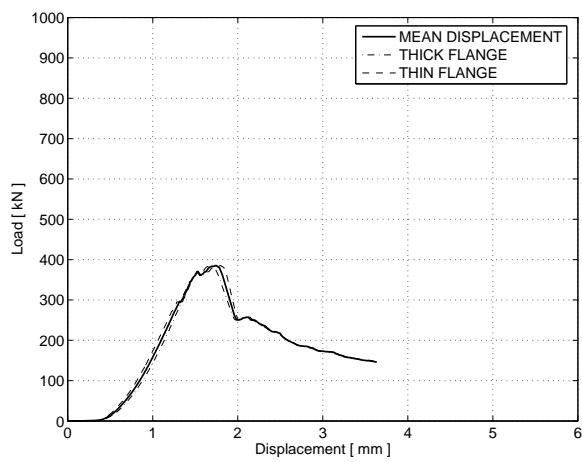
(c) 60°C



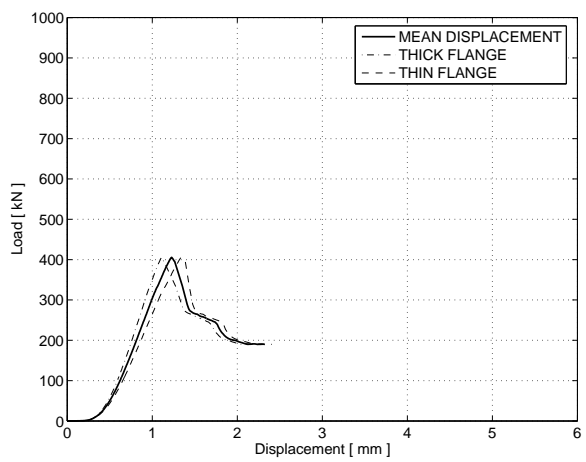
(c) 60°C

Figure B.48: Aging time: 310 days

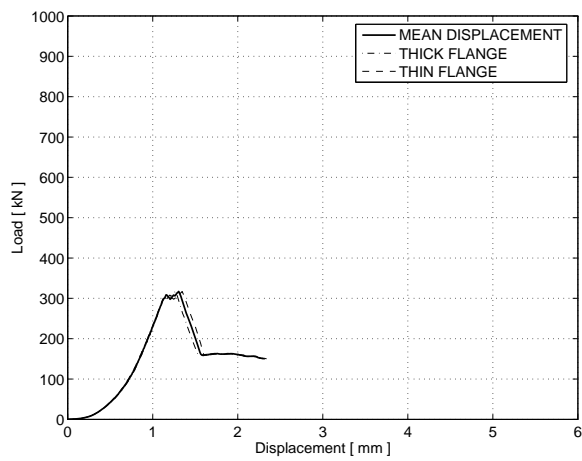
Figure B.49: Aging time: 328 days



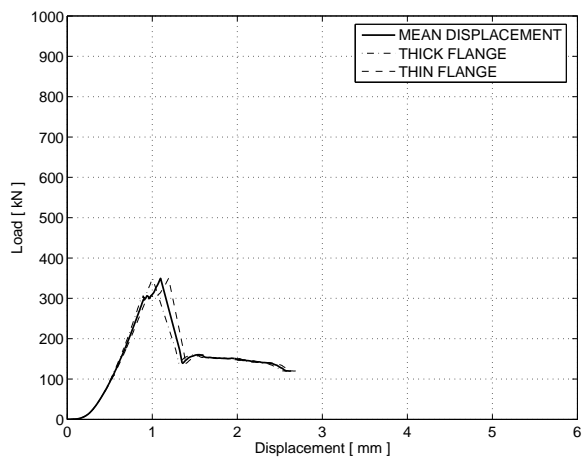
(a) 20°C



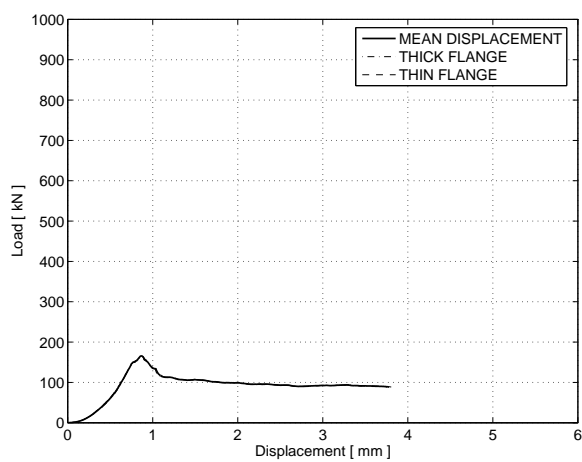
(a) 20°C



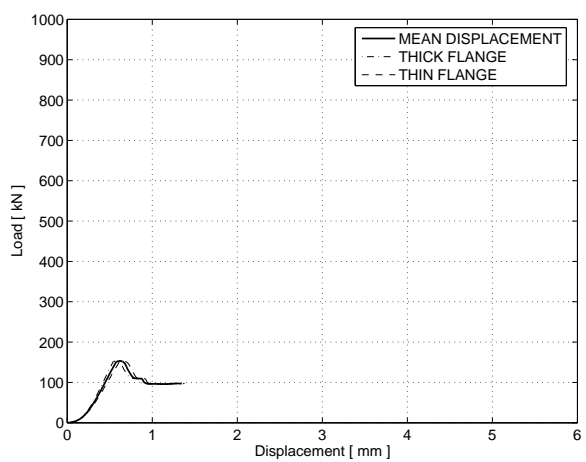
(b) 40°C



(b) 40°C



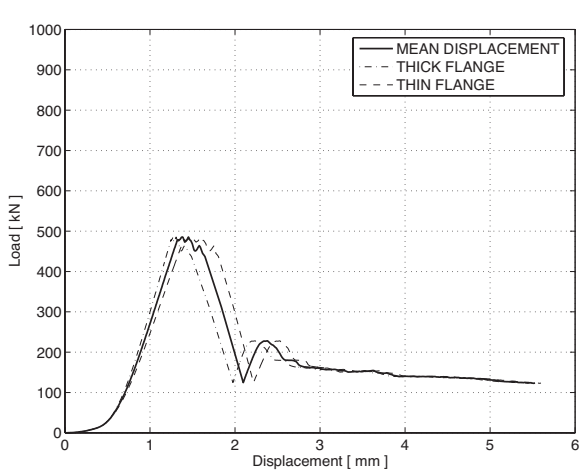
(c) 60°C



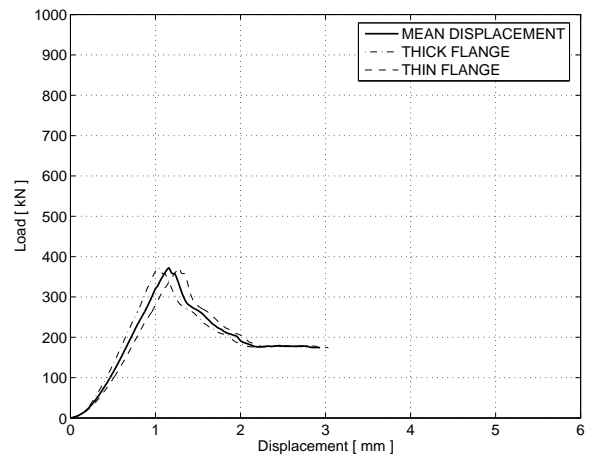
(c) 60°C

Figure B.50: Aging time: 352 days

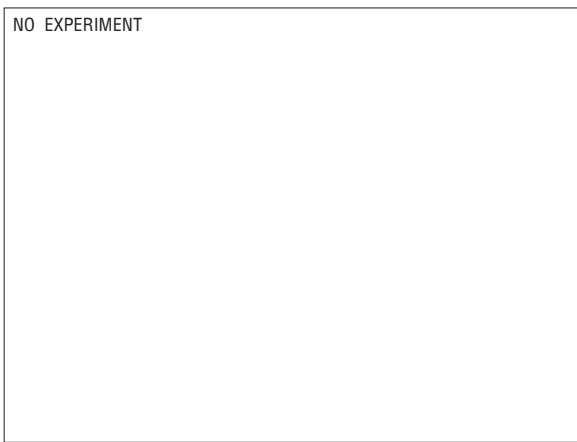
Figure B.51: Aging time: 389 days



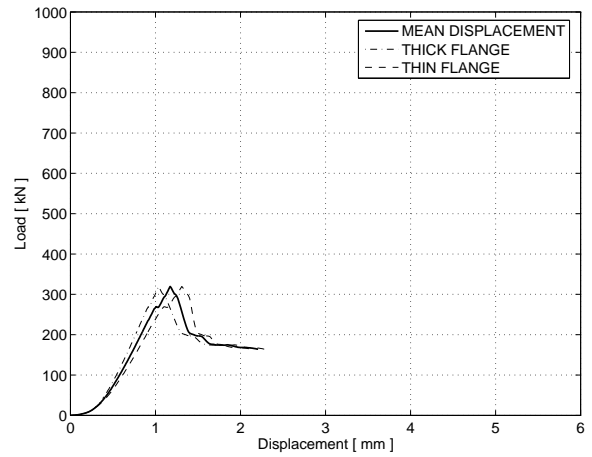
(a) 20°C



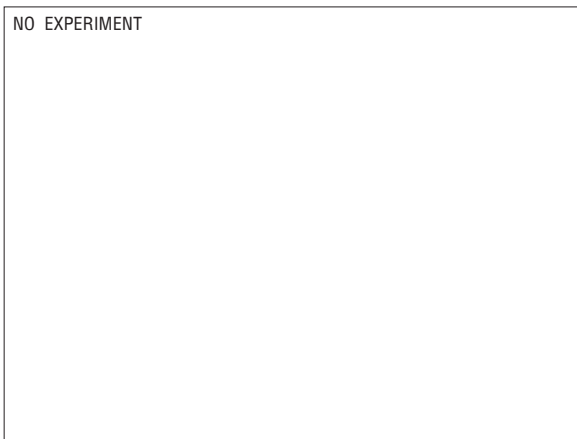
(a) 20°C



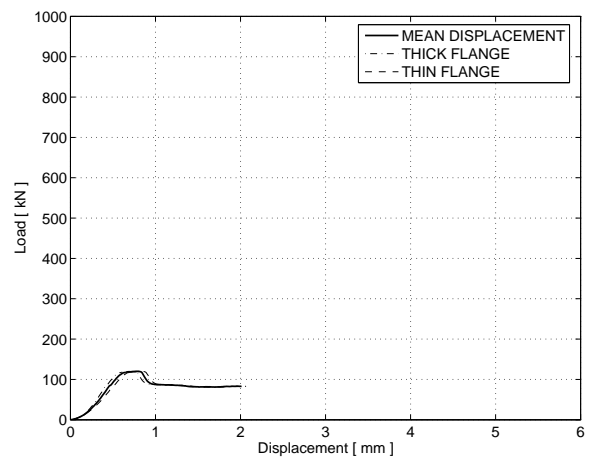
(b) 40°C



(b) 40°C



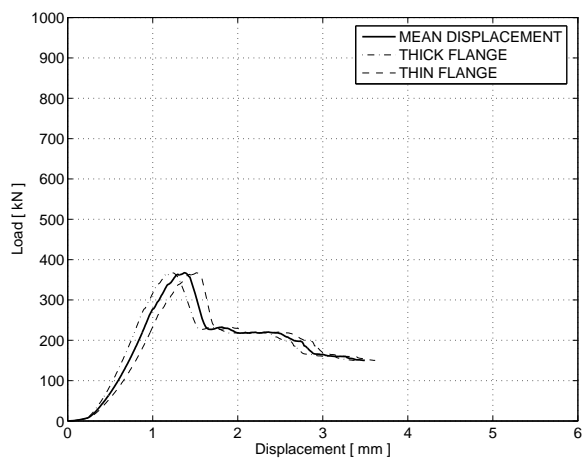
(c) 60°C



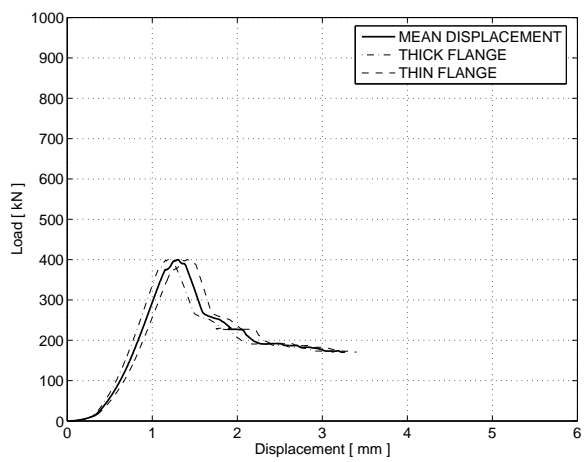
(c) 60°C

Figure B.52: Aging time: 395 days

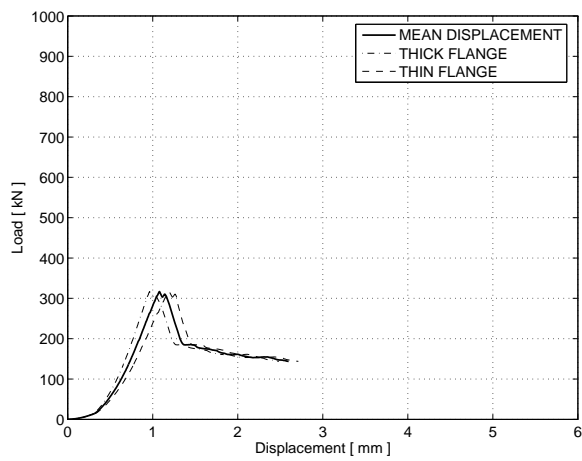
Figure B.53: Aging time: 449 days



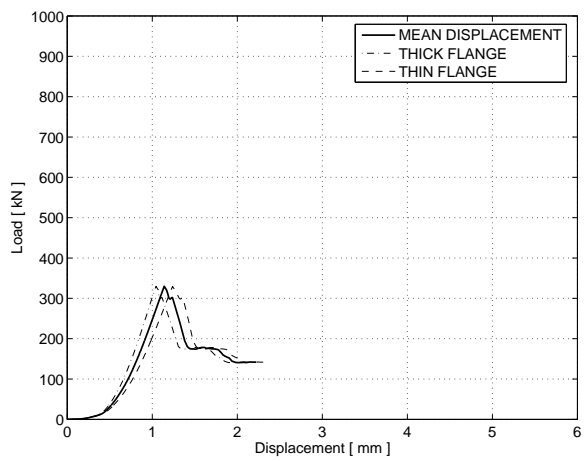
(a) 20°C



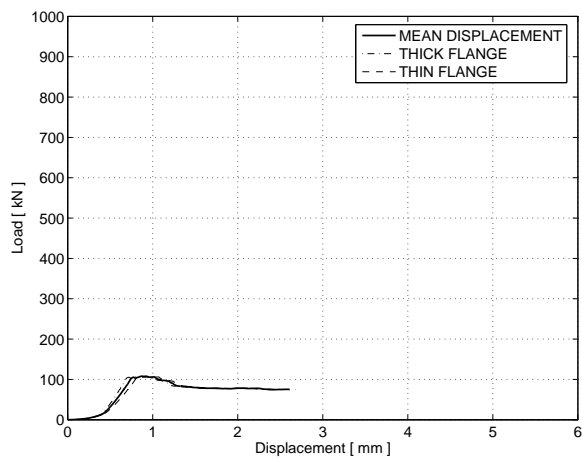
(a) 20°C



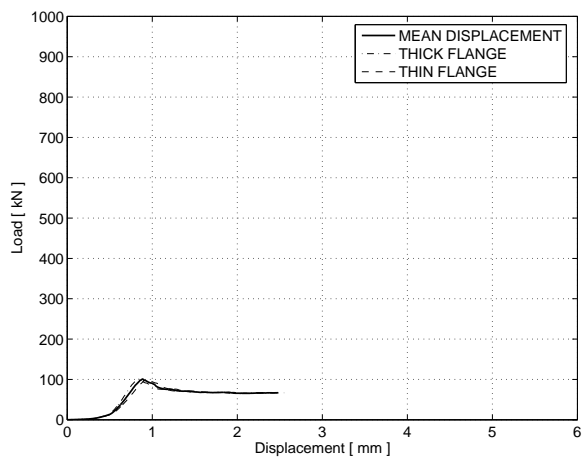
(b) 40°C



(b) 40°C



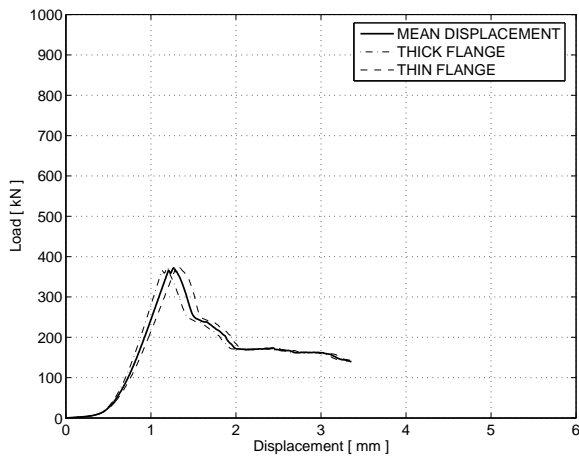
(c) 60°C



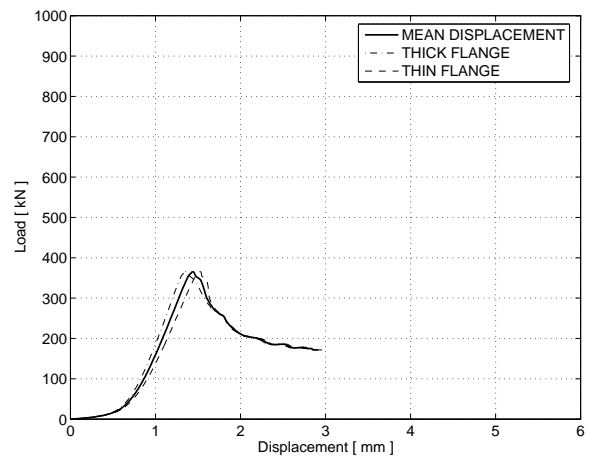
(c) 60°C

Figure B.54: Aging time: 493 days

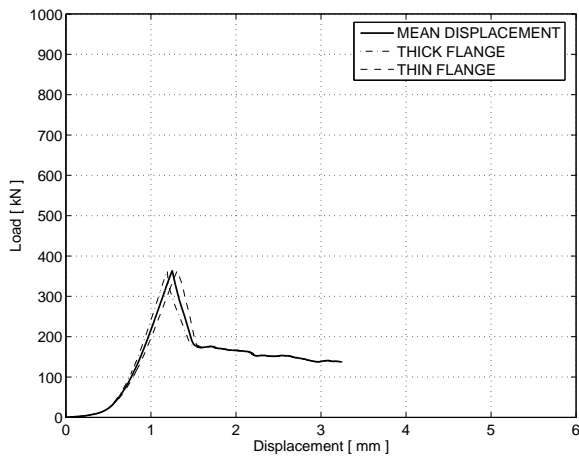
Figure B.55: Aging time: 493 days



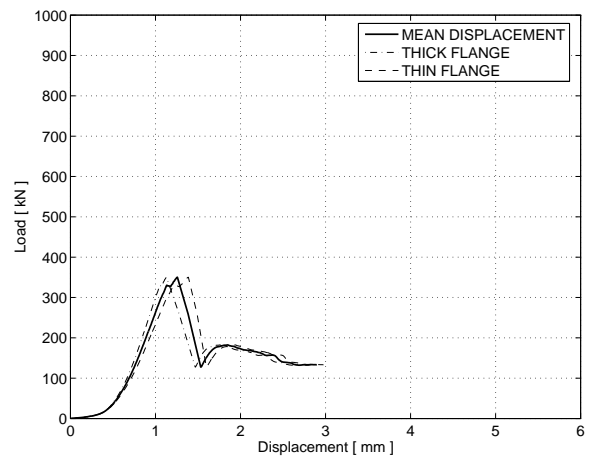
(a) 20°C



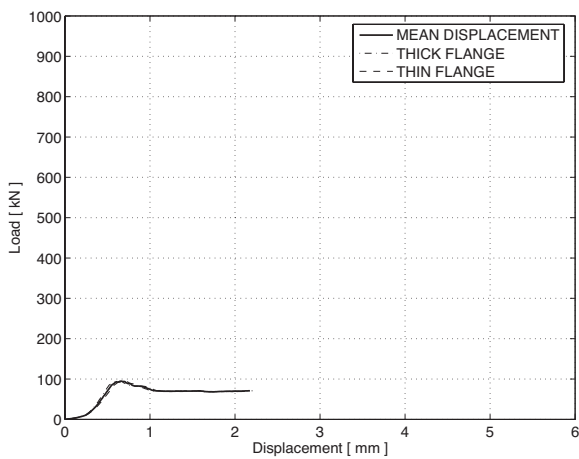
(a) 20°C



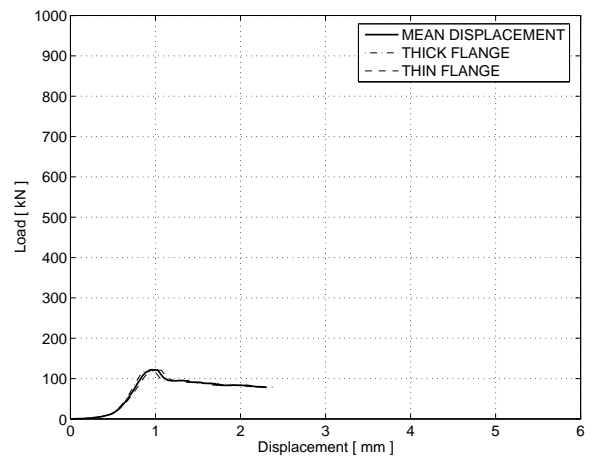
(b) 40°C



(b) 40°C



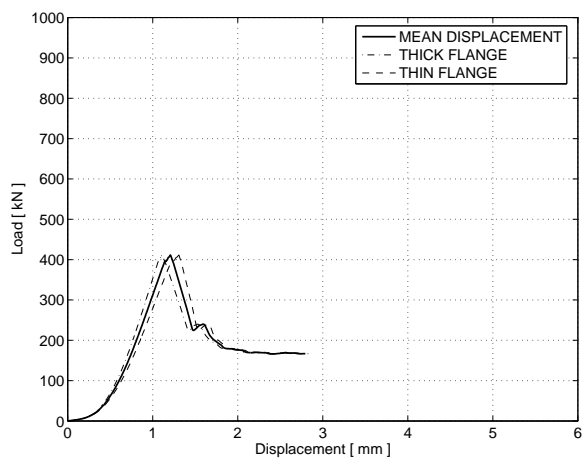
(c) 60°C



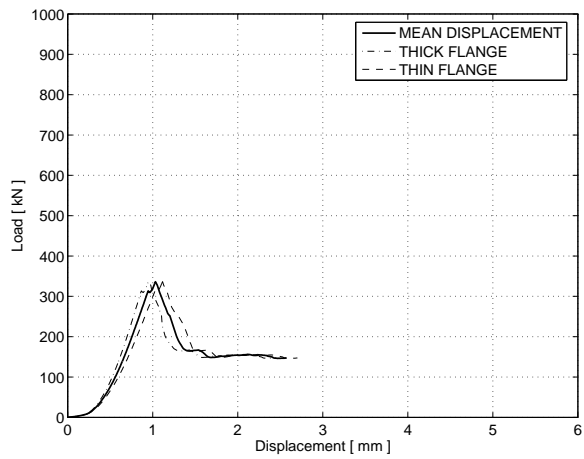
(c) 60°C

Figure B.56: Aging time: 548 days

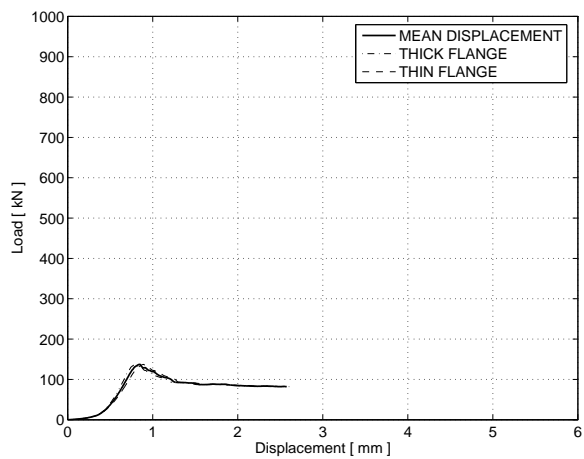
Figure B.57: Aging time: 548 days



(a) 20°C

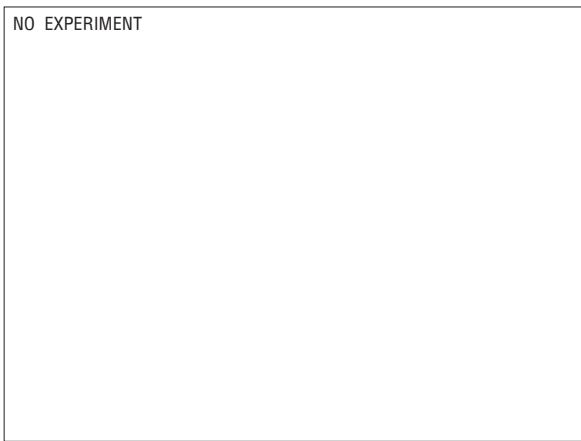


(b) 40°C

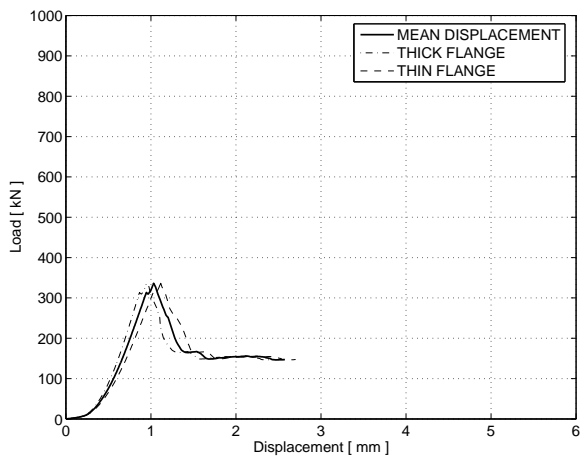


(c) 60°C

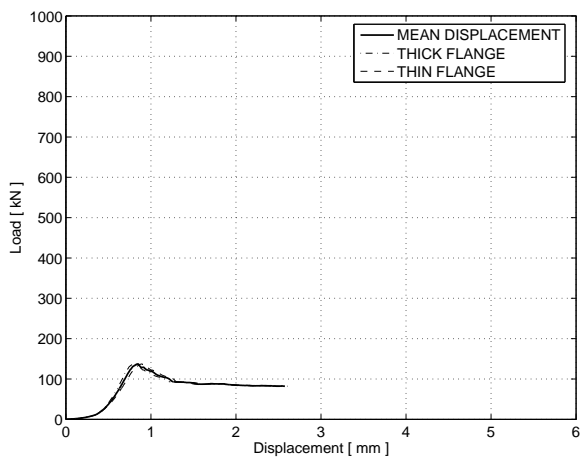
Figure B.58: Aging time: 548 days



(a) 20°C



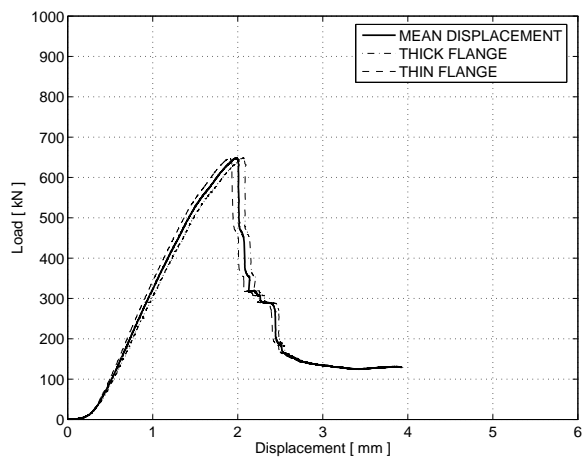
(b) 40°C



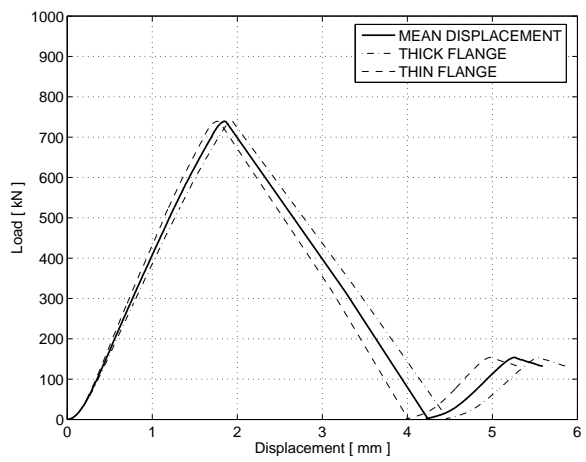
(c) 60°C

Figure B.59: Aging time: 548 days

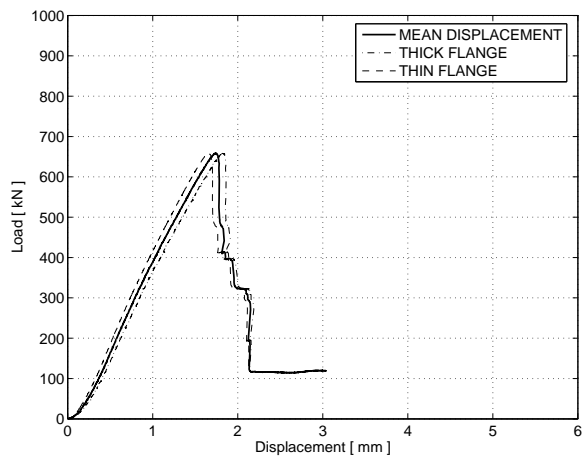
Capped elements



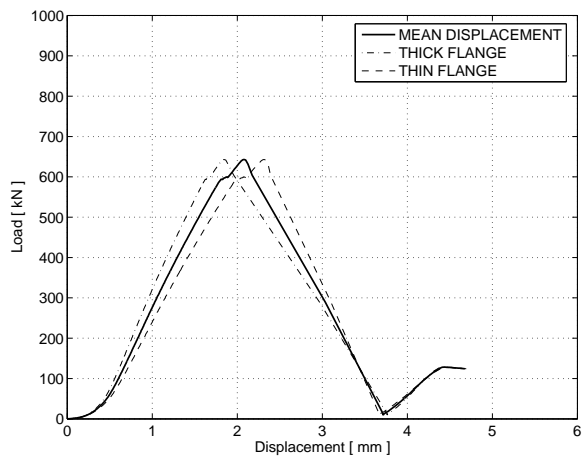
(a) 20°C



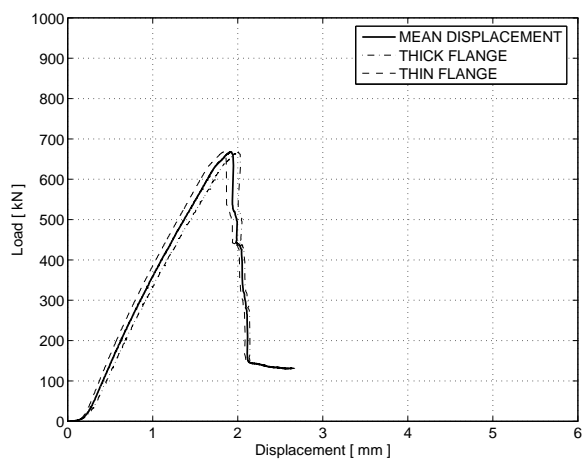
(a) 20°C



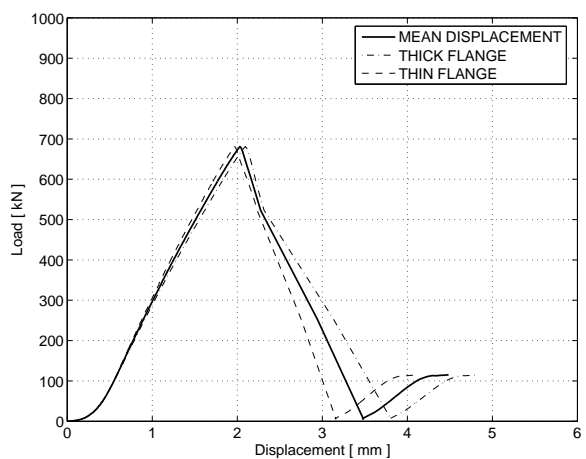
(b) 40°C



(b) 40°C



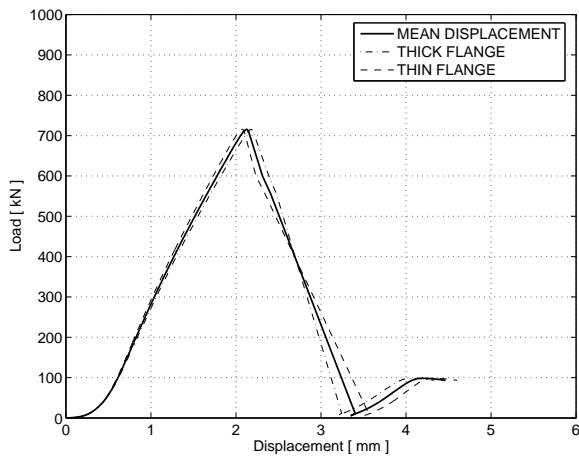
(c) 60°C



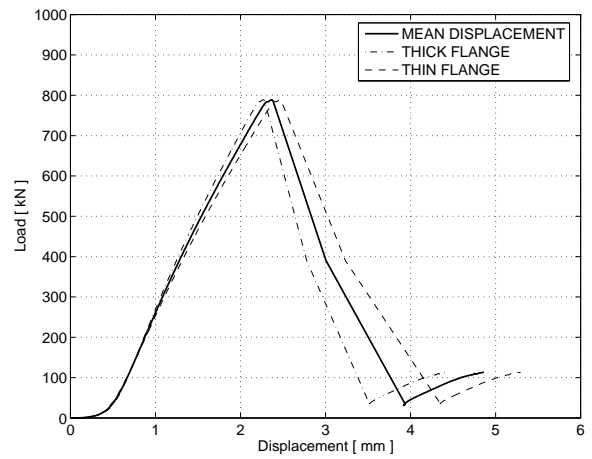
(c) 60°C

Figure B.60: Aging time: 5 days

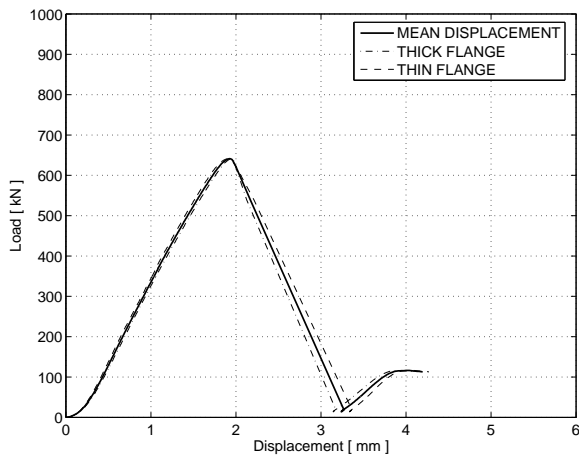
Figure B.61: Aging time: 6 days



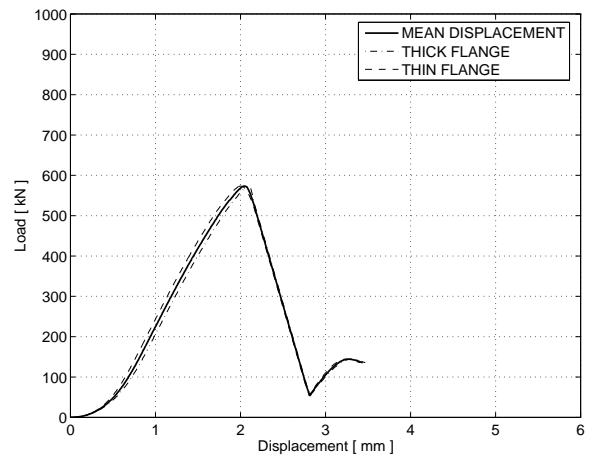
(a) 20°C



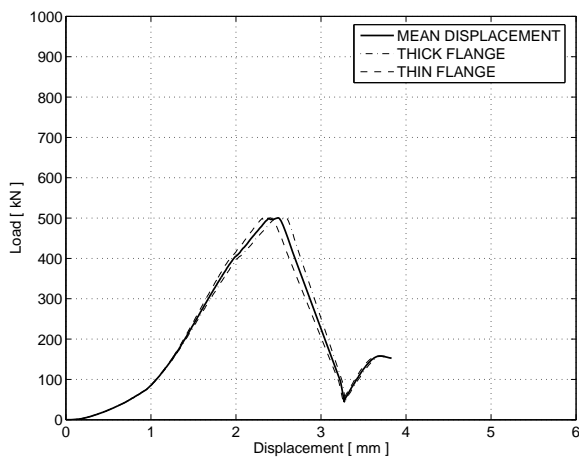
(a) 20°C



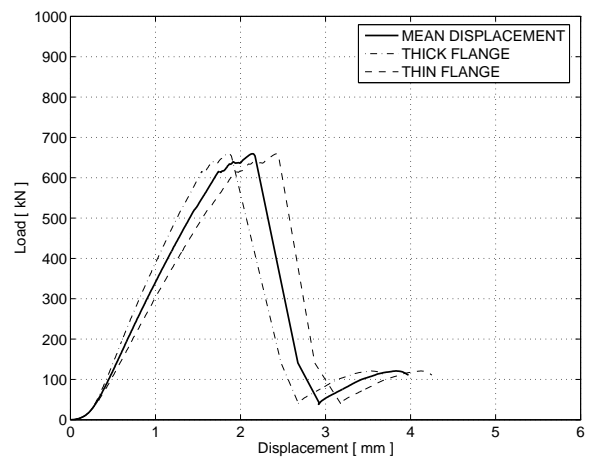
(b) 40°C



(b) 40°C



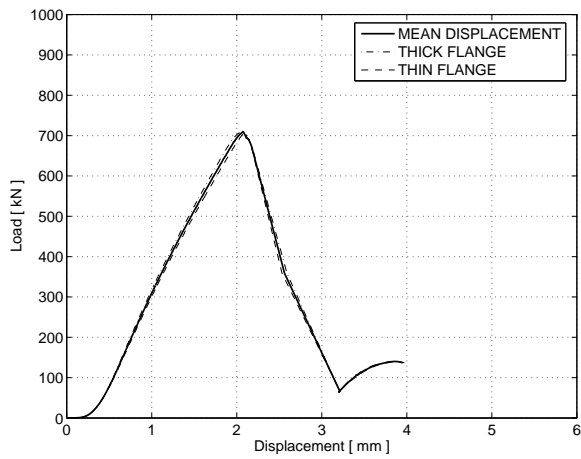
(c) 60°C



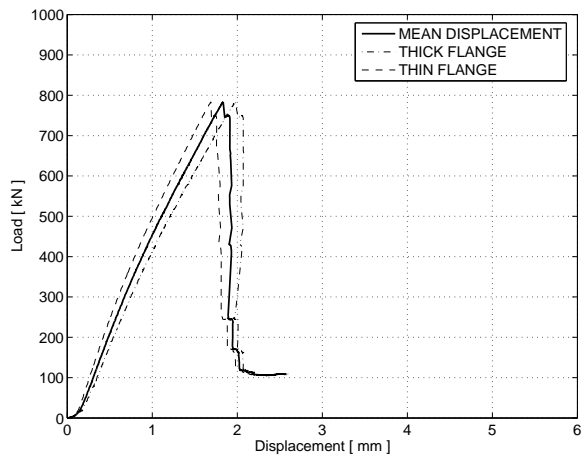
(c) 60°C

Figure B.62: Aging time: 6 days

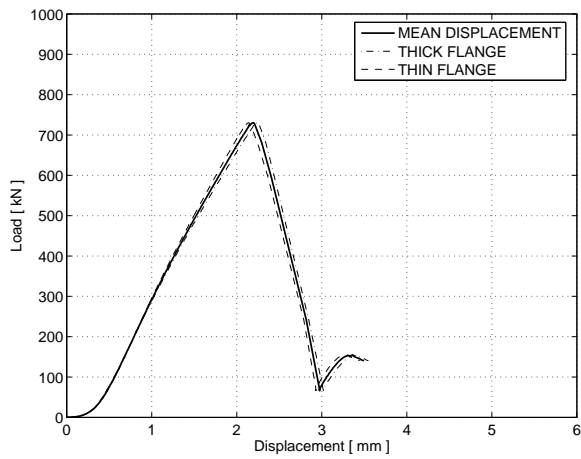
Figure B.63: Aging time: 8 days



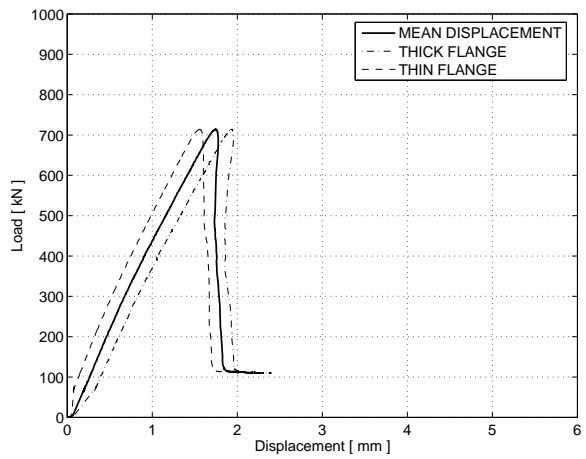
(a) 20°C



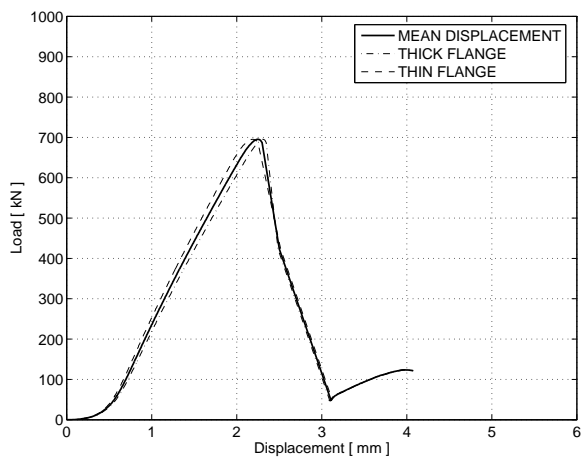
(a) 20°C



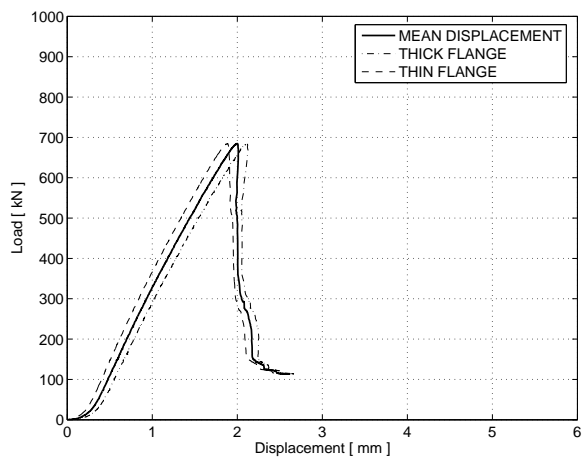
(b) 40°C



(b) 40°C



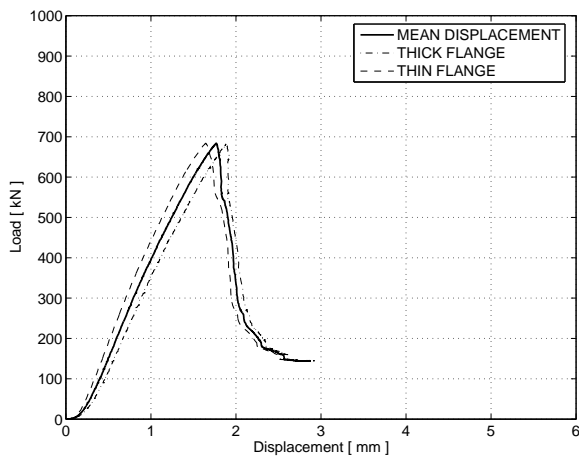
(c) 60°C



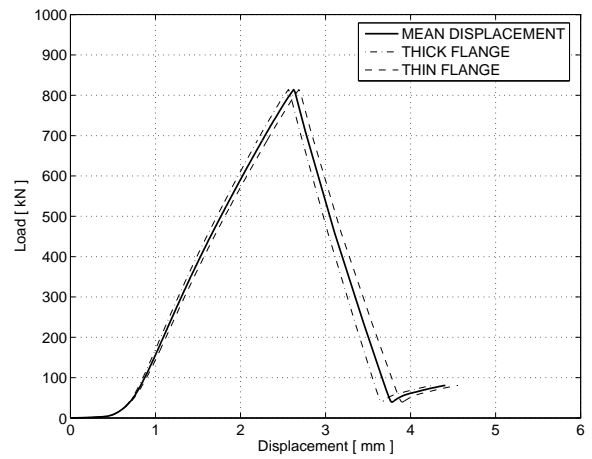
(c) 60°C

Figure B.64: Aging time: 8 days

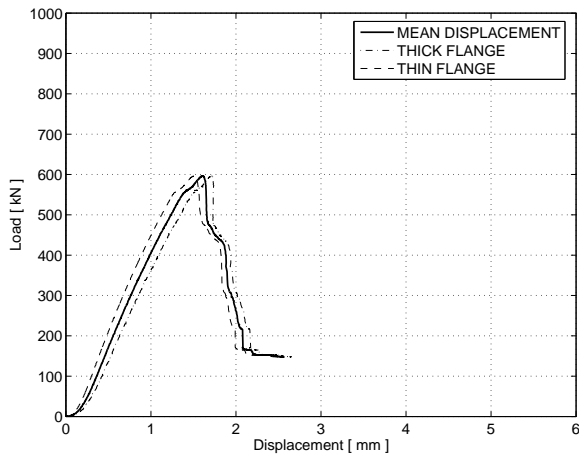
Figure B.65: Aging time: 9 days



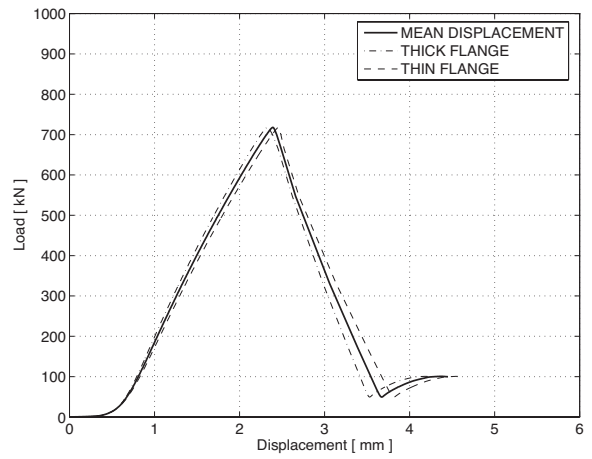
(a) 20°C



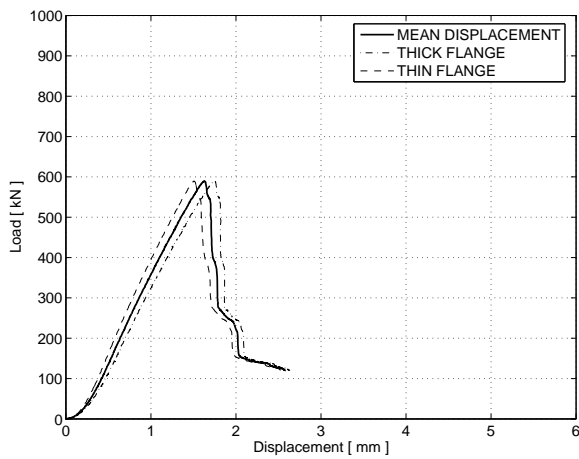
(a) 20°C



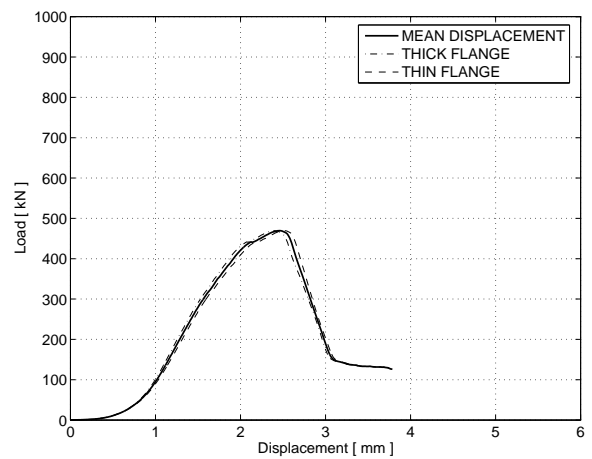
(b) 40°C



(b) 40°C



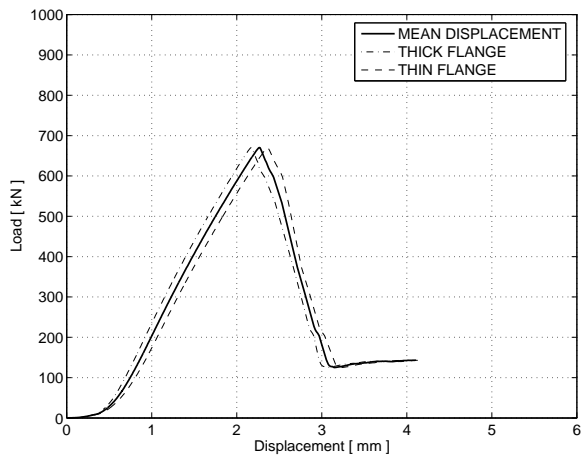
(c) 60°C



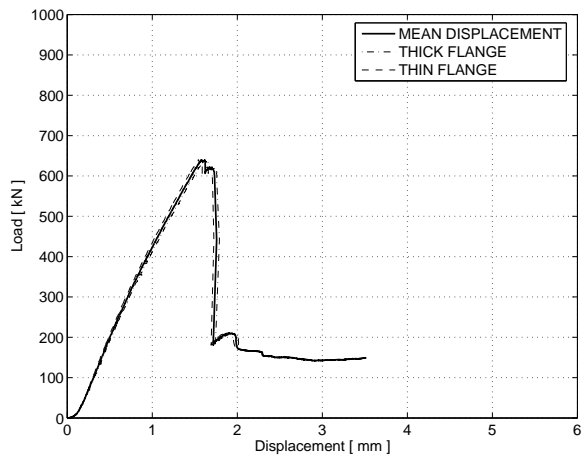
(c) 60°C

Figure B.66: Aging time: 15 days

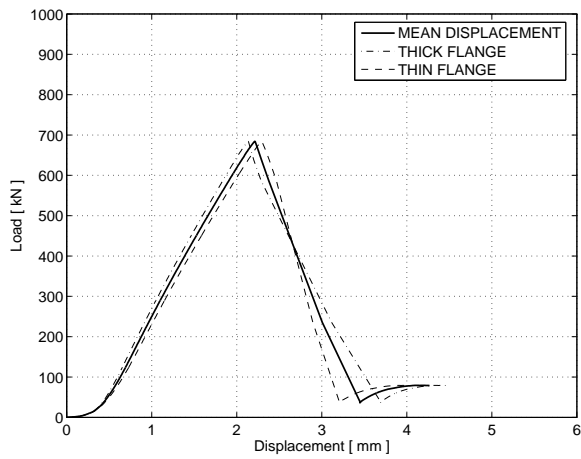
Figure B.67: Aging time: 18 days



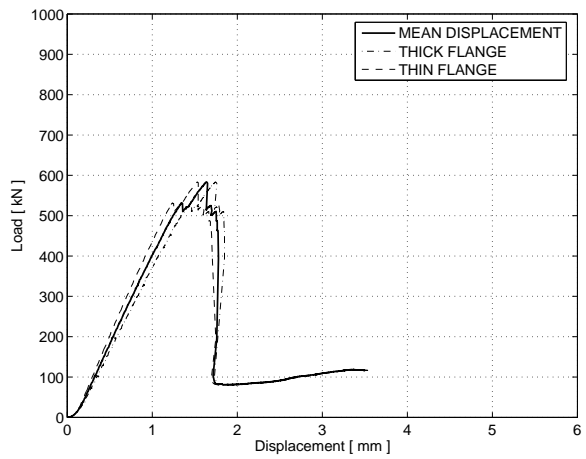
(a) 20°C



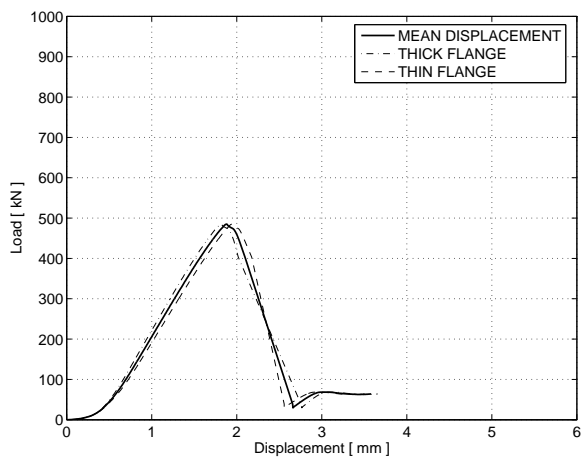
(a) 20°C



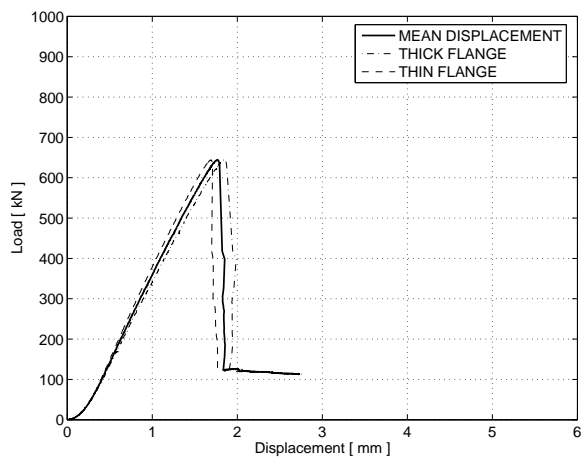
(b) 40°C



(b) 40°C



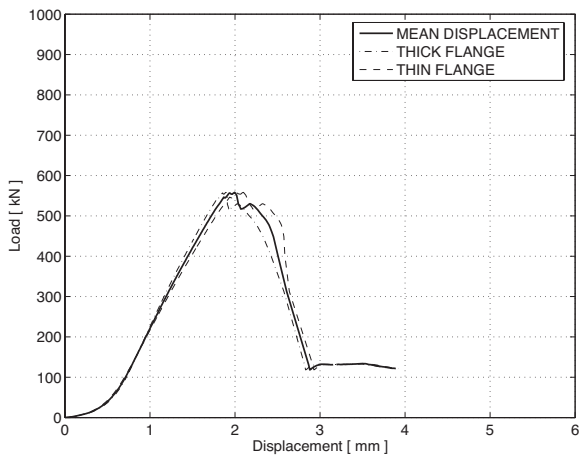
(c) 60°C



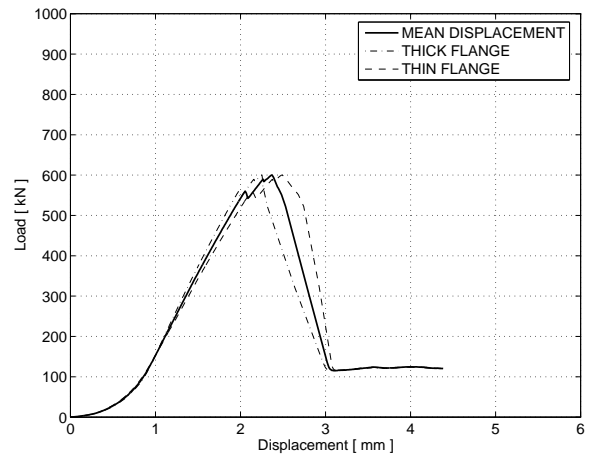
(c) 60°C

Figure B.68: Aging time: 20 days

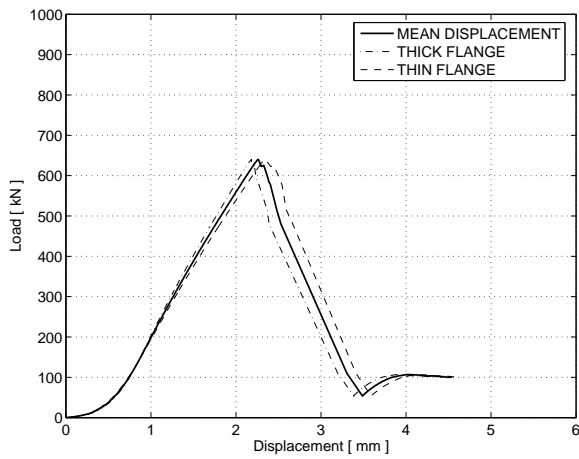
Figure B.69: Aging time: 30 days



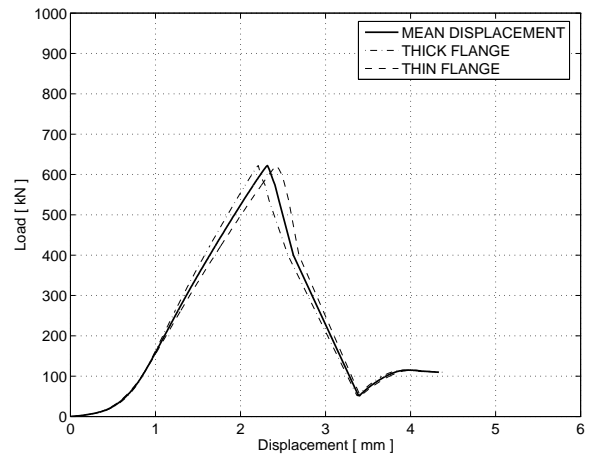
(a) 20°C



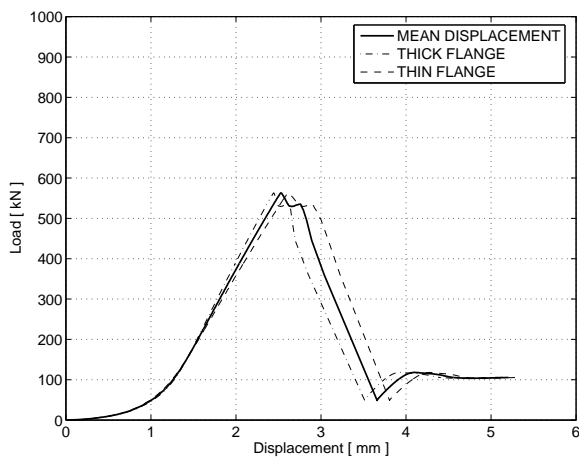
(a) 20°C



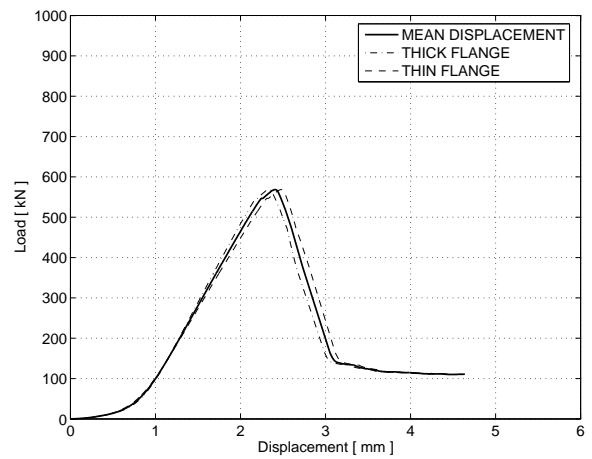
(b) 40°C



(b) 40°C



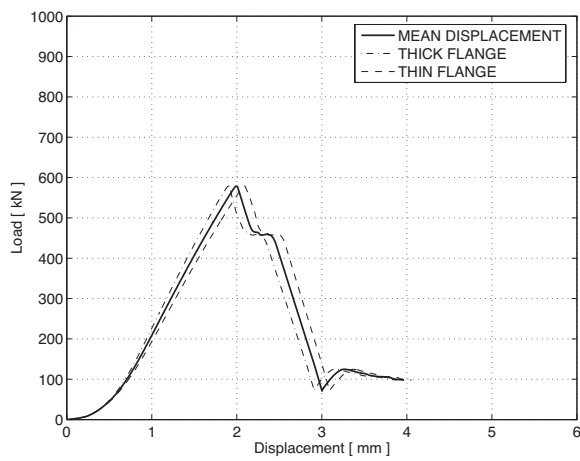
(c) 60°C



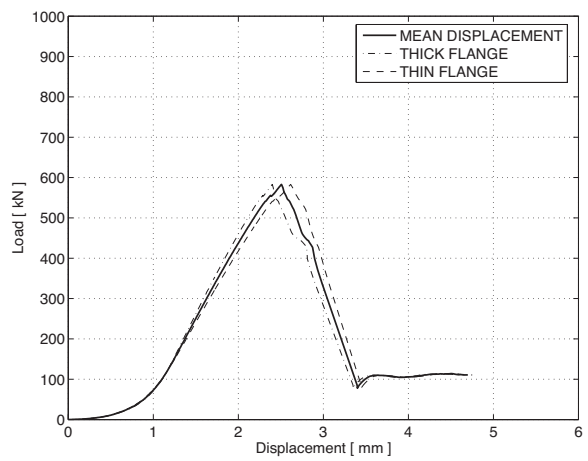
(c) 60°C

Figure B.70: Aging time: 41 days

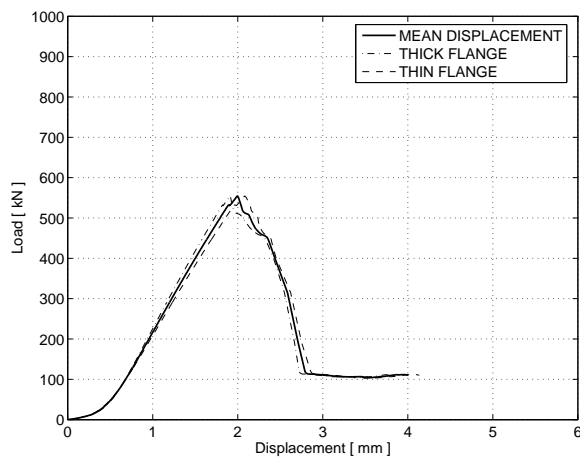
Figure B.71: Aging time: 41 days



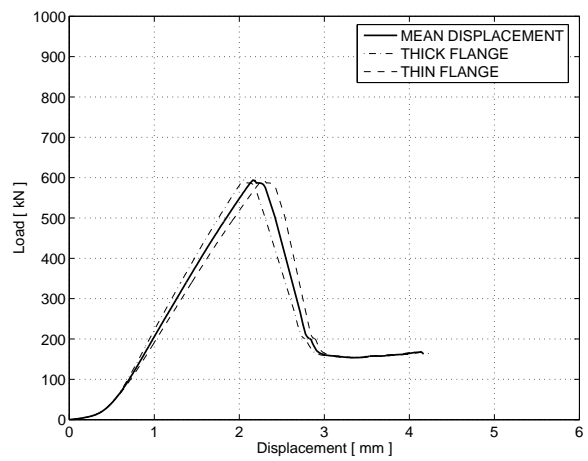
(a) 20°C



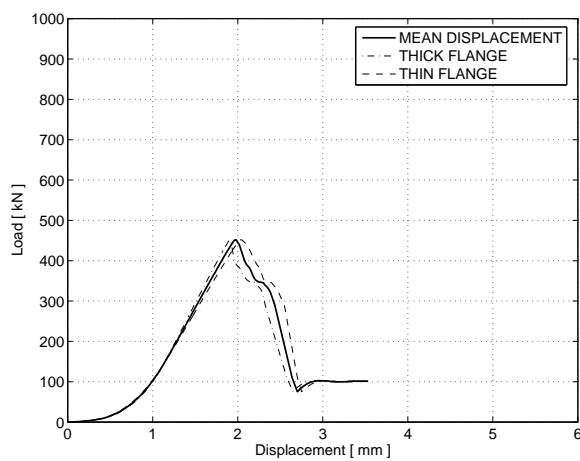
(a) 20°C



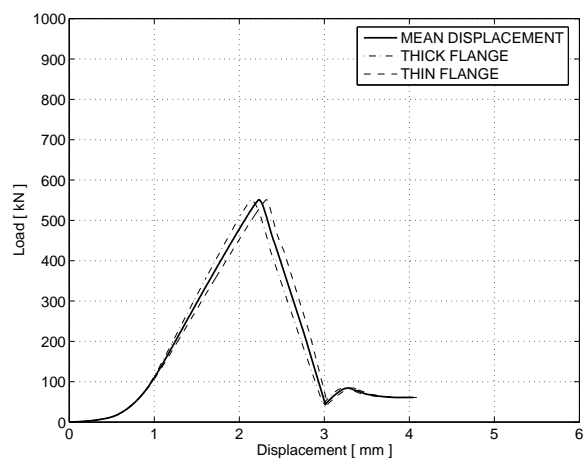
(b) 40°C



(b) 40°C



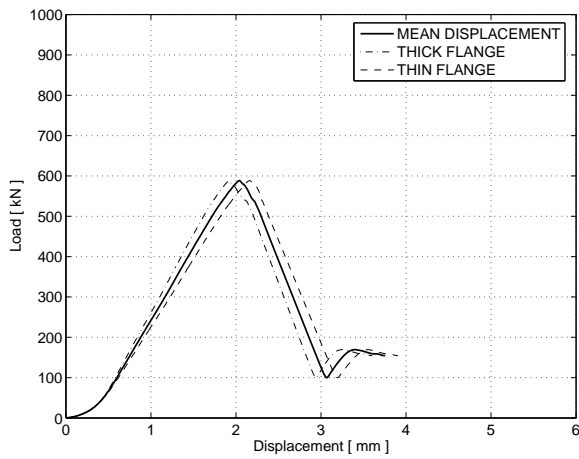
(c) 60°C



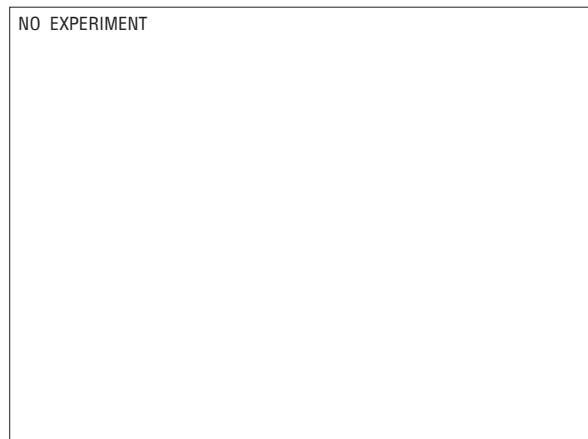
(c) 60°C

Figure B.72: Aging time: 55 days

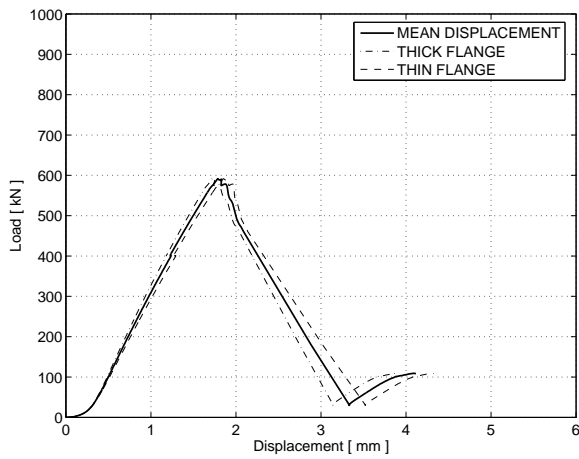
Figure B.73: Aging time: 55 days



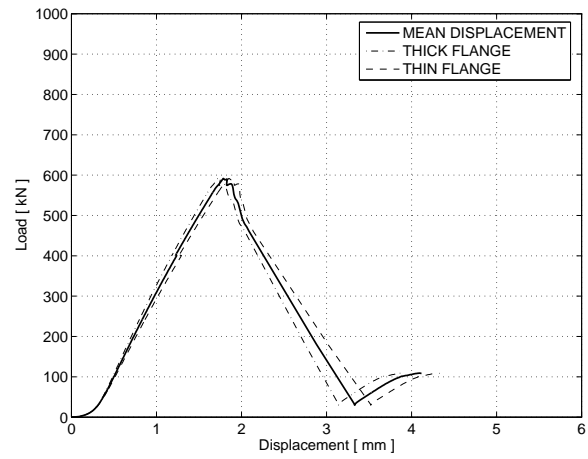
(a) 20°C



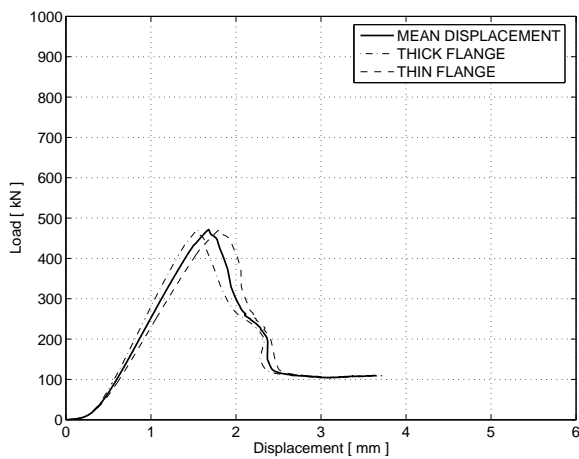
(a) 20°C



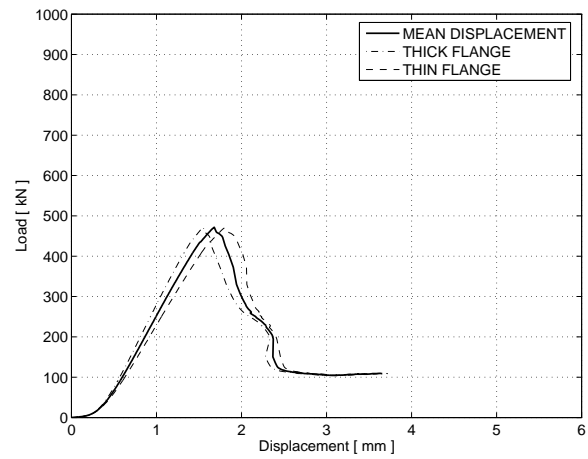
(b) 40°C



(b) 40°C



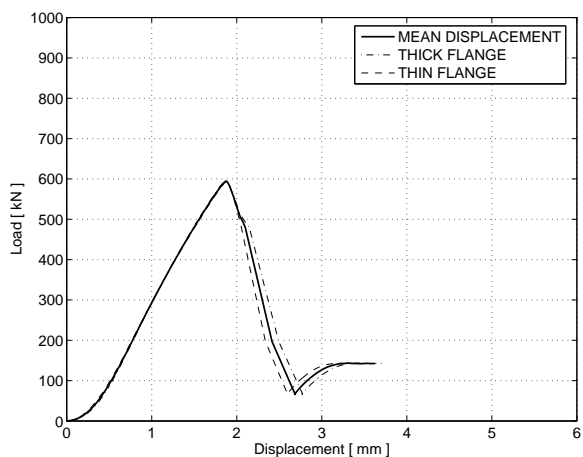
(c) 60°C



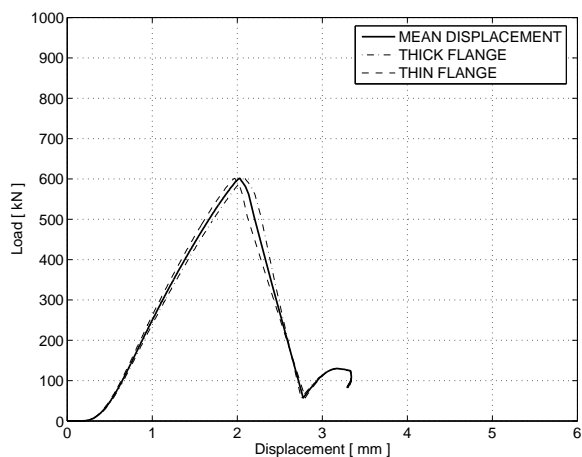
(c) 60°C

Figure B.74: Aging time: 60 days

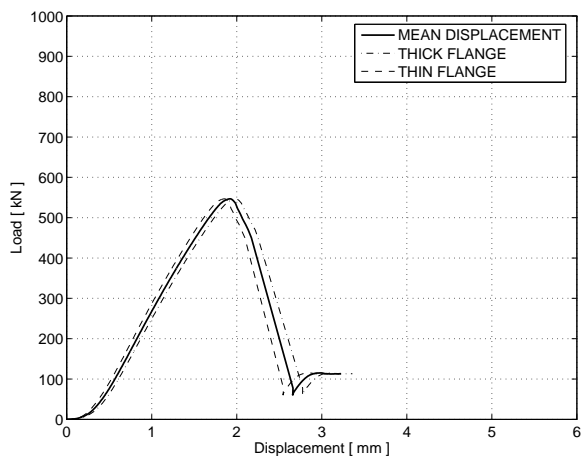
Figure B.75: Aging time: 60 days



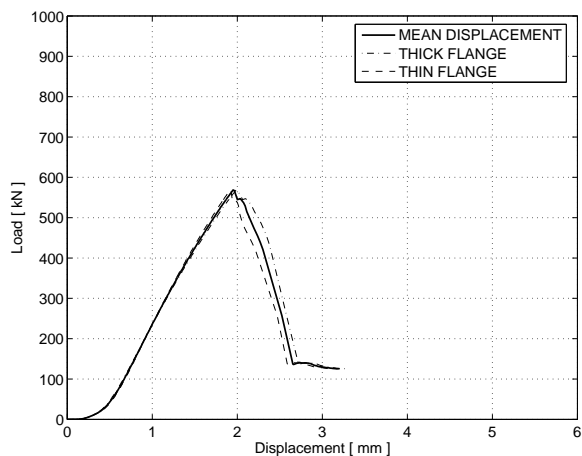
(a) 20°C



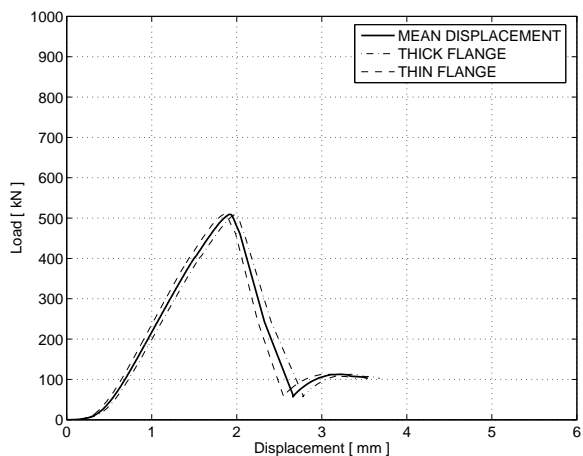
(a) 20°C



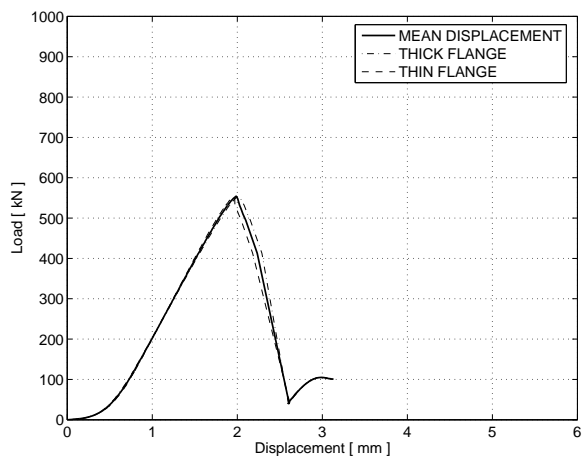
(b) 40°C



(b) 40°C



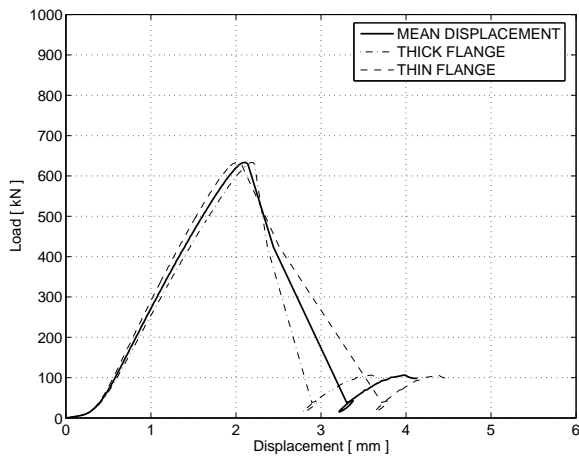
(c) 60°C



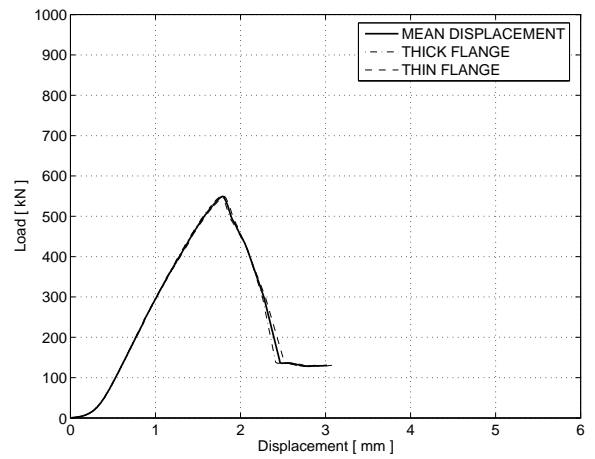
(c) 60°C

Figure B.76: Aging time: 66 days

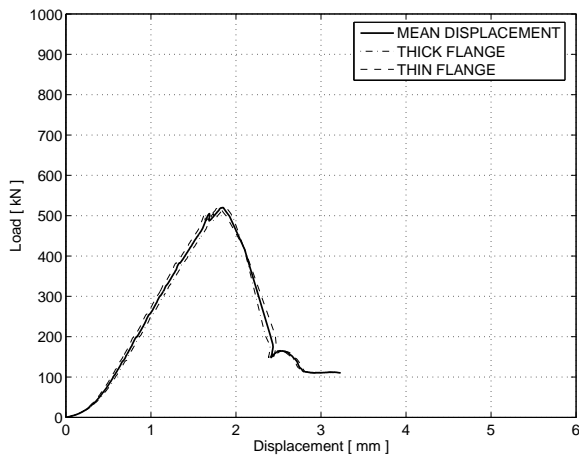
Figure B.77: Aging time: 86 days



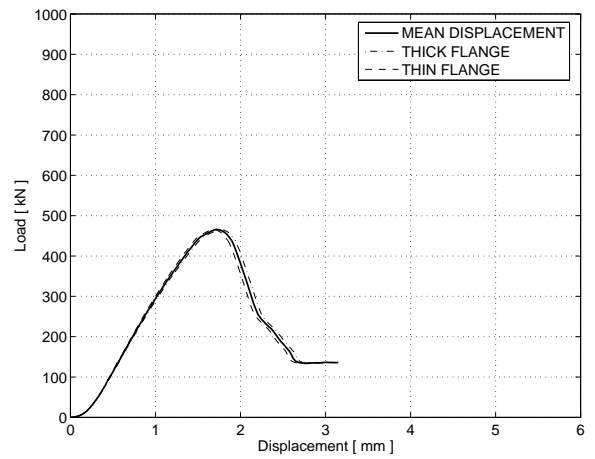
(a) 20°C



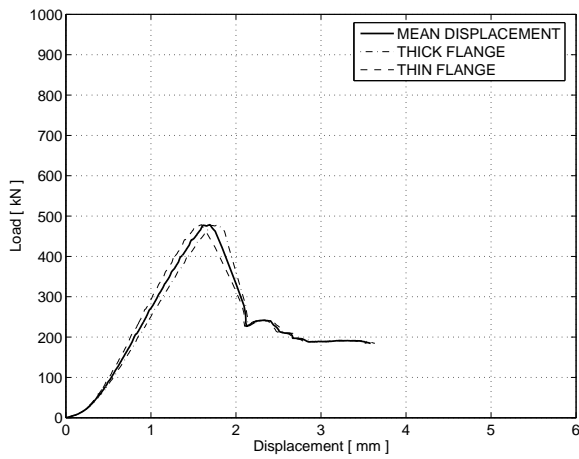
(a) 20°C



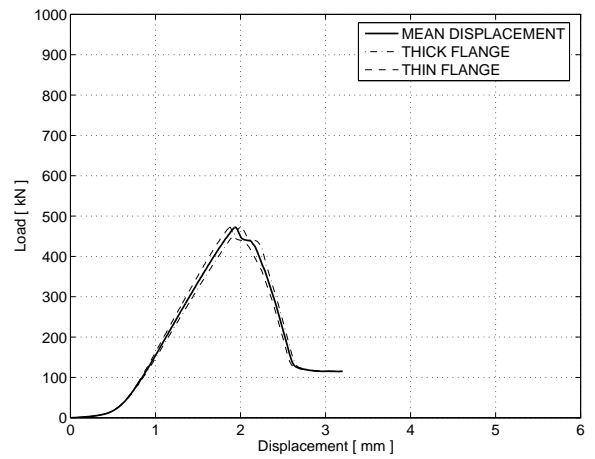
(b) 40°C



(b) 40°C



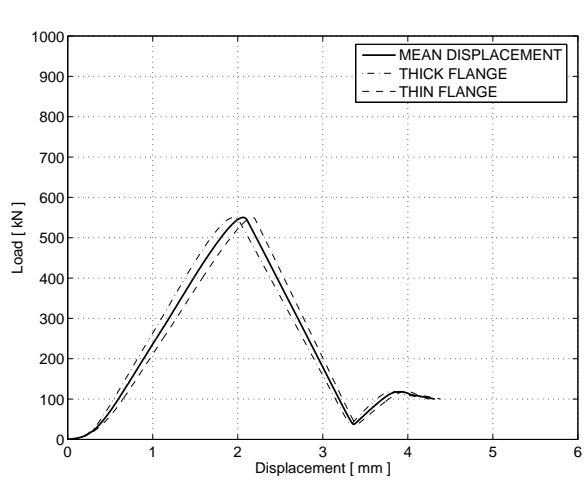
(c) 60°C



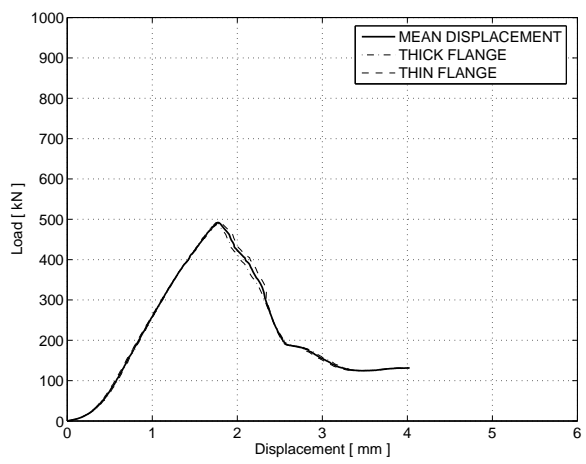
(c) 60°C

Figure B.78: Aging time: 92 days

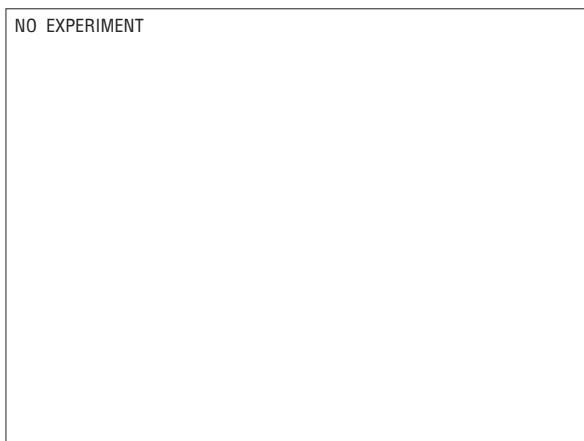
Figure B.79: Aging time: 115 days



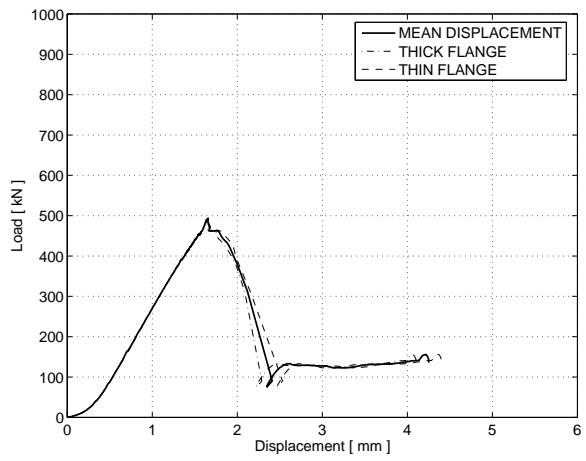
(a) 20°C



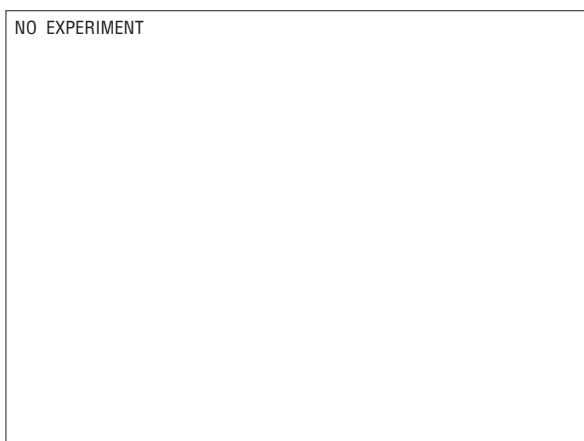
(a) 20°C



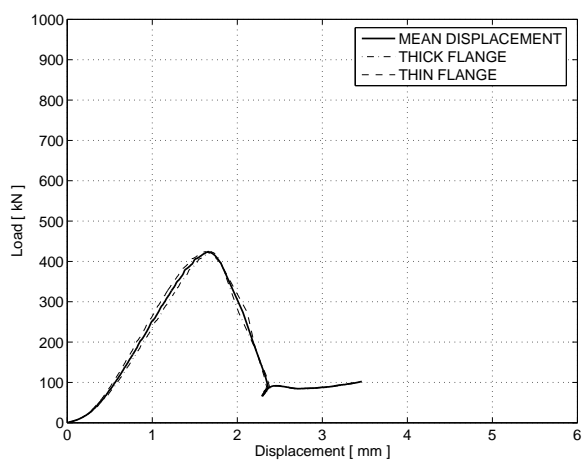
(b) 40°C



(b) 40°C



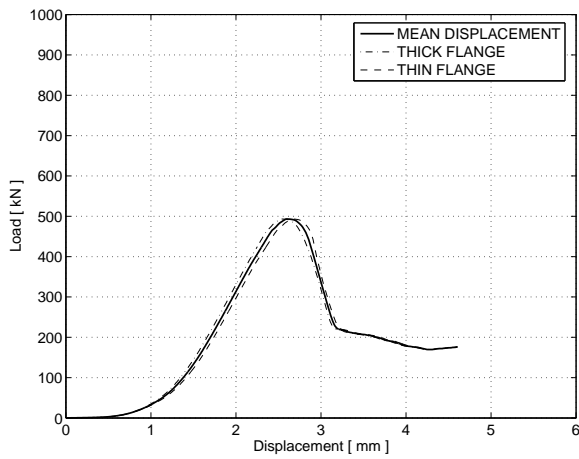
(c) 60°C



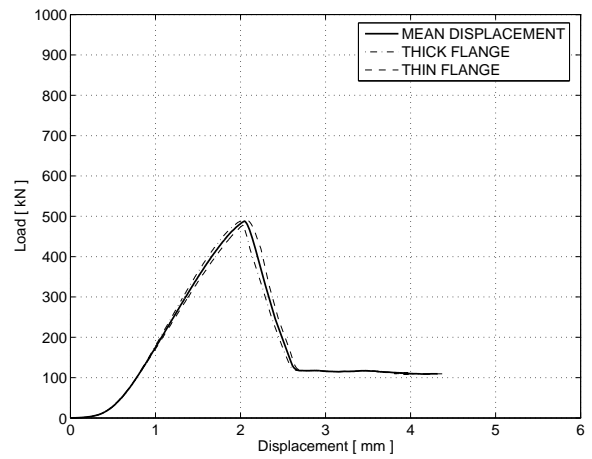
(c) 60°C

Figure B.80: Aging time: 122 days

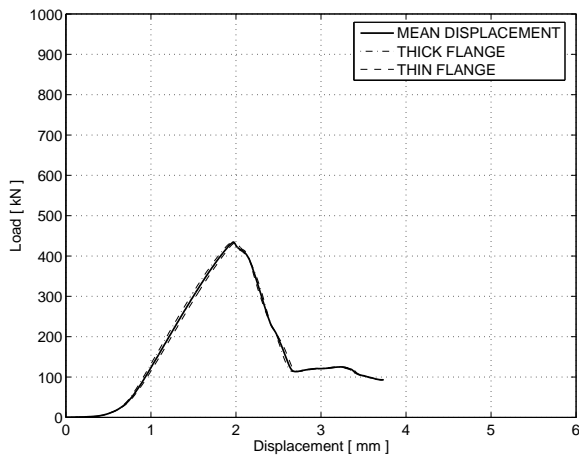
Figure B.81: Aging time: 158 days



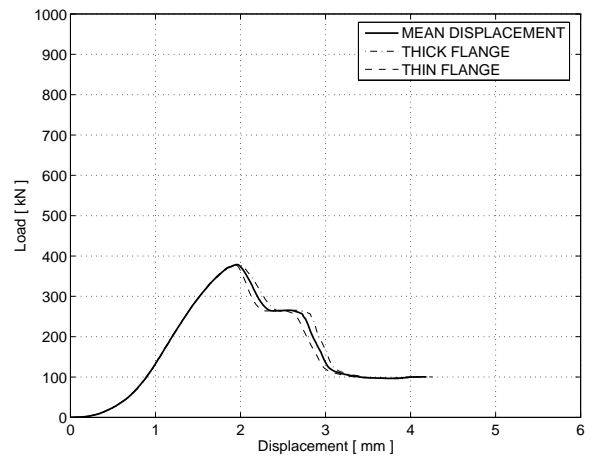
(a) 20°C



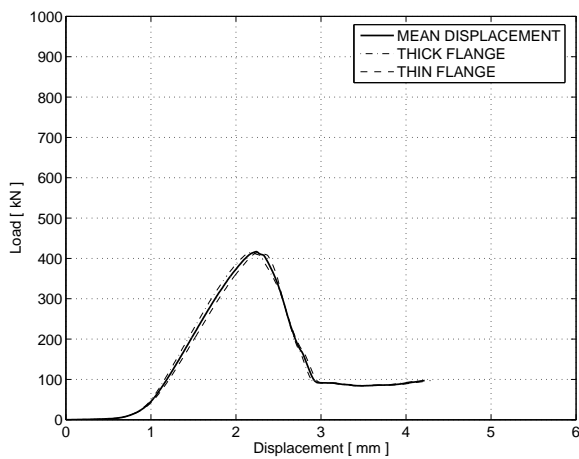
(a) 20°C



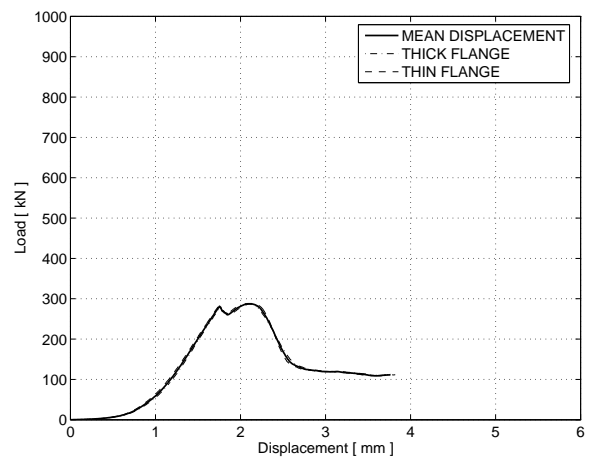
(b) 40°C



(b) 40°C



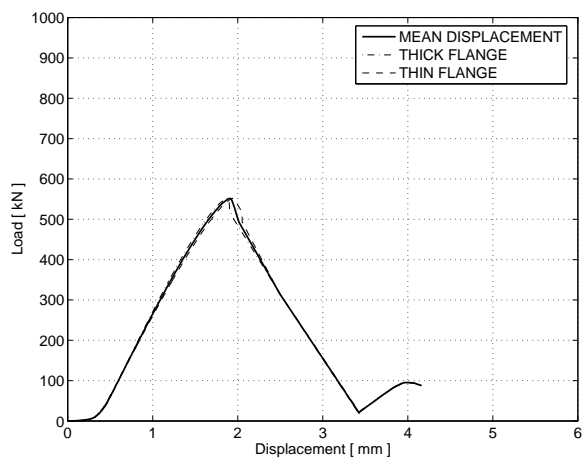
(c) 60°C



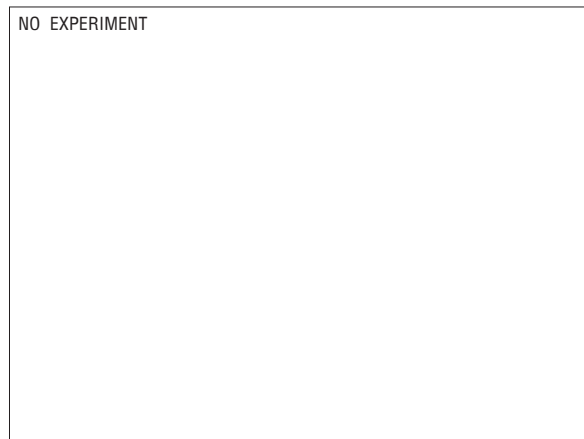
(c) 60°C

Figure B.82: Aging time: 175 days

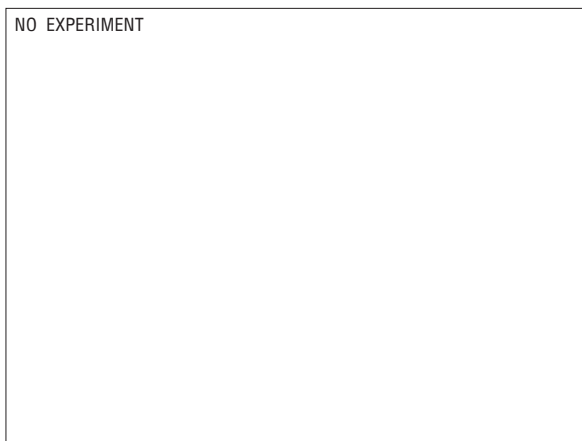
Figure B.83: Aging time: 199 days



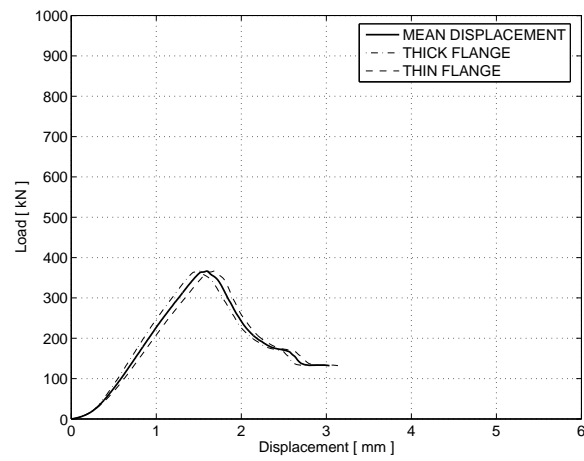
(a) 20°C



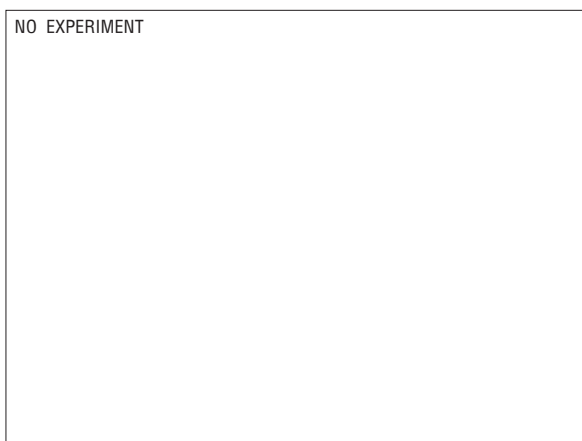
(a) 20°C



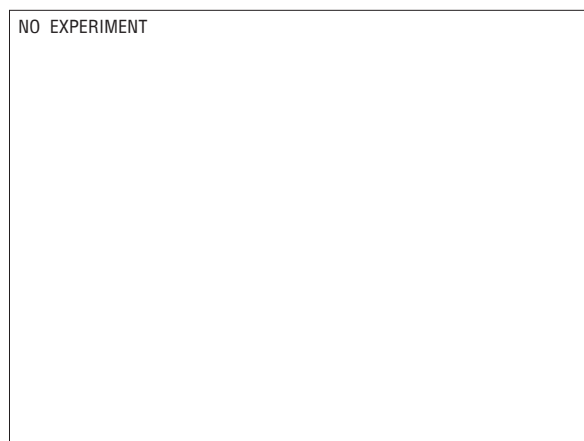
(b) 40°C



(b) 40°C



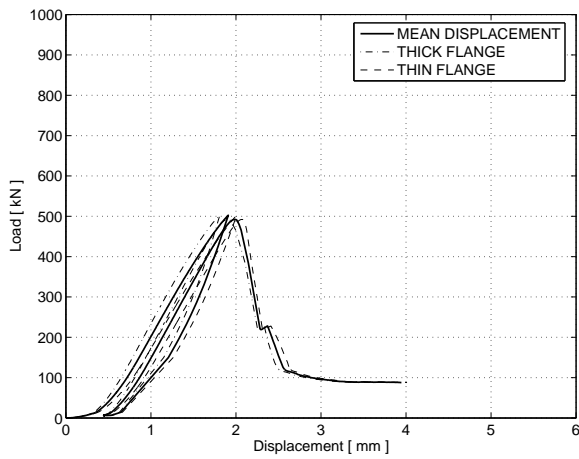
(c) 60°C



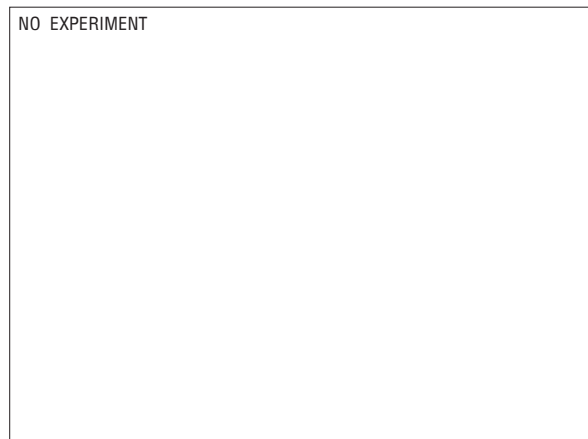
(c) 60°C

Figure B.84: Aging time: 236 days

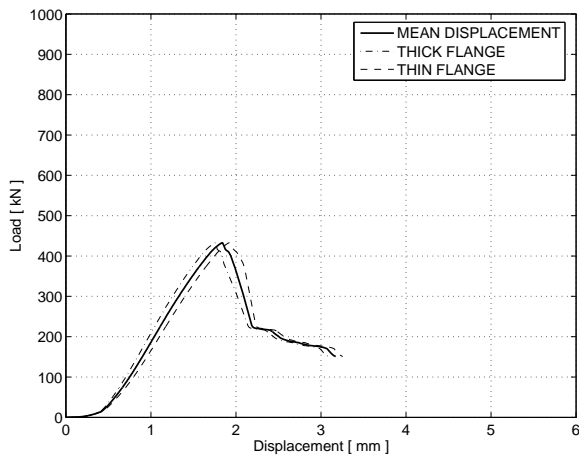
Figure B.85: Aging time: 295 days



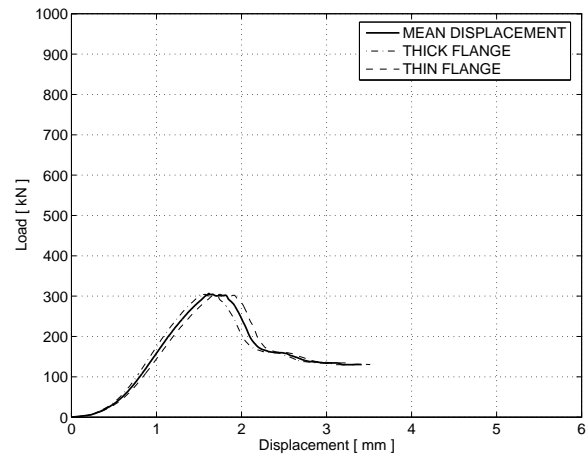
(a) 20°C



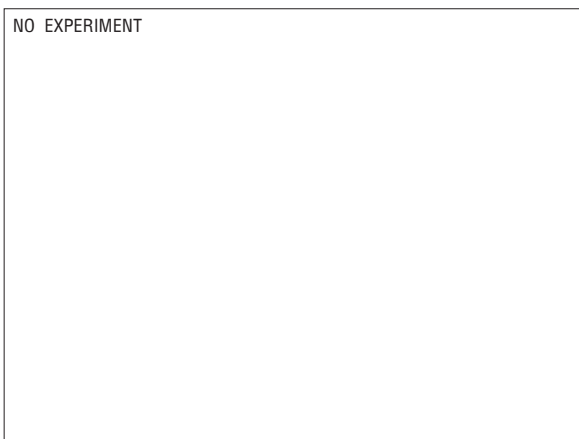
(a) 20°C



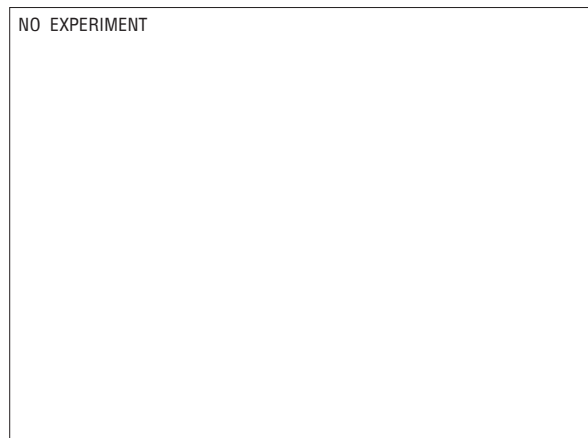
(b) 40°C



(b) 40°C



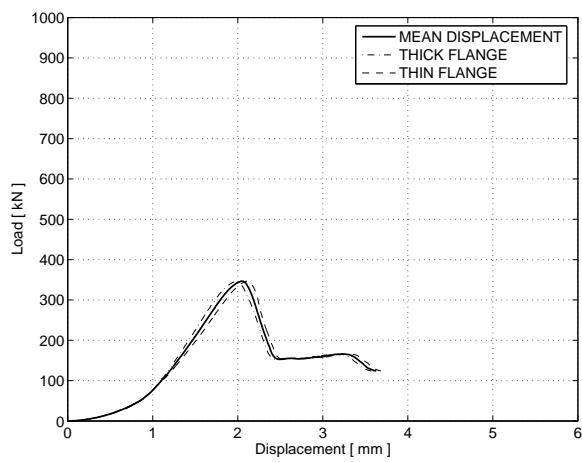
(c) 60°C



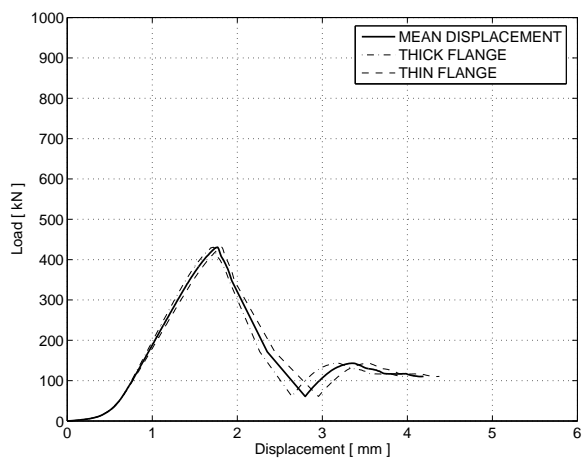
(c) 60°C

Figure B.86: Aging time: 340 days

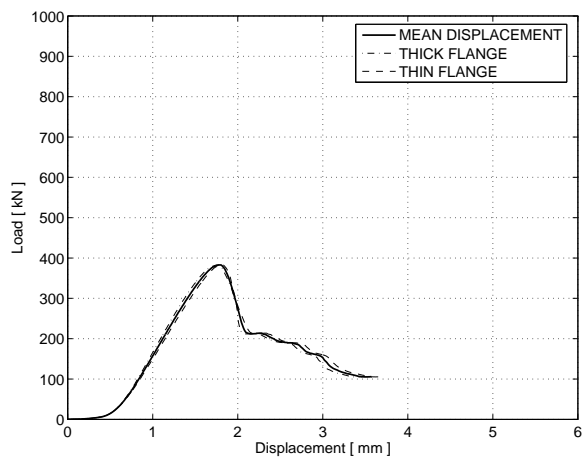
Figure B.87: Aging time: 395 days



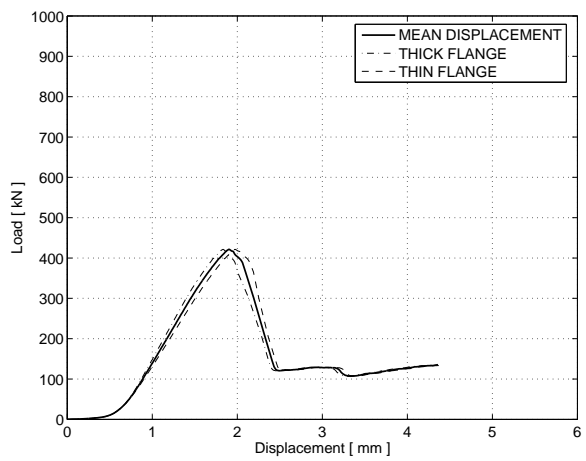
(a) 20°C



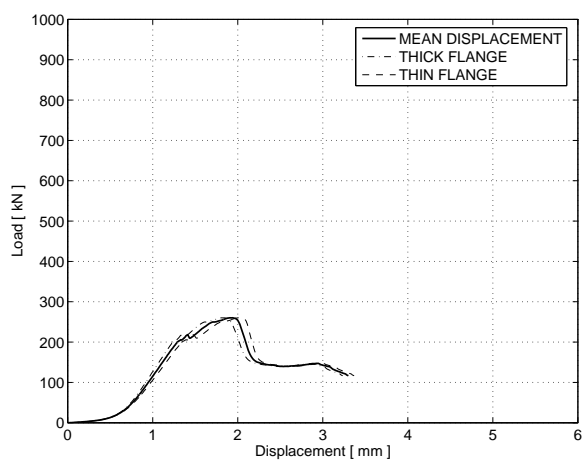
(a) 20°C



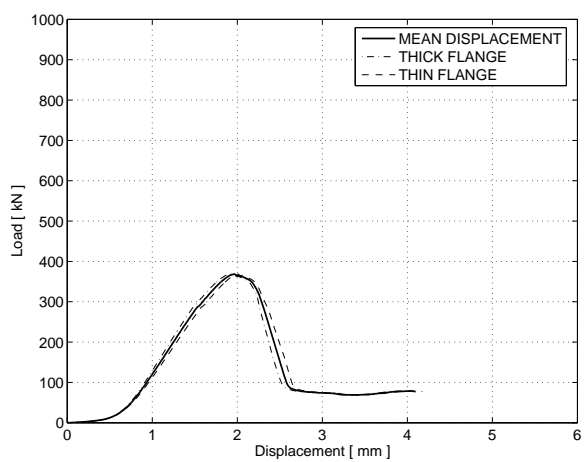
(b) 40°C



(b) 40°C



(c) 60°C



(c) 60°C

Figure B.88: Aging time: 430 days

Figure B.89: Aging time: 430 days

B.5. Failure Modes

B.5.1. Unconditioned elements



(a) Longitudinal crack on outer web

(b) Evenly distributed crushing on one end

Figure B.90: Uncapped element 01



(a) Severe asymmetric crushing

(b) Longitudinal fracture of outer web

Figure B.91: Uncapped element 02)

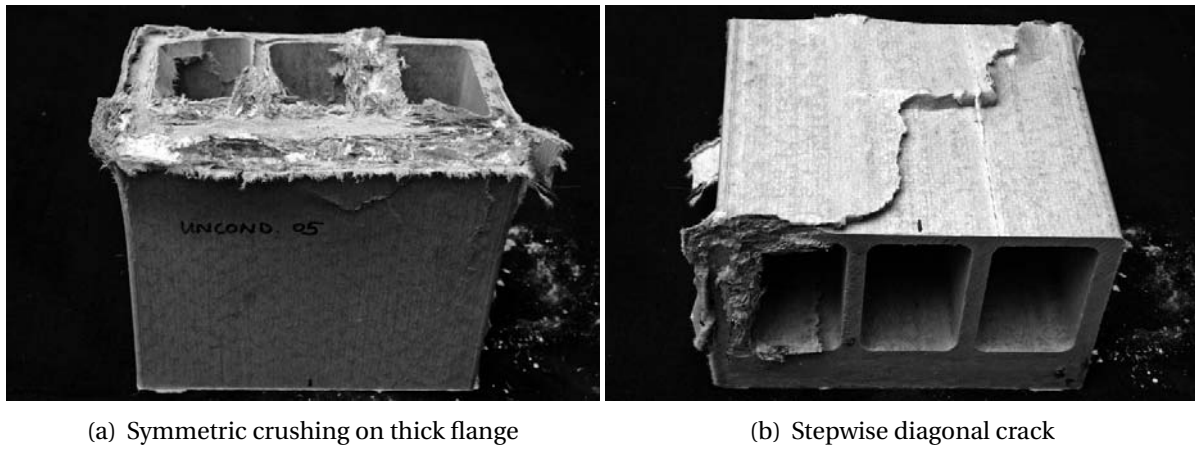


Figure B.92: Uncapped element 05

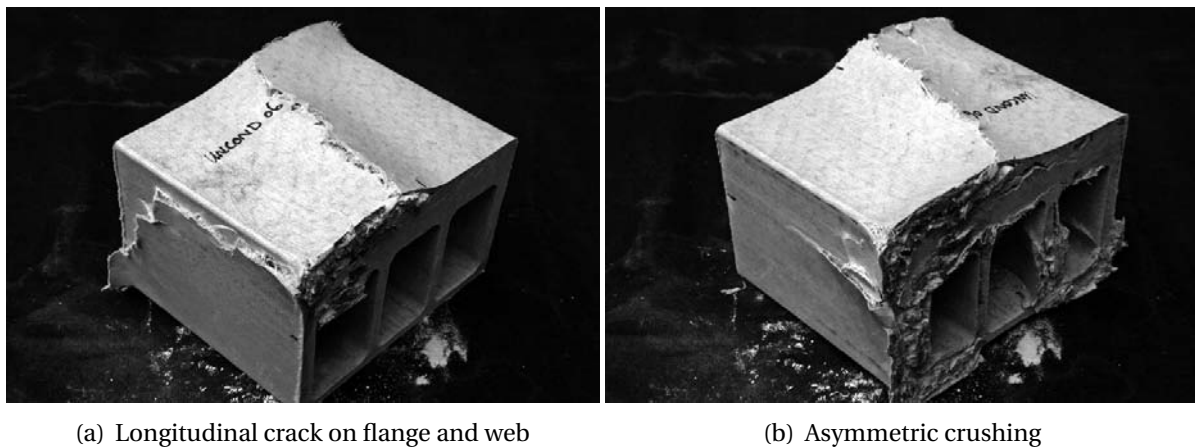


Figure B.93: Uncapped element 06

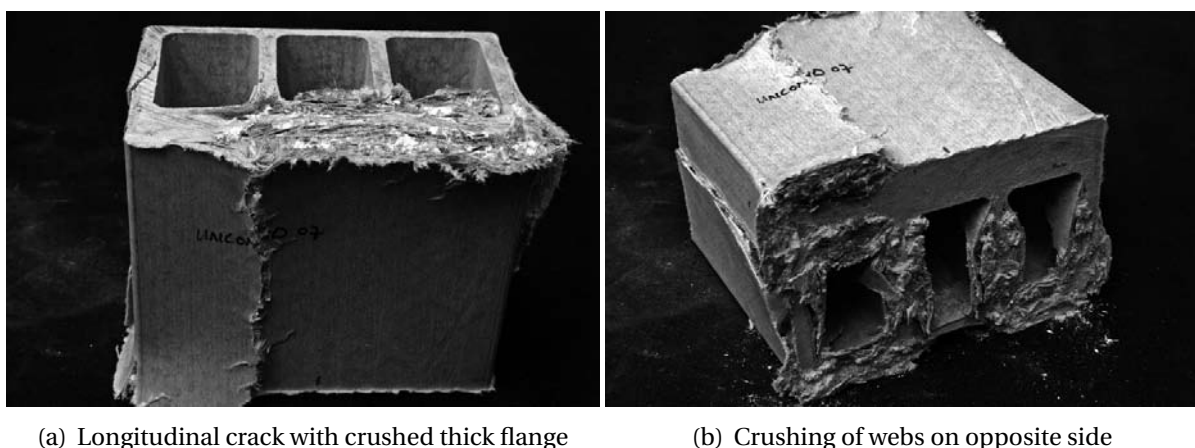
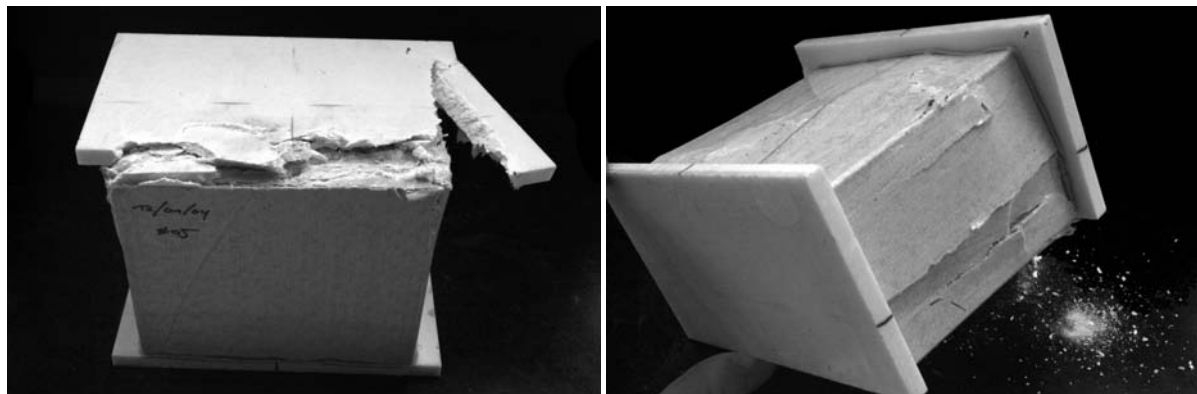


Figure B.94: Uncapped element 07



(a) Even crushing of profile end

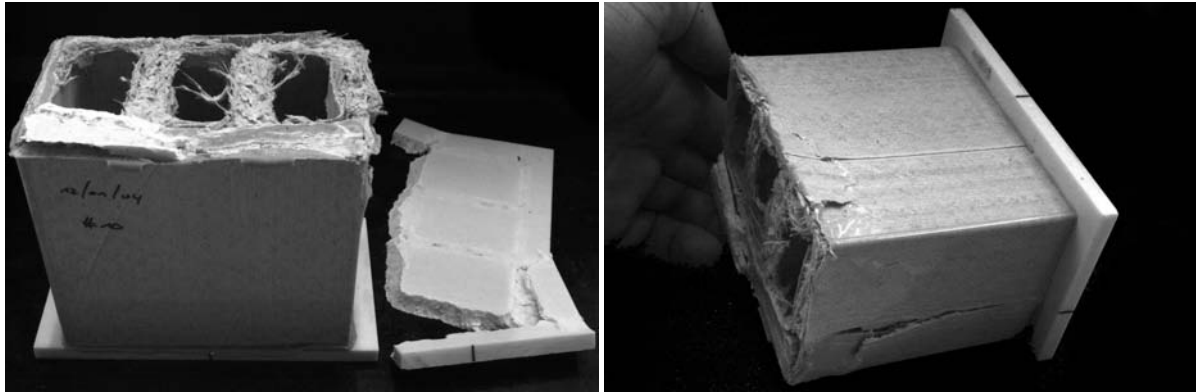
(b) Local wrinkling

Figure B.95: Capped 03

(a) Punching of cap-plate at upper side

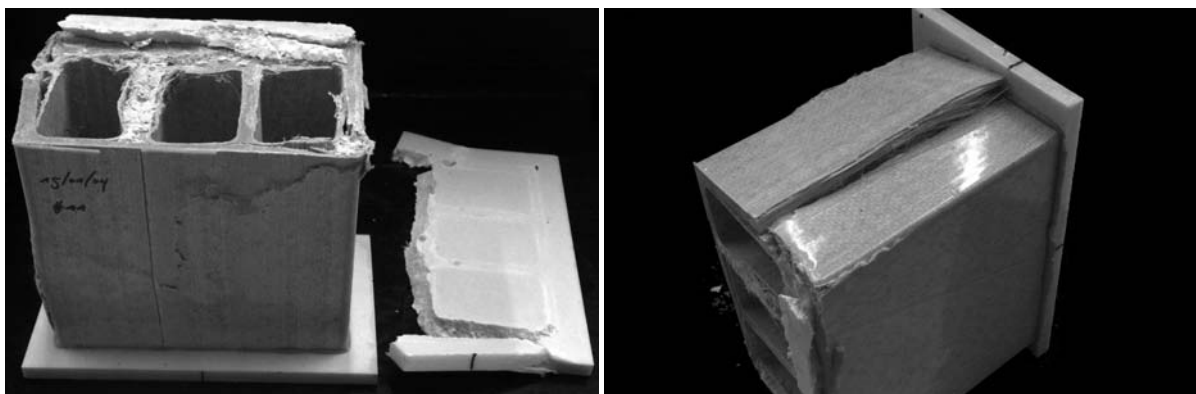
(b) Vertical cracks at junction outer webs/thick flange

Figure B.96: Capped 05



(a) Outward crushing at upper side and punched cap plate (b) Vertical cracks at at junction outer webs/thick flange

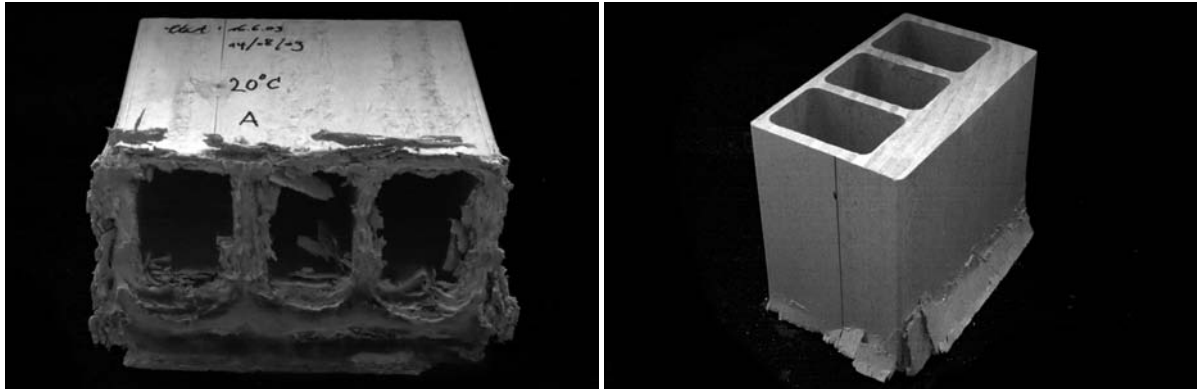
Figure B.97: Capped 10



(a) Local wrinkling and punched cap plate (b) Vertical crack on a lateral web

Figure B.98: Capped 11

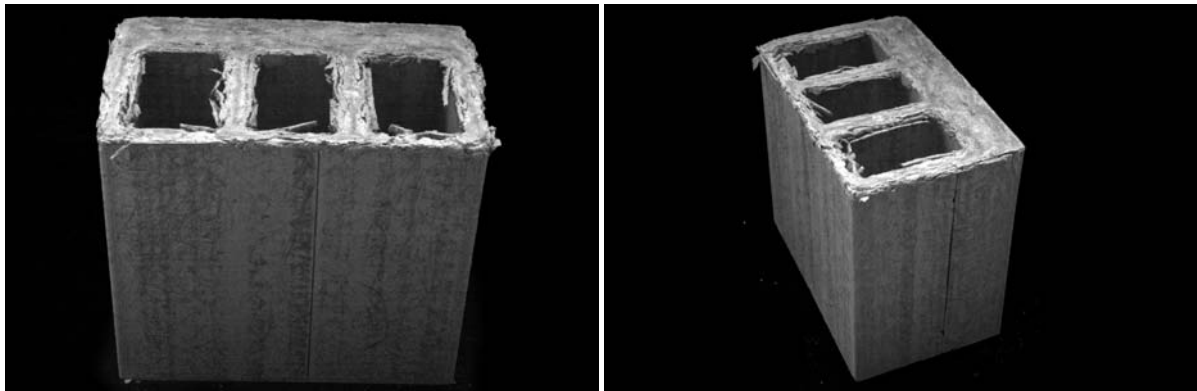
B.5.2. Conditioned elements



(a)

(b)

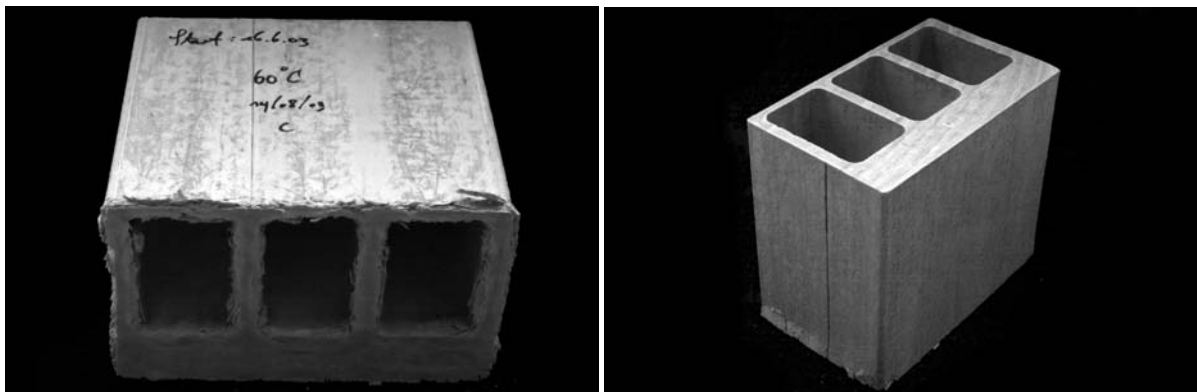
Figure B.99: Failure of uncapped element – 20°C, 59 days



(a)

(b)

Figure B.100: Failure of uncapped element – 40°C, 59 days



(a)

(b)

Figure B.101: Failure of uncapped element – 60°C, 59 days

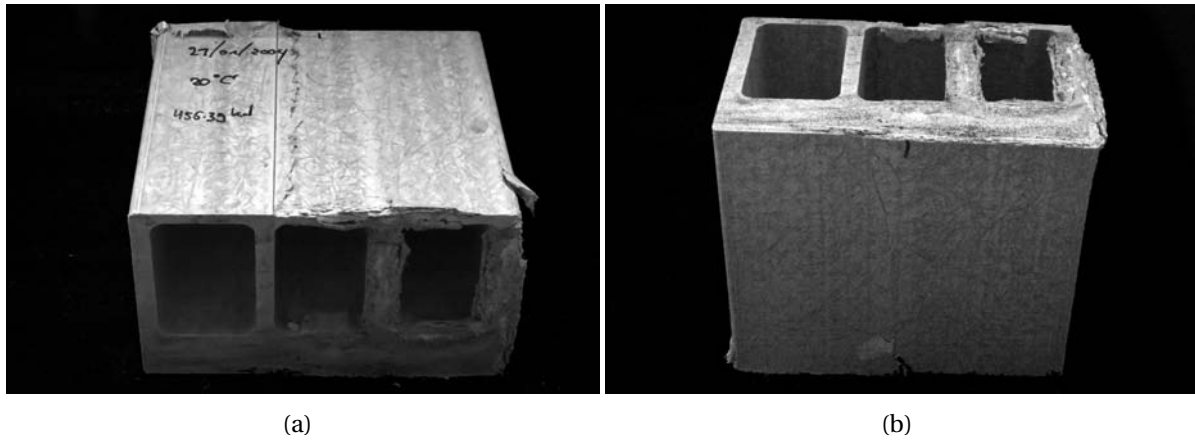


Figure B.102: Failure of uncapped element – 20°C, 219 days

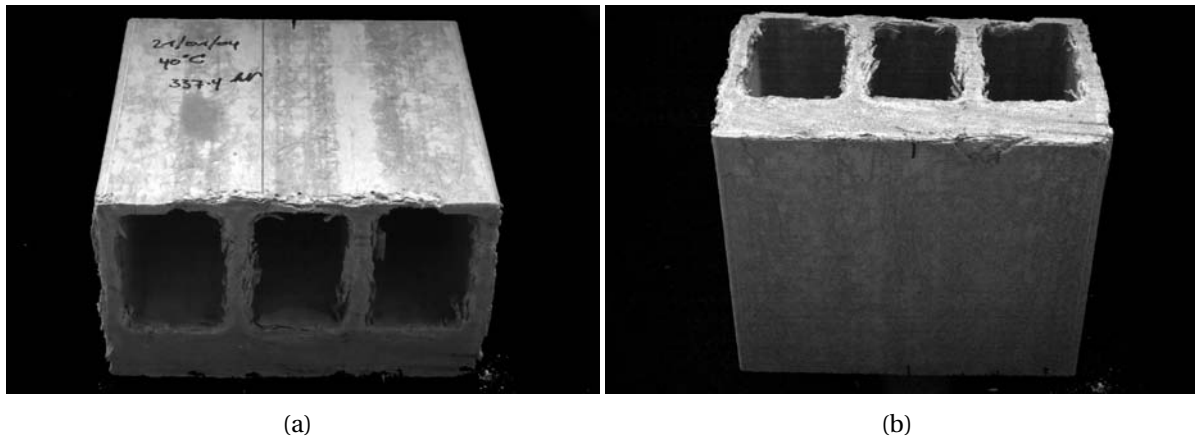


Figure B.103: Failure of uncapped element – 40°C, 219 days

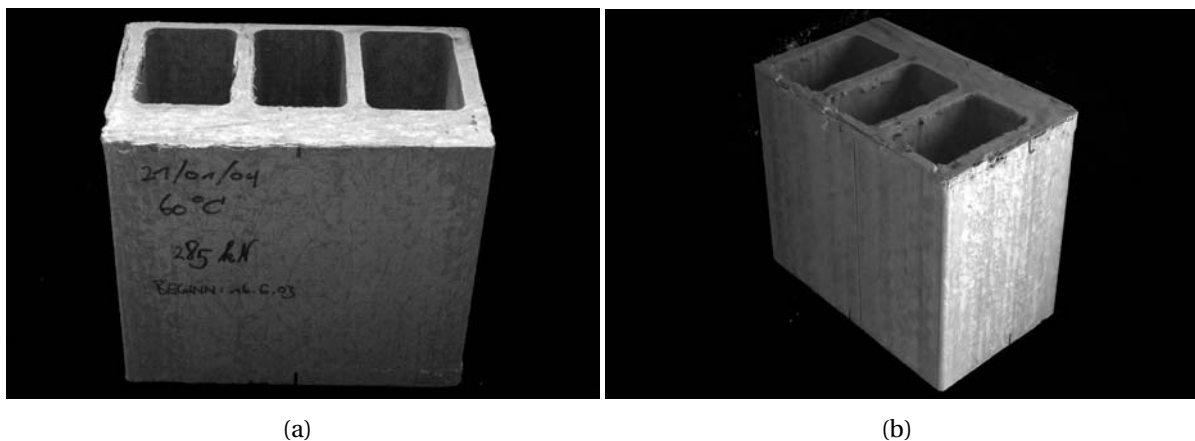


Figure B.104: Failure of uncapped element – 60°C, 219 days

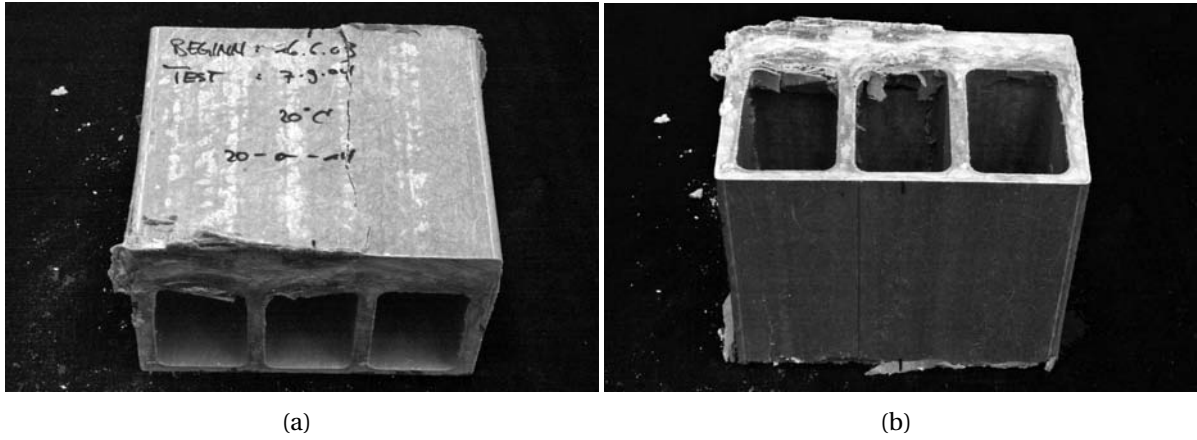


Figure B.105: Failure of uncapped element – 20°C, 448 days

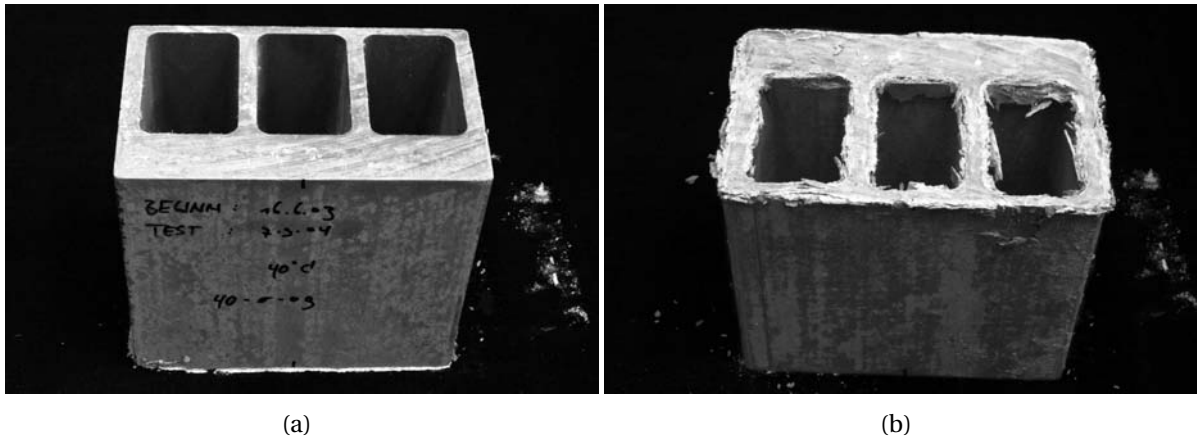


Figure B.106: Failure of uncapped element – 40°C, 448 days

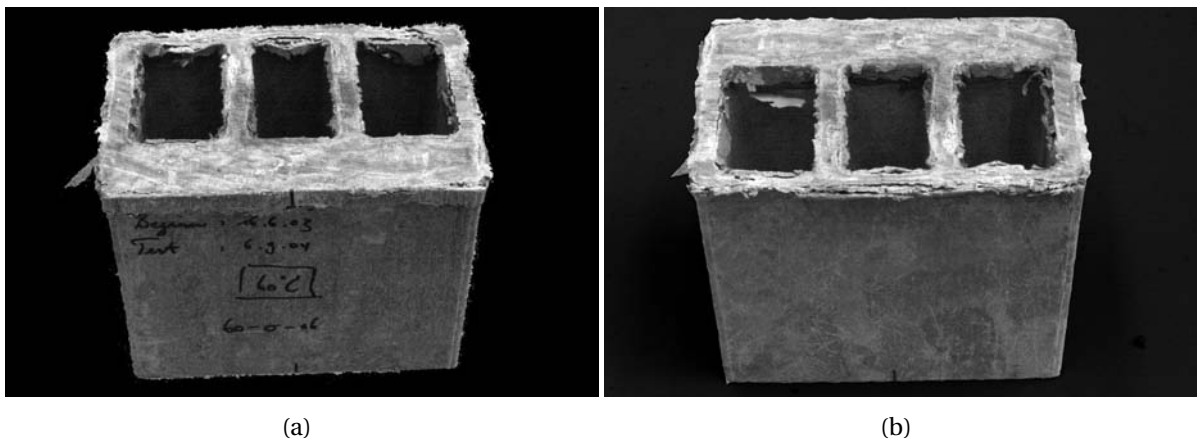
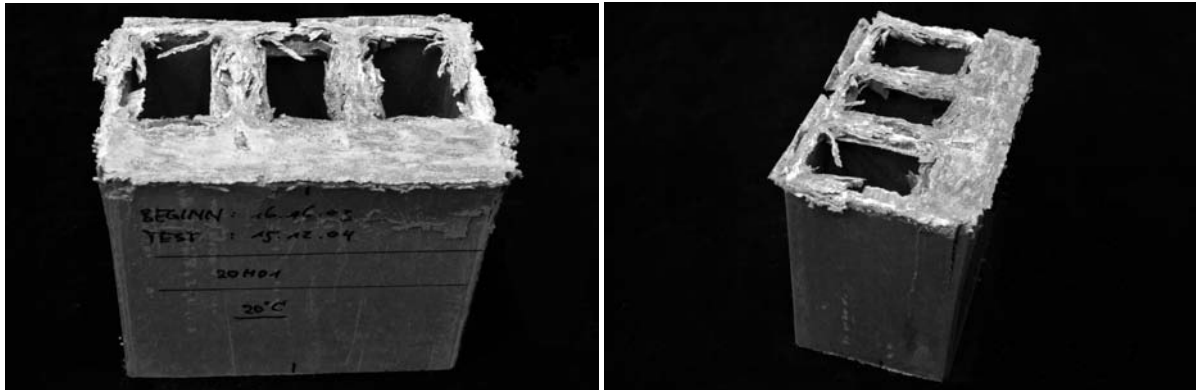


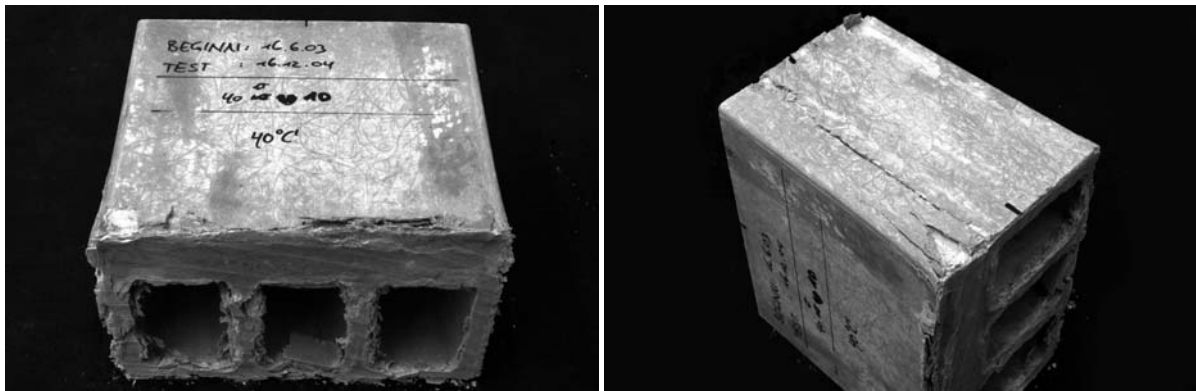
Figure B.107: Failure of uncapped element – 60°C, 448 days



(a)

(b)

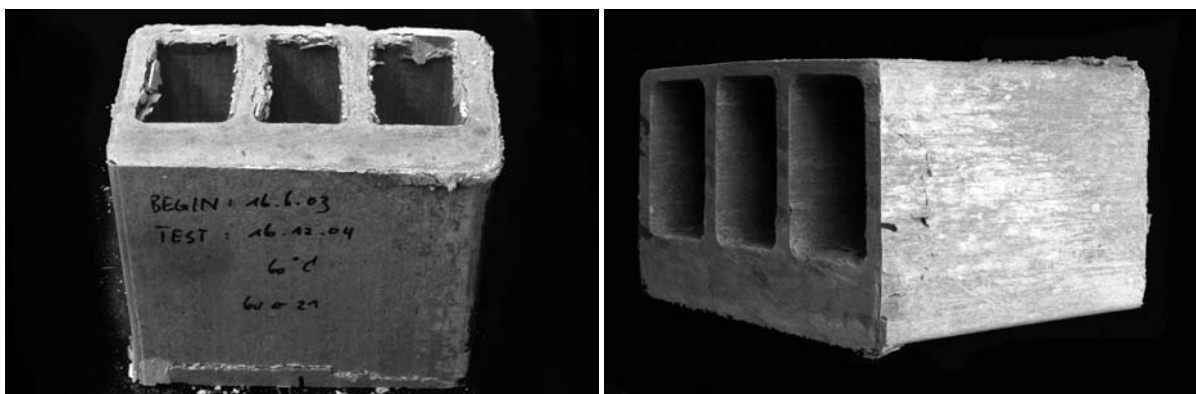
Figure B.108: Failure of uncapped element – 20°C, 548 days



(a)

(b)

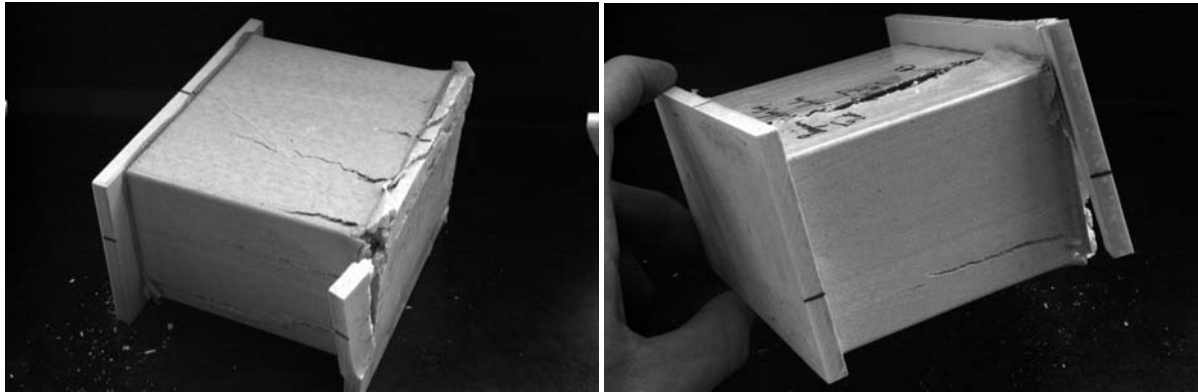
Figure B.109: Failure of uncapped element – 40°C, 548 days



(a)

(b)

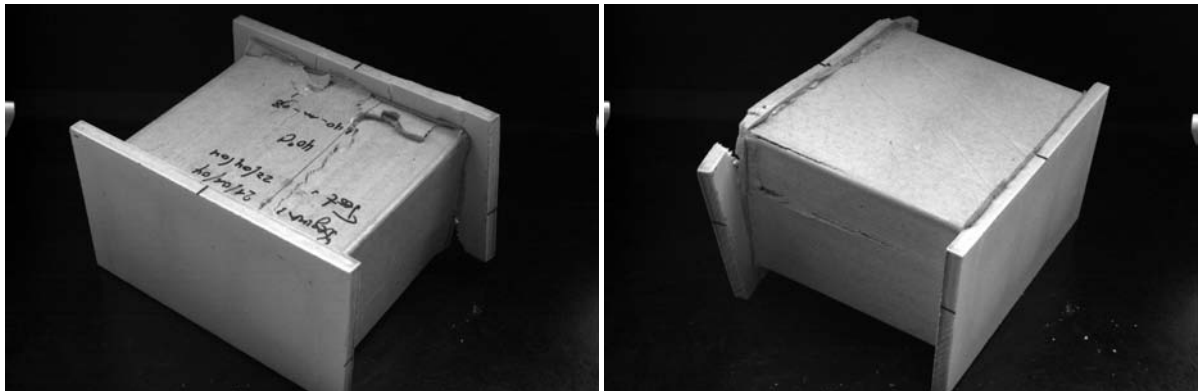
Figure B.110: Failure of uncapped element – 60°C, 548 days



(a)

(b)

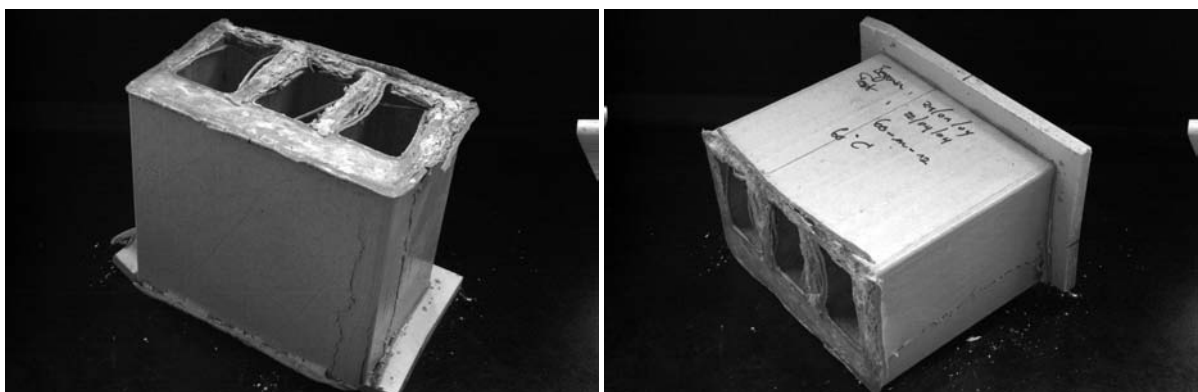
Figure B.111: Failure of capped element – 20°C, 91 days



(a)

(b)

Figure B.112: Failure of capped element – 40°C, 91 days



(a)

(b)

Figure B.113: Failure of capped element – 60°C, 91 days

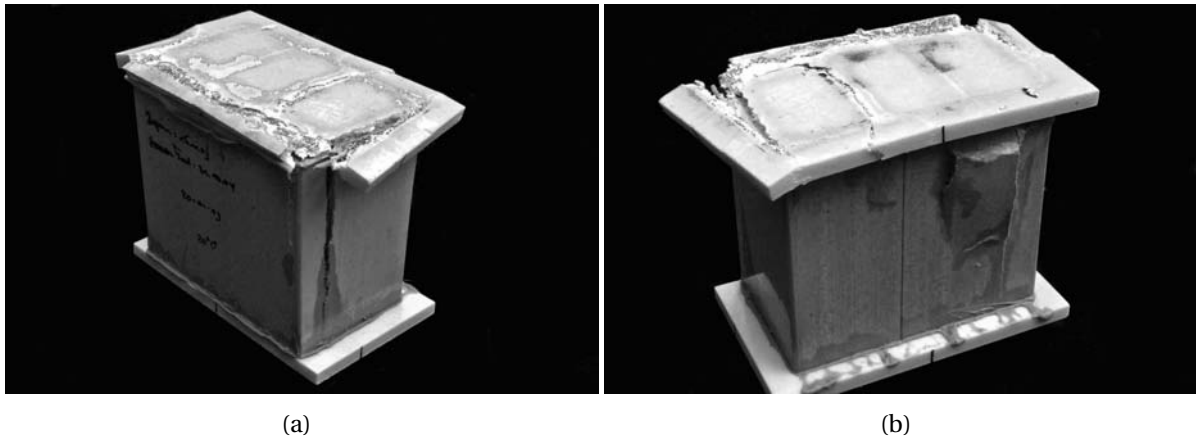


Figure B.114: Failure of capped element – 20°C, 340 days

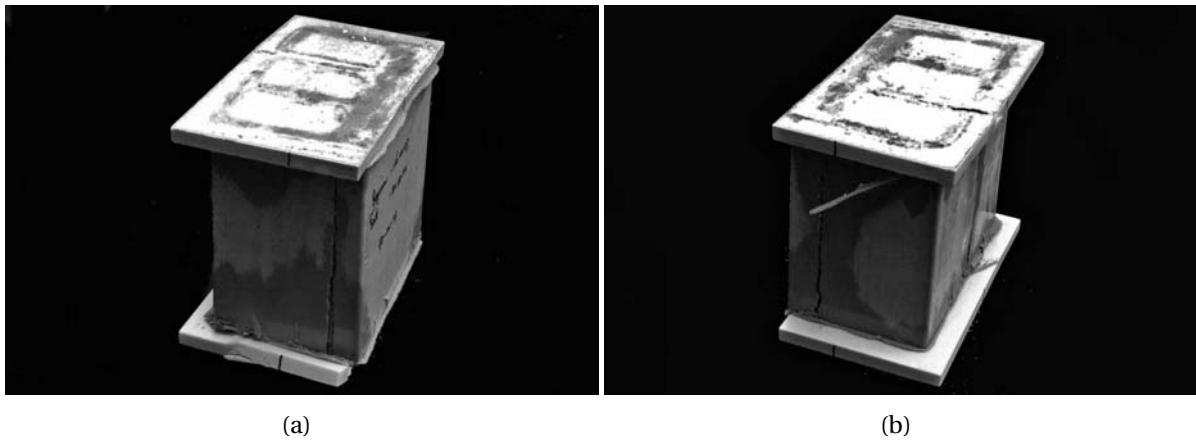


Figure B.115: Failure of capped element – 40°C, 340 days

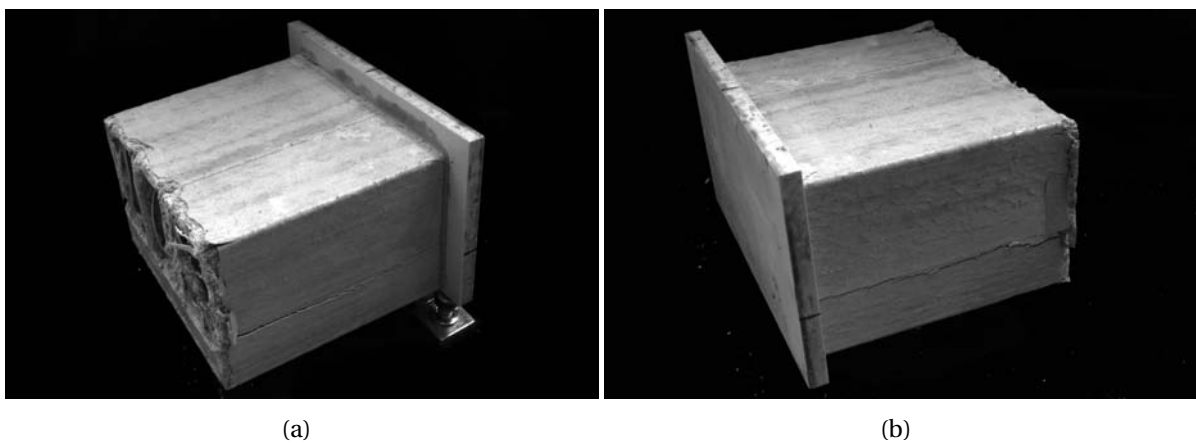


Figure B.116: Failure of capped element – 60°C, 199 days

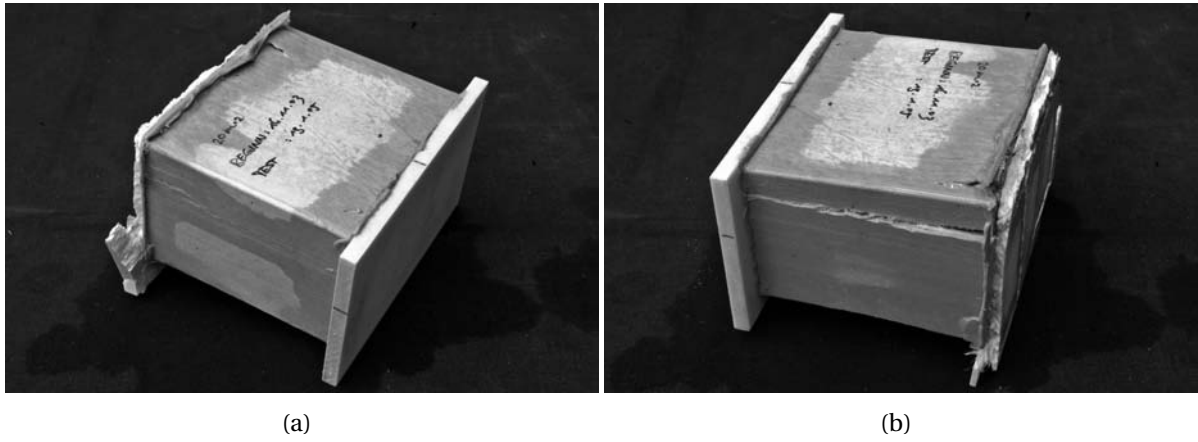


Figure B.117: Failure of capped element – 20°C, 430 days

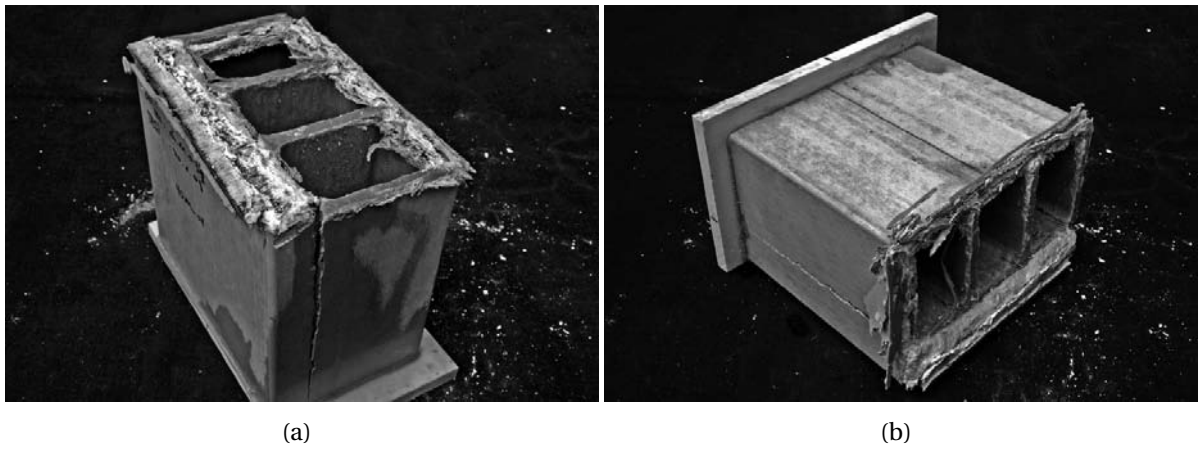


Figure B.118: Failure of capped element – 40°C, 430 days

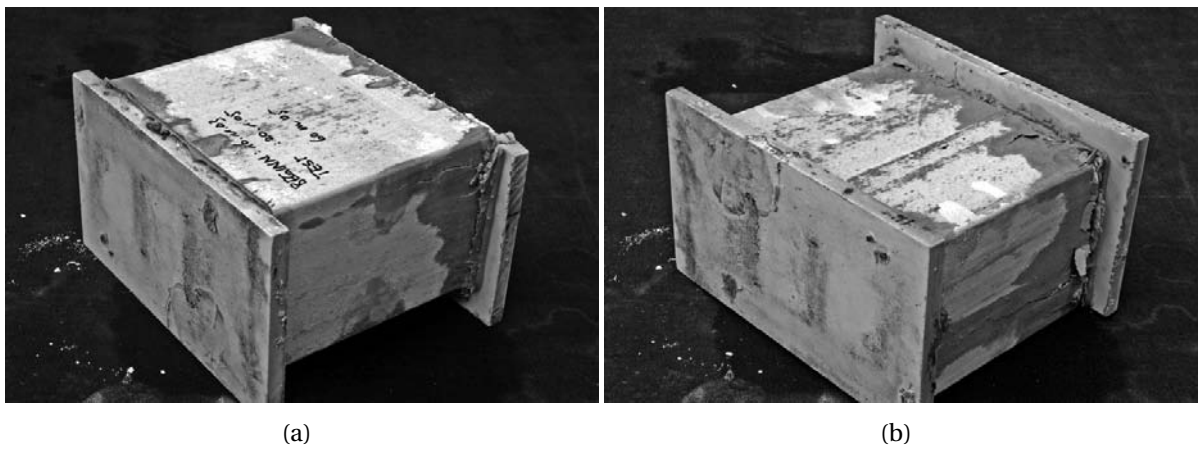


Figure B.119: Failure of capped element – 60°C, 430 days

Appendix C.

Gravimetric study

C.1. Sealing performance

The sealing material (SikaGard-63N[®]) was tested for its weight gain in 20°C alkaline solution. The testing program involved altogether eight specimens with areas of 18×73 mm² and depths between 2.8 and 10.5 mm. Their weight gain as a function of time is shown in Figure C.1. The calculated diffusion coefficient was $0.00032 \cdot 10^{-4} \frac{\text{mm}^2}{\text{sec}}$ and the maximum moisture content, M_{∞} , was 2.51 %. This value, however, was obtained by fitting, since the moisture uptake had not reached an equilibrium as can be seen in the figure.

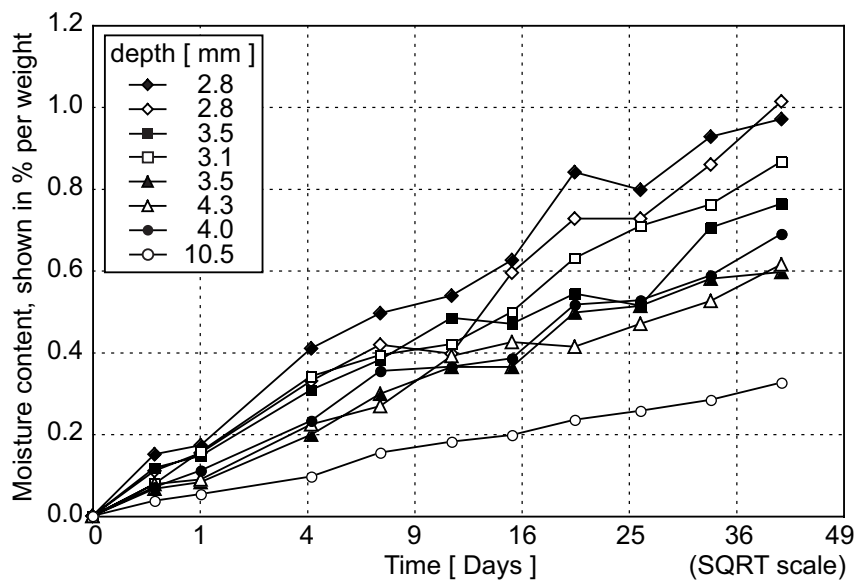
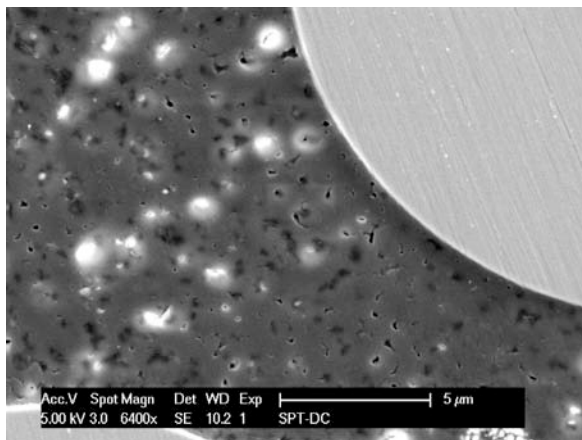


Figure C.1: Weight gain of sealing material

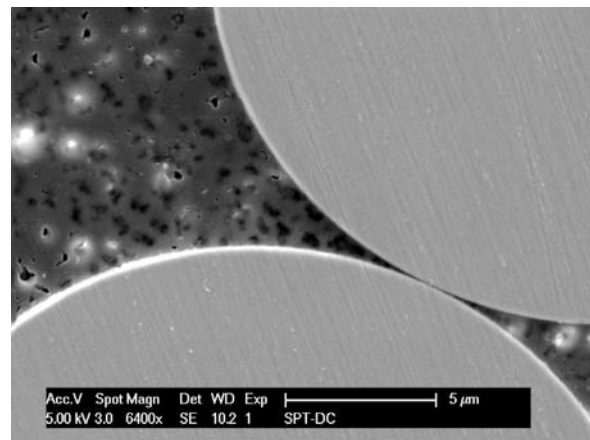
Appendix D.

Microscopic study

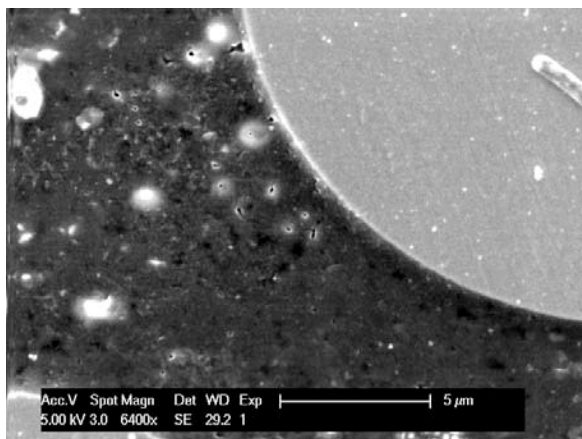
D.1. Damage progression by microscopic series



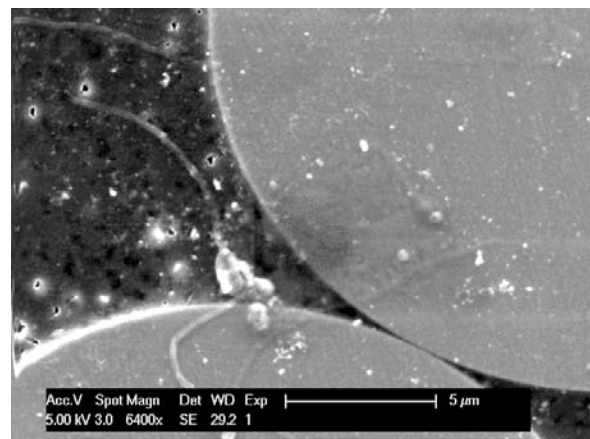
(a) As received



(b) As received

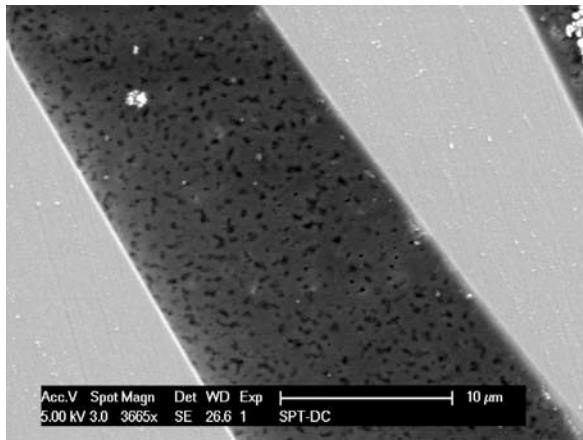


(c) After 6 days at 20°C

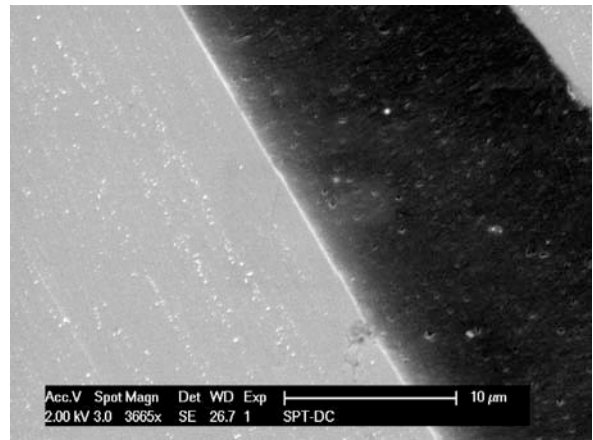


(d) After 6 days at 20°C

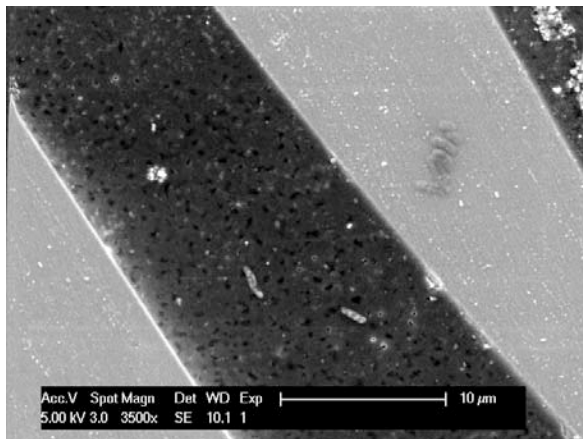
Figure D.1: Comparison of SEM images taken on a specimen with circled fiber surfaces



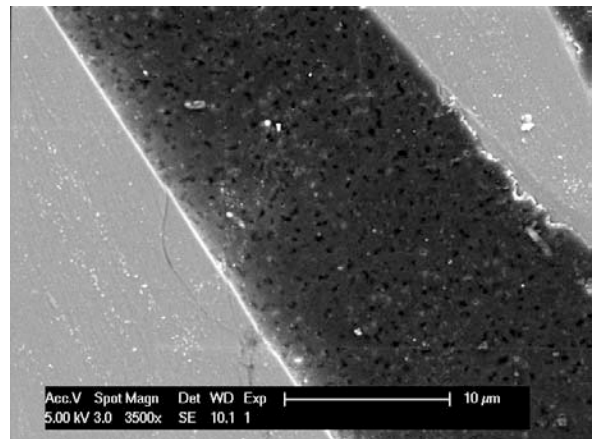
(a) As received, location 1



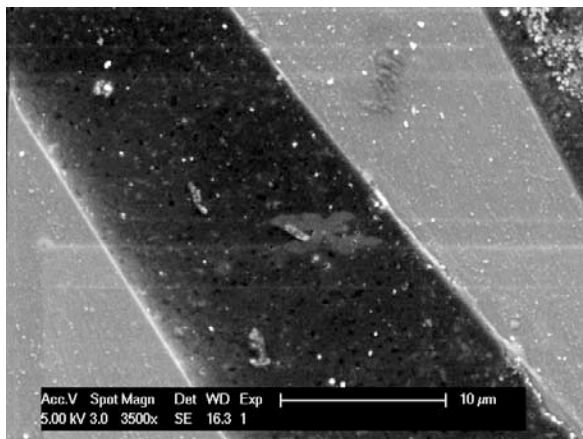
(b) As received, location 2



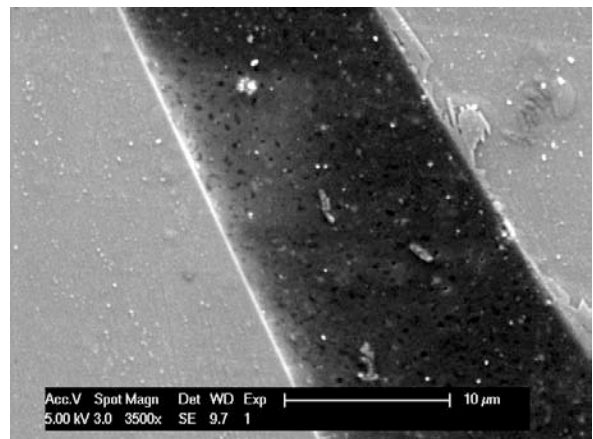
(c) After 6 days at 20°C, location 1



(d) After 6 days at 20°C, location 2

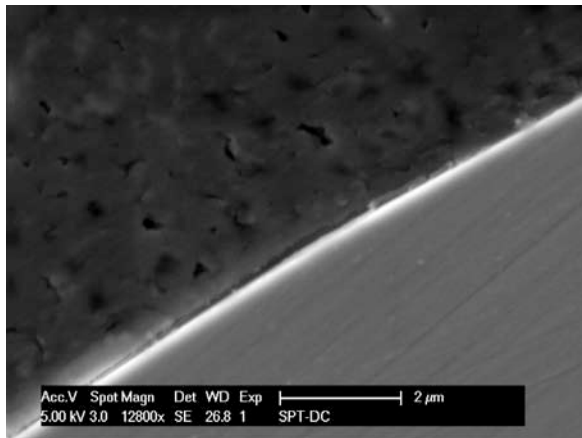


(e) After 19 days at 20°C, location 1

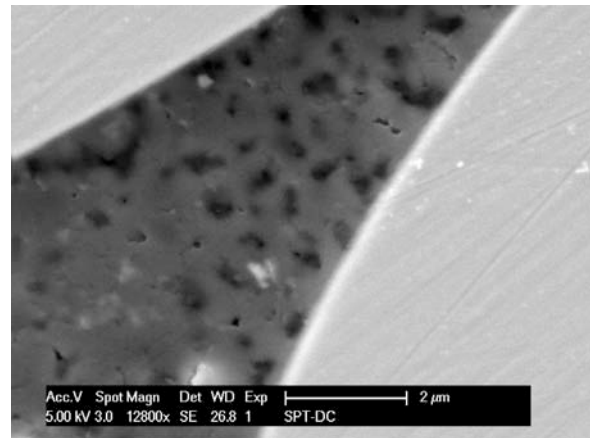


(f) After 19 days at 20°C, location 2

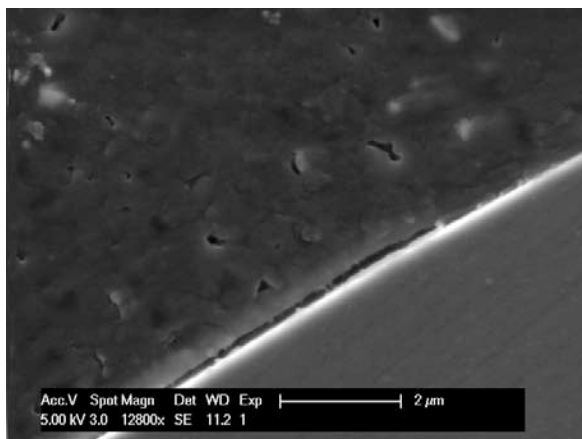
Figure D.2: Comparison of SEM images taken on a sample polished parallel to the pultrusion direction



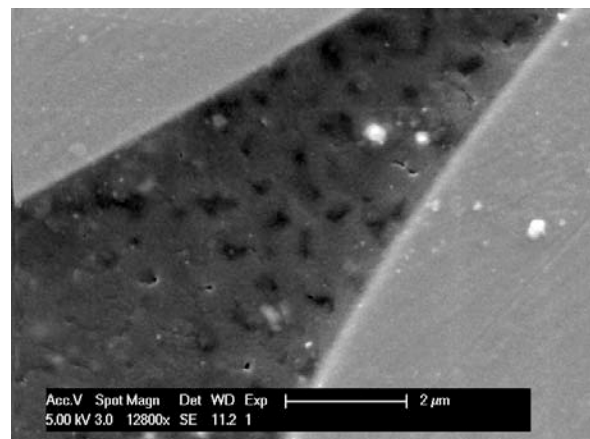
(a) As received, location 1



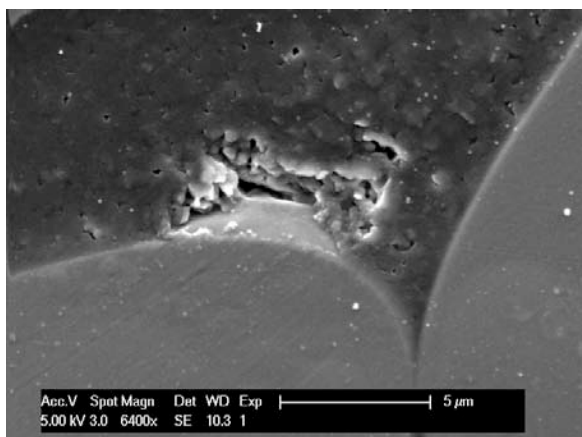
(b) As received, location 2



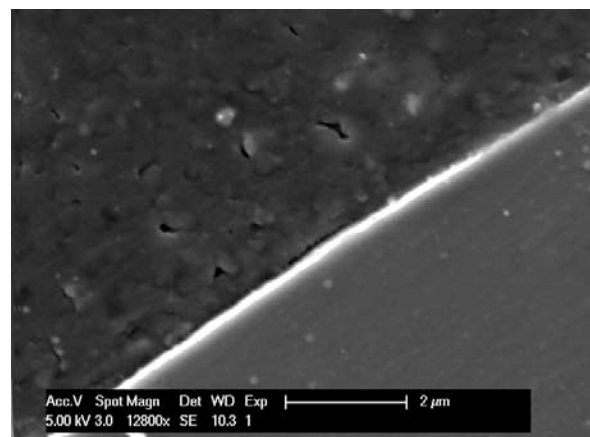
(c) After 6 days at 20°C, location 1



(d) After 6 days at 20°C, location 2

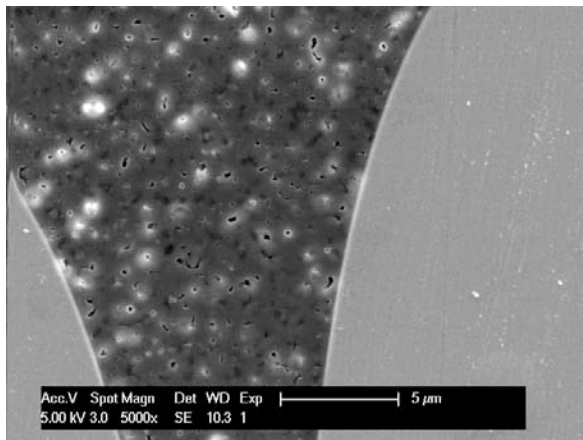


(e) After 19 days at 20°C, location 1

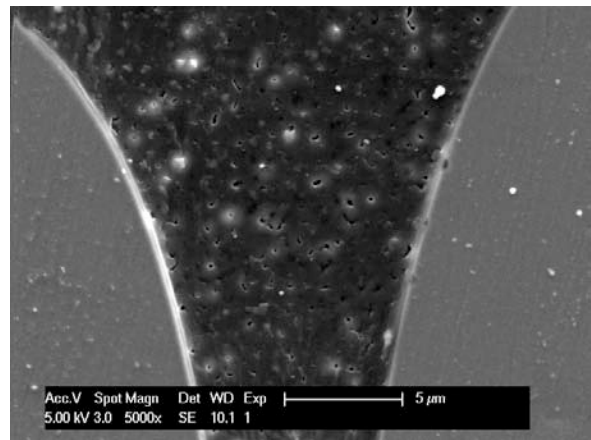


(f) After 19 days at 20°C, location 2

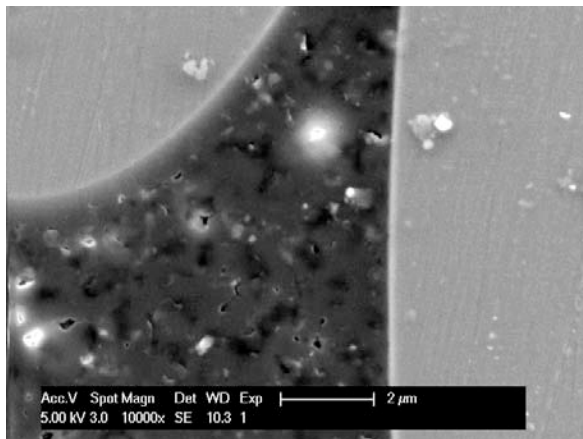
Figure D.3: Comparison of SEM images taken on a sample polished at an angle to the pultrusion direction



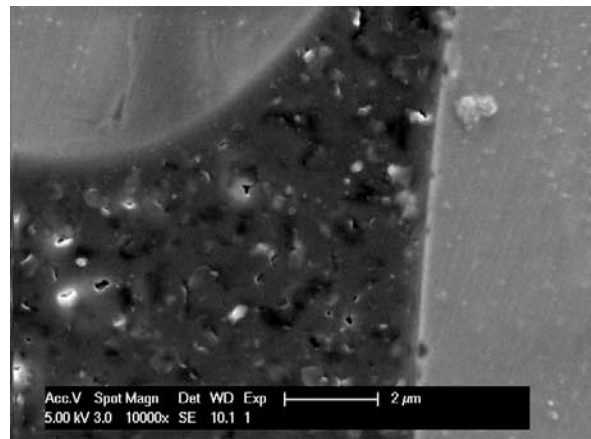
(a) As received, location 1



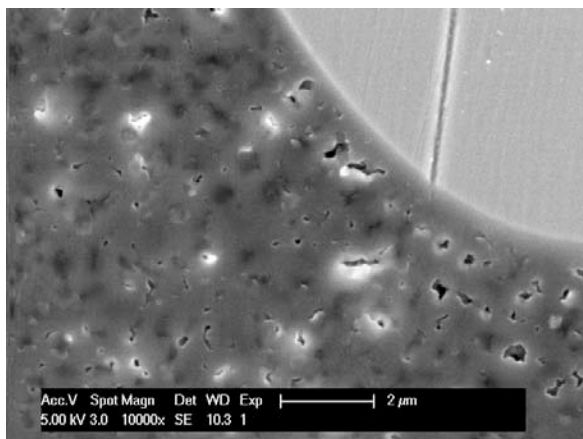
(b) After 13 days at 60°C, location 1



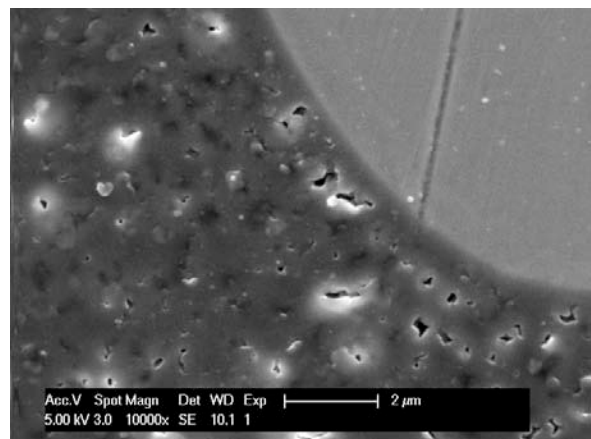
(c) As received, location 2



(d) After 13 days at 60°C, location 2



(e) As received, location 3



(f) After 13 days at 60°C, location 3

Figure D.4: Comparison of SEM images taken on a sample polished at an angle to the pultrusion direction

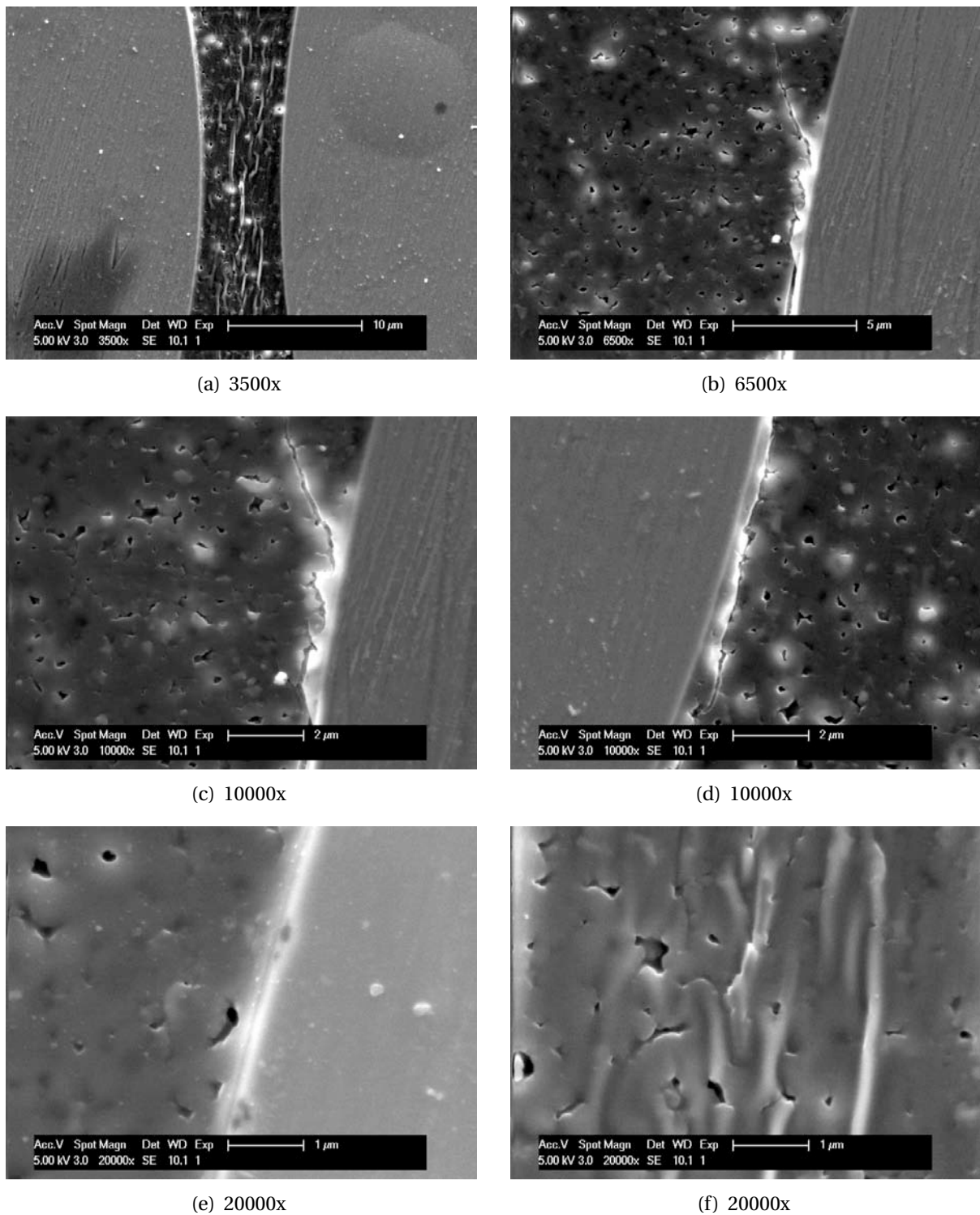
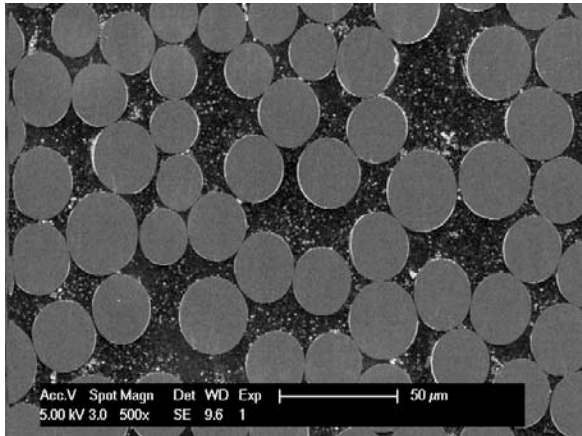
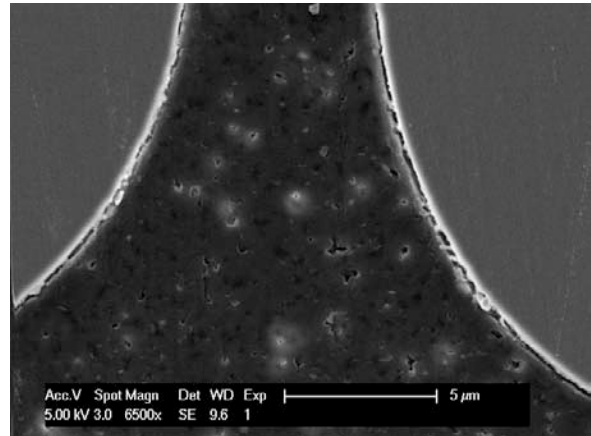


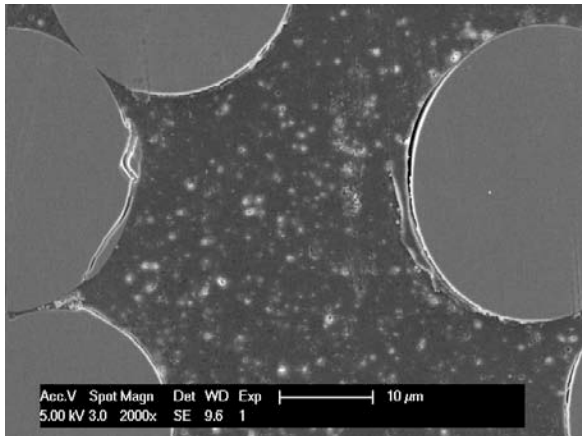
Figure D.5: SEM images taken on a sample polished at an angle to the pultrusion direction and then exposed at 60°C for 13 days

D.2. Damage after 800 days exposure at 20°C

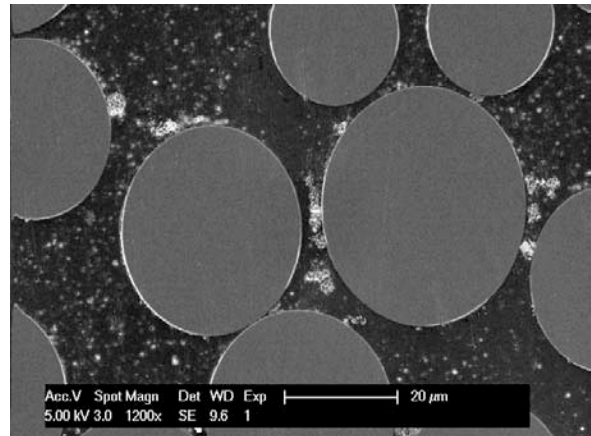
(a) Interfacial degradation



(b) Interfacial degradation - close-up



(c) Interfacial and matrix degradation



(d) Matrix degradation

Figure D.6: SEM images on profile after 800 days at 20°C (near cut end)

Appendix E.

EDX results

E.1. Results of EDX material analysis

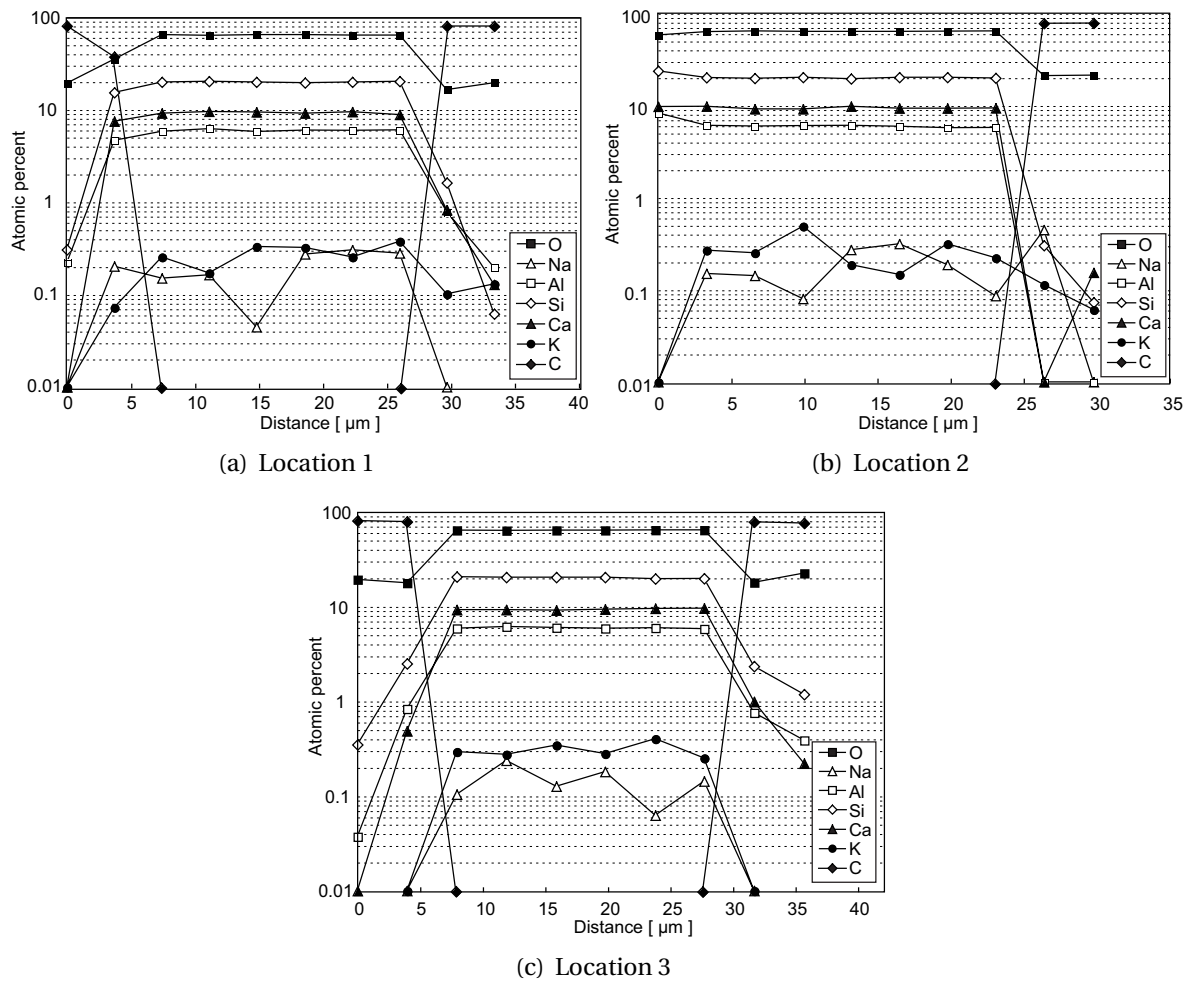


Figure E.1: Results of the EDX material analysis for unconditioned specimens

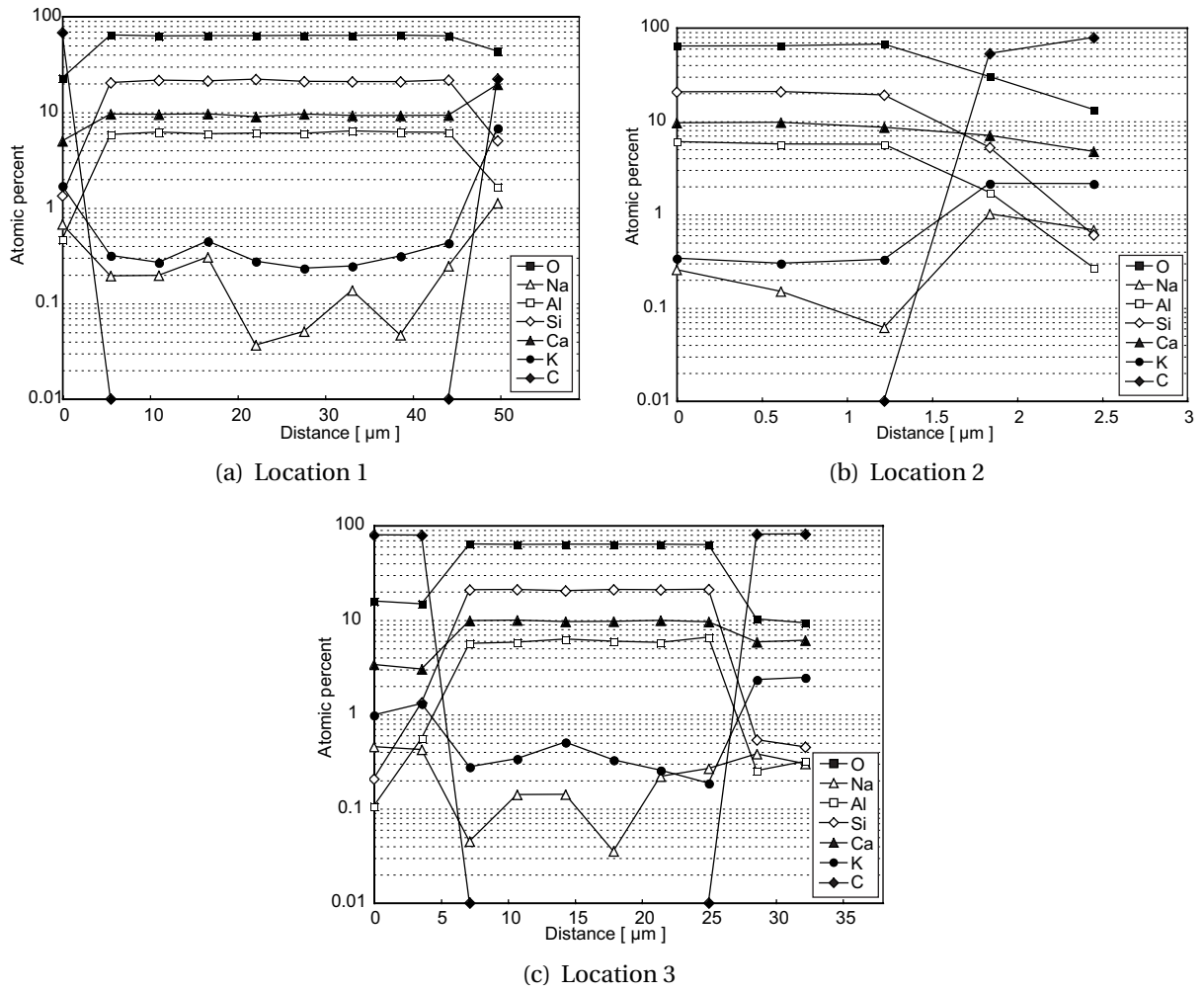


Figure E.2: Results of the EDX material analysis for specimens conditioned for 800 days at 60°C

Appendix F.

Investigations on hybrid joint

F.1. Experimental set-up

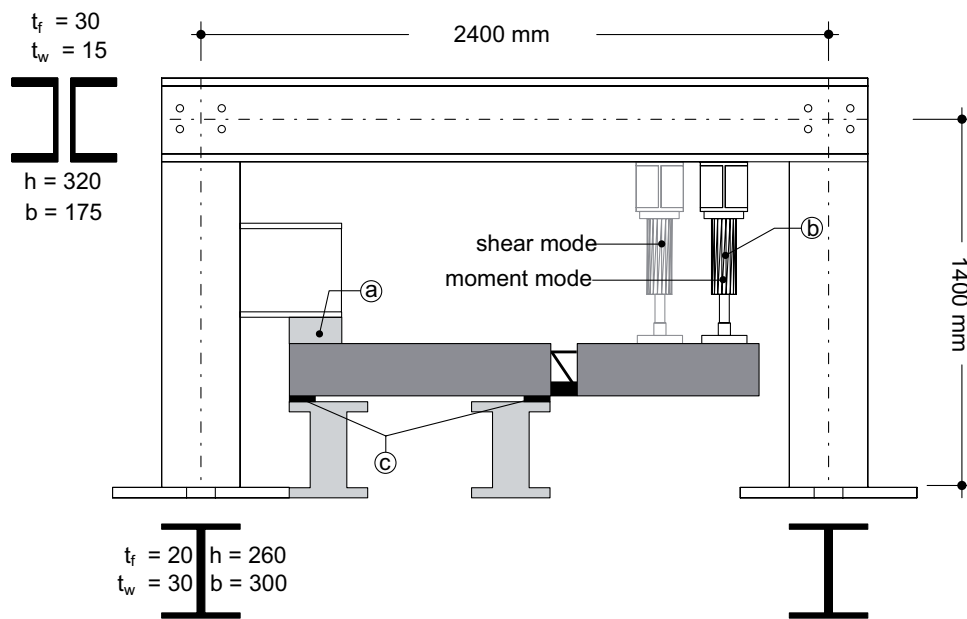


Figure F.1: Experimental set-up of hybrid beams: a) counter bearing, b) loading cylinder, c) steel plates

The loading frame consisted of steel profiles (I-shaped for the columns and U-shaped for the traverse, see figure for dimensions). The beams were placed on supporting tables and the support was fine-adjusted by 10-mm thick steel plates. At the left support, the beams were fixed against up-lift forces. The load applying cylinder had a maximum force of 200 kN and a travel of 200 mm. It was fixed on the traverse via a smaller cross girder. To change the loading position, the loading cylinder along with its cross girder was moved. In order to change the support condition in the first series, the steel plate beneath the beam was moved leaving the support table in place. Acting in this manner, however, in some cases the remaining table still served as a foothold for the compression element once spalled-off concrete accumulated on the table. Therefore, in the second series the whole supporting table was moved.

Table F.1: Pouring and testing plan

Pouring of beams		Testing of beams	
25.08.03	M200E1 / M240E1	22.09.03	
26.08.03		23.09.03	M200E1 / M240E1
27.08.03	S200E1 / S240E1	24.09.03	S200E1 / S240E1
28.08.03	M200C1 / M240C1	25.09.03	M200C1 / M240C1
29.08.03	S200C1 / S240C1	26.09.03	S200C1 / S240C1
08.09.03	M200E2 / M240E2	06.10.03	M240E2
09.09.03		07.10.03	M200E2
10.09.03	S200E2 / S240E2	08.10.03	S200E2 / S240E2
11.09.03	M200C2 / M240C2	09.10.03	M200C2 / M240C2
12.09.03	S200C2 / S240C2	10.10.03	S200C2 / S240C2
13.07.04	S200Ea / S240Ea	10.08.04	S200E3 / S240E3

Table F.2: Compressive strength of concrete after 28 days.

Beam	f_c , cube [MPa]	f_c , cube, mean [MPa]	f_c , cyl, mean [MPa]	Gravel size [mm]
M200E1/M240E1	40 / 38 / 39	39.3±0.7	31.4	16
S200E1/S240E1	44 / 44 / 45	44.6±0.6	35.7	32
M200C1/M240C1	46 / 48 / 47	47.1±0.7	37.6	32
S200C1/S240C1	50 / 51 / 51	50.6±0.8	40.5	32
M200E2/M240E2	48 / 45 / 50	47.7±2.5	38.1	32
S200E2/S240E2	49 / 47 / 49	48.4±1.1	38.7	32
M200C2/M240C2	54 / 56 / 58	55.8±1.8	44.6	32
S200C2/S240C2	55 / 54 / 55	54.5±0.5	43.6	32
S200E3/S240E3	43 / 43 / 37	43.0±3.6	34.4	32

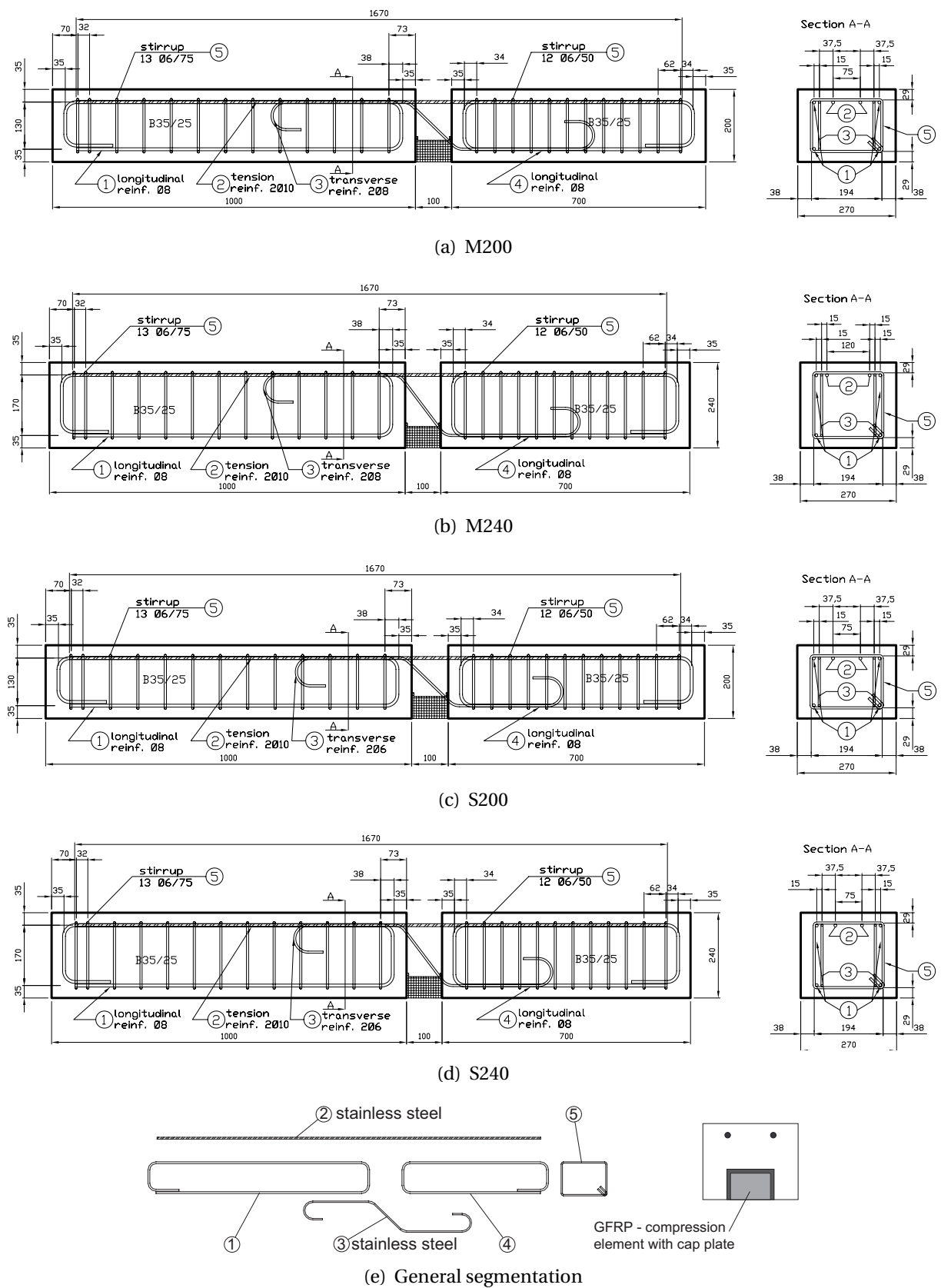
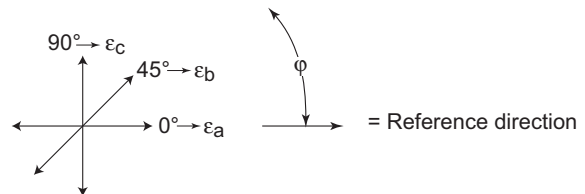


Figure F.2: Reinforcement drawing and dimensions

F.2. Calculation of principal stress angle

The correlation between strain gages in the rosette and the numbering used henceforth is shown in Figure F.3. The theory to calculate the angle of principal stress, φ^1 , from the measurements of the rosettes is based on the Mohr's circle. A two dimensional plane has two principal angles, one for σ_1 and one for σ_2 , each being orthogonal to one another.

Figure F.3: The three directions, in which strain was measured: *a* corresponds to g9 and g13, *b* corresponds to g8 and g12 and *c* corresponds to g10 and g14.



To get to φ , an auxiliary angel ψ has to be determined:

$$\tan \psi = \frac{2\epsilon_b - \epsilon_a - \epsilon_c}{\epsilon_a - \epsilon_c}$$

Here, the numerator (N) and denominator (D) will yield different signs (positive or negative), depending on the measured strain. Four combinations of different signs are possible. Each combination has its own method of calculating the first angle of principal stress φ from ψ . In Figure F.4, the dependencies between both angles for the four combinations are shown.

N	$\geq 0 (+)$	$\geq 0 (+)$	$\leq 0 (-)$	$\leq 0 (-)$
D	$> 0 (+)$	$\leq 0 (-)$	$< 0 (-)$	$\geq 0 (+)$
	I	II	III	IV
appendant quadrant				

Figure F.4: Scheme to develop the angle φ .

Since φ is the direction of the first principal stress direction, the second principal stress direction points perpendicular to it and to each φ , 90 degrees have to be added or subtracted. With the chosen arrangement of the rosettes, the angle of first principal stresses is related to the lower part of the vertical axis and runs counterclockwise. Big changes of the angle for small loading values result from the fact that the arc tangent is used to calculate φ . The function $\arctan(x)$ increases fast for small values of x .

¹In a two-dimensional plane, the first principal stress, σ_1 , always denotes the absolute highest stress, which are tension stresses in this case. The second principal stress, σ_2 , is always the absolute smaller one – in this case a compression stress.

F.3. Load-displacement curves

F.3.1. Vertical Displacements

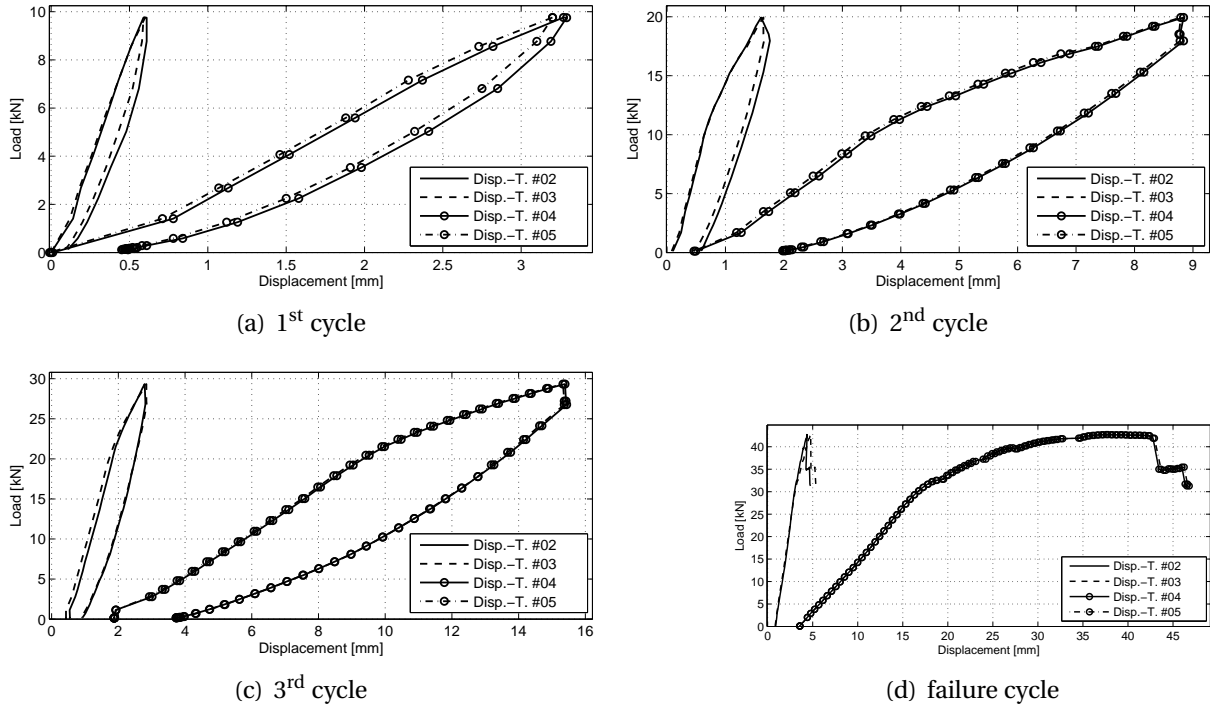


Figure F.5: Vertical displacements for M200E1

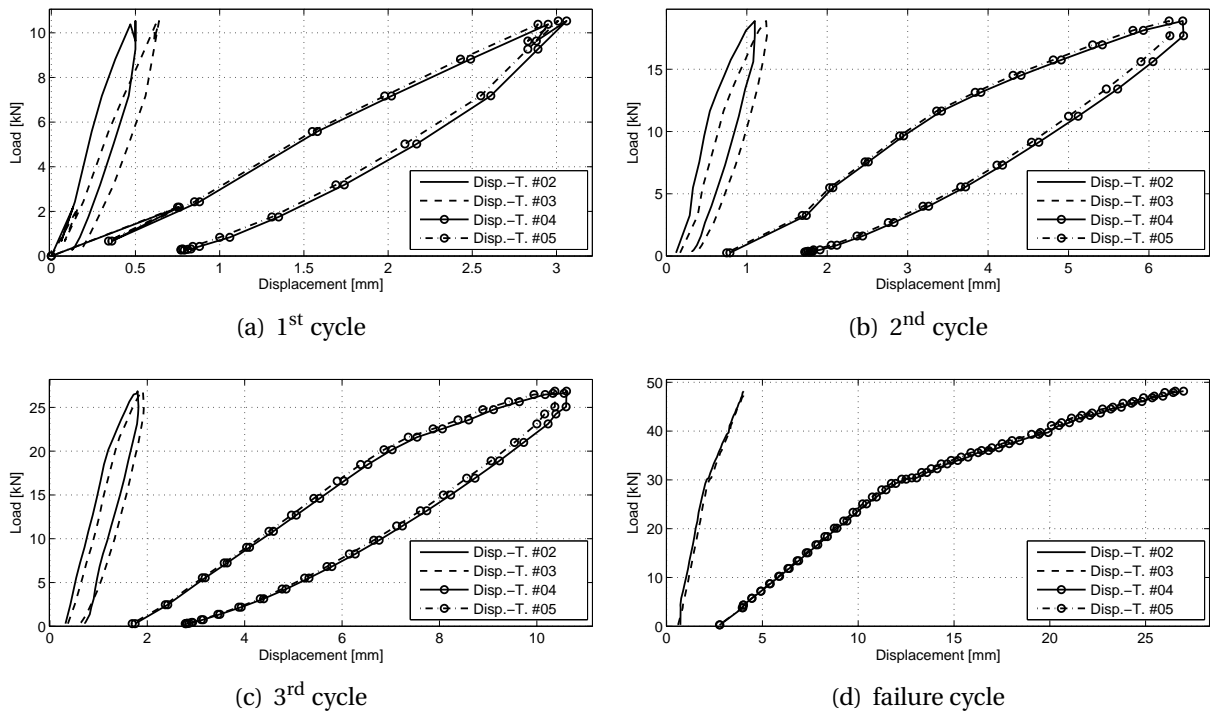


Figure F.6: Vertical displacements for M200E2

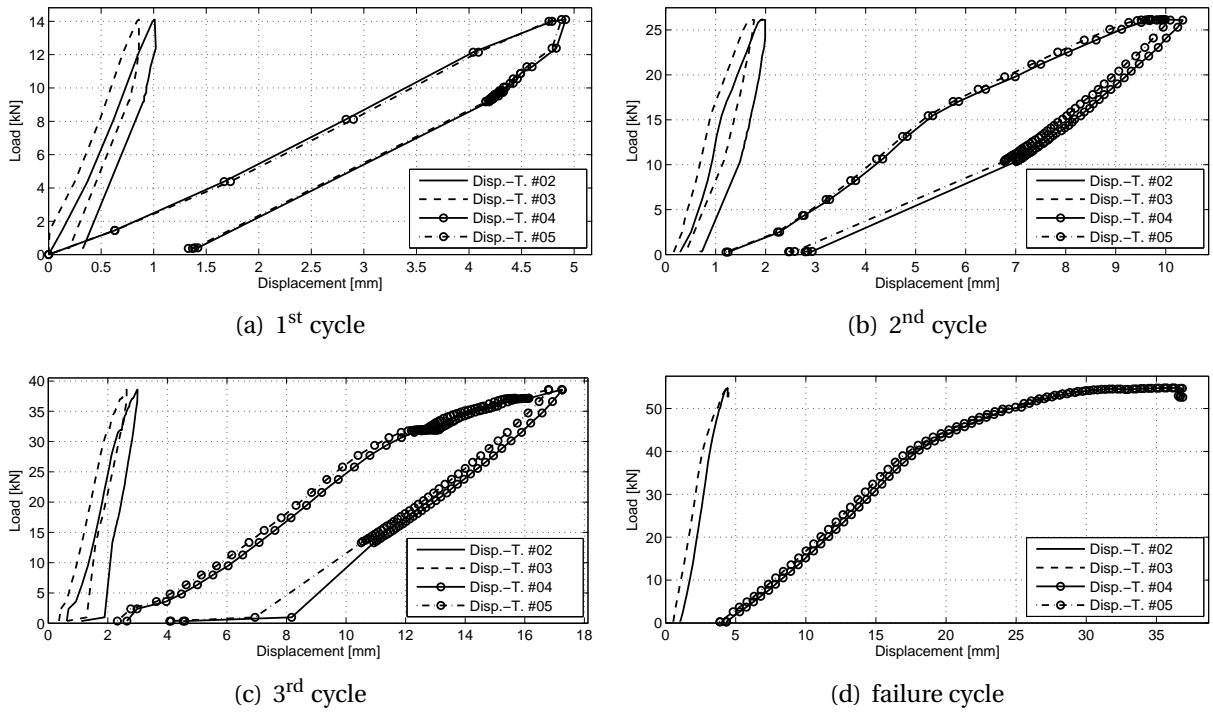


Figure F.7: Vertical displacements for M240E1

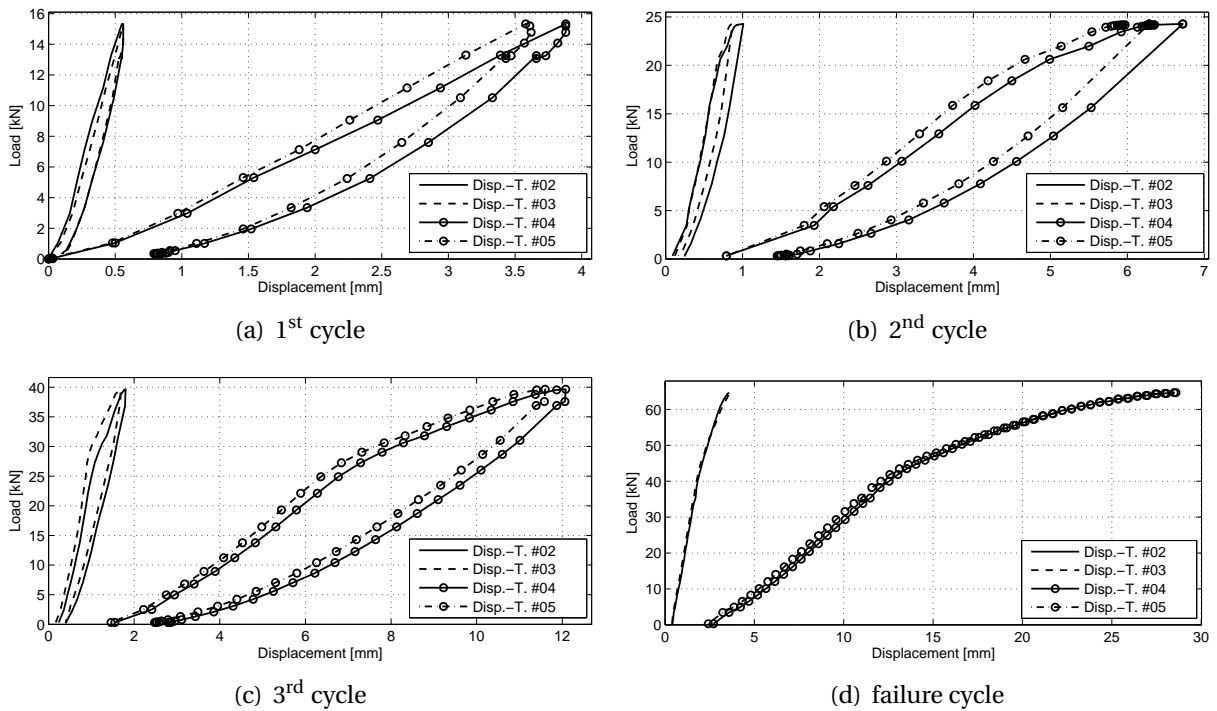


Figure F.8: Vertical displacements for M240E2

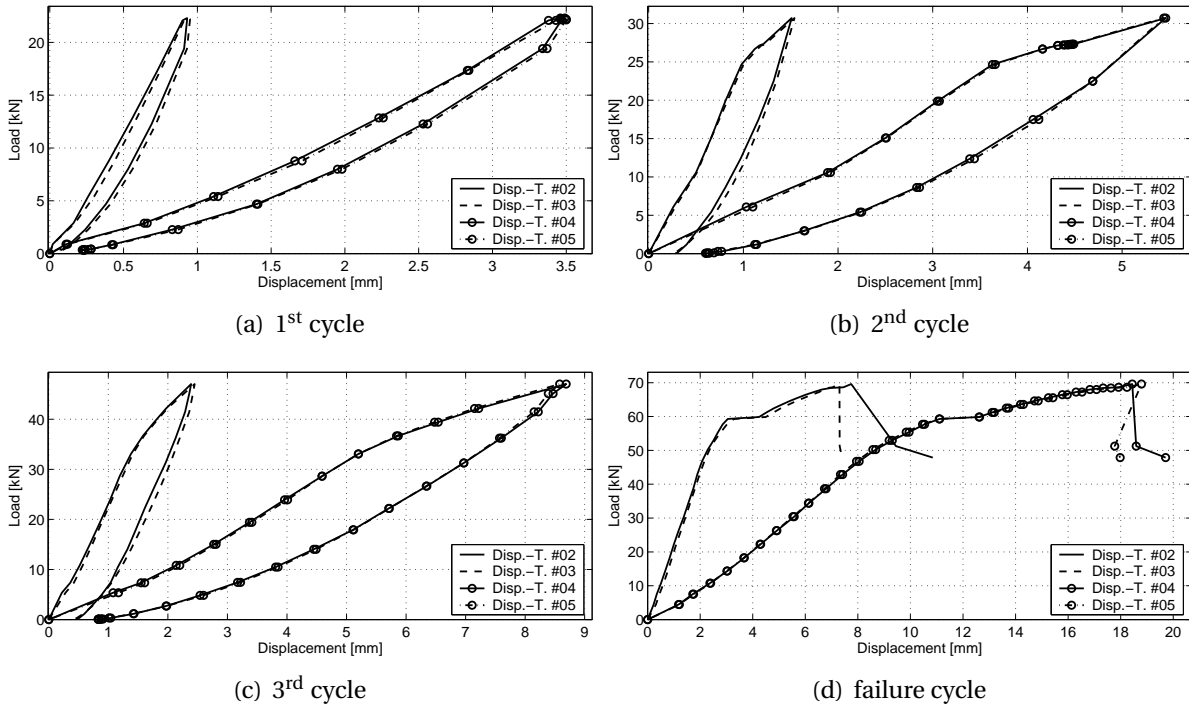


Figure F.9: Vertical displacements for S240E1

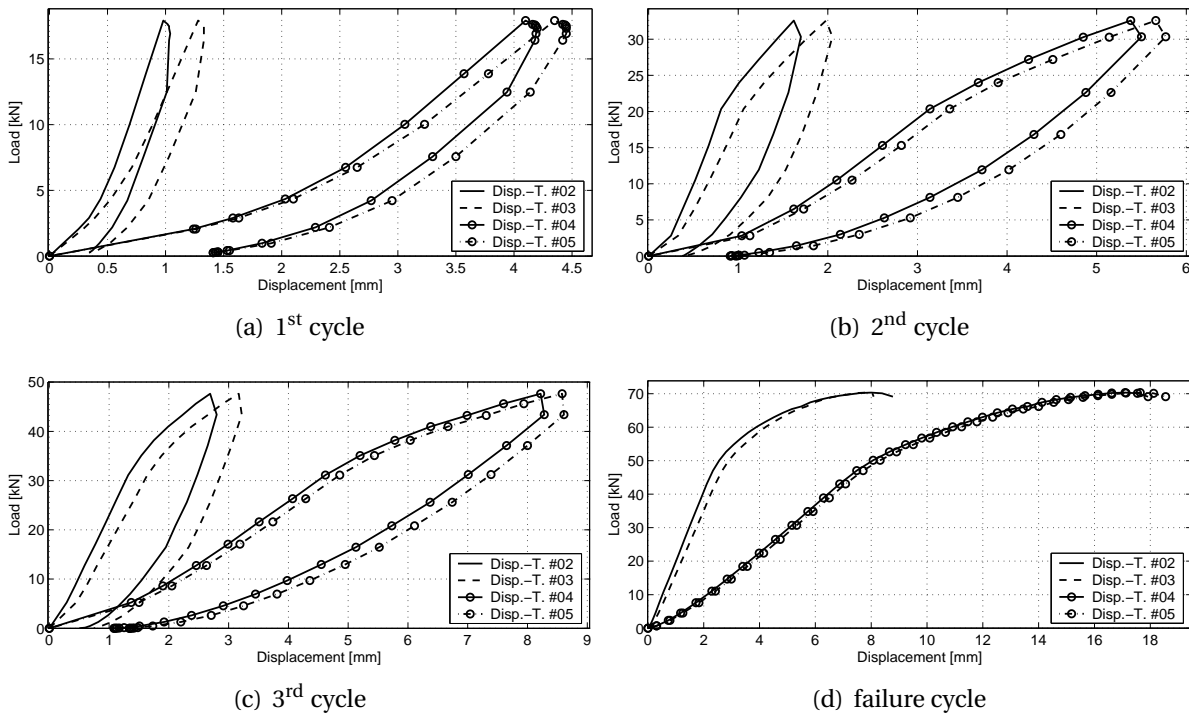


Figure F.10: Vertical displacements for S240E2

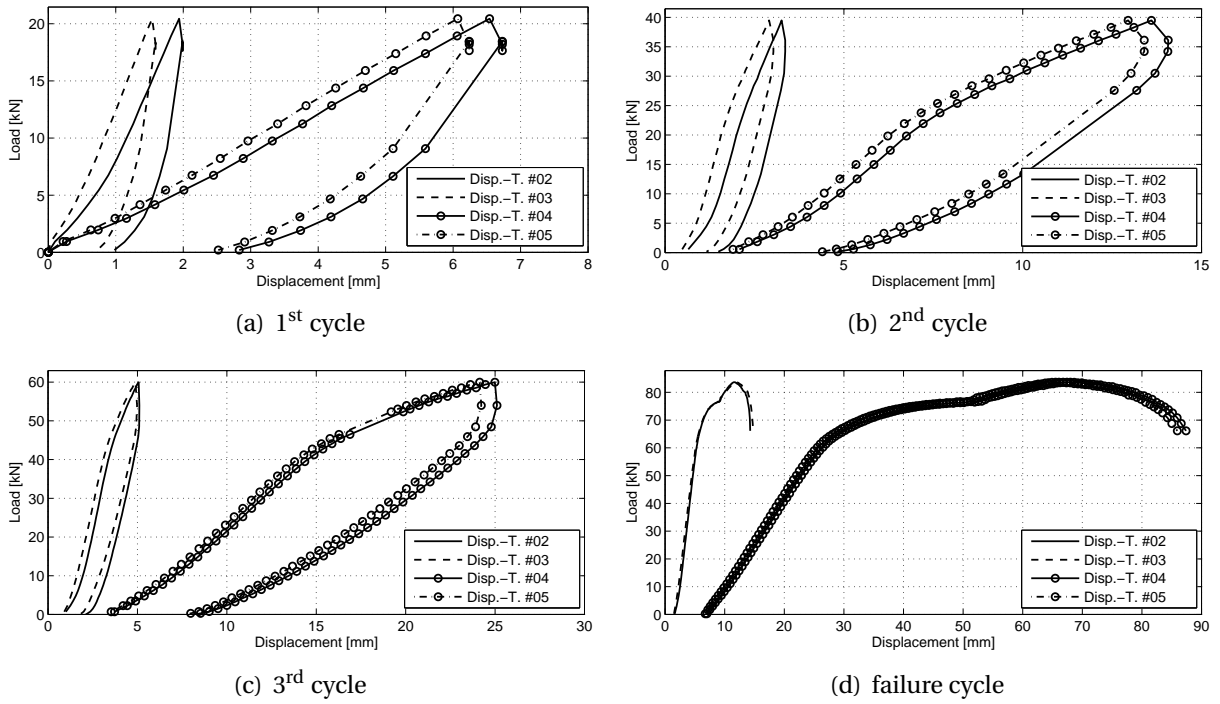


Figure F.11: Vertical displacements for S200E3

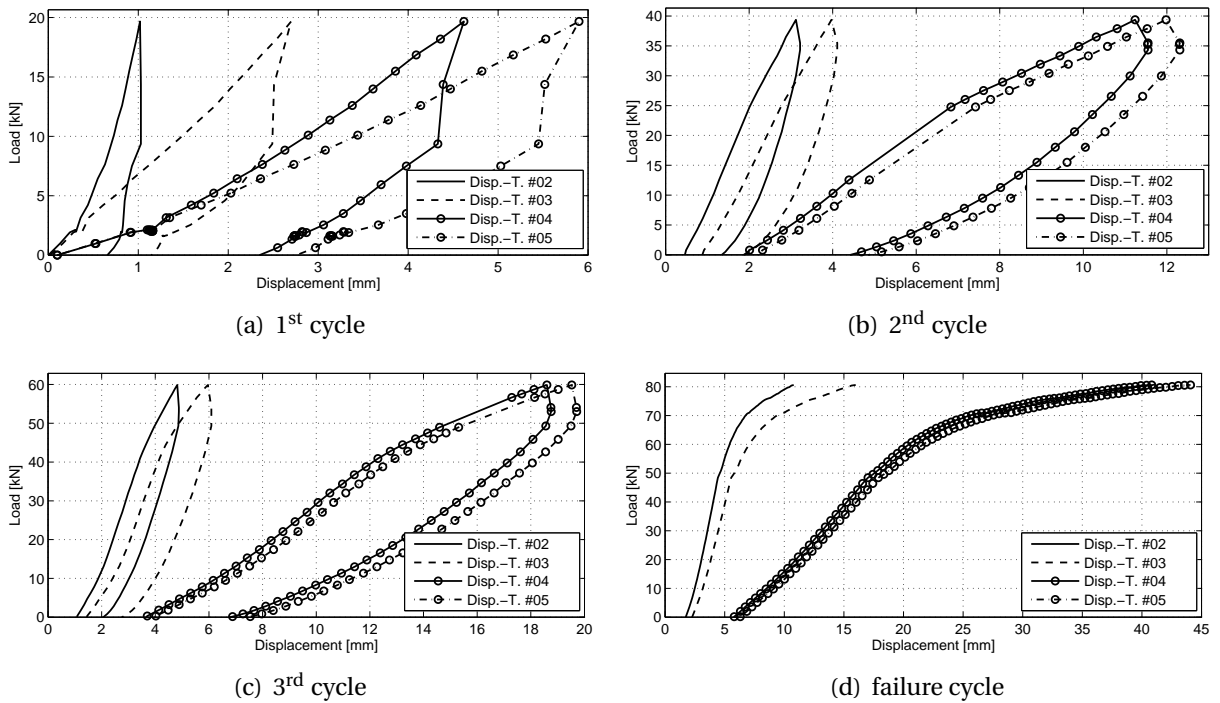


Figure F.12: Vertical displacements for S240E3

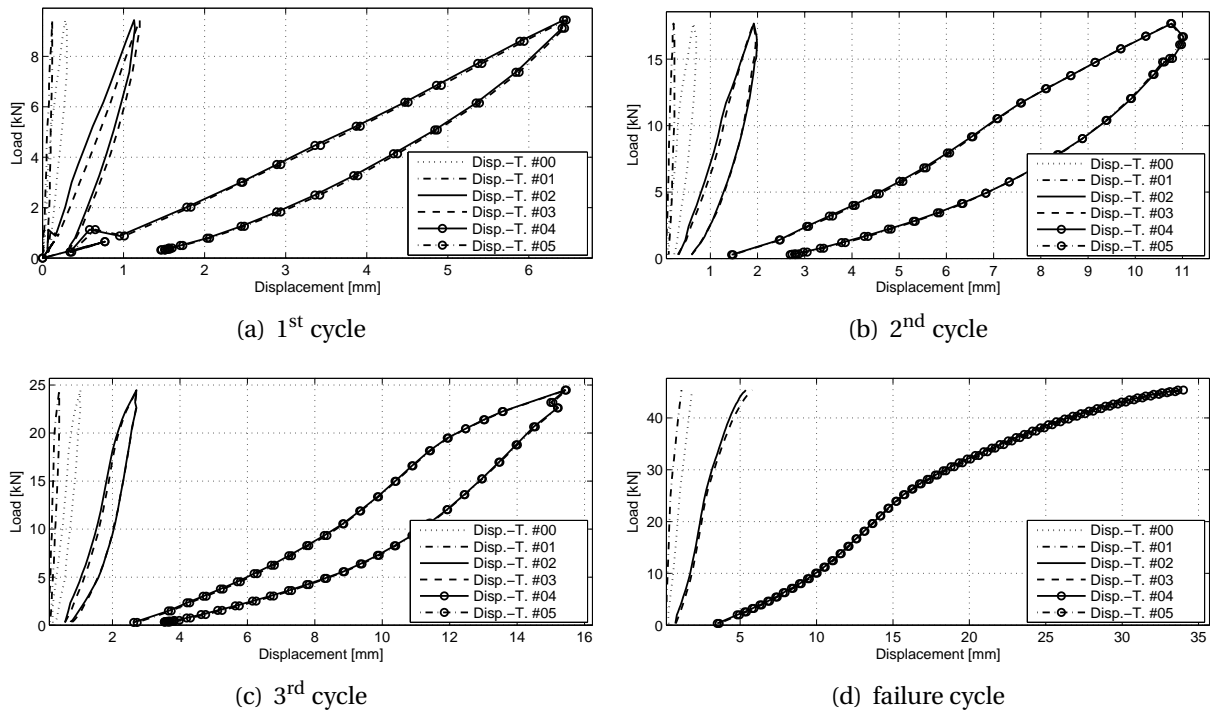


Figure F.13: Vertical displacements for M200C1

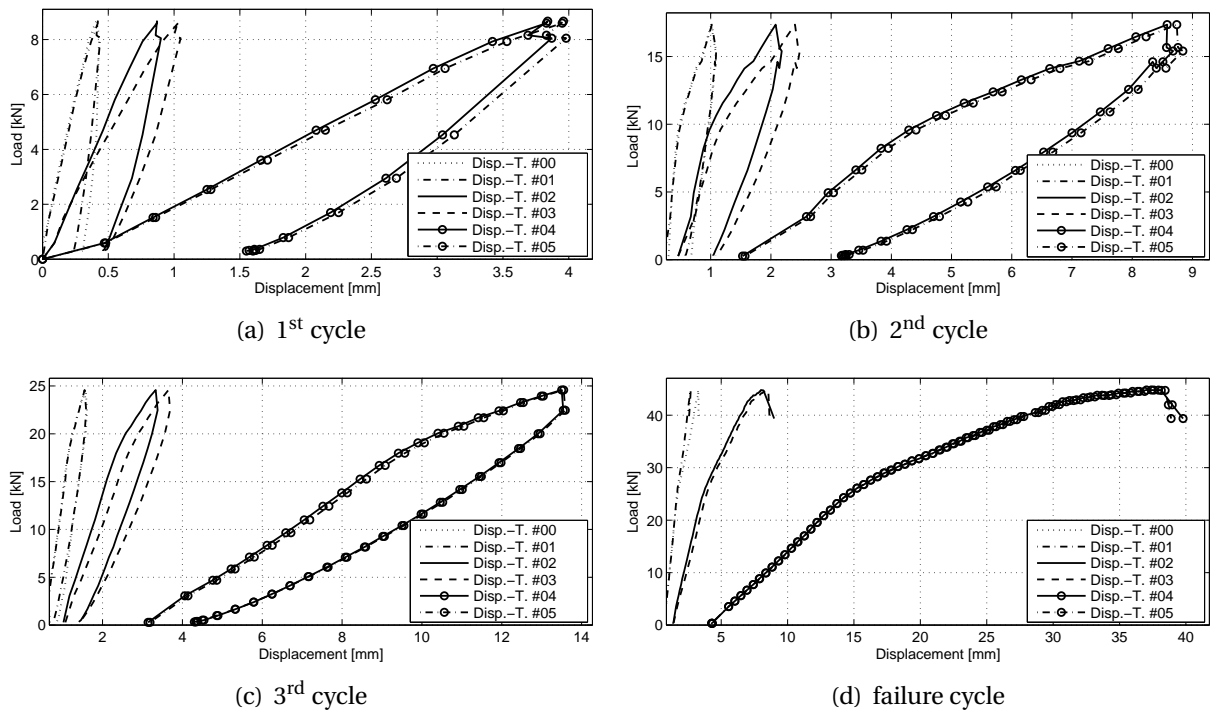


Figure F.14: Vertical displacements for M200C2

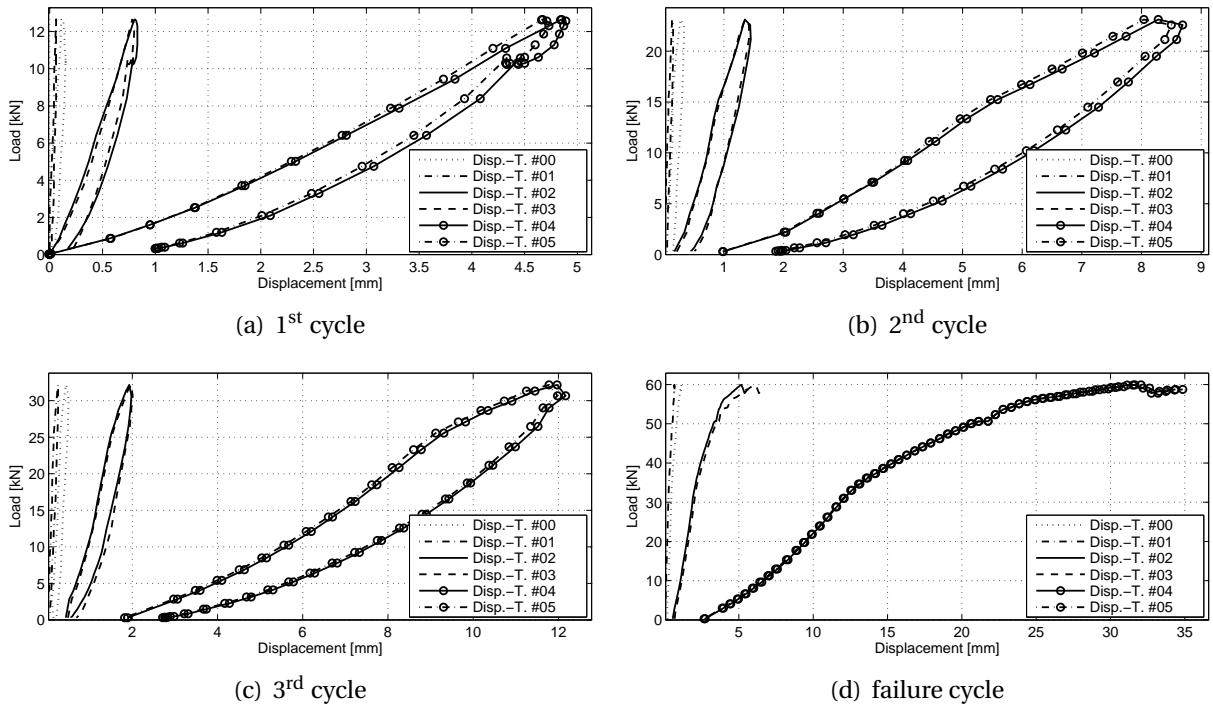


Figure F.15: Vertical displacements for M240C1

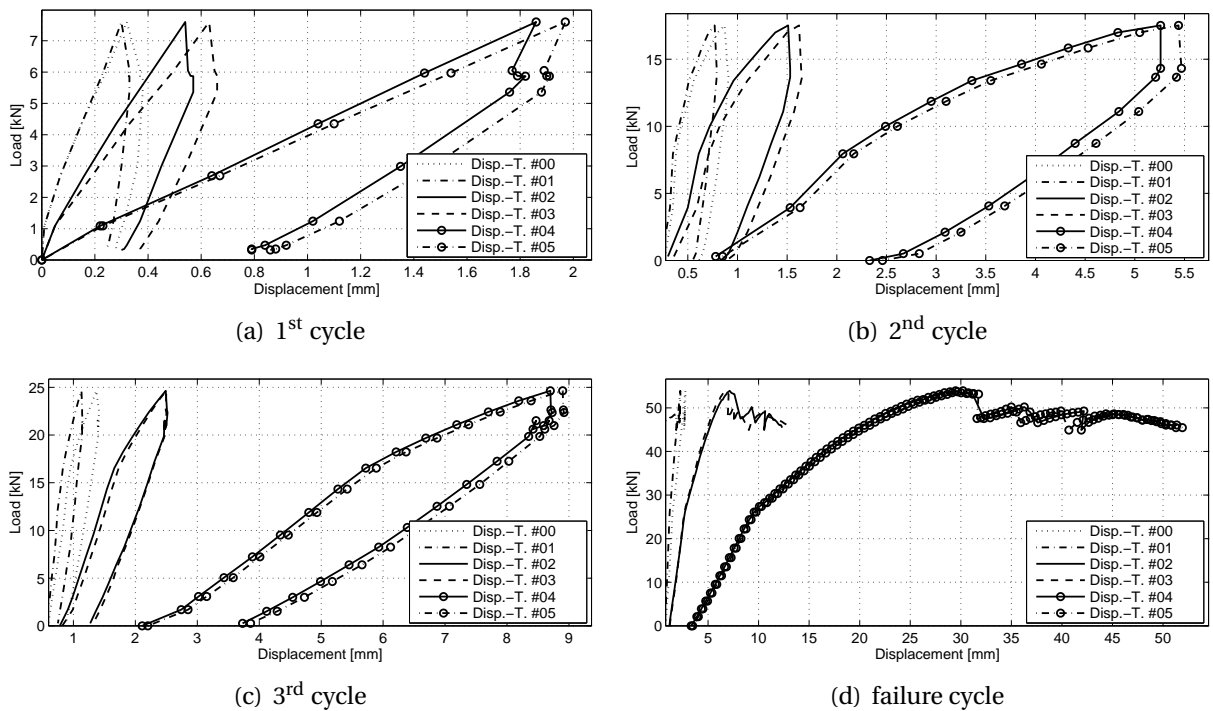


Figure F.16: Vertical displacements for M240C2

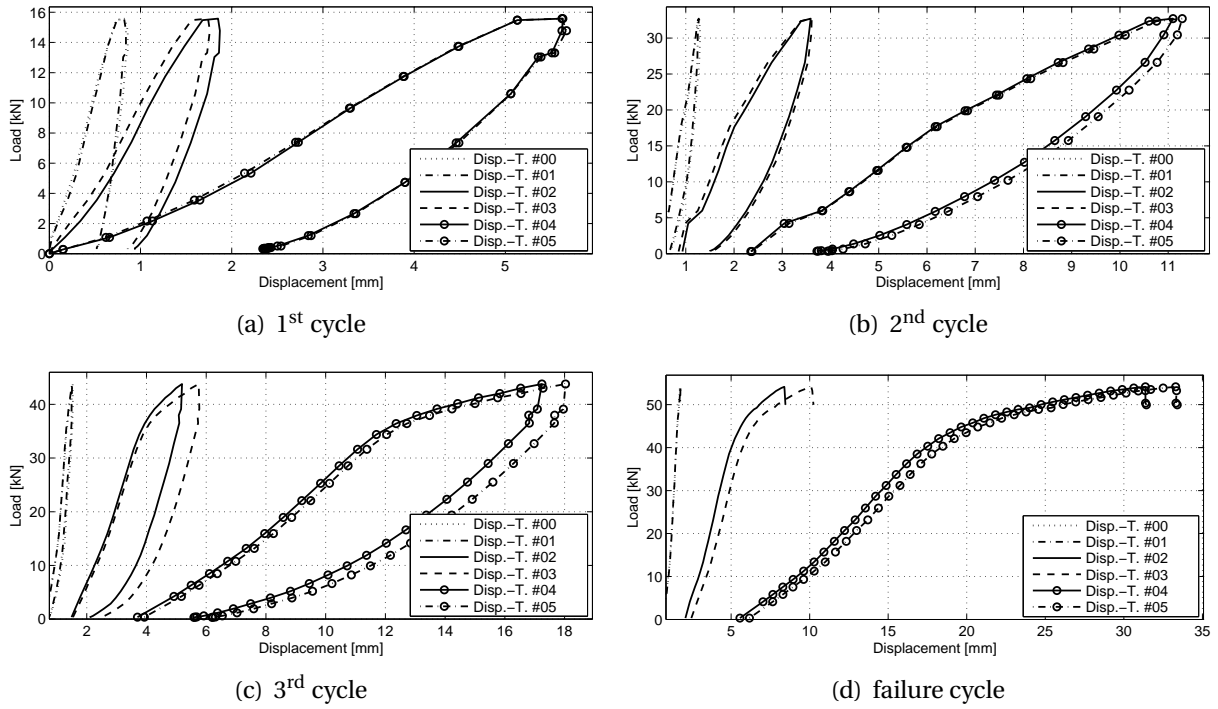


Figure F.17: Vertical displacements for S200C1

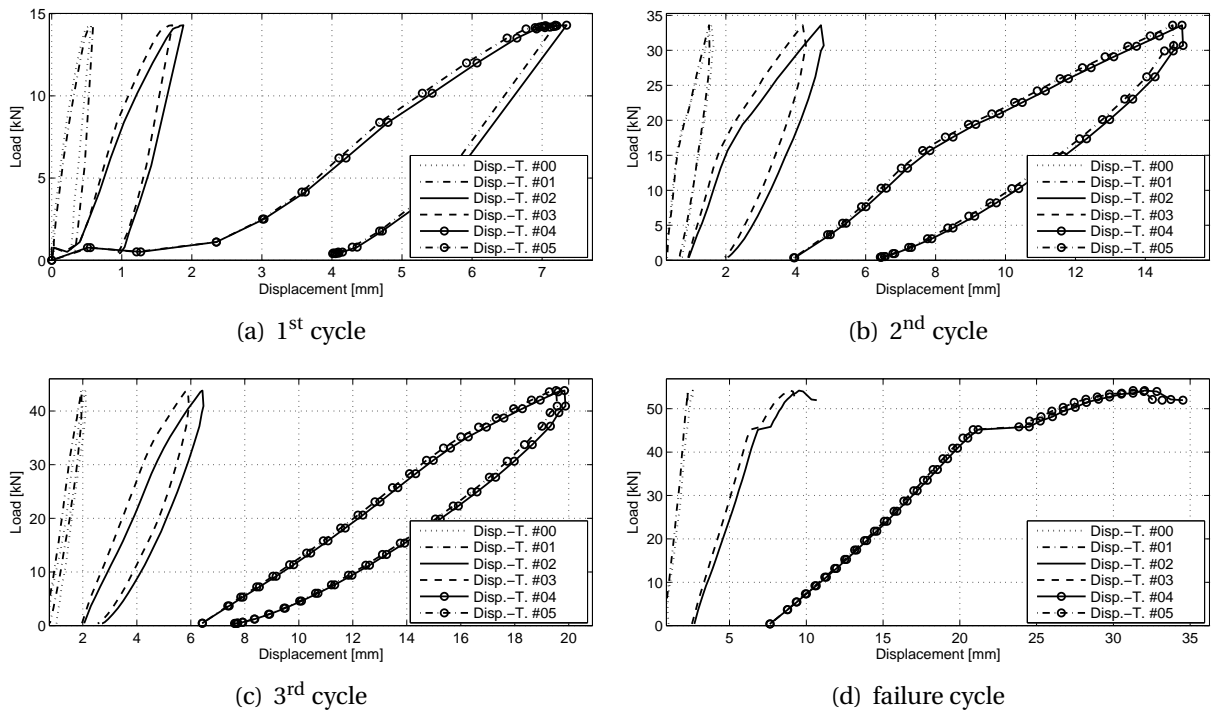


Figure F.18: Vertical displacements for S200C2

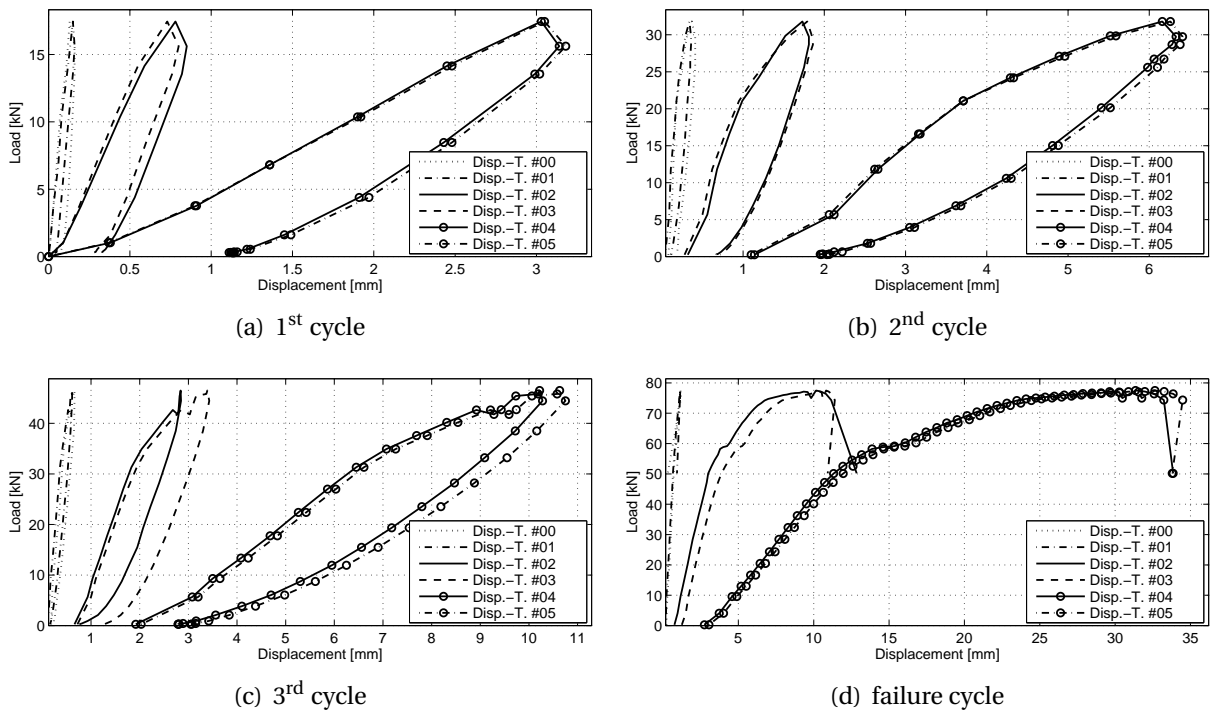


Figure F.19: Vertical displacements for S240C1

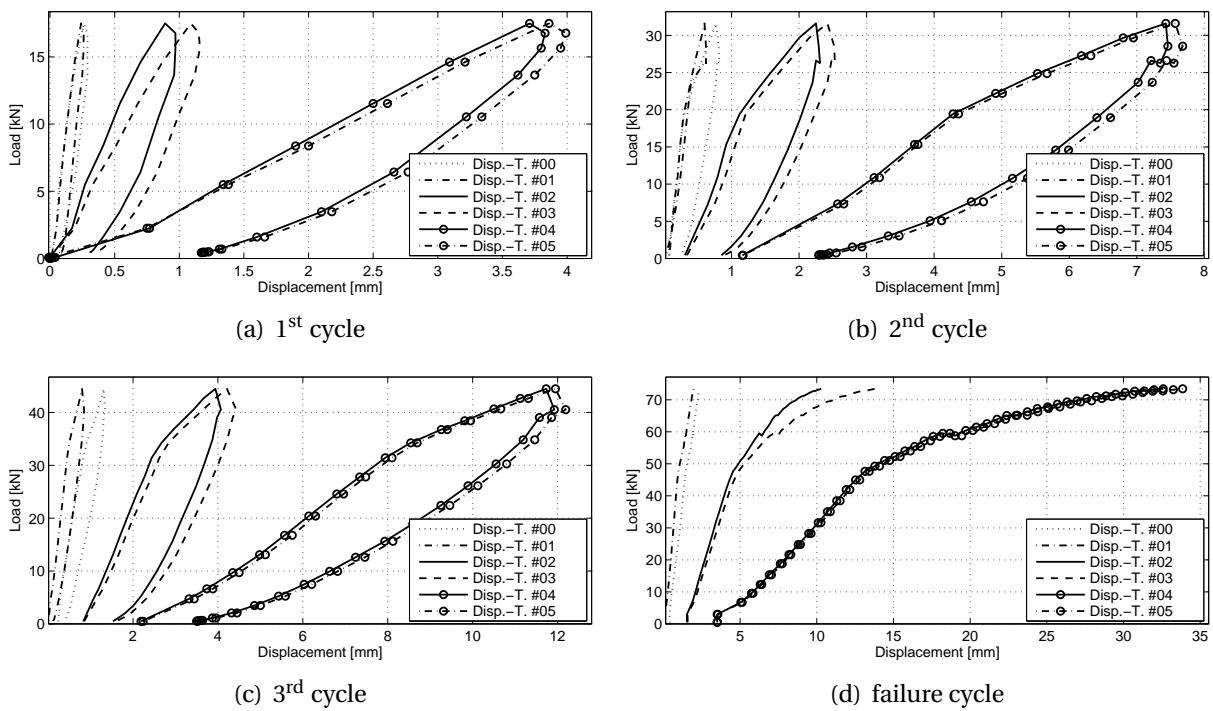


Figure F.20: Vertical displacements for S240C2

F.3.2. Horizontal Displacements

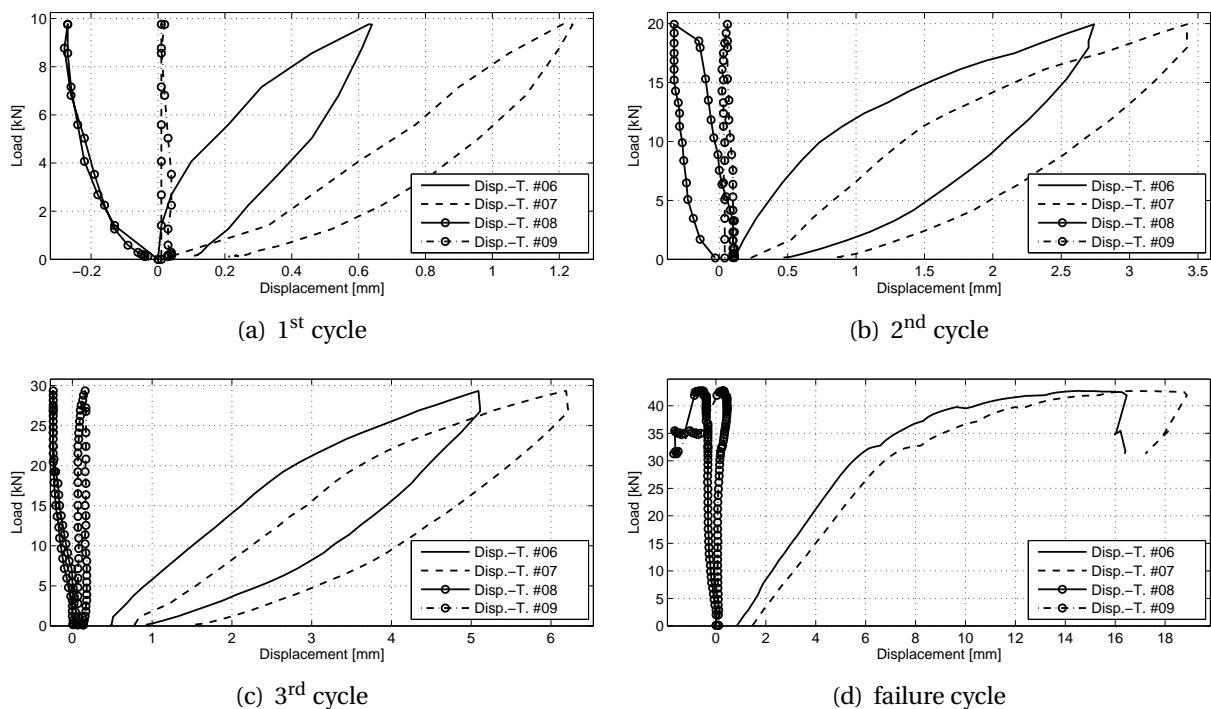


Figure F.21: Horizontal displacements for M200E1

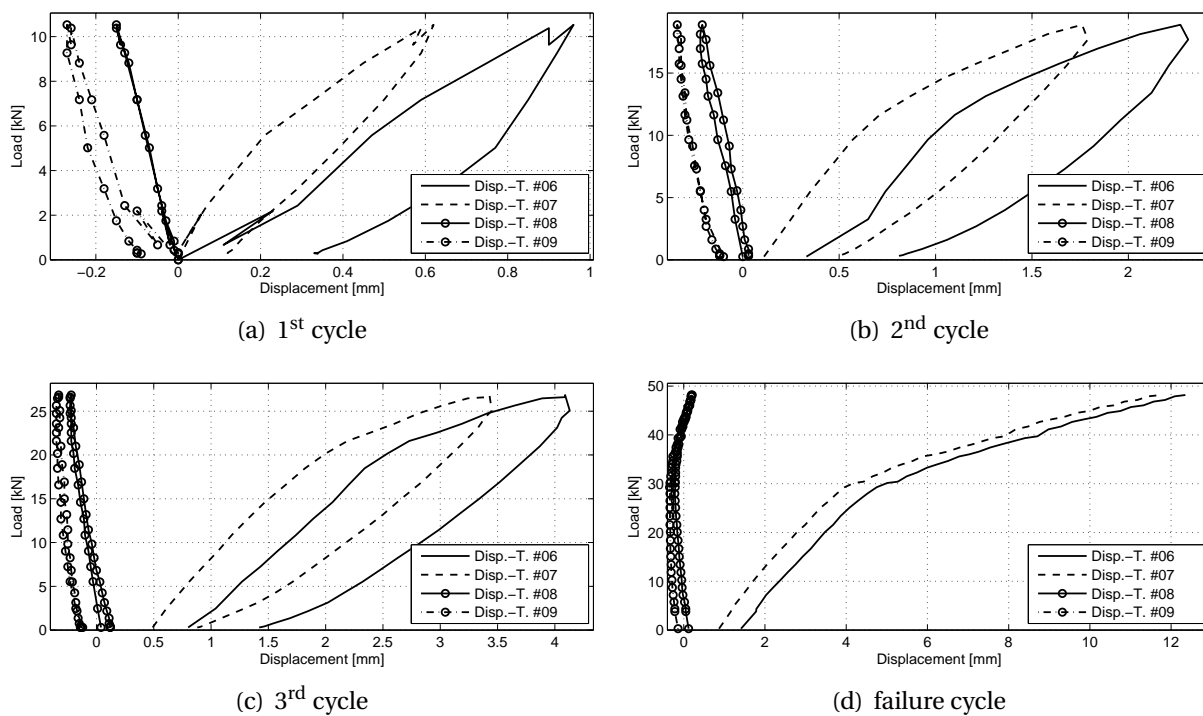


Figure F.22: Horizontal displacements for M200E2

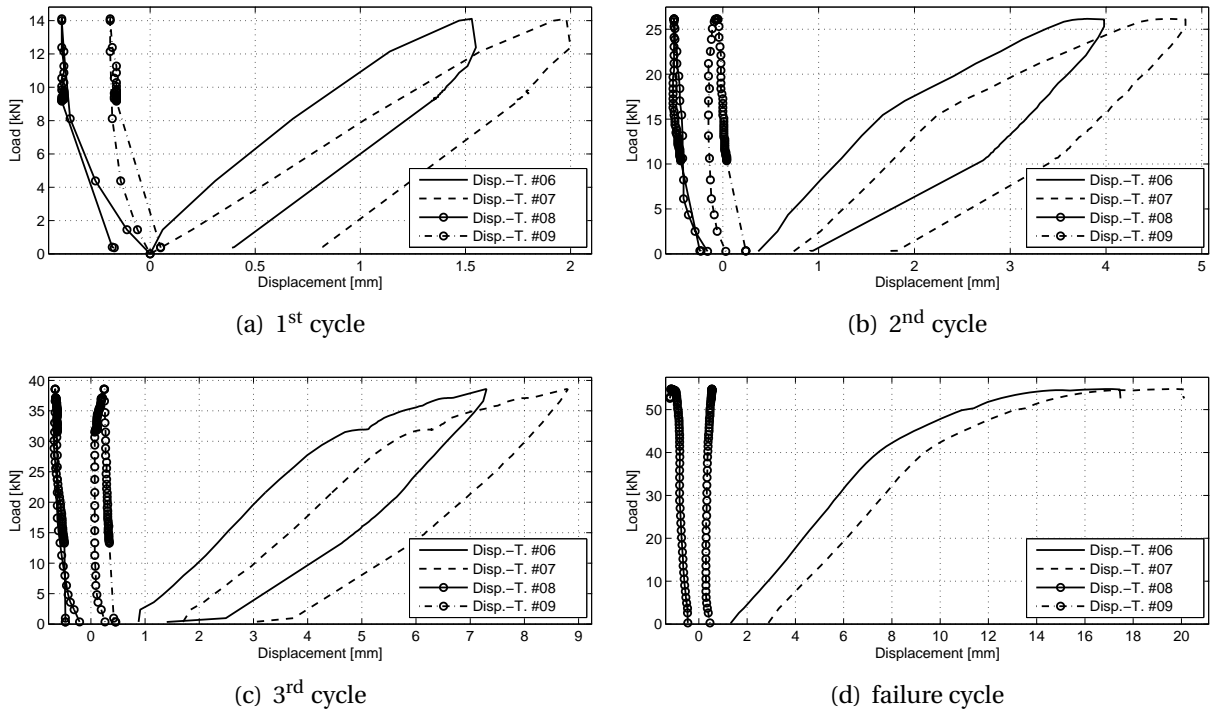


Figure F.23: Horizontal displacements for M240E1

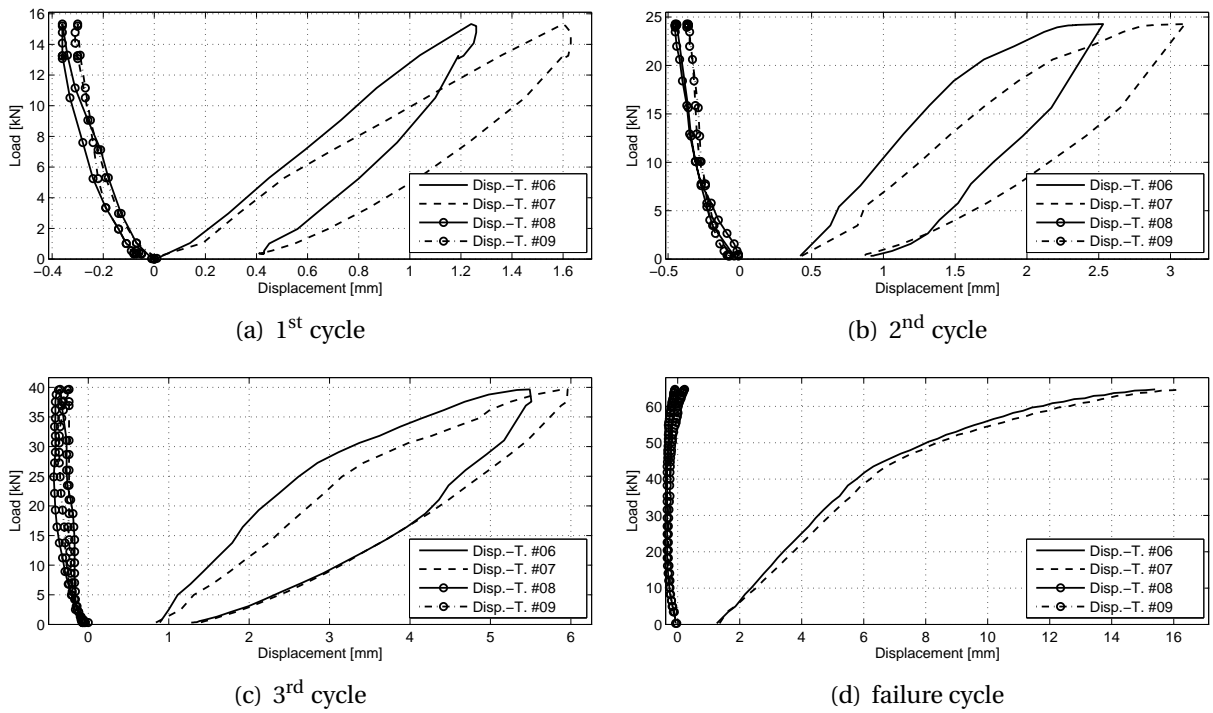


Figure F.24: Horizontal displacements for M240E2

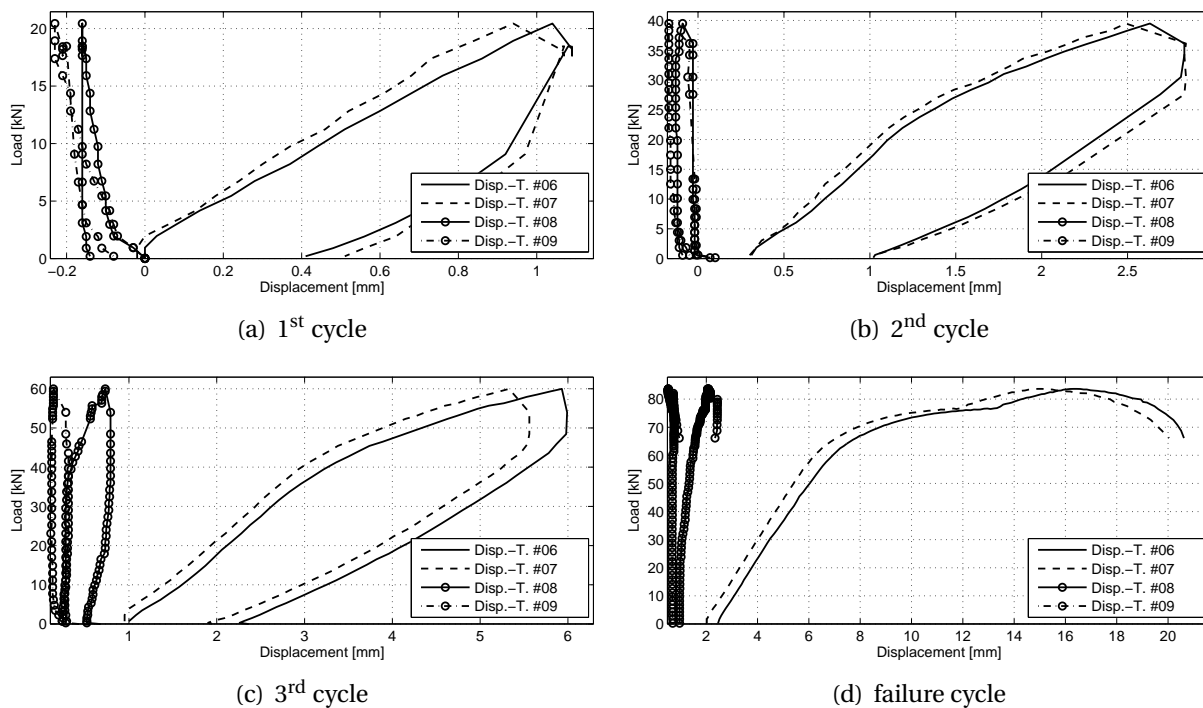


Figure F.25: Horizontal displacements for S200Ea

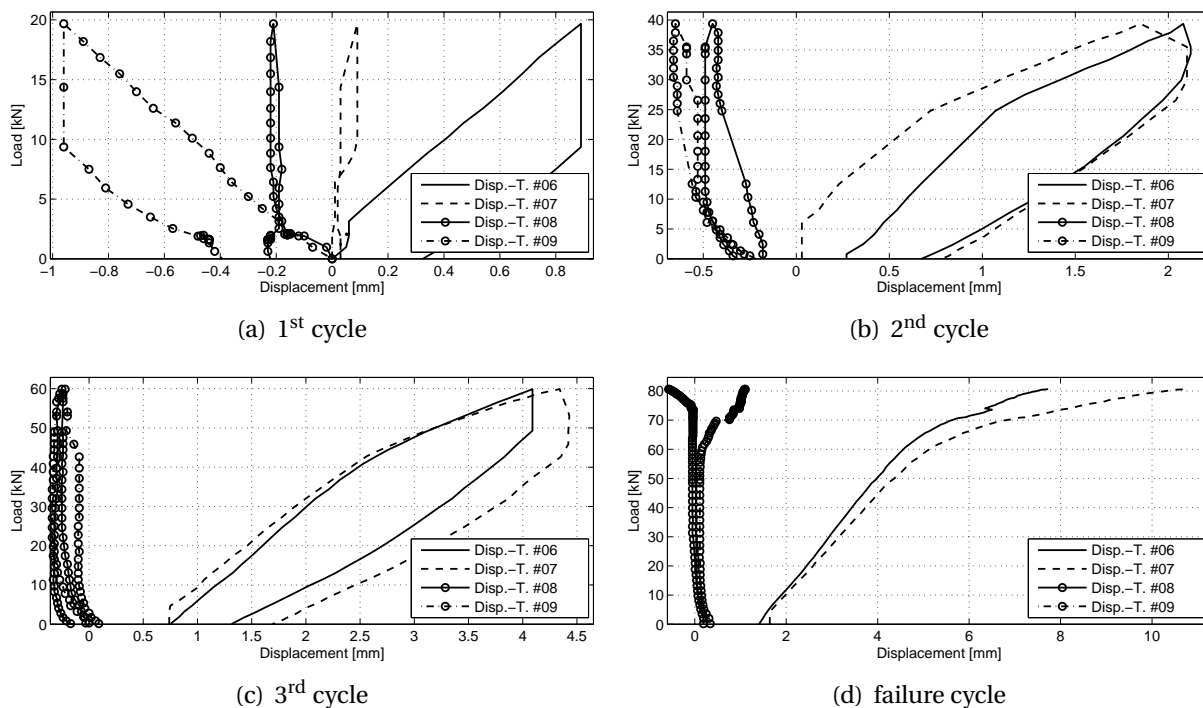


Figure F.26: Horizontal displacements for S240Ea

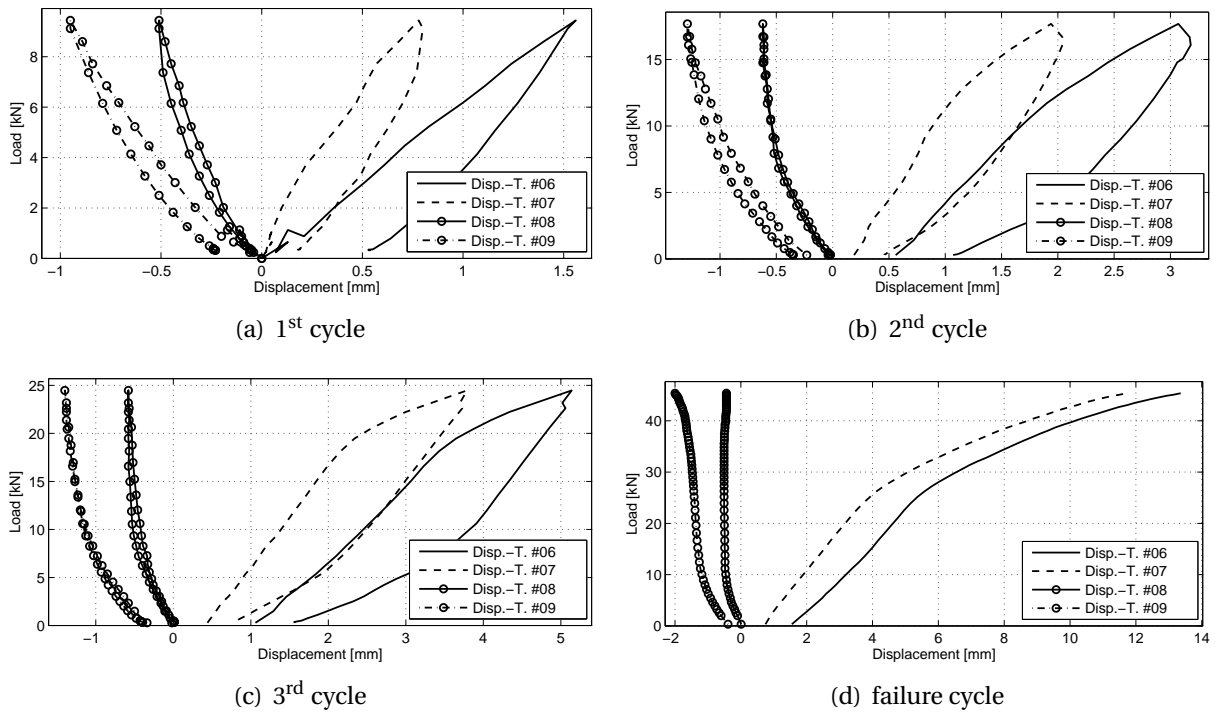


Figure F.27: Horizontal displacements for M200C1

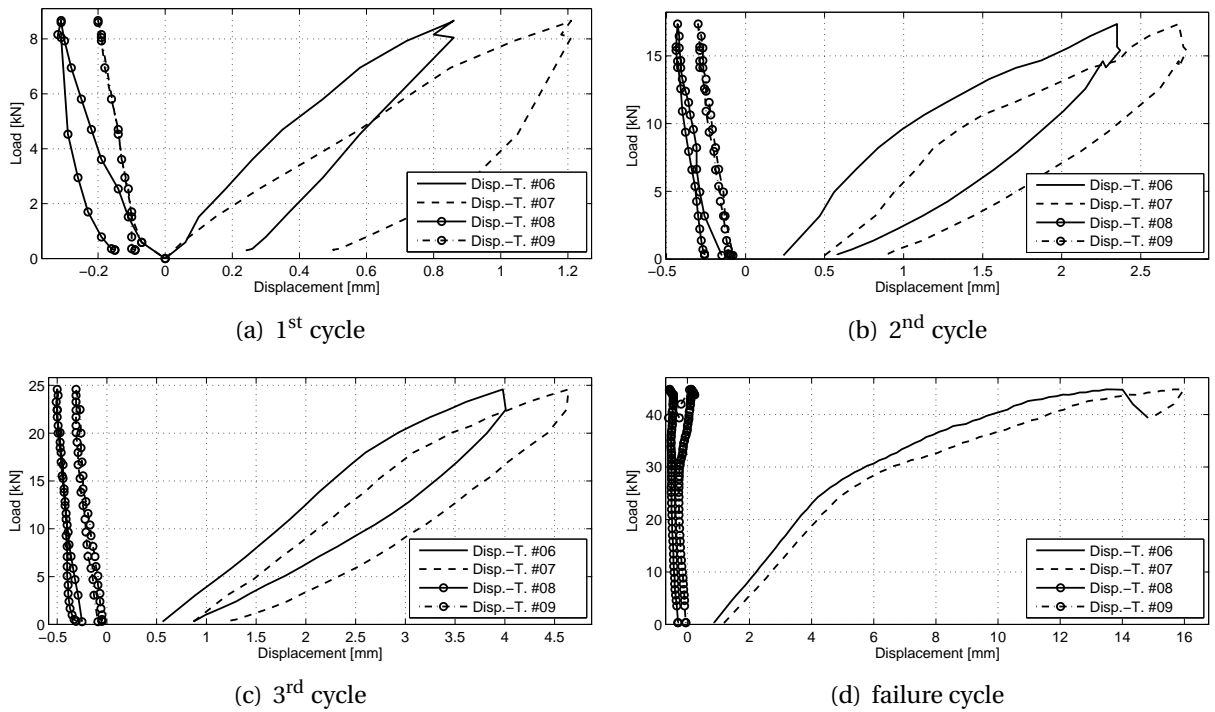


Figure F.28: Horizontal displacements for M200C2

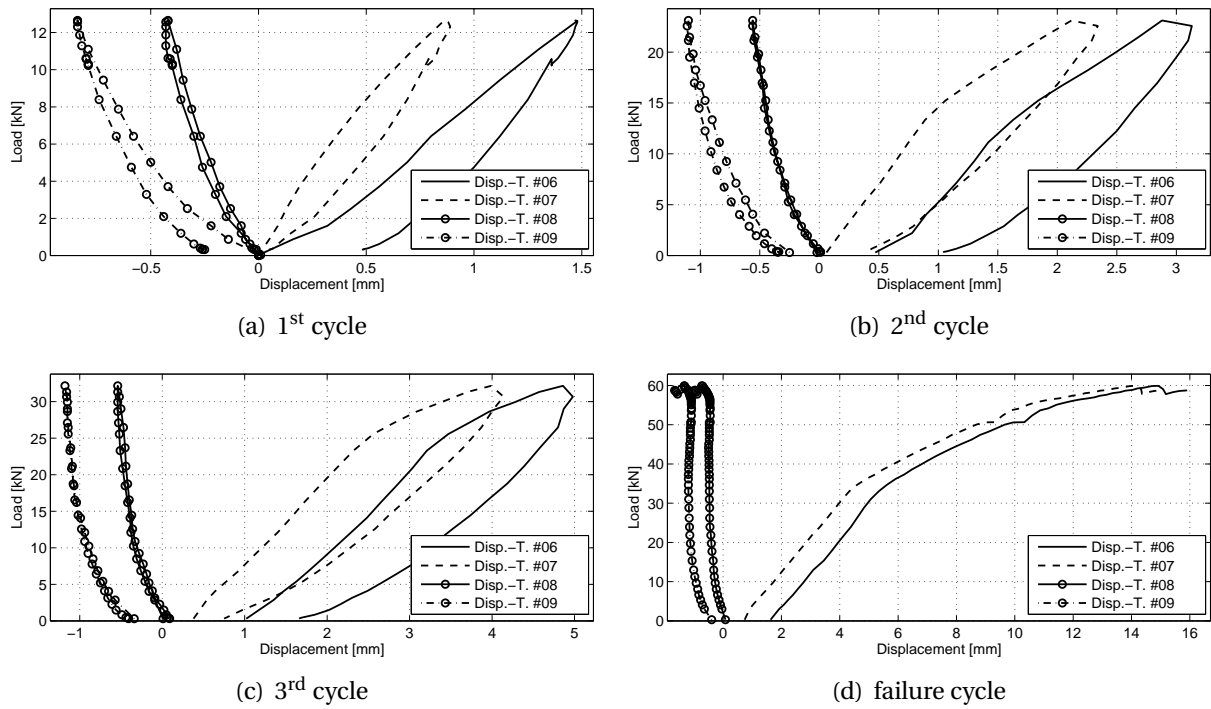


Figure F.29: Horizontal displacements for M240C1

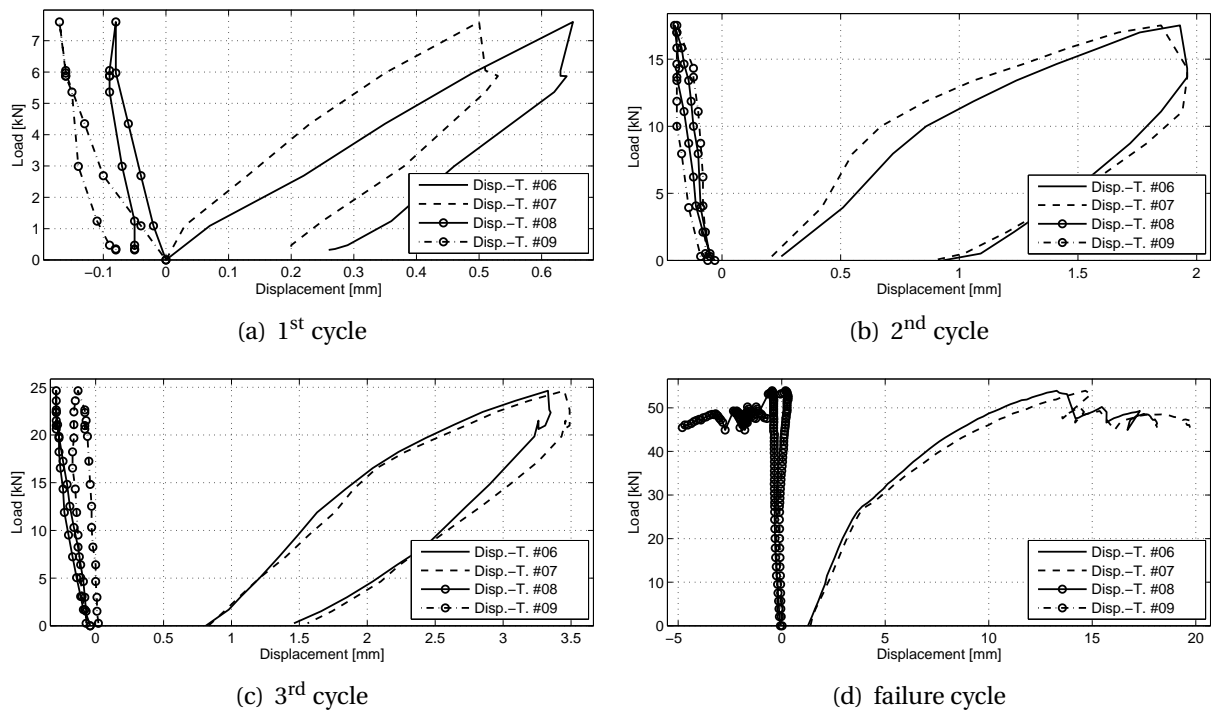


Figure F.30: Horizontal displacements for M240C2

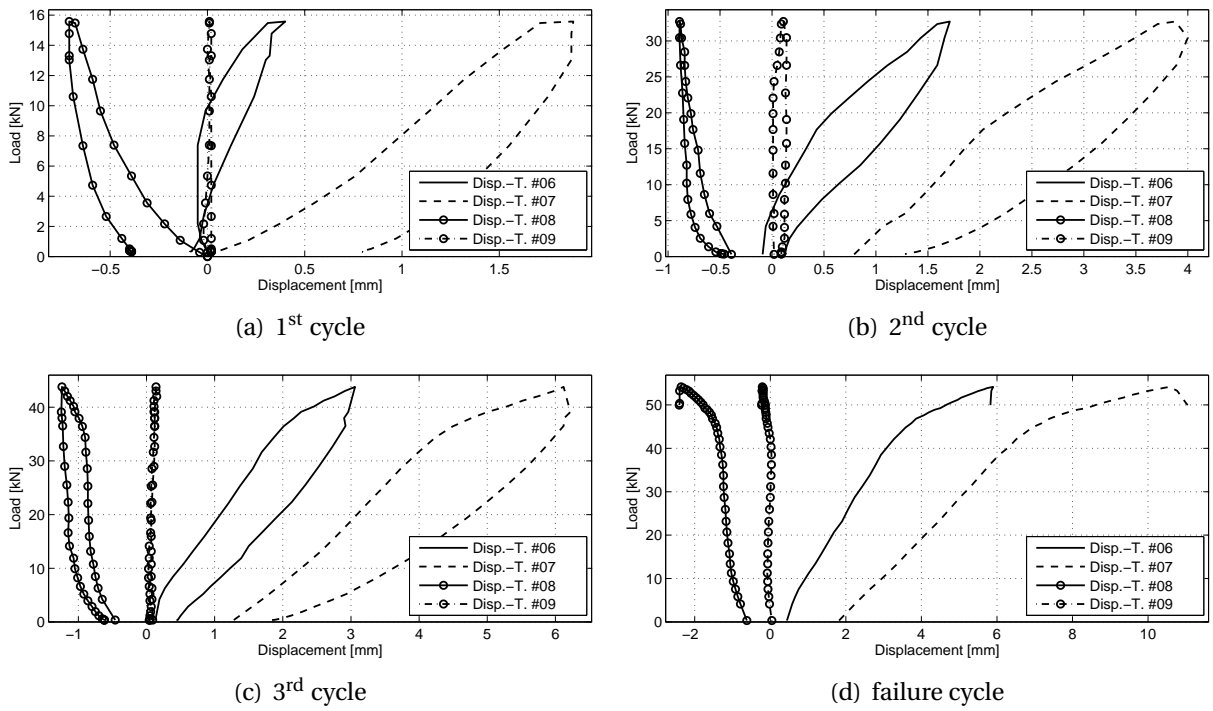


Figure F.31: Horizontal displacements for S200C1

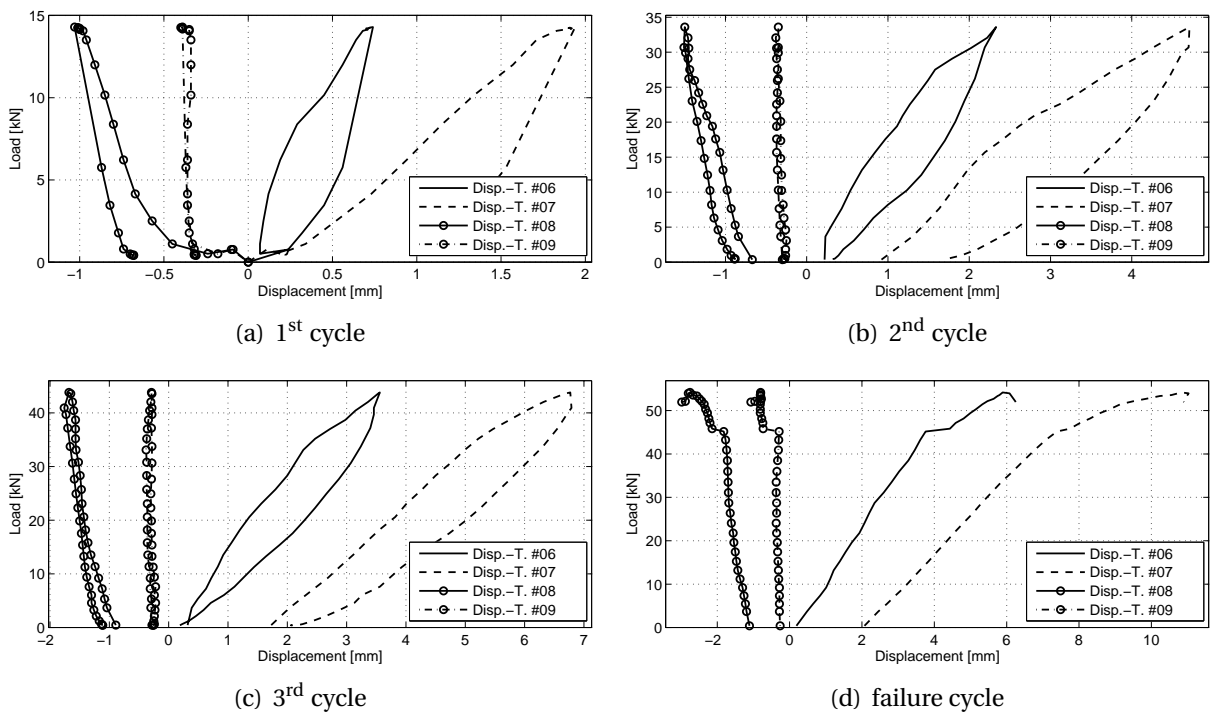


Figure F.32: Horizontal displacements for S200C2

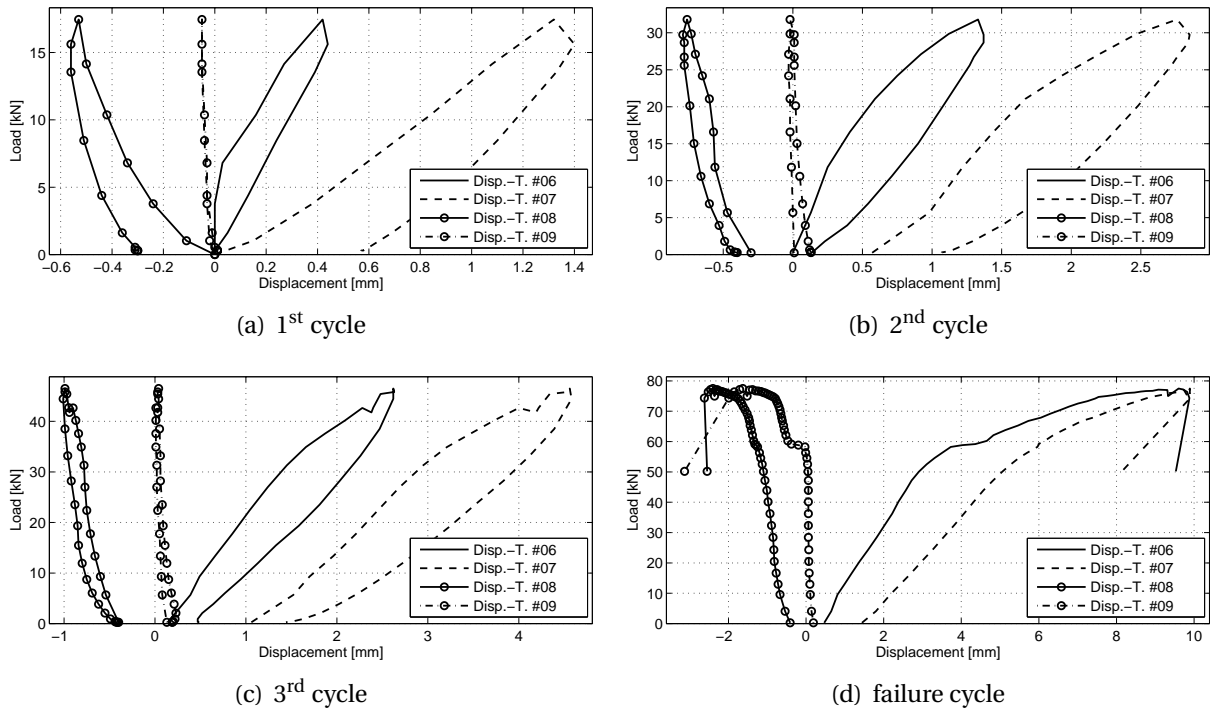


Figure F.33: Horizontal displacements for S240C1

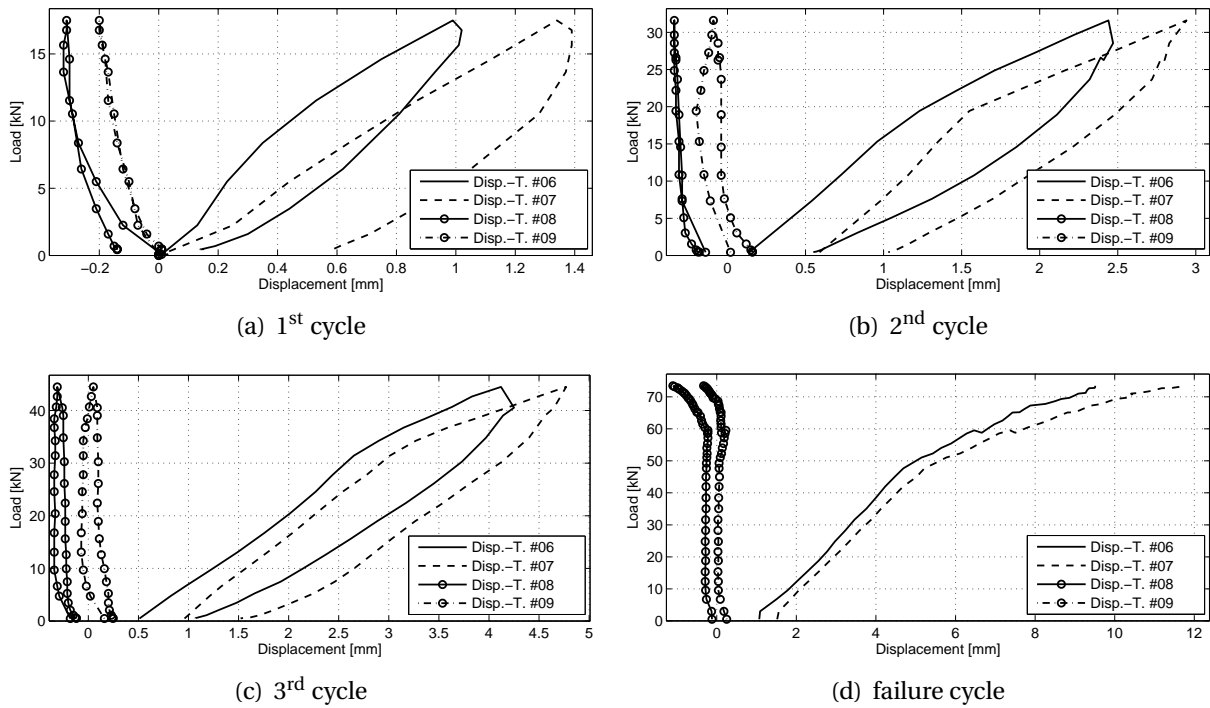


Figure F.34: Horizontal displacements for S240C2

F.4. Displacement and deformation patterns

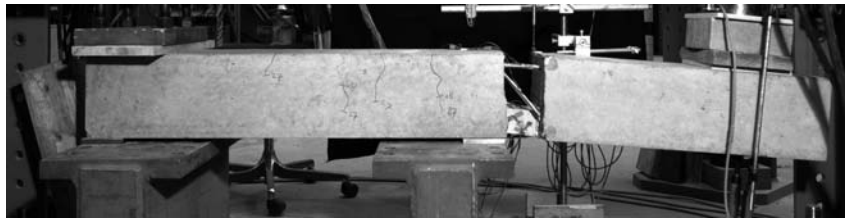


Figure F.35: M200E2



Figure F.36: M240E2

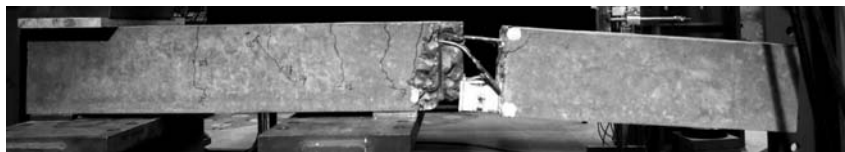


Figure F.37: M200C2

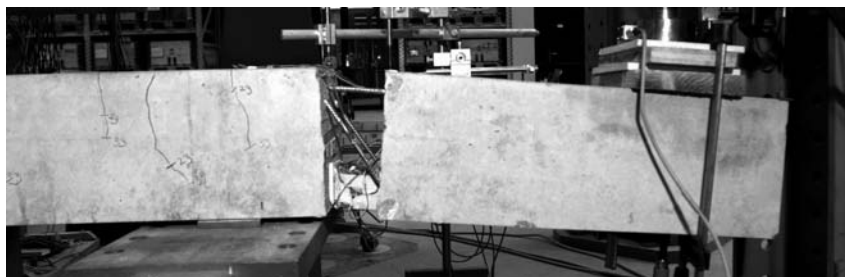


Figure F.38: M240C1

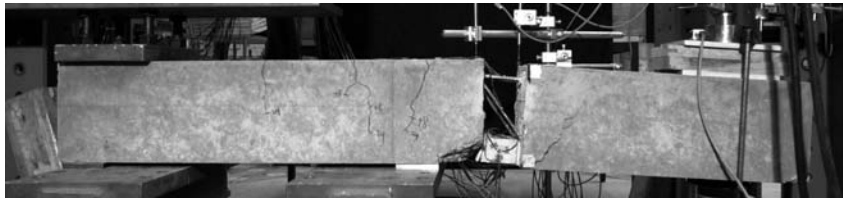


Figure F.39: M240C2



Figure F.40: S200E2

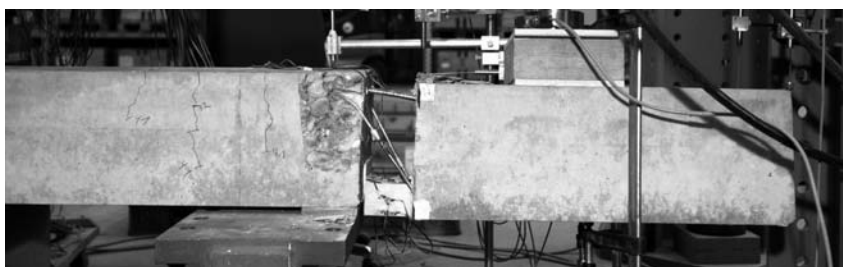


Figure F.41: S240E1

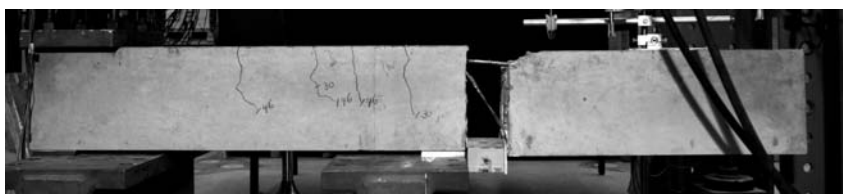


Figure F.42: S240E2

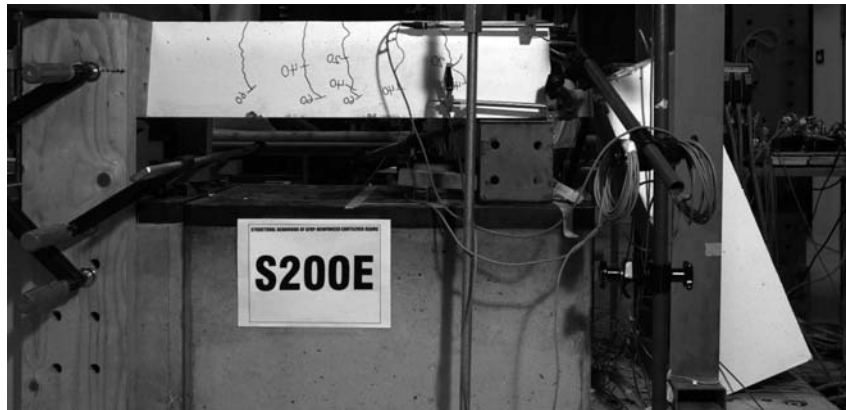


Figure F.43: S200E3

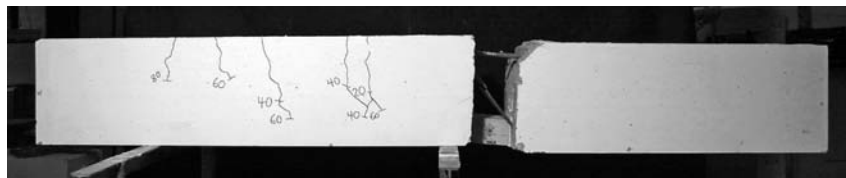


Figure F.44: S240E3

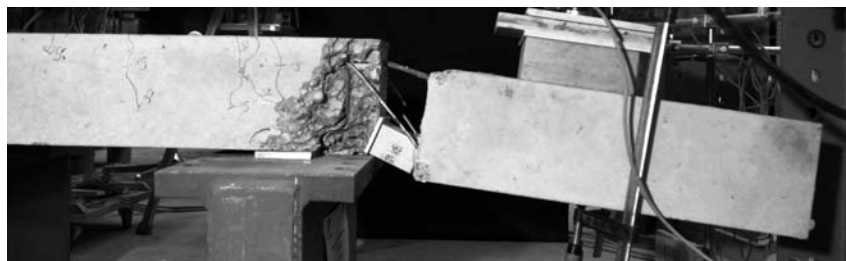


Figure F.45: S200C1

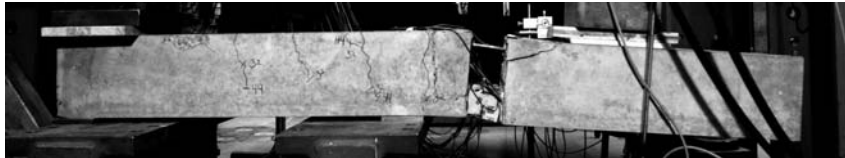


Figure F.46: S200C2



Figure F.47: S240C1



Figure F.48: S240C2



Figure F.53: M200C1



Figure F.54: M200C2



Figure F.55: M240C1

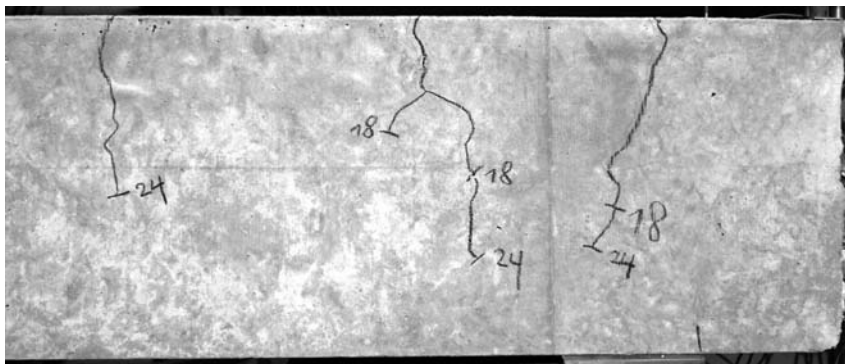


Figure F.56: M240C2

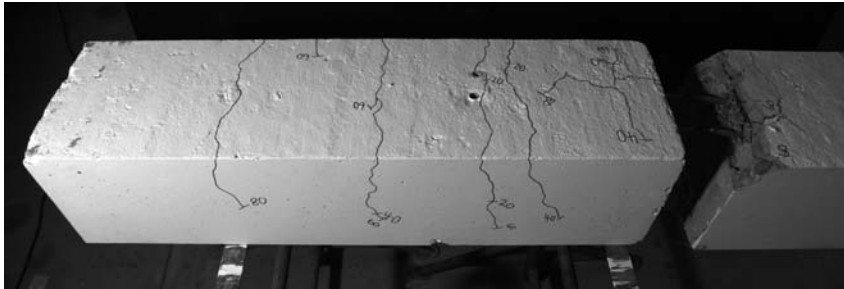


Figure F.62: S240E3



Figure F.63: S200C1

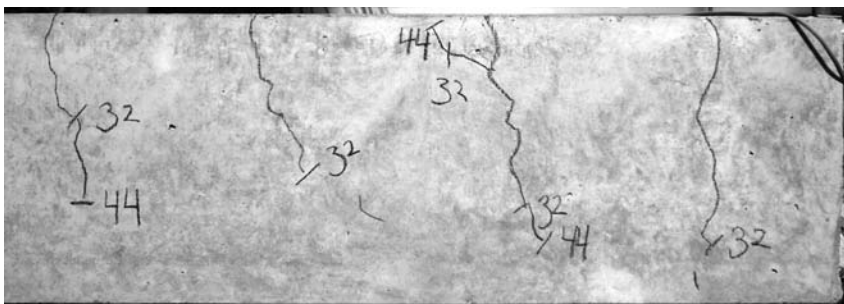


Figure F.64: S200C2

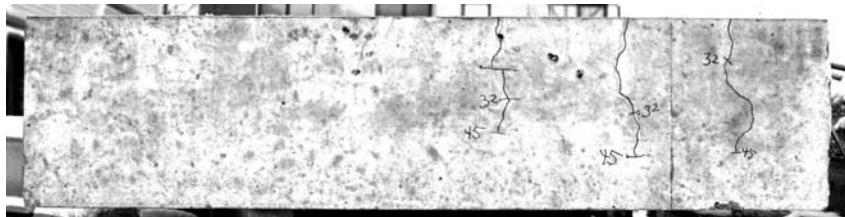


Figure F.65: S240C1

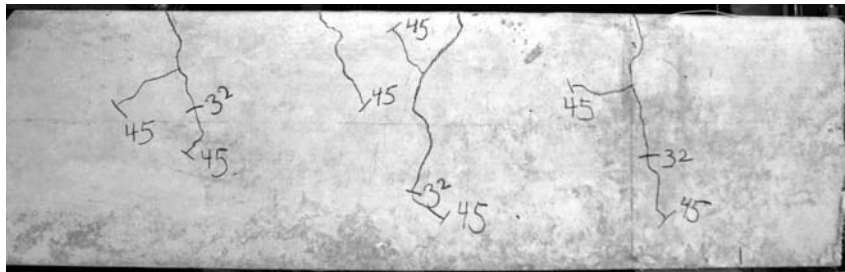


Figure F.66: S240C2

F.6. Axial strain on steel reinforcement and CS-element

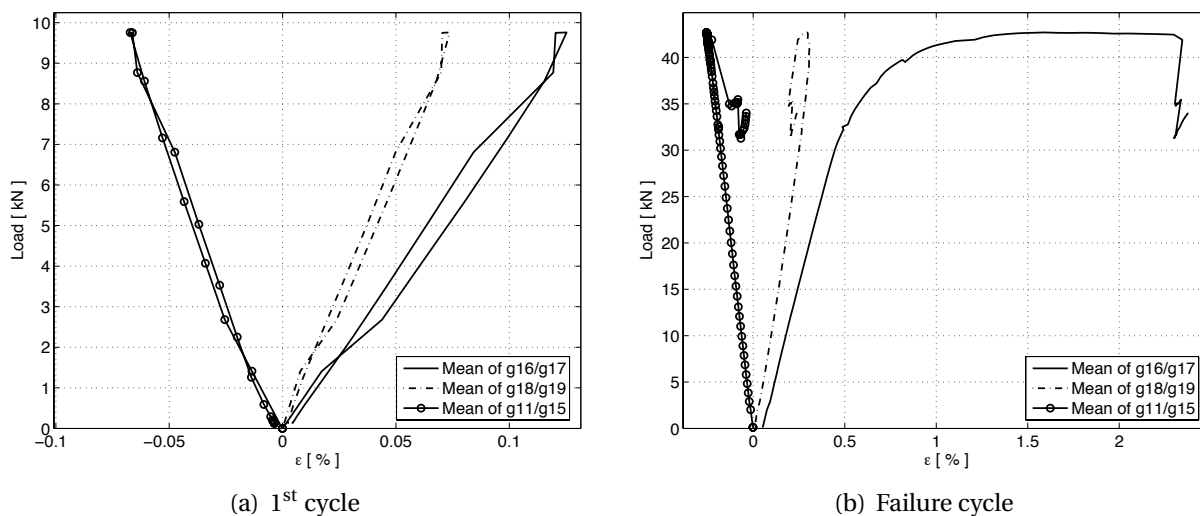


Figure F.67: M200E1

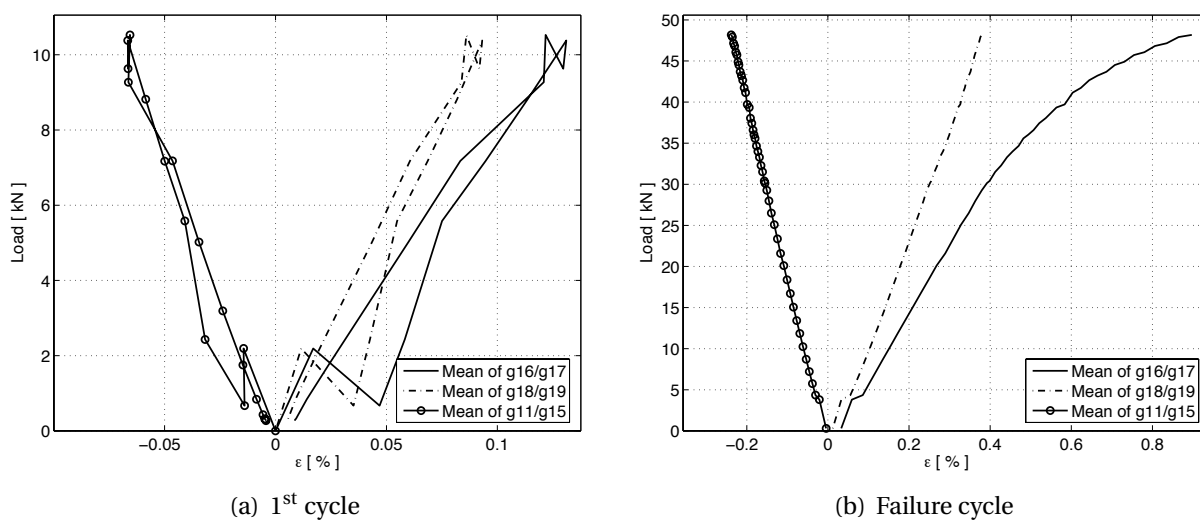


Figure F.68: M200E2

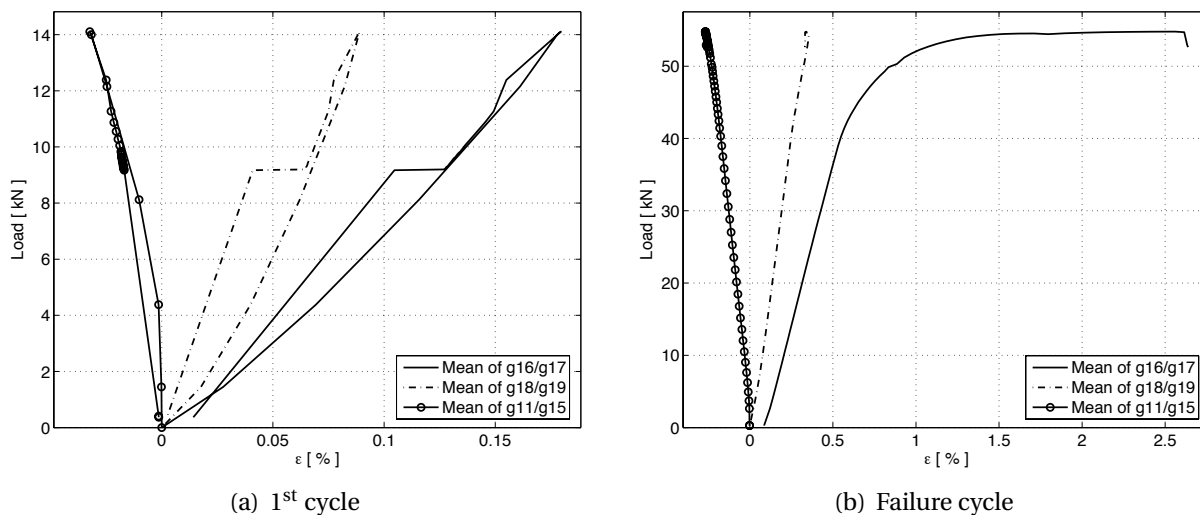
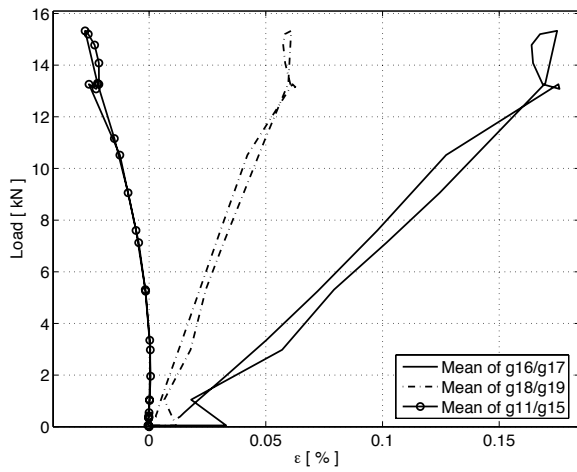
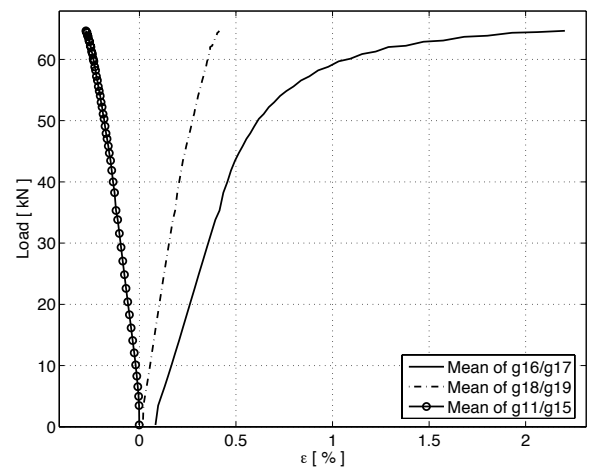


Figure F.69: M240E1

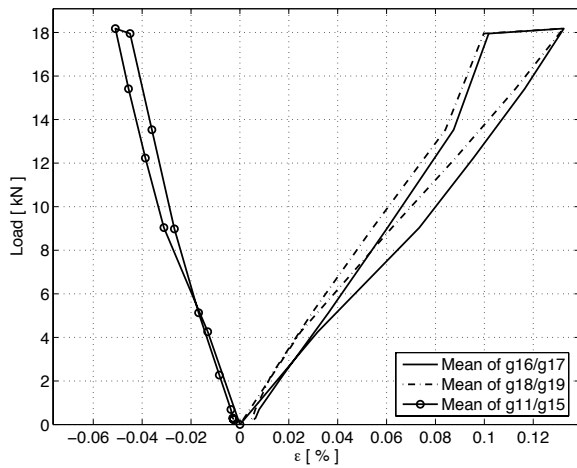


(a) 1st cycle

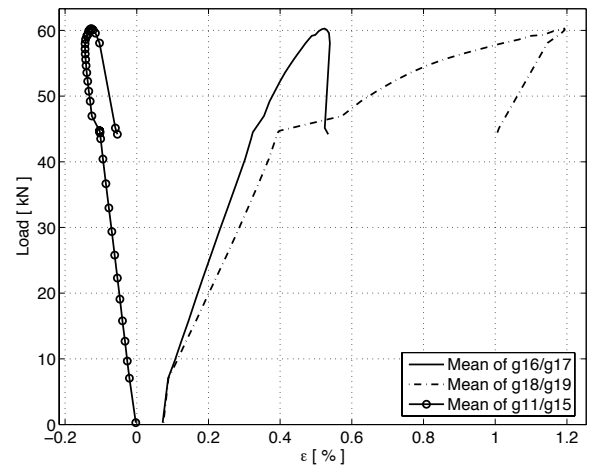


(b) Failure cycle

Figure F.70: M240E2

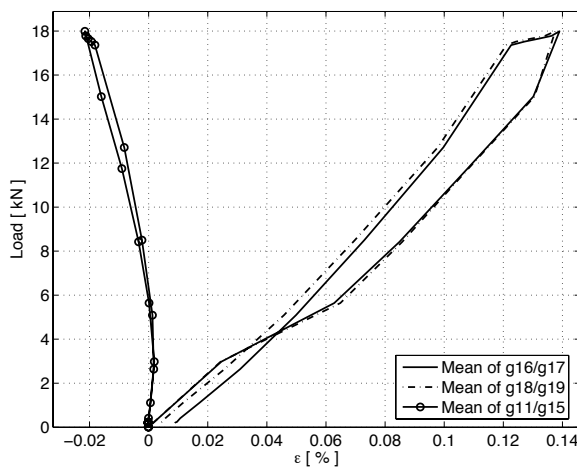


(a) 1st cycle

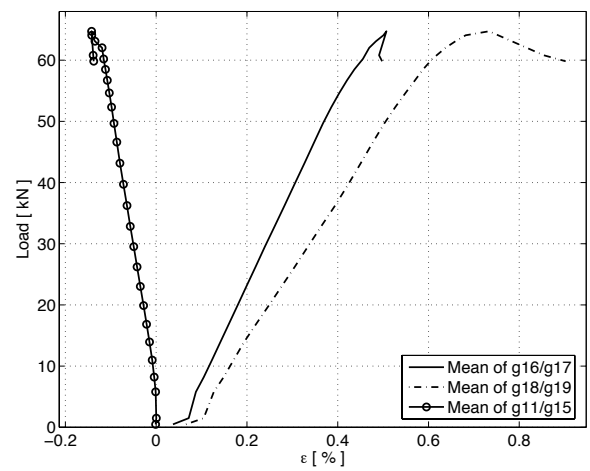


(b) Failure cycle

Figure F.71: S200E1



(a) 1st cycle



(b) Failure cycle

Figure F.72: S200E2

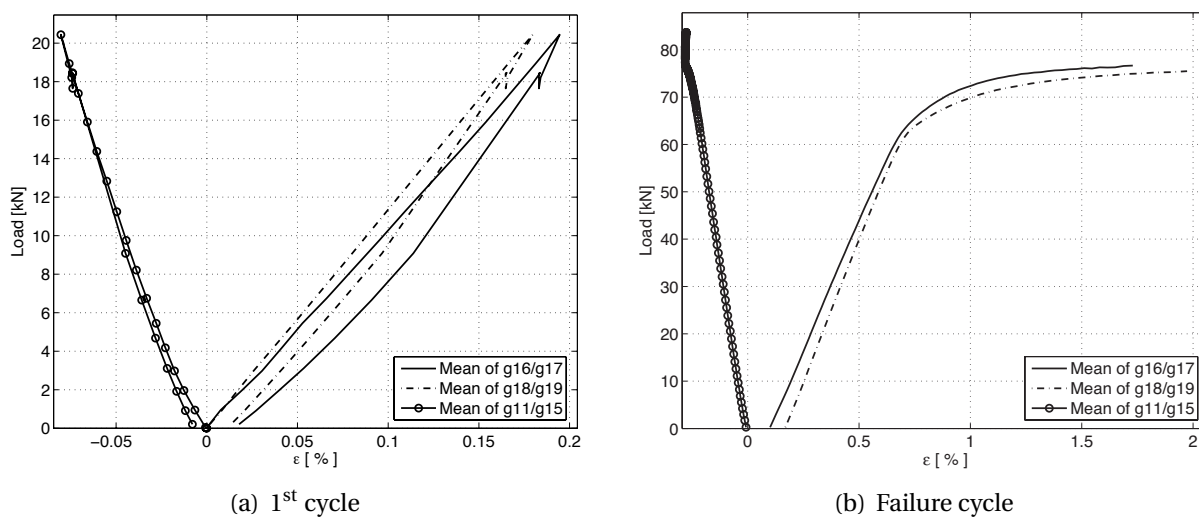


Figure F.73: S200E3

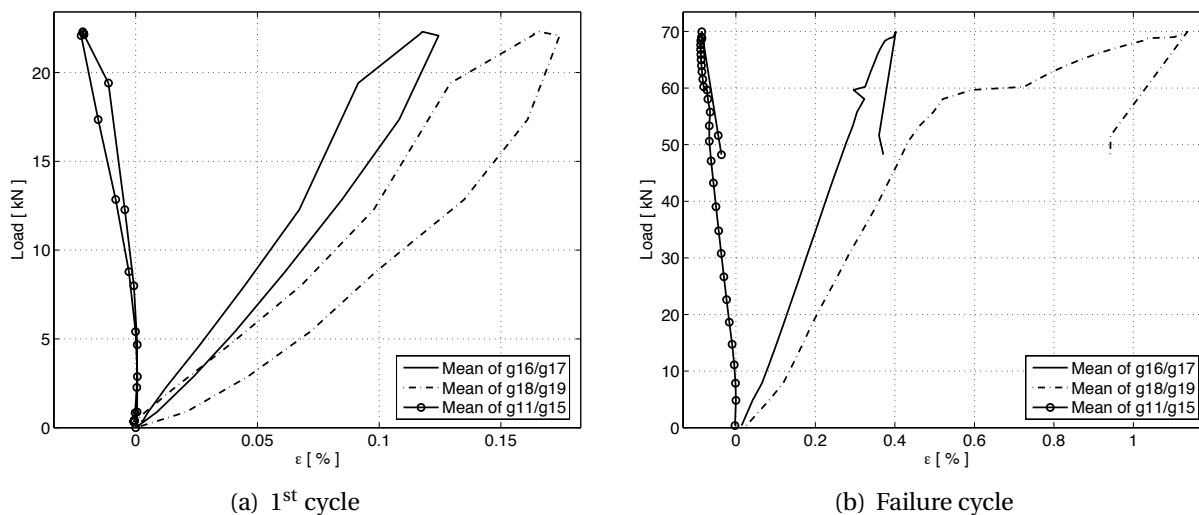


Figure F.74: S240E1

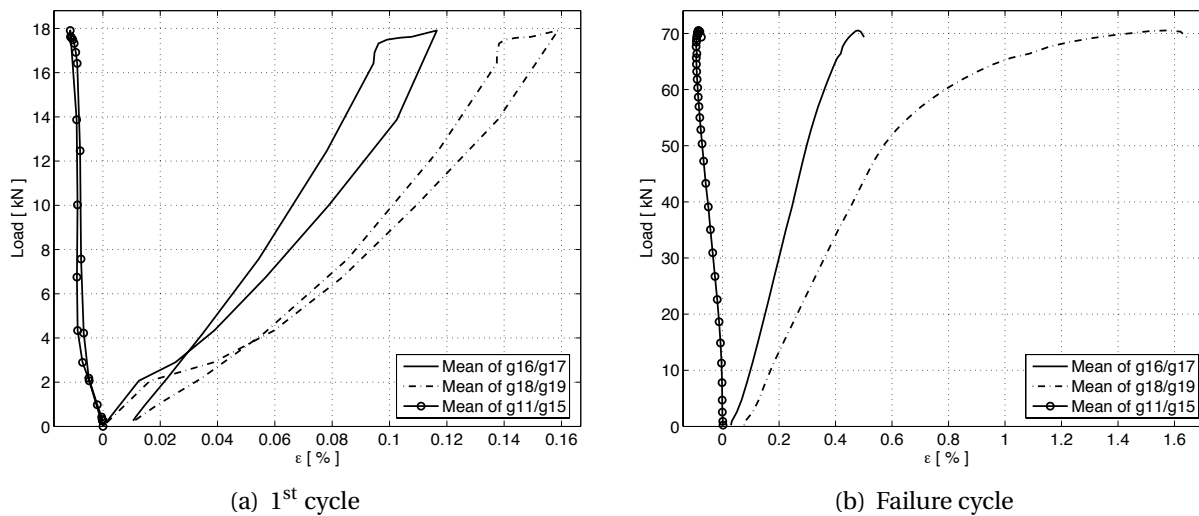
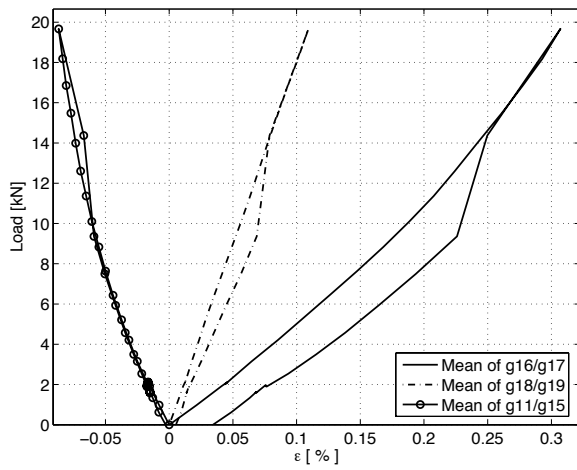
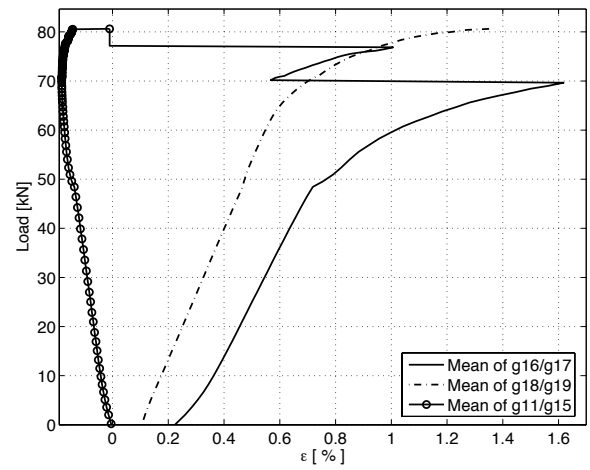


Figure F.75: S240E2

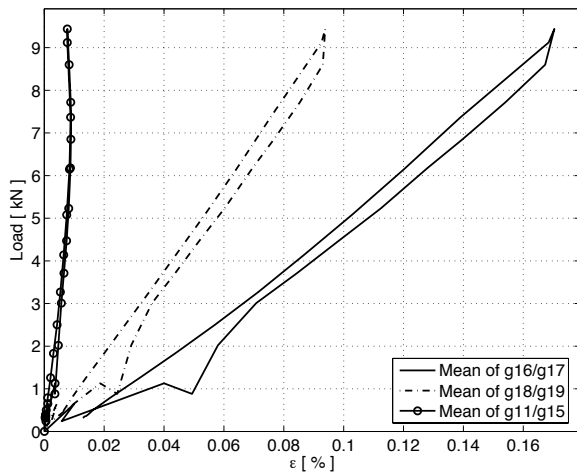


(a) 1st cycle

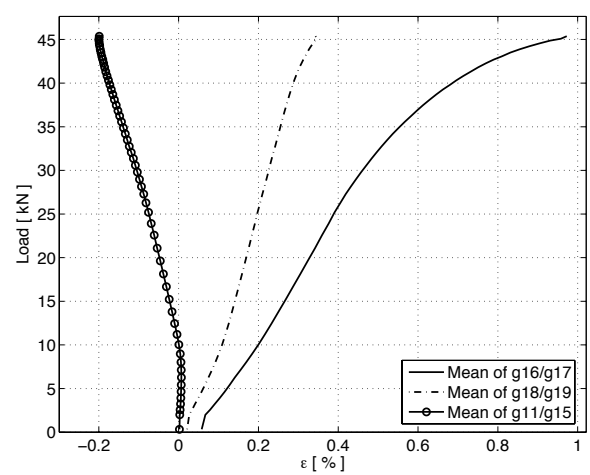


(b) Failure cycle

Figure F.76: S240E3

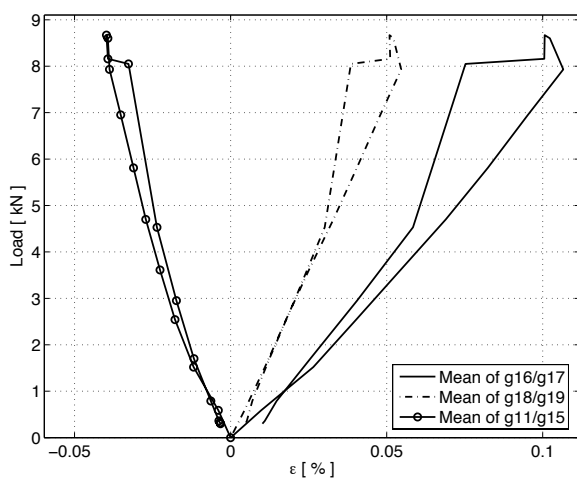


(a) 1st cycle

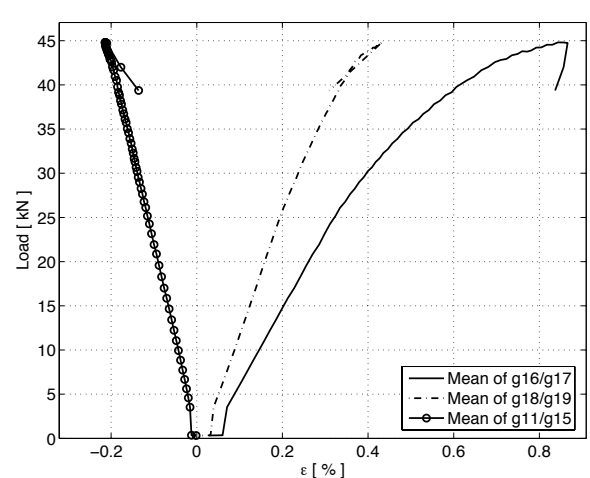


(b) Failure cycle

Figure F.77: M200C1

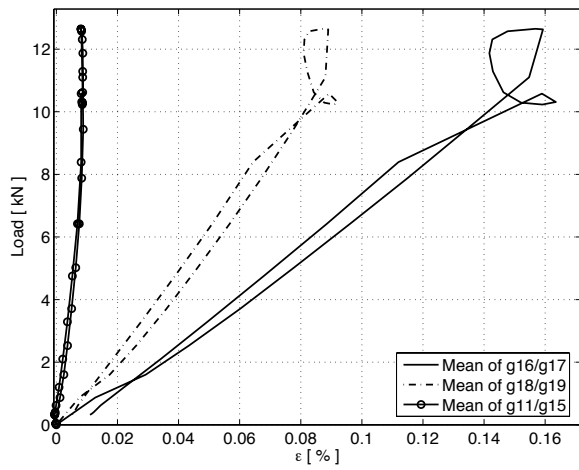


(a) 1st cycle

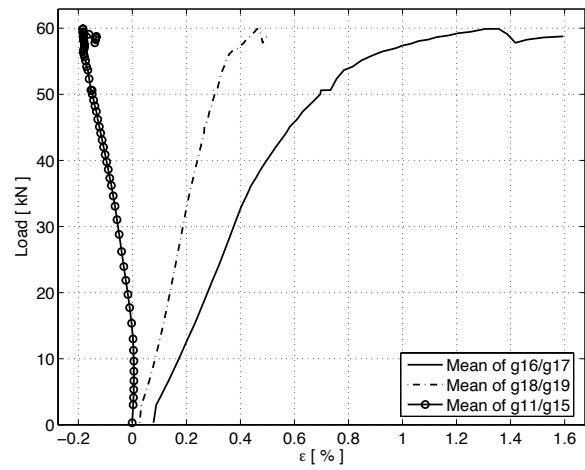


(b) Failure cycle

Figure F.78: M200C2

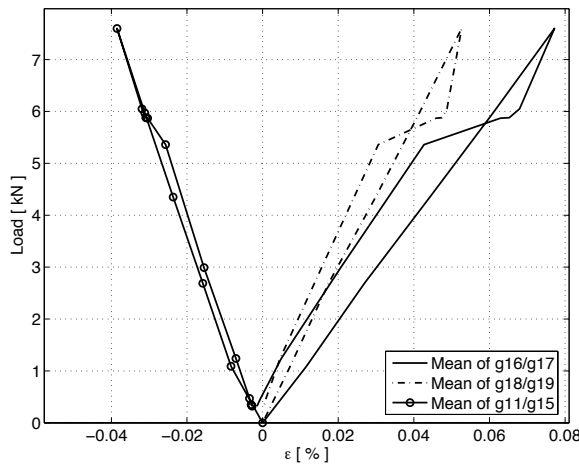


(a) 1st cycle

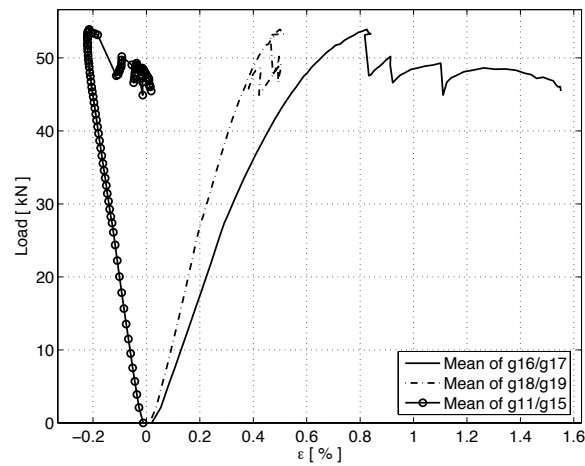


(b) Failure cycle

Figure F.79: M240C1

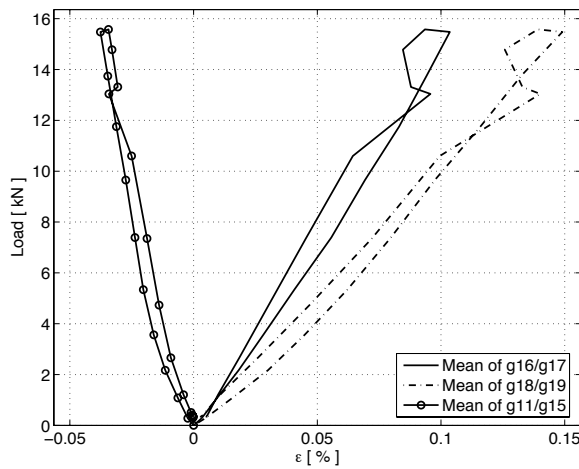


(a) 1st cycle

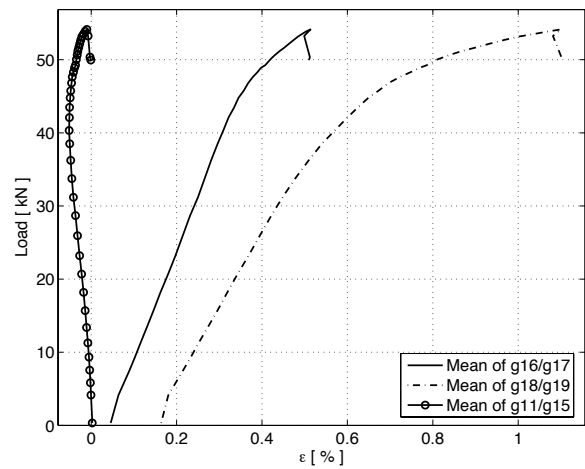


(b) Failure cycle

Figure F.80: M240C2

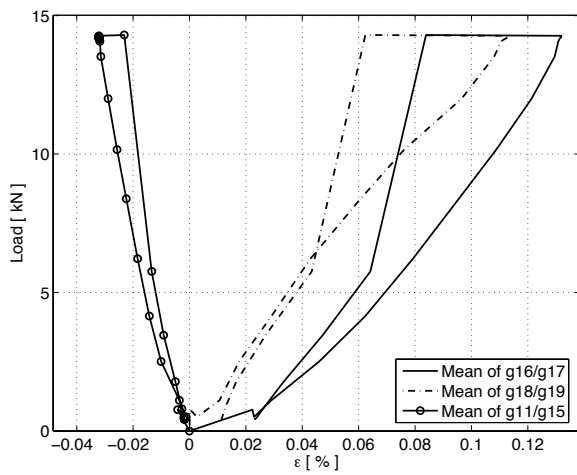


(a) 1st cycle

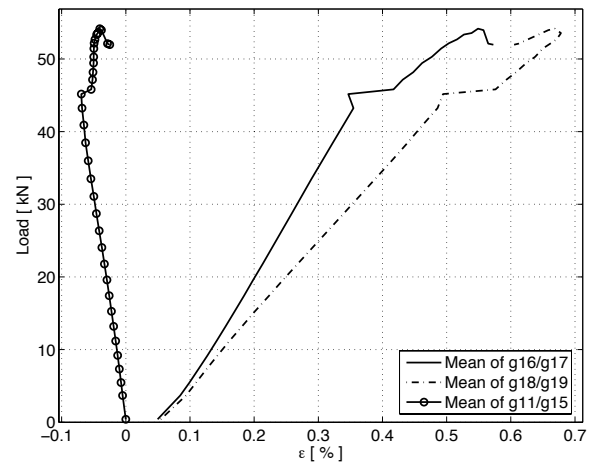


(b) Failure cycle

Figure F.81: S200C1

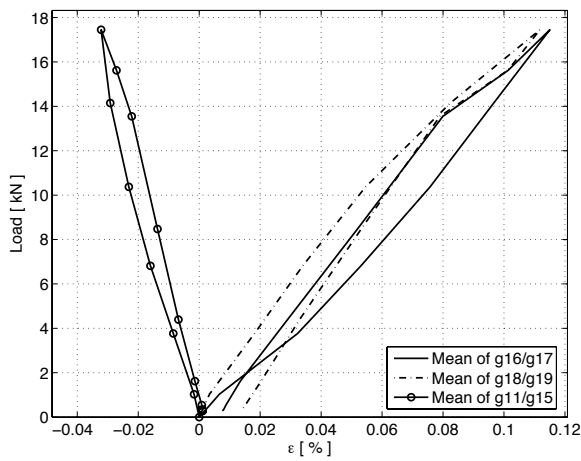


(a) 1st cycle

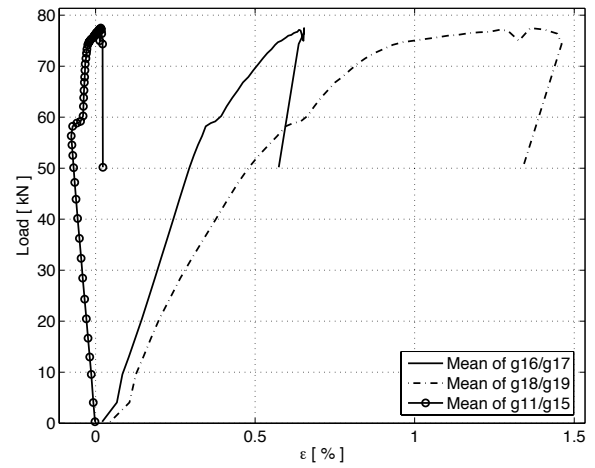


(b) Failure cycle

Figure F.82: S200C2

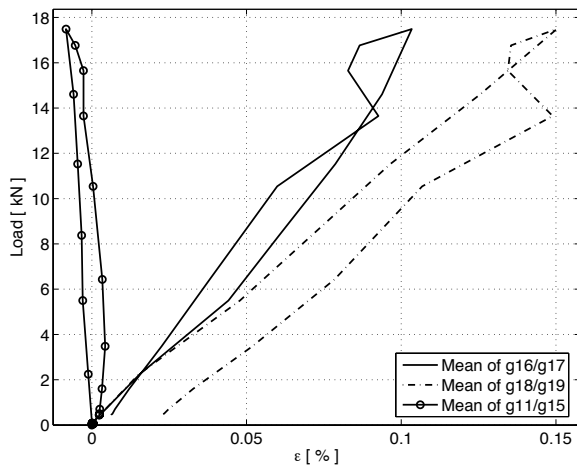


(a) 1st cycle

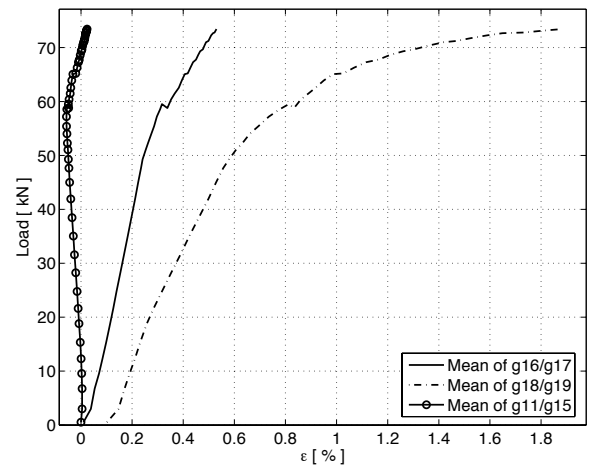


(b) Failure cycle

Figure F.83: S240C1



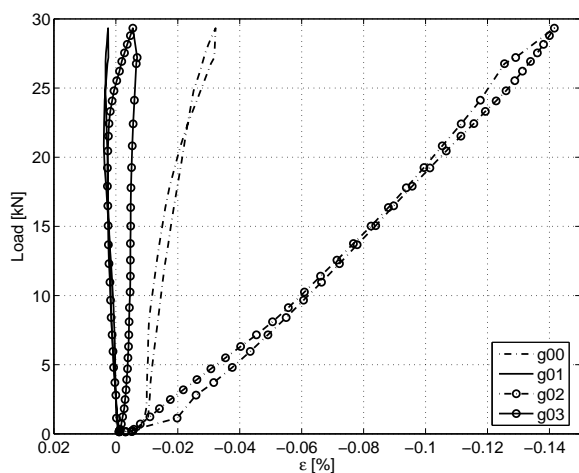
(a) 1st cycle



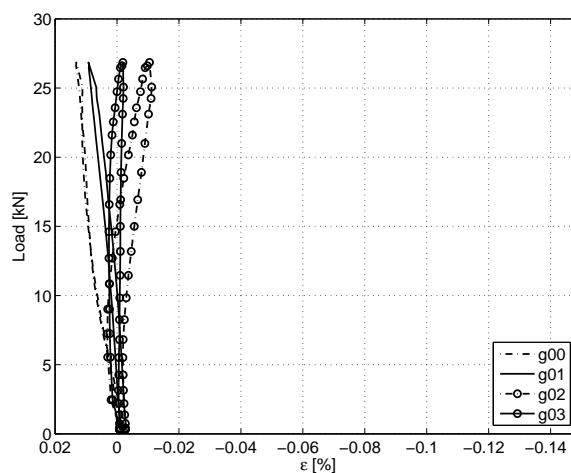
(b) Failure cycle

Figure F.84: S240C2

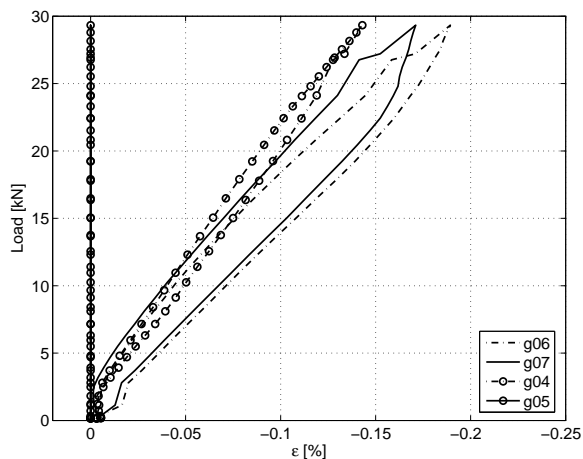
F.7. Strain on CS-element surfaces



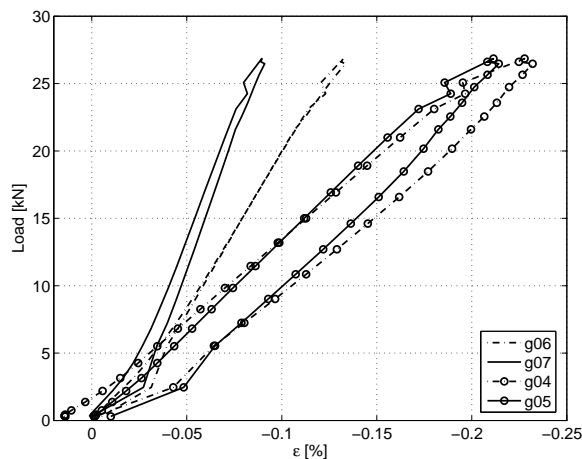
(a) Top side - 1st series



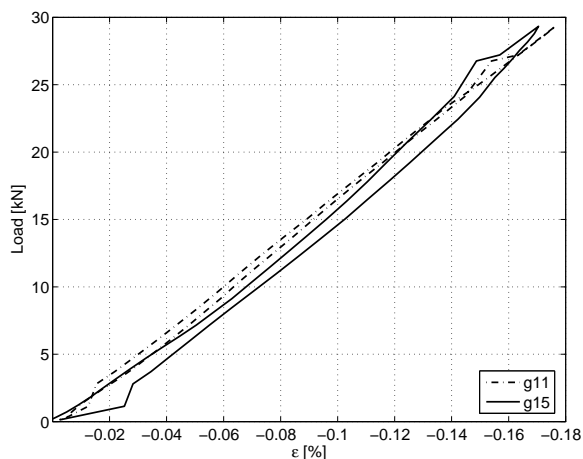
(b) Top side - 2nd series



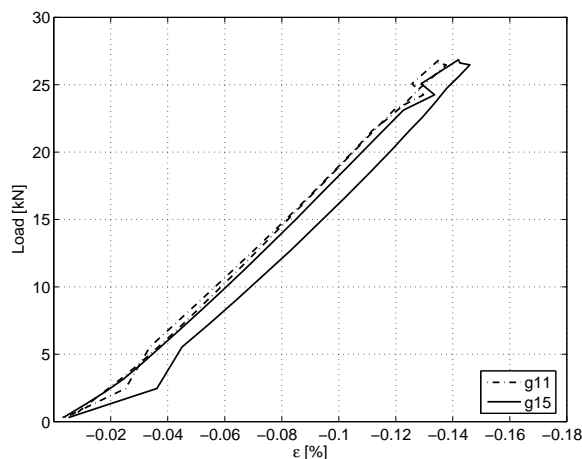
(c) Bottom side 1st series



(d) Bottom side 2nd series

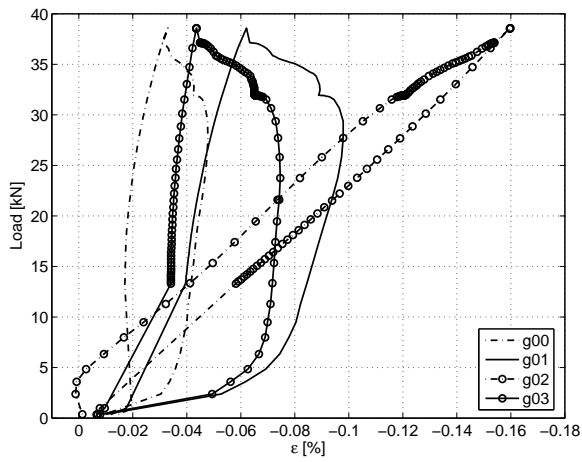


(e) Lateral sides 1st series

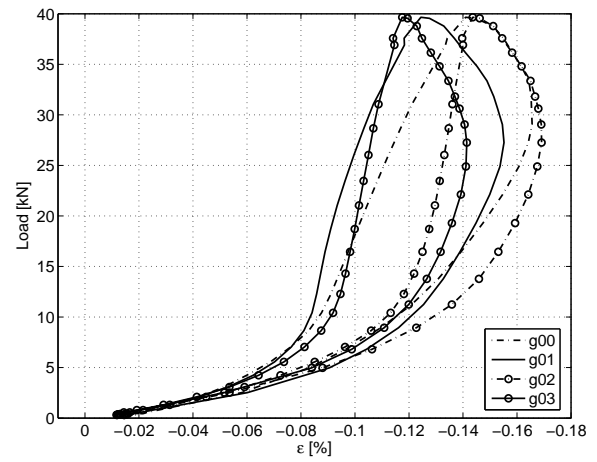


(f) Lateral sides 2nd series

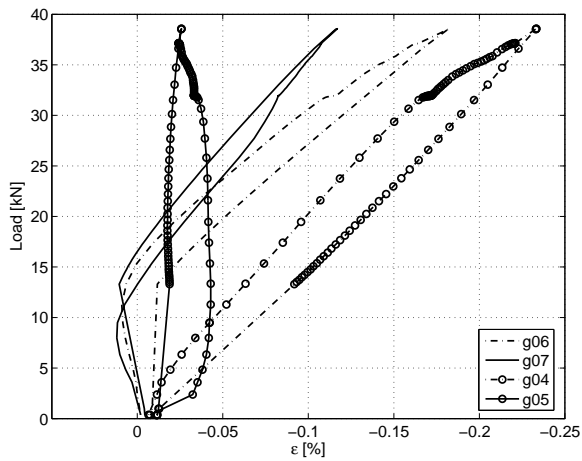
Figure F.85: M200E



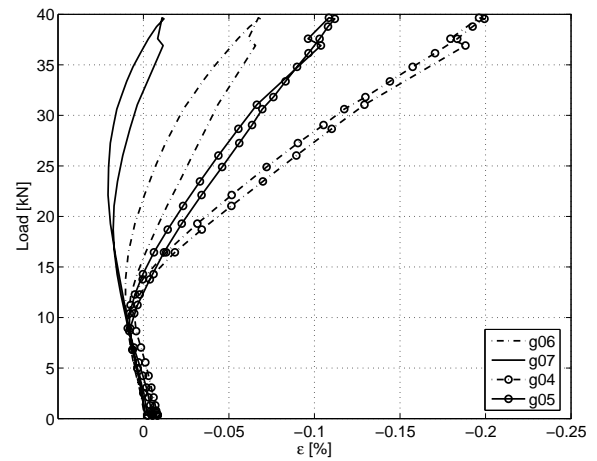
(a) Top side - 1st series



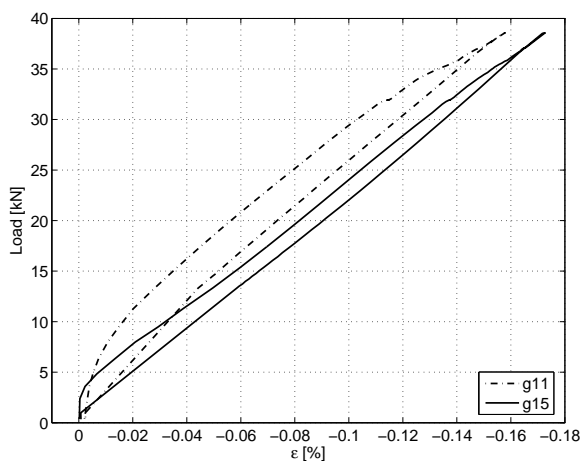
(b) Top side - 2nd series



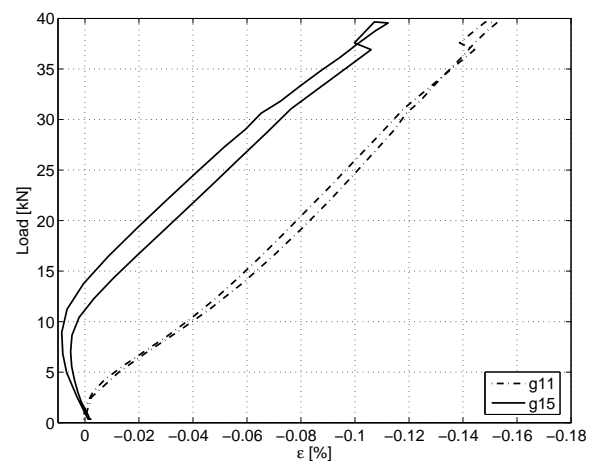
(c) Bottom side 1st series



(d) Bottom side 2nd series

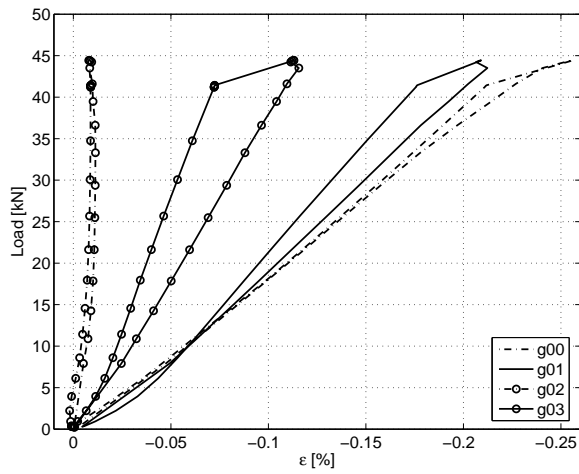


(e) Lateral sides 1st series

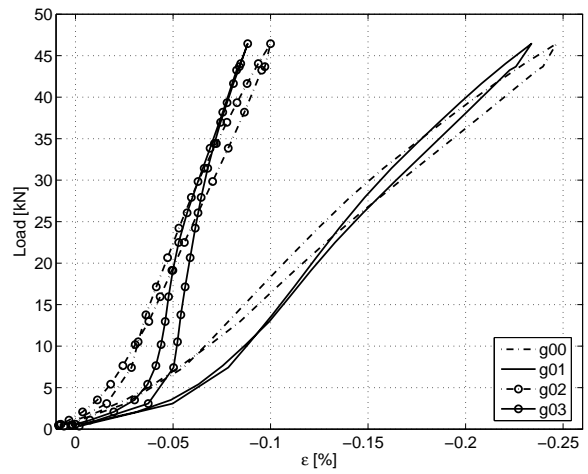


(f) Lateral sides 2nd series

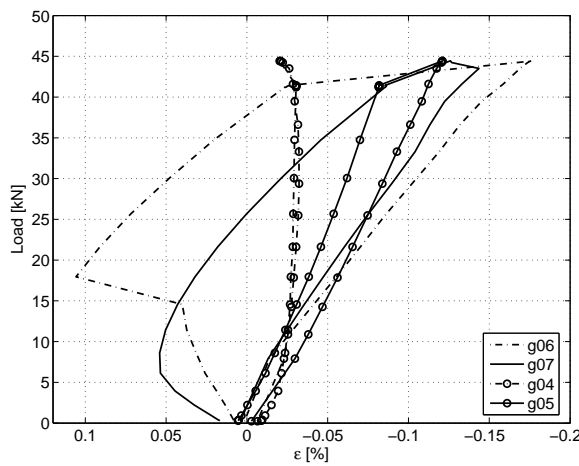
Figure F.86: M240E



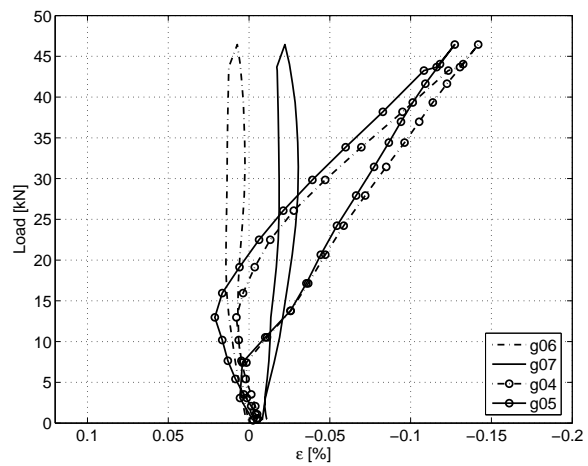
(a) Top side - 1st series



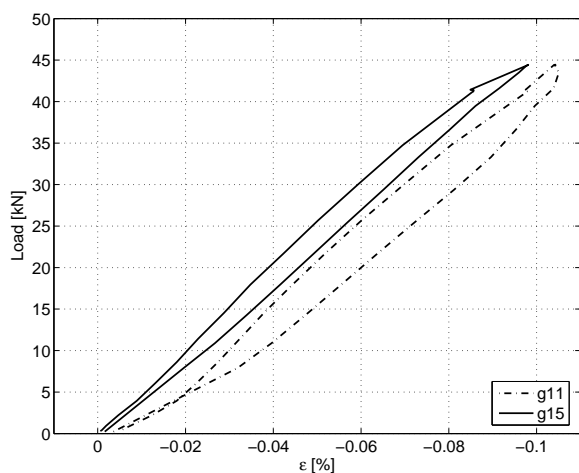
(b) Top side - 2nd series



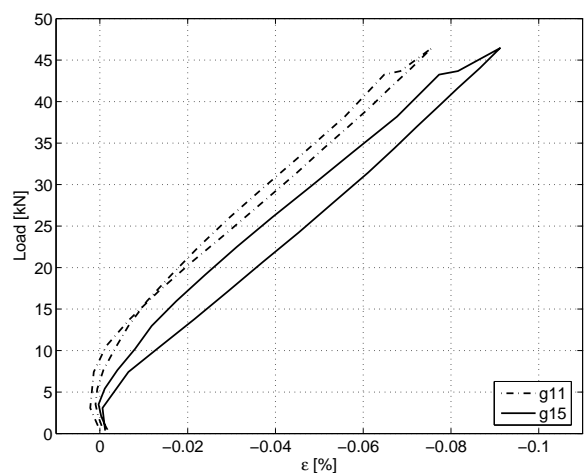
(c) Bottom side 1st series



(d) Bottom side 2nd series

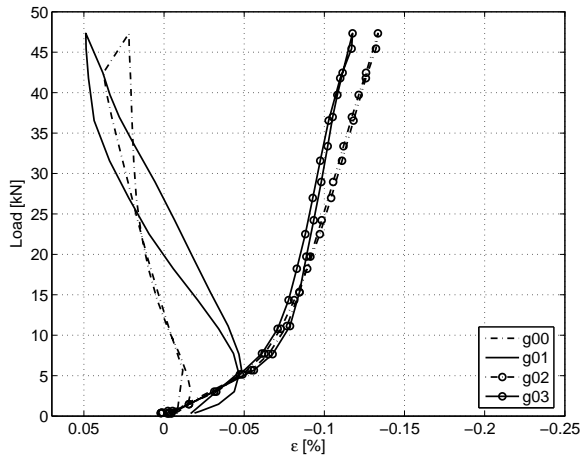


(e) Lateral sides 1st series

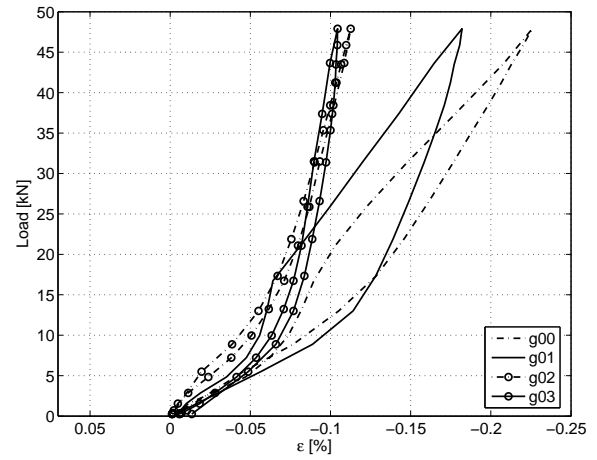


(f) Lateral sides 2nd series

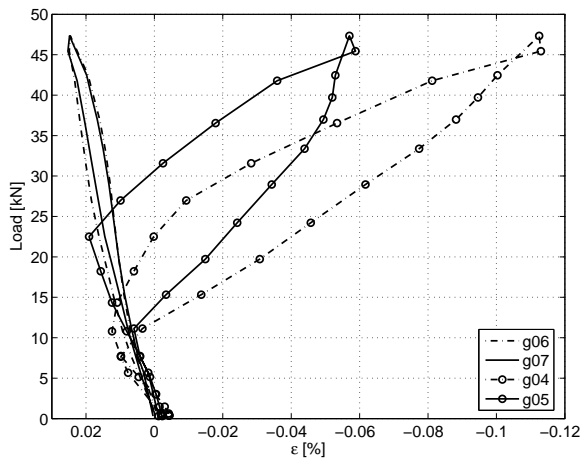
Figure F.87: S200E



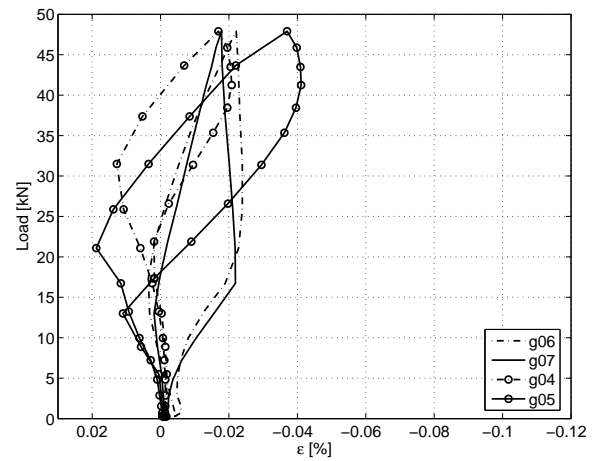
(a) Top side - 1st series



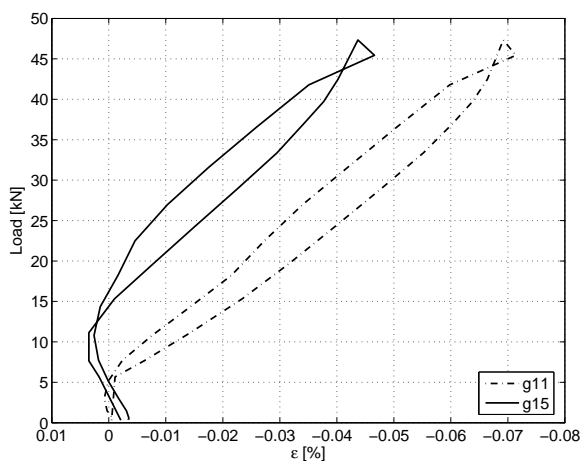
(b) Top side - 2nd series



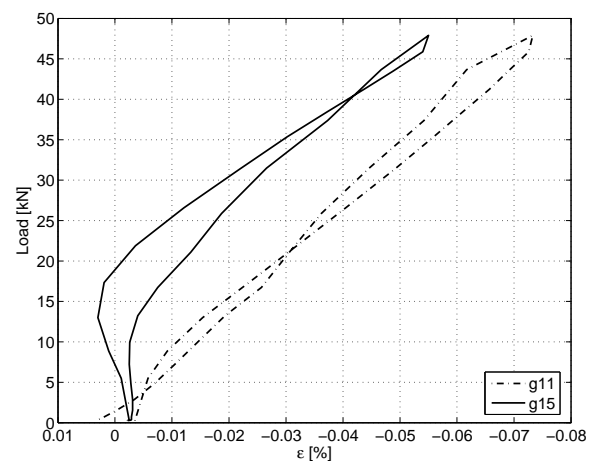
(c) Bottom side 1st series



(d) Bottom side 2nd series

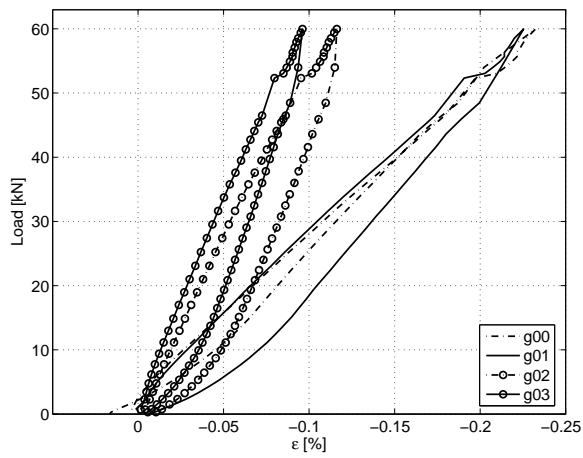


(e) Lateral sides 1st series

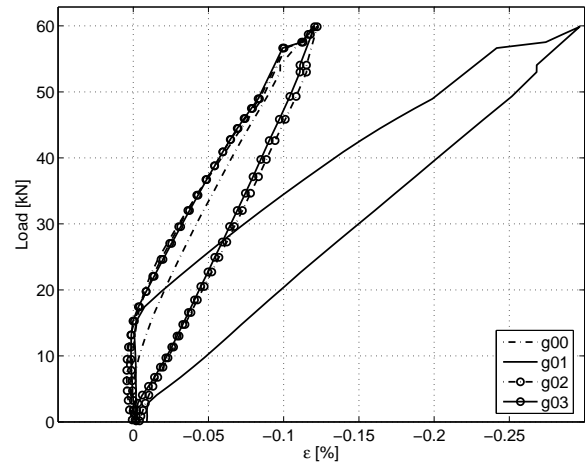


(f) Lateral sides 2nd series

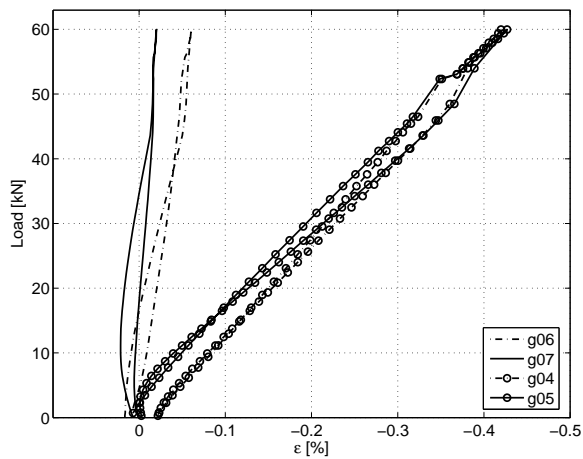
Figure F.88: S240E



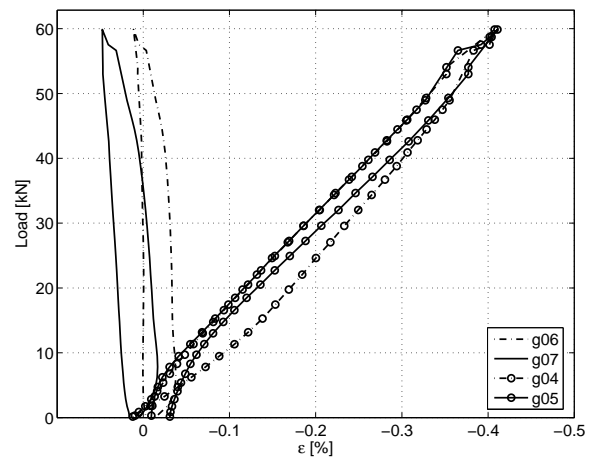
(a) Top side - 1st series



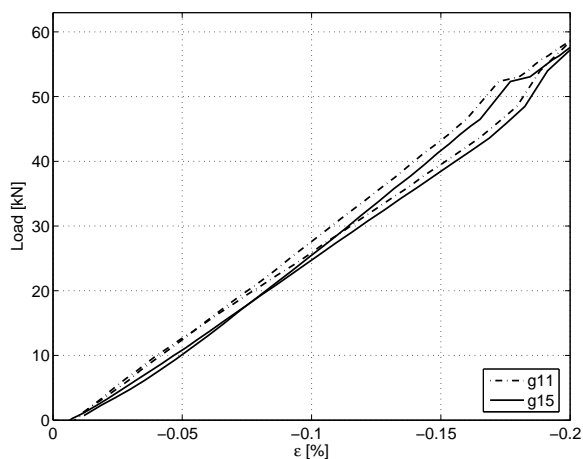
(b) Top side - 2nd series



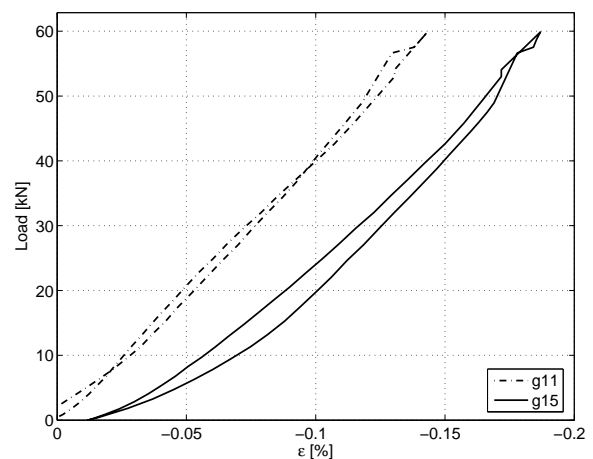
(c) Bottom side 1st series



(d) Bottom side 2nd series

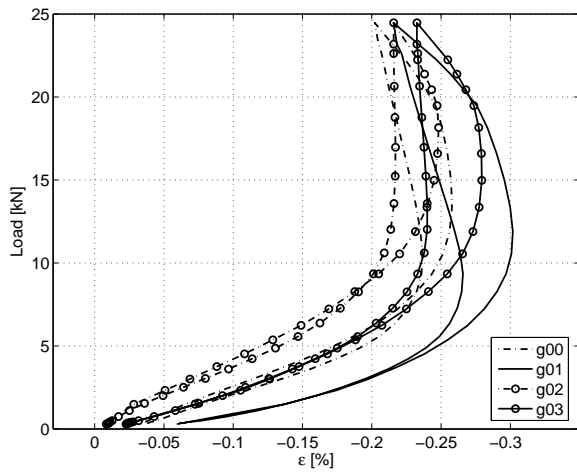


(e) Lateral sides 1st series

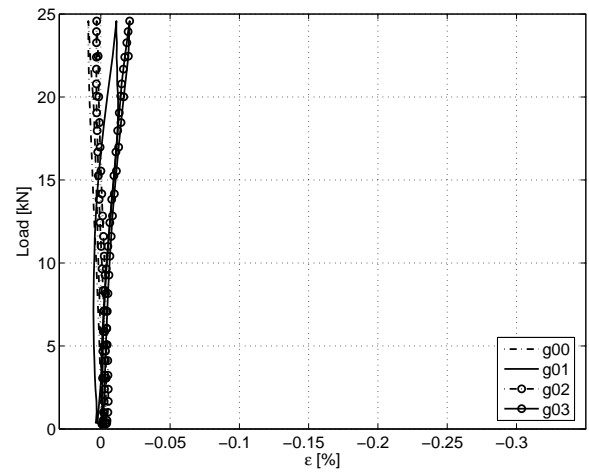


(f) Lateral sides 2nd series

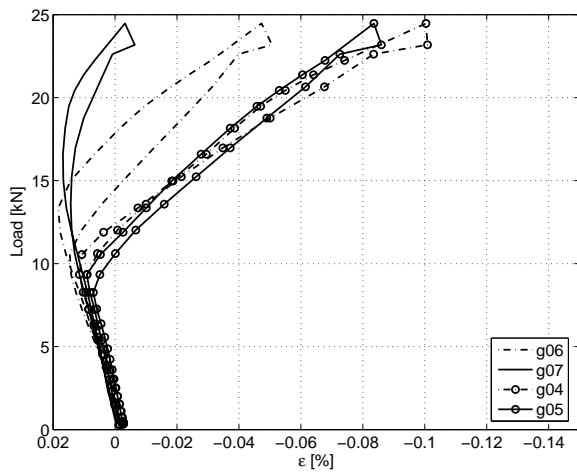
Figure F.89: S200E3 & S240E3



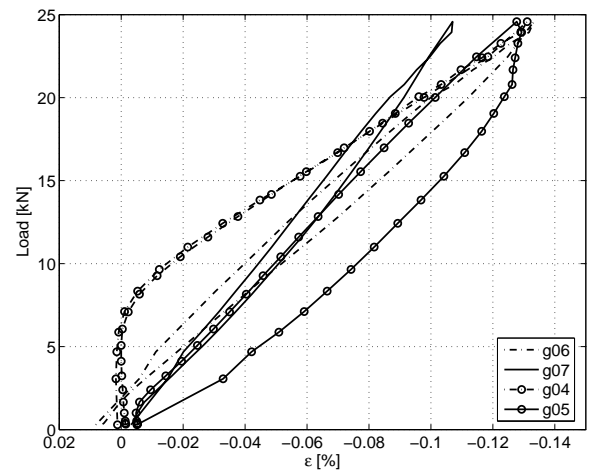
(a) Top side - 1st series



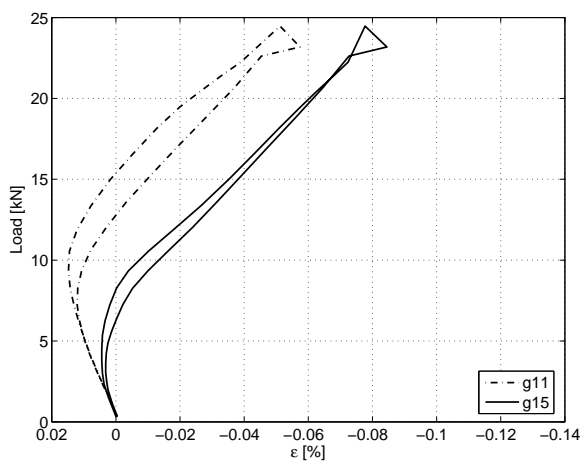
(b) Top side - 2nd series



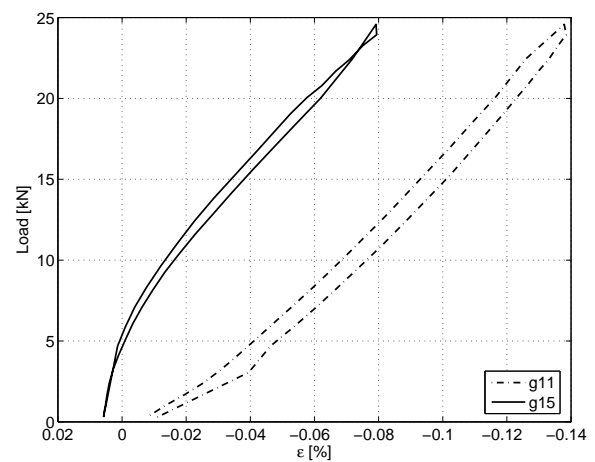
(c) Bottom side 1st series



(d) Bottom side 2nd series

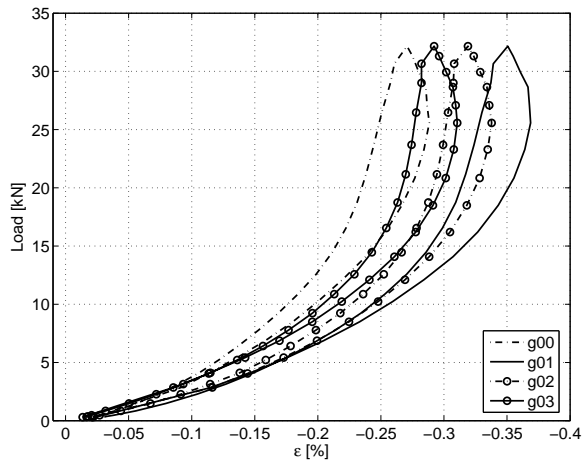


(e) Lateral sides 1st series

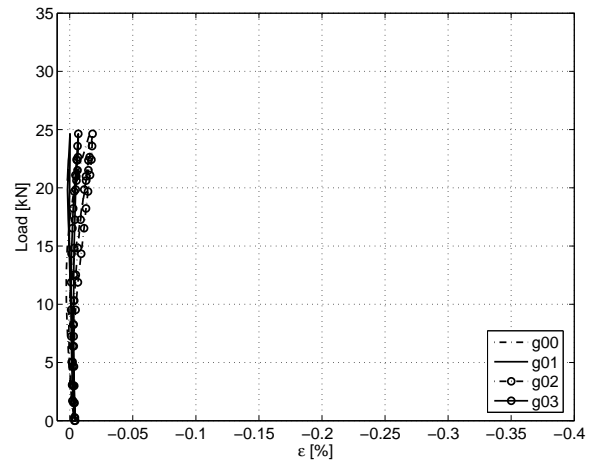


(f) Lateral sides 2nd series

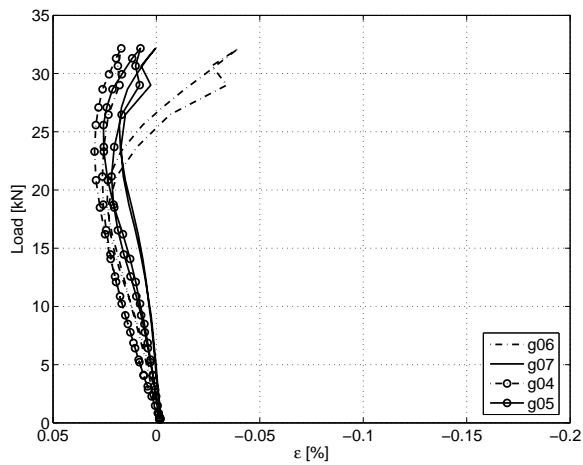
Figure F.90: M200C



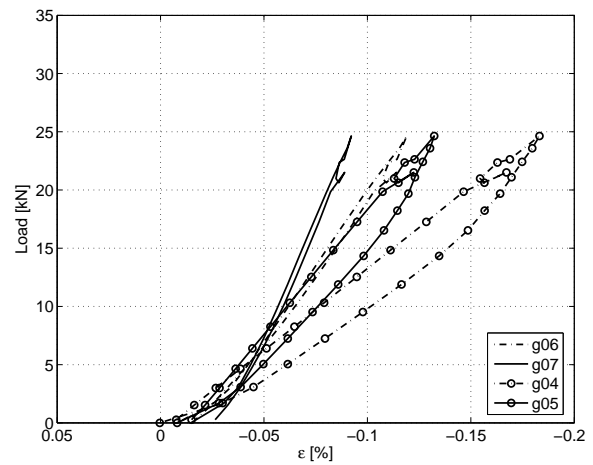
(a) Top side - 1st series



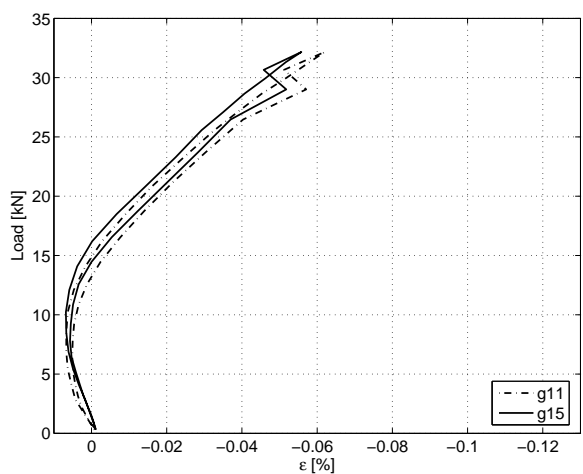
(b) Top side - 2nd series



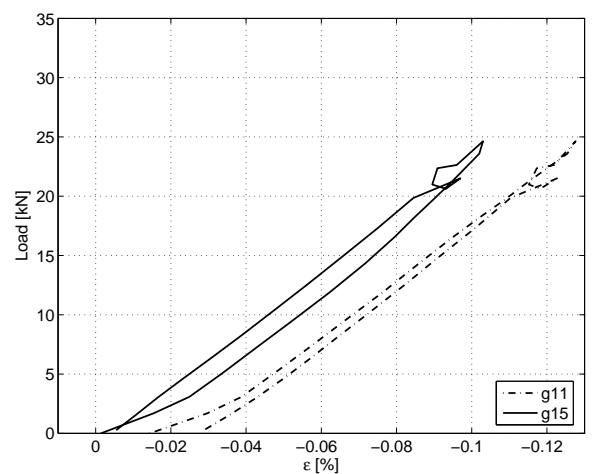
(c) Bottom side 1st series



(d) Bottom side 2nd series

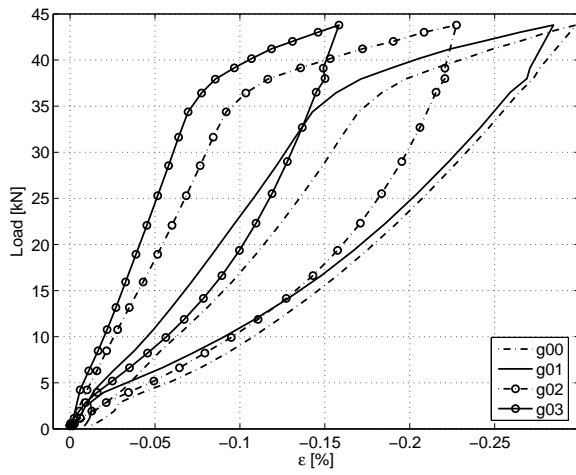


(e) Lateral sides 1st series

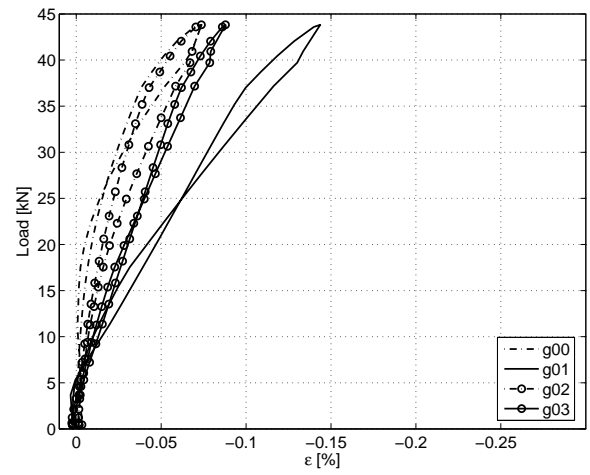


(f) Lateral sides 2nd series

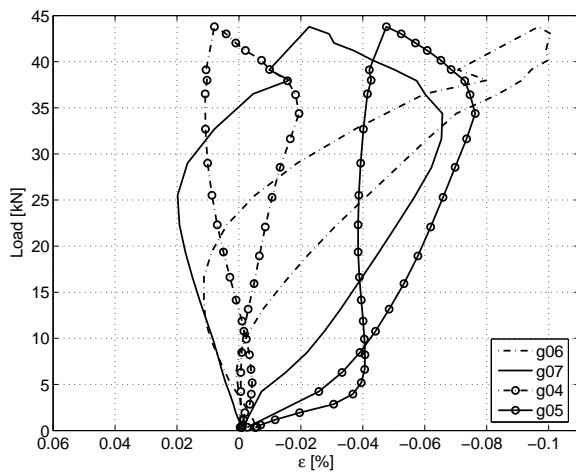
Figure F.91: M240C



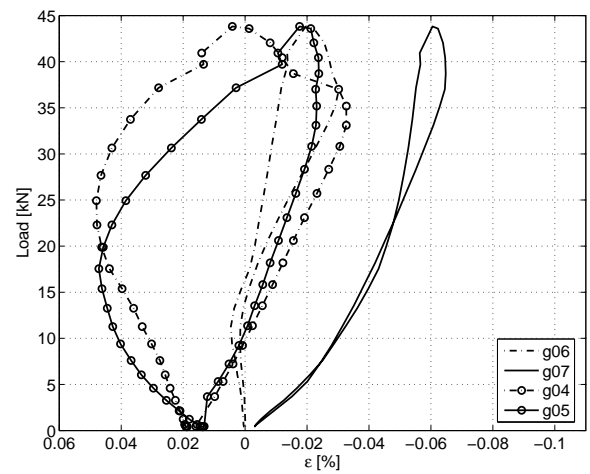
(a) Top side - 1st series



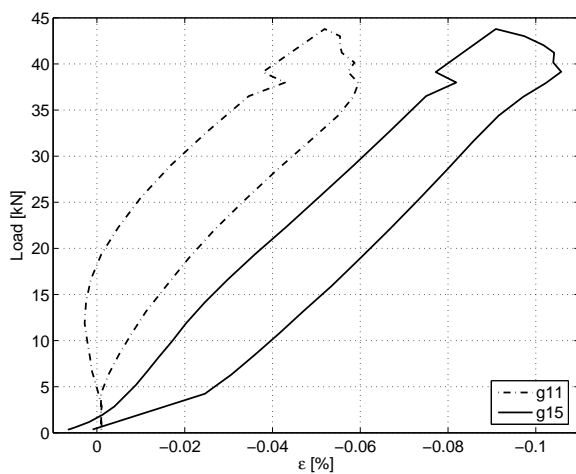
(b) Top side - 2nd series



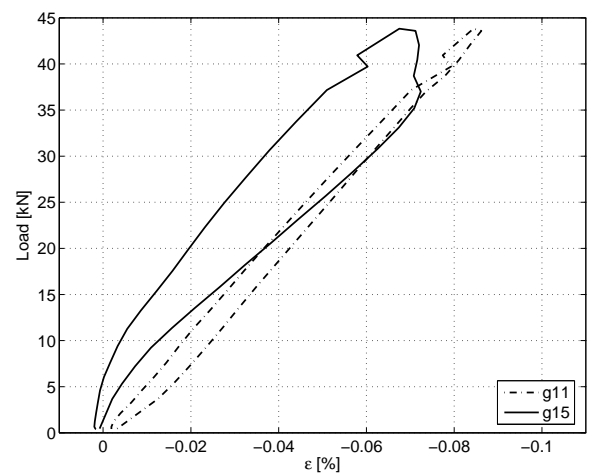
(c) Bottom side 1st series



(d) Bottom side 2nd series

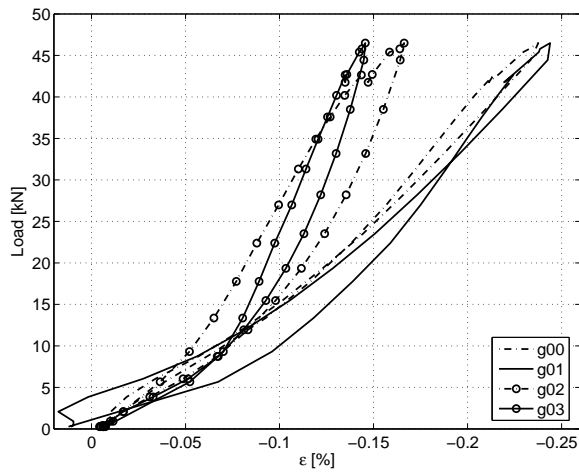


(e) Lateral sides 1st series

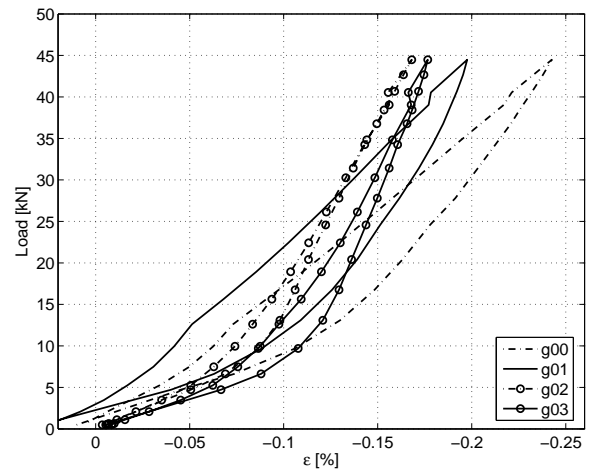


(f) Lateral sides 2nd series

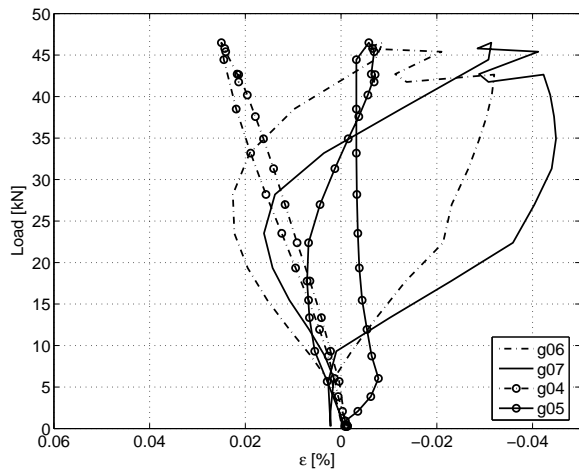
Figure F.92: S200C



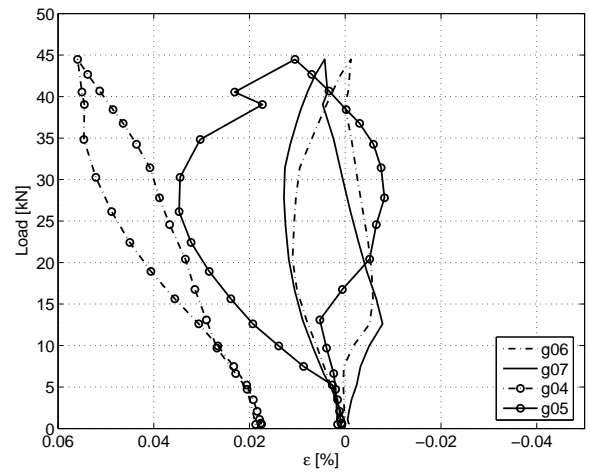
(a) Top side - 1st series



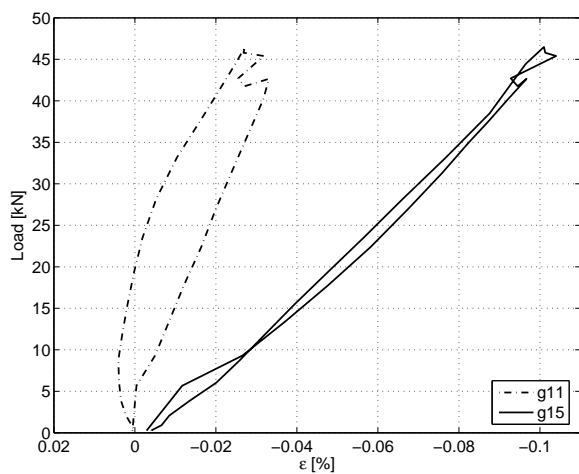
(b) Top side - 2nd series



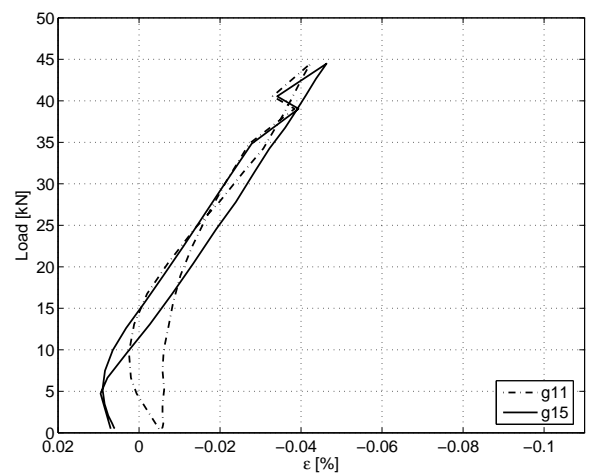
(c) Bottom side 1st series



(d) Bottom side 2nd series



(e) Lateral sides 1st series



(f) Lateral sides 2nd series

Figure F.93: S240C

F.8. Failure Modes

F.8.1. Concrete Failure at Bottom side

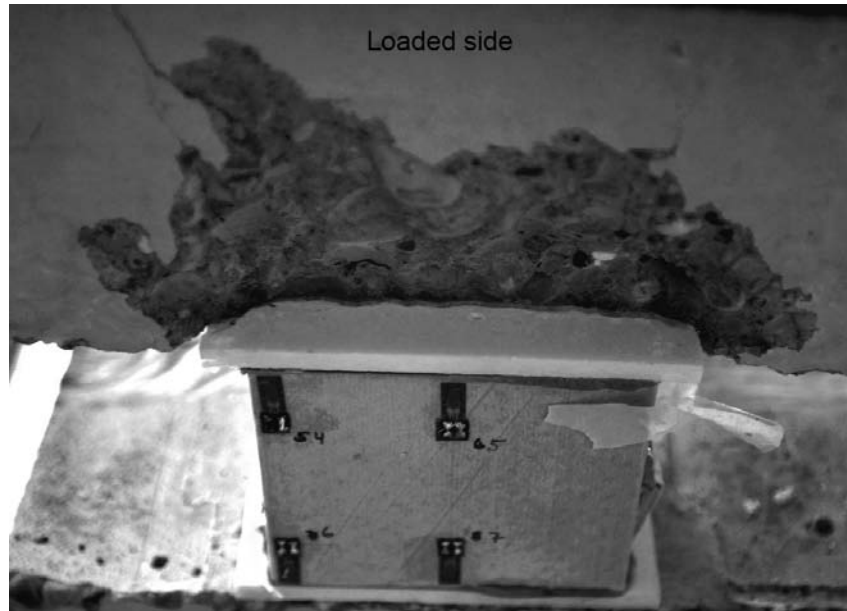


Figure F.94: M200E1



Figure F.95: M200E2

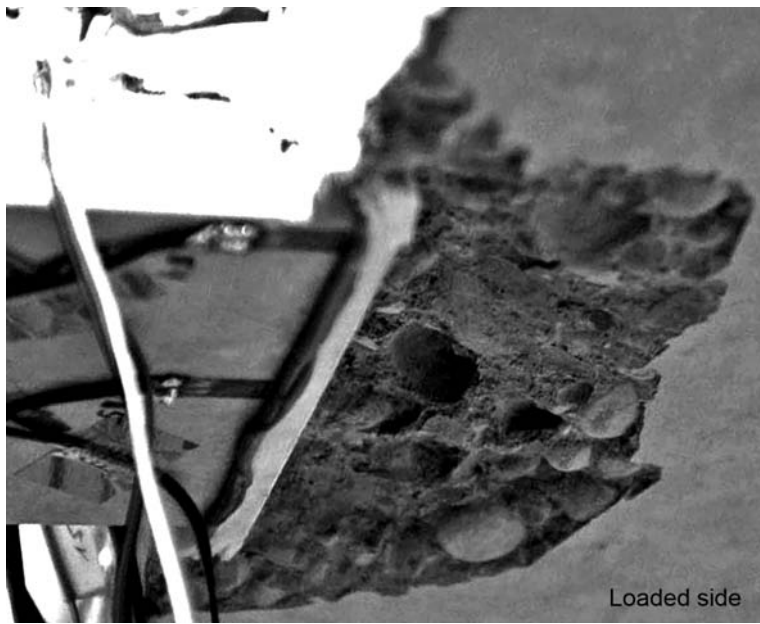


Figure F.96: M240E1

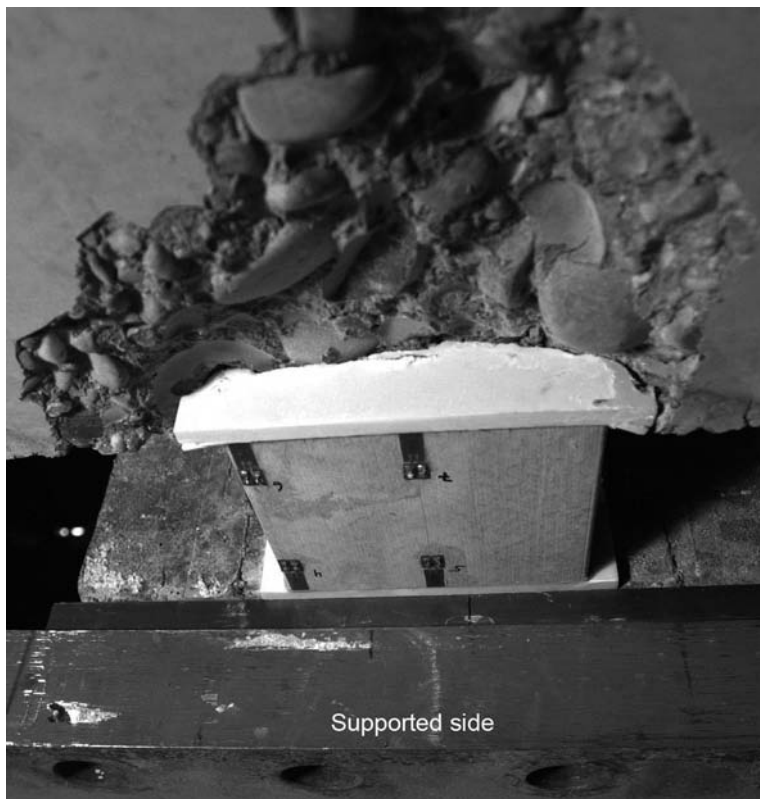


Figure F.97: M240E2

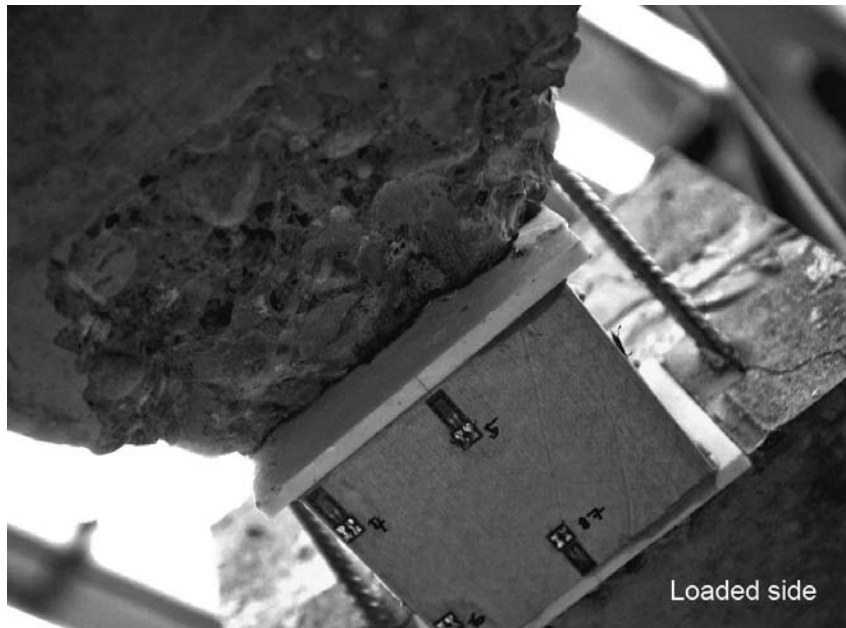


Figure F.98: M200C1



Figure F.99: M200C2



Figure F.100: M240C1

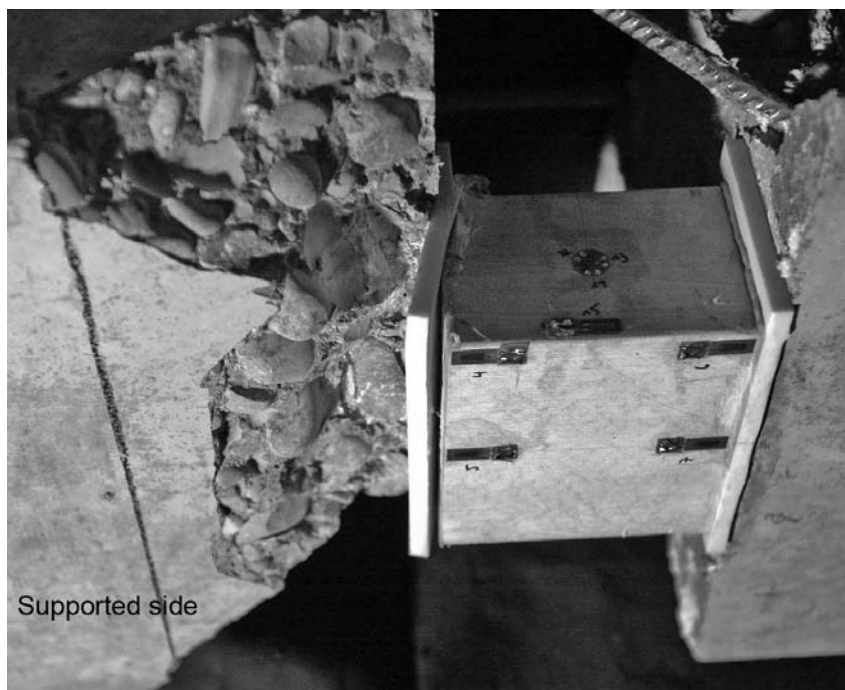
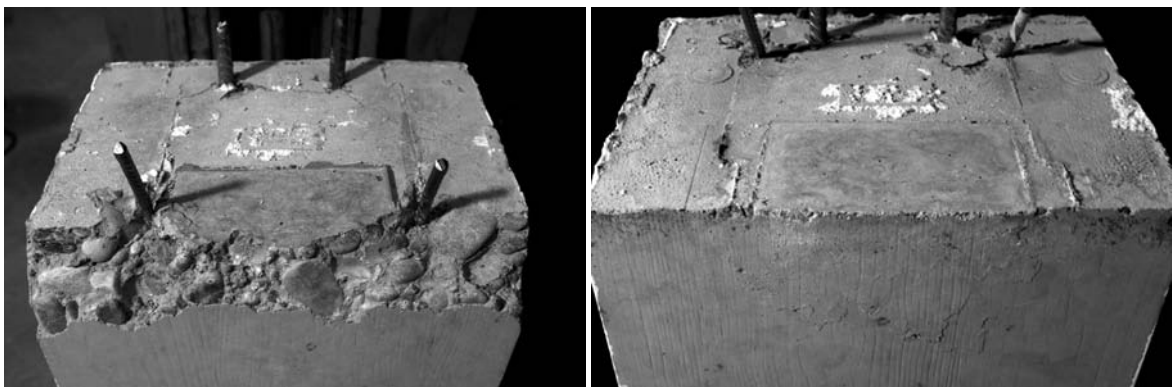


Figure F.101: M240C2



Figure F.102: S200E1



(a) loaded side

(b) supported side

Figure F.103: S200E3

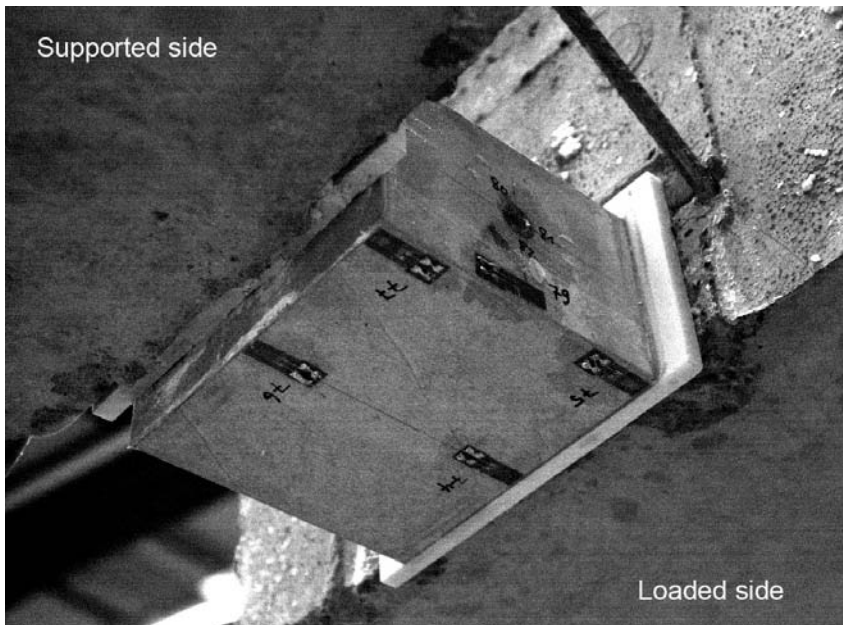


Figure F.104: S240Ea

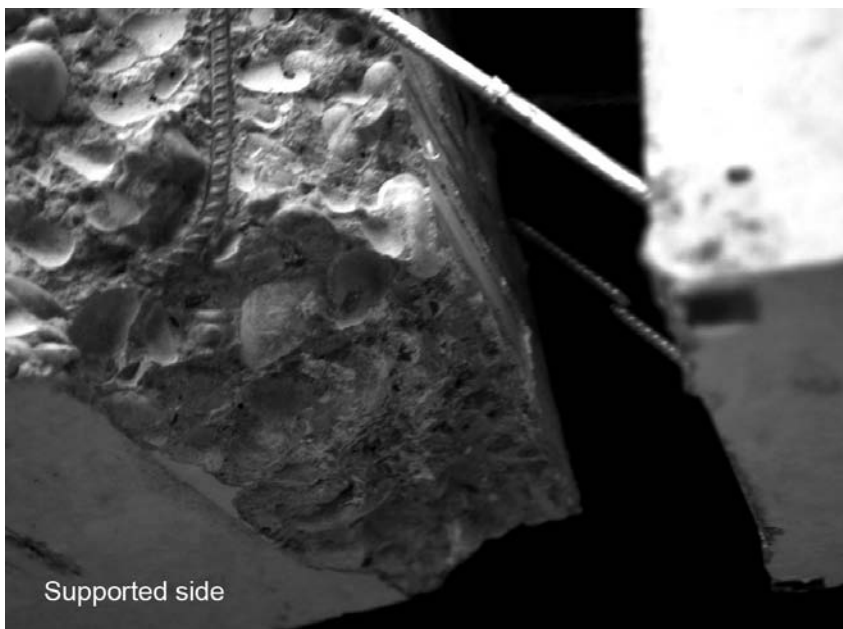


Figure F.105: S200C1

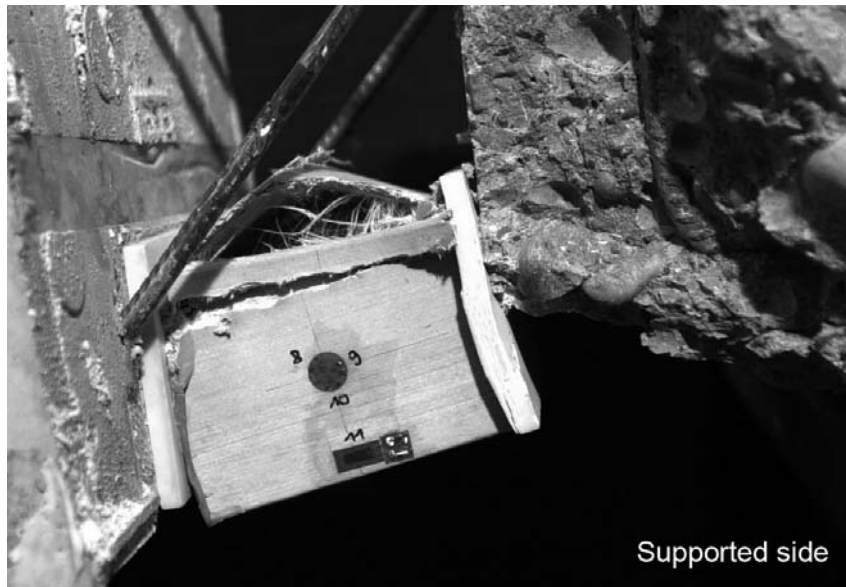


Figure F.106: S200C2



Figure F.107: S240C1

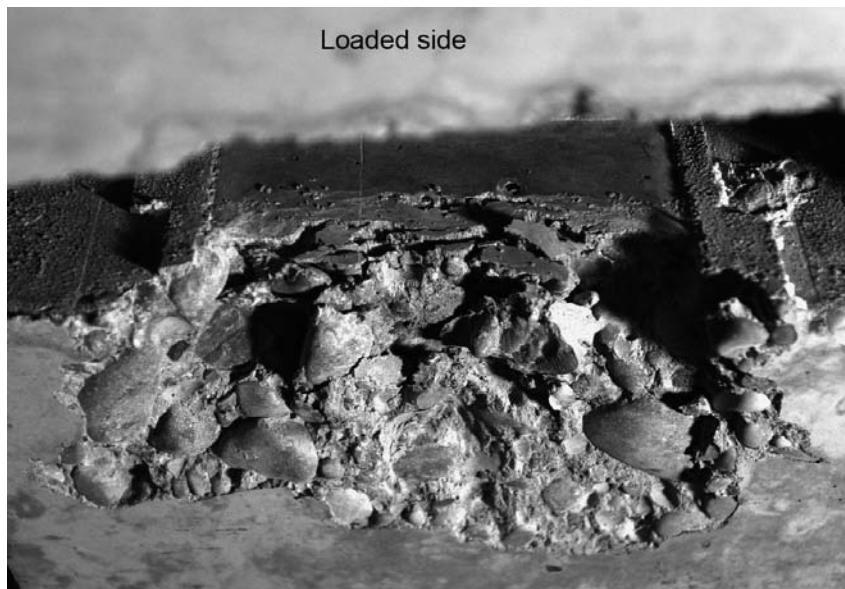


Figure F.108: S240C2

F.8.2. Detailed View of Compression Element



(a) M200E1



(b) M200E2

Figure F.109: Failure in insulating section - MDM



(a) M240E1



(b) M240E2

Figure F.110: Failure in insulating section - MDM



(a) S200E1



(b) S200E2

Figure F.111: Failure in insulating section - SDM



(a) S240E1



(b) S240E2

Figure F.112: Failure in insulating section - SDM



(a) S200E3

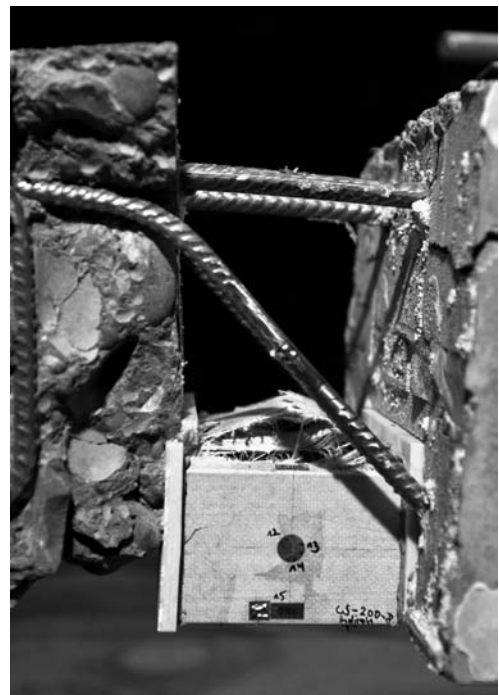


(b) S240E3

Figure F.113: Failure in insulating section - SDM



(a) M200C1



(b) M200C2

Figure F.114: Failure in insulating section - MDM



(a) M240C1

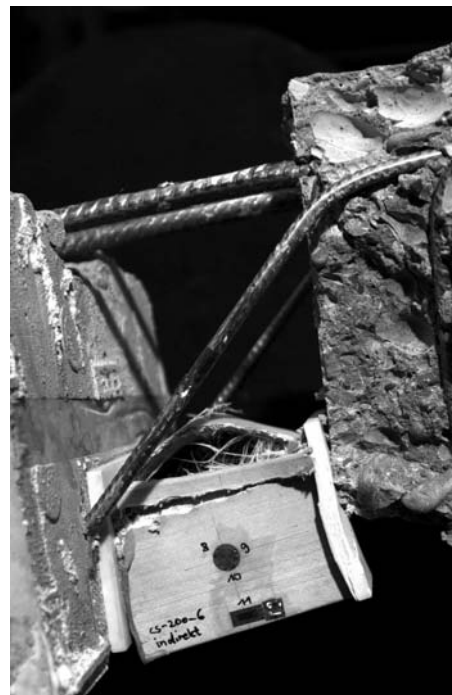


(b) M240C2

Figure F.115: Failure in insulating section - MDM



(a) S200C1



(b) S200C2

Figure F.116: Failure in insulating section - SDM



(a) S240C1



(b) S240C2

Figure F.117: Failure in insulating section - SDM

F.9. Second principal stress angle on CS-elements

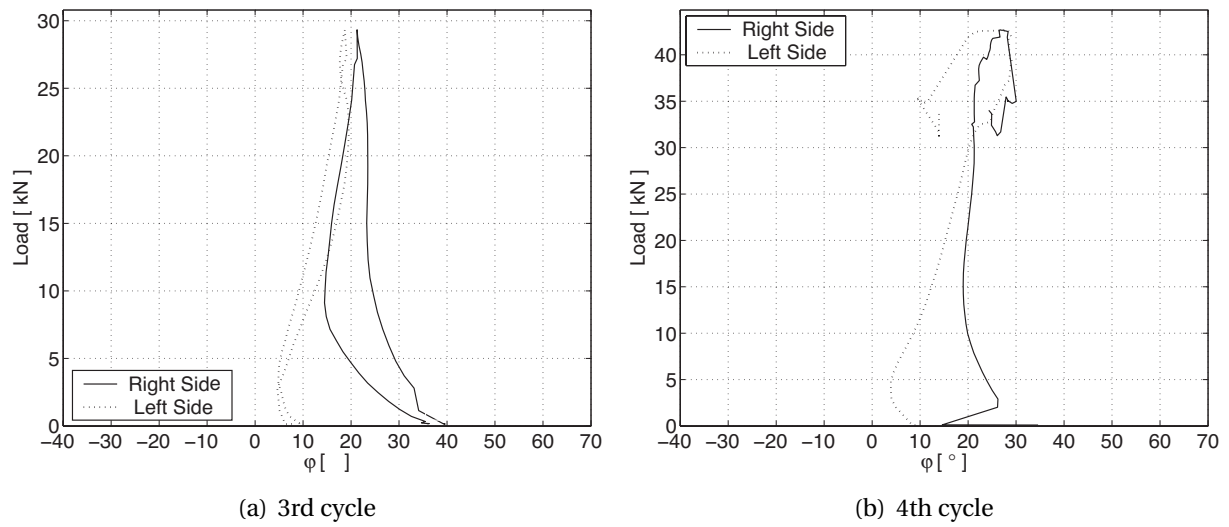


Figure F.118: M200E1

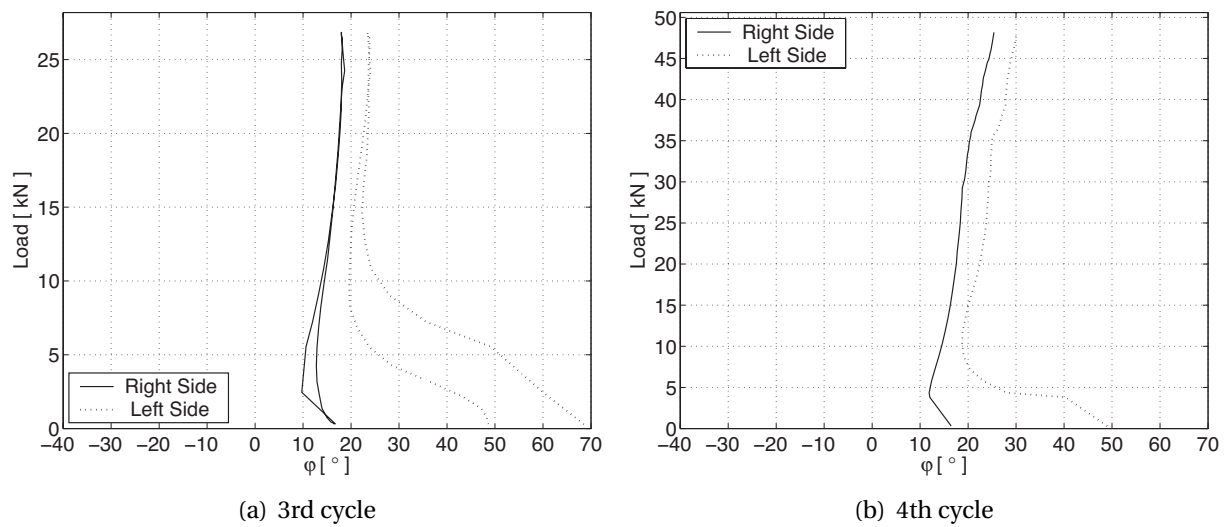


Figure F.119: M200E2

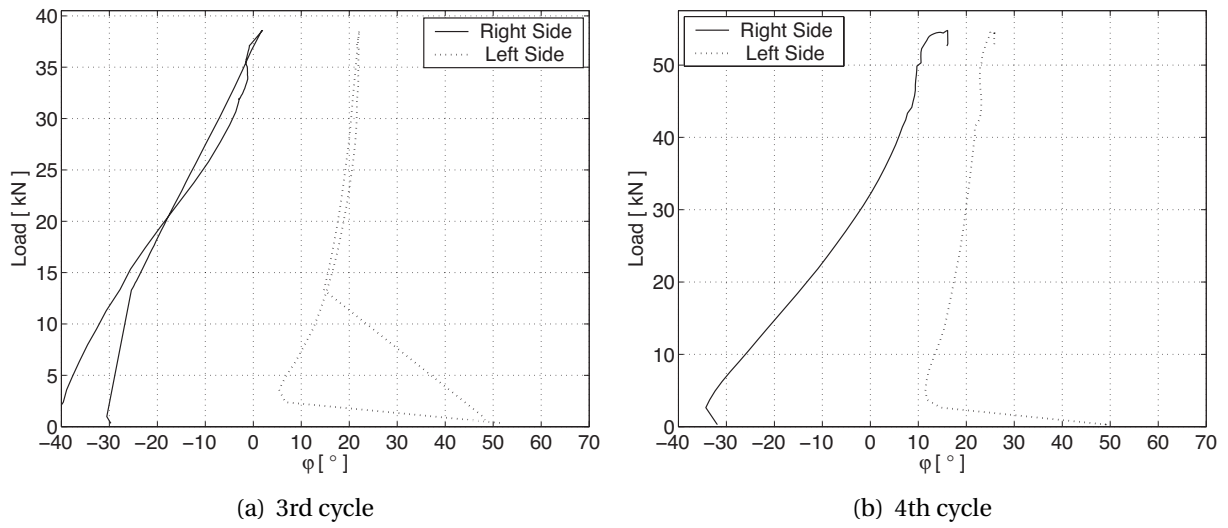


Figure F.120: M240E1

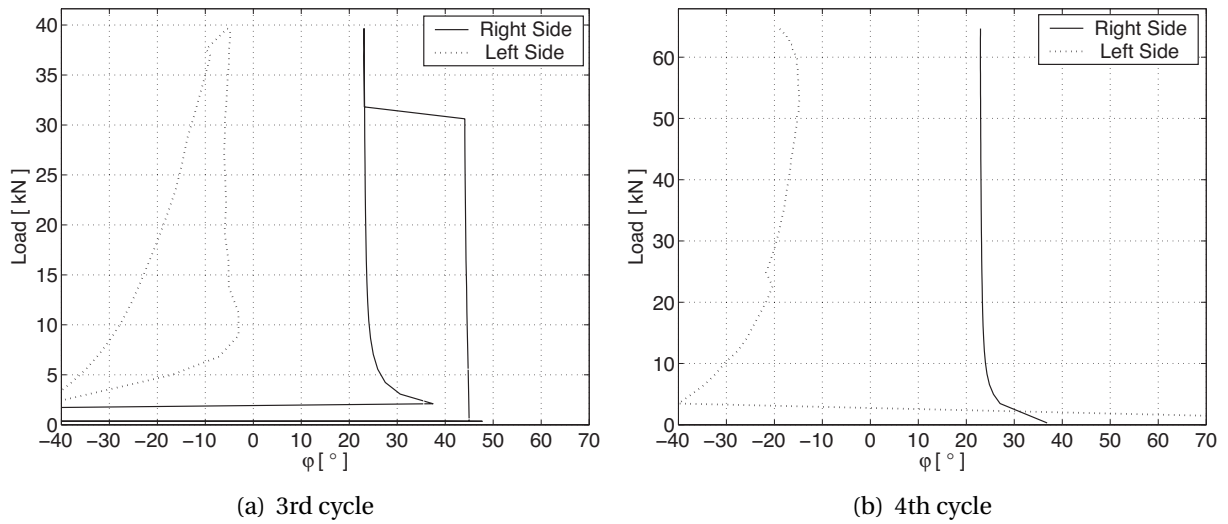


Figure F.121: M240E2

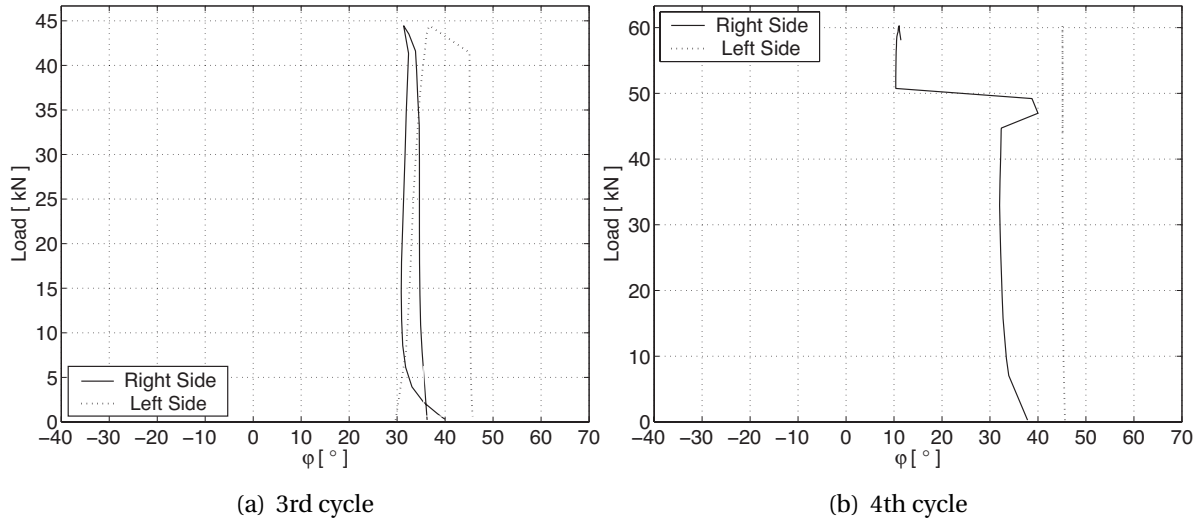


Figure F.122: S200E1

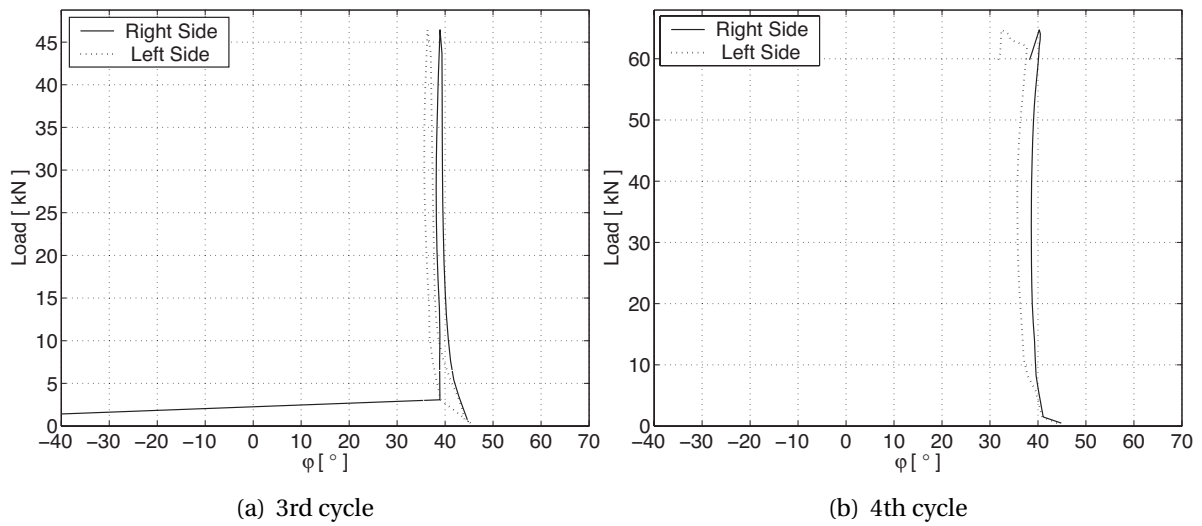


Figure F.123: S200E2

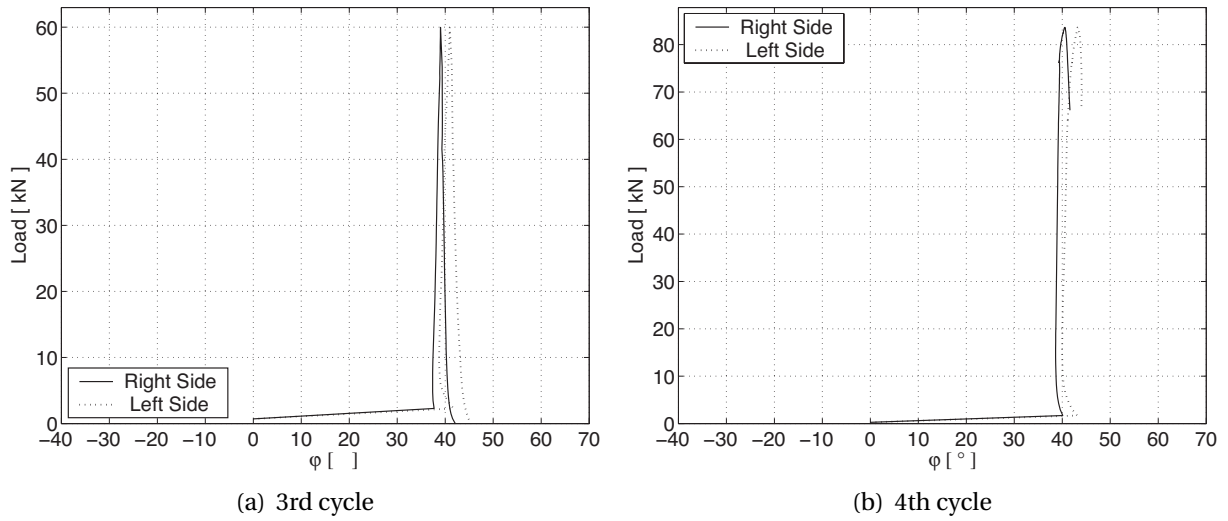


Figure F.124: S200E3

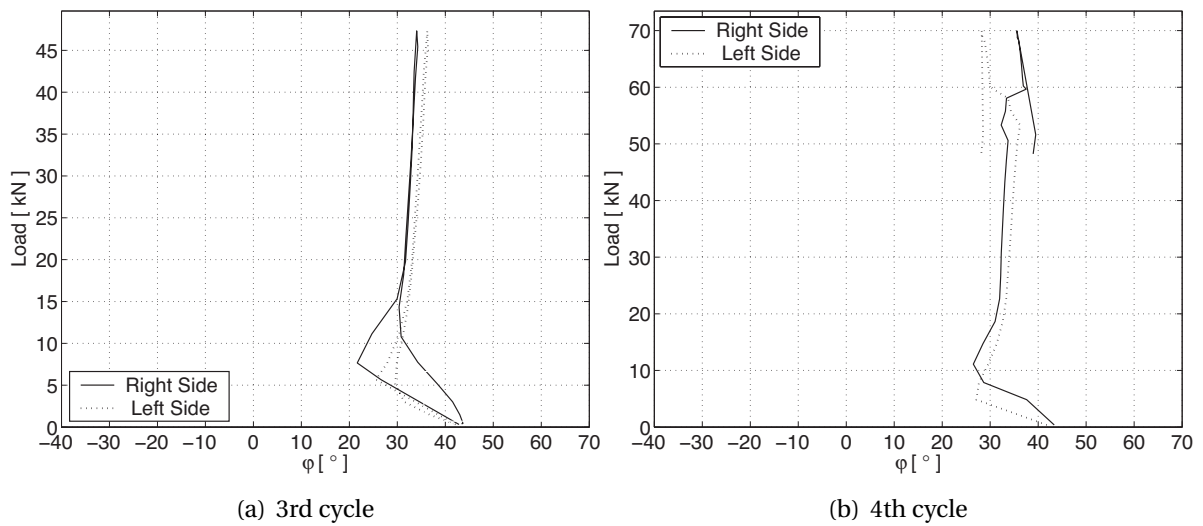


Figure F.125: S240E1

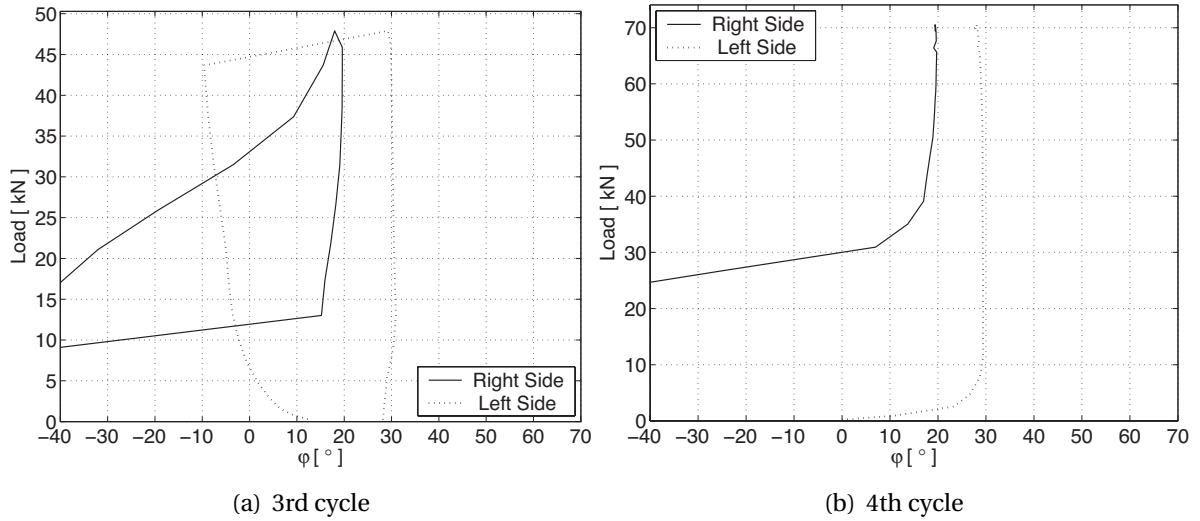


Figure F.126: S240E2

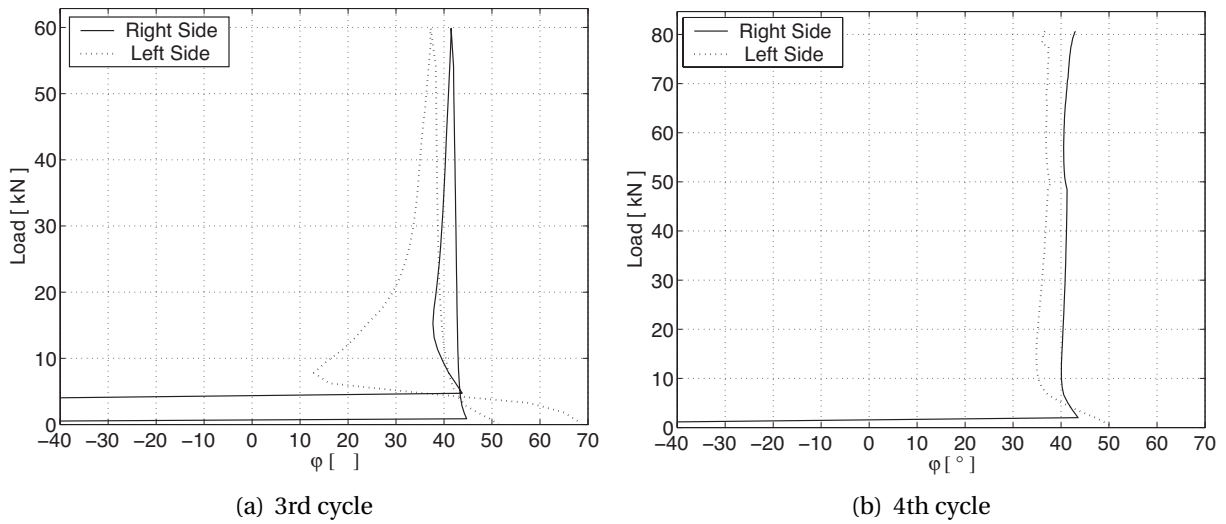


Figure F.127: S240E3

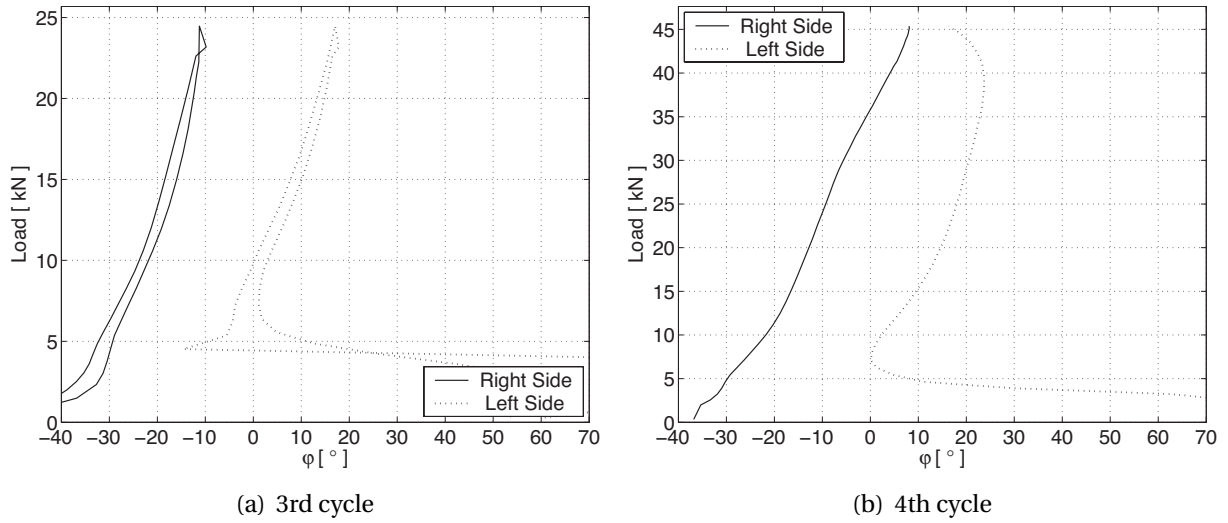


Figure F.128: M200C1

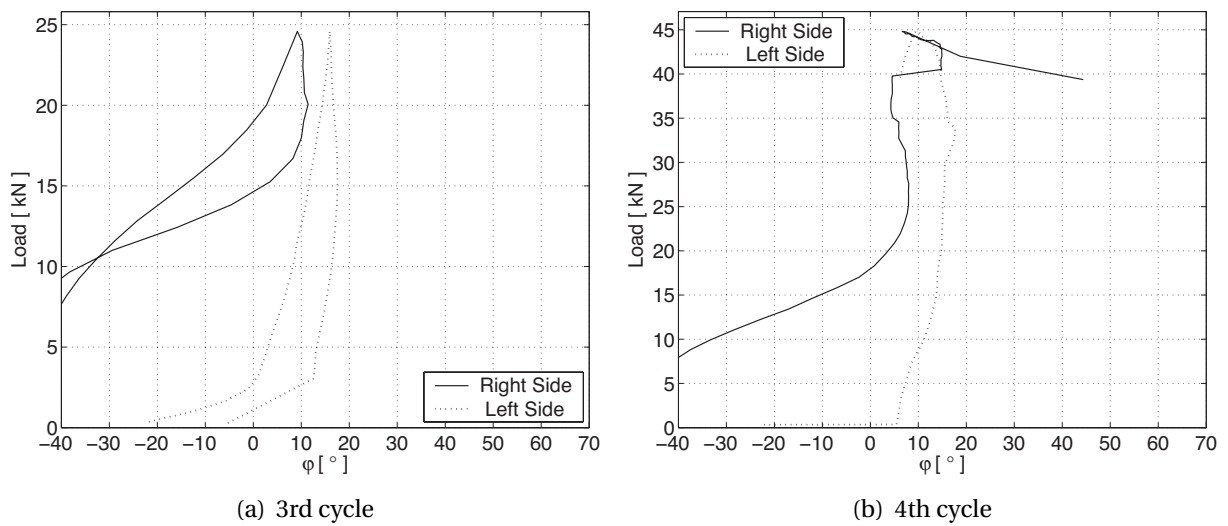


Figure F.129: M200C2

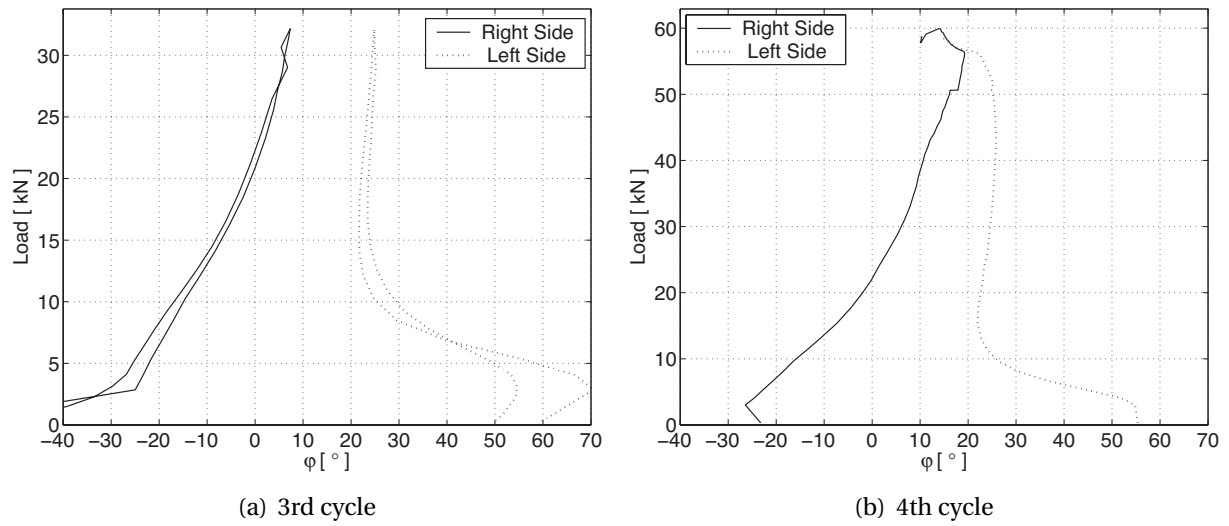


Figure F.130: M240C1

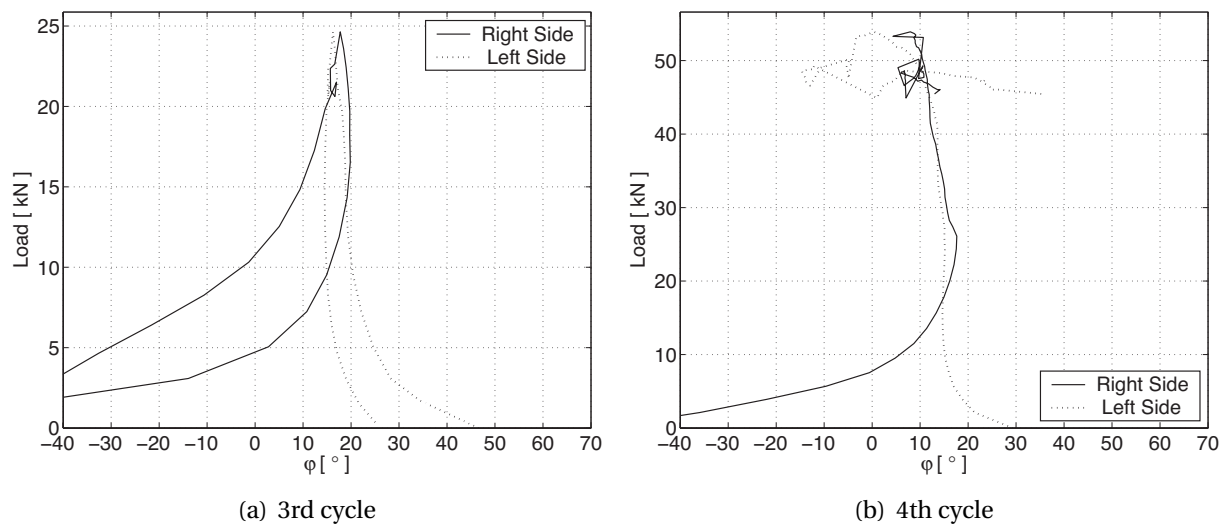


Figure F.131: M240C2

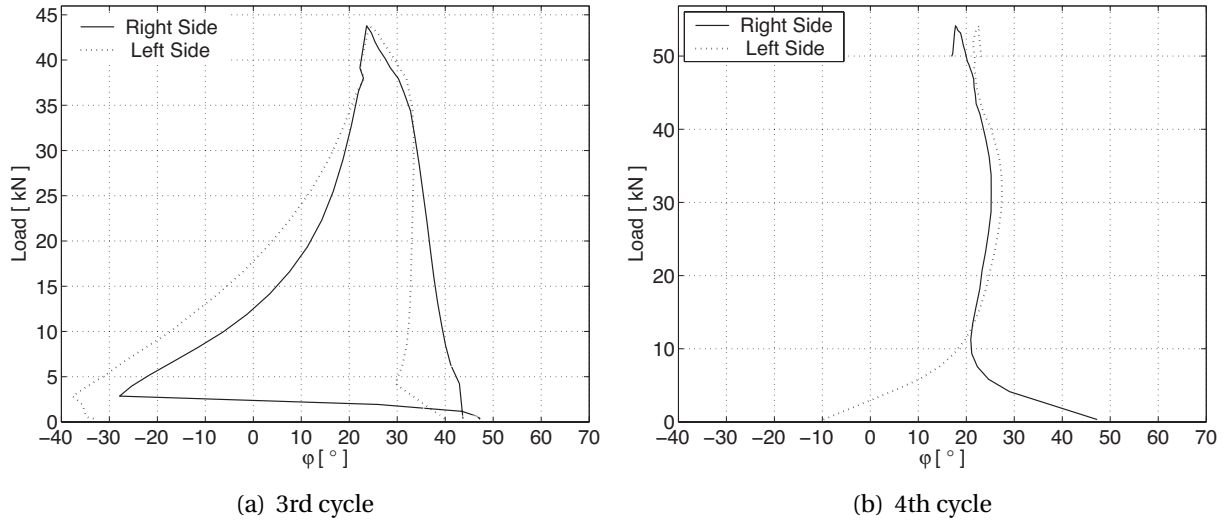


Figure F.132: S200C1

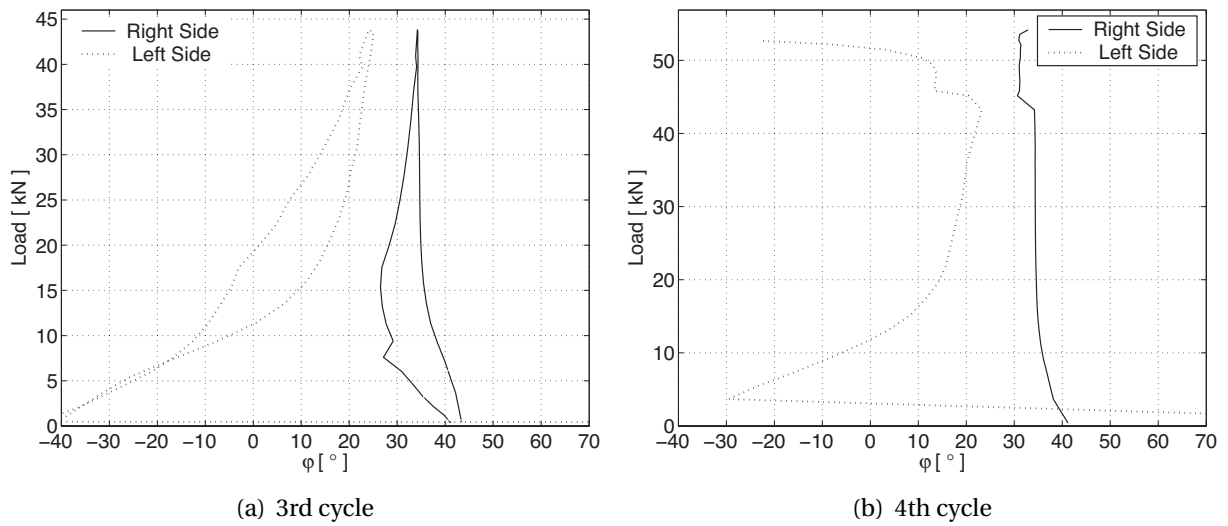


Figure F.133: S200C2

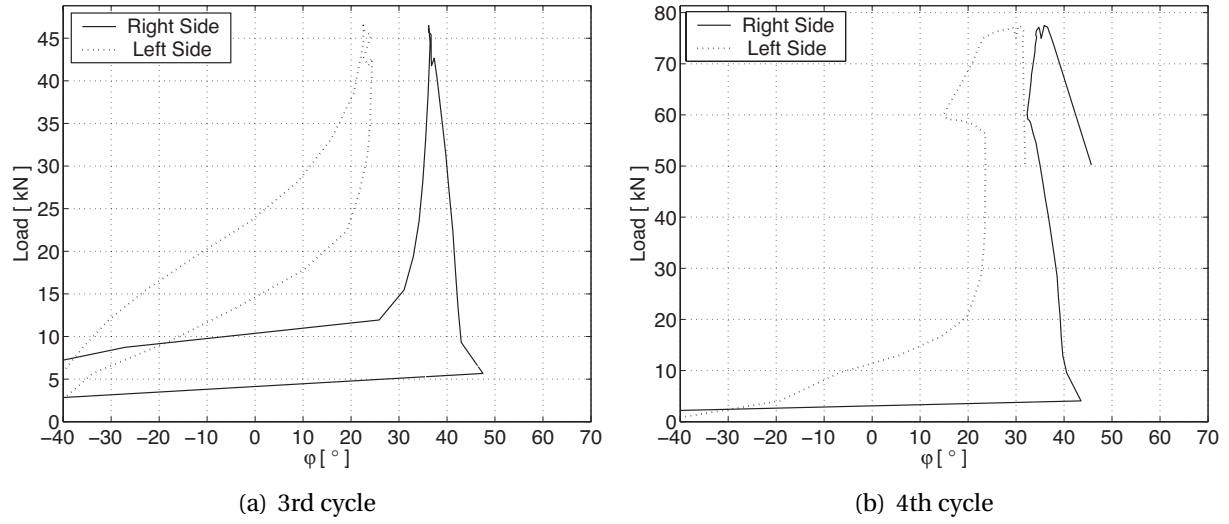


Figure F.134: S240C1

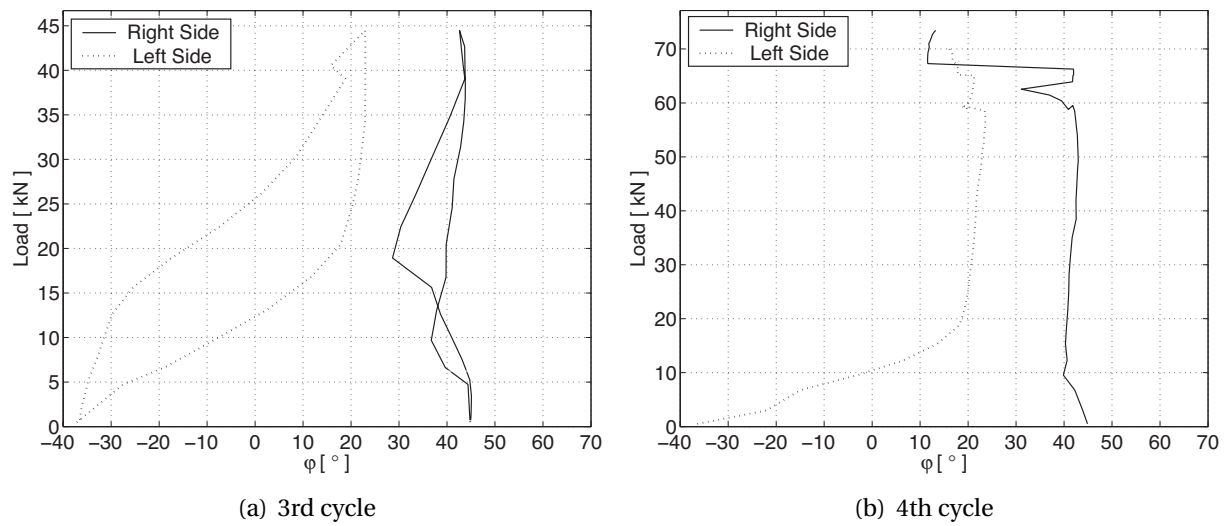


Figure F.135: S240C2

Appendix G.

Investigations on all-FRP joint

G.1. Experimental set-up

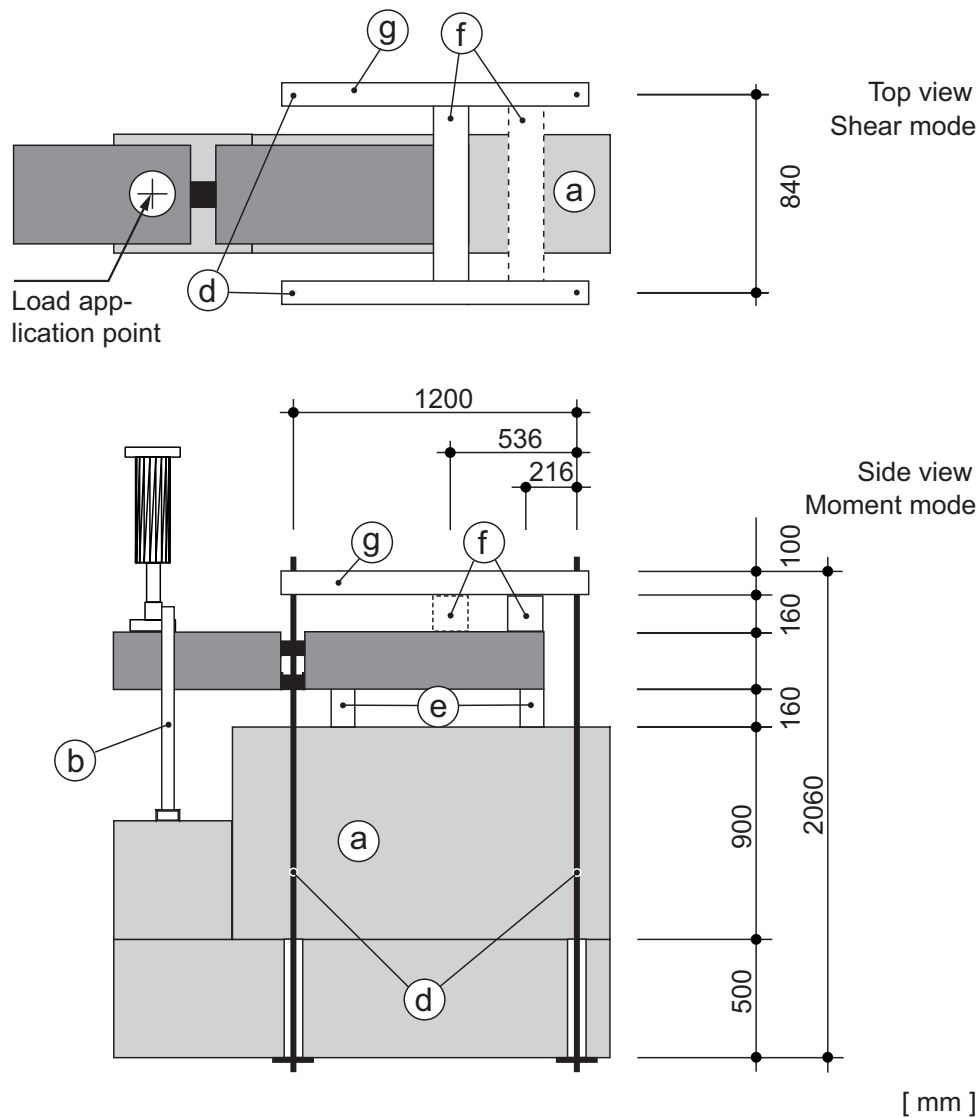


Figure G.1: Experimental set-up of all-FRP beams

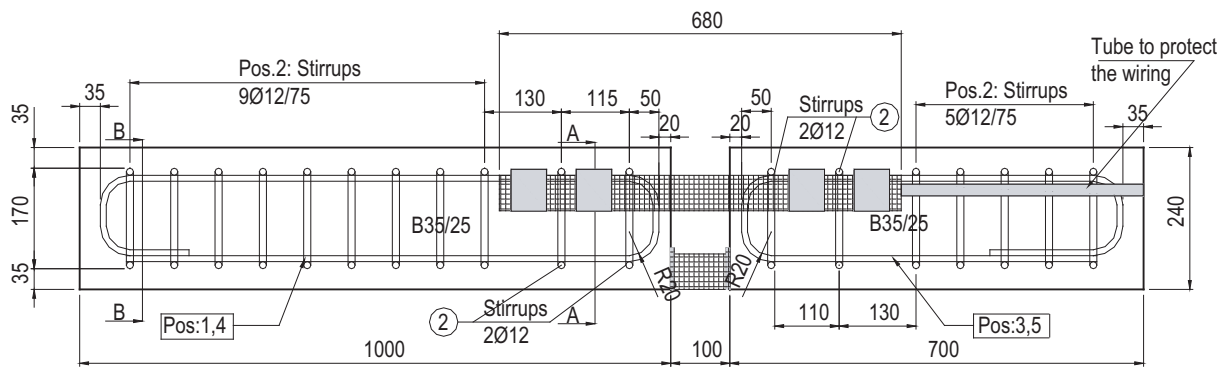
Figure G.1 shows the experimental set-up in top- and side view. Contrary to the set-up of the hybrid-joint beams, this time the beam was shifted to attain different loading modes. In

top view, a beam in shear mode position is shown, while in side view, the beam is in moment mode position. Dashed lines show alternative positions of steel profiles, which were shifted depending on the loading mode. The basis consisted of concrete blocks (a), on which the beam was placed. Supporting steel profiles (e) were moved depending on the support condition. In case of end-support condition, the profile was aligned with the concrete edge facing the joint, while, to achieve a cantilever-support condition, the profile was shifted 100 mm away from the concrete edge. To take the upward forces at the right end of the supported beam section, a system consisting of two longitudinal and one transversal profile (g) and (f) was conceived that allowed a flexible adjustment to the beam position. The longitudinal steel profiles (g) were anchored in the ground by steel bars (d). Since the beams, this time, showed a higher width to depth ratio, a guidance (b) was conceived to avoid torsional deformations of the cantilevered-beam section. The guidance was Teflon[®]-laminated to minimize friction. The load applying cylinder had a maximum force of 300 kN and a travel of 150 mm. It was fixed on a loading frame surrounding the set-up shown in Figure G.1. It was not moved during the experiments.

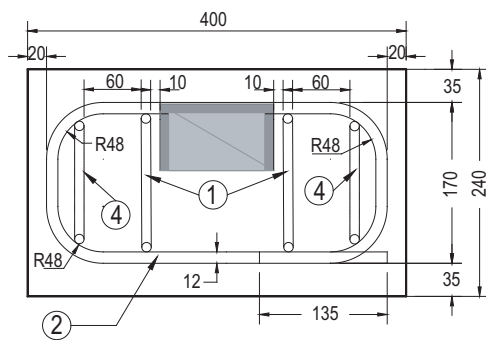
Table G.1: Compressive strength of concrete after 28 days.

Beam	$f_{c,cube}$ [MPa]	$f_{c,cube,mean}$ [MPa]	$f_{c,cyl,mean}$ [MPa]	Gravel size [mm]
Three-rib beams	– ^a / 41.52 / 44.5	40.9	32.7	32
Two-rib beams	43.43 / 42.51 / 36.82	43.0±3.6	34.4	32

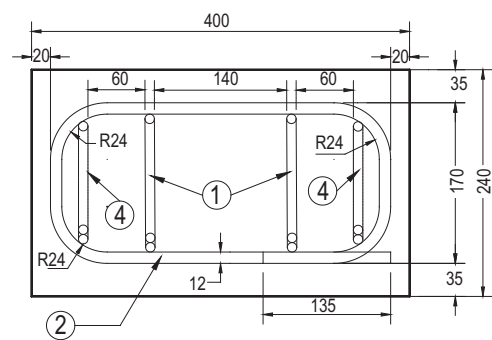
^aThe specimen was damaged and could not be tested.



(a) Beam with two-rib TS-element

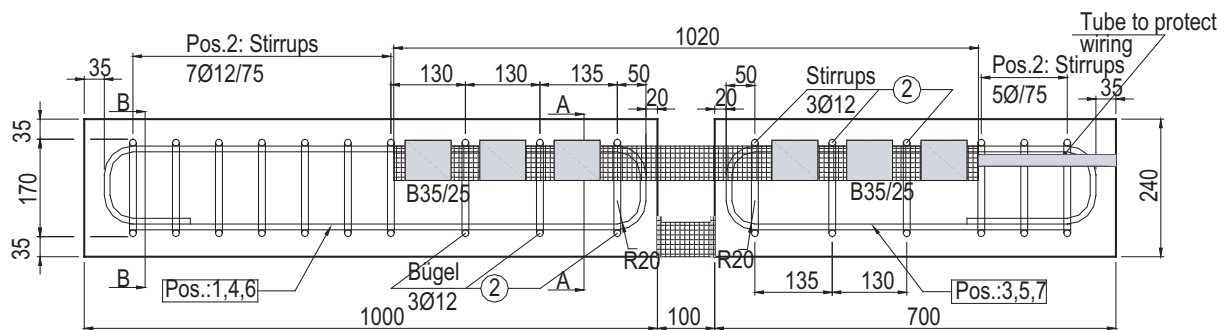


(b) Cut A-A

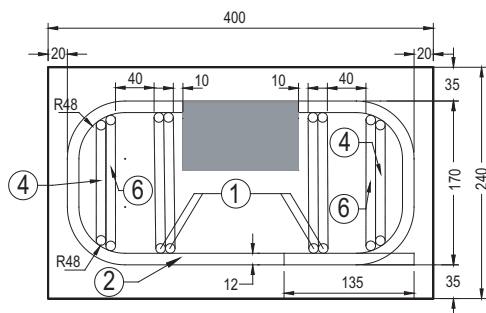


(c) Cut B-B

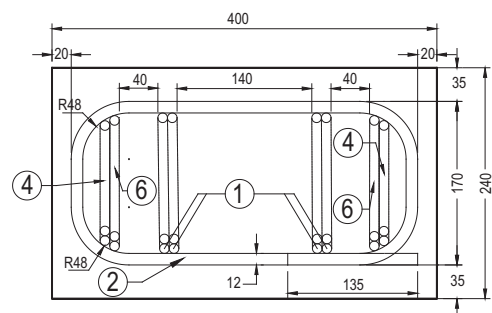
Figure G.2: Reinforcement drawing and dimensions of two-rib beam



(a) Beam with three-rib TS-element



(b) Cut A-A



(c) Cut B-B

Figure G.3: Reinforcement drawing and dimensions of a three-rib beam

G.2. Instrumentation

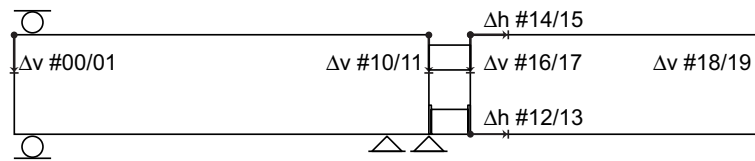


Figure G.4: Positioning of displacement transducers and support conditions

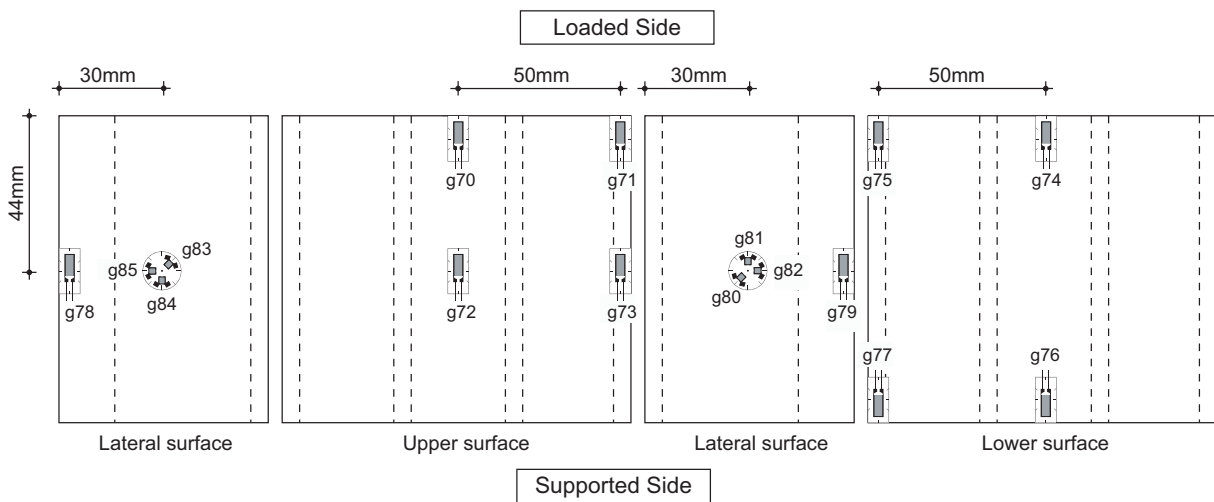
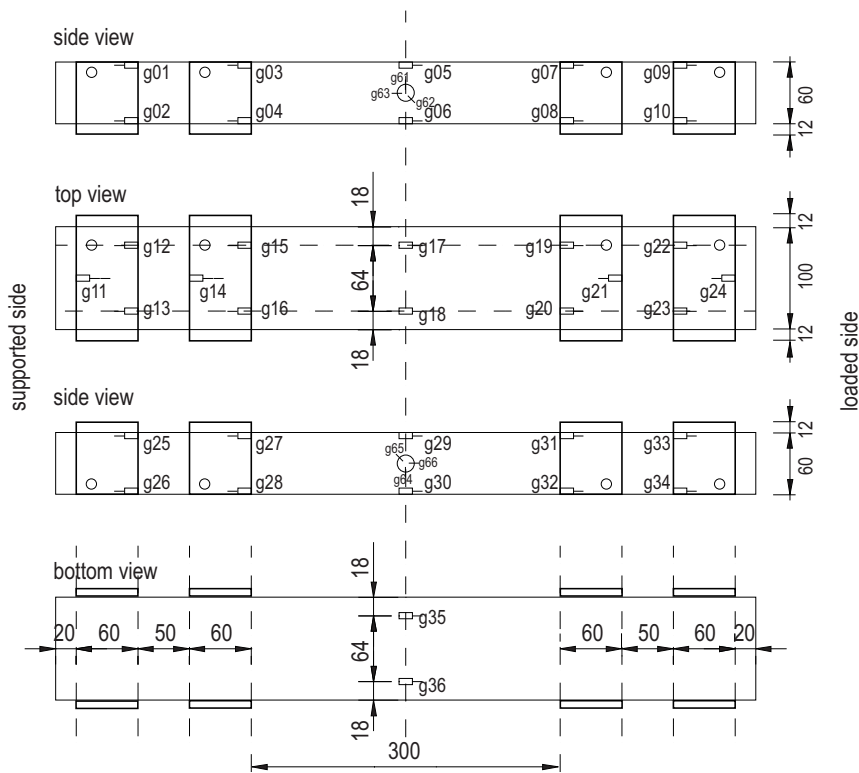


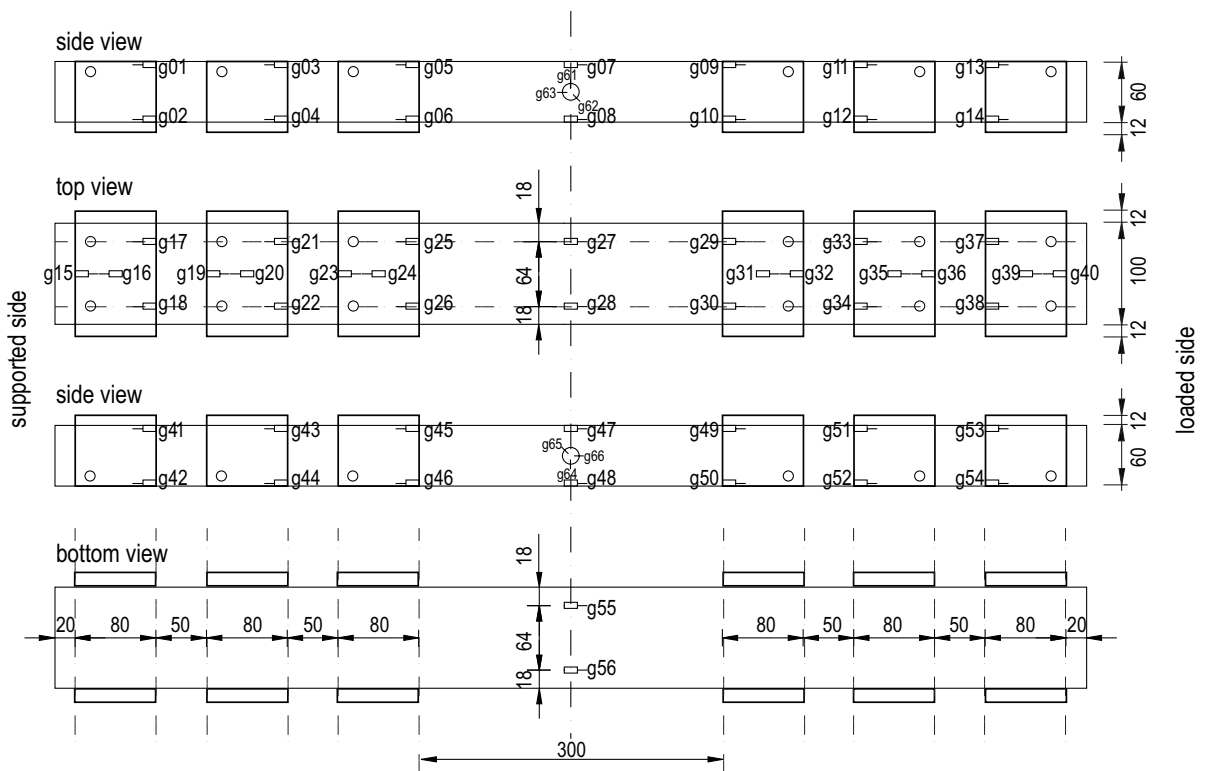
Figure G.5: Distribution of strain gages on CS-element

To determine the angle of principal stress, each two rosettes with a 0-45-90° strain gage arrangement were applied on the TS- and CS-element. The calculation of the angles from the obtained measurements is explained in Appendix F.1. With reference to Figure F.3 on page 222, the following assignment of measured directions and strain gages was applied:

Measured direction	<i>a</i>	<i>b</i>	<i>c</i>
Gages on CS-element	g82, g85	g80, g83	g81, g84
Gages on TS-element	g61, g64	g62, g65	g63, g66



(a) Tension element - two ribs, dimensions in mm

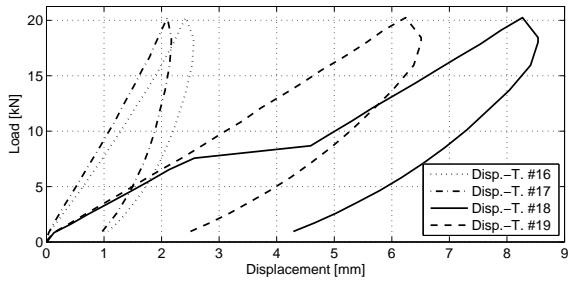


(b) Tension element - three ribs, dimensions in mm

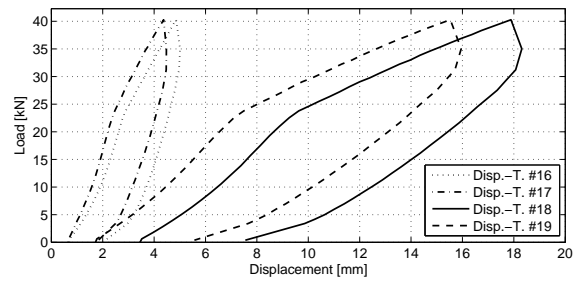
Figure G.6: Distribution of strain gages on TS-elements

G.3. Load-displacement curves

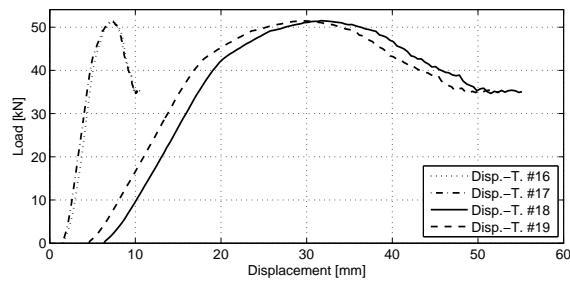
G.3.1. Vertical Displacements



(a) Cycle 20 kN

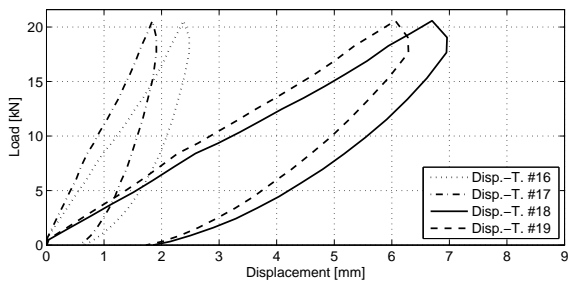


(b) Cycle 40 kN

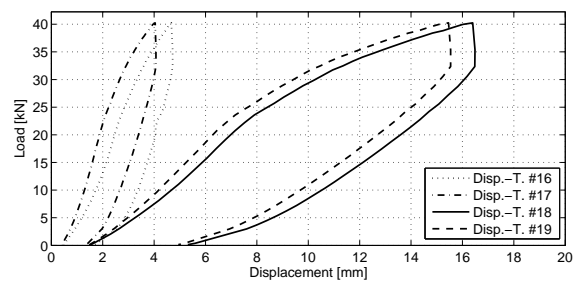


(c) Cycle 60 kN

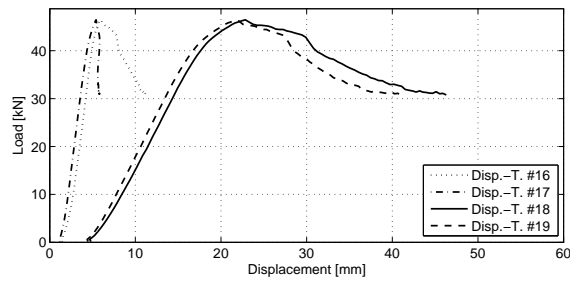
Figure G.7: Vertical displacements for M2E1



(a) Cycle 20 kN



(b) Cycle 40 kN



(c) Cycle 60 kN

Figure G.8: Vertical displacements for M2E2

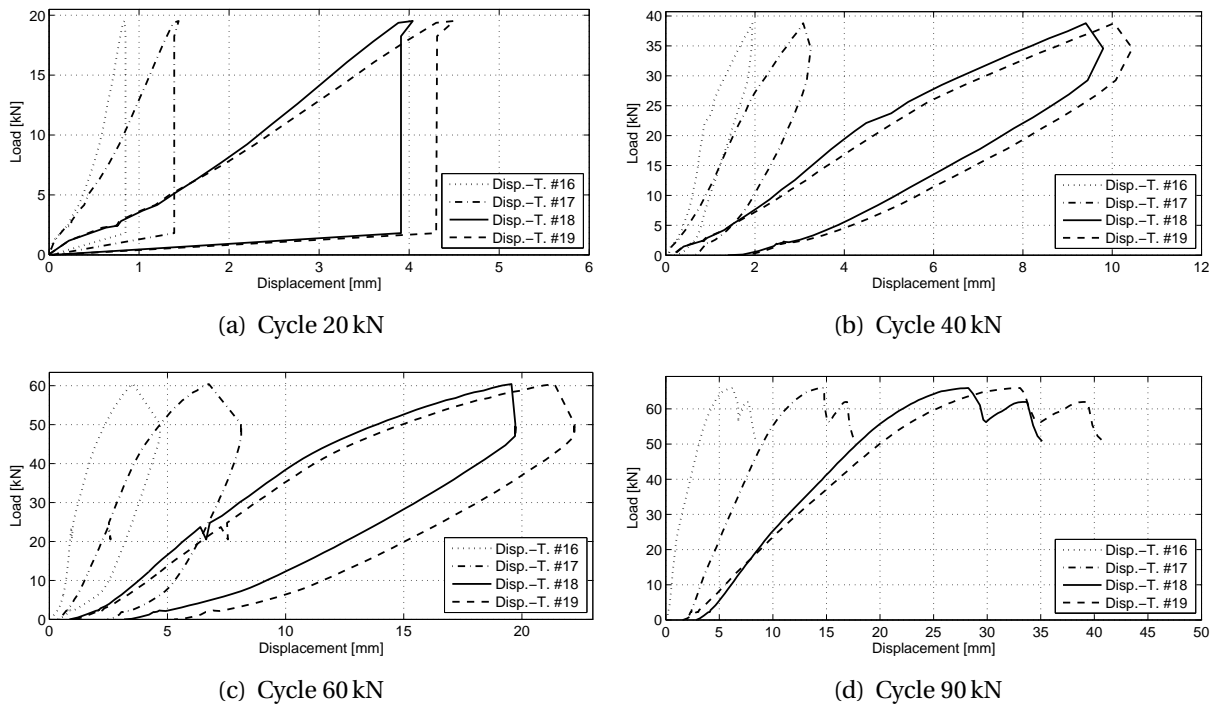


Figure G.9: Vertical displacements for M3E1

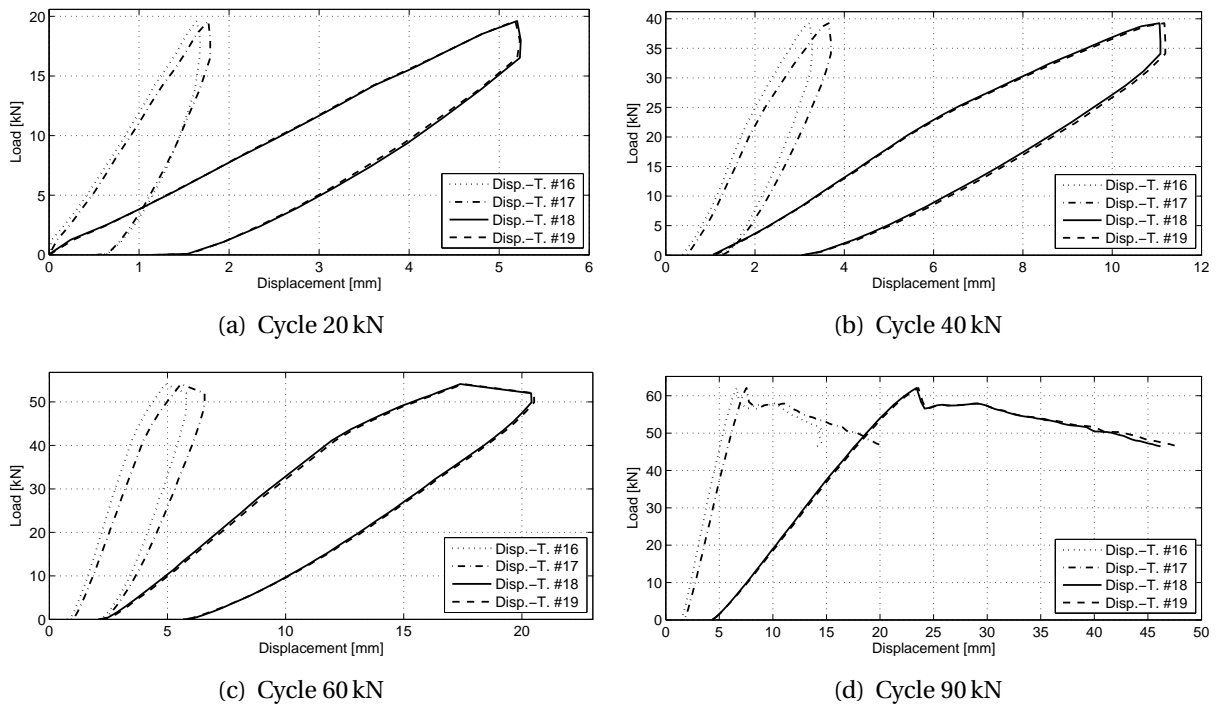


Figure G.10: Vertical displacements for M3E2

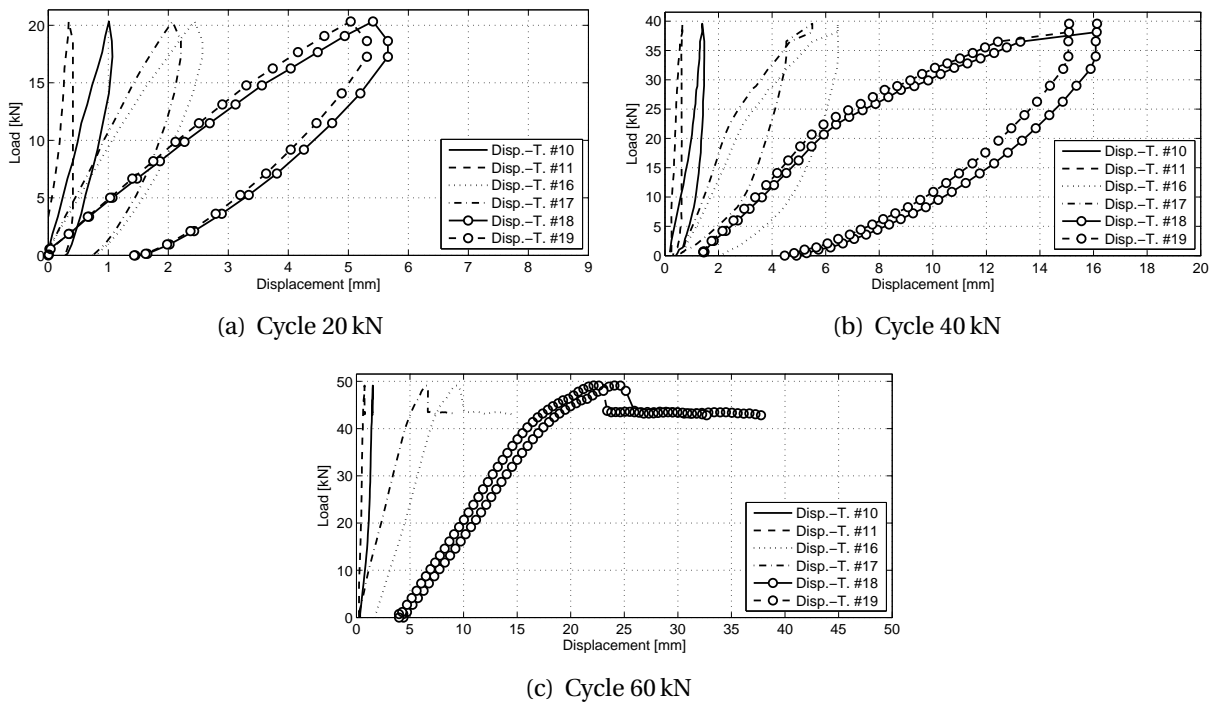


Figure G.11: Vertical displacements for S2C1

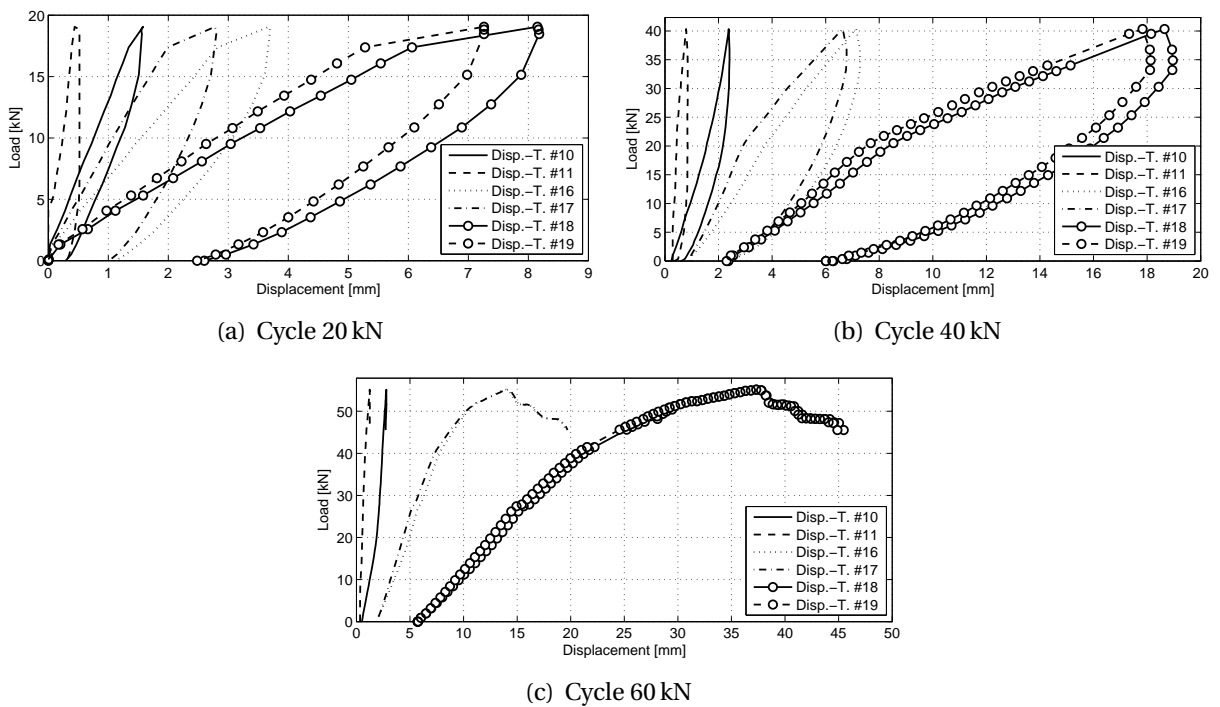
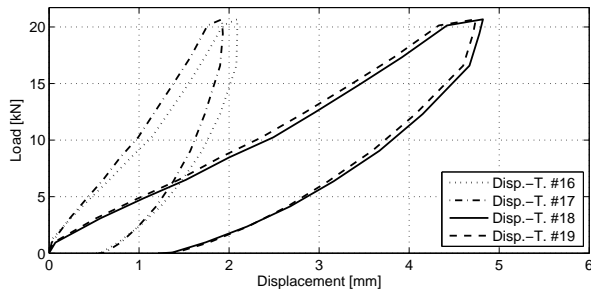
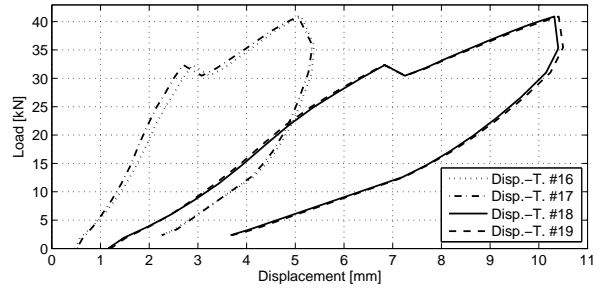


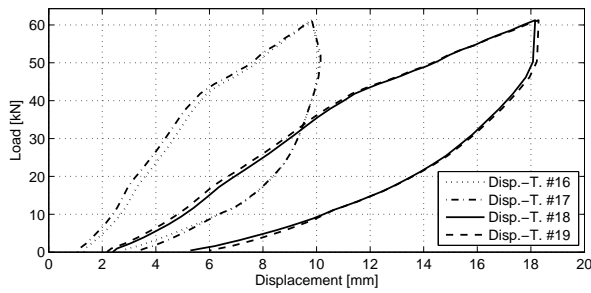
Figure G.12: Vertical displacements for S2C2



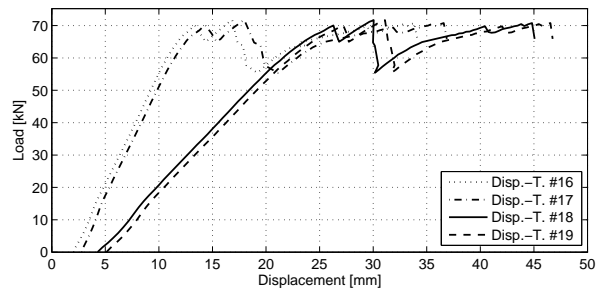
(a) Cycle 20 kN



(b) Cycle 40 kN

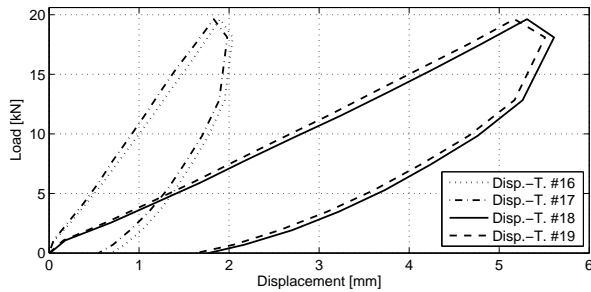


(c) Cycle 60 kN

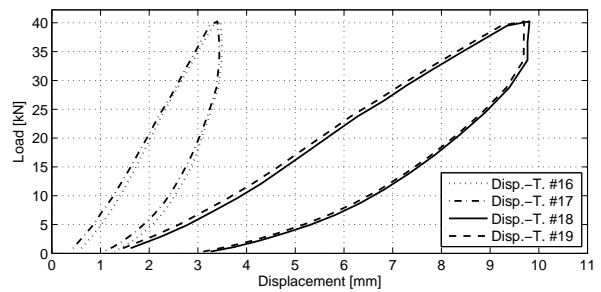


(d) Cycle 90 kN

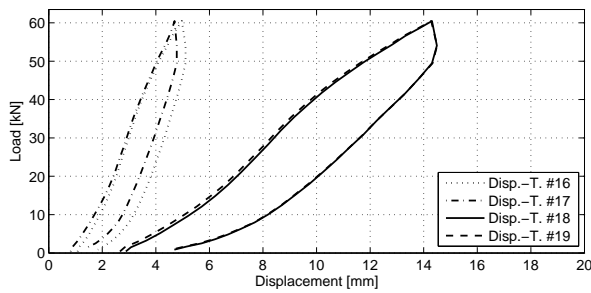
Figure G.13: Vertical displacements for S3E1



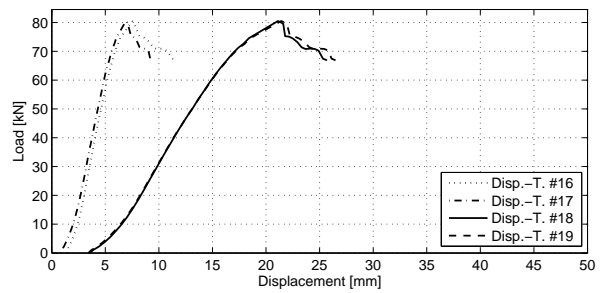
(a) Cycle 20 kN



(b) Cycle 40 kN



(c) Cycle 60 kN



(d) Cycle 90 kN

Figure G.14: Vertical displacements for S3E2

G.3.2. Horizontal Displacements

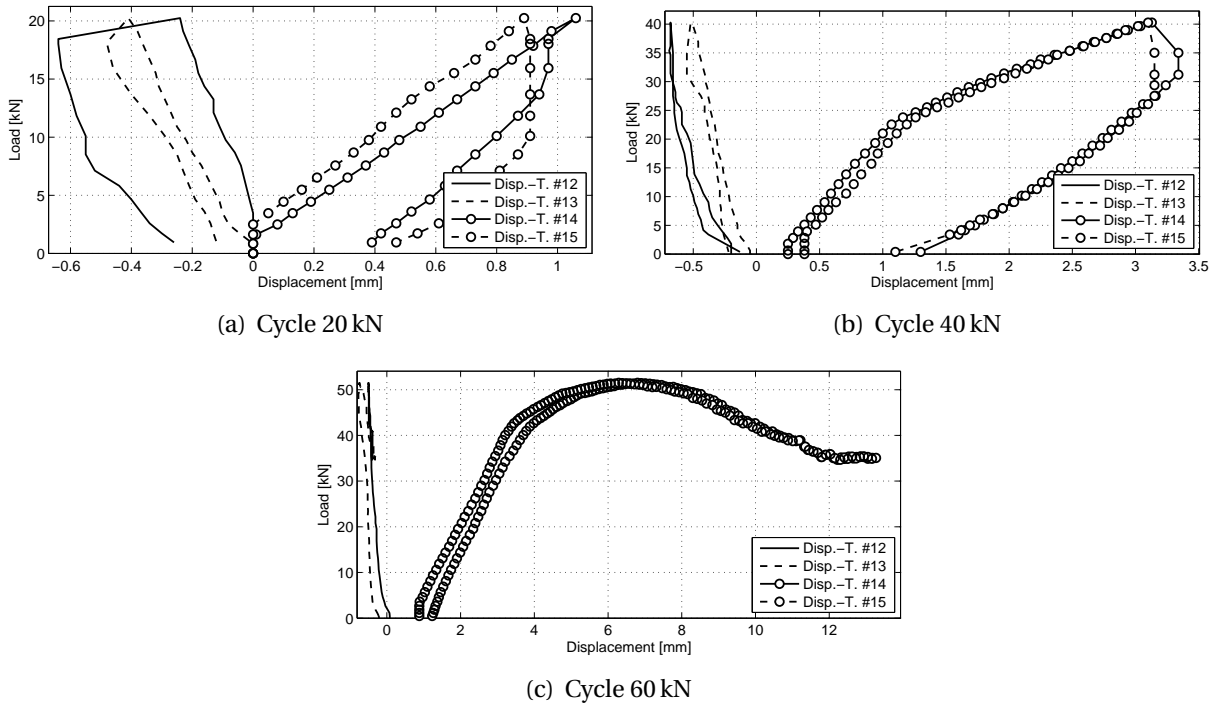


Figure G.15: Horizontal displacements for M2E1

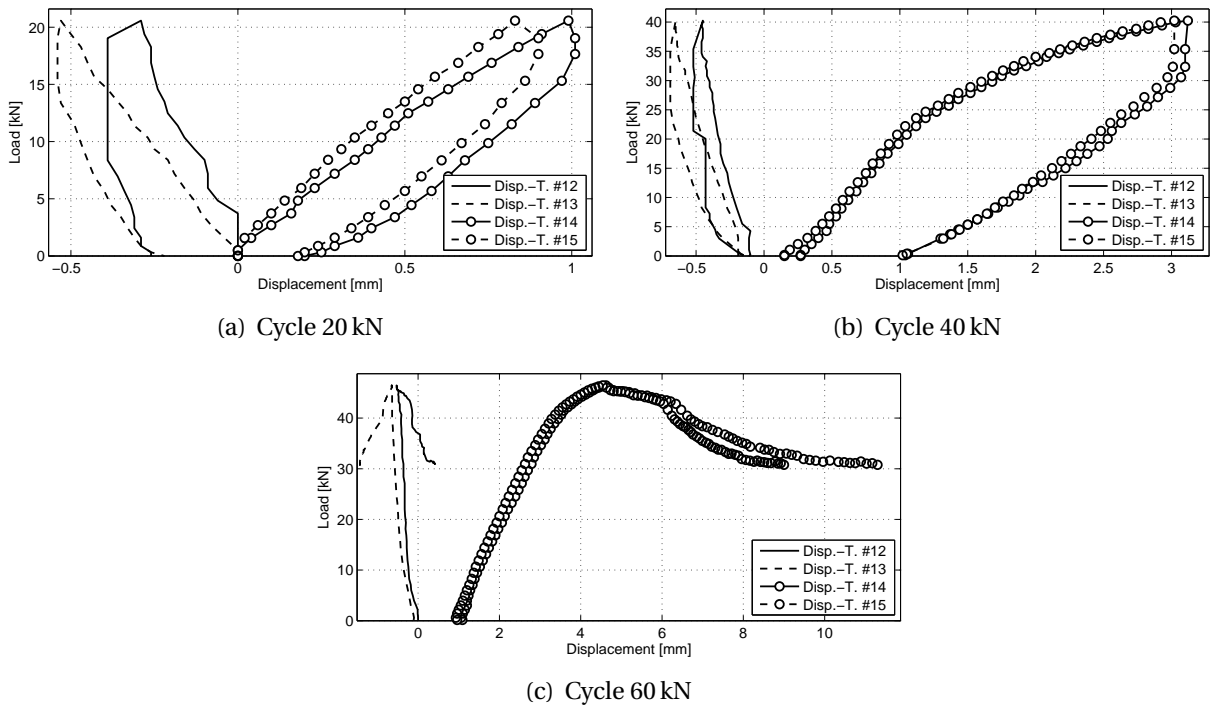


Figure G.16: Horizontal displacements for M2E2

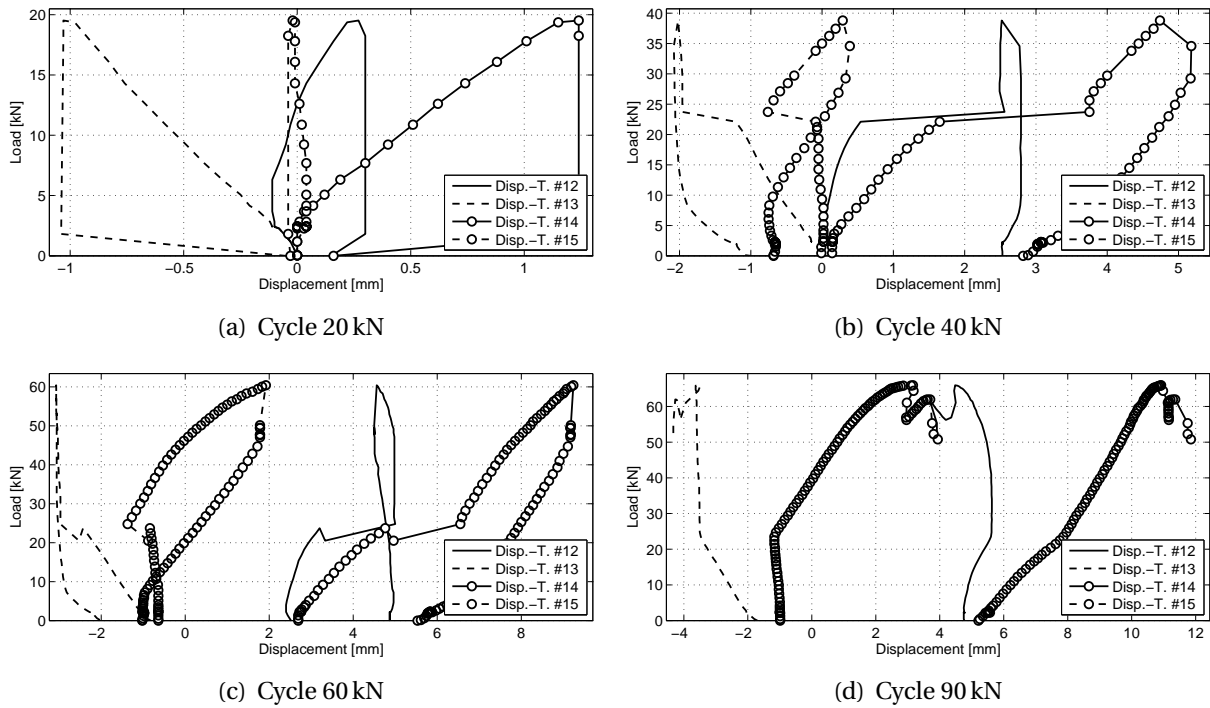


Figure G.17: Horizontal displacements for M3E1

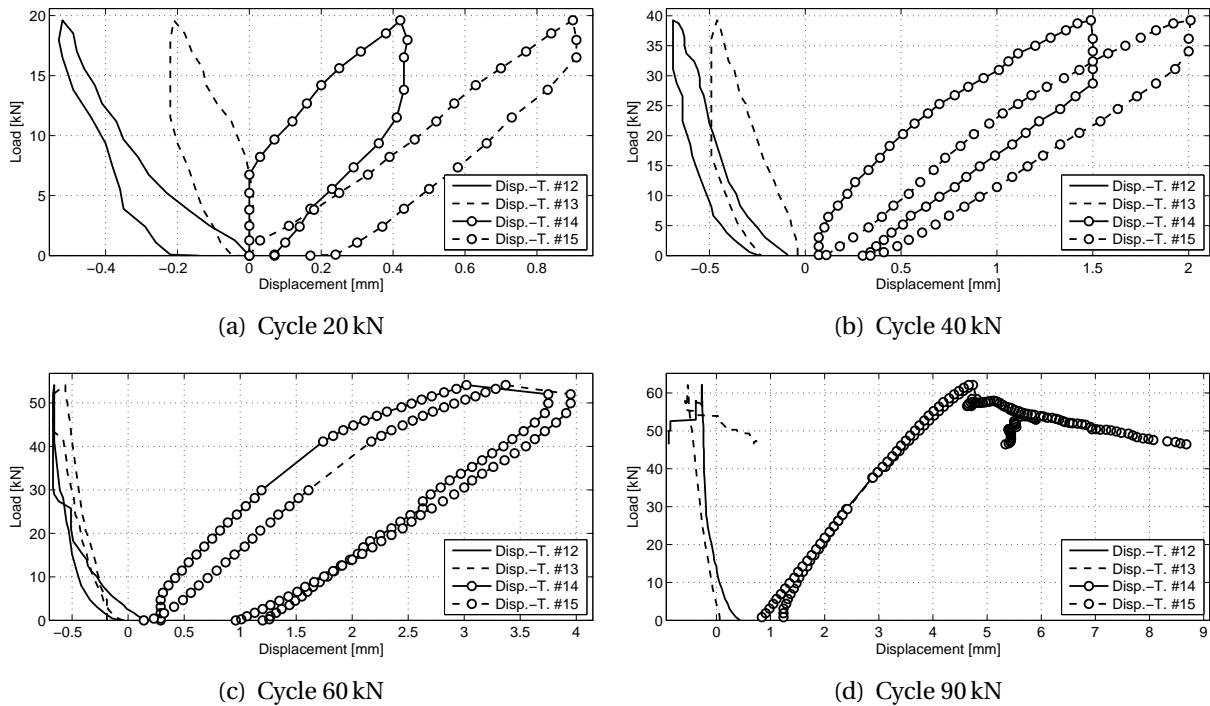


Figure G.18: Horizontal displacements for M3E2

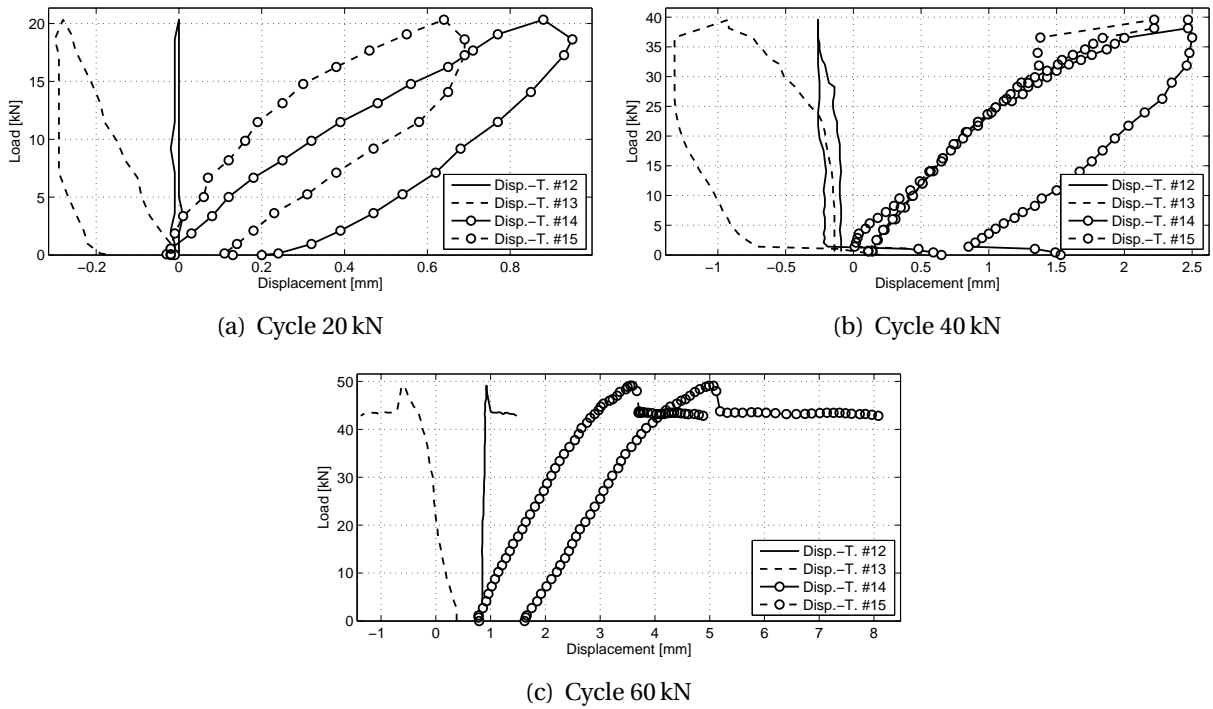


Figure G.19: Horizontal displacements for S2C1

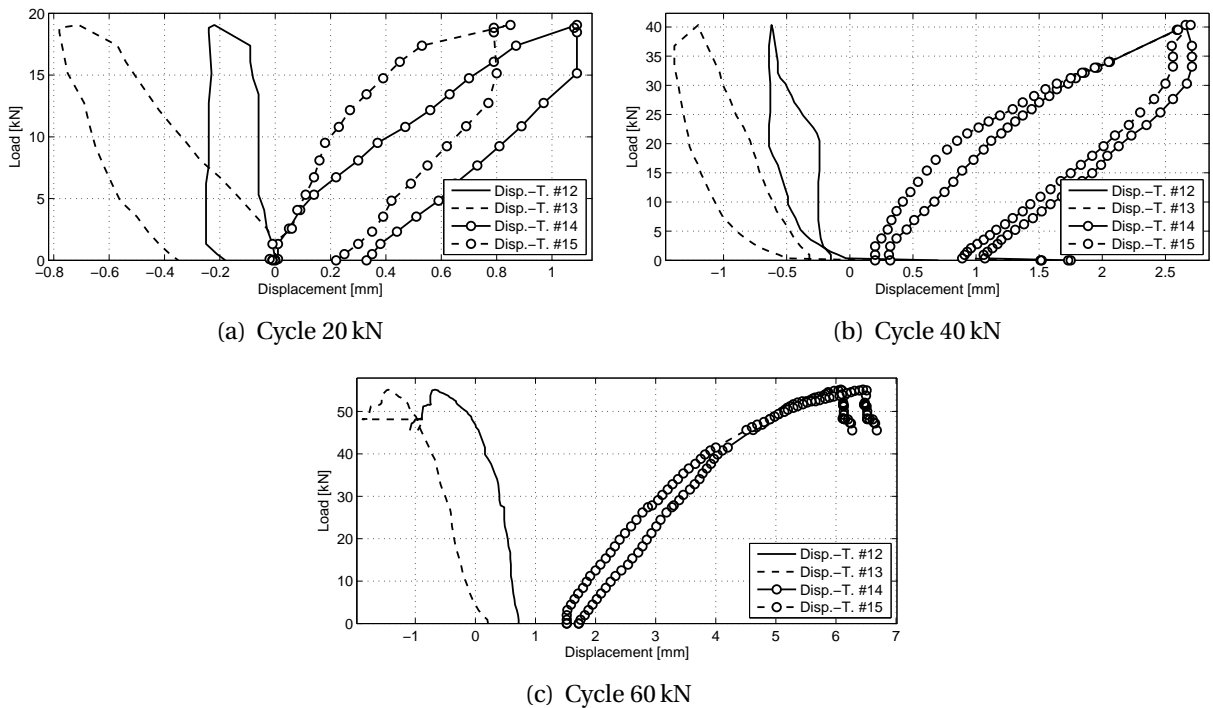
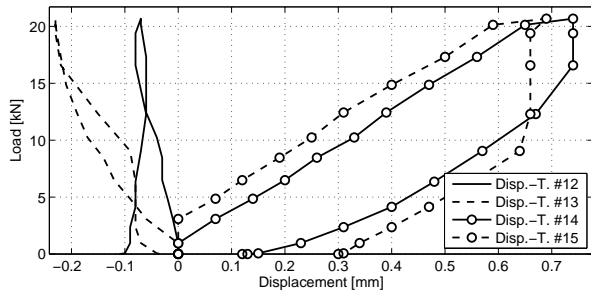
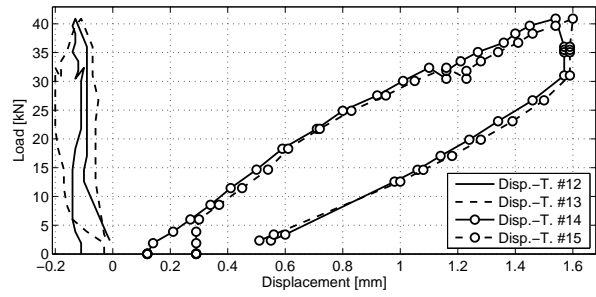


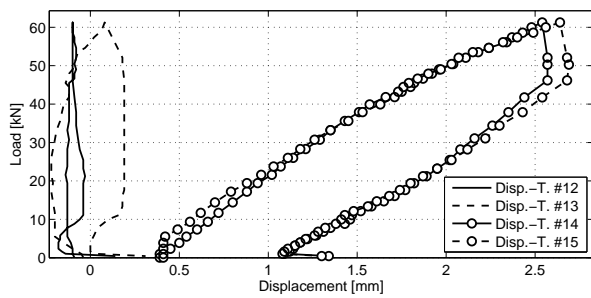
Figure G.20: Horizontal displacements for S2C2



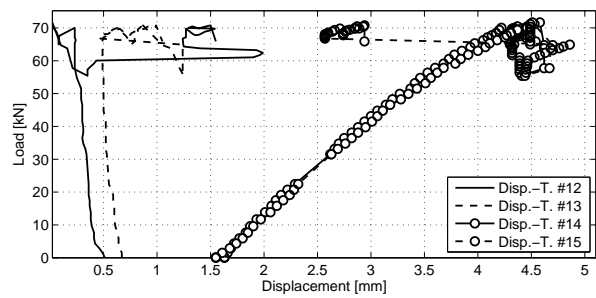
(a) Cycle 20 kN



(b) Cycle 40 kN

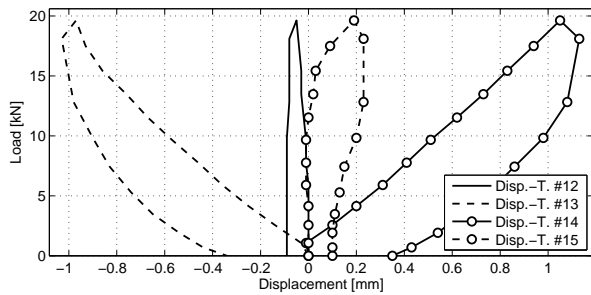


(c) Cycle 60 kN

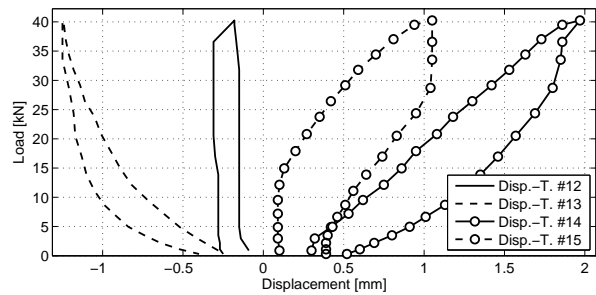


(d) Cycle 90 kN

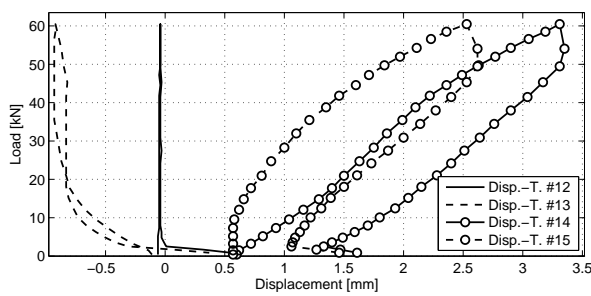
Figure G.21: Horizontal displacements for S3E1



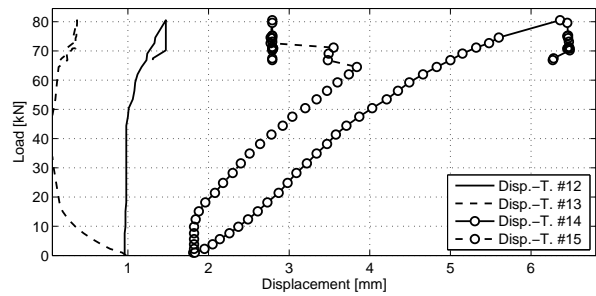
(a) Cycle 20 kN



(b) Cycle 40 kN



(c) Cycle 60 kN



(d) Cycle 90 kN

Figure G.22: Horizontal displacements for S3E2

G.4. Crack patterns

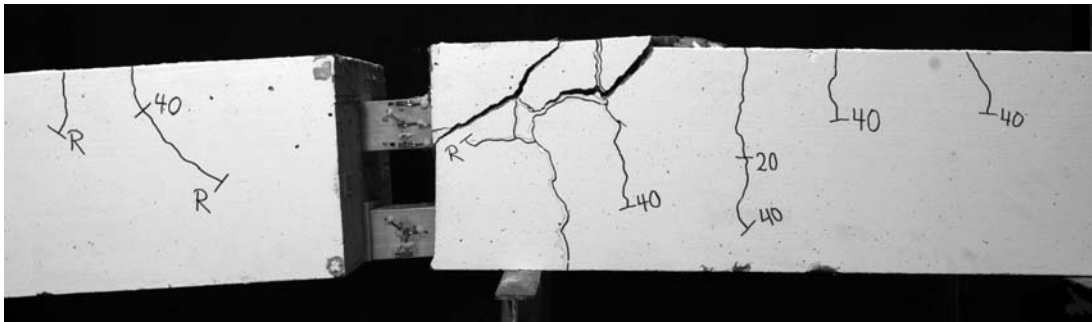


Figure G.23: Crack pattern for M2E1

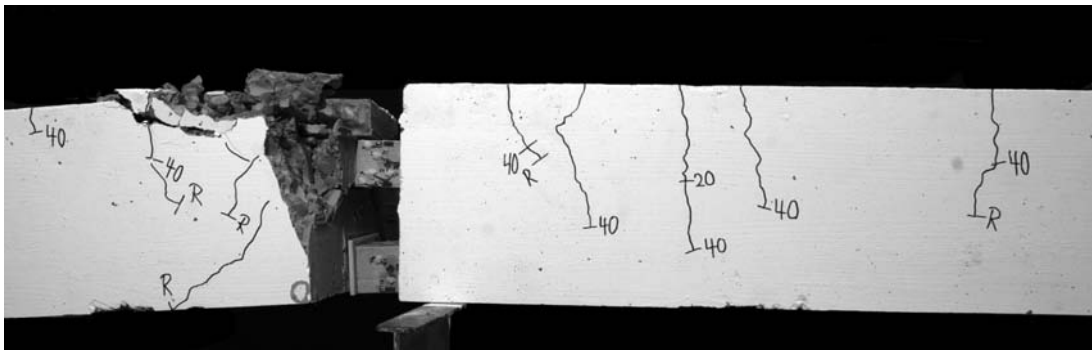


Figure G.24: Crack pattern for M2E2

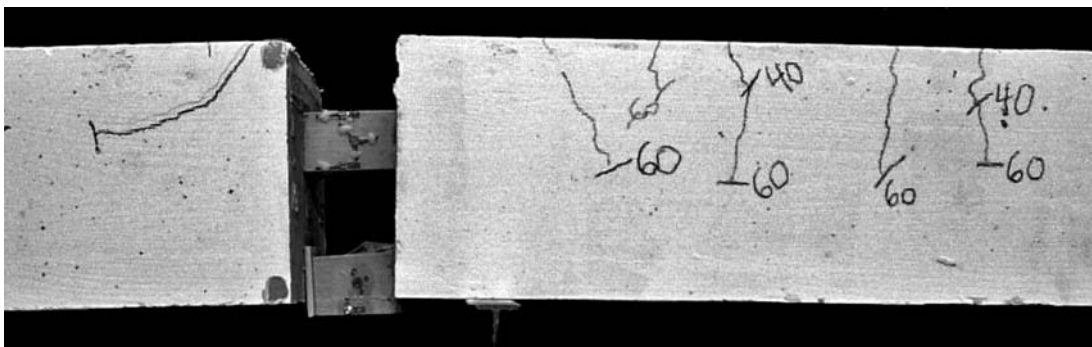


Figure G.25: Crack pattern for M3E1



Figure G.26: Crack pattern for M3E2

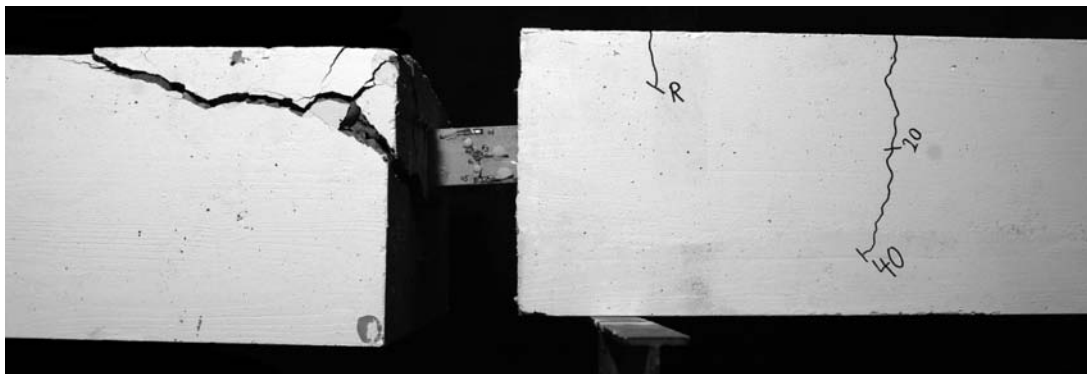


Figure G.27: Crack pattern for S2C1

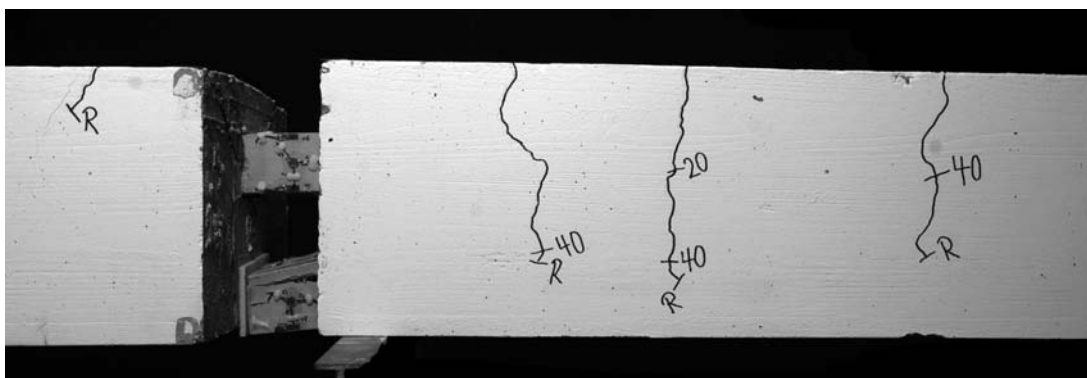


Figure G.28: Crack pattern for S2C2

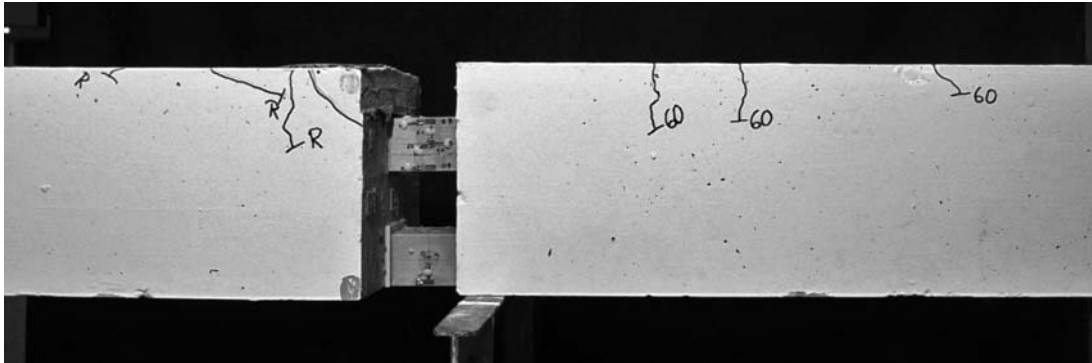


Figure G.29: Crack pattern for S3E1

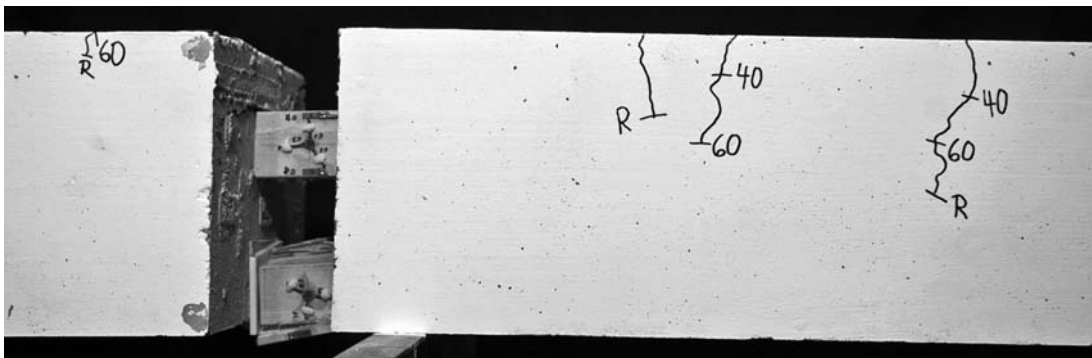


Figure G.30: Crack pattern for S3E2

G.5. Failure Modes

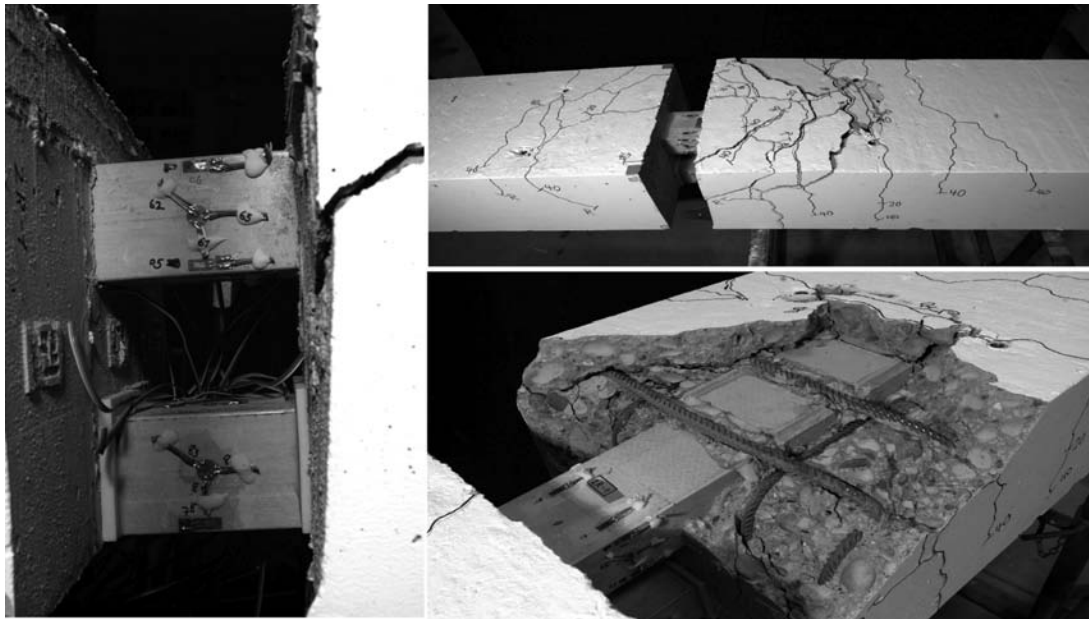


Figure G.31: Failure mode for M2E1

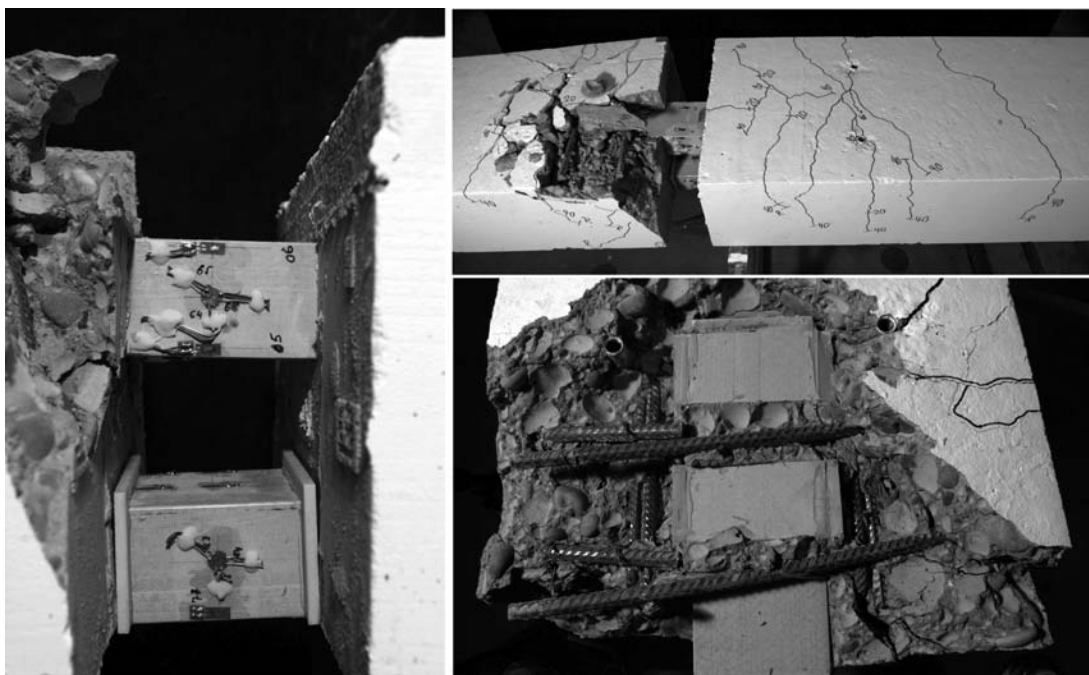


Figure G.32: Failure mode for M2E2

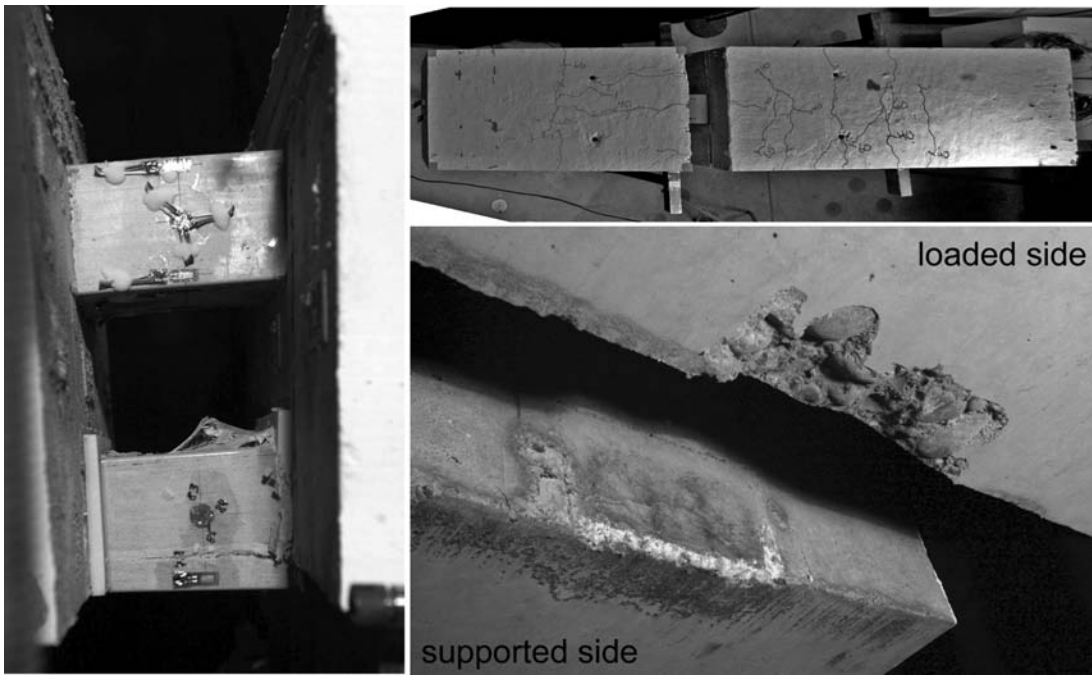


Figure G.33: Failure mode for M3E1

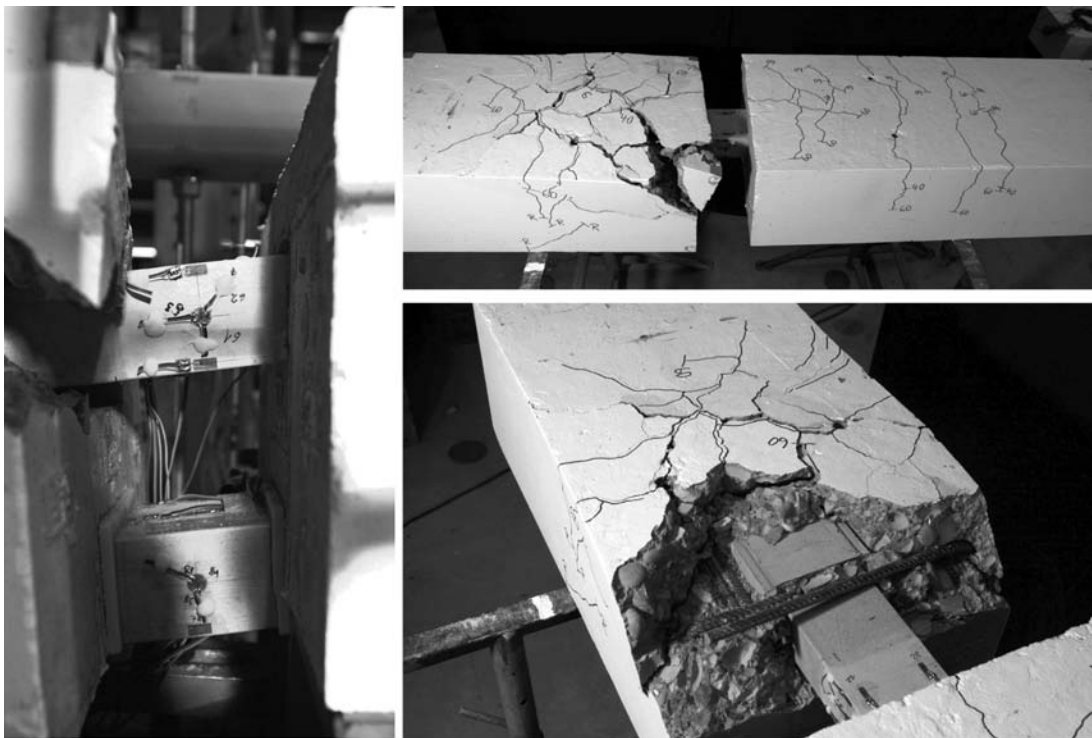


Figure G.34: Failure mode for M3E2



Figure G.35: Failure mode for S2C1

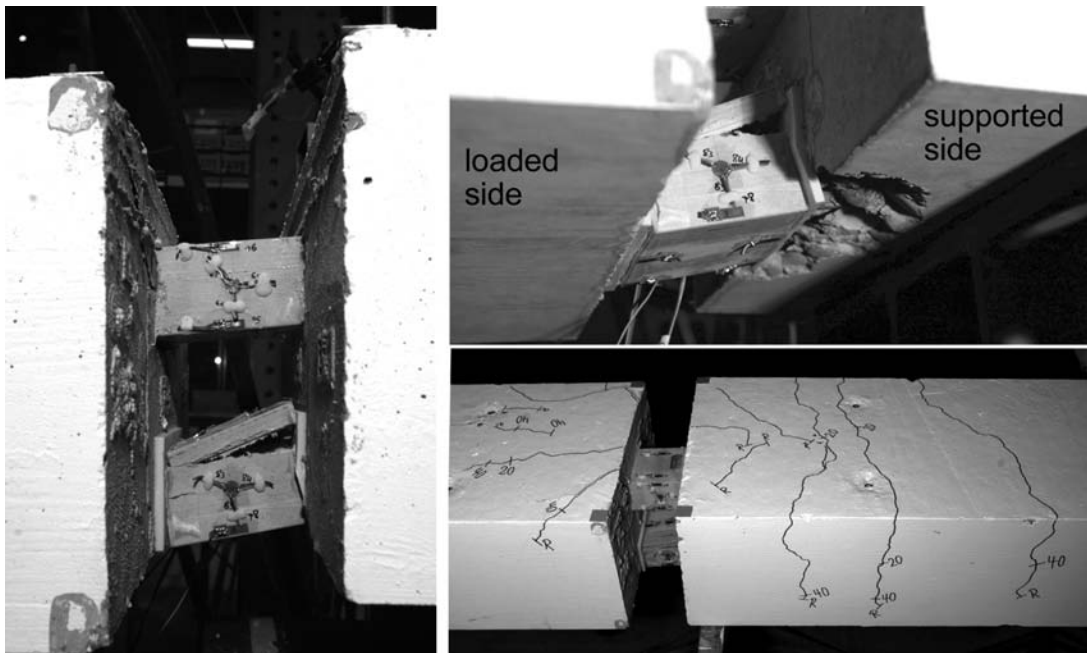


Figure G.36: Failure mode for S2C2

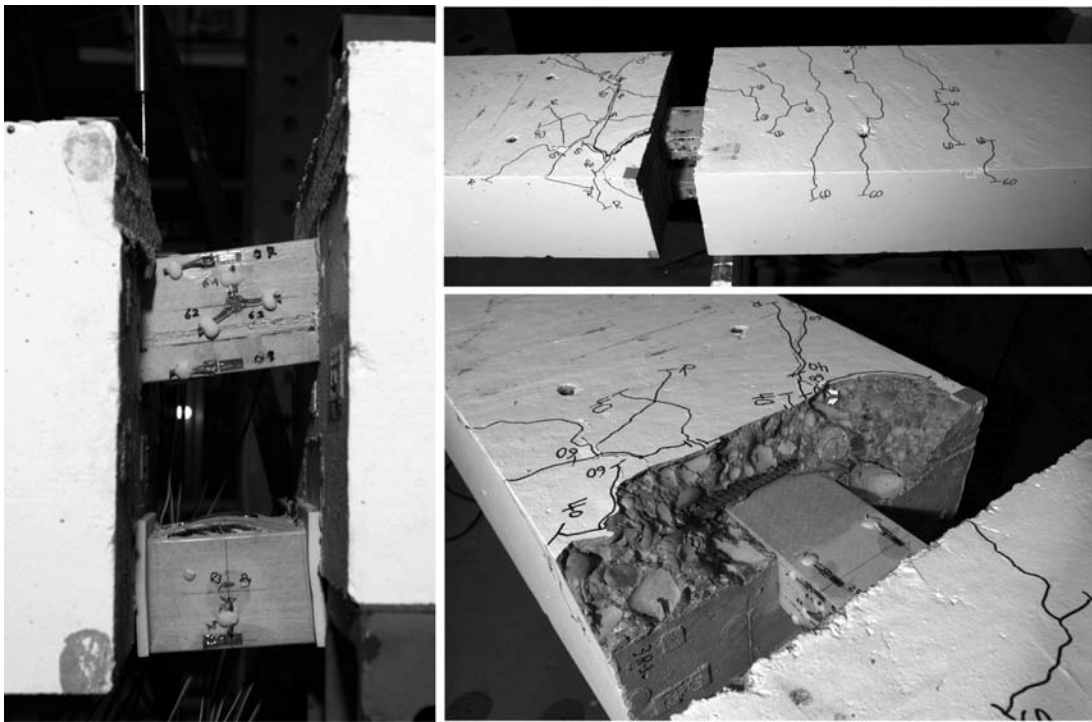


Figure G.37: Failure mode for S3E1

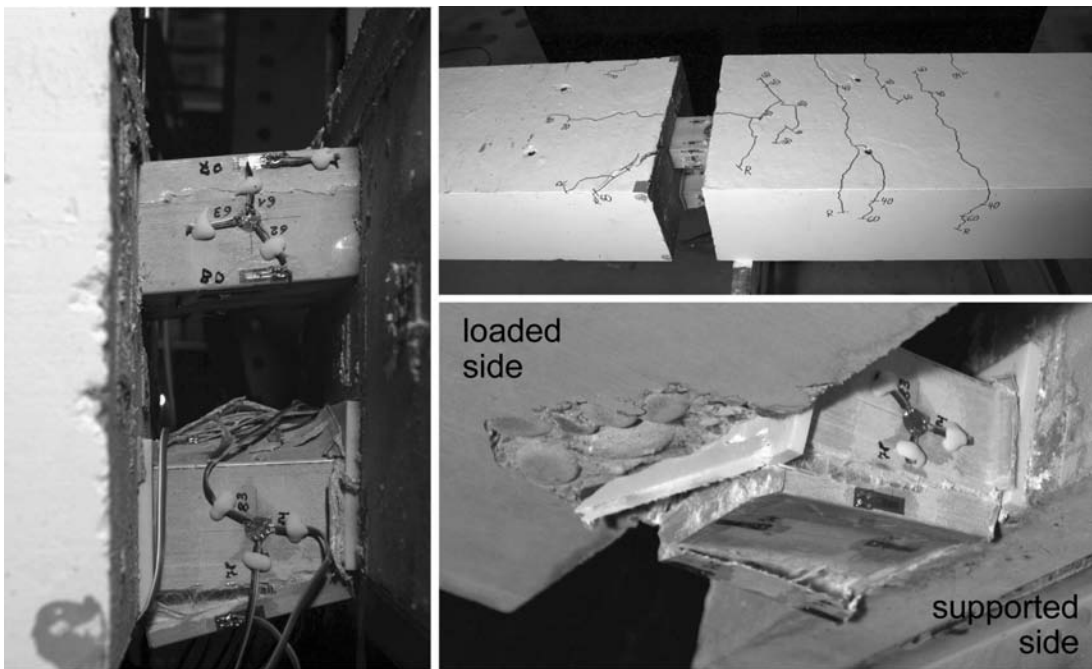
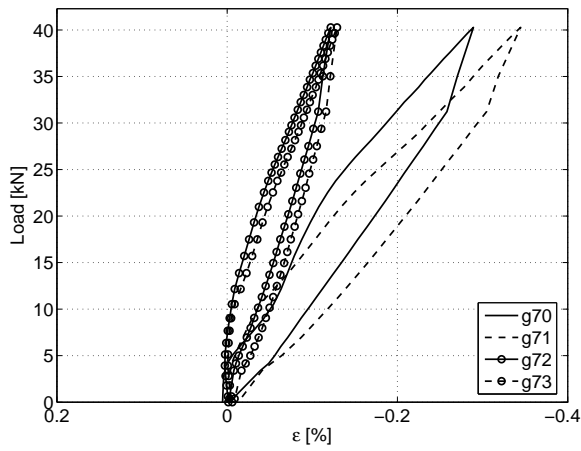
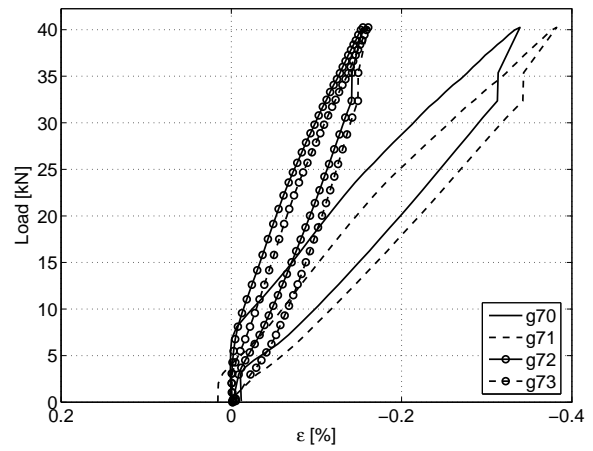


Figure G.38: Failure mode for S3E2

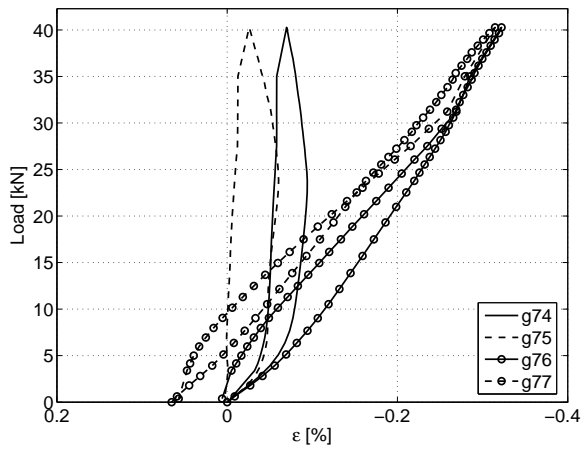
G.6. Strain on CS-element



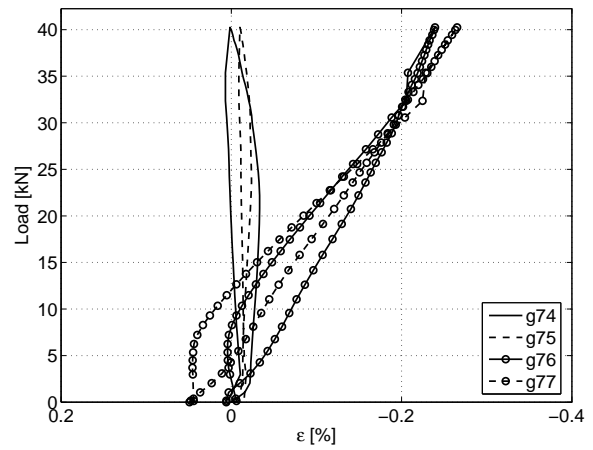
(a) Top side



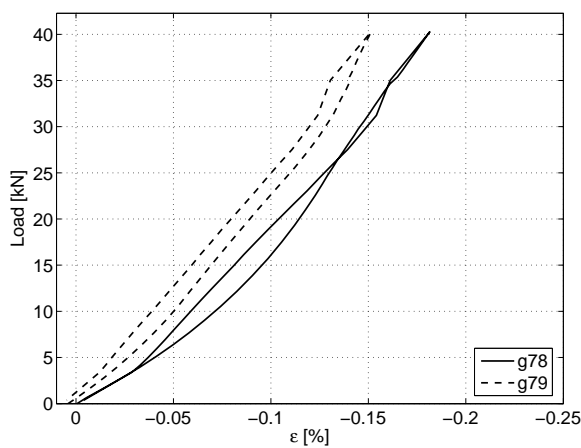
(b) Top side



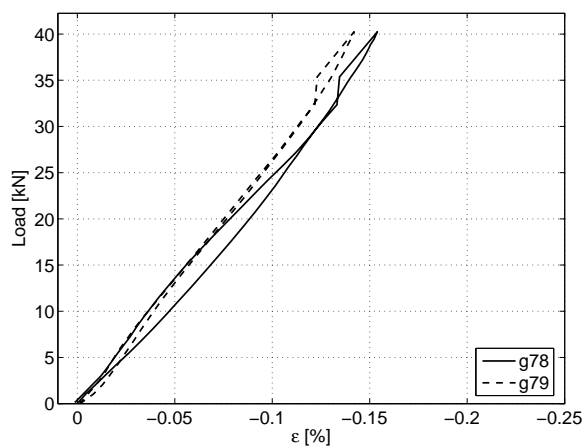
(c) Bottom side



(d) Bottom side

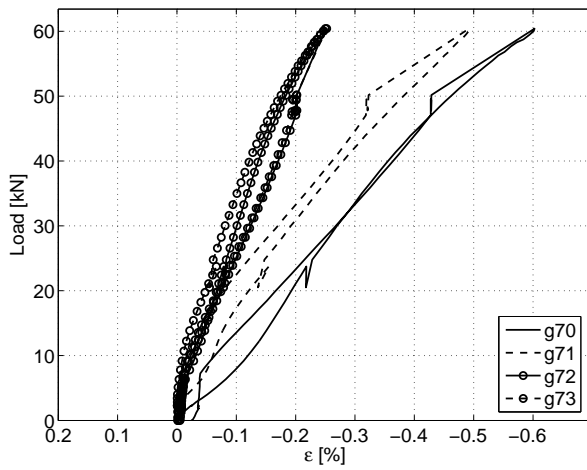


(e) Lateral sides

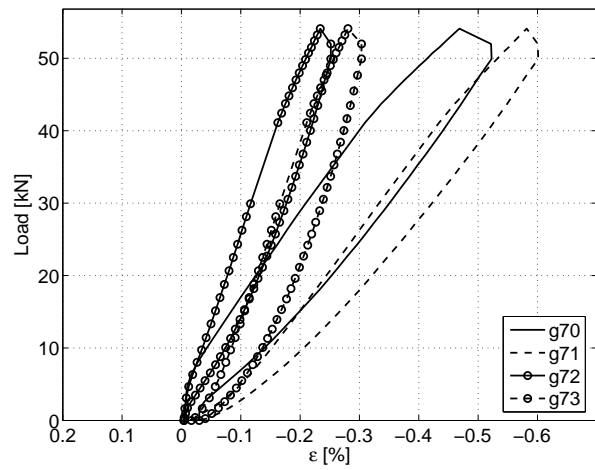


(f) Lateral sides

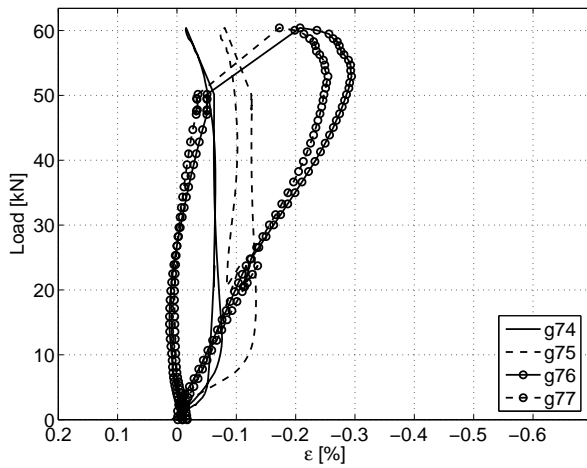
Figure G.39: M2E1 (left) & M2E2 (right)



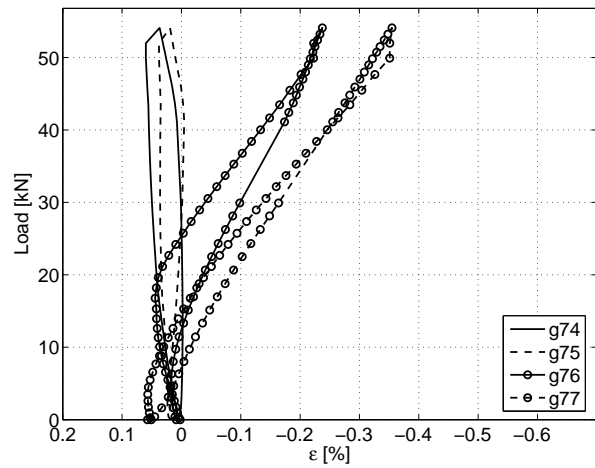
(a) Top side



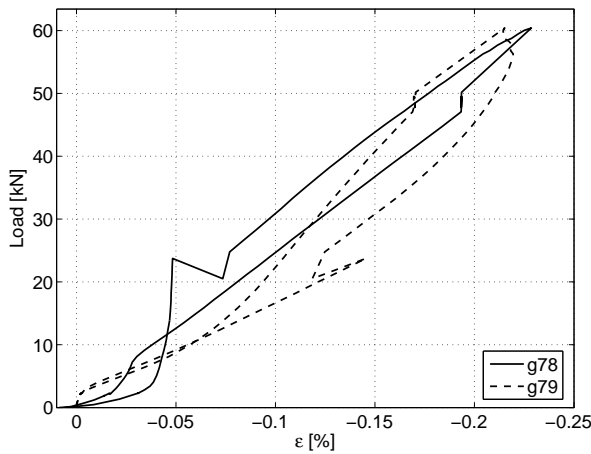
(b) Top side



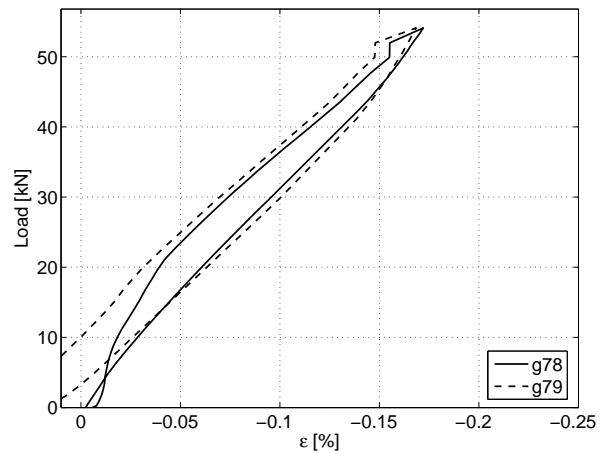
(c) Bottom side



(d) Bottom side

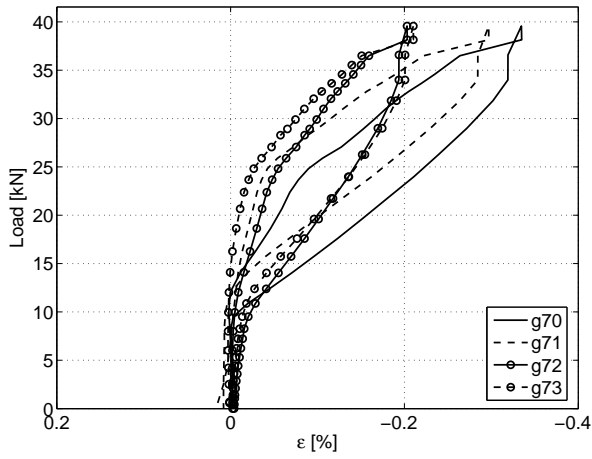


(e) Lateral sides

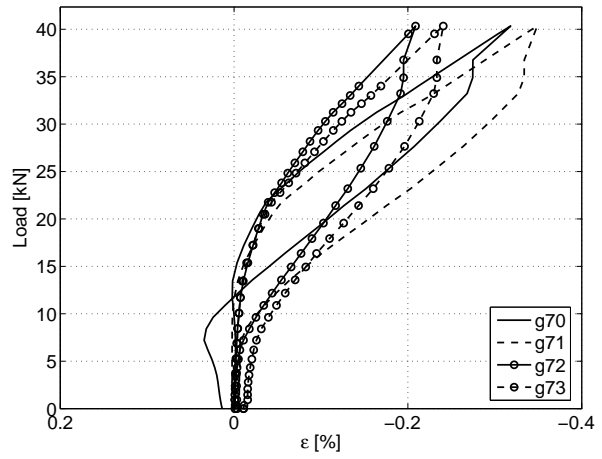


(f) Lateral sides

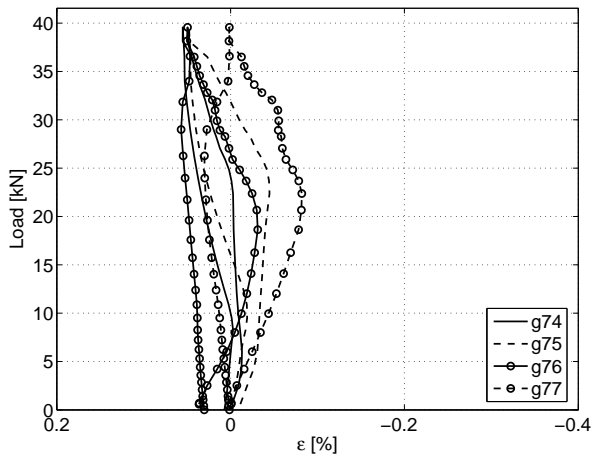
Figure G.40: M3E1 (left) & M3E2 (right)



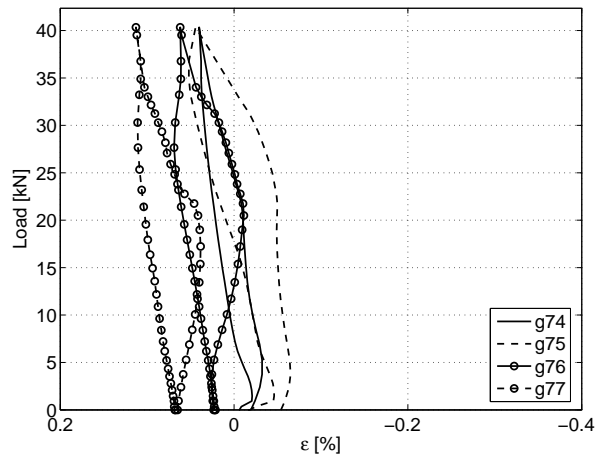
(a) Top side



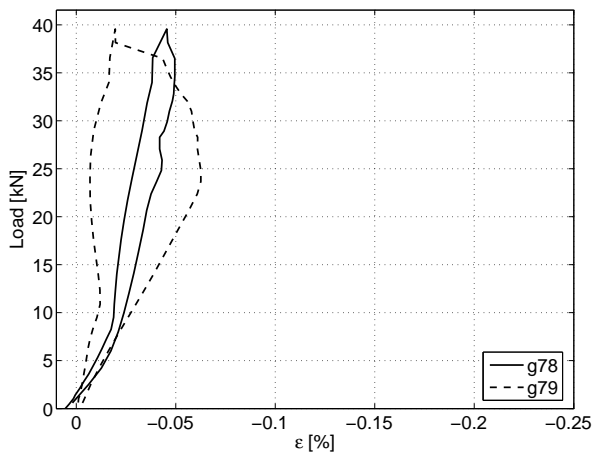
(b) Top side



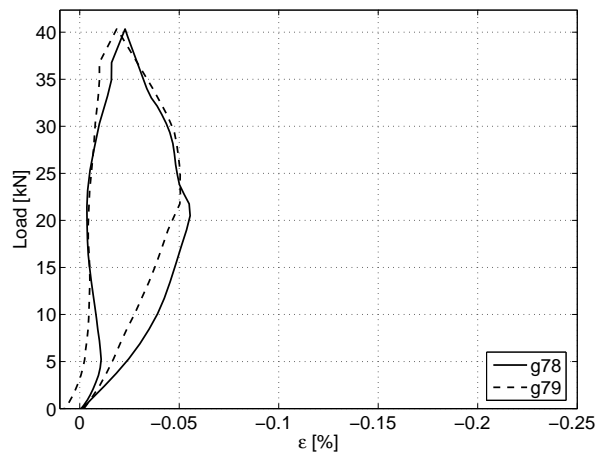
(c) Bottom side



(d) Bottom side

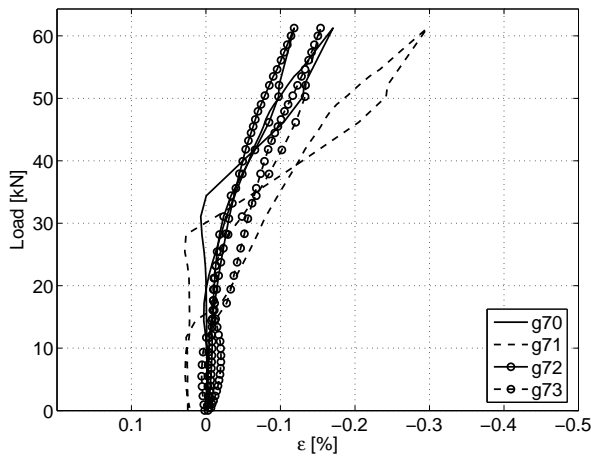


(e) Lateral sides

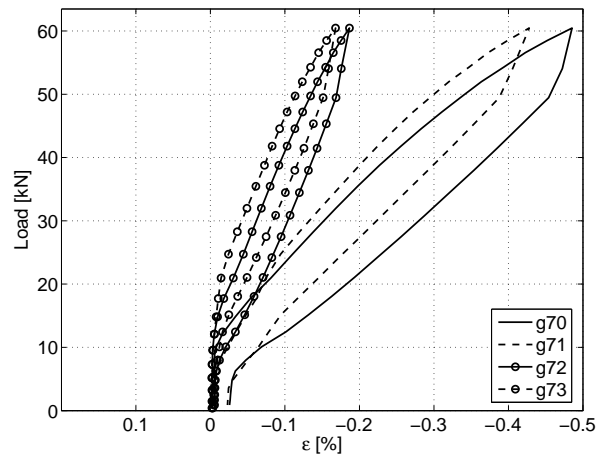


(f) Lateral sides

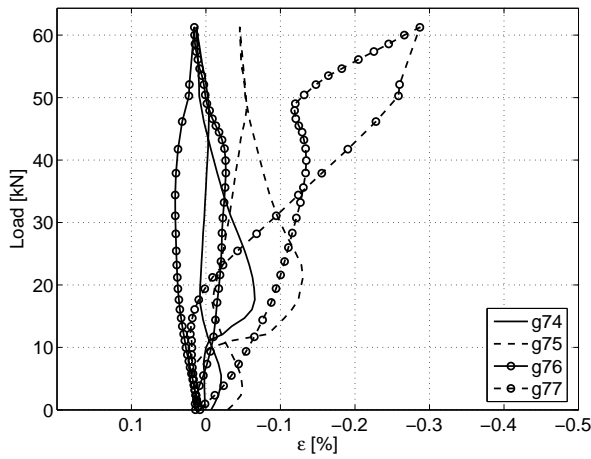
Figure G.41: S2C1 (left) & S2C2 (right)



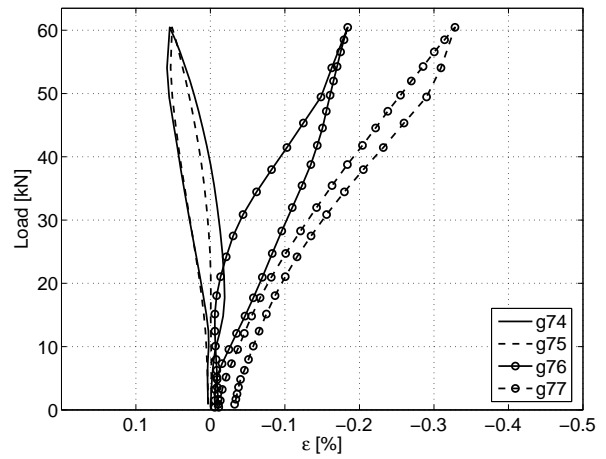
(a) Top side



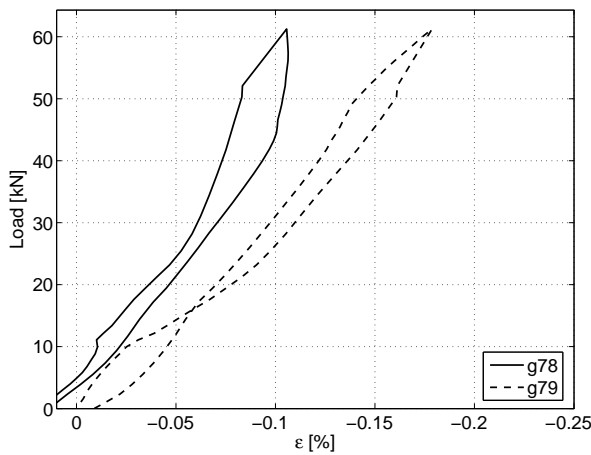
(b) Top side



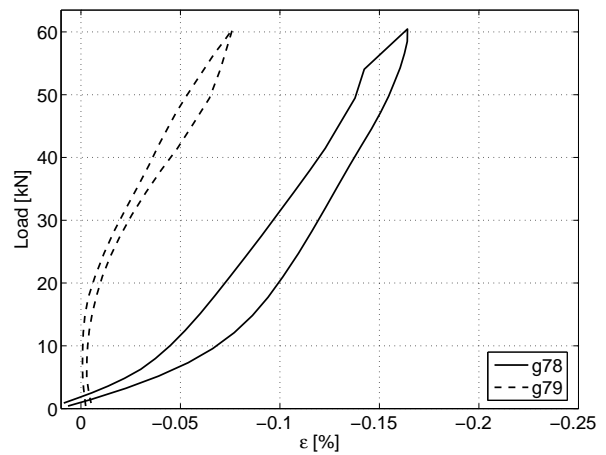
(c) Bottom side



(d) Bottom side



(e) Lateral sides



(f) Lateral sides

Figure G.42: S3E1 (left) & S3E2 (right)

G.7. Angle of principal stress on the compression element

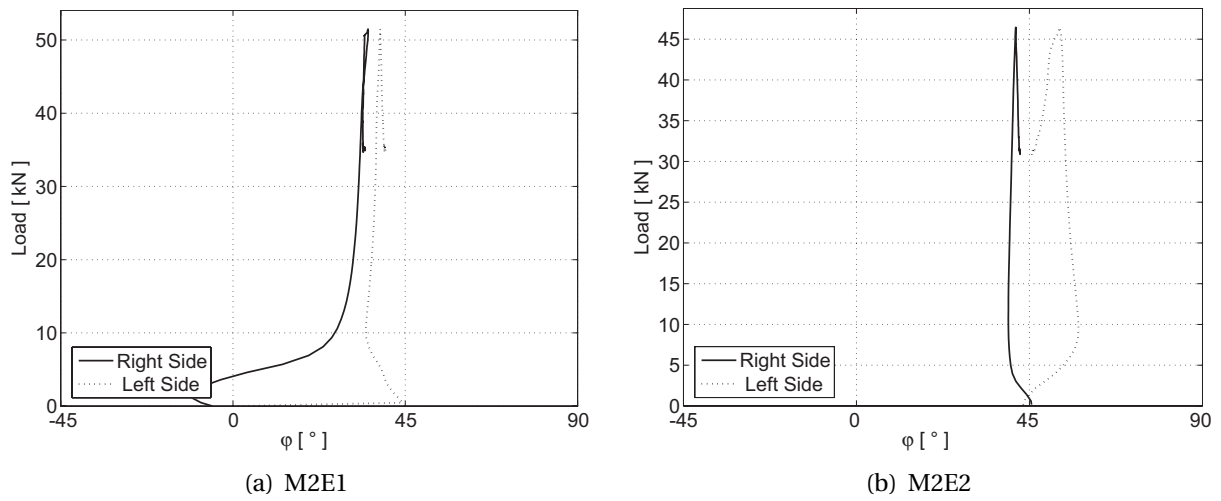


Figure G.43: M2E

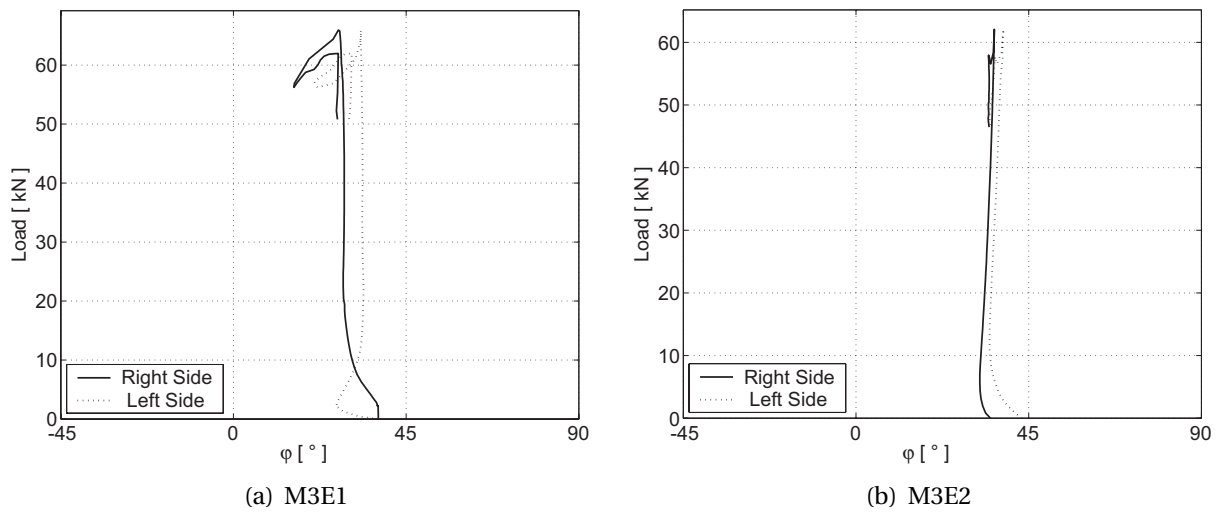


Figure G.44: M3E

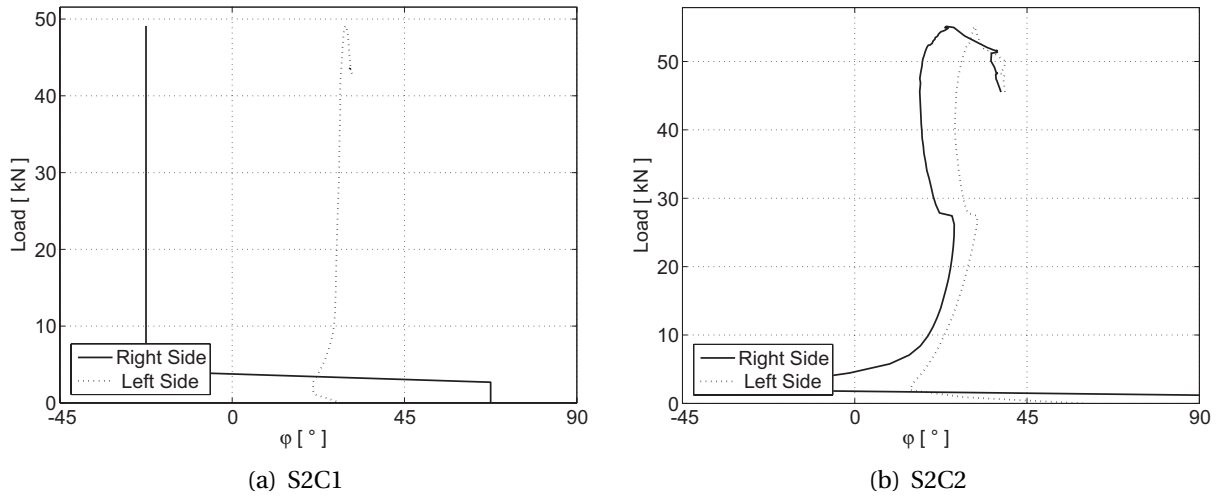


Figure G.45: S2C

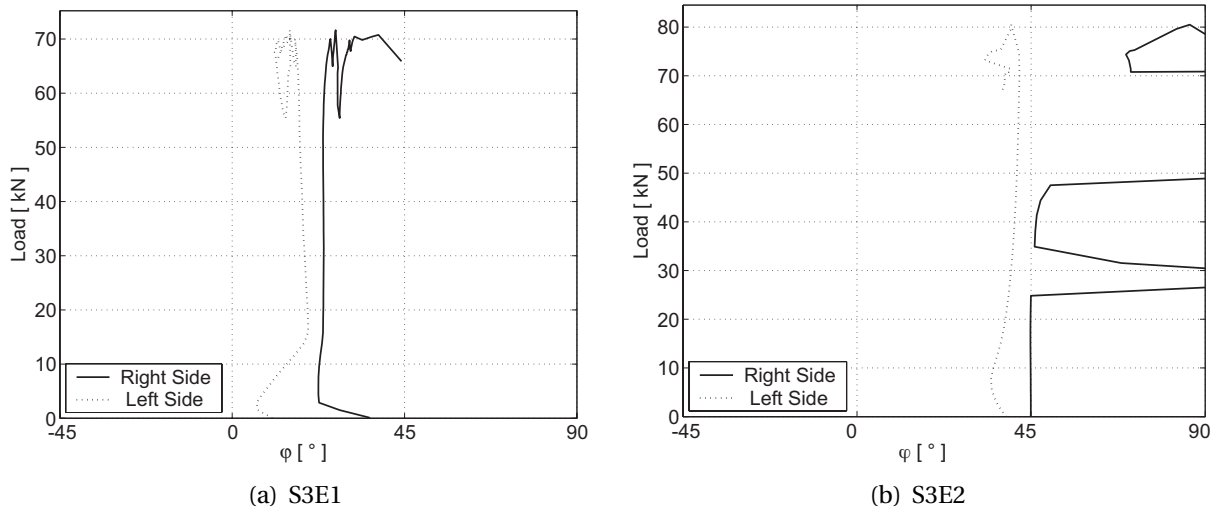


Figure G.46: S3E

G.8. Measured strain on the tension element's top-side

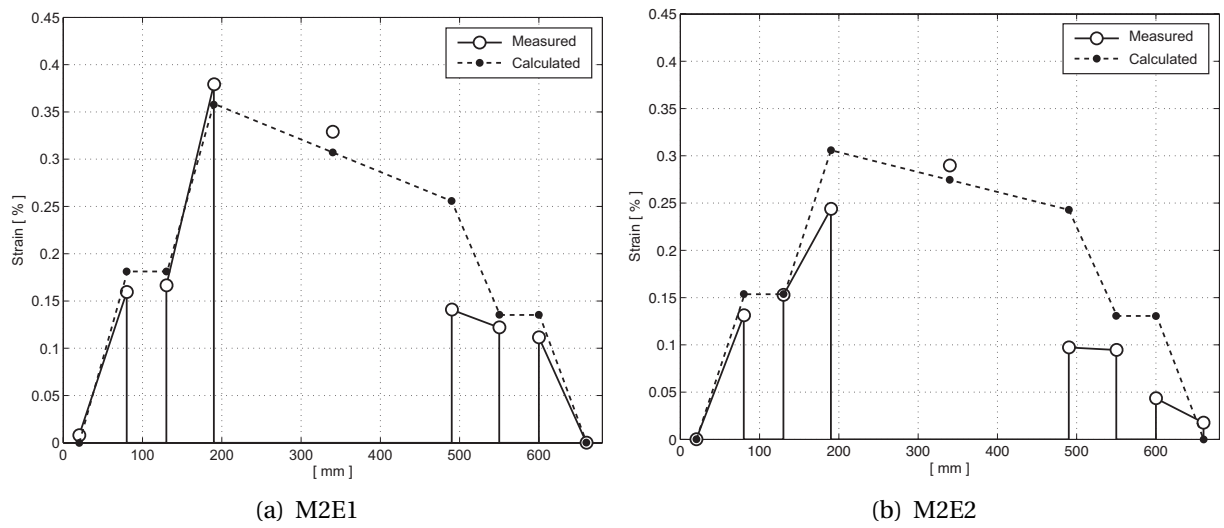


Figure G.47: Moment mode, double-rip, end support

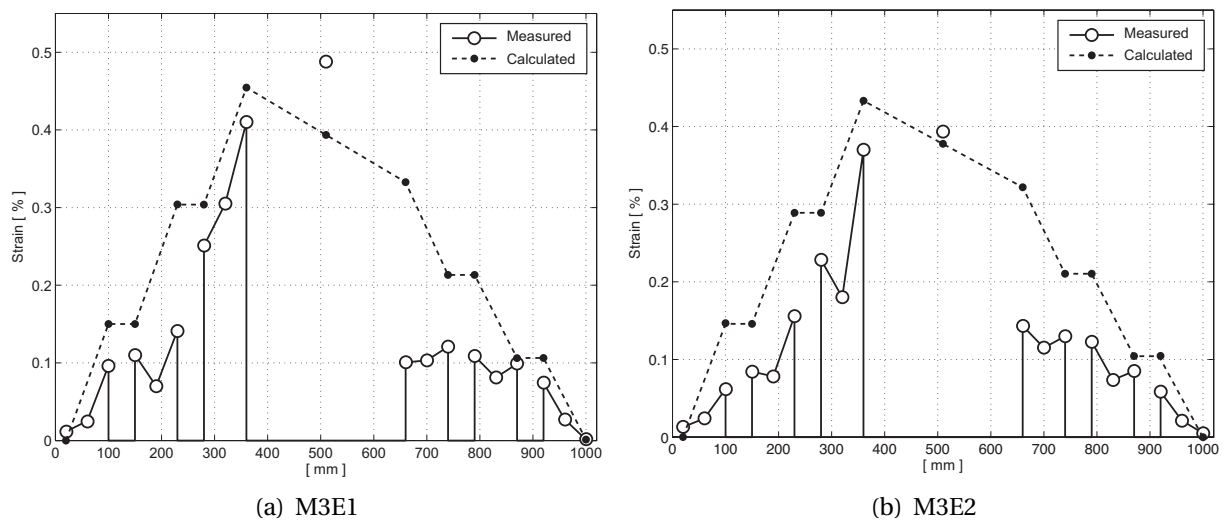


Figure G.48: Moment mode, triple rip, end support

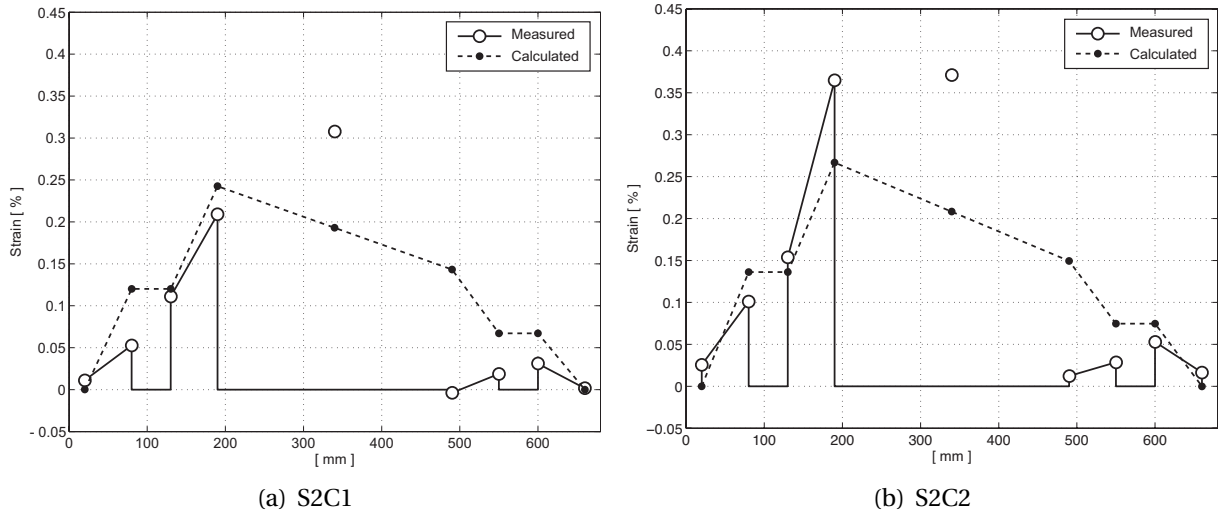


Figure G.49: Shear mode, double-rip, cantilevered support

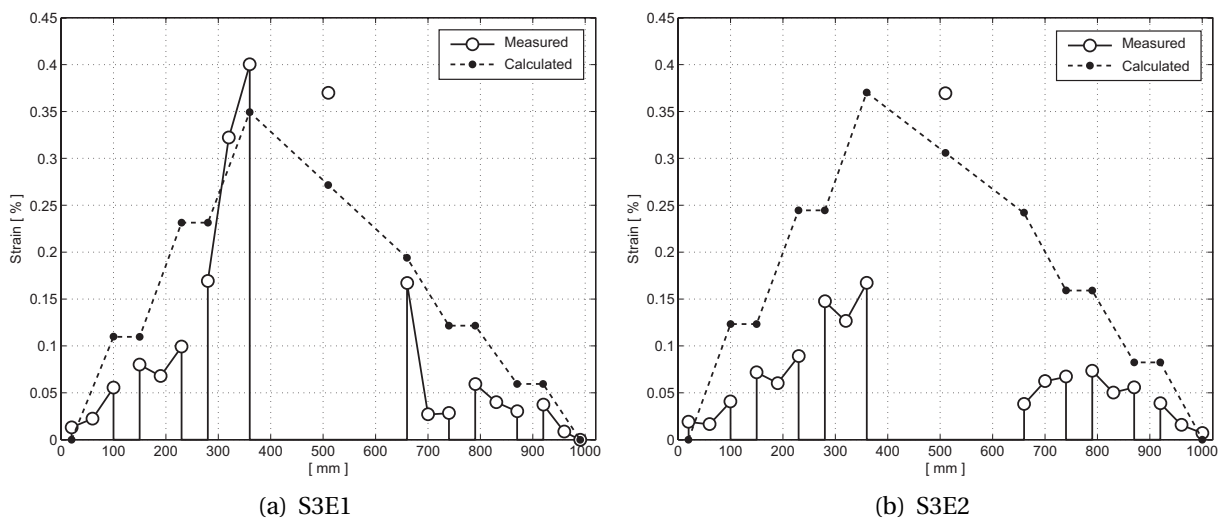


Figure G.50: Shear mode, triple rip, end support

G.9. Measured strain on the tension element's lateral sides

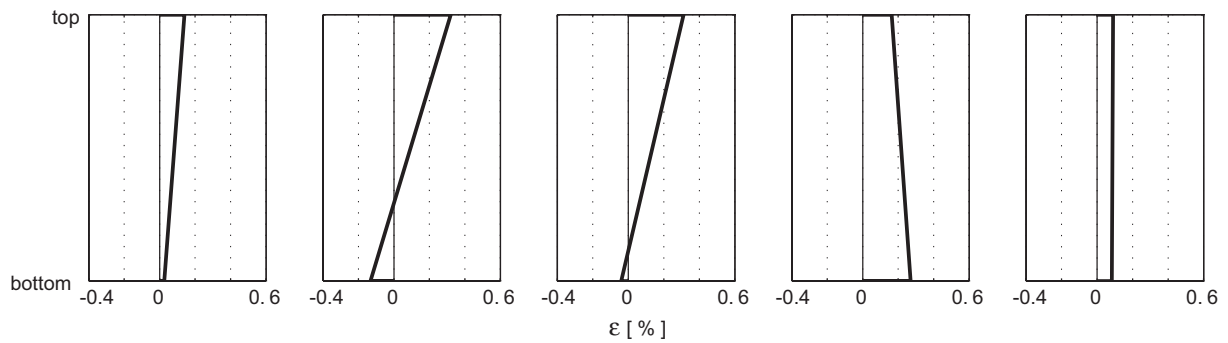


Figure G.51: Strain on tension element's lateral side – M2E1

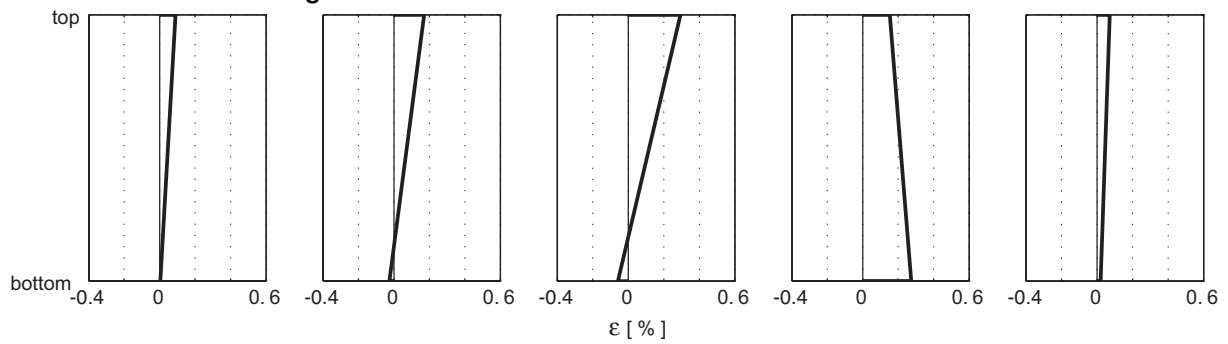


Figure G.52: Strain on tension element's lateral side – M2E2

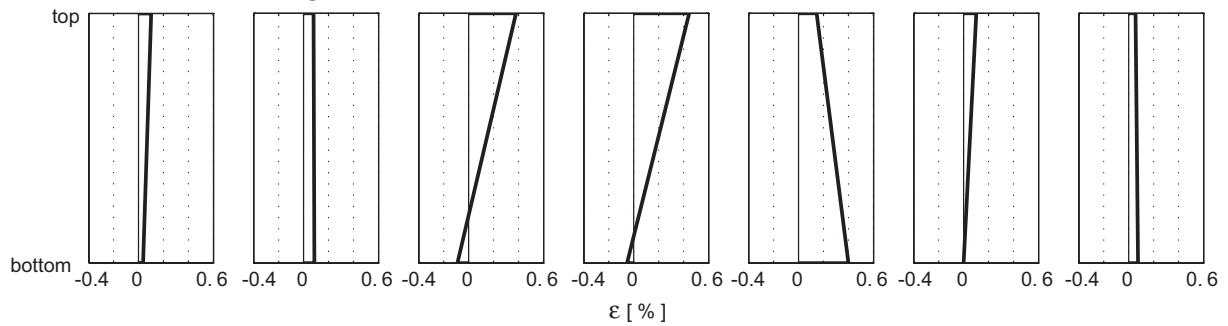


Figure G.53: Strain on tension element's lateral side – M3E1

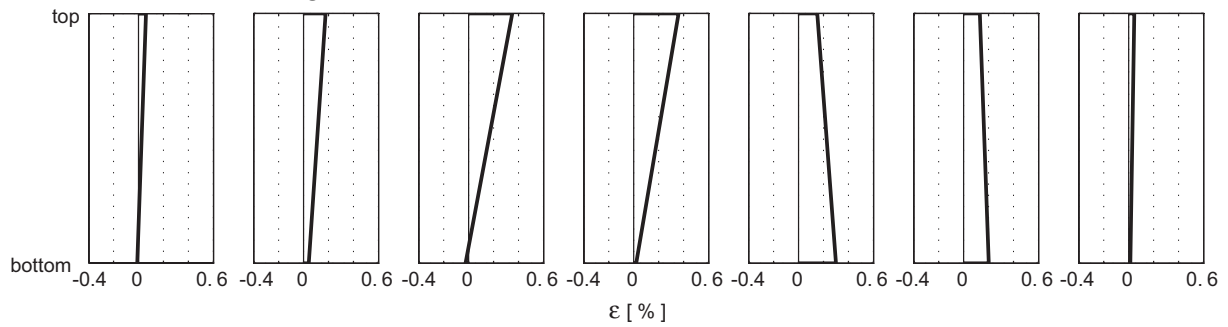


Figure G.54: Strain on tension element's lateral side – M3E2

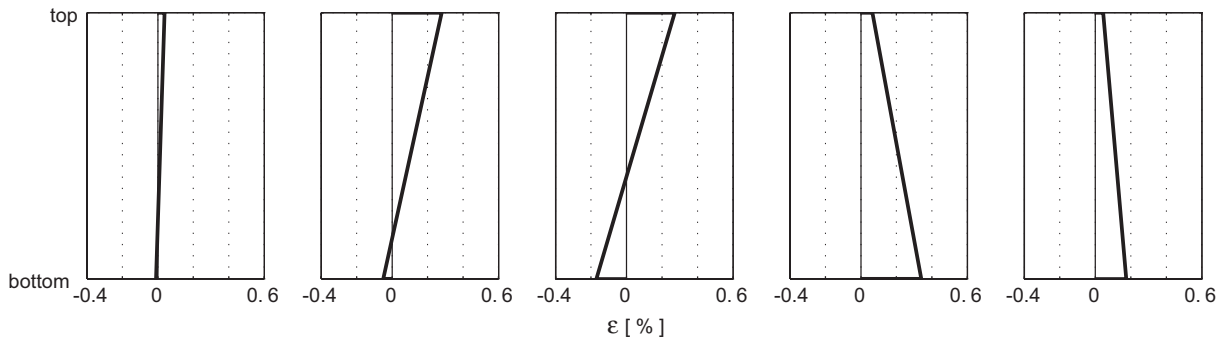


Figure G.55: Strain on tension element's lateral side – S2C1

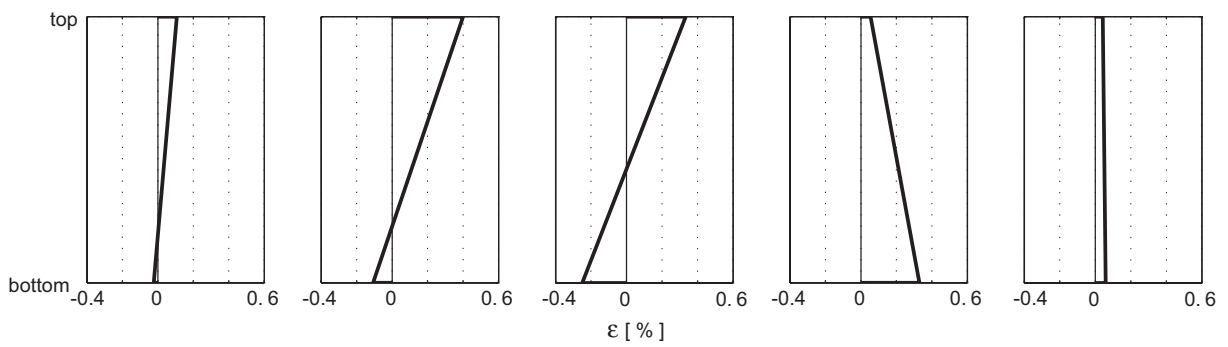


Figure G.56: Strain on tension element's lateral side – S2C2

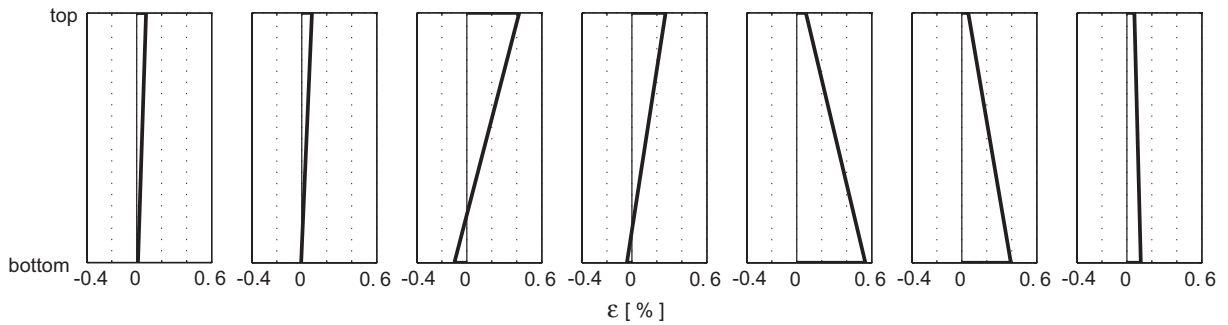


Figure G.57: Strain on tension element's lateral side – S3E1

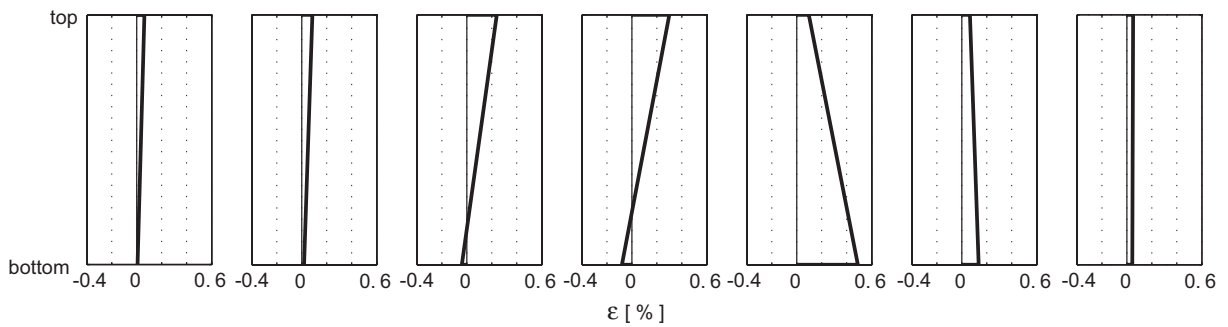


Figure G.58: Strain on tension element's lateral side – S3E2

G.10. Angle of principal stress at the tension elements middle section

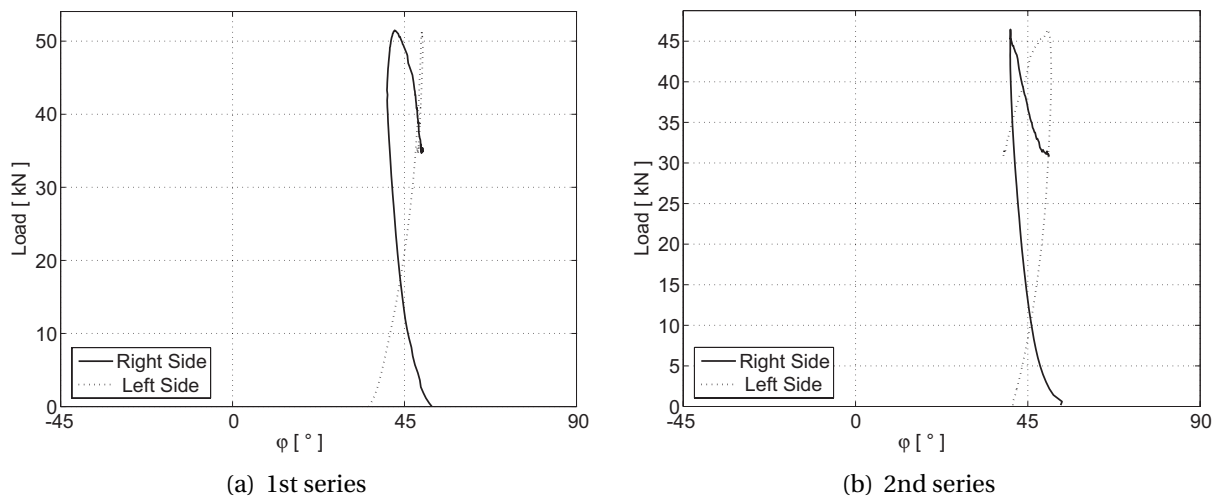


Figure G.59: M2E

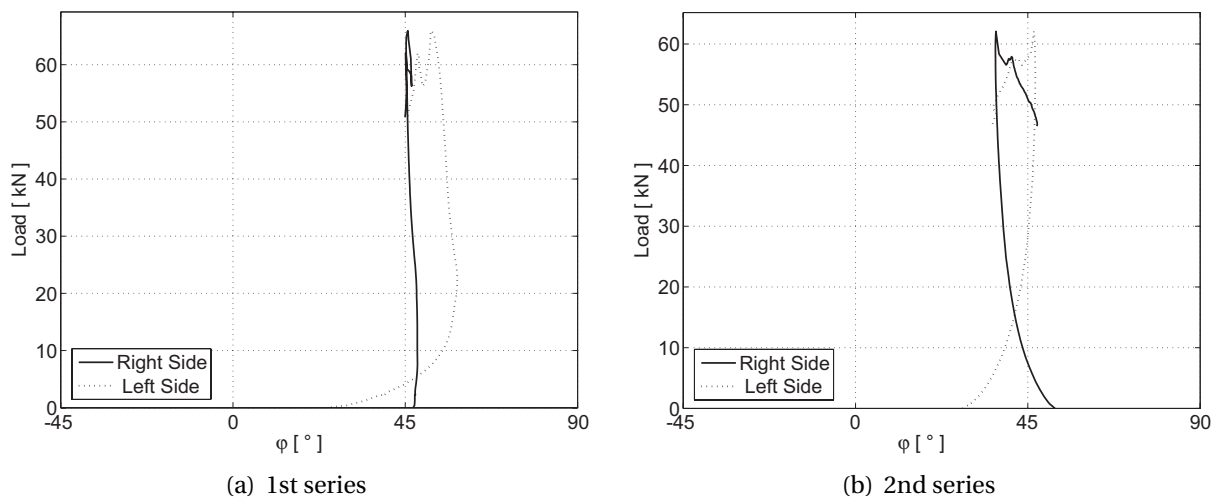


Figure G.60: M3E

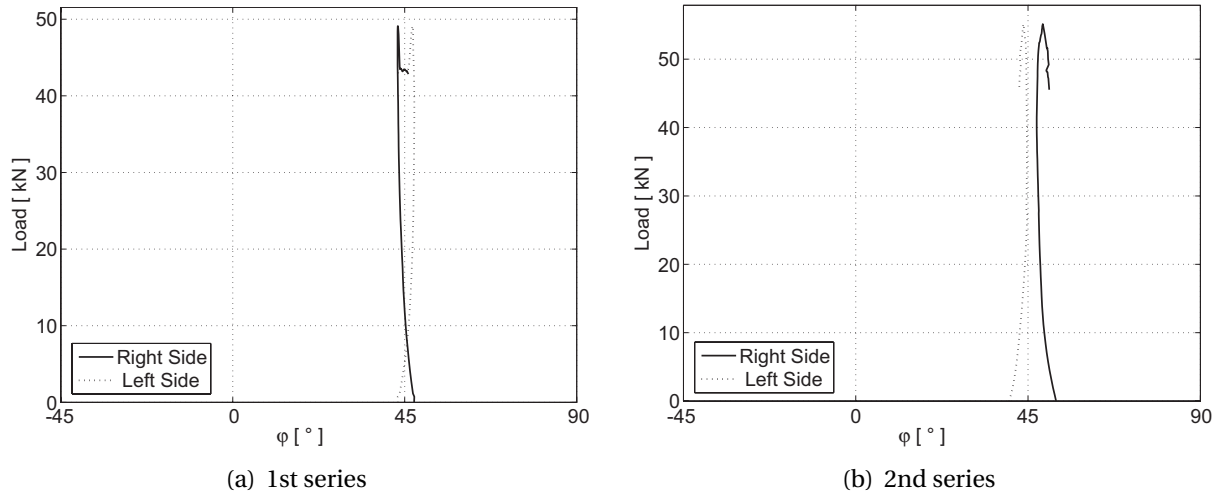


Figure G.61: S2C

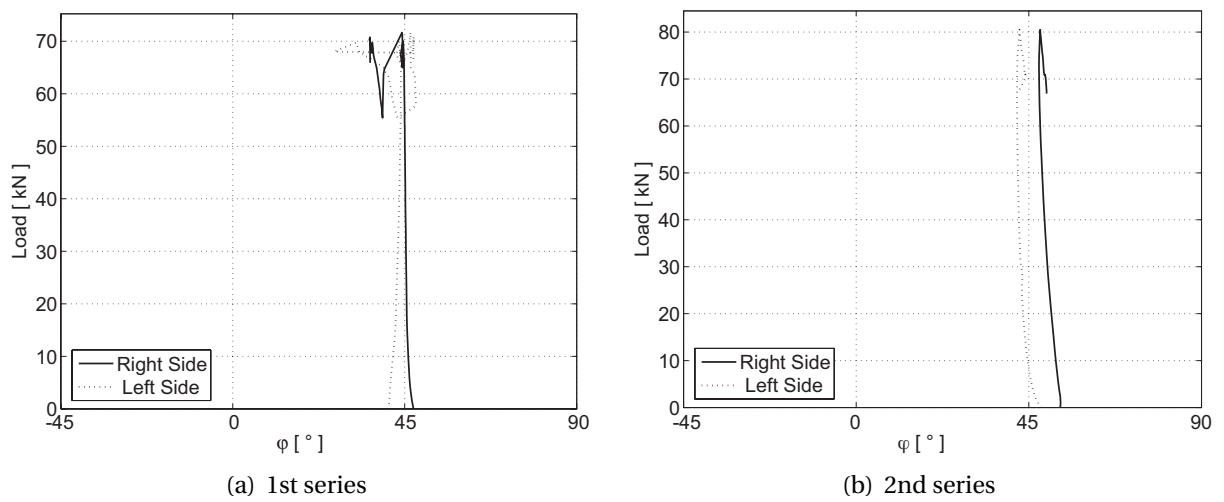


Figure G.62: S3E